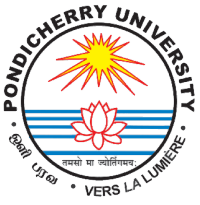
Chemodynamic studies of the Galaxy

A thesis
submitted for the degree of

Doctor of Philosophy

in

The Department of Physics,
Pondicherry University,
Puducherry - 605 014, India



by

Deepak
Indian Institute of Astrophysics,
Bangalore - 560 034, India



April 2022

Chemodynamic studies of the Galaxy

Deepak
Indian Institute of Astrophysics

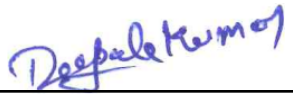


Indian Institute of Astrophysics
Bangalore - 560 034, India

Title of the thesis	:	**Chemodynamic studies of the Galaxy**
Name of the author	:	**Deepak**
Address	:	Indian Institute of Astrophysics II Block, Koramangala Bangalore - 560 034, India
Email	:	deepak@iiap.res.in deepak4astro@gmail.com
Name of the supervisor	:	**Prof. Bacham E. Reddy**
Address	:	Indian Institute of Astrophysics II Block, Koramangala Bangalore - 560 034, India
Email	:	ereddy@iiap.res.in

Declaration of Authorship

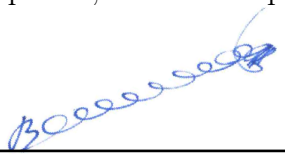
I hereby declare that the matter contained in this thesis is the result of the investigations carried out by me at the Indian Institute of Astrophysics, Bangalore, under the supervision of Prof. Bacham E. Reddy. This work has not been submitted for the award of any other degree, diploma, associateship, fellowship, etc. of any other university or institute.

Signed: 

Date: **May 13, 2022**

Certificate

This is to certify that the thesis entitled **'Chemodynamic studies of the Galaxy'** submitted to the Pondicherry University by Mr. Deepak for the award of the degree of Doctor of Philosophy, is based on the results of the investigations carried out by him under my supervision and guidance, at the Indian Institute of Astrophysics. This thesis has not been submitted for the award of any other degree, diploma, associateship, fellowship, etc., of any other university or institute.

Signed: 

Date: **May 13, 2022**

List of Publications

Refereed Publications

1. *Radial Velocity Comparison of Gaia DR2 and RAVE DR5 Survey: A Systematic Offset in Radial Velocities among a Group of Highly Accurate Radial Velocity Stars,*

   Deepak & Reddy, B. E. 2018, AJ, Volume 156, Issue 4, article id. 170, 6 pp.

   (*Chapter 2, Section 2.3*)

2. *Study of Lithium-rich giants with the GALAH spectroscopic survey,*

   Deepak & Reddy, B. E., 2019, MNRAS, Volume 484, Issue 2, p.2000-2008.

   (*Chapter 4*)

3. *Abundance analyses of Li-enriched and normal giants in the GALAH survey,*

   Deepak; Lambert, D. L. & Reddy, B. E., 2020, MNRAS, Volume 494, Issue 1, pp.1348-1365.

   (*Chapter 5*)

4. *Lithium abundances and asteroseismology of red giants: understanding the evolution of lithium in giants based on asteroseismic parameters,*

   Deepak & Lambert, D. L., 2021, MNRAS, Volume 505, Issue 1, pp.642-648.

   (*Chapter 6*)

5. *Lithium in red giants: the roles of the He-core flash and the luminosity bump,*

   Deepak & Lambert, D. L., 2021, MNRAS, Volume 5.7, Issue 1, pp. 204-225.

   (*Chapter 7*)

Publications in Conference Proceedings

6. *Lithium enrichment in the Galaxy: A study using the GALAH and Gaia surveys,*

   Deepak & Reddy, B. E., 2020, Proceedings of the International Astronomical Union, Volume 353, pp. 16-18.

   (*Chapter 3 and 8*)

7. *Lithium in the Galaxy: current status and contribution from the low-mass giants?*

   Deepak & Reddy, B. E., 2020, Memorie della Societa Astronomica Italiana, v.91, p.134-137.

   (*Chapter 3 and 8*)

Manuscript Under Preparation

8. *Stellar substructures in the Galactic halo: Properties and origin*

   Deepak et al. 2022, in preparation.

   (*Chapter 9*)

9. *Chemodynamic studies of the Galactic disc and halo*

   Deepak et al. 2022, in preparation.

   (*Chapter 10*)

Presentations

1. Poster presentation titled "Study of stellar populations in the disk of the Galaxy in the *Gaia* era" in the Galaxy Evolution and Dynamical Structures (GEDS2018) meeting, 22 - 25 January 2018, IUCAA, Pune, India.

2. An oral presentation titled "Archaeology of the Galaxy in the Era of Large Astrometric and Spectroscopic Surveys" in the International Conference on "Exploring the Universe: Near-Earth Space Science to Extragalactic Astronomy", 14 - 17 November 2018, S. N. Bose National Centre for Basic Sciences, Kolkata, India.

3. An oral presentation titled "The Galactic Halo: Stellar Populations and Formation History" in the 37^{th} Astronomical Society of India meeting, 18 - 22 February 2019, Christ (Deemed to be University), Bengaluru, India.

4. Poster presentation titled "Lithium enrichment in the Galaxy: A study of RGB stars using the GALAH and Gaia survey" in IAU Symposium 353, 30 June - 5 July 2019, Shanghai, China.

5. An oral presentation titled "Identifying emission-line objects and understanding the detection limits" in the 5^{th} Indo-French Astronomy School: Spectroscopy and Spectrographs, 16 - 24 August 2019, Inter-University Centre for Astronomy and Astrophysics (IUCAA), Pune, India.

6. An oral presentation titled "Lithium in the Galaxy: current status and contribution from the low-mass giants?" in Lithium in the Universe: to Be or Not to Be conference, 18 - 22 November 2019, Observatory of Rome, Monte Porzio Catone, Italy.

7. An oral presentation titled "Evolution of lithium in the Milky Way" in Chemical elements in the Universe: origin and evolution meeting, 16 - 19 December 2019, Indian Institute of Astrophysics (IIA), Bangalore, India.

8. Poster presentation titled "Evolution of lithium in the Milky Way" in 37^{th} Astronomical Society of India meeting, 13 - 17 February 2020, IISER, Tirupati, India.

9. An oral presentation titled “Galactic Chemical evolution in the era of the Gaia and large spectroscopic surveys: An overview on Lithium Abundance” in Gaia Symposium: DR2 and Beyond meeting, 2 - 6 November 2020, Indian Institute of Astrophysics (IIA), Bangalore, India.

Acknowledgements

First and foremost, in all honesty, I would like to thank and express my deepest regards and sincere gratitude to my thesis supervisor Professor Bacham Eswar Reddy, for his invaluable guidance, encouragement, and support throughout my Ph.D. tenure. His immense knowledge and expertise in the subject have helped me a lot during my Ph.D. There is always something new to learn from him.

I am grateful to Professor Emeritus David L. Lambert of the University of Texas at Austin and an Honorary Fellow of IIA Bangalore for his invaluable suggestions and time, which has helped me finish a significant fraction of the works covered in this thesis. I must admit that one of the most enjoyable things during my Ph.D. tenure was hunting for answers to his almost never-ending series of questions from him. His dedication to work is exceptional and inspiring. For example, in the mid of 2021, when we received a review report for one of our manuscripts, he had to visit a close family member admitted to a hospital (about 100 km away from his home) almost daily. To my surprise, even in this situation also, he carried some relevant journal articles to the hospital to offer his suggestions for the reviewer's comments. His unbiased comments and suggestions on any issue are also something to learn. In conclusion, I believe he is one of the best role models one can get. It has always been a pleasure to interact and work with him.

I sincerely thank my doctoral committee members, Prof. Gajendra Pandey (IIA) and Prof. Suraj Kumar Sinha (Pondicherry University), for their helpful comments and suggestions, which have led to an overall improvement of this thesis.

I thank IIA and the Department of Science and Technology (DST), Government of India, for all the financial support during my tenure at IIA. I am thankful to IIA for providing an excellent academic environment and facilities to carry out my research works. I want to thank Anish Parwage (Engineer, IIA Banglore)

and S. Fayaz (System Administrator, IIA Banglore) for all their help with the Delphinus and Fornax server at IIA Bengaluru, which I have used extensively for works covered in this thesis. I would also like to thank the staff at IIA Bengaluru for their timely helps throughout my Ph.D. tenure.

I also take this opportunity to thank the International Astronomical Union (IAU) for providing a travel grant to particulate in IAU Symposium 353: Galactic Dynamics in the Era of Large Surveys, held in Shanghai, China from 30^{th} June to 5^{th} July 2019. I also thank the European Cooperation in Science (e-COST) for the e-COST travel grant to attend COST Action Meeting CA16117 titled "Lithium in the Universe: to Be or Not to Be?" held at the Observatory of Rome, Monte Porzio Catone, Italy, from 18^{th} - 22^{nd} November 2019.

I also thank all my friends and colleagues at IIA for their consistent assistance and encouragement. They have definitely made my IIA stay memorable.

I also take this opportunity to thank my teachers and my family members for always encouraging and empowering me.

Last yet not least, I thank my parents, Late Smt. Neha Choudhary and Late Shri. Balwan Singh, whom I think I never thanked enough. With joy, I recognize their unconditional love and support. No amount of words will be enough to honour their sacrifices in my entire journey to date and ahead. I will always be in debt to them. I, once again, thank them and express my sincere gratitude for everything.

Data usage

The works covered in this thesis have made use of data from large spectroscopic and astrometric surveys from various ground and space-based telescopes. I thank all the institutions, funding agencies and team members of these surveys. Without the public release of data sets from these surveys, the works covered in this thesis would not have been possible. I am also very thankful to Bill Paxton (Kavli Institute for Theoretical Physics, University of California, Santa Barbara) and his colleagues for developing the *Modules for Experiments in Stellar Astrophysics* (`MESA`) suite of programs. A similar debt is due to Jo Bovy (Department of Astronomy and Astrophysics, University of Toronto, Toronto, Canada) for developing the `galpy`*: A Python Library for Galactic Dynamics* (Bovy 2015), and Ivan Ramírez (McDonald Observatory and Department of Astronomy, University of Texas at Austin, Austin, Texas, USA) and his colleague for developing *qoyllur-quipu* ($\mathtt{q}^2$) code for stellar parameters estimations (Ramírez *et al.* 2014).

The works in this thesis have made use of data from the European Space Agency (ESA) mission *Gaia* (`https://www.cosmos.esa.int/gaia`), processed by the *Gaia* Data Processing and Analysis Consortium (DPAC, `https://www.cosmos.esa.int/web/gaia/dpac/consortium`). Funding for the DPAC has been provided by national institutions, in particular, the institutions participating in the *Gaia* Multilateral Agreement.

The works in this thesis have also made use of data from the GALAH survey. The data for the GALAH survey are acquired through the Australian Astronomical Observatory, under programs: A/2013B/13 (The GALAH pilot survey); A/2014A/25, A/2015A/19, A2017A/18 (The GALAH survey phase 1); A2018A/18 (Open clusters with HERMES); A2019A/1 (Hierarchical star formation in Ori OB1); A2019A/15 (The GALAH survey phase 2); A/2015B/19, A/2016A/22, A/2016B/10, A/2017B/16, A/2018B/15 (The HERMES-TESS program); and A/2015A/3, A/2015B/1, A/2015B/19,

A/2016A/22, A/2016B/12, A/2017A/14 (The HERMES K2-follow-up program). We acknowledge the traditional owners of the land on which the AAT stands, the Gamilaraay people, and pay our respects to elders past and present. This study includes data that has been provided by AAO Data Central (`https://datacentral.org.au/`).

The works in this thesis have also used data from the LAMOST survey. The data for the LAMOST survey is acquired through the Guoshoujing Telescope. Guoshoujing Telescope (the Large Sky Area Multi-Object Fiber Spectroscopic Telescope; LAMOST) is a major national scientific project built by the Chinese Academy of Sciences. Funding for the project has been provided by the National Development and Reform Commission. LAMOST is operated and managed by the National Astronomical Observatories, Chinese Academy of Sciences.

The works in this thesis have also made use of RAVE data. Funding for RAVE has been provided by: the Australian Astronomical Observatory; the Leibniz-Institut fuer Astrophysik Potsdam (AIP); the Australian National University; the Australian Research Council; the French National Research Agency; the German Research Foundation (SPP 1177 and SFB 881); the European Research Council (ERC-StG 240271 Galactica); the Istituto Nazionale di Astrofisica at Padova; The Johns Hopkins University; the National Science Foundation of the USA (AST-0908326); the W. M. Keck Foundation; the Macquarie University; the Netherlands Research School for Astronomy; the Natural Sciences and Engineering Research Council of Canada; the Slovenian Research Agency; the Swiss National Science Foundation; the Science & Technology Facilities Council of the UK; Opticon; Strasbourg Observatory; and the Universities of Groningen, Heidelberg and Sydney. Based on data products from observations made with ESO Telescopes at the La Silla Paranal Observatory under programme ID 188.B-3002.

The works in this thesis have also made use of the Simbad database (Wenger *et al.*

2000), operated at the Centre de Données Astronomiques de Strasbourg (CDS; Genova *et al.* 2000), France, and available at `http://cdsweb.u-strasbg.fr`. The works in this thesis have also made use of NASA's Astrophysics Data System (ADS), available at `https://ui.adsabs.harvard.edu`.

Dedicated to my parents:

Late Smt. Neha Choudhary

and

Late Shri. Balwan Singh

Abstract

Based on data from large spectroscopic surveys like the GALactic Archaeology with HERMES (GALAH) and the Large Sky Area Multi-Object Fibre Spectroscopic Telescope (LAMOST), along with astrometric and photometric data from the $Gaia$ survey, we have addressed three major questions in the field of the chemical and dynamical evolution of the Galaxy. The first of these three questions is understanding the evolution of lithium (Li) in the Galaxy. For this, we used the spectroscopic data from the GALAH survey along with astrometric and photometric data from the $Gaia$ survey. We found that Li has significantly increased in the Galactic disc compared to the observed value in the metal-poor halo stars and the theoretically predicted primordial value from the Standard Big Bang Nucleosynthesis models. Search for an explanation for such large-scale Li enrichment throughout the Galactic disc led us to study the evolution of Li in low-mass stars (the second problem we have addressed). According to the standard evolutionary models, Li gets depleted as stars ascend on the red-giant branch (RGB). However, about a per cent of giants have been found to have a thousandfold higher Li than the value predicted by standard models. These rare giants with high Li, well known as the Li-rich giants, have puzzled astronomers for over four decades since their first discovery by Wallerstein and Sneden (1982).

To understand the evolution of Li in low-mass stars, we used data from the GALAH and $Gaia$ surveys. From the second data release of the GALAH survey, we discovered 335 new Li-rich giants (with A(Li) $\geq$ 1.8 dex), of which 20 are super Li-rich with A(Li) $\geq$ 3.2 dex. We further discovered that almost all of these Li-rich giants are core He-burning (CHeB) giant stars, and Li enrichment in red giants is likely associated with the He-core flash. We also found that the Li-rich giants do not belong to any particular dynamic group in the Galaxy and are found throughout the Galaxy. However, they are more prevalent among giants of the Galactic thin disc than the thick disc and

halo. We further found that chemically Li-rich and normal giants are similar except for Li abundance. We also found that the probability of becoming a Li-rich giant is approximately independent of a star's mass, although the majority of the Li-rich giants are found to be low mass ($M \leq 2$ M$_\odot$). The frequency of occurrence of Li-enriched giants among normal giants is about one per cent and slightly dependent on metallicity. Li-enriched and normal giants are also found to have a similar projected rotational velocity, suggesting that Li-enrichment in giants is not linked to scenarios such as mergers and tidal interaction between binary stars. To find more clues about the origin of Li enrichment in giants, we studied the correlation between giants' Li abundance and asteroseismic parameters. Data for the CHeB giants suggest a decrease in A(Li) with an increase in the gravity mode period spacing $\Delta\Pi_1$, which is known to increase with time at the start of the CHeB phase suggesting the enriched Li in He-core burning giants decreases as stars evolve. Based on asteroseismic data also, we found no evidence of Li enrichment at the luminosity bump. In conclusion, these studies have helped to uncover the almost four-decade-old mystery of the origin of Li-rich giant stars, and now we know that all the low-mass giants experience Li enrichment during the CHeB phase to a varying degree.

Lastly, to uncover the formation and evolution history of the Galaxy, we studied the chemical and kinematic properties of various pro-grade (like the Splash) and retrograde (like Gaia-Enceladus/Sausage (GE/S), Thamnos and Sequoia) substructures in the Galactic halo along with the Galactic thin and thick disc. We also studied the age distributions of all these Galactic components. We found that the star formation in the Splash, which is the major $in\ situ$ component of the halo and has a median [Fe/H] of -0.75 ± 0.24 dex, peaked about 13 Gyr ago. On the other hand, the star formation in the GE/S, which is the halo's largest accreted component and has a median [Fe/H] of -1.31 ± 0.23 dex, peaked about 1.5 Gyr later than the Splash. The Galactic thin and thick discs are found to have peak ages of about 5.0 and 11.5 Gyr, respectively. The GE/S and Sequoia are also found to have a distinct chemical evolution from the Splash, whose chemical composition is found to be similar to the metal-poor stars

of the thick disc. In conclusion, our studies support the idea of galaxy formation by hierarchical clustering in a Lambda cold dark matter universe.

Contents

Abstract **i**

List of Figures **xi**

List of Tables **xxv**

Abbreviations **xxvii**

Glossary of Symbols **xxix**

1 Introduction **1**

1.1 The Milky Way system 1
1.2 Chemodynamic studies of the Galaxy 4
1.3 Chemical and kinematic populations of stars in the MW 5
1.3.1 The Bulge 7
1.3.2 The Thin disc and the thick disc 8
1.3.3 The Halo 9
1.4 Formation of the Galaxy: An overview of different formation models 10
1.4.1 Top-down model: 13
1.4.2 Bottom-up model 15
1.4.3 ΛCDM model 16
1.5 Stars, their evolution and contribution towards the chemical evolution of the Galaxy 18
1.5.1 Evolution of stars of different mass range 19
1.5.2 Stars' role in the chemical evolution of galaxies 24
1.6 Lithium: A trace element from the BBN to the Galaxy and stars . . 25
1.6.1 Primordial Lithium 25
1.6.2 Stellar evolution of Li 26
1.6.3 Galactic evolution of Li 27
1.7 Scope of the Thesis 28
1.8 Plan of the Thesis 29
1.9 Resource summary 33

2 Data samples and methodology 35
2.1 Data samples . . . 36
2.1.1 Astrometric data . . . 36
2.1.2 Spectroscopic data . . . 38
2.2 Methodology . . . 42
2.2.1 Stars' galactic space velocities . . . 43
2.2.2 Stars' kinematic membership probabilities . . . 47
2.2.3 Orbital properties of stars . . . 48
2.2.4 Stellar ages and mass . . . 49
2.2.5 Stellar evolutionary models . . . 51
2.3 Radial Velocity Comparison of *Gaia* DR2 and RAVE DR5 Survey: A Systematic Offset in Radial Velocities among a Group of Highly Accurate Radial Velocity Stars . . . 51
2.3.1 Data Sample . . . 52
2.3.2 Analysis . . . 53
2.3.3 Discussion . . . 58
2.3.4 Conclusion . . . 62
2.4 Resource summary . . . 62

3 Evolution of Lithium in the Galaxy 65
3.1 Introduction . . . 65
3.2 Data sample . . . 66
3.2.1 Li abundances of sample stars . . . 68
3.3 Results and discussion . . . 69
3.3.1 Sample in the form of the Toomre diagram . . . 69
3.3.2 Li versus rotational velocity . . . 71
3.3.3 Li versus [Fe/H] . . . 72
3.3.4 Lower Li at super-solar metallicity . . . 74
3.4 Concluding remarks . . . 75

4 Evolution of Lithium in stars: the origin of Li-rich red giant stars 79
4.1 Introduction . . . 79
4.2 Stellar Sample . . . 82
4.3 Analysis . . . 83
4.3.1 Sample stars in L - $T_{\rm eff}$ plane . . . 83
4.3.2 Li abundances of sample stars . . . 84
4.4 Results . . . 85
4.4.1 Li-rich giants on RGB . . . 85
4.4.2 Stellar Evolutionary Phase of Li-rich Giants . . . 87
4.4.3 Li-rich Giants in the Galaxy . . . 89
4.5 Discussion . . . 90
4.5.1 External versus in-situ Li enrichment . . . 91
4.5.2 In-situ nucleosynthesis at luminosity bump versus He-flash . 97

4.6 Conclusion 100

5 Properties of Li-enriched and normal giants in the GALAH survey: mass, metallicity, stellar rotation and chemical composition 103
5.1 Introduction 103
5.2 Data sample 105
5.2.1 Samples by Luminosity 107
5.3 Analysis 108
5.4 Lithium and other stellar properties 119
5.4.1 Lithium and luminosity 119
5.4.2 Lithium and mass 121
5.4.3 Lithium and rotational velocity 124
5.4.4 Lithium and the Carbon Abundance 127
5.5 Creation of a Lithium enriched giant 135
5.5.1 Thoughts on the external reservoir 137
5.5.2 Thoughts on the internal reservoir 140
5.6 Concluding remarks 142

6 Li abundances and asteroseismology of red giants: understanding the evolution of lithium in giants based on asteroseismic parameters 145
6.1 Introduction 145
6.2 Data sample 147
6.3 Results 151
6.3.1 Asteroseismic mass for sample stars 151
6.3.2 Li as a function of stellar mass 152
6.3.3 Predicted evolution in the $\Delta\Pi_1 - \Delta\nu$ plane 154
6.3.4 Li as a function of $\Delta\nu$ and $\Delta\Pi_1$ in giants 158
6.4 Discussion and Conclusions 161

7 Lithium in red giants: the roles of the He-core flash and the luminosity bump 165
7.1 Introduction 165
7.2 Data sample 168
7.2.1 Elemental abundances 170
7.3 Lithium-rich giants: overview 172
7.3.1 He-core burning giants - the red clump 176
7.4 MESA modelling for low-mass stars 181
7.4.1 Predicted Li abundances to the RGB tip 181
7.4.2 MESA predictions for the red clump 199
7.5 Lithium enrichment at the luminosity bump? 201
7.6 Compositions of red clump giants 204
7.7 Concluding remarks 206

8 Contribution of low-mass stars towards the Galactic Li evolution 211
8.1 Introduction . . . 211
8.2 Evolution of Li in low-mass giant stars: an overview . . . 212
8.2.1 Li production in low-mass giants . . . 214
8.2.2 Contribution of low-mass giants towards the Galactic Li-enrichment . . . 215
8.3 Summary and future plan . . . 216

9 Study of stellar substructures in the Galactic halo based on the data from the LAMOST and *Gaia* surveys 217
9.1 Introduction . . . 217
9.2 Data sample . . . 220
9.3 The Galactic halo: An overview . . . 223
9.4 Stellar Substructures in the Galactic halo . . . 225
9.4.1 Hot disc sample: Stars with the Galactic disc-like properties but hotter kinematics in our halo sample . . . 227
9.4.2 Splash . . . 227
9.4.3 Helmi stream . . . 228
9.4.4 Gaia-Enceladus/Sausage . . . 230
9.4.5 Thamnos and Sequoia . . . 230
9.5 Low- and high-α disc stars in the HD sample . . . 230
9.6 Comparison of CMDs of the halo's components and importance of kinematic segregation of these components . . . 232
9.7 Metallicity, age, and kinematic properties of the halo's components 234
9.7.1 HD population . . . 238
9.7.2 Splash . . . 239
9.7.3 Gaia-Enceladus/Sausage (GE/S) . . . 241
9.7.4 Thamnos and Sequoia . . . 242
9.7.5 Helmi stream (H99) . . . 243
9.8 Discussion and concluding remarks . . . 243

10 Chemodynamic studies of the Galactic disc and halo 249
10.1 Introduction . . . 249
10.2 Data Sample . . . 250
10.2.1 Stellar sample of the Galactic halo and its substructures . . 253
10.2.2 Selection of the thin and thick disc stars . . . 255
10.3 Metallicity for the thin-disc, thick-disc and halo sub-structures . . . 256
10.4 Eccentricity functions for the thin disc, thick disc and halo sub-structures . . . 259
10.5 Stellar ages of the thin disc, thick disc and halo's sub-structures . . 260
10.6 Chemical compositions of the thin disc, thick disc, and components of the Galactic halo: Abundances of the α-process elements . . . 264

10.6.1 Insights into the formation of different Galactic components based on [α/Fe] trends 269
10.7 Lithium abundance across the components of the Galactic halo and disc 271
10.7.1 Li in the Galactic thin and thick disc 272
10.7.2 Li across the components of the Galactic halo 279
10.8 Summary 280

11 Conclusions, key results and future plan **281**
11.1 Thesis conclusions and key results 281
11.2 Future plan 289

Bibliography **291**

List of Figures

1.1 An optical view of the Milky Way from the Indian Astronomical Observatory located in Hanle, Ladakh, India. The Himalaya Chandra Telescope (HCT) is visible in the foreground. Image credit: Dorje Angchuk, IAO, Hanle, Ladakh, India. 2

1.2 Edge on view of the Milky Way in near-infrared from the Diffuse Infrared Background Experiment (DIRBE), Cosmic Background Explorer (COBE) mission. Image credit: E. L. Wright, DIRBE, the COBE Project, NASA. 3

1.3 A cartoon representation of the Galaxy showing its four major stellar components. 6

1.4 History of the Universe: From the Big Bang to present. Here, WIMPs refer to weakly interacting massive particles. (Image credit: NASA/CXC/M.Weiss) 11

1.5 Cartoon illustrations of the top-down and bottom-up models for the formation of a complex structures galaxy like the MW. Red arrows indicate the direction of contraction due to gravity, while circular grey arrows indicate the sense of rotation of the system (galaxy). . . 13

1.6 Cartoon illustration of the evolution of a Sun-like low-mass star from birth to He-core burning phase. Here, H is hydrogen, He is helium, C is carbon, and O is oxygen. 19

1.7 Cartoon illustration of the evolution of stars of different masses from birth to death. Objects like novas and supernovas, shown as circles with spikes, are known to alter the chemical composition of the universe through feedback as they shed their mass during explosions. With each life cycle, stars process the existing chemical elements and, in the end, enrich the universe with newly cooked heavy elements. 22

2.1 A cartoon illustration of stellar spectroscopy. Cases for continuous spectrum, absorption spectrum and emission line spectrum are shown. 38

2.2 Cartoon illustration showing the relationship between a star's space velocity and the astrometric parameters (like, parallax Π and proper motion μ) measured by the *Gaia* satellite. Here, V_r is the radial component of space velocity and is well known as the LoS radial velocity (RV), while V_T is the tangential component of space velocity. $V_T \approx 4.74\mu/\Pi$, where μ and Π are the star's proper motion and parallax in mas per year, respectively. A cartoon of the MW with its four major components is also shown in the background. NGP and SGP stand for the north and south galactic poles, respectively. 43

2.3 Cartoon illustration showing the U, V, W components of a star's Galactic space velocity with respect to the centre of the solar system. Components of the Sun's velocity with respect to the local standard of rest (LSR) are also shown. A cartoon of the MW with its four major components is shown in the background. 44

2.4 Distribution of $\mathrm{RV_{RAVE}}$ and $\mathrm{RV_{Gaia}}$ velocities for RAVE DR5 and Gaia DR2 cross-matched data with (a) no error limit, (b) $\mathrm{SD(RV_{RAVE})} \leq 2$ km s^{-1}, $\mathrm{MAD(RV_{RAVE})} \leq 2$ km s^{-1}, (c) $\mathrm{SD(RV_{RAVE})} \leq 2$ km s^{-1}, $\mathrm{MAD(RV_{RAVE})} \leq 2$ km s^{-1}, and cross-correlation error (σ_{RV}) ≤ 2 km s^{-1} or 2% in $\mathrm{RV_{Gaia}}$ and $\mathrm{RV_{RAVE}}$. (d) A section of the normalized histogram of difference in $\mathrm{RV_{Gaia}}$ and $\mathrm{RV_{RAVE}}$. The histogram is normalized with respect to the maximum count, and the bin size used is 2 km s^{-1}. 54

2.5 Normalized distribution and corresponding normal distribution fit of difference in velocities for Group-01 and Group-02 stars. Histogram bin size for Group-01 and Group-02 are 0.2 km s^{-1} and 2 km s^{-1} respectively, and are in agreement with Freedman-Diaconis rule. 55

2.6 (a) Distribution of the difference between $V_{\mathrm{j,Gaia}}$ and $V_{\mathrm{j,APASS}}$ for all the Gaia DR2 and RAVE DR5 cross-matched stars for which both $V_{\mathrm{j,Gaia}}$ and $V_{\mathrm{j,APASS}}$ are available (441,106 stars), and corresponding normal distribution fit. (b) Distribution of $V_{\mathrm{j,APASS}}$ and $V_{\mathrm{j,Gaia}}$ for stars belonging to Group-02 (red) and Group-03 (blue). Here, $V_{\mathrm{j,Gaia}}$ is calculated from Gaia's G-band magnitudes and $V_{\mathrm{j,APASS}}$ is provided in RAVE DR5. 56

2.7 Distribution of difference in position coordinates of Group-02 stars from Gaia DR2 and RAVE DR5 catalog when corresponding proper motions (pm) from Gaia DR2 along (a) right ascension (RA), and (b) declination (DEC) are used as weights. Distribution of difference in position coordinates of Group-03 stars from Gaia DR2 and RAVE DR5 catalog when corresponding proper motions (pm) from Gaia DR2 along (c) right ascension (RA), and (d) declination (DEC) are used as weights. 57

2.8 (a) Toomre diagram for stars in Group-02 with kinematics deduced using RV_{Gaia} (black) and RV_{RAVE} (magenta). The two concentric circles delineate constant peculiar velocities (V_{tot} = (U^2_{LSR} + V^2_{LSR} + W^2_{LSR})$^{1/2}$) of 80 km s^{-1} and 200 km s^{-1}, and represent kinematic boundary for thin disc ($|V_{tot}| < 80$ km s^{-1}), thick disc (80 $< |V_{tot}| <$ 200 (km s^{-1})) and halo ($|V_{tot}| >$ 200 (km s^{-1})) which are in accordance with results in Reddy *et al.* (2006). (b) Distribution of [α/Fe] with respect to [Fe/H] of Group-02 stars (red) with Group-01 in background (blue). Measurements of [α/Fe] are given in RAVE DR5, and out of 272 stars of Group-02, both [α/Fe] and [Fe/H] are available for 227 stars which are plotted here. 59
2.9 (a) Sky distribution, and (b) Color-Luminosity diagram for stars in our sample. Here green, red and blue color represent Group-01, Group-02 and Group-03 stars respectively. 61
2.10 Flow chart showing methodology and data flow for conducting chemodynamic studies of the Galaxy. 63

3.1 Sample stars in the HR diagram. 68
3.2 Distribution of the selected sample of dwarfs in the form of the Toomre diagram. Stars' Li abundance, A(Li), is encoded in the colour of the data point as per the colour bar given on the right side. The green-coloured circular arc, with V_{total} = 80 kms^{-1}, represents the approximate boundaries between the Galactic thin and thick disc, where stars on the inner side of the circle are thin-disc stars while the stars on the outside are thick disc stars. Similarly, the blue-coloured circular arc, with V_{total} = 200 kms^{-1}, represents the approximate boundaries between the Galactic thick disc and halo, where stars on the outer side of the circle are halo stars while stars between the green circle and blue circle are the thick disc stars. . . 70
3.3 Li versus galactic rotational velocity V_{LSR} for selected sample of dwarfs. The solid red line at A(Li) = 2.72 dex mark the theoretically predicted primordial Li abundances from the standard BBN models. 71
3.4 Li versus [Fe/H] distribution for the selected sample of low-mass dwarfs. The solid red line marks the theoretically predicted primordial Li abundances from the standard BBN models. 72
3.5 Li abundance as a function of temperature T_{eff} for the selected sample of dwarfs sampled in different metallicity ranges. 75

4.1 Sample stars in the HR diagram. 84
4.2 Lithium abundance versus metallicity of RGB sample stars. 86
4.3 The HR diagram and log(L/L$_\odot$) vs A(Li) distribution for our selected RGB sample stars from the GALAH DR2 and the *Gaia* DR2 survey with mass $M \leq 2M_\odot$. In the left-hand side panel, we have also shown the approximate positions of the RGB bump (red rectangle) and the RGB clump (black rectangle). 87

4.4 Distribution of selected RGB sample in A(Li) vs V_{LSR} plane and in the form of Toomre Diagram. In Figure 4.4b, we have plotted the approximate boundaries separating thin and think disc (V_{Total}=80 km s^{-1}, continuous red circle), and thick disc and halo (V_{Total}=200 km s^{-1}, dotted red circle). 89
4.5 The HR diagram showing Li-rich giants' positions a) prior to extinction correction, b) with the size of representative point proportional to extinction, and c) post extinction correction. 92
4.6 The HR diagram showing super Li-rich giants' positions a) prior to extinction correction, b) with size of representative point proportional to extinction, and c) post extinction correction. 96

5.1 HR diagram showing the location of Li-rich giants ($1.8 \leq A(\mathrm{Li}) \leq 3.2$ dex) (black dots) and super Li-rich giants ($A(\mathrm{Li}) > 3.2$ dex) (red dots), with the complete sample of giants in the background. The outlines of the two most prominent evolutionary regions – the red clump (RC) and the luminosity bump (LB) – are taken from Deepak & Reddy (2019). Some of the cooler giants within the RC luminosity range are not included here to avoid possible contamination between RC and LB. 104
5.2 Distribution of elemental abundances of Li-normal, rich and super-rich giants of red-clump (RC) sample. The yellow contours in each panel represent the density of Li normal giants and are provided to ease the visualisation of the positions of the Li-rich and super Li-rich giants with respect to the Li normal giants. 109
5.3 Lithium versus [Fe/H] for the GALAH sample across the four luminosity samples RC^+, RC, LB and LB^-. 118
5.4 Normalized frequency distribution for Li-enriched and normal giants along [Fe/H]-axis. 120
5.5 Normalized frequency distributions for Li-enriched and normal giants along mass-axis. 122
5.6 Normalized frequency distributions for Li-enriched and normal giants of RC^+, RC, LB and LB^- samples along mass-axis. 122
5.7 A(Li) versus the projected stellar rotational velocity ($V_{\mathrm{rot}}\sin i$) for our sample of giants from the GALAH survey. The projected rotational velocities are based on spectral line widths, which also consist of effects of macro- and micro-turbulence velocities; their combined effect on spectral width is not insignificant. 125
5.8 Normalized density distribution in projected stellar rotational velocity ($V_{\mathrm{rot}}\sin i$) for our sample of RC^+, RC, LB and LB^- normal giants. 125
5.9 [C/Fe]] versus [Fe/H] for Li-normal, rich and super-rich giants of RC^+, RC, LB and LB^- samples. 126

5.10 [C/Fe] versus [O/Fe] for Li-normal, rich and super-rich giants of RC^+, RC, LB and LB^- samples. 126
5.11 Abundances of C and N for known Li-enriched (including a few normal) giants in literature. For carbon, the RGB sample extracted from the GALAH survey is also plotted in the background. 130
5.12 $^{12}C/^{13}C$ versus Li abundances for known Li-enriched (along with a few normal) giants in the literature. 133
5.13 Distribution of [N/Fe] versus [Fe/H] for a sample of common giants among the GALAH and LAMOST surveys (sample RGB_{GL}). . . . 134
5.14 [C/Fe], [O/Fe], and [Na/Fe] versus [Fe/H] for common giants among GALAH and LAMOST. The left and right panels show the abundance from the GALAH and LAMOST surveys, respectively. . . . 135

6.1 The spectroscopic HR diagram for giants in the KRBS sample along with *Kepler* DR25 stars in the background. Here, RGB are inert He core stars with H-shell burning, and CHeB are core He-burning giants, while 'Unknown' are the ones with unclassified evolutionary phases. 147
6.2 A(Li) as a function of stellar mass estimated from the scaling relation (top panel) and from `PARAM` (bottom panel). Errors in mass estimates are shown as black error bars. Filled red and blue circles are core He-burning giants with Li detections and upper limits, respectively. Filled black and green squares are RGB giants with H-shell burning with Li detections and upper limits, respectively. . 153
6.3 Distribution for our sample stars in the $\Delta\Pi_1 - \Delta\nu$ plane. Used labels are the same as in Figure 6.2. 154
6.4 Evolutionary tracks for solar-metallicity model stars with masses 0.8 (blue line), 1.0 (red line) and 1.2 $M_\odot$ (black line) in $\Delta\Pi_1 - \Delta\nu$ plane. The RGB phase is shown in the top and middle panels, while the CHeB phase is shown in the bottom panel. Arrows indicate the global direction of the evolution of model stars. Open circles in the top panel indicate the position of the luminosity bump for each of the three masses. In the middle panel, the luminosity bump occurs at the obvious 'S-type' loop in the tracks. The initial He core flash at $\Delta\nu < 0.1$ μHz) is very strong. However, the actual peak value may be even higher and missed due to the finite step size. This and other early episodes of He core flash occur in a brief phase at a luminosity well above the RC. 155
6.5 Variation of $\Delta\nu$, $\Delta\Pi_1$, luminosity and $T_{\rm eff}$ as a function of time (in millions of years) during the CHeB phase for solar-metallicity model stars of masses 0.8, 1.0 and 1.2 $M_\odot$. A base-10 log scale is used for the time axis to highlight the fact that giants in the CHeB phase spend almost their entire life in a relatively stable state except for the brief He-flashing region at the start. 156

6.6 A(Li) as a function of $\Delta\nu$ for our sample stars. Used labels are the same as in Figure 6.2. 159
6.7 Li abundances in RGB and core-He-burning (CHeB) giants as a function of their gravity-mode period spacing ($\Delta\Pi_1$). Used labels are the same as in Figure 6.2. 160

7.1 Sample stars in a HR diagram also showing the selection of red giants (the RBS) within the green box. For all the stars, uncertainty in luminosity and temperature are also plotted in the background as red error bars. 170
7.2 HR diagram and A(Li) as a function of luminosity for the RBS giants with masses $M/\mathrm{M}_\odot = 1.10 \pm 0.02$ and metallicity [Fe/H] $= 0.00 \pm 0.10$ dex. The left and middle panels show giants with both Li detections and upper limits with light yellow colour, indicating a higher density of stars. In the right-most panel, giants with Li detections are shown in red, while giants with Li upper limits are in blue. 172
7.3 The HR diagram for the RBS giants. The colour in the left and right panels represents the linear density and maximum A(Li) abundances, respectively. Note that the density visualization scale in the left-side panel is linear, but in Figure 7.1 scale is logarithmic. . . . 172
7.4 HR diagrams for the RBS giants for Li abundances in different abundance intervals. All giants shown here have a Li detection (i.e., flag_Li_fe=0). 173
7.5 Li abundance maps along with metallicity and mass information in colour for the RBS giants in the HR diagram. All the giants shown here have Li detections (i.e., flag_Li_fe=0). 174
7.6 Top row: Metallicity and mass histograms for giants plotted in Figure 7.5. Histograms are shown for different Li abundance intervals, as shown in the keys in the two panels. Bottom row: Metallicity and mass histograms for entire RBS sample with $\log(L/\mathrm{L}_\odot) > 1.5$. 175
7.7 HR diagram (odd-numbered rows) and A(Li) as a function of luminosity (even-numbered rows) for the RBS stars selected with mass and metallicity range as mentioned in panels' titles. In luminosity-A(Li) panels, giants with Li detections are shown in red, while giants with Li upper limits are shown in blue. 182
7.8 HR diagrams and A(Li) as a function of luminosity for solar mass and solar metallicity models with different α_{ML} and α_{th}. The top and bottom panels show a model's sensitivity to α_{ML} and α_{th}, respectively. Dashed lines show pre-main-sequence evolution, while solid lines show the evolution from the zero-age main sequence (ZAMS). On each track, the LB's position is marked by the green coloured blob. 184

7.9 Temporal evolution of Li for solar mass and solar metallicity models with different $\alpha_{\rm ML}$ and $\alpha_{\rm th}$. Time is shown relative to the onset of LB. Model's sensitivity to both $\alpha_{\rm ML}$ and $\alpha_{\rm th}$ is shown. The left-hand side panel covers evolution from about the sub-giant phase to the CHeB phase, while the right-hand side panel covers evolution from near RGB on-wards. Evolution up to the RGB tip is shown as solid lines, while dashed lines show the evolution in the CHeB phase. On each track, the LB's position is marked by the green coloured blob. Timestep in each case varies from about 0.1 to 0.2 million years (Myr) during the LB, and further decreases as the star ascend the RGB. 184

7.10 Left-hand side panel: Predicted evolution of A(Li) as a function of luminosity for solar metallicity (Z = 0.0143) giants. Masses of 0.8 $M_\odot$ to 2.0 $M_\odot$ are shown, as labelled. Right-hand side panel: Predicted evolution of A(Li) as a function of luminosity for $1M_\odot$ mass models with metallicities Z = 0.0045, 0.0080, 0.0143, and 0.0254, which are equivalent to [Fe/H] = -0.50, -0.25, 0.00, and 0.25 dex, respectively. For all models, we use $\alpha_{\rm ML} = 1.85$, $\alpha_{\rm th} = 100$ and initial surface rotation $\Omega_{int}/\Omega_{crit} = 0$. For each of the case, evolution is shown from the ZAMS to the RGB tip. For all the masses, LBs are marked by green coloured blobs. The abrupt change in A(Li) occurring at about $\log(L/L_\odot) \sim 1.5$ is attributable to the onset of thermohaline mixing at the LB. 185

7.11 Observed and predicted HR diagram (top panel) and A(Li) as a function of luminosity (middle and bottom panels) for RBS giants of masses 1.10 ± 0.02 $M_\odot$ and metallicity 0.0 ± 0.1 dex. Predictions are shown for best fit model with $\alpha_{\rm ML} = 1.85$ along with $\alpha_{\rm th} =$ 50, 100, 150 and 200. The bottom panel shows luminosity-A(Li) trends after adjustment to Li abundance level. In A(Li)-luminosity panels, giants with Li detections are shown in red, while giants with Li upper limits are shown in blue. 186

7.12 Observed and predicted HR diagram (top panel and middle panel) and A(Li) as a function of luminosity (bottom panel) for RBS giants of masses 1.10 ± 0.02 $M_\odot$ and metallicity 0.0 ± 0.1 dex. Predictions are shown for the best-fit model with $\alpha_{\rm ML} = 1.85$ and $\alpha_{\rm th} = 100$ along with initial surface rotation $\Omega_{\rm int}/\Omega_{\rm crit} = 0.00$, 0.05, and 0.10, which are equivalent to an initial surface rotation of about 0, 15, and 30 $\rm kms^{-1}$, respectively. In A(Li)-luminosity panels, giants with Li detections are shown in red, while giants with Li upper limits are shown in blue. 187

7.13 Observed and predicted HR diagram (top panel) and A(Li) as a function of luminosity (middle and bottom panel) for RBS giants of masses 1.10 ± 0.02 $M_\odot$ and metallicity -0.50 ± 0.10 dex. Prediction are shown for best fit models with α_{ML} = 1.80 along with α_{th} = 50, 100, 150 and 200. In A(Li)-luminosity panels, giants with Li detections are shown in red, while giants with Li upper limits are shown in blue. 188

7.14 Observed and predicted HR diagram (top panel) and A(Li) as a function of luminosity (bottom panel) for RBS giants of masses 1.50 ± 0.02 $M_\odot$ and metallicity -0.25 ± 0.10 dex. Prediction are shown for best fit model with α_{ML} = 1.95 and α_{th} = 100, 200, 300 and 400. The bottom panel shows luminosity-A(Li) trends after adjustment to Li abundance level. In A(Li)-luminosity panels, giants with Li detections are shown in red, while giants with Li upper limits are shown in blue. 189

7.15 Left panel: HR diagram showing tracks for RGB phase for solar metallicity (Z = 0.0143) models of masses from 0.8 to 2.2 in steps of 0.2 $M_\odot$. Right panel: RGB tracks for solar mass models of metallicity Z = 0.0045, 0.0080, 0.0143, and 0.0254, which is equivalent to [Fe/H] = -0.50, -0.25, 0.00 and 0.25, respectively. Shown tracks are for models with α_{ML} = 1.85 and α_{th} = 100. The luminous end for each of the tracks marks the position of the RGB tip. Also, in each case, the green blob marks the position of LB. 199

7.16 Variation of luminosity, T_{eff} and A(Li) as a function of time (in million years) during the CHeB phase for solar-metallicity model stars of masses 0.8, 1.0 and 1.2 $M_\odot$ with α_{ML} = 1.85 and α_{th} = 100. For the time axis, a base-10 log scale is used to highlight the fact that CHeB giants spend almost their entire life in a relatively stable state except for the brief He-flashing region, which lasts for about 1-2 Myr from the He-core flash. In the CHeB phase, giants also experience additional Li depletion. This Li depletion starts at approximately about 5 Myr after the He-core flash for a solar mass and solar metallicity star. 204

8.1 Top panel: Li as a function of luminosity for the sample of low-mass giants from Deepak and Reddy (2019). Bottom panel: Li as a function of large frequency spacing $\Delta\nu$ for the sample of giants from Deepak and Lambert (2021a). In the bottom panel, errors in Li abundance and $\Delta\nu$ are shown using black-colored error bars corresponding to each of the stars. Also, Filled red and blue circles are core He-burning giants with Li detections and upper limits, respectively. Filled black and green squares are RGB giants with H-shell burning with Li detections and upper limits, respectively. . . 213

9.1 Color-magnitude diagram and metallicity function for the selected sample of halo stars. A bi-modal distribution is clearly visible in both CMD and metallicity function. 223
9.2 Energy-L_Z distribution for the kinetically selected halo stars. . . . 225
9.3 Kinetically selected sample of halo stars in E-L_Z plane. Stars' sky coordinates, radial distance from the Galactic center R, radial velocity V_R, ϕ, and circular velocity V_ϕ are shown in color in the top two panels. Stars' position coordinates (X, Y, Z) and space velocities (V_X, V_Y, V_Z) are shown in color in the bottom two panels. The dotted black line represents the quadratic equation $E = -2 \times 10^5 + 35 \times L_Z - 0.002 \times L_Z^2$ and separates the probable disc stars with large tangential velocity (i.e., stars with $E < -2 \times 10^5 + 35 \times L_Z - 0.002 \times L_Z^2$) from more certain halo stars (with $E > -2 \times 10^5 + 35 \times L_Z - 0.002 \times L_Z^2$). 226
9.4 Kinetically selected sample of halo stars in E-L_Z plane. The dotted black and red lines represent the quadratic equation $E = -2 \times 10^5 + 35 \times L_Z - 0.002 \times L_Z^2$ and ($E = -1.7 \times 10^5 + 35 \times L_Z - 0.002 \times L_Z^2$), respectively, and encloses the stars belong to the Splash. Selection of Splash's stars is further restricted to $L_Z > 0.4 \times 10^3$ kpc km s^{-1} to avoid contamination from retro-grade populations. Members of the Helmi stream (H99) are shown in cyan color. 228
9.5 Selection of Gaia-Enceladus/Sausage, Thamnos and sequoia. The whole sample of kinematically selected halo stars is shown in the background. GE/S stars are selected with $E \gtrsim -1.5 \times 10^5$ km s^{-2} and -600 $\leq L_Z \leq$ 400 kpc km s^{-1}. The dotted yellow line represents the quadratic equation $E < -2 \times 10^5 - 40 \times L_Z$. Stars below the dotted yellow line and with $-1.8 \times 10^5 < E < -1.5 \times 10^5$ km^2 s^{-2} and $-1700 < L_Z < -500$ kpc km s^{-1} are classified as Thamnos stars, while Sequoia's selection is restricted to stars with $-1.5 \times 10^5 < E < -0.9 \times 10^5$ km^2 s^{-2} and $-3300 < L_Z < -1900$ kpc km s^{-1}. 229
9.6 [α/Fe] versus [Fe/H] distribution for the hot-disc (HD) sample is shown in the top-left panel while the remaining panels show histograms for various spatial and kinematic properties of the HD's high- and low-α stars. Selection of the HD's high- and low-α samples is shown in the top-left panel, where the red horizontal line (with [α/Fe] = 0.1 dex) separates the high-α stars (with [α/Fe] > 0.1) from the low-α stars having [α/Fe] < 0.1. 231
9.7 Color-magnitude diagram for the halo sample along with all the identified components/substructures of the halo. 233
9.8 Metallicity and age histograms for all the substructures in the Galactic halo. Histograms for the low- and high-α populations in the HD samples are also shown. 235

9.9 Histograms of the orbital eccentricity and maximum vertical distance from the Galactic plane ($|Z|_{\rm max}$) for all the substructures in the Galactic halo. Histograms for the low- and high-α populations in the HD samples are also shown. 236
9.10 Orbital eccentricity as a function of metallicity for all the substructures in the Galactic halo. Distributions for the low- and high-α populations in the HD samples are also shown. 240

10.1 Top-left panel: The distribution of the GALAH DR3 stars in the form of the Toomre Diagram. Top-right panel: The Toomre diagram for the selected sample of halo stars from the GALAH survey (Halo$_G$). The selected samples of thin and thick disc stars from the GALAH survey are shown in the bottom left and right panels, respectively. 252
10.2 The left and right-hand panels show the Toomre diagram for the samples of halo stars from the LAMOST survey (Halo$_{\rm L}$) and the GALAH survey (Halo$_{\rm G}$). The sample Halo$_{\rm G}$ from the GALAH survey is about eight times smaller than the sample Halo$_{\rm L}$ from the LAMOST survey. The number of retrograde stars (i.e. the stars with $V_{\rm LSR}$ < -200 km s^{-1}) in the Halo$_{\rm G}$ sample is also relatively less than the Halo$_{\rm L}$ sample. 253
10.3 Top-left panel: The distribution of the GALAH DR3 stars in Energy-L_Z plane. Top-right panel: Energy-L_Z distribution for the kinetically selected sample of halo stars. Energy-L_Z distribution for the kinetically selected samples of thin and thick disc stars are shown in the bottom left and right panels, respectively. 254
10.4 The left and right-hand panels show the distribution in Energy-L_Z plane for the samples of halo stars from the LAMOST survey (Halo$_{\rm L}$) and the GALAH survey (Halo$_{\rm G}$). Compared to the Halo$_{\rm L}$ sample, the Halo$_{\rm G}$ has relatively fewer stars with retrograde orbits (i.e. stars with $L_Z < 0$). 255
10.5 Top-left and top-right hand panels show the normalized metallicity functions for the selected samples of the thin and thick disc stars, respectively. A single peak Gaussian fit to the metallicity distribution is also shown as the red dotted line for both thin and thick samples. The thin disc sample has a mean [Fe/H] of about -0.111 with a standard deviation (SD) of about 0.248. The thick disc sample has a slightly lower mean [Fe/H] of -0.396 with a SD of 0.294. The normalized metallicity function for the selected samples of halo stars from the LAMOST survey (Halo$_{\rm L}$) and GALAH survey (Halo$_{\rm G}$) is shown in the bottom-left panel. Metallicity functions with actual star count in the metallicity bins are shown in the bottom-right panel. 257

10.6 Metallicity functions for the samples of halo's sub-structures selected from the GALAH and LAMOST survey (shown in magenta and black, respectively). The letters 'L' and 'G' in the sample's subscripts indicate their parent survey name. 258
10.7 Orbital eccentricity functions for the thin and thick disc are shown in the top-left and top-right hand panels, respectively. The eccentricity function for the samples of halo's substructures selected from the GALAH and LAMOST surveys is shown in the bottom-left and bottom-right panels, respectively. The letters 'G' and 'L' in the subscript of the samples' names shown in the legends indicate the sample's parent survey. 259
10.8 Comparison of stellar ages determined in this study using $\mathtt{q}^2$ and ages provided along with the third data release of the GALAH survey. A single peak Gaussian fit, with mean ≈ -0.2569 Gyr and SD ≈ 0.9786 Gyr is also shown in red. 261
10.9 Age functions for the thin disc (top-left panel) and the thick disc (top-right panel). The bottom two rows show the age function for four major substructures in the selected samples of halo stars from the GALAH and LAMOST surveys shown in the filled magenta histogram and black histograms, respectively. The letter 'G' and 'L' in the subscript of the sample's name stands for GALAH and LAMOST survey and indicates the parent survey from which samples are withdrawn. 262
10.10 Abundance ratio [X/Fe] as a function of [Fe/H] for α-process elements O, Mg, Si, Ca and Ti provided in the GALAH DR3 survey for selected samples of the thin and thick disc along with five major substructures in the halo. All the stars shown here have measured abundances in the GALAH DR3 survey and are selected using `flag_X_fe` = 0. For example, a plot for abundance ratio [X/Y] includes only the stars with abundance flag `flag_X_fe` = 0 and `flag_Y_fe` = 0. Except in the case of the Thamnos and Sequoia, plots show density distribution with 'rainbow' as the adopted colour scheme in which red represents the highest density while dark violet (or black) represents the lowest density. 266
10.11 Abundance ratio [Mg/Fe] as a function of [Fe/H] for selected samples of the thick disc and five major substructures in the halo. All the stars shown here have measured Mg and Fe abundances in the GALAH DR3 survey and are selected using `flag_mg_fe` = 0 and `flag_fe_h` = 0. The linear fits to the Splash, GE/S and Sequoia are shown as the black, yellow and blue lines, respectively. 268

10.12The HR diagram for the selected sample of stars from the GALAH DR3 survey. Uncertainty in luminosity and temperature are plotted in the background as magenta error bars for all the stars. The dotted-black line $\log(L/\mathrm{L}_\odot) = 0.001 \times T_{\rm eff} - 4.8$ marks the approximate separation between dwarfs (below the line) from giants (above the line). These dwarfs are further used to understand the distribution of Li in the Galactic disc and the various substructures in the Galactic halo. 271

10.13Distribution of lithium abundance A(Li) as a function of metallicity for dwarfs of the thin and thick disc are shown in the top-left and top-right panels, respectively. The bottom two rows show the distribution of Li abundance as a function of metallicity for substructures in the Galactic halo. For each of the stars, the error in Li abundance A(Li) and metallicity [Fe/H] are also shown in the background using cyan-coloured error bars. Except in the case of the Thamnos and Sequoia, plots show density distribution with a 'rainbow' colour scheme in which red represents the highest density while dark violet (or black) represents the lowest density. Thamnos and Sequoia's stars are shown in the bottom-right panel as filled red circles and blue squares, respectively. All the shown stars have measured Li abundance in the GALAH DR3 survey. 273

10.14Top-left and top-right panels show the distribution of the thin and thick disc dwarfs in luminosity versus temperature plane. The bottom two rows show the distribution of the halo's substructures in the luminosity versus temperature plane. In each case, maximum Li abundance at a pixel is encoded in the data point's colour using a 'rainbow' colour scheme. The amount of Li corresponding to each colour is provided in the colour bar. For each star, errors in the luminosity and temperature are also shown in the background using cyan-coloured error bars. All the shown stars have measured Li abundance in the GALAH DR3 survey. 274

10.15The top-left and top-right panels show the distribution of Li abundance as a function of surface brightness temperature for dwarfs of the thin and thick disc, respectively. The bottom two rows show distributions for dwarfs in the Galactic halo's substructures. For each star, errors in the A(Li) and temperature are also shown in the background using cyan-coloured error bars. Except in the case of the Thamnos and Sequoia, plots show density distribution with a 'rainbow' colour scheme in which red represents the highest density while dark violet (or black) represents the lowest density. The Thamnos and Sequoia's stars are shown in the bottom-right panel as filled red circles and blue squares, respectively. All the shown stars have measured Li abundance in the GALAH DR3 survey. . . 275

10.16The top-left and top-right panels show lithium abundance A(Li) as a function of stellar age for dwarfs of the Galactic thin and thick disc, respectively. The bottom two rows show lithium abundance A(Li) as a function of stellar age for dwarfs in the Galactic halo's substructures. For each star, the error in the A(Li) and ages are also shown in the background using cyan-coloured error bars. Except in the case of the Thamnos and Sequoia, plots show density distribution with a 'rainbow' colour scheme in which red represents the highest density while dark violet (or black) represents the lowest density. The Thamnos and Sequoia's stars are shown in the bottom-right panel as filled red circles and blue squares, respectively. All the stars shown here have measured Li abundance in the GALAH DR3 survey. Also, only the dwarfs with reliable age estimates are plotted here (see Section 10.5 for more details). 277

List of Tables

2.1 Kinematic definitions, i.e. characteristic velocity dispersion (D_U, D_V, and D_W) and the asymmetric drift velocities V_{ad} relative to local standard of rest for the Galactic thin-disc, thick-disc and halo, adopted from Bensby *et al.* (2003); Reddy *et al.* (2006). Relative number density (f_i) of the Galactic thin-disc, thick-disc and halo stars in the GALAH survey sample is adopted from Bland-Hawthorn *et al.* (2014). 47

2.2 RV of three common stars from Gaia, RAVE and LAMOST of Group-02. 60

4.1 Estimated evolutionary timescales for a representative $1M_{\odot}$ star with metallicities,[Fe/H]=0.0 dex and -0.5 dex. 93

4.2 Stellar parameters of Super Li-rich giants with Li abundance of $A(\mathrm{Li}) \geq 3.2$ dex in our sample. 95

5.1 Mean [Fe/H], A(Li) and [X/Fe] abundances with the standard error of the mean (SEM) for all the 21 elements given in the GALAH survey for Li-normal and Li-rich giants of each of the four luminosity samples. Results are tabulated for four [Fe/H] ranges. In the cases where the number of stars (data points) is less than five, we have provided the average of the abundance error given in the GALAH survey, and all such cases are marked with an asterisk (*). 111

7.1 The initial temperature, luminosity and A(Li) along with their values at ZAMS, at the onset of LB and at the tip of the RGB for the models shown in Figure 7.10 and 7.15. 193

7.2 Input parameters for the best-fit models along with lithium abundances at the start of the different evolutionary phases for the three (M, [Fe/H]) cases studied in details in Section 7.4.1.1. 199

9.1 Mean, SD, median, median absolute deviation (MAD), mode and skew values for metallicity, age, eccentricity and $|Z|_{\max}$ distributions for selected samples of halo's substructures. The data entries in bold are the best possible measures for the central/ peak values for each sample are given in bold. 237

Abbreviations

BB	**B**ig **B**ang
BBN	**B**ig **B**ang **N**ucleosynthesis
CDM	**C**old **D**ark **M**atter
COBE	**C**osmic **B**ackground **E**xplorer
CoRoT	**Co**nvection, **Ro**tation and planetary **T**ransits mission
DEC	**Dec**lination
DIRBE	**Dec**iffuse **I**nfrared **B**ackground **E**xperiment
DOI	**D**igital **O**bject **I**dentifier
DRx	**D**ata **R**elease **x**
GALAH	**GAL**actic **A**rchaeology with **H**ERMES
GC	**G**alactic **c**entre
GE/S	**G**aia-**E**nceladus/**S**ausage
HCT	**H**imalayan **C**handra **T**elescope
HRD	**H**ertzsprung–**R**ussell **d**iagram
IAO	**I**ndian **A**stronomical **O**bservatory
ISM	**I**nter-**S**tellar **M**edium
LAMOST	**L**arge Sky **A**rea **M**ulti-**O**bject Fibre **S**pectroscopic **T**elescope
LoS	**L**ine **o**f **S**ight
LSR	**L**ocal **S**tandard of **R**est
`MESA`	**M**odules for **E**xperiments in **S**tellar **A**strophysics
`MIST`	**MESA** **I**sochrones & **S**tellar **T**racks
`MISTv1.2`	**MESA** **I**sochrones & **S**tellar **T**racks's **v**ersion **1.2**

MNRAS	**M**onthly **N**otices of the **R**oyal **A**stronomical **S**ociety
MW	**M**ilky **W**ay
NASA	**N**ational **A**eronautics and **S**pace **A**dministration
PMDEC	**P**roper **M**otion in **Dec**lination direction
PMRA	**P**roper **M**otion in **R**ight **A**scension direction
RA	**R**ight **A**scension
RAVE	**RA**dial **V**elocity **E**xperiment
RV	**R**adial **V**elocity
WIMPs	**W**eakly **I**nteracting **M**assive **P**articles
WMAP	**W**ilkinson **M**icrowave **A**nisotropy **P**robe

Glossary of symbols

$\mathrm{M}_\odot$	Solar mass
$\mathrm{L}_\odot$	Solar luminosity
$T_{\mathrm{eff},\odot}$	Sun's surface brightness temperature
Π	Parallax
μ_α	Proper motion in right-ascension (RA) direction
μ_δ	Proper motion in declination (DEC) direction
V_r	Line of sight radial velocity (RV)
V_T	Transverse velocity
V_sp	$= \sqrt{V_\mathrm{r}^2 + \mathrm{V}_\mathrm{T}^2}$; star's galactic spatial velocity
U	Radial component of V_sp; positive towards the Galactic center (GC)
V	Circular component of V_sp; positive in the direction of the Galactic disk rotation
W	Vertical component of V_sp; positive towards the north galactic pole (NGP)
L	Total angular momentum
L_X, L_Y, L_Z	X, Y, and Z component of angular momentum L
e	Orbital eccentricity

Chapter 1

Introduction

1.1 The Milky Way system

On a clear, moonless night, when the Sun has gone below the horizon, it is possible to see thousands of celestial objects like asteroids, planets, stars, galaxies, etc., in the sky. If the night is dark enough, one may even see a broad stream of white light across the sky, resembling a flowing milk river. The ancient Greeks named it '*galaxìas kyklos*', which translates to "milky circle." Since then, several variants of this name have been used to refer to it, but today, it is most commonly known by the Milky Way (MW). The studies of MW and other objects we see in the night sky have been going on for many millenniums. From rather basic technology and methodologies, each new clue kept on surprising us and made us more curious to know about the MW and other objects in the night sky. A significant turning point in our understanding came in the early 1600s when the legendary Italian polymath Galileo Galilei pointed his newly perfected telescope to the MW and

realized that it consists of many individual stars. Now, after almost 400 years, with the help of more powerful telescopes, we know that it consists of not only billions of individual stars but also gas and dust with a complex structure.

A photograph of the MW, taken from the Indian Astronomical Observatory (IAO; Hanle, Ladakh, India), is shown in Figure 1.1. The Himalaya Chandra Telescope (HCT) is visible in the foreground. The broad bright band with patches of dark regions at the center is a section of the MW's inner region. This broad bright band is a result of the light emitted from billions of stars, while the dark patches are due to obstruction of this light by dust and gas, which are abundant in the MW's inner region. Most of the scattered faint dots, whose number density decreases with distance from the central band, are stars, clusters of stars, or distant galaxies.



FIGURE 1.1: An optical view of the Milky Way from the Indian Astronomical Observatory located in Hanle, Ladakh, India. The Himalaya Chandra Telescope (HCT) is visible in the foreground. Image credit: Dorje Angchuk, IAO, Hanle, Ladakh, India.

The dust and gas are relatively transparent to wavelengths in infrared (IR) radiation. Hence, mapping the inner region of MW is possible in IR wavelength. Figure 1.2 shows an edge-on view of the MW in IR band from the Diffuse Infrared Background Experiment (DIRBE), Cosmic Background Explorer (COBE) mission. The image reveals a much clear structure of the MW. Combinedly, these two images (Figure 1.1 and 1.2) readily suggest that most of the MW's stars are present in a narrow plane, and their numbers decrease with vertical distance from this plane. The number density of stars also decreases as one moves radially away from the central point of the plane. Additionally, the two figures suggest an abundance of gas and dust in the narrow central plane.

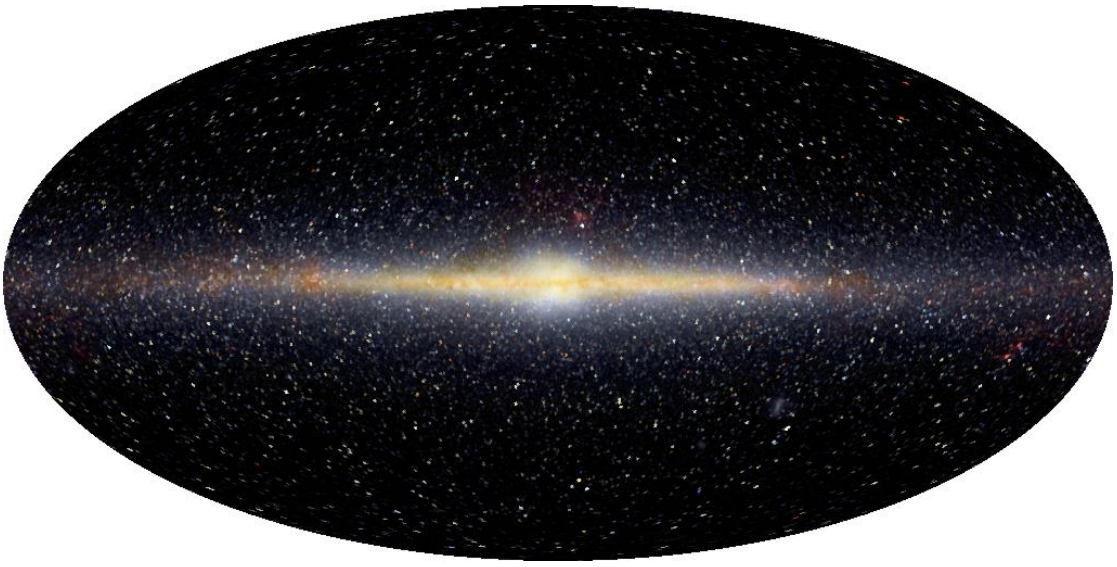


FIGURE 1.2: Edge on view of the Milky Way in near-infrared from the Diffuse Infrared Background Experiment (DIRBE), Cosmic Background Explorer (COBE) mission. Image credit: E. L. Wright, DIRBE, the COBE Project, NASA.

These two simple yet powerful images are enough to make anyone curious and generate thought-provoking questions about the structure and history of the Galaxy. A few of these questions are: Why do most of the stars reside in the central plane? Why stars' number density decreases as one moves vertically away from the central plane and radially away from the centre of this plane? Why do most of the gas and dust reside in the central region of the MW? Are the stars from the inner and

outer regions of the MW similar or different, and do they have different origins? Why is the MW the way it is? What leads to such complicated distributions of stars and gas in the MW? Moreover, what is the MW made of, and how has its content and shape evolved over time? This thesis aims to address some of these and related questions about the formation and evolution histories of the MW.

For centuries, star count has been extensively used to understand the stellar structure of the MW. For example, the earlier models of the MW were constructed based on star count by the likes of Herschel (1785) and Kapteyn (1922). However, to fully understand the formation and evolution of the MW, one needs more than the stellar count. As discussed in the next section, stars' spatial, kinematic and chemical properties, along with their ages, can be used to accurately understand the formation and evolution of the MW.

1.2 Chemodynamic studies of the Galaxy*

One of the most significant outstanding astronomical issues is deciphering the history of the origin and growth of our home galaxy, the MW. In the 1950s, it began to be understood that combining stars' kinematics, chemistry (metallicities estimated based on photometry), and ages may help build a picture of the Galactic creation and learn more about its evolution (e.g. Roman 1954). From an observational standpoint, the quantitative study of the Galaxy based on kinematics and chemical properties of a large sample of nearby stars by Eggen, Lynden-Bell, Sandage (ELS; Eggen *et al.* 1962) set the stage for systematic studies of the Galaxy's formation and evolution. In simple words, the study of the formation and evolution histories of the Galaxy is similar to traditional archaeology, which deals with the study of

*Throughout the literature, 'Galaxy' with a capital 'G' refers to the Milky Way, while 'galaxy' with a lower-case 'g' is used to refer to any galaxy in general. The same notations are adopted in this thesis.

human history based on artefacts (remains of objects that human-created, modified, or used) and features (like pyramids and depressions on the Earth's surface where a human-made structure once stood) which can be excavated and observed today. Because of this similarity, the study of the formation and evolution histories of the Galaxy is also known as Galactic archaeology. However, unlike traditional archaeology, all the investigations in the Galactic archaeology case are based on pieces of information collected by detailed observations of the basic building blocks of the Galaxy like the stars, gas and dust, and other structures (like stars clusters, galactic nuclei, etc.). The study of stars in the Galaxy, as noted by Freeman and Bland-Hawthorn (2002), gives substantial clues regarding the circumstances that prevailed in the early Universe.

1.3 Chemical and kinematic populations of stars in the MW

An edge-on view of the Galaxy, as shown in Figure 1.2, reveals that most of these stars, gas and dust are concentrated in the central plane. Further, at the centre of this relatively thin plane, one can also see a bright spherical distribution corresponding to the swelled-up over-density of stars relative to the thin planner distribution. Distribution in Figure 1.2 is stars' instantaneous positional distribution only, and in actuality, they move in complex orbits governed by a complicated Galactic gravitational potential. However, even after being in continuous motion, their combined positional distribution stays approximately the same as in Figure 1.2 for millions of years which is much less than the Galactic time scale. Also, as stars age, their atmospheric parameters and composition change and when they explode, they enrich the interstellar medium with various metals. The newly formed stars from such altered ISM clouds will have enhanced metal content and also acquire the cloud's kinematics. Sun-like stars are known to conserve the signatures

of these acquired chemical elements in their outer atmosphere for most of their life. However, the acquired kinematics may change with time due to the continuous influence of the Galactic gravitational potential. For decades, astronomers have been using stars' spatial, kinematic and chemical properties to classify them into different stellar populations, find distinct stellar groups, and finally build a picture of the Galaxy. We now know that the Galaxy has a complex structure with four key internal components: the bulge, thin disc, thick disc, and halo, as well as one external component: accreted material (e.g. Gilmore *et al.* 1989; Freeman and Bland-Hawthorn 2002; Helmi 2008; Ivezić *et al.* 2012, and references therein). These components are typically defined by the phase spaces in which we observe them spatially, kinematically and chemically, and constitute the basis for any attempt to model, simulate and understand the birth and evolution histories of the Galaxy.

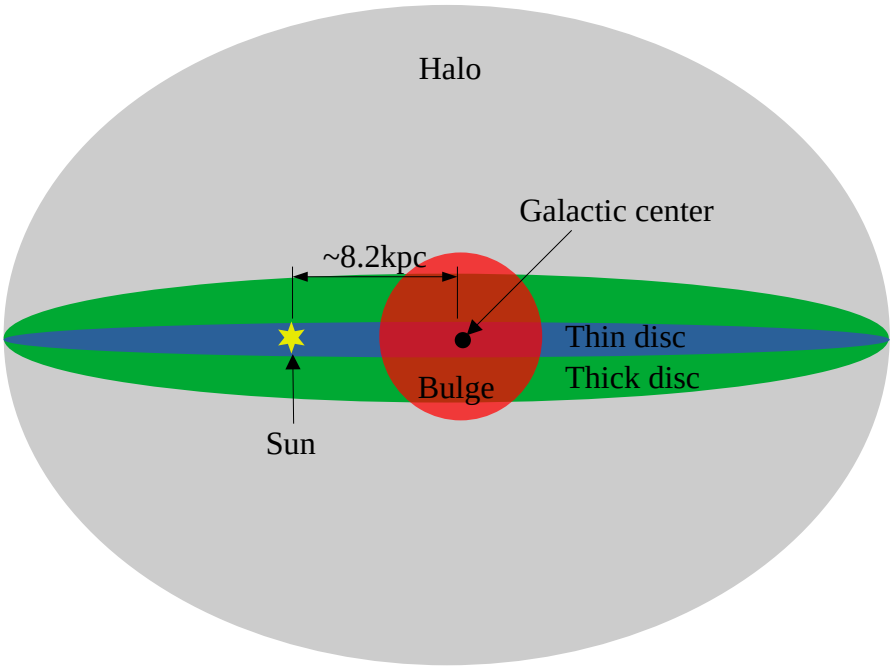


FIGURE 1.3: A cartoon representation of the Galaxy showing its four major stellar components.

A cartoon depiction of our Galaxy highlighting the four primary internal components is shown in Figure 1.3. Detailed discussion on each of these components is

provided in the below sections.

1.3.1 The Bulge

The innermost component of the MW, the bulge, is a dense concentration of stars in a roughly spheroidal shape. Most of the stars in the bulge are predominantly old (e.g. Gonzalez and Gadotti 2016; Hasselquist *et al.* 2020, and reference therein). Early low-resolution spectroscopic studies and photometric metallicity calculations revealed that the bulge stars span a wide range in metallicity with [Fe/H] ranging from about -1.0 to 0.4 dex (e.g. Sadler *et al.* 1996; Ramírez *et al.* 2000; Zoccali *et al.* 2003). Thanks to the availability of large multi-object spectroscopic surveys, we now know that the bulge is a mixture of many stellar populations rather than a single homogeneous one. These populations have different dynamical and morphological characteristics and show evidence for a multiple-component scenario.

Metallicity distribution of bulge stars suggests the presence of more than one population (Hill *et al.* 2011; Rojas-Arriagada *et al.* 2014). The two dominant populations – metal-poor and metal-rich bulge populations – peak at [Fe/H] -0.3 and 0.3 dex, respectively. Kinematically, the metal-poor bulge population stars follow a spheroidal distribution, while the metal-rich bulge population stars rotate cylindrically (see, e.g. the review of Gonzalez and Gadotti 2016, and references therein).

The metal-poor bulge stars, with [Fe/H] $<$ -0.3, are found to be enhanced in [α/Fe] by about 0.3 dex, suggesting a fast stars formation scenario (McWilliam and Rich 1994; Rich and Origlia 2005; Cunha and Smith 2006; Fulbright *et al.* 2007; Lecureur *et al.* 2007; Rich *et al.* 2007). The metal-rich, however, stars show the expected decreasing trend in [α/Fe] relative to [Fe/H], reaching a solar value

for metallicities higher than the Solar metallicity. More interestingly, not all the chemical elements in bulge stars follow the expected yield trends.

1.3.2 The Thin disc and the thick disc

About three-quarters of the Galaxy's stars, along with most of the gas and dust, reside in its disc. Radially, the Galactic disc extends up to 15 kiloparsecs (kpc), but most of the stars are centrally concentrated, i.e. their number density falls off exponentially as we move away from the centre. For a long time, based on the density distribution of stars, the Galactic disc is known to have two main components, namely the thin disc and the thick disc (e.g. Yoshii 1982; Gilmore and Reid 1983). These findings are further confirmed by different kinematics and chemical compositions of thin and thick disc stars. Now we know that the thin and thick disc stars are spatially, kinematically and chemically different (e.g. Gilmore and Reid 1983; Gilmore and Wyse 1985; Edvardsson *et al.* 1993; Freeman and Bland-Hawthorn 2002; Bovy *et al.* 2012; Haywood *et al.* 2013; Rix and Bovy 2013). Also, most of the disc stars (about 95%) lie in the thin disc and remaining forms the thick disc.

Spatially, the thin disc is defined by an exponential power law with a vertical height of about 300 pc and a radial scale length of 3.4 kpc (e.g. Bovy *et al.* 2012; Haywood *et al.* 2013, and references therein). Thin disc stars have modest velocity dispersion and follow near-circular, co-rotational orbits (Edvardsson *et al.* 1993; Reddy *et al.* 2003; Rix and Bovy 2013). Chemically, the thin disc is found to have a metallicity range of $-0.7 < [\mathrm{Fe/H}] < 0.1$ dex, and abundances of *alpha*-process elements similar to that of the Sun (Reddy *et al.* 2003; Bensby *et al.* 2005).

The thick disc, on the other hand, is defined spatially by an exponential power law with a large vertical scale height of about 900 pc and smaller radial scale length

of about 1.8 kpc compared to the thin disc (Bensby *et al.* 2011; Haywood *et al.* 2013). Kinematically, similar to the thin disc stars, the thick disc stars co-rotate with the Galactic disc but with a smaller rotational velocity about the Galactic centre and overall have hotter orbits than stars of the thin disc (e.g. Edvardsson *et al.* 1993; Reddy *et al.* 2003; Haywood *et al.* 2013). Chemically, thick disc stars are significantly metal-poor compared to their thin disc counterparts (Gilmore and Wyse 1985; Reddy *et al.* 2003; Bensby *et al.* 2014). Unlike the thin disc, the metallicity of the thick disc extends well below [Fe/H] < -1.0 dex (Beers *et al.* 2002; Reddy *et al.* 2003).

1.3.3 The Halo

The bulk of the observable part of the Galaxy that is outside the disc is known as the Galactic halo (or simply halo). Unlike the Galactic disc, it lacks gas and dust and consists of individual stars and dense, compact clusters of stars (known as globular clusters). All the halo stars are predominantly old, as due to a lack of cold gas and dust, there is no new star formation going on in the halo. Kinematically, the Galactic halo consists of stars with a wide range in rotational velocity from small pro-grade rotation to highly retrograde rotation (see, e.g., Carollo *et al.* 2007; Helmi 2008, and references therein). Chemically, halo stars are predominately metal-poor and enriched in the alpha-elements (see, e.g., Chiba and Beers 2000; Ishigaki *et al.* 2012). For a long time, the halo is also known to have a bi-model metallicity distribution. It is believed to consist of many small components but can be divided into two major components: a metal-rich halo and a metal-poor halo (see, e.g., Carollo *et al.* 2007; Helmi 2008, and references therein). Recent discoveries based on the data from the *Gaia* survey in combination with data from the large spectroscopic surveys suggest that the metal-poor halo is a remnant of dwarf galaxy Gaia-Enceladus/Sausage (GE/S) which merged with the MW about

some 10 billion years ago (Haywood *et al.* 2018; Gallart *et al.* 2019). The metal-rich halo is understood to be *in situ* component and is believed to be a mixture of the stars of MW's original halo and the ones that were knocked out from the inner region of the MW during the merger events.

1.4 Formation of the Galaxy: An overview of different formation models

In the last section, we learned about the Galaxy's structure along with some of the properties of its four major stellar components. But what led to the formation of such a complex Galactic system, and how various components of this Galactic system have evolved over time? To answer these and similar questions related to the formation and evolution of the Galaxy and galaxies in general, we first need to understand the history of the Universe and understand how the structures were formed and evolved in it.

Based on the works of Willem de Sitter and Albert Einstein, the Belgian Catholic priest and cosmologist Georges Lemaître in his seminal paper in 1927, proposed the idea that the Universe is expanding and is not static. In 1931, to further explain the origin of the Universe, Lemaître proposed the "Hypothesis of the Primeval Atom". According to this hypothesis, the Universe began with the explosion of the primeval atom, and this explosion occurred at a finite point in time. This led to the foundation of the well-known and widely accepted Big Bang theory. According to the Big Bang theory, the observable Universe originated from the singular cataclysmic event Big Bang (BB) about 13.7 billion years ago. From this singular point, the Universe stretched and expanded to get as big as it is today.

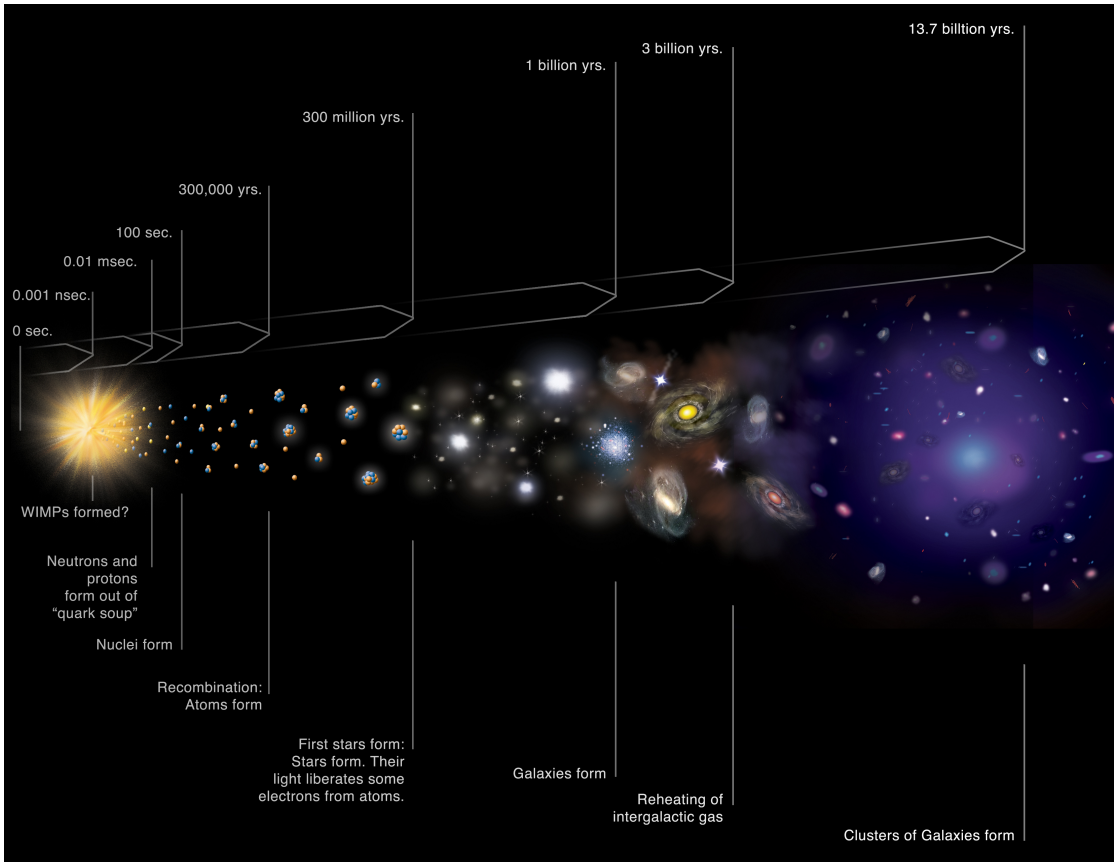


FIGURE 1.4: History of the Universe: From the Big Bang to present. Here, WIMPs refer to weakly interacting massive particles. (Image credit: NASA/CXC/M.Weiss)

A rough timeline of the evolution of the Universe since the BB is shown in Figure 1.4. Within a fraction of a second of the BB, the newly formed universe expanded very rapidly and cooled down, allowing the formation of weakly interacting massive particles (WIMPs). A further drop in temperature allowed the formation of subatomic particles, which later clubbed together to form atoms. This epoch of the formation of the first atoms in the Universe began about one minute after the Big Bang and is known as the Big Bang Nucleosynthesis (BBN). The BBN is believed to be responsible for forming the neutral hydrogen (^{1}H), deuterium (D, or ^{2}H), helium isotopes ^{3}He and ^{4}He along with a small amount of the lithium isotope ^{7}Li (see, e.g., Peebles 1966a,b; Wagoner *et al.* 1967; Reeves *et al.* 1973; Wagoner 1973; Schramm and Wagoner 1977; Boesgaard and Steigman 1985, and

references therein).

When the Universe was about 300 million years old, the newly formed giant gas clouds were cold enough to collapse under their own gravity. The collapse of these giant clouds of primordial gas resulted in the birth of the Universe's first stars. These first stars, believed to be very massive, quickly evolved and died. In this process, they cooked chemical elements heavier than hydrogen and enriched the Universe with these elements. The new stars, which formed from these clouds, inherited these enriched elements. (For more details on how stars contribute towards the chemical evolution of galaxies, see Section 1.5.)

In the meantime, when the Universe was just about a billion years old, more prominent structures like galaxies also started forming from the gravitational collapse of primordial gas clouds. Over time, these initial structures in the Universe interacted and evolved and acquired different shapes and sizes. At present, many of these galaxies, typically with a stellar halo of roughly spherical shape and a disc full of gas and stars, look like our home galaxy, the Milky Way.

Understanding the formation and evolution of larger structures in the Universe, like the galaxies, involves two competing approaches: the top-down and the bottom-up approach. According to the top-down approach, large systems like galaxies are formed by the monolithic collapse of vast clouds of primordial gas. Contrary to this, in the bottom-up approach, smaller structures formed first, which then merged to form larger systems like the galaxies. Cartoon illustrations of models for the formation of a MW-like galaxy through these two approaches are shown in Figure 1.5. A brief introduction to the origins of these two models, along with their limitations, is provided below.

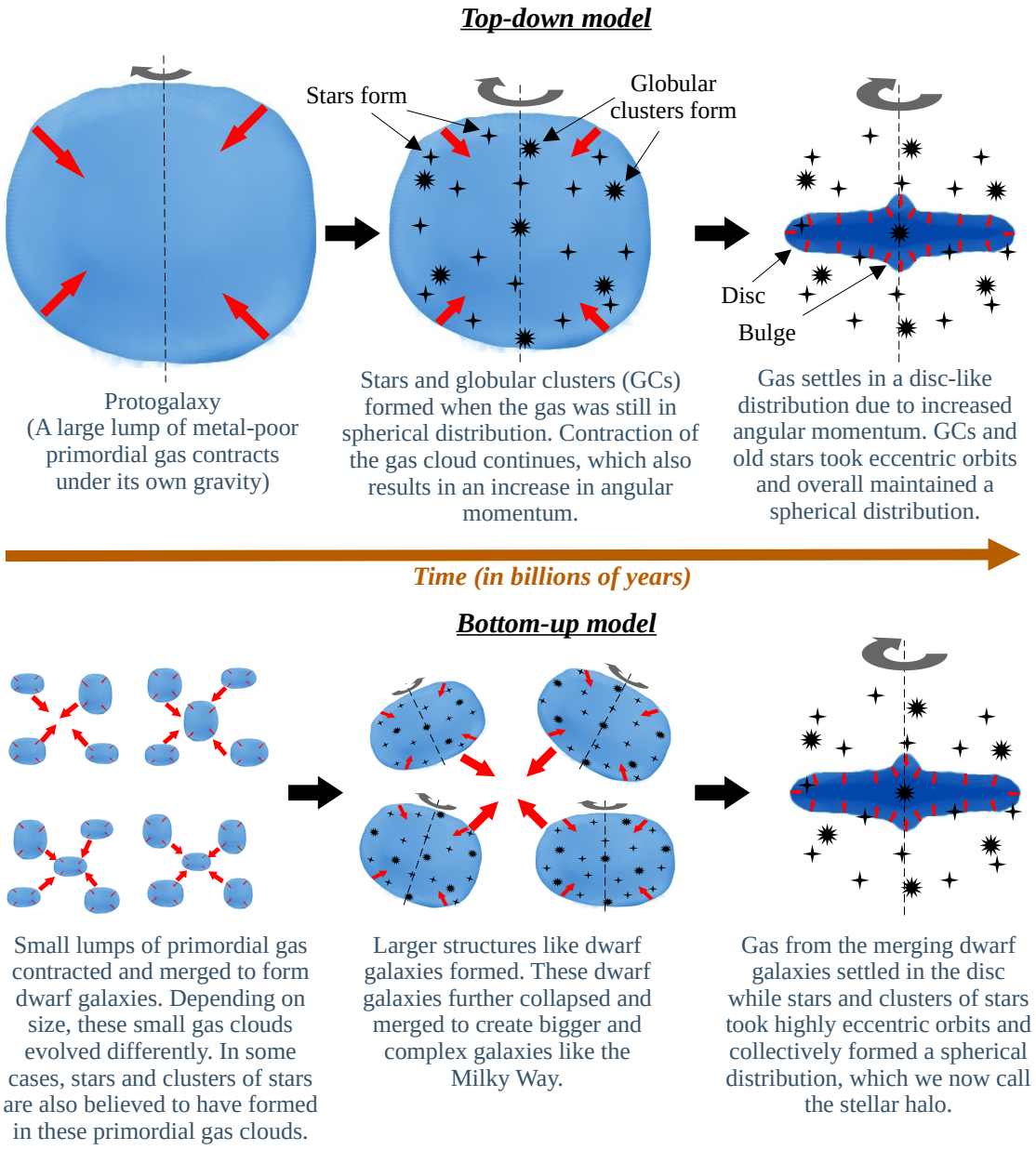


FIGURE 1.5: Cartoon illustrations of the top-down and bottom-up models for the formation of a complex structures galaxy like the MW. Red arrows indicate the direction of contraction due to gravity, while circular grey arrows indicate the sense of rotation of the system (galaxy).

1.4.1 Top-down model:

Proposed by ELS in their seminal paper in 1962, this model is also well known as the ELS model and the 'monolithic collapse' model and is based on the relative

motions and chemical compositions of populations I and II stars. The population II stars are relatively old, metal-poor, and follow more eccentric orbits than the population I stars. In this model, galaxies are formed by the gravitational collapse of a giant gas cloud (also known as the protogalactic cloud). The collapse is countered by increasing outward centrifugal force, which is the result of increasing angular momentum of the galaxy due to infalling gas. The system eventually reaches a dynamical equilibrium when the centrifugal force is large enough to equal the gravitational collapse. Further, in this model, halo stars and globular clusters are thought to form first, and their formation may have started as early as when the protogalactic cloud was still contracting. The current relatively spherical distribution of halo stars and globular clusters suggests that they formed from the protogalactic gas cloud when it was still somewhat spherical. In addition, the production of stars and globular clusters in the halo took place on a time scale similar to that of free-fall. With time, as the cloud further contracted, gas settled in a disc-like distribution due to increased angular momentum. Because of this, the already collapsing halo stars and globular clusters (held together by their self-gravity) took eccentric orbits about the Galactic centre. Additionally, younger generations of stars are formed from the newly settled gas in the disc. This model is known as the closed box model, as gas (or any other material) does not leave or enter the system. Although this classical model adequately describes numerous properties of the Galaxy, it fails to explain several features, such as the Galaxy's observed paucity of metal-poor G-dwarfs (well known as the G-dwarf problem, van den Bergh 1962; Rana 1991), the existence of a large number of halo stars with counter-rotating motion relative to the Galactic disc, significant spread in the ages of globular clusters, etc. The G-dwarf problem is also known to exist in other galaxies too (Worthey *et al.* 1996). Also, similar to the G-dwarfs problem, there is an observed paucity of K and M dwarfs in the Galaxy (Casuso and Beckman 2004; Mould 1978; Woolf and West 2012). The discovery of dark matter and dark energy based on the data from the Wilkinson Microwave Anisotropy Probe (WMAP) also presents a significant challenge to this classical model.

1.4.2 Bottom-up model

This model, also known as the Hierarchical Clustering model, states that enormous structures like galaxies formed through the hierarchical clustering of small systems. In 1965, Canadian-American astrophysicist, astronomer, and theoretical cosmologist Phillip James Edwin Peebles suggested domination of small-scale density perturbations over large scale density perturbations due to high radiation pressure during the early stage of the Universe (Peebles 1965). This prevented the formation of large structures at the early stage of the Universe, and only small clusters of stars, not bigger than the current day globular clusters, are believed to have formed from the collapse of chunks of the primordial gas cloud. Searle and Zinn (1978) proposed that these small systems of gas and stars merged to create dwarf galaxies which later merged to form large galaxies (like our own Milky Way) and clusters of galaxies. They also suggested that these mergers happened over a large time scale. This idea of a large timescale is supported by observational evidence about the lack of correlation between the characteristics of globular clusters (like metal abundances, age, stellar mass function, etc.) and halo stars with the Galactocentric distance. Also, unlike the monolithic collapse scenario, the merger scenario can explain the existence of elliptical galaxies. To add to this, Toomre and Toomre (1972a,b) claimed that all galaxies began as disc galaxies, with some merging to form elliptical galaxies later on. Two of the Toomres' objects, NGC 3921 and NGC 7252, were found to be post-starburst objects, leading to the realisation that mergers cause a burst of star formation that exhausts the available gas in these systems, resulting in a merger with mostly old stellar systems and little star formation activity. This is in complete agreement with the recent discoveries of remnants of a number of accreted dwarf galaxies in the Galactic halo and bulge, having mostly metal-poor stars and showing signs of sudden drops in star formation (see, e.g., Haywood *et al.* 2018; Gallart *et al.* 2019; Horta *et al.* 2021). The first-ever detection of the infant protogalaxies by Rauch *et al.* (2008) has given a significant boost to the bottom-up model. Rauch *et al.* found that all the 27

galaxies in their sample are of irregular shapes and with very low star-formation rates. Also, the stars that formed were very massive, so they evolved very rapidly and exploded as supernovae. However, the discoveries of supermassive black holes with masses over billion $M_{\odot}$ and ages more than 13 billion years, i.e., from the time when the Universe was just a billion-year-old or younger (e.g. Mortlock *et al.* 2011; Bañados *et al.* 2018; Wang *et al.* 2018; Belladitta *et al.* 2020; Wang *et al.* 2021; Yang *et al.* 2021, and references therein), present a big challenge to the bottom-up model because there was not enough time and favourable conditions (due to high radiation pressure) for such gargantuan mass to accumulate at that early age of the Universe. Several mechanisms – like many massive stars colliding and collapsing to form a black hole, the collapse of early stars powered by dark matter, over-dense regions of space-time collapsed into black holes, and the collapse of an entire galaxy – has been proposed to explain the existence of supermassive black holes, but each of these has their own limitations.

Of these two competing models, the bottom-up model better explains most, but not all, features of the MW. But, as discussed above, the bottom-up model also faces some tough challenges in explaining the formation and evolution histories of the Galaxy. This model, however, has led to the creation of a more acceptable model known as the ΛCDM Model, which is briefly discussed below.

1.4.3 ΛCDM model

Currently, the *Lambda*CDM model is the most widely accepted and successful model for explaining observable Universe features such as large-scale structures and expansion (Solà and Gómez-Valent 2015). In this model, CDM refers to the cold dark matter whereas Λ denotes a cosmological constant representing the dark energy, which is a hypothetical force and assists in accelerating the expansion of the Universe(Blumenthal *et al.* 1984). It is also known as the big bang's standard

model. Visible matter, cold dark matter and dark energy make up the Universe in this model. According to this model, soon after the BB, the Universe was essentially homogeneous, extremely hot, and extraordinarily smooth. However, with time small fluctuations in density began to appear and grow. Due to these small density fluctuations, clumps of dark matter began to condense as the Universe cooled. Gas molecules also started forming within these regions of condensed dark matter. The gravitational attraction among these molecules further accelerated the collapse leading to the formation of high-density regions. More gas and dark matter are attracted to these high-density regions leading to the formation of mini-halos and, thus, the seeds that later will become the first galaxies. Once these mini-haloes became more massive, they collapsed under their own weight and became protogalaxies. In the meantime, fragments of clouds of hydrogen and helium gas within these halos collapsed and led to the formation of the first stars. Also, over time, these grown-up mini-halos merged and resulted in larger and more complex structured galaxies. This continuous merging of smaller structures to create larger systems is known as hierarchical merging. Computer simulations, especially in the last two decades, have enabled theoretical astrophysicists to track the evolutionary changes to the Universe and galaxies in it from immediately after the BB to the present time (for example, see Vogelsberger *et al.* 2014; Feng *et al.* 2016). According to these simulations, the formation of galaxies in CDM's presence occurs hierarchically, with small dwarf galaxies forming initially and then merging to create larger and more complex galaxies. Hundreds of small dwarf galaxies must have been swallowed by big galaxies like the MW over time. However, many of these small dwarf galaxies are currently so mingled with their parent galaxy's stars that they are difficult to distinguish.

1.5 Stars, their evolution and contribution towards the chemical evolution of the Galaxy

Stars, one of the basic building components of galaxies, are found with an extensive range of intrinsic properties like colour, luminosity, temperature, mass, size, and composition. In Section 1.3, we learned that the stars belonging to different components of the Galaxy have distinct chemical signatures. For example, halo's stars have higher α-process elements, while the disc stars are more enriched in iron group elements. The chemical evolution of galaxies is directly linked to how stars are born and evolve in their lifetime. They are born by the gravitational collapse of a dust and gas cloud. Depending on the parent cloud's temperature, density, and size, stars can be of different masses. This initial mass of stars plays a crucial role in its evolution. The required amount of heat energy from the fusion of light elements like hydrogen and helium is proportional to the inward gravitational pressure, which is further dependent on the star's mass. Most of the stars can be roughly divided into three mass ranges: 1) low-mass stars having masses from about 0.7 to 2.0 $M_\odot$, 2) intermediate-mass stars having masses from 2.0 to 8 $M_\odot$, and finally, high mass stars having masses higher than 8 $M_\odot$. (Here, we have not categorized the stars with masses of less than 0.7 $M_\odot$ as their main-sequence lifetime is more than the universe's present age, and so we can expect no contribution from these stars towards the chemical evolution of the universe.) A brief discussion on the evolution of stars belonging to these three mass ranges is provided below.

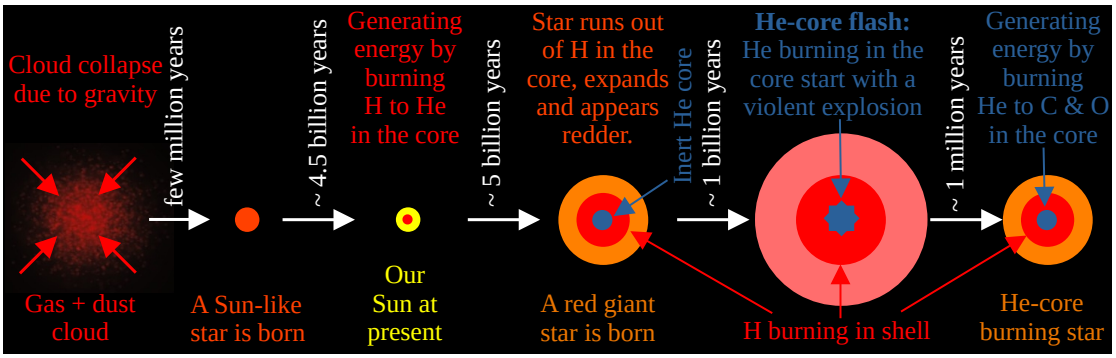


FIGURE 1.6: Cartoon illustration of the evolution of a Sun-like low-mass star from birth to He-core burning phase. Here, H is hydrogen, He is helium, C is carbon, and O is oxygen.

1.5.1 Evolution of stars of different mass range

1.5.1.1 Low mass stars

Low-mass stars like our Sun take billions of years to exhaust hydrogen fuel in the core to the point that the heat generated from the conversion of hydrogen to helium is not enough to counter the inward gravitational pressure. With this star cools down and expands. The newly formed helium atoms accumulate in the core, which results in increased pressure and temperature of the core. The increased core temperature facilitates the burning of hydrogen in a shell around the core, which by now primarily has He. This results in an increase in the star's luminosity, and it further expands and cools down. This phase of hydrogen burning in a shell around the inert helium core is known as the red giant phase (RGB). The newly produced helium from hydrogen burning keeps accumulating in the core, resulting in a further increase in the core's pressure and temperature. With more and more addition of helium, the core's temperature eventually increases to the extent that the fusion of helium atoms is possible, and three helium atoms fuse together to form a carbon atom through the well-known triple-α process. The onset of helium ignition in the core is predicted to be very violent and is known as the He-core flash. Due to additional energy generation from the fusion of He in the core,

the star's radius shrinks and its surface temperature increases. For the next few million years, the star is mainly powered by the conversion of helium to carbon. Stars' in this evolutionary phase are known as helium core burning giant stars (Paczyński 1970; Eggleton 1971). A cartoon illustration of a Sun-like star from its birth to the He-core burning phase is shown in Figure 1.6. With time, like hydrogen, stars also run out of helium fuel, and now the core is mainly occupied by carbon and the remaining helium move to a shell around this inert carbon core. Same as the formation of the red giant, the star contracts and heat up. Because of the increased temperature in the core, the fusion of helium atoms in the shell is possible. Helium fuses in the shell around the inert carbon core, while hydrogen atoms fuse in a shell around the helium shell. This causes the star to expand again and become redder. This phase is known as the early asymptotic giant branch (EAGB) phase (also known as the second red giant stage) and lasts for only about a million years for Sun-like low-mass stars. The core temperature never rises high enough to start carbon fusion in low-mass stars. Hence, in low-mass stars, other heavy elements are not produced except for some oxygen produced by the fusion of a carbon atom with a helium atom. Also, the ignition of helium in the shell around the inert carbon core often happens in a series of flashes which pushes the outer layer of the star more outward and as the star is gigantic in size (with weak inward gravitational force on the outer shells of gas) so a large amount of material from the outer layers of star escape and gets added to the ISM. During this stage, Sun-like stars eject their outer layers of helium and hydrogen. These ejected layers are hot and glow bright and are known as a planetary nebula (e.g. Osterbrock 1964; Kwok *et al.* 1978; Kwok 1982, and references therein). After shedding the hydrogen and helium layers, the star is left with no option for heat generation through fusion to counter the inward gravitational contraction. Hence, the remaining core (mainly consisting of carbon and oxygen) gets compressed more and more until it reaches an equilibrium when the outward electron degeneracy pressure equals the inward gravitational pressure. At this stage, if the remaining

mass of the stars is less than the Chandrasekhar limit of about 1.4 $M_\odot$[†], it turns into a white dwarf (see, e.g., Shapiro and Teukolsky 1983; Chandrasekhar 1984, and references therein). However, if the remaining mass is higher than about 1.4 $M_\odot$, the electron degeneracy pressure would be insufficient to withstand the inward gravitational pressure (Paczyński 1971). So the star will continue shrinking and finally explode, leaving behind a neutron star or a black hole. Since there is no new thermonuclear reaction once a star turns into a white dwarf, it only glows from the leftover heat energy. However, due to continuous energy loss from radiation, it slowly cools and starts fading away. When it cools enough that the thermal kinetic energy of carbon ions is less than their mutual electrostatic potential energy, they begin forming bonds with each other. With this, the gaseous white dwarf slowly turns into a giant spherical rock with very low self-luminosity and is known as a black dwarf. In a total of about a few thousand of million years since the star lost its hydrogen and helium envelope, its temperature drops to zero, which is the end of a star's life. However, in a binary system, white dwarfs can acquire mass from the companion star and explode as the type Ia supernova and enriches the ISM with various heavy elements, especially the iron group elements. The life cycle of low-mass stars is illustrated in Figure 1.7.

1.5.1.2 High mass star

Like the low-mass stars, high-mass stars (with masses higher than eight times the sun's mass) also undergo hydrogen and helium burning but at a much-accelerated

[†]The maximum mass limit for a stable white dwarf is dependent on its composition and is given by $M_{CH} = 1.44 \times (2Y_e)^2\ M_\odot$, where Y_e = (number of electrons)/(number of nucleons i.e. number of protons plus neutrons) is electron fraction of the core (Chandrasekhar 1931, 1935). For example, a carbon atom has 6 electrons and 12 nucleons (6 protons + 6 neutrons), and so Y_e for carbon core is 0.5, giving $M_{CM,Carbon} = 1.44\ M_\odot$, which is the well known Chandrasekhar mass limit. Similarly, an iron-56 atom has 26 electrons and 56 nucleons (26 protons + 30 neutrons), and so for a core composed of iron-56, $Y_e = 26/56 \approx 0.464$ and $M_{CM,Iron-56} \approx 1.242\ M_\odot$. Hence, white dwarfs composed of heavy elements have a lower mass limit.

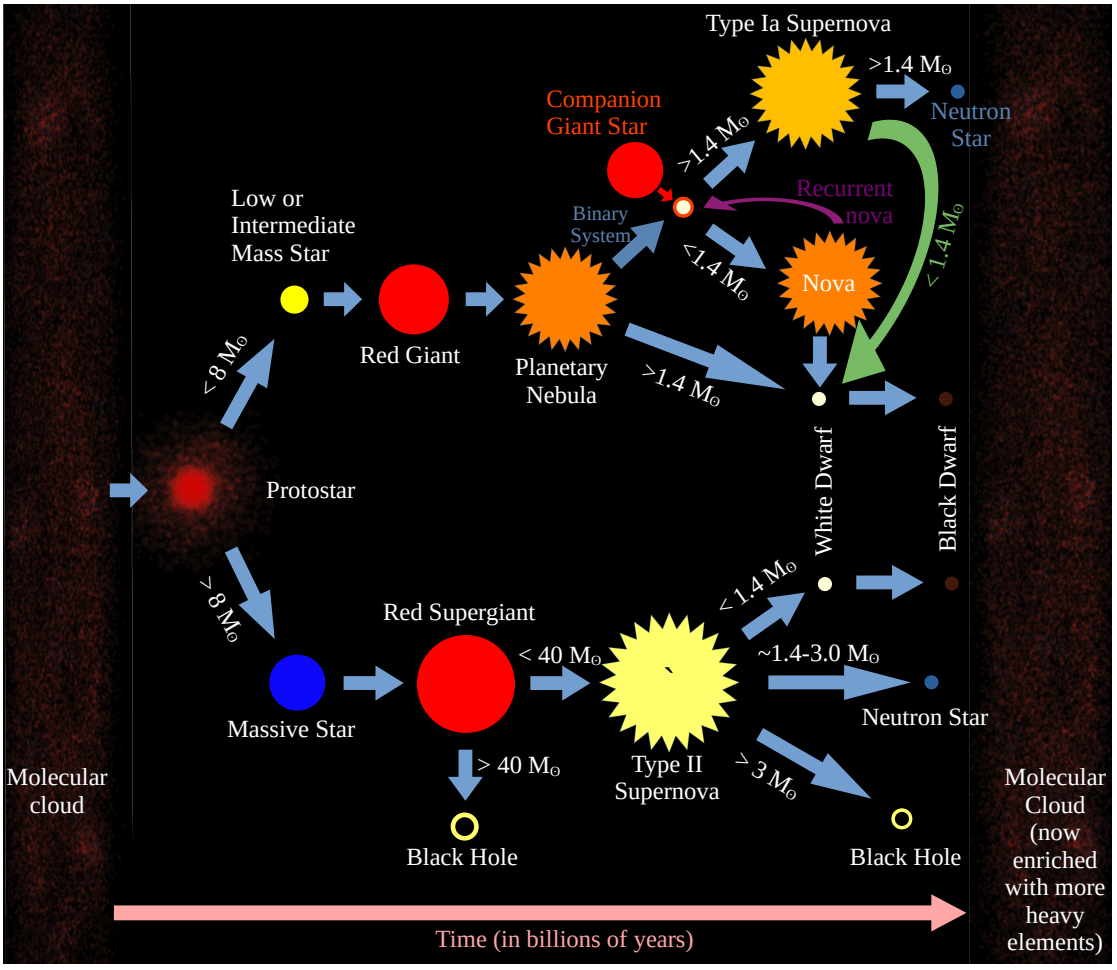


FIGURE 1.7: Cartoon illustration of the evolution of stars of different masses from birth to death. Objects like novas and supernovas, shown as circles with spikes, are known to alter the chemical composition of the universe through feedback as they shed their mass during explosions. With each life cycle, stars process the existing chemical elements and, in the end, enrich the universe with newly cooked heavy elements.

pace. For example, an eight-solar-mass star takes only a few million years compared to billions of years for a solar-mass star to finish off core hydrogen and helium. After the He-core burning phase, high-mass stars' evolution is significantly different from low-mass stars (Heger *et al.* 2003). Unlike low-mass stars, the temperature in the core of a high-mass star is high enough to start the fusion of carbon atoms and then atoms of other heavy elements to produce elements all the way up to the iron. Also, the cores of high-mass stars are non-degenerate, so the carbon ignition starts quietly. The fusion of iron atoms and the atoms of other

heavier elements is not feasible as the amount of energy required for such fusion to take place is higher than the amount of energy released from such fusion. Another major difference between the low-mass and the high-mass stars is how their life cycle ends. Unlike low-mass stars, once a high-mass star runs out of nuclear fuel to counter the inward gravitational pressure, it collapses within fractions of a second and then explodes as a Type II supernova and enriches the surrounding ISM with heavy elements, especially the α-capture elements like oxygen (O), magnesium (Mg), silicon (Ca), calcium (Ca) and titanium (Ti). Stars with initial masses in the narrow mass range $\sim$8 - 10 $M_{\odot}$ form degenerate oxygen and neon cores which can ignite very violently, resulting in the loss of the star's outer envelope and leaving behind a core composed of heavy elements (Garcia-Berro and Iben 1994; Ritossa *et al.* 1996). Post a significantly large mass loss, even in the case of high-mass stars, the leftover core with a mass of less than 1.4 $M_{\odot}$ turns into a white dwarf (Weidemann 1977). However, if the mass of the core is higher than 1.4 $M_{\odot}$ then gravity will overcome the electron degeneracy pressure, and the star will collapse further. When this happens, electrons and protons combine to form neutrons through electron capture. For stars with remnant core mass from about 1.4 to 3.0 $M_{\odot}$, the collapse will continue until it is contained by the outward pressure due to strong repulsive force between nucleons and neutrons degeneracy and results in a neutron star's formation (Oppenheimer and Volkoff 1939; Miyaji *et al.* 1980; Nomoto 1984, 1987; Miyaji and Nomoto 1987; Nomoto and Hashimoto 1988; Douchin and Haensel 2001). In the case of stars with remnant core mass heavier than 3.0 $M_{\odot}$, the inward gravitational pressure will be so high that even the neutron degeneracy pressure will not be enough to stop the star's collapse, and eventually, the star turns into a black hole. Stars with masses more than about 40 $M_{\odot}$ can directly turn into a back hole through core collapse without going supernova (see, e.g., Fryer 1999; Heger *et al.* 2003, and references therein).

1.5.1.3 Intermediate mass star

The intermediate-mass stars' evolution is somewhat between evolutions of the low and high mass stars (Iben 1974; Dominguez *et al.* 1999). Post hydrogen and helium burning, the remnant carbon core of these stars is massive enough to start the fusion of carbon and then other heavier elements. However, unlike high-mass stars, intermediate-mass stars have degenerate carbon cores, and so the onset of carbon ignition is always explosive (Arnett 1969, 1971; Couch and Arnett 1975). Similarly, cores composed of other heavier elements like oxygen and neon are also degenerate; hence an intermediate-mass star experiences many explosive runaway fusion reactions, which results in strong oscillations. With each of these strong oscillations, stars experience significant mass loss (e.g., Fusi-Pecci and Renzini 1976; Weidemann 1977; Knapp and Morris 1985; Knapp 1986; Ramstedt *et al.* 2008) and contaminate the surrounding ISM region with primeval and synthesised chemical elements. Post mass loss, if the mass of the remnant core is less than 1.4 $M_{\odot}$, the star ends up as a white dwarf composed of higher mass elements. But in many cases, the mass of the remnant core is higher than this limit and so similar to the high-mass stars, collapse in these stars also continues, and they end up as neutron stars (if the remnant core mass is in the range $\sim$ 1.4-3.0 $M_{\odot}$) or a black hole if core grows heavier than about 3.0 $M_{\odot}$ due to falling back of material on the neutron stars (Fryer 1999).

1.5.2 Stars' role in the chemical evolution of galaxies

As discussed in the previous section, stars of different mass ranges evolve differently and produce various chemical elements throughout their lifetime. Stars spill these newly cooked elements into their surrounding space during explosive events throughout their lifetime, altering the chemical composition of the gas and

dust cloud in their vicinity. For example, high-mass stars (with an initial mass higher than about 8 $M_{\odot}$) evolve at a much-accelerated pace and contribute more α-process elements compared to low- and intermediate-mass stars (with masses $\leq$ 8 $M_{\odot}$), which contribute more iron peak elements and also evolve at a slower pace. The new generation of stars formed from these altered gas and dust clouds inherent these chemical elements. Same as the previous generation of stars, this new generation of stars also goes through a similar evolution phase and alters the surrounding ISM region with more newly cooked elements when they explode. This cycle of stars' evolution and their contribution to the enrichment of different chemical elements in the galaxies keeps repeating endlessly. A cartoon illustration of the cycle of low- and high-mass stars' evolution is shown in Figure 1.7.

1.6 Lithium: A trace element from the BBN to the Galaxy and stars

1.6.1 Primordial Lithium

As discussed previously in Section 1.4, lithium's isotope ^{7}Li (hereafter, Li) is the heaviest element produced in a significant amount in the BBN. Along with ^{7}Li, ^{6}Li was also produced but in a very small quantity: $^{6}\mathrm{Li}/^{7}\mathrm{Li} \lessapprox 10^{-4}$ (Thomas *et al.* 1993; Vangioni-Flam *et al.* 1999). The fraction of elements produced in BBN is sensitive to the baryon-to-photon ratio at that time. Although direct measurements of chemical elements produced in the BBN are not possible, their indirect measurements are possible from the measurements of the baryon-to-photon ratio. At present, with the help of space-based experiments such as the *Wilkinson Microwave Anisotropy Probe* (WMAP; Jungman *et al.* 1996; Komatsu *et al.* 2011)

and the Planck mission (Planck Collaboration *et al.* 2014), the measurement of primordial baryon-to-photon ratio is possible. Using baryon density measurements from the WMAP, the standard BBN models predict primordial Li abundance, $A(\mathrm{Li}) = 2.72 \pm 0.06$ dex (Cyburt *et al.* 2008; Coc *et al.* 2012).[‡] A similar value of primordial Li abundance is found based on baryonic density measurements from the Plank mission (Coc *et al.* 2014). As the fragments of the primordial gas cloud collapsed and formed stars and galaxies, this trace amount of primordial lithium also ended up in them, where it further evolved based on local conditions.

1.6.2 Stellar evolution of Li

Li is a fragile element as it easily gets destroyed at temperatures of about $2.5 \times 10^6 K$. Stars' interior temperatures are much higher than this limit, so Li can not survive there; however, it can survive in the stars' outer thin envelope known as the atmosphere, where the temperature is relatively lower. The survival of surface Li is further sensitive to a star's evolution. (Greenstein and Richardson 1951) provided the first measurement of Li in the Sun and also discovered that the Sun has about 100 times lower Li than what is found on the Earth and meteorites, which are understood to be representatives of the natal gas cloud from which Sun has formed. Further, from early observational studies of a relatively large sample of stars, it became clear that Li's destruction in stars is highly variable, and destruction increases with decreasing temperature (Bonsack 1959; Bonsack and Greenstein 1960). We now understand that the depletion of Li in stars starts as early as the pre-main-sequence (PMS) phase when stars are fully convective. The amount of depletion during the PMS phase depends on parameters like the star's mass, metallicity and age along with the efficiency of processes like convection (see,e.g. Bildsten *et al.* 1997; Pinsonneault 1997; D'Antona and Montalbán 2003).

[‡]Elemental abundances of Li are given on the traditional scale: $A(\mathrm{Li}) = \log[N(\mathrm{Li})/N(\mathrm{H})] + 12$ where $N(\mathrm{Li})$ and $N(\mathrm{H})$ are the number density of Li and H, respectively.

During the MS phase also stars are known to further deplete their Li to a varying degree. For example, our Sun and similar star are believed to have depleted their Li during the MS phase rather than during the PMS phase (see, e.g., Zappala 1972; Jeffries *et al.* 2009; Dumont *et al.* 2021, and reference therein). Once stars leave the MS phase, they experience further major depletion of Li. Events like enhanced mixing during the first dredge-up lead to rapid dilution of Li in stars' outer envelopes as they evolve from the main sequence (Pinsonneault 1997). In conclusion, stars act as a sink for the Li as for most of their life they destroy it. However, evolved stars such as RGB stars are known to create Li in their innards via the Cameron-Fowler process under certain conditions (Cameron and Fowler 1971). This has been observed in a small group of RGB stars which are known in the literature as Li-rich giants with $A(\mathrm{Li}) \geq 1.5$, an upper limit set by stellar models (Iben 1967).

1.6.3 Galactic evolution of Li

Halo stars are relics from the early formation history of the MW. They are believed to hold the chemical fingerprints of the natal gas clouds from which the MW has formed. Hence measurements of Li abundances in the atmosphere of these stars can be thought to provide a direct estimation of the primordial Li abundance. In a sample of metal-poor halo stars, Spite and Spite (1982) discovered a remarkably constant Li abundance. Li in these stars is found to be independent of the star's temperature, and further distribution is found to be remarkably flat when plotted as a function of the star's metallicity and is well known as the Spite plateau. However, stars' metallicity increase with time as the Galaxy evolves chemically due to the recycling of elements on stars. Thus a flat Spite plateau indicates that the Li in halo stars is primordial. Subsequent follow-up studies (e.g., Pinsonneault *et al.* 1992; Bonifacio and Molaro 1997; Thorburn 1994; Pinsonneault *et al.* 1999; Ryan *et al.* 1999; Meléndez and Ramírez 2004; Asplund *et al.* 2006, to name a few) has

confirmed the existence of this plateau, although with some very slight variation in the height with respect to what was found in Spite and Spite (1982). The plateau's existence has also been confirmed in other accreted dwarf galaxies, implying that it is universal (e.g. Monaco *et al.* 2010; Matteucci *et al.* 2021; Simpson *et al.* 2021). Currently, the most accepted value of Li abundance at spite plateau is $A(\mathrm{Li}) = 2.27 \pm 0.03$ (Lind *et al.* 2009b) which is about three times lower than the theoretically predicted value from the standard BBN models. The striking difference between the predicted and observed amount of Li is well known as the primordial Li abundance problem. The present value of Li abundance in the ISM, as measured in meteorites and young galactic disc stars, is approximately A(Li) *approx* 3.32 dex, which is about ten times greater than the Li found in metal-poor dwarfs and three times higher than the value predicted by the BBN models (e.g., see Guiglion *et al.* 2016; Deepak and Reddy 2020b, references therein).

In conclusion, Li is an exciting element due to its primordial origin and fascinating journey in stars and the Galaxy. Understanding its evolution and distribution in the Galaxy can provide insight into the chemical and dynamic history of the Galaxy. In this regard, one of the aims of this thesis is to understand the production of Li in low-mass stars and their possible contribution towards the Galactic evolution of Li.

1.7 Scope of the Thesis

This thesis aims to understand the chemo-dynamical evolution of the Galaxy using publicly available data from large spectroscopic and astrometric surveys. However, as already discussed in this chapter, Galaxy's chemo-dynamical evolution is a vast topic. So it is not possible to answer all the unanswered questions through one

single thesis. Listed below are some of the main goals of this thesis to help advance our understanding of the Galaxy's formation and evolution history.

1. To understand the distribution and evolution of Li in the Galaxy.
2. To understand the stellar evolution of Li.
3. To understand the origin of Li-rich red giant stars and see if their origin is linked to the dynamic history of the Galaxy.
4. To Understating roles of mixing, luminosity bump and He-core flash based on a comparison between observational data and stellar models created using *Modules for Experiments in Stellar Astrophysics* (`MESA`).
5. To understand the contribution of low-mass stars towards the Galactic Li.
6. Uncovering the formation and evolution histories of the Galactic halo based on stars' kinematic properties, metallicity and stellar ages.
7. Uncovering the formation and evolution histories of the Galactic halos as well as the Galaxy based on stars' chemical compositions.
8. To provide a context for future work.

1.8 Plan of the Thesis

Following is the chapter-wise plan of the thesis:

- Chapter 1: Introduction

  This chapter contains a brief introduction to the Galaxy, its formation model and how its formation and evolution history can be studied. A quick review

of previous studies in this regard is also provided. This chapter also provides a brief introduction to the origin and evolution of Li in the Universe, stars and the Galaxy. The chapter also highlights the usefulness of Li as a tool to understand the formation and evolution history of the Galaxy.

- Chapter 2: Data samples and methodology

  This chapter introduces various astrometric and spectroscopic surveys from which data is used in this thesis. A brief introduction to used methodologies like the determination of stars' kinematic and orbital properties along with the determination of stars' age and masses are also provided.

- Chapter 3: Evolution of Li in the Galaxy

  In this chapter, we discuss the distribution and evolution of Li in the Galaxy based on observational data from the GALAH survey. Data clearly suggest an enrichment of Li in the Galactic disc compared to both theoretically predicted and observed primordial Li in the metal-poor halo stars. We further discuss various sources contributing towards the Galactic Li. Results from this study are published in the Memorie della Societa Astronomica Italiana (Deepak and Reddy 2020b) and Proceedings of the International Astronomical Union (Deepak and Reddy 2020a).

- Chapter 4: Evolution of Lithium in stars: the origin of Li-rich red giant stars

  In this chapter, we provide our study on the evolution of Li in red giant stars. In this study, we have looked into the origins of Li-rich giant stars, which have been a hot topic of discussion for more than the last four decades and are believed to be one of the major contributors of the Galactic Li. In the study covered in this chapter, we have discovered more than three hundred new Li-rich giant stars, which helped in doubling the number of known Li-rich giant stars at the time of publication in early 2019. Results from this study are published in the *Monthly Notices of the Royal Astronomical Society* (MNRAS; see Deepak and Reddy 2019).

- Chapter 5: Properties of Li-enriched and normal giants in the GALAH survey: mass, metallicity, stellar rotation and chemical composition

  We further looked into the distribution of these Li-rich stars to see if they belong to any particular kinetic group in the Galaxy. Also, to learn more about the Li enrichment process in low-mass stars, we looked into the chemical compositions of Li-rich and Li-normal red giant stars. Results from this study are published in the MNRAS (see Deepak *et al.* 2020).

- Chapter 6: Li abundances and asteroseismology of red giants: understanding the evolution of lithium in giants based on asteroseismic parameters

  In this study, we use the asteroseismic data from the literature for giants with known Li abundances to understand the evolution of Li in these giants. Results from this study are published in the MNRAS (see Deepak and Lambert 2021a).

- Chapter 7: Lithium in red giants: the roles of the He-core flash and the luminosity bump

  To further understand the evolution of Li in low-mass stars, we looked into roles of mixing, luminosity bump and He-core flash. For this, we used more recent data from the third data release of the GALAH survey. For this study, we also used the `MESA` suites of programs to create stellar evolution models, including the evolution of Li. Results from these studies have been published in the MNRAS (Deepak and Lambert 2021b).

- Chapter 8: Contribution of low-mass stars towards the Galactic Li evolution

  This chapter discusses the possible contribution of low-mass stars towards the Galactic Li evolution. We also discuss plans to further this study which can help get a quantitative estimate of the amount of Li low-mass stars can contribute to the Galaxy. Results from this study are published in the *Memorie della Societa Astronomica Italiana* (Deepak and Reddy 2020b) and

Proceedings of the International Astronomical Union (Deepak and Reddy 2020a).

- Chapter 9: Study of stellar substructures in the Galactic halo based on the data from the LAMOST and *Gaia* surveys

  This chapter contains preliminary results from our ongoing study on the formation and evolution histories of the Galactic halo. Based on data from the large spectroscopic and astrometric surveys, we identified various pro-grade (like Splash and Helmi stream) and retrograde (like Gaia-Enceladus/Sausage, Thamnos and Sequoia) substructures in the halo. We then probed their spatial, kinematic and orbital properties along with ages to get clues about the formation and evolution history of the Galactic halo.

- Chapter 10: Chemical compositions of the Galactic disc and halo components: An insight into the formation and evolution histories of the Galaxy

  This chapter discusses preliminary results from our ongoing study on the formation and evolution histories of the Galactic disc and halo components based on spectroscopic samples of the Galactic disc and halo's stars drawn from the GALAH DR3 survey in combination with the astrometric data from the *Gaia* survey. To find clues about the origin and differences in the evolution of the Galactic disc and halo's components, we search for the differences in the chemical abundance among these samples. For this, we used about 30 chemical species from the GALAH DR3 survey. We also look into the kinematics, metallicity and age distributions of the components of the Galactic halo in comparison with the Galactic thin and thick disc.

- Chapter 11: Summary, conclusions and future work

  In this chapter, we summarise all the works in this thesis. We further discuss the novel aspects of these works and also talk about the implications of these in future studies. Finally, we close this chapter and these with future plans to further our understanding of the formation and evolution of the Galaxy.

1.9 Resource summary

In this chapter, we presented a basic introduction to the Galaxy, its various components, formation scenarios and how it can be studied (see Section 1.1 to 1.4). An in-depth introduction to the evolution of stars of different masses and their contribution towards the chemical evolution of galaxies is provided in Section 1.5. In Section 1.6, we have provided a brief introduction to the origin and evolution of lithium in the cosmos, which is a trace element from BBN to the Galaxy and stars. The goals of this thesis are presented in Section 1.7. Finally, in Section 1.8, we provided a chapter-wise plan for this thesis. The primary resources other than the in-text references we used for the discussion in this chapter are Shapiro and Teukolsky (1983); Böhm-Vitense (1992); Arnett (1996); Kippenhahn *et al.* (2012); Matteucci (2012); Iben (2012a,b).

Chapter 2

Data samples and methodology

This chapter covers a brief introduction to the data samples and methodology used in the studies in this thesis. An introduction to the sources of data samples is provided in Section 2.1. However, this data introduction is very general, and an in-depth introduction to the selection of data samples specific to a particular study is provided in the corresponding chapters. Section 2.2 covers a brief introduction to methodologies used to process the raw data. In Section 2.3, we have provided a comparison between the RVs from the *Gaia* DR2 and RAVE DR5 Survey. Section 2.3 also covers an additional introduction to *Gaia*'s photometry and provides descriptions of quantifying Galactic disc and halo stars based on the distribution in the Toomre Diagram, which is not covered in the earlier sections of this chapter. Lastly, in Section 2.4, we have summarized the entire chapter.

2.1 Data samples

For this thesis, we have primarily used two types of data to study the MW's stars: 1) five-parameter astrometric solution (i.e., stars' position coordinates, proper motions and parallaxes) from the *Gaia* survey, and 2) spectroscopically determined information like stars' temperature, gravity, radial velocity and chemical abundances, which are available from extensive spectroscopic surveys like the GALAH, APOGEE, LAMOST and RAVE. A brief introduction to both types of data sets is covered in the following sections.

2.1.1 Astrometric data

The key parameters needed to pinpoint a star in the night sky are its position coordinates, e.g., ascension (RA) and declination (DEC). Stars do shift their positions due to their actual motion in the Galaxy with respect to the center of the Galaxy and relative to the solar system. The relative shifts vary from star to star and depend on the star's distance from us, actual speed, and the direction of motion with respect to the line of sight (LoS). In astronomy, these apparent motions of stars along with celestial coordinates and at a right angle to the observer's LoS are known as proper motions (μ), e.g., proper motion along RA (PMRA or $\mu_{\rm RA}$ or μ_α) and proper motion along DEC (PMDEC or $\mu_{\rm DEC}$ or μ_δ). The astronomical distance is usually determined based on trigonometric parallax (Π) measurements, which is the apparent displacement of an object due to a change in the observer's position (distance = $1/\Pi$, where distance and parallax Π are in parsec and arcsec, respectively). Even though most of the stars in the Galaxy move at an average speed of thousands of kilometres per hour, their apparent position in the sky changes varies slightly due to large distances of stars from the observer (i.e. earth or the solar system). This makes the measurement of the apparent shift in the

star's position a challenging task. The task becomes more complicated when a ground-based facility is used as involved errors due to the time-dependent nature of astrometric measurements, atmospheric perturbations, low visibility, and thermal and gravitational flexure of used telescopes. Because of these reasons, astrometric measurements from early studies are available only for a handful of high proper motion nearby stars. These measurements also lack accuracy due to the involved complexity and errors. So the only solution to overcome these limitations was to make astrometric observations from space. Launched in 1989 and operated until 1993, the *Hipparcos* mission was the first space-based mission for astrometric measurements (see, e.g., HIP 1997; Perryman *et al.* 1997, and references therein). Following the success of the *Hipparcos* mission and with the aim to get more precise astrometric measurements, the European Space Agency launched the *Gaia* mission in 2013. In all the works in this thesis, we have used data from the *Gaia* survey. A brief introduction to the *Gaia* survey is provided in the below section.

2.1.1.1 The *Gaia* survey

Gaia, a European space telescope mission meant for recording accurate astrometry of more than a billion stars in the Galaxy, began its scientific observations in 2014 July (Gaia Collaboration *et al.* 2016a). Since then, *Gaia* has been scanning the whole sky and observing all the stars within *Gaia* G-band magnitude limits of 2.0 $\lesssim G \lesssim$ 20.7. Published in 2018b, the second data release from the *Gaia* survey (hereafter *Gaia* DR2) provides five parameter solution (i.e., position coordinates, proper motions and parallax, along with corresponding errors) and photometric data in the *Gaia* G, BP, and RP-band magnitudes covering wavelength bands of [330-1050], [330-680], and [630-1050] nm, respectively, for about 1.5 billion stars (Jordi *et al.* 2010a; Gaia Collaboration *et al.* 2018b). *Gaia* DR2 also provides line-of-sight median radial velocity (RV; over 22 months) of about 7.2 million stars.

In all the works in this thesis, we have extensively used *Gaia*'s five-parameter astrometric solution.

2.1.2 Spectroscopic data

Another critical ingredient for chemo-dynamic studies of the Galaxy is stellar spectroscopic data like stars' surface brightness temperatures, specific gravity and chemical abundances. Using Doppler correction to the observed spectrum, one can also get an accurate estimate of the star's line of sight RV. A brief introduction to astronomical spectroscopy is provided below, and then in the following sections, we have provided a brief introduction to the spectroscopic survey used in the study.

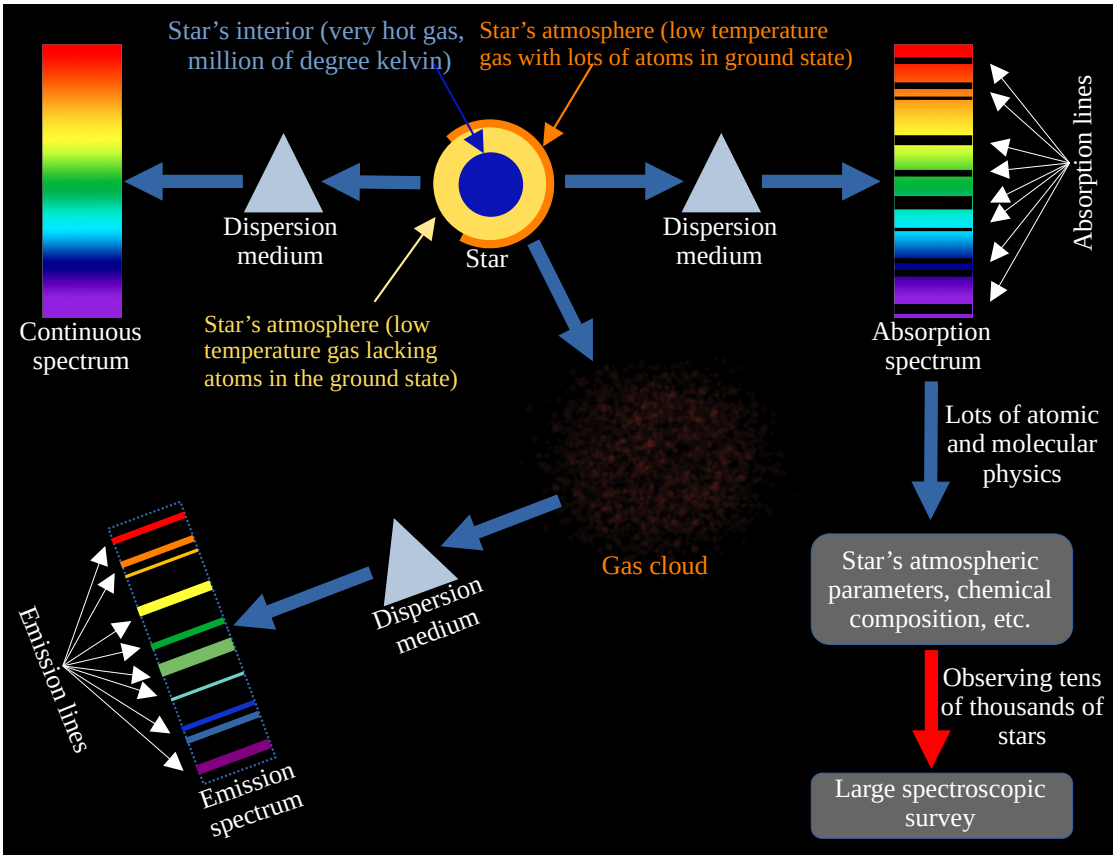


FIGURE 2.1: A cartoon illustration of stellar spectroscopy. Cases for continuous spectrum, absorption spectrum and emission line spectrum are shown.

2.1.2.1 Astronomical spectroscopy

The basic idea behind astronomical spectroscopy is shown as a cartoon illustration in Figure 2.1. We know that every object with a temperature higher than absolute zero kelvin emits electromagnetic radiation at virtually all wavelengths due to random motions of the object's constituents particles, atoms and molecules because of their thermal energy. Also, the amount of electromagnetic radiation emitted at a given wavelength is a function of the object's temperature only and does not depend on any other property of the object like chemical composition (Planck 1910, 1912).

Stars' cores are millions of degrees hot, so most of the emitted radiation will be at a shorter wavelength compared to the visible spectrum. However, the high energy radiations get trapped inside the star due to thick layers of gas between the core and atmosphere (or photo-sphere). The trapped energy slowly gets transported to the surface via convection and results in the surface temperature from about a thousand kelvin to tens of thousand kelvin, and the peak emission wavelength corresponding to which falls in and near the visible spectrum. The lost energy from a star's surface due to continuous radiation is replenished by a continuous supply of energy keeping the surface at an approximately constant temperature. Because of this, stars can be assumed as black bodies and emission from them can be approximated as black-body radiation.

Now, if the star's atmosphere is composed of ionised atoms only, then we can expect that there will be no absorption of energy from the emitted black-body radiation. The spectrum (i.e., intensity as a function of wavelength) for such radiation is continuous and is known as a continuum spectrum. The case of continuum spectrum is shown in the top left corner of Figure 2.1.

In general, the stars' atmosphere has many atoms of different elements in the

ground energy state or partially excited state. The atoms can capture photons and acquire an excited state or become fully ionised. During de-excitation or recombination of ionised atoms and electrons, photons are emitted in all directions (i.e., in 4π steradian) regardless of the original direction of the captured photon. This results in a deficiency of photons at some particular wavelengths along the LoS and leads to the formation of dark lines in the spectrum. Such a spectrum with dark lines is known as the absorption line spectrum or absorption spectrum. In Figure 2.1, the case of an absorption spectrum is shown in the top-right corner. The dark lines in this spectrum correspond to the atomic ionisation level, which is possible to identify using atomic data. Based on the relative depth of these lines compared to the continuum spectrum and relevant atomic and molecular physics, finding the number of chemical elements corresponding to these absorption lines is possible. In large spectroscopic surveys, spectra of thousands of stars are obtained, which are then used to estimate various stellar parameters and chemical abundances based on absorption lines. A brief introduction to the large spectroscopic survey used in works covered in this thesis is discussed in the following sections.

Lastly, as shown in the bottom left corner of Figure 2.1, gas clouds present in the ISM can absorb emitted light from stars and then re-emit it in all directions. Such spectrum is known as emission line spectrum or emission spectrum. Similar to the absorption spectrum, analysis of the emission spectrum can provide a great deal of information about the composition of the gas cloud.

2.1.2.2 GALAH survey

The Galactic Archaeology survey with the HERMES spectrograph (GALAH) is a large-scale spectroscopic survey. The stellar spectra are obtained with the HERMES spectrograph mounted on the 4-m Anglo-Australian Telescope (AAT) at a

spectral resolution (R = $\lambda/\Delta\lambda$) of $\sim 28,000$. In the second data release of the GALAH survey (hereafter GALAH DR2), the GALAH team has provided stellar parameters (Teff, log$g$, micro-turbulence velocity) along with quantitatively derived abundances of 23 elements, from Li to Eu for 342,682 stars (see Buder *et al.* 2018).* Additional information about sample selection from the GALAH DR2 catalogue are provided in Chapter 3, 4 and 5.

More recently published third data release of the GALAH survey (hereafter GALAH DR3) provides stellar parameters and elemental abundances of about 30 chemical species derived from 678,423 spectra for 588,571 unique stars observed between November 2013 and February 2019 (see Buder *et al.* 2021, for more detail on the data release).† This catalogue also includes abundances derived for each individual line for all the elements. More details about the sample selection from the GALAH DR3 catalogue are provided in Chapter 7 and 10.

2.1.2.3 LAMOST survey

The Large Sky Area Multi-Object Fibre Spectroscopic Telescope (LAMOST) survey is a spectroscopic survey of millions of stars from the LAMOST, also known as the Guo Shoujing Telescope (named after the famous Chinese astronomer Guo Shoujing from the 13^{th}-century; see Zhao *et al.* 2012, for more details). In our work, we make use of a catalogue of stellar parameters and abundances of about six million stars provided by Xiang *et al.* (2019) based on the fifth data release of the LAMOST survey (hereafter we refer to catalogue by LAMOST DR5).‡ The catalogue provides abundances of 16 elements (C, N, O, Na, Mg, Al, Si, Ca, Ti, Cr, Mn, Fe, Co, Ni, Cu, and Ba) of about 6 million stars from $\sim$ 8 million

*The GALAH DR2 data is publicly available at `https://datacentral.org.au/teamdata/GALAH/public/GALAH_DR2/`

†The GALAH DR3 data is publicly available at `https://cloud.datacentral.org.au/teamdata/GALAH/public/GALAH_DR3/`

‡The LAMOST DR5 catalogue is publicly available at `http://dr5.lamost.org/doc/vac`.

low-resolution (R $\sim$ 1800) spectra from the fifth data release. Abundances were extracted from the LAMOST spectra using training sets of high-resolution spectra provided by GALAH and Sloan Digital Sky Survey's Apache Point Observatory Galactic Evolution Experiment (APOGEE) abundances (see Xiang *et al.* 2019, for more details). More details on sample selection from the LAMOST DR5 survey are provided in Chapters 4 and 7.

2.1.2.4 RAVE survey

The Radial Velocity Experiment (RAVE) is a ground-based magnitude-limited spectroscopic survey of randomly selected MW's stars from the southern hemisphere (Steinmetz *et al.* 2006; Munari *et al.* 2014). Observations are conducted using the 1.2-meter UK Schmidt Telescope (UKST) of the Australian Astronomical Observatory (AAO). From the start of observations on 12 April 2003 to completion on 4 April 2013, about half a million stars were observed in the spectral region (8410–8750 Å) covering the CaII triplet with an effective spectral resolution, R $\sim$ 7500. In our work, we have used the RAVE survey's fifth data release (hereafter RAVE DR5), which includes stellar parameters, RVs and individual elemental abundances of Mg, Al, Si, Ca, Ti, Fe, and Ni, of 457,588 unique stars from 520,781 spectra (Kunder *et al.* 2017).[§]

2.2 Methodology

This section provides a brief introduction to various methods, techniques and calculations of various secondary parameters (estimated based on primary data from data sources discussed in the previous section) we have used in this thesis.

[§](The RAVE survey data is publicly available at RAVE project website `https://www.rave-survey.org/`

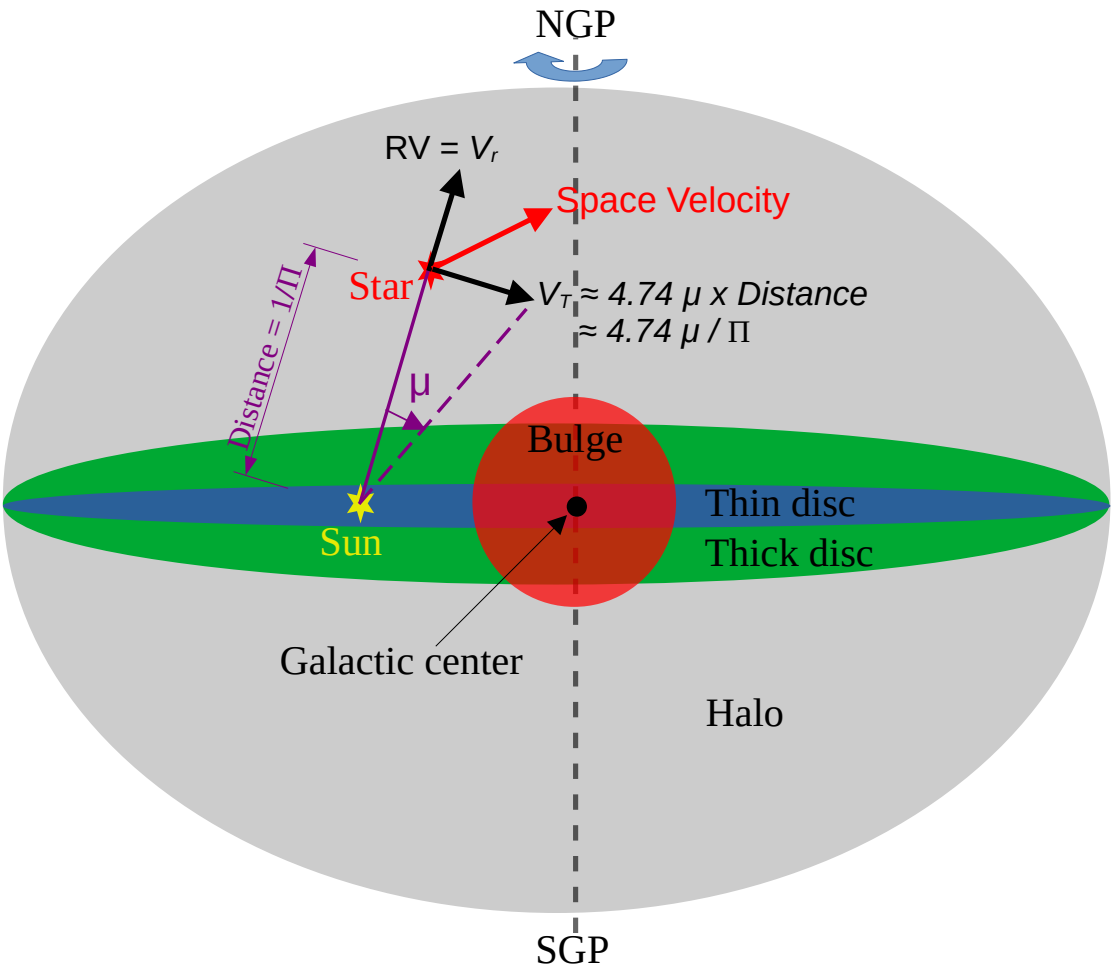


FIGURE 2.2: Cartoon illustration showing the relationship between a star's space velocity and the astrometric parameters (like, parallax Π and proper motion μ) measured by the *Gaia* satellite. Here, V_r is the radial component of space velocity and is well known as the LoS radial velocity (RV), while V_T is the tangential component of space velocity. $V_T \approx 4.74\mu/\Pi$, where μ and Π are the star's proper motion and parallax in mas per year, respectively. A cartoon of the MW with its four major components is also shown in the background. NGP and SGP stand for the north and south galactic poles, respectively.

2.2.1 Stars' galactic space velocities

Stellar kinematics is one of the critical ingredients needed in chemo-dynamical studies of the Galaxy. With the availability of highly precise five-parameter astrometric solution from the *Gaia* survey along with RVs either from *Gaia* or from medium to high-resolution spectroscopic surveys like the GALAH, stars' space

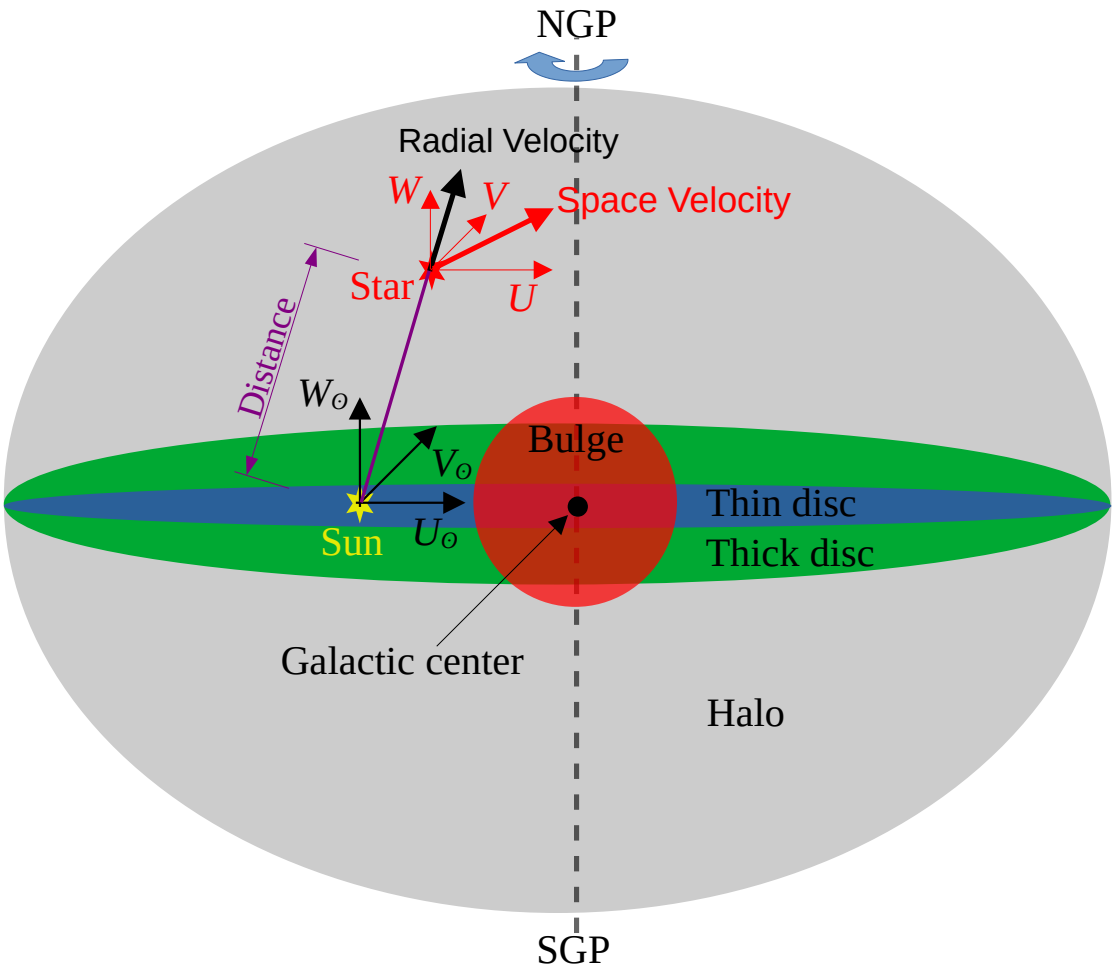


FIGURE 2.3: Cartoon illustration showing the U, V, W components of a star's Galactic space velocity with respect to the centre of the solar system. Components of the Sun's velocity with respect to the local standard of rest (LSR) are also shown. A cartoon of the MW with its four major components is shown in the background.

velocity can be estimated. The cartoon illustration in Figure 2.2 shows the relationship between a star's space velocity and the astrometric parameters (like, parallax Π and proper motion μ) measured by the *Gaia* satellite. The star's space velocity's radial component (i.e., line of sight radial velocity, RV) is determined spectroscopically by estimating Doppler shift to the observed spectra. However, calculating the transverse component (V_T) of the space velocity is difficult and precise measurements of the star's distance and proper motion (μ) are needed. Thanks to the *Gaia* satellite, now we have precise estimates of parallax (Π) and proper

motion ($\mu = \sqrt{\mu_\alpha^2 + \mu_\delta^2}$) for about 1.5 billion stars. Based on simple trigonometric relation, we can write $V_T \approx 4.74 \times \mu/\Pi$, where both μ and Π are in mas per year and V_T is in km s^{-1}.

For simplicity and easier interpretation when handling the space velocities of a large sample of stars, the Milky Way's Galactic coordinate system is used. In this coordinate system, the space velocity's components are designated U, V, and W, with U, V, and W positive in the direction of the GC, Galactic rotation, and north galactic pole (NGP), respectively (see Figure 2.3). For calculation of these space velocity components, we use the following transformations relations from Johnson and Soderblom (1987).

$$\begin{bmatrix} U \\ V \\ W \end{bmatrix} = B. \begin{bmatrix} V_r \\ k\mu_\alpha/\Pi \\ k\mu_\delta/\Pi \end{bmatrix} \tag{2.1}$$

where,

$$B = \begin{bmatrix} -0.06699 & -0.87276 & -0.48354 \\ +0.49273 & -0.45035 & +0.74458 \\ -0.86760 & -0.18837 & +0.46020 \end{bmatrix} \cdot \begin{bmatrix} \cos\alpha\cos\delta & -\sin\alpha & -\cos\alpha\sin\delta \\ \sin\alpha\cos\delta & \cos\alpha & -\sin\alpha\sin\delta \\ \sin\delta & 0 & \cos\delta \end{bmatrix} \tag{2.2}$$

k=4.74057, V_r is the radial velocity (km/sec), Π is parallax (mas yr^{-1}), α and δ are RA and DEC, and μ_α and μ_δ are proper motion along RA and DEC in mas per year.

The expression for the uncertainties in the galactic space velocity components are the following:

$$\begin{bmatrix} \sigma_U^2 \\ \sigma_V^2 \\ \sigma_W^2 \end{bmatrix} = C \begin{bmatrix} \sigma_{V_r}^2 \\ (k/\Pi)^2[\sigma_{\mu_\alpha}^2 + (\mu_\alpha \sigma_\Pi/\Pi)^2] \\ (k/\Pi)^2[\sigma_{\mu_\delta}^2 + (\mu_\delta \sigma_\Pi/\Pi)^2] \end{bmatrix} + 2\mu_\alpha \mu_\delta k^2 \sigma_\Pi^2/\Pi^4 \begin{bmatrix} b_{12}.b_{13} \\ b_{22}.b_{23} \\ b_{32}.b_{33} \end{bmatrix} \tag{2.3}$$

where, the elements of the matrix C are the square of the individual elements of B, i.e. $c_{ij} = b_{ij}^2$ for all i and j. $\sigma_{V_r}, \sigma_\alpha, \sigma_\delta, \sigma_{\mu_\alpha}, \sigma_{\mu_\delta}$ are errors in radial velocity, RA, DEC, proper motion μ_α and proper motion μ_δ, respectively.

These components are relative to the Solar system, which itself is moving at a peculiar velocity with respect to the LSR (e.g., Dehnen and Binney 1998; Francis and Anderson 2009). Let $U_\odot$, $V_\odot$, and $W_\odot$ are the components of the Sun's velocity relative to the LSR and $\sigma_{U_\odot}$, $\sigma_{V_\odot}$, and $\sigma_{W_\odot}$ are corresponding uncertainties, then the star's velocity components relative to the LSR are given by

$$\begin{bmatrix} U_{\rm LSR} \\ V_{\rm LSR} \\ W_{\rm LSR} \end{bmatrix} = \begin{bmatrix} U \\ V \\ W \end{bmatrix} + \begin{bmatrix} U_\odot \\ V_\odot \\ W_\odot \end{bmatrix} \tag{2.4}$$

and corresponding uncertainties are,

$$\begin{bmatrix} \sigma_{U_{\rm LSR}} \\ \sigma_{V_{\rm LSR}} \\ \sigma_{W_{\rm LSR}} \end{bmatrix} = \begin{bmatrix} \sqrt{\sigma_U^2 + \sigma_{U_\odot}^2} \\ \sqrt{\sigma_V^2 + \sigma_{V_\odot}^2} \\ \sqrt{\sigma_W^2 + \sigma_{W_\odot}^2} \end{bmatrix} \tag{2.5}$$

2.2.2 Stars' kinematic membership probabilities

As discussed in the previous chapter, on average, stars from the different components of the Galaxy have distinct kinematics and collectively follow approximately Gaussian distributions. The star's probability in these components can be estimated using these distribution functions and the estimated value of the star's space velocity. For estimating these probabilities, we adopt the methodology used in previous studies like Bensby *et al.* (2003); Reddy *et al.* (2006). Similar to previous studies, we assume that our sample is a mixture of the three populations (think disc, think disc and halo). Kinematic definitions, i.e., the values of the characteristic mean velocity dispersion (D_U, D_V, and D_W) and the asymmetric drift velocities V_{ad} relative to the LSR for the three major Galactic components are tabulated in Table 2.2.2 and are adopted from previous studies Bensby *et al.* (2003); Reddy *et al.* (2006). The relative fractions (f_i) of the thin disc, thick disc and halo stars in the GALAH survey sample are adopted from Bland-Hawthorn *et al.* (2014).

TABLE 2.1: Kinematic definitions, i.e. characteristic velocity dispersion (D_U, D_V, and D_W) and the asymmetric drift velocities V_{ad} relative to local standard of rest for the Galactic thin-disc, thick-disc and halo, adopted from Bensby *et al.* (2003); Reddy *et al.* (2006). Relative number density (f_i) of the Galactic thin-disc, thick-disc and halo stars in the GALAH survey sample is adopted from Bland-Hawthorn *et al.* (2014).

Component	Index, i	D_{U_i}	D_{V_i}	D_{W_i}	V_{ad_i}	Relative fraction, f_i
Thin disc	1	43	28	17	-9	0.75
Thick disc	2	67	51	42	-48	0.24
Halo	3	131	106	85	-220	0.01

Expressions for the star's probability to be in the thin disc ($P_{\rm thin}$), the thick disc ($P_{\rm thick}$), or the halo ($P_{\rm halo}$) are:

$$\begin{aligned} P_{\rm thin} &= f_1 \frac{P_1}{P} \\ P_{\rm thick} &= f_2 \frac{P_2}{P} \\ P_{\rm halo} &= f_3 \frac{P_3}{P} \end{aligned} \tag{2.6}$$

where,

$$P = \sum_{i=1}^{3} f_i P_i \tag{2.7}$$

$$P_i = K_i exp\left[-\frac{U_{LSR}^2}{2D_{U_i}^2} - \frac{(V_{LSR} - V_{ad_i})^2}{2D_{V_i}^2} - \frac{W_{LSR}^2}{2D_{W_i}^2} \right] \tag{2.8}$$

and

$$K_i = \frac{1}{(2\pi)^{3/2} D_{U_i} D_{V_i} D_{W_i}} \qquad (i = 1, 2, 3) \tag{2.9}$$

2.2.3 Orbital properties of stars

Properties of stars' orbit about the Galactic centre can provide a great deal of information about their origin. For estimation of sample stars' orbital parameters, we used `galpy`, a `Python` package for galactic-dynamics calculations (Bovy 2015; Mackereth and Bovy 2018).[¶]. We used `galpy`'s version `v1.7`. For each of the sample stars, we integrated the orbit in `McMillan17` potential (McMillan 2017) for 10 Gyr at 1 Myr intervals by specifying the observed quantities (like astrometric parameters and RV) as the initial conditions using `radec=True`. (The choice of the Galactic potential leads to significant differences in the estimated orbital parameters. For example, `MWPotential2014` potential (Bovy 2015) results in an offset of about 10^5 km^2 s^{-2} in the estimated orbital energies (see, for example Feuillet *et al.* 2020) along with a large fraction of sample stars with positive energies when compared to the energies based on `McMillan17` potential, which is commonly used

[¶]The `galpy` Code is available at `http://github.com/jobovy/galpy`

in more recent studies.) The astrometric input parameters (i.e., stars' spatial positions, proper motions, and parallax) are taken from the *Gaia* catalogue, while RV is from the ground-based spectroscopic survey as *Gaia*'s RV are available for a relatively small fraction of our sample stars. The output provides several orbital parameters like pericenter and apocenter radii ($R_{\rm peri}$ and $R_{\rm apo}$, respectively), eccentricity (e), the maximum vertical distance from the Galactic plane ($|Z_{\rm max}|$), angular momentum components along X, Y, Z-axis (i.e., L_X, L_Y, L_Z), total orbital energy (E), etc., along with the galactic space velocities (U, V, W) for each of the sample star.

2.2.4 Stellar ages and mass

Stellar ages and masses are two other key parameters needed to understand the origin scenarios of different stellar populations. They hold information like when stars were formed and in what kind of environment (i.e., information regarding gas density). Age and mass are estimated using the *qoyllur-quipu* or `q`^{2} code which is a `Python` based package developed by Ivan Ramirez for determining the stellar parameters (see Ramírez *et al.* 2014, for more details).[‖] This code provides estimates of stellar ages based on Yonsei-Yale isochrons (see Yi *et al.* 2001; Kim *et al.* 2002, for more details) and combination of input stellar-parameters like star's temperature, luminosity, log$g$, metallicity, etc. along with their respective errors. `q`^{2} can be used in two different modes: *plx*-mode and *logg*-mode. In the case of *plx*-mode, the required input stellar parameters are the star's temperature, parallax, apparent V-band magnitude, and metallicity. While in the case of *logg*-mode, the needed input stellar parameters are the star's temperature, log$g$, and metallicity. For our work, we used the `q`^{2} code in the *plx*-mode. The required stars' apparent V-band magnitudes are calculated from the *Gaia*'s G-band magnitudes based on conversion formulas provided by the *Gaia Collaboration* (see Evans *et al.* 2018).

[‖] The `q`^{2} code is available at `https://github.com/astroChasqui/q2`

Stars' total metallicity, [M/H], and corresponding error $\sigma_{[\mathrm{M/H}]}$ are estimated by accounting for α-enhancement using following expression from Salaris *et al.* (1993):

$$[\mathrm{M/H}] = [\mathrm{Fe/H}] + \log\left[C \cdot 10^{[\alpha/\mathrm{Fe}]} + (1 - C)\right] \tag{2.10}$$

$$\sigma_{[\mathrm{M/H}]} = \sqrt{\sigma^2_{[\mathrm{Fe/H}]} + \left(\frac{C \cdot 10^{[\alpha/\mathrm{Fe}]}}{C \cdot 10^{[\alpha/\mathrm{Fe}]} + (1 - C)}\right)^2 \cdot \sigma^2_{[\alpha/\mathrm{Fe}]}} \tag{2.11}$$

where, $C = 0.638$, and [Fe/H] and [α/Fe] are taken from the spectroscopic survey like the GALAH and LAMOST (depending on the study). $\sigma_{[\mathrm{Fe/H}]}$ and $\sigma_{[\alpha/\mathrm{Fe}]}$ are the SD in [Fe/H] and [α/Fe], respectively, are also taken from the corresponding survey. Finally, from the outputs, the stars' mean age and corresponding standard deviation (SD) are used for further study. (More details about errors estimated ages are provided in the corresponding chapter.)

With the availability of accurate distance, photometry and stellar parameters, stellar masses can also be estimated using well-known mass-luminosity-gravity-temperature relation $log(M/\mathrm{M}_\odot) = log(L/\mathrm{L}_\odot) + logg - log\mathrm{g}_\odot + 4 \times log(\mathrm{Teff}_\odot/\mathrm{T}_{\mathrm{eff}})$, where, $\log g_\odot = 4.44$ dex and $\mathrm{Teff}_\odot = 5772$ K for the solar values. Values of effective temperature, T_{eff}, and logarithmic surface gravity, $\log g$, are adopted from the spectroscopic survey (depending on the study) and the values of luminosities are based on parallaxes and apparent magnitudes taken from the *Gaia* catalogue. (More details on the determination of masses using this method are available in Chapter 4.)

Stellar masses and ages can also be determined to very high precision using asteroseismic data (see Chapter 6 for more details). However, due to the limited availability of asteroseismic data, mass and age using this method can only be

calculated for a very small fraction of giant stars.

2.2.5 Stellar evolutionary models

As discussed in the previous chapter (1), stars play a very crucial role in the evolution of galaxies. Hence, it is of great interest to understand their evolution. For this, we used the `MESA` suite of computer programmes (Paxton *et al.* 2011, 2013, 2015, 2018, 2019). For more details see Chapter 6 and 7.

2.3 Radial Velocity Comparison of *Gaia* DR2 and RAVE DR5 Survey: A Systematic Offset in Radial Velocities among a Group of Highly Accurate Radial Velocity Stars**

The *Gaia* DR2 provides median radial velocity (over 22 months) of about 7.2 million stars (Gaia Collaboration *et al.* 2018b). The radial velocities are determined with the Radial Velocity Spectrometer (8450 -8720Å) having a spectral resolution of R $\sim$ 11,700 (RVS; Katz *et al.* 2019; Cropper *et al.* 2018). The typical uncertainty in radial velocities is within 2 km s^{-1}. On the other hand, the Radial Velocity Experiment (RAVE) is a ground-based magnitude-limited survey of stars (see Section 2.1.2.4 for more details). The selection criteria and the magnitude distribution have been discussed in Steinmetz *et al.* (2006) and in Munari *et al.* (2014), respectively. Spectral region (8410-8750 Å) with effective spectral resolution, R = $\lambda/\Delta\lambda \sim$ 7,500 was selected to cover the Ca_{II} triplet which is similar

**The work in this section is published in Deepak and Reddy (2018).

to Gaia's RVS (Steinmetz *et al.* 2006). The fifth data release of the RAVE survey includes radial velocities of 457,588 unique stars from 520,781 spectra, with typical accuracy better than 2 km s^{-1} (Kunder *et al.* 2017).

Radial velocity (RV) is a key parameter along with accurate astrometry for computing a star's kinematics. While selecting a sample of stars from the publication of Gaia DR2 and RAVE DR5, we noticed an offset of about -104 km s^{-1} in radial velocities between the two surveys for a tiny group of stars ($\approx 0.08\%$ of the total stars), although the remaining radial velocities from the two surveys turn out to be in good agreement. Here we highlight the existence of this tiny faulty group and its consequences. We have not attempted to provide solutions for the discrepancy or corrections; rather, we looked at different possibilities that might have caused the offset in radial velocities between the two surveys.

2.3.1 Data Sample

For this study, we adopted radial velocity data directly from a catalogue of stars which resulted from cross-matching of RAVE DR5 and Gaia DR2 (rave_DR2_gaia_source.csv available at *Rave survey website* (`https://www.rave-survey.org/`) and added RAVE DR5 table to this using RAVE_OBS_ID (Unique Identifier for RAVE objects, Observation Date, Fieldname, Fibernumber). We took only those stars that are common in the two surveys and for which both the radial velocities (RV_{RAVE} and RV_{Gaia}) are available. This resulted in 456,316 stars out of the total number of 512,971 stars.

2.3.2 Analysis

Radial velocity data of all the common stars between the two surveys is shown in Figure 2.4*a*. Though most RV values agree well with each other; there are a number of stars for which differences between the two surveys are quite large, at the central portions in particular (see Figure 2.4*a*). Both the surveys provide RV along with the formal error, $\sigma_{\rm RV}$, which are measures of how well the cross-correlation of their spectrum is against the template spectrum. RAVE DR5 also provides standard deviation (SD) (it is not the same as $\sigma_{\rm RV}$) and the median absolute deviation (MAD), which provide independent measures of the $\rm RV_{RAVE}$ uncertainties calculated by re-sampling a spectrum ten times (for more details see Kunder *et al.* 2017). On checking, we found that these stars are the reason for the very large scatter at the central portions, as shown in Figure 2.4*a*. Considering the typical accuracy of $\rm RV_{RAVE}$ in RAVE survey, which is better than 2 km s^{-1} (Kunder *et al.* 2017), we excluded all those stars from the sample for which $\rm SD(RV_{RAVE}) >$ 2 km s^{-1} and $\rm MAD(RV_{RAVE}) > 2$ km s^{-1}. This resulted in a total of 448,726 stars from RAVE DR5. The resultant data set of radial velocities from RAVE DR5 is compared in Figure 2.4*b* with corresponding values of $\rm RV_{Gaia}$ from Gaia. Larger scatter that is present in Figure 2.4*a* is almost absent in Figure 2.4*b*. But one can notice a sharp line parallel to the central line of the majority of stars for which RV values in both the catalogues are in good agreement.

To further cull out the data with relatively large uncertainties (see Figure 2.4*b*) and to retain good quality radial velocities, we chose only those stars from both the surveys that have $\sigma_{\rm RV}$ values either maximum of 2 km s^{-1} (for retaining stars with small RV) or maximum percentage error of 2% (for retaining stars with larger RV) from both the catalogs. These filters yielded a sample of 322,878 stars. Figure 2.4*c* shows distribution of $\rm RV_{Gaia}$ and $\rm RV_{RAVE}$ velocities. In this figure, the parallel line substructure along with the central line (where the majority of sample stars are lying) is clearly visible. The distribution of differences in $\rm RV_{Gaia}$ and $\rm RV_{RAVE}$

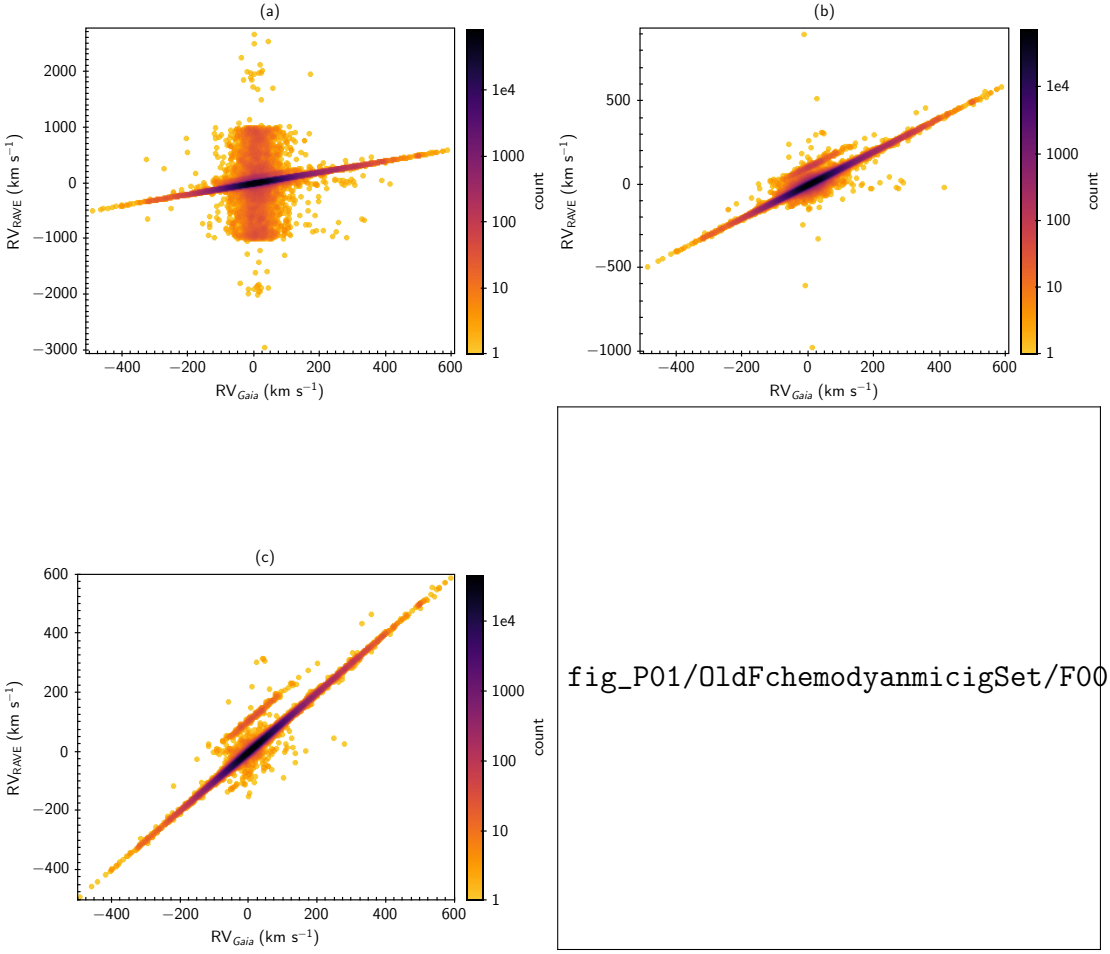


FIGURE 2.4: Distribution of RV_{RAVE} and RV_{Gaia} velocities for RAVE DR5 and Gaia DR2 cross-matched data with (*a*) no error limit, (*b*) $SD(RV_{RAVE}) \leq 2$ km s^{-1}, $MAD(RV_{RAVE}) \leq 2$ km s^{-1}, (*c*) $SD(RV_{RAVE}) \leq 2$ km s^{-1}, $MAD(RV_{RAVE}) \leq 2$ km s^{-1}, and cross-correlation error (σ_{RV}) ≤ 2 km s^{-1} or 2% in RV_{Gaia} and RV_{RAVE}. (*d*) A section of the normalized histogram of difference in RV_{Gaia} and RV_{RAVE}. The histogram is normalized with respect to the maximum count, and the bin size used is 2 km s^{-1}.

is shown as a normalized histogram (Figure 2.4*d*).

Based on Figure 2.4*c* and Figure 2.4*d*, we divide the entire sample into three groups: (*1*) **Group-01:** the majority group consisting of 322,449 stars with a mean difference ($RV_{Gaia} - RV_{RAVE}$) of 0.28 km s^{-1} with a spread given by σ= 1.49 km s^{-1} (Figure 2.5), (*2*) **Group-02:** a small group consisting of about 272 stars with a large offset between RV_{Gaia} and RV_{RAVE}, the normal distribution for the

difference in RV_{Gaia} and RV_{RAVE} velocities is given in Figure 2.5, which shows that the mean difference between the velocities is -104.50 km s^{-1} with spread given by $\sigma = 4.92$ km s^{-1}, and (*3*) **Group-03:** the remaining 156 stars, which lie on either side of the main group distribution.

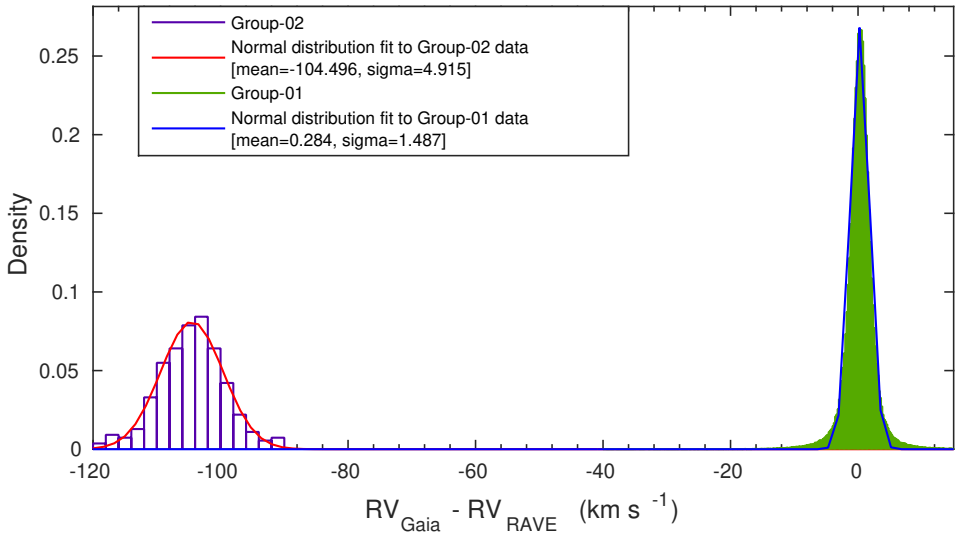


FIGURE 2.5: Normalized distribution and corresponding normal distribution fit of difference in velocities for Group-01 and Group-02 stars. Histogram bin size for Group-01 and Group-02 are 0.2 km s^{-1} and 2 km s^{-1} respectively, and are in agreement with Freedman-Diaconis rule.

In general, one would expect a distribution in differences in high-quality radial velocities between the two surveys similar to the main group (Group-01). However, the large offset of -104 km s^{-1} between the two surveys for the small group (group-02) is surprising. There is a possibility of mistakenly matching fore or background stars. For making sure that the V_{rad} values of the sample under consideration are, in fact, of the same stars in the respective surveys, we compared the star's magnitudes and positions between the two surveys. To eliminate this possibility, we made sure that the apparent magnitudes of common stars are the same or within reasonable limits. But the problem is that the photometric passbands used for apparent magnitude measurements are not common in the two surveys. Gaia DR2 provides photometric G, G_{BP}, and G_{RP}-band magnitudes in

wavelength bands of [330-1050] nm, [330-680] nm, and [630-1050] nm respectively (Jordi *et al.* 2010b). RAVE does not have its own measurements, but it has magnitudes collected from various surveys such as Hipparcos, TYCHO2 and APASS. Of all, the AAVSO Photometric All-Sky Survey (APASS) Data Release 9 (DR9) is the most comprehensive and precise, with two Johnson broadband filters (B and V) and three Sloan filters. Survey is complete from 7 to 17^{th} V-magnitude, hereafter $V_{\rm j,APASS}$ (Henden *et al.* 2015). Cross-match between APASS and RAVE has been discussed in Munari *et al.* (2014). To compare $V_{\rm j,APASS}$ with Gaia's magnitude, both of these need to be put on the same scale. We converted Gaia's G-band photometric magnitudes to Johnson V magnitude (hereafter $V_{\rm j,Gaia}$) using conversion formulas provided by Gaia Collaboration (Evans *et al.* 2018).

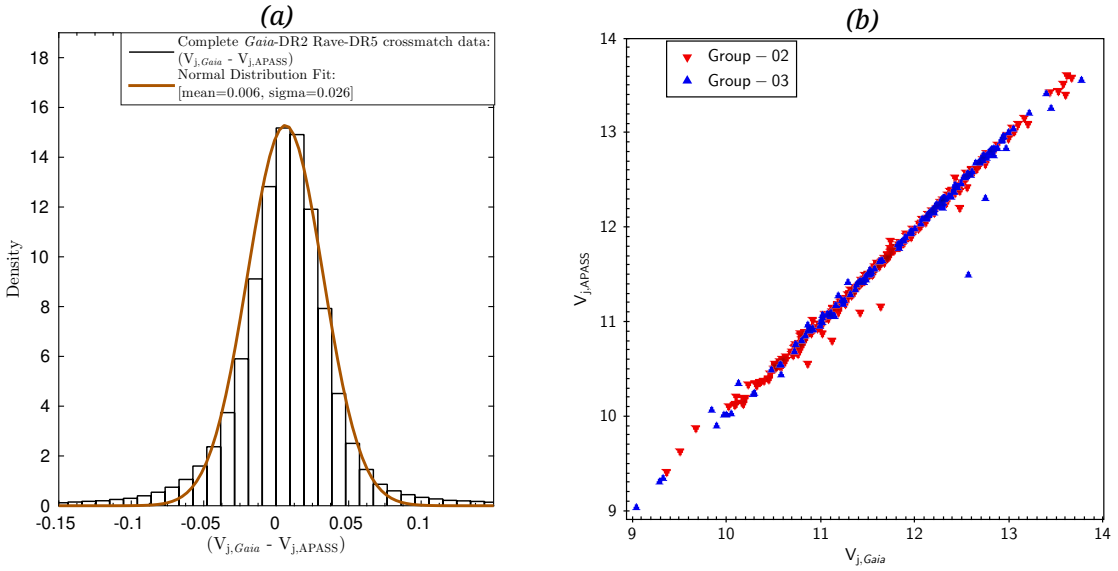


FIGURE 2.6: (*a*) Distribution of the difference between $V_{\rm j,Gaia}$ and $V_{\rm j,APASS}$ for all the Gaia DR2 and RAVE DR5 cross-matched stars for which both $V_{\rm j,Gaia}$ and $V_{\rm j,APASS}$ are available (441,106 stars), and corresponding normal distribution fit. (*b*) Distribution of $V_{\rm j,APASS}$ and $V_{\rm j,Gaia}$ for stars belonging to Group-02 (red) and Group-03 (blue). Here, $V_{\rm j,Gaia}$ is calculated from Gaia's G-band magnitudes and $V_{\rm j,APASS}$ is provided in RAVE DR5.

In Figure 2.6, we plotted the distribution of magnitude difference ($V_{\rm j,Gaia} - V_{\rm j,APASS}$) for the entire sample of stars for which magnitudes are available in both the surveys. The distribution shows that the magnitudes in both the surveys agree well with a mean difference of 0.006 with sigma = 0.026 (see Figure 2.6*a*). Magnitude

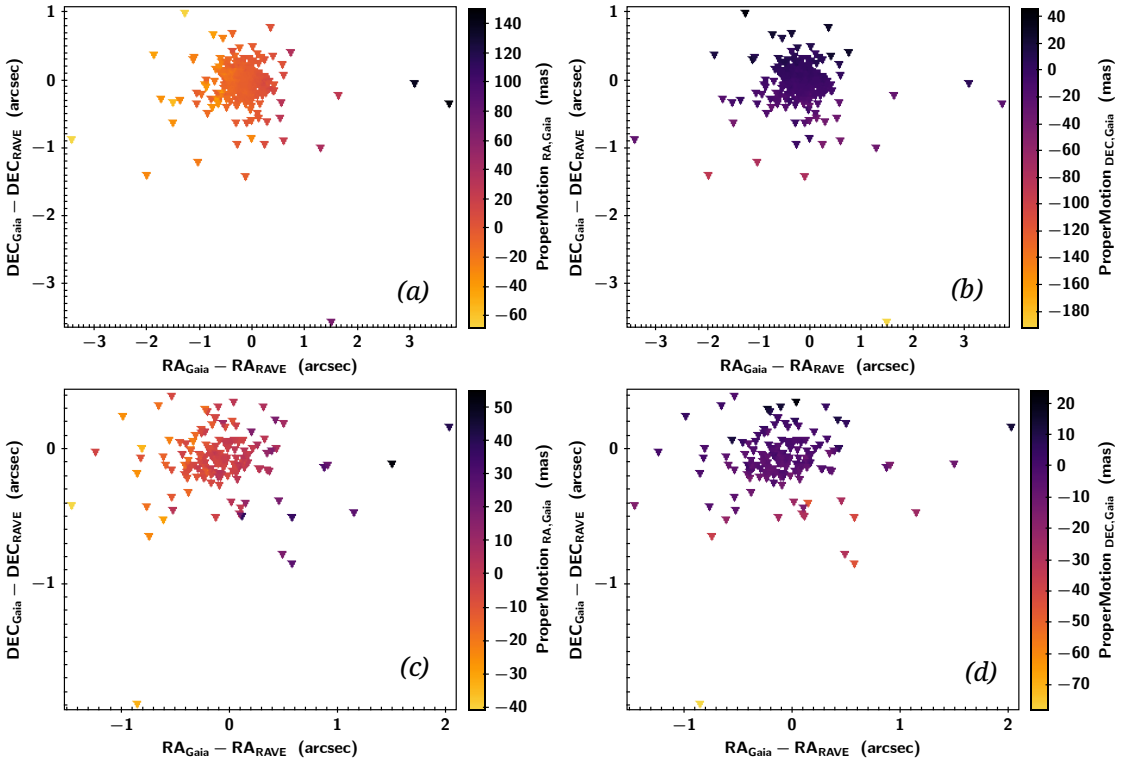


FIGURE 2.7: Distribution of difference in position coordinates of Group-02 stars from Gaia DR2 and RAVE DR5 catalog when corresponding proper motions (pm) from Gaia DR2 along (a) right ascension (RA), and (b) declination (DEC) are used as weights. Distribution of difference in position coordinates of Group-03 stars from Gaia DR2 and RAVE DR5 catalog when corresponding proper motions (pm) from Gaia DR2 along (c) right ascension (RA), and (d) declination (DEC) are used as weights.

agreement between the two data sets with the exemption of a couple of outliers (Figure 2.6b) validates the cross-matching of stars in the two surveys provided by RAVE. This shows that the systematic difference in RV is not an artifact arising from a mismatch of stars between the two surveys. For stars of Group-01 and Group-02, comparison of positions of stars (RA & DEC) in the surveys are given in Figure 2.7a, 2.7b and Figure 2.7c, 2.7d respectively. The difference in position is quite small, except in cases where stars have comparatively large proper motion. Given the different epochs of surveys, such small differences in position are expected.

Of 272 stars in Group2, there are 51 stars for which radial velocities are given

in RAVE DR5 from more than one spectrum observed at different times. Out of these 51 stars with multiple spectra, on checking RV for the same star from different RAVE observations, we found that 50 stars have at least one spectrum which gave almost similar values as RV_{Gaia} along with the ones which gave a difference of approximately -104km/sec. Exception is the star 'Gaia DR2 5913047541322494080' for which the two listed velocities in RAVE DR5 from two different spectras ('20100803_1726m56_003' and '20100731_1726m56_003') differ from that of RV_{Gaia} by approximately -107 km s^{-1}. Our understanding is that the same reduction methodology was used to derive the radial velocities from the multiple spectra for the same star, and yet for a small group, there seems to be a problem.

2.3.3 Discussion

The relatively small spread in radial velocities in the case of the main group (i.e. Group-01) is probably due to intrinsic errors related to different instrumental setups and measurement methods. One also cannot rule out the possibility of such differences as a result of measuring intrinsic random motions of stars, including low-amplitude pulsations (both radial and non-radial) frequently present on giant stars, the spectroscopic binaries and gravitational redshifts at two different epochs (Lindegren and Dravins 2003). The Gaia DR2 data provides median radial velocities averaged over the first 22 months of observations since its launch in July 2014. On the other hand, RAVE velocities are from the spectra observed from April 2003 to April 2013. The two surveys measured radial velocities in a time difference of about 2 to 12 years.

However, it is not clear why such a large offset exists for stars of Group-02 between the two surveys. Though the fraction of faulty stars form a very small percentage

($\approx 0.08\%$) of the total sample of highly accurate radial velocity stars considered, it is important to highlight the issue of discrepancy to avoid misleading results. For example, Kinematic velocities (U, V, W) computed using RV values from RAVE DR5 and Gaia DR2 for Group-02 stars differ significantly.

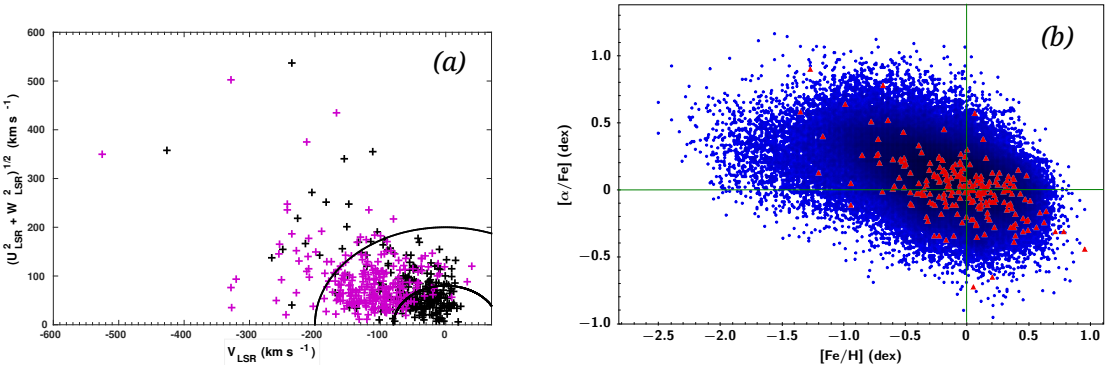


FIGURE 2.8: (a) Toomre diagram for stars in Group-02 with kinematics deduced using RV_{Gaia} (black) and RV_{RAVE} (magenta). The two concentric circles delineate constant peculiar velocities ($V_{tot} = (U^2_{LSR} + V^2_{LSR} + W^2_{LSR})^{1/2}$) of 80 km s^{-1} and 200 km s^{-1}, and represent kinematic boundary for thin disc ($|V_{tot}| <$ 80 km s^{-1}), thick disc (80 $< |V_{tot}| <$ 200 (km s^{-1})) and halo ($|V_{tot}| >$ 200 (km s^{-1})) which are in accordance with results in Reddy *et al.* (2006). (b) Distribution of [α/Fe] with respect to [Fe/H] of Group-02 stars (red) with Group-01 in background (blue). Measurements of [α/Fe] are given in RAVE DR5, and out of 272 stars of Group-02, both [α/Fe] and [Fe/H] are available for 227 stars which are plotted here.

Probabilities computed based on the two different sets of kinematics using the recipe given in Reddy *et al.* (2006) lead to different Galactic components to which stars belong. Stars' kinematics based on RV_{Rave} suggest that most of the stars belong to the thick disc. On the other hand, the kinematics based on RV_{Gaia} values suggest that most of the stars belong to the Galactic thin disc component. This has been illustrated in Figure 2.8a in the form of the Toomre diagram, which represents the relationship between the sum in quadrature of the vertical and radial velocities (i.e. kinetic energy) and the rotational velocity (i.e. rotational energy) relative to the LSR (Sandage and Fouts 1987). Star's heliocentric velocities (U, V, W) are corrected for the solar motion (using U_o=10, V_o=5.3, W_o=7.2 (km s^{-1}) from Dehnen and Binney (1998)) to get velocities with respect to the LSR (U_{LSR}, V_{LSR}, W_{LSR}).

TABLE 2.2: RV of three common stars from Gaia, RAVE and LAMOST of Group-02.

Object ID	RV (km s^{-1})			σ_{RV} (km s^{-1})		
Gaia DR2	Gaia	RAVE	LAMOST	Gaia	RAVE	LAMOST
5763571271979913472	60.47	164.54	56.7	0.49	0.78	-
3831262427493102976	79.43	196.79	84.5	1.05	1.57	-
3831274998862303360	21.66	132.48	19.1	1.63	1.48	-

To understand the source for this discrepancy, we examined the star's metallicity ([Fe/H]) provided by RAVE DR5. The distribution shows that the [Fe/H] ranges from -1.2 to $+0.5$ dex (Figure 2.8*b*), which is typical of the Galactic disc metallicity range (Reddy *et al.* 2006). Combined with the available [Fe/H] and kinematics implies that the stars may belong to the Galactic thin disc and the kinematics based on velocities from Gaia seems to be consistent with the star's [Fe/H] distribution. Though the thick disc's [Fe/H] overlaps with the thin disc metallicities, one would expect most of the stars on the metal-poor side beyond -1.2 dex in the case of the thick disc. Another piece of evidence could be α-process elements for distinguishing thin disc stars from thick disc (Reddy *et al.* 2003). Abundances taken from the RAVE survey are plotted against [Fe/H] (Figure 2.8). Though the majority of stars do show normal α-process, it does not provide clear separation.

Further, we searched for radial velocity measurements of Group-02 stars among LAMOST and APOGEE spectroscopic surveys. Unfortunately, we found just three stars that are common with the LAMOST survey. In Table 2.2, we have summarized RV values of these three common stars from all three surveys. LAMOST values match well with those from the Gaia data suggesting that the large offset is probably caused by the RAVE data set.

The more intriguing part is the near constant offset of -104.5 km s^{-1} with a small dispersion. To search for clues for the discrepancy in radial velocity data, we examined whether these stars were of some particular kind or localized in space.

In Figure 2.9*a*, we showed Group-02 & 03 stars superposed with the entire sample as background. Stars are all over the sky without any spatial clustering ruling out the possibility that these stars belong to spatially localized cluster or clusters. We also checked whether these stars are of any particular type. As shown in Figure 2.9*b*, the distribution of stars in the HR diagram suggests that they are uniformly distributed across the stellar evolutionary phases and have no particular trend with either T_{eff} or log g with respect to the main group.

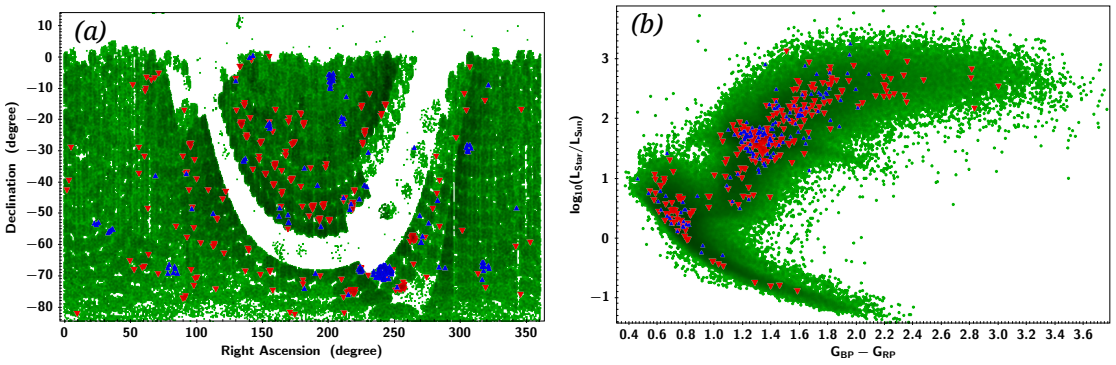


FIGURE 2.9: (*a*) Sky distribution, and (*b*) Color-Luminosity diagram for stars in our sample. Here green, red and blue color represent Group-01, Group-02 and Group-03 stars respectively.

Another possibility may be cluster evaporation, in particular, the short-lived open cluster with loosely bound member stars, which may become disrupted and the member stars escape due to encounters with other massive structures in the galaxy like clusters and clouds of gas, and tidal force in the galactic gravitational field as they orbit the galactic center (Trumpler 1930; Shapley 1930; Wielen 1988)). Members of such open clusters will be spread along the path traced by it and continue to orbit the galaxy with inherited velocities with certain dispersion (Trumpler 1930). However, this will not explain the offset in the difference between the two surveys but will provide a clue that the members might have belonged to a particular group in the past. A closer scrutiny of data reveals that these stars are at different distances ranging from about 80 pc to 3 Kpc, and also do not seem to be kinematically similar as well. Thus, it is unlikely that the offset in difference is due to the stars that belonged to a single group, either in the past or present.

2.3.4 Conclusion

While comparing radial velocity data from the two major surveys, the RAVE and the Gaia, we noticed a significant difference in radial velocity with an offset of -104.5 km s^{-1} for a small group of 272 stars. While kinematics based on RAVE suggest that most of the stars in the group are of the thick disc, velocities from Gaia suggest the stars are of the thin disc. However, the [Fe/H] range of stars in the group from -1.2 to $+0.5$ dex suggests that most of the stars are, in fact, from thin disc origin, agreeing with Gaia velocity data. This is corroborated by LAMOST velocity data for three common stars among the three surveys (i.e., the RAVE, the Gaia and the LAMOST), which are in agreement with Gaia values. Though the source for the offset is not clear, our study suggests that the offset is due to the RAVE data set.

2.4 Resource summary

In this chapter, we discussed the various types of data samples we have used in all the works in this thesis. Brief introductions to sources of these data sets and basic observation techniques are also discussed. Introduction to various methods, techniques and calculations of various secondary parameters needed for chemo-dynamical studies of the Galaxy are also discussed. The adopted methodology and data flow for conducting chemodynamic studies of the Galaxy is summarised in Figure 2.10. In Section 2.3, we have provided a comparison between the RVs from the *Gaia* DR2 and RAVE DR5 Survey. In this study, we found an offset of about -104 km s^{-1} in radial velocities between the two surveys for a tiny group of stars ($\approx 0.08\%$ of the total stars), although the remaining radial velocities from the two surveys turn out to be in good agreement. We have not attempted to provide solutions for the discrepancy; instead looked at different possibilities that

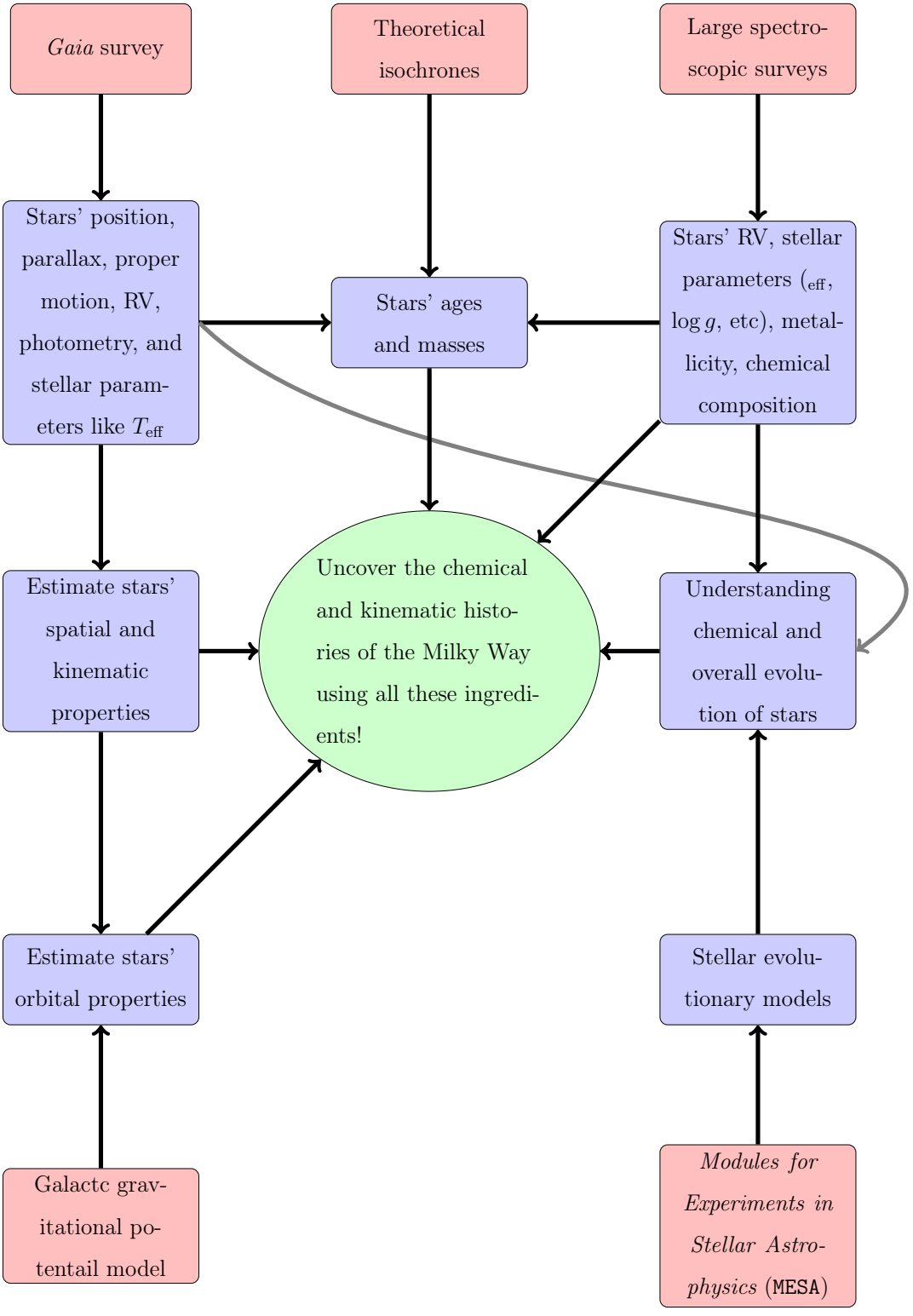


FIGURE 2.10: Flow chart showing methodology and data flow for conducting chemodynamic studies of the Galaxy.

might have caused the offset in radial velocities between the two surveys. We also highlighted the consequences of such discrepancy. This study also covers an additional introduction to *Gaia*'s photometry and provides a demonstration of some of the kinematic techniques, like, quantifying Galactic disc and halo stars based on the distribution in the Toomre Diagram, etc., which are not covered in the earlier sections of this chapter.

Chapter 3

Evolution of Lithium in the Galaxy*

3.1 Introduction

Li is one of the three primordial elements produced in the Big Bang Nucleosynthesis (BBN), apart from H and He. Standard BBN Models, in combination with input parameter value of baryonic density measured from space missions such as the Wilkinson Microwave Anisotropy Probe (WMAP), predict primordial Li abundance of A(Li) = 2.72 ± 0.06 dex (Cyburt *et al.* 2008), about three times higher than the widely suggested primordial Li abundance based on observations of metal-poor dwarfs which is also known as Spite-Plateu, A(Li) = 2.27 ± 0.03 (Lind *et al.* 2009b). The discrepancy between the observed and predicted primordial Li is not very clear. On the other hand, Li abundance measured in young stars, interstellar medium, and meteorites is A(Li) = 3.32 dex, which is about ten times higher than the Li found in metal-poor dwarfs and about three times higher

*This chapter is published in Deepak and Reddy (2020a,b).

than the value predicted by BBN models. This clearly suggests Li enrichment in the Galaxy from its initial value (Guiglion *et al.* 2016). Studies suggest various sources of Li contribution to the Galaxy: cosmic ray spallation in ISM (Mitler 1972), novae explosions (Tajitsu *et al.* 2015) and nucleosynthesis in evolved stars. Here, we briefly discuss Li contribution by stars.

In general, stars are known to be sinks for Li as Li burns at relatively low temperatures of about 2.5×10^6 K, and is sensitive to enhanced mixing during first dredge-up, which leads to rapid dilution of Li in stars' outer envelopes as they evolve from the main sequence. However, under particular conditions, evolved stars such as red giant branch (RGB) stars are known to produce Li in their interiors via the Cameron-Fowler mechanism (Cameron and Fowler 1971). This has been observed in a small group of RGB stars which are known in the literature as Li-rich giants with $A(\mathrm{Li}) \geq 1.5$, an upper limit set by stellar models (Iben 1967). In section 3.3.3 and 3.3.4, we discuss the evolution of Li in the Galaxy at different metallicity.

3.2 Data sample

For this study, we use the second data from the GALAH survey (GALAH DR2), which provides stellar parameters (like the star's surface brigantines temperature, surface gravity and rotational velocity) and quantitatively derived abundances of about 23 elements, including the light element Li, which is the focus of this study, for a sample of 342,682 stars (Buder *et al.* 2018). The sample is searched for corresponding astrometric and photometric data from the second data release of *Gaia* survey (hereafter the *Gaia* DR2), which is a catalogue of about 1.7 billion stars. Source matching is done using the *Gaia* DR2 source identifier provided in the GALAH DR2 data set (see Buder *et al.* 2018; Gaia Collaboration *et al.*

2018b). This resulted in a sample of 340,299 common stars among the two data sets. The provided stellar parameters and abundances in the GALAH's catalogue are derived using the reduction software `Cannon`. In the GALAH DR2, an index of `flag_cannon` against each star, which indicates accuracy or level of confidence in derived stellar parameters, is provided. `flag_cannon` index range from 0 to 128, with 0 being the most reliable, and other numbers indicating issues such as binary companion, fitting accuracies, S/N ratio, etc. (for more details see Buder *et al.* 2018). We restricted our sample to stars with reliable stellar parameters by culling out all the stars with a nonzero value of `flag_cannon`. We further culled out stars for which $\sigma_{T_{\rm eff}} \geq 150\ k$, parallax ($\Pi$) is negative and fractional error in parallax, $\sigma_{\Pi}/\Pi \geq 0.20$ yielding a total sample of 228,753 stars.

We estimated the luminosity for each of the sample stars using the relations given in Andrae *et al.* (2018) and bolometric corrections based on $T_{\rm eff}$ from the GALAH survey. Values of luminosities given in the Gaia and those derived in this study agree well with each other. The difference between the two values is quite small with $\sigma \approx 0.02$ dex. Uncertainties in the derived luminosity values due to errors in parallax and $T_{\rm eff}$ are also estimated and are found to be quite small, typically $\sigma_{L/{\rm L}_{\odot}}$ ≤ 0.05 dex for most of the stars. Using these luminosities, we further estimated the masses of our sample stars using the following well-known mass-luminosity-temperature relationship:

$$\log(M/{\rm M}_{\odot}) = \log(L/{\rm L}_{\odot}) + \log {\rm g} - \log {\rm g}_{\odot} + 4 \times \log({\rm T}_{\rm eff,\odot}/{\rm T}_{\rm eff}) \tag{3.1}$$

where the values of effective temperature, $T_{\rm eff}$, and logarithmic surface gravity, $\log {\rm g}$, are adopted from the GALAH catalog (Buder *et al.* 2018). Also, we used $\log g_{\odot} = 4.44$ dex and ${\rm Teff}_{\odot} = 5772$ K as solar values, which are the same as used in the GALAH survey (Buder *et al.* 2018). We restricted the sample to low-mass stars with $M \leq 2{\rm M}_{\odot}$. This entire sample of low-mass stars plotted in luminosity

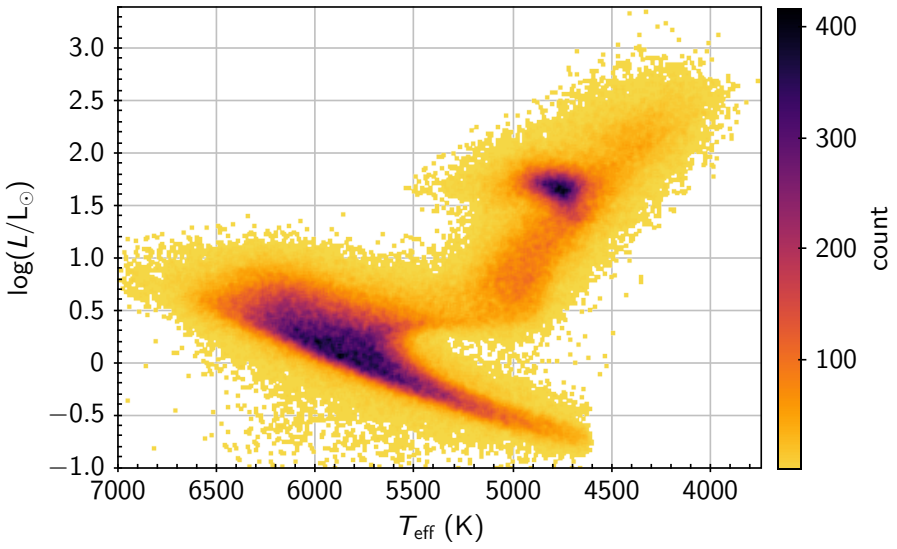


FIGURE 3.1: Sample stars in the HR diagram.

versus temperature diagram (Figure 3.1) shows a well-defined main sequence (MS) and RGB. To study the evolution of Li in the Galaxy, we restrict our sample to MS dwarfs with Teff $>$ 5500 K. Cooler dwarfs (with Teff $<$ 5500 K) are rejected as their spectra are complex and derived abundances may be having large uncertainties. This resulted in a sample of about 60 000 stars.

For each of our sample stars, we also estimated the Galactic space velocity components (U, V, W) using the procedure discussed in Section 2.2.1. We further applied correction for the solar motion from Dehnen and Binney (1998) to estimate the stars' Galactic space velocity components $(U_{\rm LSR}, V_{\rm LSR}, W_{\rm LSR})$ with respect to the local standard of rest (LSR).

3.2.1 Li abundances of sample stars

The GALAH DR2 provides Li abundances in the form of [Li/Fe] (= [Li/H] - [Fe/H], where [Li/H] = A(Li) − $A(\rm Li)_\odot$) along with associated error and a flag indicating the level of confidence in the measured abundance. The GALAH also provides

metallicity, [Fe/H], for all the stars in the catalogue. Commonly, Li abundance is expressed as $A(\mathrm{Li}) = \log[\mathrm{n(Li)/n(H)}]+12$, where n(Li) and n(H) are number Li and H atoms per unit volume, respectively. For a better comparison with the literature, [Li/Fe] values of the GALAH are converted into A(Li) using the expression $A(\mathrm{Li}) = [\mathrm{Li/Fe}] + [\mathrm{Fe/H}] + A(\mathrm{Li})_{\odot}$, where $A(\mathrm{Li})_{\odot}$ is the solar Li abundance. We adopted $A(\mathrm{Li})_{\odot} = 1.05 \pm 0.10$ dex, which is the same one used for the GALAH data (see Buder *et al.* 2018). The corresponding error is $\sigma_{A(\mathrm{Li})} = (\sigma^2_{[\mathrm{Li/Fe}]} + \sigma^2_{[\mathrm{Fe/H}]} + 0.10^2)^{1/2}$.

The level of confidence in measured lithium abundances of the sample has been encoded in the form of a lithium abundance flag (`flag_li_fe`) against each star. `flag_li_fe` index ranges from 0 to 9, with 0 being the most reliable, flag one is raised when line strength is below 2σ, flag two is raised when cannon fitting starts extrapolating, flag three is when both flag one and two are raised, flag four is when χ^2 of the best fitting model spectrum is very high or low, flag eight is raised when `flag_cannon` is not zero, and the remaining flags are combinations of these flags (see Buder *et al.* 2018, for more details). For this study, we restrict our sample to stars with `flag_li_fe` ≤ 3.

3.3 Results and discussion

3.3.1 Sample in the form of the Toomre diagram

The distribution of the selected sample of low-mass dwarfs in the form of the Toomre diagram is shown in Figure 3.2. The Toomre diagram represents the relationship between the quadrature sum of the galactic space velocity's radial and vertical components, $\sqrt{U^2_{\mathrm{LSR}} + W^2_{\mathrm{LSR}}}$ (i.e., kinetic energy), and the rotational component (i.e., rotational energy) with respect to the local standard of rest (Sandage and Fouts 1987). Li abundances of the stars are given as the colour of the data

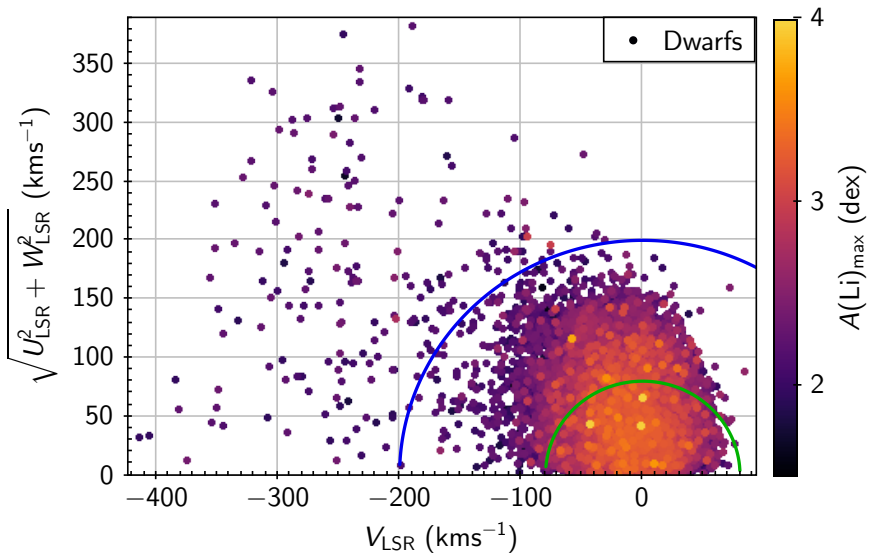


FIGURE 3.2: Distribution of the selected sample of dwarfs in the form of the Toomre diagram. Stars' Li abundance, A(Li), is encoded in the colour of the data point as per the colour bar given on the right side. The green-coloured circular arc, with $V_{\rm total}$ = 80 kms^{-1}, represents the approximate boundaries between the Galactic thin and thick disc, where stars on the inner side of the circle are thin-disc stars while the stars on the outside are thick disc stars. Similarly, the blue-coloured circular arc, with $V_{\rm total}$ = 200 kms^{-1}, represents the approximate boundaries between the Galactic thick disc and halo, where stars on the outer side of the circle are halo stars while stars between the green circle and blue circle are the thick disc stars.

points. Approximate segregation between the Galactic thin-disc, thick disc and halo stars is also provided based on the definitions adopted from literature (e.g., Reddy *et al.* 2006; Gallart *et al.* 2019). In the figure, the green-coloured circular arc, with $V_{\rm total}$ = 80 kms^{-1}, represents the approximate boundaries between the Galactic thin and thick disc, where stars on the inner side of the circle are thin-disc stars while the stars on the outside are thick disc stars. Similarly, the blue-coloured circular arc, with $V_{\rm total}$ = 200 kms^{-1}, represents the approximate boundaries between the Galactic thick disc and halo, where stars on the outer side of the circle belong to the Galactic halo while stars between the green circle and blue circle are the thick disc stars. The figure readily suggests that the Galactic thin disc stars have higher Li than the thick disc and halo stars. The figure also indicates that most of the thick disc stars with high Li abundance are the ones with higher kinetic energy (i.e. larger $\sqrt{U_{\rm LSR}^2 + W_{\rm LSR}^2}$). However, there is no such

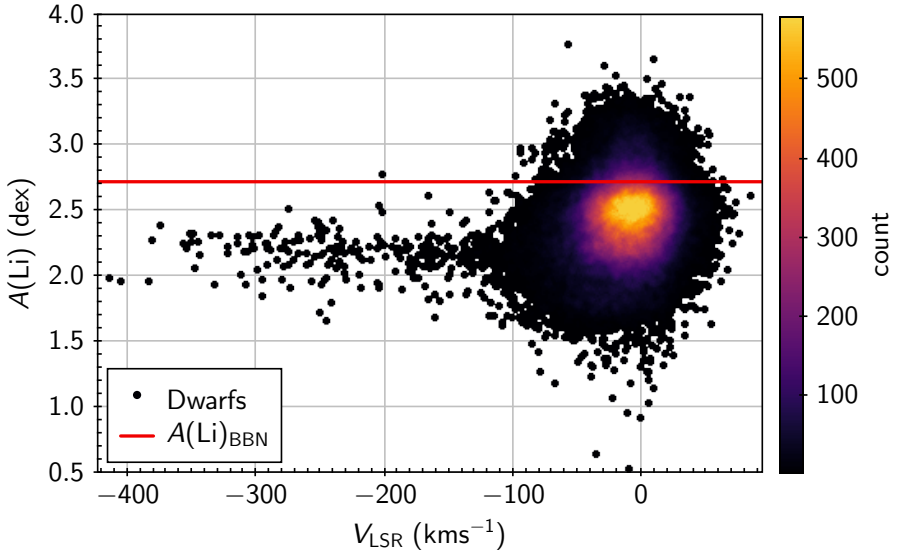


FIGURE 3.3: Li versus galactic rotational velocity $V_{\rm LSR}$ for selected sample of dwarfs. The solid red line at $A(\rm Li) = 2.72$ dex mark the theoretically predicted primordial Li abundances from the standard BBN models.

apparent dependence of Li abundance on kinetic energy or rotational energy in the case of halo stars. This suggests that the Galactic Li enrichment is limited to the disc only.

3.3.2 Li versus rotational velocity

To get a better quantitative estimate of the Li distribution in the Galaxy, in Figure 3.3, we have plotted Li as a function of the galactic rotational velocity. The solid red line at $A(\rm Li) = 2.72$ marks the theoretically predicted primordial Li abundances from the standard BBN models (Cyburt *et al.* 2008; Coc *et al.* 2012). Depending on mass, metallicity and age, stars can deplete their Li during most of their lifetime; hence the upper envelope of the distribution is considered to be the representative of the natal cloud's Li abundance. The figure suggests that most of the halo stars, i.e. the stars having $V_{\rm LSR} \lesssim -200$ kms^{-1}, have a maximum Li abundance of about 2.3 dex, which is about three times lower than the theoretical prediction. This value is in agreement with the Spite plateau

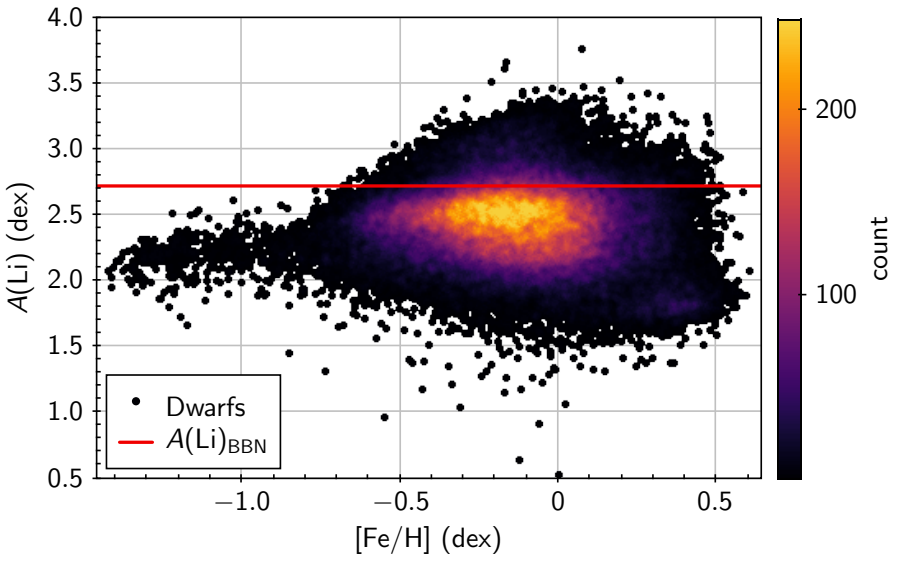


FIGURE 3.4: Li versus [Fe/H] distribution for the selected sample of low-mass dwarfs. The solid red line marks the theoretically predicted primordial Li abundances from the standard BBN models.

from other studies (e.g., Spite and Spite 1982; Lind *et al.* 2009b). This constant plateau-like distribution continues up to around $V_{\rm LSR} \sim -100$ kms^{-1} because of the presence of halo stars with high kinetic energy and old, metal-poor thick disc stars. For $V_{\rm LSR} > -100$, maximum Li abundance increases sharply. This velocity range is dominated primarily by thin-and thick-disc stars with higher kinetic energy (i.e. stars with larger $\sqrt{U^2_{\rm LSR} + W^2_{\rm LSR}}$).

3.3.3 Li versus [Fe/H]

Metallicity [Fe/H] is a good indicator of the Galactic chemical evolution. Hence, the distribution of Li as a function of [Fe/H] can be used to understand the relationship between the evolution of Li and the chemical evolution of the Galaxy. The distribution of Li abundance as a function of [Fe/H] for our selected sample of halo dwarfs is shown in 3.4. This plot can be divided into three main evolutionary phases in the [Fe/H] domain: a) [Fe/H] $<$ -0.8 dex, b) -0.8 $<$ [Fe/H] $<$ 0 dex, and

c) [Fe/H] $>$ 0 dex. A brief discussion of the evolution of Li during these three phases is provided below.

a) [Fe/H] $<$ -0.8 dex: Stars in this metallicity range have approximately constant mean Li of A(Li) = 2.20 dex with a standard deviation of 0.14 dex. This mean value is slightly less (by about 0.1 dex) than the observed primordial Li abundance in the old, metal-poor halo stars, which is defined by the upper limit of the distribution. Another important fact this sample of metal-poor stars suggest is a slightly increasing trend in Li with increasing metallicity. This slightly increasing trend is understood to be because of Li addition due to the cosmic ray spallation over time (Ryan *et al.* 2000). However, possible contamination from the Galactic disc, where the initial Li is found to be higher, can not be neglected.

b) -0.8 $<$ [Fe/H] $<$ 0 dex: The maximum Li in dwarfs of this sub-solar metallicity range is following a sharply increasing trend with an increase in [Fe/H]. Also, most of the stars in this metallicity range belong to the Galactic disc, in which metallicity is known to be correlated with the radial distance. This suggests that in the case of the Galactic disc also, Li abundance is higher in the inner region of the Galaxy compared to the outer region. This also indicates continuous enrichment of Li in the Galactic disc.

c) [Fe/H] $>$ 0 dex: Dwarfs of super solar metallicity are showing a decreasing trend in the Li. This decreasing trend is speculated to be related to the metallicity dependence of stellar evolution and the Galactic dynamic history (Guiglion *et al.* 2019). We comment more on this in section 3.3.4.

3.3.4 Lower Li at super-solar metallicity

It is thought that the lower Li in super-solar metallicity stars might be related to the dynamical history of the Galaxy (Guiglion *et al.* 2019). Based on both observations and Galactic chemodynamical evolution models, stars in this metallicity group are known to be about $5 - 10$ Gyr old (e.g., Casagrande *et al.* 2011; Trevisan *et al.* 2011; Anders *et al.* 2017; Minchev *et al.* 2013, 2014b,a). Considering higher metallicity and older age, these stars are thought to have formed in the Galaxy's inner region and later radially migrated to the solar neighbourhood where we currently observe them. Also, these stars are believed to have depleted their Li over time, resulting in the presently observed decrease in Li at the super-solar metallicity. To find evidence of the dynamical migration, we compared these stars' spatial and kinematic properties (like distribution in the UVW planes, the Toomre diagram and orbital eccentricity) with the dwarfs of solar metallicity. We found no significant difference suggesting no connection between the lower Li at super solar metallicity and radial migration. More recent studies (Randich *et al.* 2020; Charbonnel *et al.* 2021) support this conclusion and suggest that the lower Li at super-solar metallicity is a result of sample selection. Randich *et al.* (2020) found no evidence of Li depletion at super-solar metallicity in a sample of 18 clusters. Further, Charbonnel *et al.* (2021) suggest that the bias in sample selection is one of the reasons for the apparently lower Li in super-solar metallicity stars. They found that the difference in the temperature of the selected stars is one of the main reasons for the decreasing trend in the super-solar metallicity stars, and if stars of similar metallicity are considered, then this trend disappears. Figure 3.5, shows the Li as a function of temperature for our selected sample of stars sampled in different [Fe/H] bins. The figure readily suggests a correlation between the stars' Li abundance and temperature. The figure also indicates a lack of warm dwarfs in higher metallicity bins than the bins of lower metallicity.

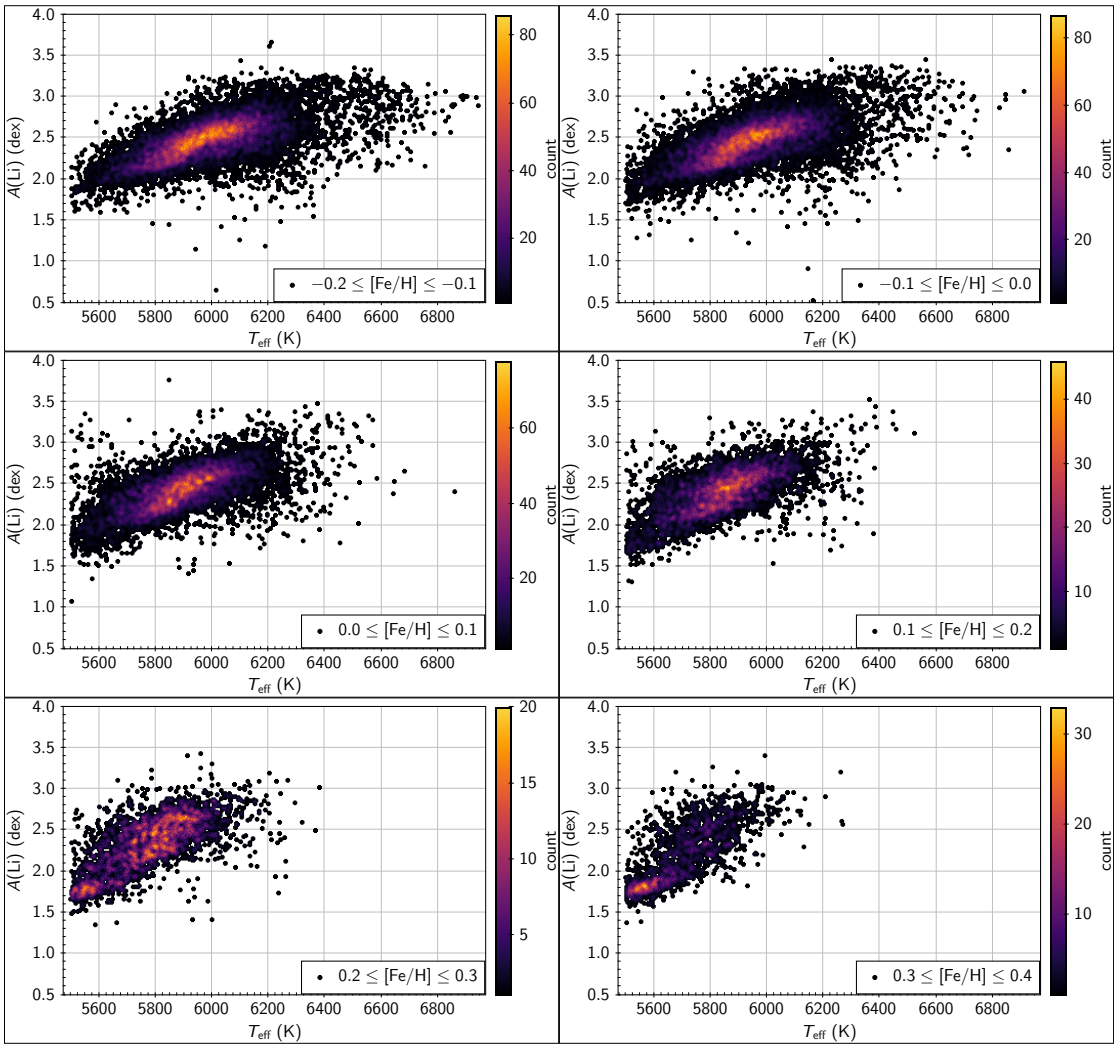


FIGURE 3.5: Li abundance as a function of temperature $T_{\rm eff}$ for the selected sample of dwarfs sampled in different metallicity ranges.

3.4 Concluding remarks

Based on the data from the *Gaia* and GALAH surveys, we looked into the evolution of Li in the Galaxy. Data for the metal-poor stars (with [Fe/H] $<$ -0.8 dex) confirm the existence of Spite plateau at A(Li) of $\sim$ 2.3 dex. These metal-poor dwarfs are found to have a mean A(Li) of 2.20 $\pm$ 0.14 dex but with a slightly increasing trend which is understood to be because of Li addition due to the cosmic ray spallation over time. Also, the absence of any correlation between Li abundance and kinematic parameters (like galactic space velocities), as well

as metallicity, suggests that Li in these metal-poor stars is primordial. It is, however, not clear if the amount of Li in these metal-poor stars is the same as the initial Li produced in the BBN or has decreased over time through astration by spallation processes (Mathews *et al.* 1990). In the sub-solar metallicity range (-0.8 $<$ [Fe/H] $<$ 0 dex), Li has increased significantly from the initial value of about 2.3 dex to a present value of about 3.3 dex (Figure 3.4). Super-solar metallicity dwarfs, which are known to be more than $\sim$ 5 Gyr old, follow a decreasing trend in Li with an increase in [Fe/H]. This decrease was thought to be related to the Galaxy's dynamical history, like the radial migration of stars (Guiglion *et al.* 2019). However, we found no significant difference in the kinematic properties of super-solar metallicity dwarfs compared to dwarfs with solar metallicity. More recent studies, like Randich *et al.* (2020); Charbonnel *et al.* (2021), are at variance with previous findings of decreasing Li in super solar metallicity stars and suggest that the observed lower Li for super solar metallicity stars in Li-[Fe/H] plot is due to sample selection effect. The super solar metallicity dwarfs in our sample are relatively cooler than the solar metallicity stars (Figure 3.5). This difference in temperature is believed to be one of the main reasons for the lower Li in super-solar metallicity stars. Further studies are needed to understand the temperature-dependent difference in diffusion mechanism and resulting Li depletion among cool and warm dwarfs.

In conclusion, Li has significantly increased in the Galactic disc. Li in young metal-rich disc stars is about ten times higher than the metal-poor halo stars and about three times higher than the theoretically predicted value from SBBN models. The gradual rise of the maximum Li envelope in the disc metallicity range in Figure 3.4 suggests a correlation between the Galactic Li evolution and Galactic nucleosynthesis. However, the source of such a large-scale Li production throughout the Galaxy (especially in the Galactic disc) is not clear. Other than the primordial Li from the BBN, some of the sources which are known to produce Li and may have contributed towards such a large scale Li enrichment throughout the Galaxy

are cosmic ray spallation (Meneguzzi *et al.* 1971; Mitler 1972), novae explosions (Arnould and Norgaard 1975; Starrfield *et al.* 1978; Izzo *et al.* 2015; Tajitsu *et al.* 2015), white dwarf mergers (Longland *et al.* 2012; Zhang and Jeffery 2013) and nucleosynthesis in evolved stars (see, e.g., Audouze and Truran 1973; Romano *et al.* 2001; Ventura *et al.* 2013; Deepak and Lambert 2021b, and references therein). The actual contribution of Li from these studies towards the Galactic Li is uncertain and varies among studies (e.g., Scalo 1976; Romano *et al.* 2001; Rukeya *et al.* 2017). However, most of of the studies agrees that the low-mass stars are one of the most significant contributors and can help increase in the Galactic Li. For example, Romano *et al.* (2001) found that the low-mass stars contribute about 41% of the currently observed Li in the solar neighbourhood. However, the evolution of Li during the post-main sequence phases is not very well understood, and there are disagreements between the theoretical predictions and observed Li in evolved stars. For example, about 1% of low-mass giants stars are known to have higher Li than the predicted values by the standard stellar evolutionary models (Brown *et al.* 1989b). The availability of measured Li abundances for thousands of stars from the large spectroscopic surveys provides a golden opportunity to understand the evolution of Li in stars which will further help to know how these stars are contributing towards the evolution of Li in the Galaxy.

Chapter 4

Evolution of Lithium in stars: the origin of Li-rich red giant stars*

4.1 Introduction

The measured abundance of $A(\mathrm{Li}) = 3.32$ dex in young stars and interstellar medium (ISM) suggest that Li enriched significantly in the Galaxy from the primordial value of $A(\mathrm{Li}) = 2.72$ dex, a value predicted from the big bang nucleosynthesis (BBN) models based on the results from WMAP (Cyburt *et al.* 2008). One of the known sources for Li enrichment, apart from cosmic ray spallation (Mitler 1972), an interaction of high energy cosmic ray particles with carbon and oxygen atoms, and novae explosions (Tajitsu *et al.* 2015; Izzo *et al.* 2015), is nucleosynethsis in evolved stars. Though stars, in general, are considered as Li sinks, highly evolved stars such as asymptotic giant branch (AGB) stars are known to produce

*This chapter is published in Deepak and Reddy (2019)

fresh Li (Smith and Lambert 1989) via Cameron-Fowler mechanism (Cameron and Fowler 1971) which add to the Li enrichment of the Galaxy through mass loss. It is understood Li production in AGB happens only in relatively massive stars of $M \geq 3$ $M_{\odot}$ through a process known as hot bottom burning (Mowlavi 1995; Lattanzio *et al.* 1996). However, the discovery of high Li abundance in relatively less evolved low mass red giant branch (RGB) stars was unexpected (Wallerstein and Sneden 1982). Since then, observational studies revealed more Li-rich giants, and systematic surveys suggest Li-rich giants are rare, $< 1\%$ (e.g., Brown *et al.* 1989b; Charbonnel and Balachandran 2000). There are close to 200 Li-rich RGB stars (Casey *et al.* 2016) known so far with Li ≥ 1.5 dex, an upper limit commonly used in the literature and attributed to the standard models of first-dredge-up on RGB (Iben 1967). In some cases, Li abundance was found to be more than the star's initial abundance of $A(\mathrm{Li}) = 3.2$ dex, which are known as super Li-rich giants (e.g., Yan *et al.* 2018). In fact, observations in general show much less Li than the expected limit (Fields 2011) and are attributed to the extra-mixing process, post first dredge-up, during luminosity bump evolution (Deliyannis 1990), which is not part of the standard models. Thus, Li enhancement in RGB giants is a puzzle, and its origin is being debated since a few decades.

To explain high Li in RGB stars, two hypotheses have been proposed in the literature: 1) the addition of Li-rich material through the merger of sub-stellar objects, and 2) internal nucleosynthesis and mixing-up of fresh Li with photosphere. There is no consensus on any of these two hypotheses. If the mechanism is in-situ nucleosynthesis as suggested by a few studies (Cameron and Fowler 1971; Mowlavi 1995; Lattanzio *et al.* 1996), RGB stars should be counted for Li enrichment in the Galaxy. On the other hand, if the enhancement is due to an external origin, we are simply observing the locked-up Li in sub-stellar objects. Thus, understanding the mechanism of Li enhancement in RGB may not only provide clues to our understanding of RGB nucleosynthesis but to the larger issue of Li enrichment in the Galaxy.

The clue probably lies in finding the evolutionary phase of Li-rich giants on RGB. The evolutionary phase may be determined either by using the star's position in the HR diagram or using asteroseismology (Bedding *et al.* 2011) or secondary calibrations based on asteroseismology (Ting *et al.* 2018). Most of the currently known Li-rich giants have been classified based on their positions in the HR diagram. Due to the small separation in values of luminosity and $T_{\rm eff}$ between different phases on RGB, in particular between the red clump and the luminosity bump, there are conflicting reports in the literature about the true evolutionary phase of Li-rich giants on RGB. With regards to asteroseismic analysis, which has been proven to be a gold standard to separate He-core burning giants (red clump) from those of H-core burning giants ascending RGB for the first time. Asteroseismic data is mostly based on either Kepler or CoRoT missions. Unfortunately, data is not available for all the stars as these observations are made for specific sky fields. Presently, the evolutionary phase is accurately known, based on Kepler asteroseismic data and CoRoT asteroseismic data, only for half a dozen Li-rich stars (Jofré *et al.* 2015; Kumar *et al.* 2018; Singh *et al.* 2019b; Smiljanic *et al.* 2018). Interestingly, all of them are red clump stars with He-core burning except the star studied by Jofré *et al.* (2015), which is on RGB with H-core burning phase whose Li-rich giant status is discussed later in the discussion section. None of the previously known Li-rich giants is in the Kepler field.

This necessitates exploring alternate ways to find the evolutionary phase of Li-rich giants. One of the ways is to undertake a large-scale survey for Li-rich giants in globular clusters, which have well-defined RGB with visible luminosity bumps and red clumps with a significant number of stars. However, getting a reasonable resolution spectrum for a large number of fainter stars in globular clusters, even with 10-m class telescopes, is difficult and time-consuming. Another way is to employ a large data set of giants with measured Li abundance and accurate astrometry.

Fortunately, while analyzing large data sets from the *Gaia* and the GALAH spectroscopic surveys to understand elemental abundance patterns in the Galaxy, we noticed a strikingly well-populated red clump and RGB in the HR diagram of L-$T_{\rm eff}$ of the GALAH stars. This could potentially be used to find clues to Li enhancement origin in RGB stars if we search for Li-enhanced giants along the RGB. Combining the *Gaia* astrometry and the GALAH Li abundances, we provide evidence that most of the Li-rich stars belong to the red clump with implications for Li enhancement origin scenarios.

4.2 Stellar Sample

For this study, we started with the cross-match between the second data releases of the GALAH and *Gaia* surveys (i.e., GALAH DR2 and *Gaia* DR2 catalogues) which yielded a sample of 340,299 common stars among these two data sets (see Section 3.2 for details about this cross-match). From this sample, we culled out stars for which $\sigma_{\rm Teff_{GALAH}} \geq 100$ k, parallax (Π) is negative and fractional error in parallax, $\sigma_{\Pi}/\Pi \geq 0.15$ yielding a total sample of 246,390 stars (see Section 3.2 for details about this cross-match). We further restrict the sample to stars having the most reliable stellar parameters, i.e. the stars with `flag_cannon` = 0.

In addition, to avoid stars of higher masses of early AGB and stars evolved from hotter spectral types from the main sequence, as some of them are found to be having higher Li abundances due to inefficient mixing, we have restricted our sample to low mass RGB stars of $M \leq 2{\rm M}_{\odot}$, which are expected to evolve through both luminosity bump and He-flash (Carlberg *et al.* 2016; Cassisi *et al.* 2016). For this, we first estimated luminosities for all our sample stars and then mass using the mass-luminosity-temperature relationship as discussed in Section 3.2. We also calculated the Galactic space velocities for each of our sample stars using the

methodology discussed in Section 2.2.1. These space velocities are corrected for solar motion using Sun's motion with respect to the LSR from Dehnen and Binney (1998). After the implementation of all the above-discussed selection criteria, we finally have a sample of 188,679 low-mass stars.

4.3 Analysis

4.3.1 Sample stars in L - $T_{\rm eff}$ plane

Sample data plotted in the HR diagram of Luminosity versus effective temperature (Figure 4.1) shows stellar evolution with well defined main sequence and red giant branch. Since our interest lies in the Li enhancement during RGB evolution, RGB has been separated from the data set as defined by a box with the dashed line in Figure 4.1. The box includes giants from the base of RGB through its tip and red clump in the L - $T_{\rm eff}$ plane defined by 3800K $\leq T_{\rm eff} \leq$ 5200K and 0.3 $\leq \log(L/{\rm L}_{\odot})$ $\leq$ 3.0. This yielded 51,982 red giant branch stars, which are the focus of this study. The data sets also show two visible concentrations of stars which are identified as luminosity bump and red clump regions and have been marked by red and black rectangles, respectively. The two clusters are defined in L - $T_{\rm eff}$ plane by (1.5, 1.9; 4650, 5200) for the red clump and (1.3, 1.5; 4500, 5000) for the luminosity bump. The concentrations at these two phases are direct consequences of their relatively longer evolutionary timescales compared to any other place on RGB. The well-defined stellar concentrations could be used to decipher the origin of Li excess by searching for Li-rich giants among the well-defined RGB, luminosity bump and red clump.

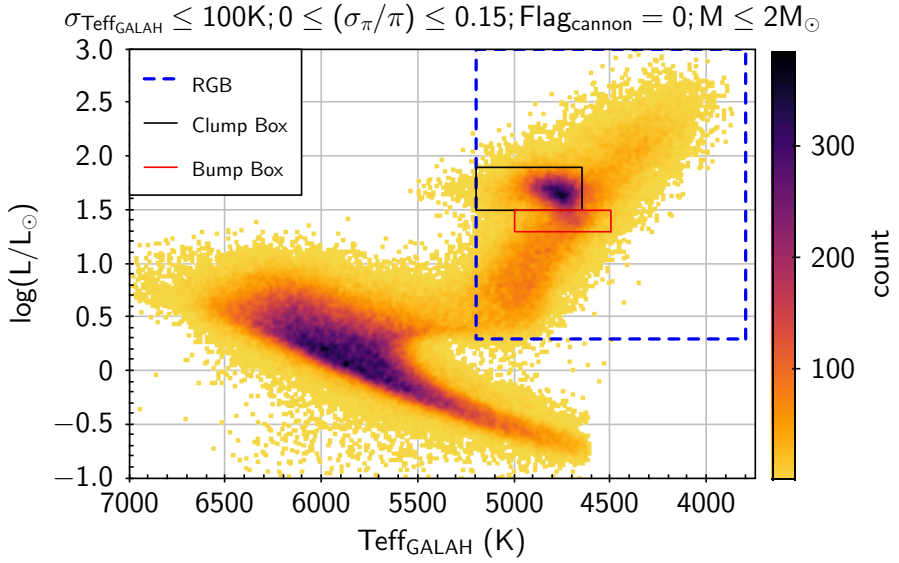


FIGURE 4.1: Sample stars in the HR diagram.

4.3.2 Li abundances of sample stars

As discussed in the previous chapter (3), the GALAH DR2 provides Li abundances in the form of [Li/Fe] (= [Li/H] - [Fe/H], where [Li/H] = A(Li) - A(Li)$_\odot$) along with associated error and a flag indicating the level of confidence in the measured abundance. For each of the sample stars, we converted the provided abundance ratio [Li/Fe] to A(Li) and also estimated the corresponding error (see Section 3.2 for more details). On checking, we found that all the stars with relatively higher values of Li, for example A(Li) $\geq$ 1.6 dex, has `flag_li_fe` $\leq$ 3, while for some of the Li-low stars `flag_li_fe` $\geq$ 3. A higher `flag_li_fe` value for Li-low stars is expected as the Li absorption line in those stars is weaker. We consider all RGB stars for which Li abundance is measured by the GALAH, as this would enable us to comment on the relative fraction of Li-rich giants among RGB stars and the evolution of Li itself along the RGB.

4.4 Results

4.4.1 Li-rich giants on RGB

Standard models of stellar evolution (Iben 1967) predict dilution of Li in RGB stars by a factor of 30 to 60 from its main sequence value. Models, however, do not prescribe the value of initial Li abundance on the main sequence, which is a function of age, mass, metallicity, and its pre-main sequence evolution (Lambert and Reddy 2004). If we assume RGB stars evolved off the main sequence with an initial value of $A(\mathrm{Li}) = 3.32$ dex, according to the standard models, one would expect $A(\mathrm{Li}) \approx 1.5$ to 1.8 dex for RGB giants in the mass range of 1 to 1.5 $\mathrm{M}_{\odot}$, lower the mass, lesser is the dilution factor. However, in the literature, commonly, a single upper limit of $A(\mathrm{Li}) = 1.5$ dex is used for Li-normal giants, and giants with $A(\mathrm{Li})$ higher than this are considered Li-rich. But for the question "What is a Li-rich giant?", the answer seems to be not a single limit, but probably multiple limits depending on mass and metallicity. Also, see Smiljanic *et al.* (2016) and Aguilera-Gómez *et al.* (2016b) who discussed lower limit for Li-rich giants in connection with two giants (Trumpler 20 MG 340 and 591) with $A(\mathrm{Li}) \sim 1.6$ dex which is at the borderline for qualifying them as Li-rich giants. Here, we use Li trends with metallicity to define Li abundance limits on RGB.

In a plot of $A(\mathrm{Li})$ versus [Fe/H] (Figure 4.2), one can notice varying Li trend with metallicity. The trend can be grouped into three: very metal-poor stars with $[\mathrm{Fe/H}] \leq -1.5$ dex, metal-poor stars with $-1.5 < [\mathrm{Fe/H}] \leq -0.5$ dex, and metal-rich stars with $[\mathrm{Fe/H}] > -0.5$ dex. The metal-poor giants show a well-defined upper limit of $A(\mathrm{Li}) \approx 1.5$ dex for Li-normal giants, which is commonly used in the literature. For very metal-poor giants, the nice horizontal trend breaks down at $[\mathrm{Fe/H}] = -1.5$ dex, and Li abundance starts rapidly decreasing with decreasing [Fe/H]. Though it is interesting in the context of Li evolution in the early Galaxy,

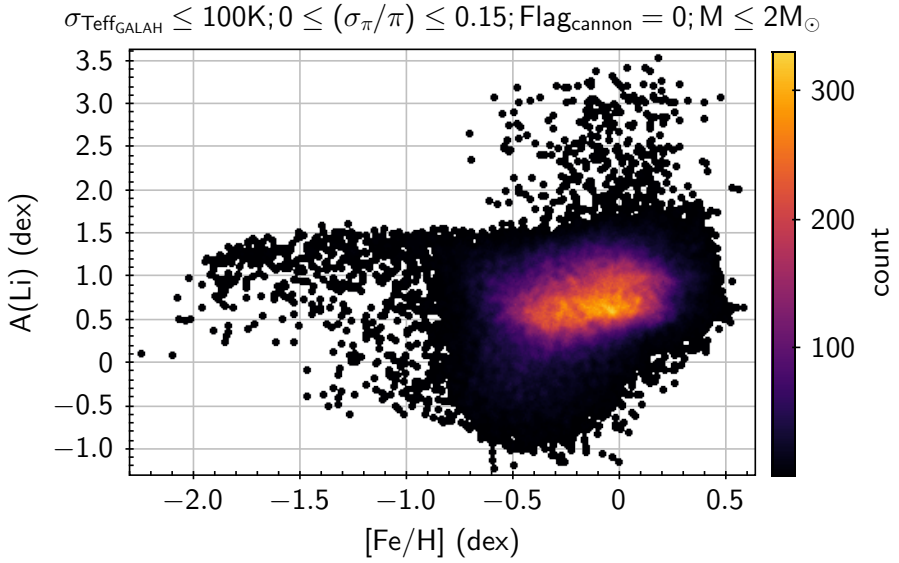


FIGURE 4.2: Lithium abundance versus metallicity of RGB sample stars.

for the present study, we concentrate on Li-rich giants among RGB. It is also interesting to note that there are no Li-rich giants among giants with [Fe/H] $\leq$ -0.7 dex. However, on our loosely defined metal-rich side, the Li abundance upper limit for Li-normal stars seems to be slightly higher with a range of $A(\mathrm{Li}) \approx 1.6$ - 1.8 dex than the commonly used upper limit of $A(\mathrm{Li}) = 1.5$ dex for Li-normal giants.

For the current study, we adopt a single limit of $A(\mathrm{Li}) = 1.8$ dex, instead of using two upper limits, as most of the Li-rich giants in the sample are in the higher metallicity group (i.e [Fe/H] > -0.6 dex) as shown in Figure 4.2. This is also the same upper limit set by standard models for low mass ($\sim 1\mathrm{M}_\odot$) Li-normal giants. In addition, given the relatively larger uncertainties ($\approx \pm 0.14$) involved in the derivation of Li abundances from the spectra, the adoption of a slightly higher limit to avoid contamination with Li-normal giants is justified. With this definition, we found 335 giants with $A(\mathrm{Li}) \geq 1.8$ dex. This is about 0.64% of total RGB giants considered in this study and confirms the previous survey results (Brown *et al.* 1989b; Kumar *et al.* 2011; Kirby *et al.* 2012) that Li-rich giants are a rare group.

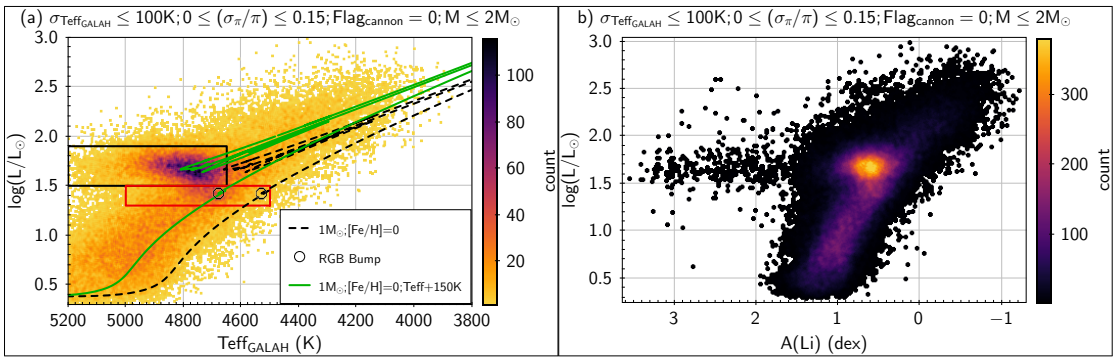


FIGURE 4.3: The HR diagram and $\log(L/\mathrm{L}_\odot)$ vs A(Li) distribution for our selected RGB sample stars from the GALAH DR2 and the *Gaia* DR2 survey with mass $M \leq 2\mathrm{M}_\odot$. In the left-hand side panel, we have also shown the approximate positions of the RGB bump (red rectangle) and the RGB clump (black rectangle).

4.4.2 Stellar Evolutionary Phase of Li-rich Giants

Determination of the stellar evolutionary phase of Li-rich giants is the key motivating factor of this study and has been elusive for a long time due to the lack of large data set with Li abundances coupled with accurate astrometry. The current larger data set of the GALAH Li abundances and the *Gaia* astrometry is ideally suited for this purpose. In Figure 4.3, the selected sample of 51,982 giants for which Li abundances have been measured and have accurate T_{eff} and luminosity have been shown. Clump stars are concentrated within the luminosity range of $\log(\mathrm{L/L}_\odot)$ = 1.5 - 1.9 (blue rectangle box). Bump stars appear to be slightly at a lower luminosity below the much larger group of clump stars. To demonstrate that RGB, bump and clump regions are well identified in the data (Figure 4.3), we superposed a representative theoretical evolutionary track of $1\mathrm{M}_\odot$ star with [Fe/H] = 0.0, taken from MESA Isochrones & Stellar Tracks' latest version 1.2 (`MISTv1.2`) available at `http://waps.cfa.harvard.edu/MIST/index.html` and for details see Paxton *et al.* (2011). The solar-like model is used as the mass and metallicity distribution of the current data set peaks at about $1\mathrm{M}_\odot$ and [Fe/H] = 0.0 dex. However, the theoretical track is systematically cooler by about 150 K (Figure 4.3a, broken line). If the track is shifted by 150 K towards the hotter side,

it coincides well with the observed locations of the bump and clump stars and runs through the middle of RGB. Note, the theoretical models, due to differences in input assumptions, disagree by more than 100 K in $T_{\rm eff}$ among themselves and in some cases with observations (Salaris *et al.* 2002).

To test the occurrence of Li-rich giants on RGB, we have shown in Figure 4.3b, a plot of Luminosity versus A(Li). It is known that Li abundance is a function of $T_{\rm eff}$ in which A(Li), in general, decreases with decreasing $T_{\rm eff}$. As a result, the plot of $\log(\mathrm{L/L_{\odot}})$ versus A(Li) (Figure 4.3b) mimics the HR diagram of $\log(\mathrm{L/L_{\odot}})$ verses $\mathrm{Teff_{GALAH}}$. Most of the giants follow this general rule and show, on average, a decreasing Li trend as they ascend RGB towards the tip. Contrary to this general rule, however, a small group of giants show enhanced Li abundance, in particular, at a region which coincides with red clump, post He-flash. There are also Li-rich giants below and above the red clump luminosity range as indicated in Figure 4.3a. Interestingly, Li-rich giants with $\log(\mathrm{L/L_{\odot}}) \leq 1.5$ are far less compared to those at the clump. Giants above the clump luminosity are probably early AGB stars, about which we comment further in section 4.5.

It appears from Figure 4.3 that most of the Li-rich giants are concentrated at the red clump. Out of the total 335 Li-rich giants, as mentioned above, there are 253 that seem to fall in the red clump luminosity range of $\mathrm{L/L_{\odot}} = 1.5 - 1.9$ dex (see Figure 4.3a). A bump with a relatively lesser number of Li-rich giants (24), appears to be just below and rightwards of the clump and falls in the luminosity range of $\mathrm{L/L_{\odot}} \approx 1.3 - 1.5$ dex. Given the small difference between the luminosities of the red clump and the RGB bump, about 0.3 dex (the difference between the mid values), and the typical errors in luminosities, about 0.05 dex (maximum 0.1 dex), we can not rule out the possibility of small overlap of giants among bump and clump. There are also a few Li-rich giants that are below the bump luminosity about which we comment on later.

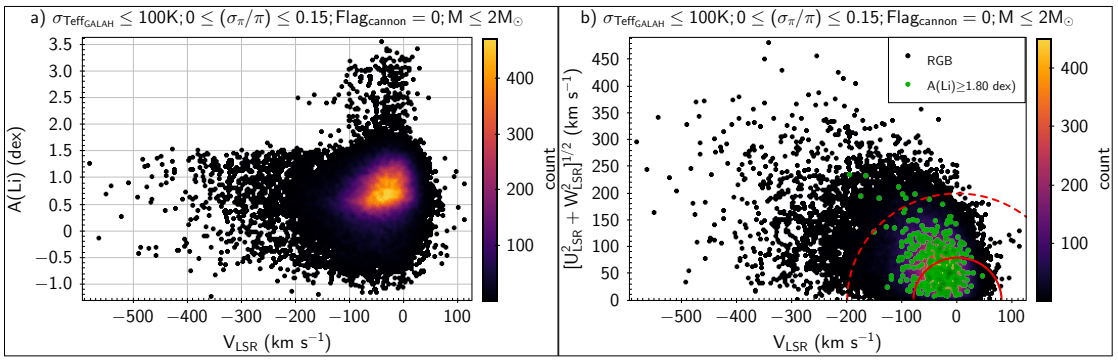


FIGURE 4.4: Distribution of selected RGB sample in A(Li) vs $\mathrm{V_{LSR}}$ plane and in the form of Toomre Diagram. In Figure 4.4b, we have plotted the approximate boundaries separating thin and think disc ($\mathrm{V_{Total}}$=80 km s^{-1}, continuous red circle), and thick disc and halo ($\mathrm{V_{Total}}$=200 km s^{-1}, dotted red circle).

4.4.3 Li-rich Giants in the Galaxy

To understand the distribution of Li-rich giants among different stellar components of the Galaxy, we have computed membership probability, based on the recipe given in Reddy *et al.* (2006) and references therein, for each of the stars in the selected RGB sample for belonging to one of the three main components of the Galaxy, namely; thin disc, thick disc and halo. For this, the heliocentric velocities (U, V, W) for each of the sample giant is calculated using the *Gaia* astrometry (positions, parallax, and proper motions) and radial velocities (RV) from the GALAH DR2. The heliocentric velocities are corrected for the solar motion using U_o=10, V_o=5.3, W_o=7.2 (km s^{-1}) from Dehnen and Binney (1998) to get velocities with respect to the LSR ($\mathrm{U_{LSR}}$, $\mathrm{V_{LSR}}$, $\mathrm{W_{LSR}}$). The entire sample is shown in the Toomre Diagram of rotational velocity ($\mathrm{V_{LSR}}$) and the sum of quadrature of radial and vertical velocities ($[\mathrm{U_{LSR}^2} + \mathrm{W_{LSR}^2}]^{1/2}$) (Sandage and Fouts 1987). Li-rich giants are identified by coloured symbols as shown in Figure 4.4. We used kinematic boundaries for thin disc ($|\mathrm{V_{Total}}| = [\mathrm{U_{LSR}^2} + \mathrm{V_{LSR}^2} + \mathrm{W_{LSR}^2}]^{1/2}$ $\leq$ 80 km s^{-1}), thick disc (80 $<$ $|\mathrm{V_{Total}}|$ $\leq$ 200 km s^{-1}) and halo ($|\mathrm{V_{Total}}|$ $>$ 200 km s^{-1}) which are in accordance with the results in Reddy *et al.* (2006). Further, to quantify the number of giants belonging to different components of the Galaxy, we used a probability of 70% or more for any star being considered as a member

of a particular component. We found 223 Li-rich thin disc stars, which is about 0.8% of total thin disc RGB stars with $P_{\rm thin} \geq 70\%$ and 69 Li-rich thick disc stars consisting of 0.5% of total thick disc RGB stars with $P_{thick} \geq 70\%$. We have found just 3 Li-rich giants among 1442 halo giants with $P_{halo} \geq 70\%$. This shows that Li-rich giants are rare ($< 1\%$) across stellar components but are relatively more prevalent among metal-rich thin disc components compared to thick disc and very metal-poor halo.

4.5 Discussion

Surveys based on large pre-selected low mass RGB stars such as Kumar *et al.* (2011) and Smiljanic *et al.* (2018) using data from Hipparcos and *Gaia* catalogue respectively, suggested that Li-rich giants occupy a luminosity range in the HR diagram overlapping the luminosity of RC and RGB bump regions. This led to suggestions of internal nucleosynthesis as both regions are associated with key phases of stellar evolution: removal of H-profile discontinuity and He-flash, respectively. There are observational reports suggesting the existence of Li-rich stars before and after the luminosity bump on RGB, which indicates that Li-rich giants may occur anywhere on RGB, implying external origin for Li excess, such as the engulfment of sub-stellar objects. Now the question is whether the Li-rich giants happen anywhere along RGB or at a particular phase on RGB. The answer to this is a key to understanding the origin of excess Li in RGB stars.

Thanks to the Kepler and CoRoT missions, which provided a wealth of time-resolved photometric data for stars in certain fields of the sky. Using asteroseismic analysis, one can distinguish RGB giants of H-core burning from those of red clump giants of He-core burning (Bedding *et al.* 2011). Recently, half a dozen Li-rich giants which are in the Kepler fields have been reported by different studies (Silva

Aguirre *et al.* 2014; Kumar *et al.* 2018; Singh *et al.* 2019b; Smiljanic *et al.* 2018). All of them have been classified as red clump stars with He-core burning based on asteroseismic data analysis with seismic parameters; average period spacing between g- and p-modes, $\Delta \mathrm{p} \geq 150$ and frequency separation, $\Delta\nu \leq 5$. There is also a lone Li-rich giant (KIC 9821622), which is in Kepler field and has been classified as RGB star with H-core burning (Jofré *et al.* 2015). Values of luminosity and $T_{\rm eff}$ suggest its location below the luminosity bump on RGB. Though the star is a bona fide RGB, given its reported large difference in derived Li abundance between the stronger resonance line at 6707Å ($A(\mathrm{Li})_{\rm LTE} = 1.49$ dex; $A(\mathrm{Li})_{\rm NLTE} = 1.65$ dex) and weaker sub-ordinate line at 6103Å ($A(\mathrm{Li})_{\rm LTE} = 1.80$ dex; $A(\mathrm{Li})_{\rm NLTE} = 1.94$ dex), its status being Li-rich giant needs further studies. Also, the star's average Li abundance of ($A(\mathrm{Li}) = 1.80 \pm 0.2$ dex for a star with [Fe/H] $= -0.49 \pm 0.03$ dex) is at the border of the limit for Li-normal giants. However, in the absence of Kepler data for most of the known Li-rich stars and a lack of systematic surveys for Li-rich giants among asteroseismically known RGB and RC stars, one cannot affirm that Li-rich stars belong only to the RC region based on a small number of Li-rich stars randomly discovered. The large data set assembled here is quite suitable to find the likely occurrence of Li-rich giants in different locations on RGB and possible origin mechanisms: external versus in-situ scenarios.

4.5.1 External versus in-situ Li enrichment

We examine the external scenario of a planet or sub-stellar material accretion for excess Li in RGB stars. If this scenario has to hold, one would expect Li-rich giants across RGB with relatively higher concentrations both at luminosity bump and red clump as their evolutionary timescales are relatively longer. In Table-4.1, we have given approximate evolutionary periods for different phases of RGB evolution for a representative $1\mathrm{M}_{\odot}$ mass star of the metallicity of [Fe/H] $= 0.0$ dex and -0.5 dex. Timescales are based on theoretical tracks taken from

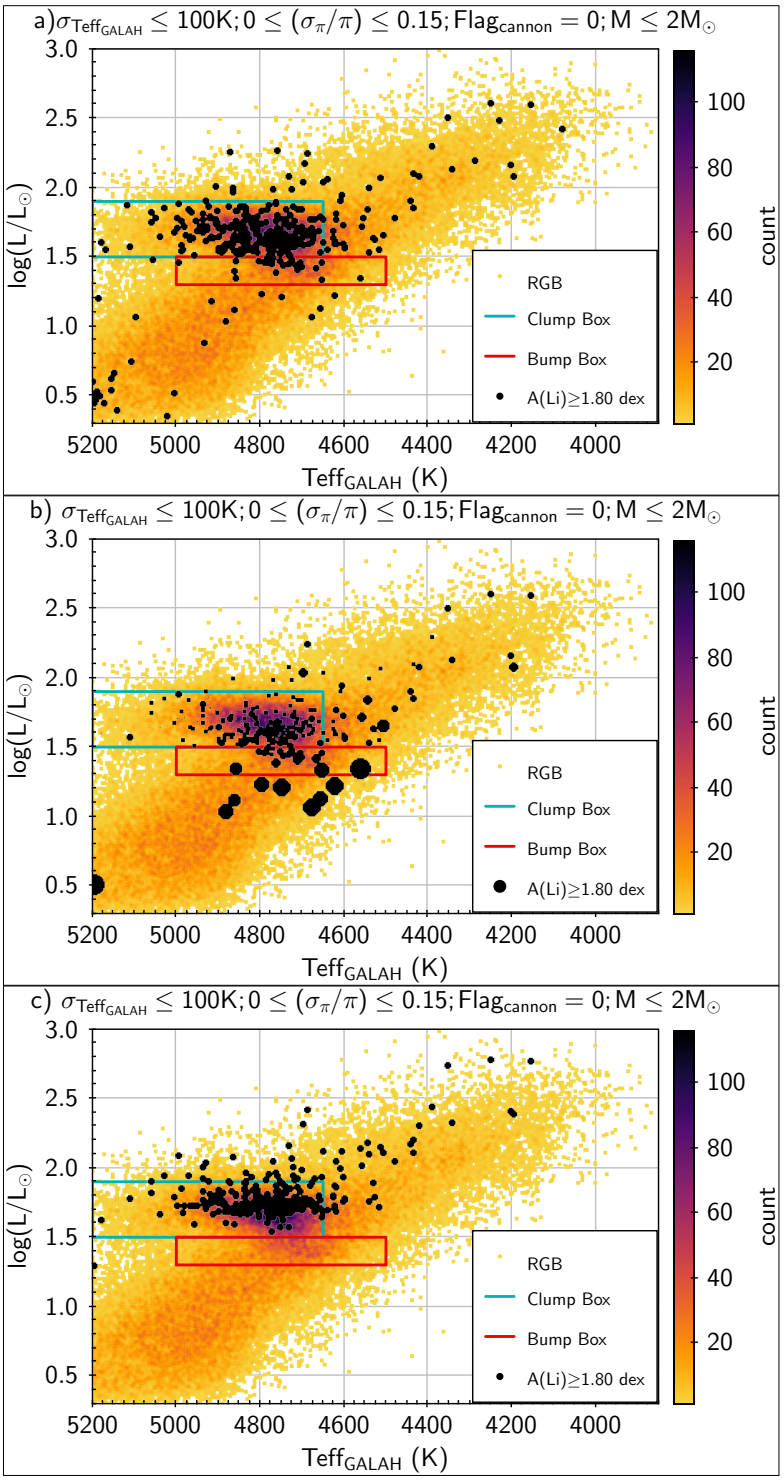


FIGURE 4.5: The HR diagram showing Li-rich giants' positions a) prior to extinction correction, b) with the size of representative point proportional to extinction, and c) post extinction correction.

TABLE 4.1: Estimated evolutionary timescales for a representative $1M_{\odot}$ star with metallicities,[Fe/H]=0.0 dex and −0.5 dex.

Evolutionary Phase	For M=$1M_{\odot}$ & [Fe/H]=0 dex t_e (Gyr)	For M=$1M_{\odot}$ & [Fe/H]=−0.5 dex t_e (Gyr)
MS Turn-off to RGB tip	1.416	0.931
RGB base to tip	0.659	0.466
RGB base to Bump	0.555	0.402
RGB Bump	0.014	0.006
RGB Bump to RGB tip	0.100	0.059
He Core Burning	0.111	0.102

MESA Isochrones & Stellar Tracks' latest version 1.2 (`MISTv1.2`) available at `http://waps.cfa.harvard.edu/MIST/index.html` and see Paxton *et al.* (2011) for more details. The evolutionary period for giants between the base of RGB and the tip of RGB is about six times more than that of the evolutionary period of giants at the clumps, which is about 110 Myrs. This means one should expect a number of Li-rich giants by a similar factor more on RGB in ascending phase, including the bump compared to a number of Li-rich giants at the red clump region. Contrary to this, we found less than one-third of the total Li-rich giants (about 106) outside the red clump box (see Figure 4.5a). Some of these, about 16, are lying just above the red clump box, which probably are either evolving off the red clump phase towards early AGB or descending from the RGB tip. Quite a few (about 16) appear to be located below $L/L_{\odot} < 0.8$ dex, at the base of the RGB. Probably, these may still be in the sub-giant phase, and their higher Li abundance may be due to insufficient mixing as they might not have fully experienced the first dredge-up phase. In this context, we would like to mention the recent discovery of a number of metal-poor sub-giants with Li abundances $A(\mathrm{Li}) \geq 2.0$ dex and in some cases exceeding ISM values (Li *et al.* 2018b). There are also suggestions that Li excess seen in the post-first-dredge-up on RGB giants probably originated from

sub-giants (Kirby *et al.* 2016), though the origin of high Li in subgiants itself is not known yet.

Though the number of Li-rich stars on RGB is less, it is important to know if they are really on RGB in ascending phase or if they are misplaced in the HR diagram due to errors. One of the errors that could be specific to individual giants is extinction, which can affect the stars' brightness and hence their position in the HR diagram. In the present study, we have not taken into account the extinction in deriving luminosities, as the extinction values are not available for the majority of the sample stars. Moreover, the corrections for most of the stars in the sample are small as the stars are nearby ($d < 5$ kpc) bright giants (with $9 \leq m_v \leq 14$). However, on scrutiny of extinction among Li-rich giants, we found the extinction values only for 269 Li-rich giants out of 335. Interestingly, most of the Li-rich giants that are below the bump have relatively larger extinction values compared to others. In Figure 4.5b, Li-rich giants with extinction values are shown. The level of extinction is represented by the size of the symbol. If we correct m_v values for extinction given in the *Gaia* DR2, many of the Li-rich giants that are below the bump on RGB move towards the brighter clump box (Figure 4.5c). Some of them also moved out of the clump box towards higher luminosities. Particularly interesting is the fact that there are no Li-rich giants at the bump and also below the bump. Though it is compelling to suggest, based on the current data as shown in Figure 4.5c, that Li-rich giants belong only to RC, we note extinction has not been applied to the entire sample as it is not available for the majority of the sample. One thing that emerges from Figure 4.5 is that a large number of Li-rich giants seems to be at RC even though the evolutionary period of RGB is many-fold longer than RC giants.

In Table-4.2, we have separately given super Li-rich giants with $A(\mathrm{Li}) \geq 3.2$ dex. There are 20 of them. Except for one super Li-rich giant, all are closer to solar metallicity ([Fe/H] within ± 0.30 dex and belongs to the Galactic thin disc. Super

TABLE 4.2: Stellar parameters of Super Li-rich giants with Li abundance of $A(\mathrm{Li}) \geq 3.2$ dex in our sample.

S.No.	Object ID	T_{eff} (K)	log$g$ (dex)	[Fe/H] (dex)	m$_V$ (mag)	log(L/L$_\odot$)	A(Li) (dex)
1	Gaia DR2 6423511482552457344	4828.68 ± 58.32	2.84 ± 0.14	0.18 ± 0.05	12.15	1.56 ± 0.03	3.54 ± 0.12
2	Gaia DR2 6216747182780840576	4773.08 ± 58.40	2.69 ± 0.15	0.12 ± 0.06	12.54	1.54 ± 0.07	3.41 ± 0.12
3	Gaia DR2 3080569351805501824	4995.53 ± 95.89	2.60 ± 0.17	0.03 ± 0.07	11.07	1.71 ± 0.04	3.41 ± 0.12
4	Gaia DR2 5920543908525756800	4815.52 ± 76.34	2.68 ± 0.18	0.14 ± 0.07	11.71	1.54 ± 0.04	3.39 ± 0.13
5	Gaia DR2 5676420200792553600	4854.10 ± 97.57	2.31 ± 0.16	-0.11 ± 0.06	12.40	1.83 ± 0.07	3.38 ± 0.12
6	Gaia DR2 6721793108675117440	4911.04 ± 90.19	2.45 ± 0.17	-0.04 ± 0.07	11.36	1.64 ± 0.04	3.33 ± 0.12
7	Gaia DR2 4488063566731544960	4778.94 ± 86.05	2.37 ± 0.16	-0.02 ± 0.06	12.34	1.52 ± 0.05	3.27 ± 0.12
8	Gaia DR2 2939800046333110272	4985.20 ± 83.68	2.56 ± 0.18	-0.13 ± 0.08	12.98	1.55 ± 0.06	3.26 ± 0.13
9	Gaia DR2 4168437628181576192	4749.88 ± 89.58	2.71 ± 0.18	0.19 ± 0.07	13.23	1.21 ± 0.06	3.26 ± 0.13
10	Gaia DR2 5229729170925959552	5038.38 ± 70.89	2.79 ± 0.17	-0.15 ± 0.07	11.13	1.65 ± 0.02	3.24 ± 0.13
11	Gaia DR2 5293680581122445184	4832.25 ± 68.88	2.50 ± 0.15	-0.01 ± 0.06	12.68	1.65 ± 0.04	3.23 ± 0.12
12	Gaia DR2 5242382659974594688	4786.39 ± 51.84	2.80 ± 0.14	0.28 ± 0.05	11.57	1.60 ± 0.03	3.23 ± 0.12
13	Gaia DR2 6721685773156936064	4751.60 ± 58.24	2.52 ± 0.15	0.11 ± 0.06	10.87	1.68 ± 0.04	3.23 ± 0.12
14	Gaia DR2 5628302754467688576	4868.94 ± 93.16	2.37 ± 0.17	-0.20 ± 0.07	13.47	1.57 ± 0.04	3.21 ± 0.13
15	Gaia DR2 3202012502737830784	4906.32 ± 86.59	2.42 ± 0.16	-0.14 ± 0.06	12.78	1.77 ± 0.11	3.21 ± 0.12
16	Gaia DR2 5460011229840058880	4813.14 ± 50.93	2.63 ± 0.13	0.16 ± 0.05	12.17	1.70 ± 0.05	3.21 ± 0.12
17	Gaia DR2 5452473905831060480	4711.60 ± 70.91	2.17 ± 0.15	-0.30 ± 0.06	12.41	1.84 ± 0.07	3.20 ± 0.12
18	Gaia DR2 6162898261508964992	4835.99 ± 77.44	2.58 ± 0.17	0.01 ± 0.07	12.59	1.70 ± 0.12	3.20 ± 0.13
19	Gaia DR2 6779302244026689920	4541.30 ± 69.25	2.17 ± 0.15	-0.48 ± 0.06	12.02	1.99 ± 0.08	3.20 ± 0.12
20	Gaia DR2 3496188144418768640	4776.14 ± 72.41	2.59 ± 0.16	0.04 ± 0.06	12.12	1.63 ± 0.05	3.20 ± 0.12

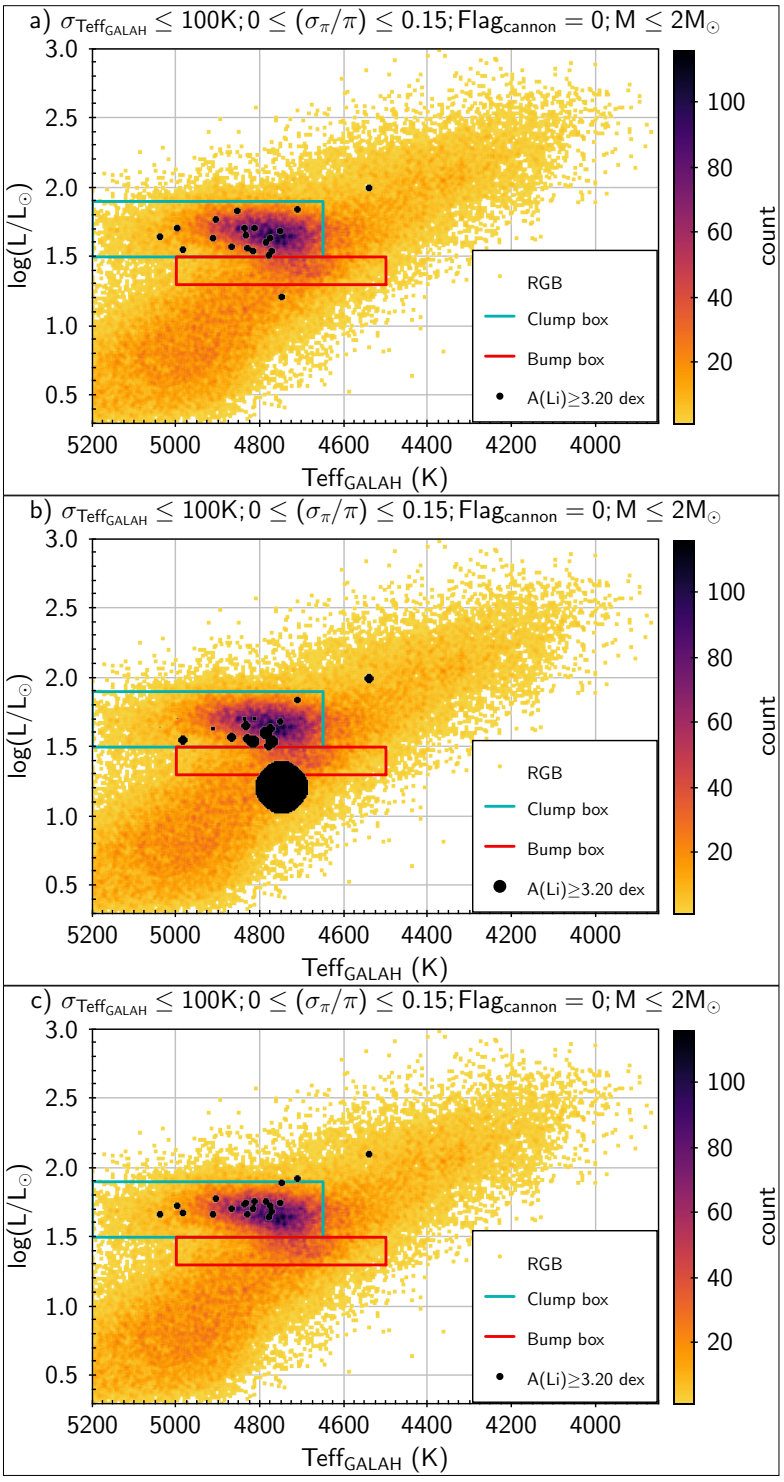


FIGURE 4.6: The HR diagram showing super Li-rich giants' positions a) prior to extinction correction, b) with size of representative point proportional to extinction, and c) post extinction correction.

Li-rich giants are plotted in the HR diagram of Figure 4.6a. With the exemption of two, all fall in the RC region defined by a turquoise colour box. Of two, one is below the bump, and the second is above the clump region. Interestingly, the super Li-rich giant that appears below the bump has a much larger extinction (the larger the symbol, the higher the extinction) value, as shown in Figure 4.6b. Post-extinction correction, the lone super Li-rich giant below the bump moves up into the red clump box. After extinction correction, super Li-rich giants seem to fall in the center of the RC region as shown in Figure 4.6c. Two of the giants also move slightly upward towards the brighter side, away from the central region of RC. The giants above the clump are not RGB but are slightly leftwards. Probably, they are either post-clump giants evolving toward early AGB or post-He-flash giants. Most importantly, none of the super Li-rich giants is either at bump or even on RGB. Given the transient nature of Li enrichment and the very high Li abundance of super Li-rich giants, the Li enrichment, most probably, would have happened very recently. Clustering of super Li-rich stars only at the clump, as revealed by the data shown in Figure 4.6, is the most compelling evidence against the external scenario for Li-excess origin. There is no reason to believe that the conditions for sub-stellar engulfment at RC are more favourable than at any other RGB phase. This clearly points towards the in-situ scenario either at the luminosity bump or its immediate preceding phase of He-flash at the RGB tip.

4.5.2 In-situ nucleosynthesis at luminosity bump versus He-flash

There are two likely phases at which nucleosynthesis and dredge-up of Li may happen: luminosity bump and He-flash at the RGB tip. Both phases are associated with significant internal changes in the stars. It is at the bump at which the H-burning shell moves upward and gets encroached by the outer convective shell resulting in a slowdown of stellar evolution, which manifests as luminosity bump

(Christensen-Dalsgaard 2015). Also, it is at the bump H-profile discontinuity, a barrier for convective mixing, which gets removed and resumes mixing up of $p-p$- chain products with the photosphere. Mixing at the bump, also known as extra-mixing, is attributed to a rapid decrease in Li abundance and lowering of carbon isotopic ratios, $^{12}C/^{13}C$ (Gilroy 1989; Smiljanic *et al.* 2009). On the other hand, He-flash at the tip of RGB terminates the RGB phase by removing electron degeneracy in the core (Iben and Renzini 1984). Post He-flash, stars settle at the red clump quiescently burning He at the core with an outer H-burning shell before climbing up towards AGB.

There are a number of theoretical models dealing with extra mixing at the bump (Eggleton *et al.* 2008; Charbonnel and Lagarde 2010; Denissenkov and Merryfield 2011; Denissenkov 2012). The models do suggest a synthesis of Li via the Cameron-Fowler mechanism in H-shell and somehow dredge up with photosphere. The models were invoked with the presumption that Li-rich giants occur at the bump as reported by many observational studies (Charbonnel and Balachandran 2000; Kumar *et al.* 2011; Yan *et al.* 2018). However, it is not clear how the same mechanism that is responsible for the rapid depletion of Li is also responsible for Li enhancement. The lack of clarity on Li's origin probably stems from the fact that the evolutionary phase of Li-rich giants has not been identified without ambiguity. The reported Li-rich giants fall in a narrow luminosity range which overlaps both bump and clump regions. The difference between clump and bump values of luminosity and $T_{\rm eff}$ are small, and many a time, they are within the measurement uncertainties. This degeneracy even led to the suggestion that Li-rich giants may make a zigzag motion and appear as clump or bump giants due to internal rotation (Denissenkov 2012). Let us tackle this issue using this large data set and evolutionary period argument, as it requires a large number of stars to define the luminosity bump.

Among 335 Li-rich giants, there are only 106 giants which appear outside the red

clump. Only one-third of these seem to be either at the bump or above the bump. The large concentration of Li-rich giants at RC suggests, probably, that the origin of Li enhancement lies at or post He-flash rather than at the luminosity bump. If Li enhancement occurred at the bump, the enhanced Li has to be sustained till RC, which is quite unlikely given the deep convection post-bump evolution. One would also expect a significant number of Li-rich giants both at the bump and between the bump and the RGB tip because the evolutionary periods of giants between the bump to RGB tip (100 Myrs) and the red clump (100 Myrs) are similar (see Table-4.1). This is not the case as shown in Figure 4.4, as there is a factor of about four more Li-rich giants at the clump compared to those at the bump or post-bump evolution. One could make another argument against the bump as the site for Li origin based on very short Li depletion periods compared to the evolutionary time of luminosity bump (see Palacios *et al.* 2001; Kumar *et al.* 2015). The enhanced Li may deplete within 60% of the evolutionary period of the bump, i.e. Li-rich giants may become Li-normal within a few million years, which is much shorter than the evolutionary periods between the bump and RC. Based on this argument, it is reasonable to suggest that all the Li-rich giants are, most likely, in He-core burning phase rather than at multiple phases on RGB for Li origin. Of course, we need to have further studies to understand a minority of Li-rich giants that are outside of the RC region. This conclusion is also strengthened by the fact that all the presently known six Li-rich giants (e.g., Singh *et al.* 2019b) that are in the Kepler field are red clump giants. Data assembled in Figure 4.5 and Figure 4.6 suggests that most of the Li-rich giants are at red clump, which implicitly points towards He-flash, a major stellar event preceding red clump, for Li enrichment. However, we do not have much insight into the nucleosynthesis and dredge-up processes during He-flash, except for a couple of studies to understand Li-rich giants at the red clump or the early AGB stars of J-type. For example, the study Mocák *et al.* (2011) deals with Li production during He-flash, but in the case of very metal-poor giants. They show that the requirement of proton injection into the convective shell powered by He burning during the He-flash phase may not be met in the

case of metal-rich giants as He-ignition occurs relatively farther away from the H-burning shell. For explaining large Li abundances in J-type stars, Zhang and Jeffery (2013) explored merging up of He white dwarfs (WDs) of different masses with the He-core of RGB giants and showed that they could produce observed values for certain combinations.

4.6 Conclusion

In this paper, we have searched for Li-rich giants among a large data set of red giant branch stars given in the GALAH catalogue for which the *Gaia* astrometry is available. We found 335 giants with $A(\mathrm{Li}) \geq 1.80$ dex, an abundance which is more than the maximum Li abundance expected from canonical stellar models for stars in the mass range of 1 to 1.5$\mathrm{M}_{\odot}$. Among these, we found 20 super Li-rich giants with $A(\mathrm{Li}) \geq 3.20$ dex. This is the largest number of Li-rich giants ever reported in a single study. Values of Luminosity based on the *Gaia* parallax and T_{eff} given in the GALAH suggest that the majority of the Li-rich giants are red clump giants as defined in the HR diagram. Only a minority of them are outside it. About a dozen of Li-rich giants are found below the bump, which may be sub-giants. The high Li in them may be due to insufficient mixing and dilution from the initial values. There are a couple of Li-rich giants which are above RC and leftwards of the RGB, which may either be evolving off the red clump or just on their way to RC after experiencing He-flash at the RGB tip. A few Li-rich giants that seem to fall in the bump region, as defined in the HR diagram, need to be studied further.

With the advantage of large data set with well-defined evolutionary phases on RGB, we addressed the key issue of origin scenarios: external accretion versus in-situ nucleosynthesis. If the cause for Li excess is due to external accretion, one

would expect Li-rich giants across RGB. However, the disproportionately large concentration of Li-rich giants at a single evolutionary phase of red clump compared to those on RGB phase, between RGB base and its tip, suggest that external origin for Li enrichment is an unlikely scenario. Though the large data set provides compelling evidence that Li-rich giants may belong to RC with He-core burning phase, we cannot dismiss the possibility of a few Li-rich giants on other phases on RGB with different sources of Li enhancement. To firmly establish whether there are single or multiple sites on RGB for Li origin, it is important to conduct further studies such as asteroseismic analysis and detailed abundance studies of all the known Li-rich giants.

Chapter 5

Properties of Li-enriched and normal giants in the GALAH survey: mass, metallicity, stellar rotation and chemical composition*

5.1 Introduction

In the previous chapter (4), we covered the search for a clue to the origin of Li enrichment in giants based on their distribution in the HR diagram. We found that the great majority of the Li-rich giants are relatively long-lived He-core burning

*This chapter is published in Deepak *et al.* (2020).

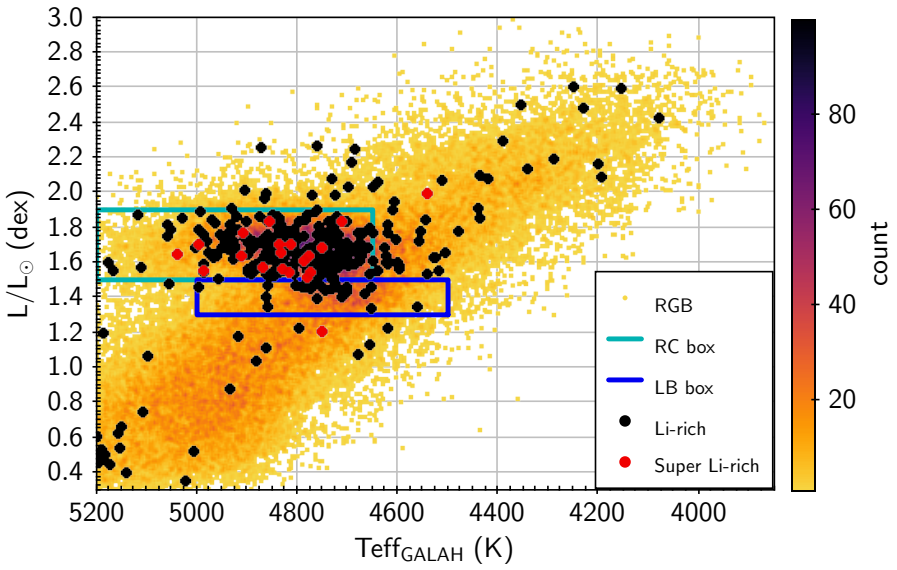


FIGURE 5.1: HR diagram showing the location of Li-rich giants ($1.8 \leq A(\mathrm{Li}) \leq 3.2$ dex) (black dots) and super Li-rich giants ($A(\mathrm{Li}) > 3.2$ dex) (red dots), with the complete sample of giants in the background. The outlines of the two most prominent evolutionary regions – the red clump (RC) and the luminosity bump (LB) – are taken from Deepak & Reddy (2019). Some of the cooler giants within the RC luminosity range are not included here to avoid possible contamination between RC and LB.

('clump') giants. A few have a luminosity above the clump, i.e., are on the early-AGB but prior to the onset of the third dredge-up when activation of the Cameron-Fowler mechanism is predicted and observed to provide strong Li enhancements in very luminous giants (Smith and Lambert 1989). In addition, a few Li-rich giants have the luminosity of the "luminosity bump" on the red giant branch well prior to the clump phase. The bump on the RGB occurs at the point when the H-burning shell moves outwards across the H-discontinuity. At this point in its evolution, models show that a star's evolution reverses course and moves down the RGB slightly before reversing again and continuing to evolve up the RGB. Li-rich giants at luminosities below that of clump and bump stars are assumed to have yet to complete their first dredge-up. Figure 5.1 shows the H-R diagram for all giants with Li-rich ($A(\mathrm{Li}) \geq 1.8$ dex) and super Li-rich giants ($A(\mathrm{Li}) \geq 3.2$ dex) highlighted, drawn by Deepak and Reddy (2019) from the selection of giants included in the GALAH survey.

In this study, to further understand the mechanism behind the Li enrichment in giants, the abundances of elements from Li to Eu are used to search for abundance differences between Li-rich and normal giants drawn from the GALAH survey (Buder *et al.* 2018). Stars are chosen by luminosity and metallicity. Discussion is limited to giants of the Galactic disc, i.e., [Fe/H] ≥ -1. To minimize the intrusion of systematic errors, samples of normal and Li-rich giants are compared for common intervals of luminosity and metallicity. Sample selections and their compositions are discussed in Section 5.2 and 5.3, respectively. This is the first such comprehensive examination of the composition of a large sample of Li-rich giants and an even larger sample of thoroughly otherwise comparable normal giants. In Section 5.4, we discuss various properties (like mass, rotational velocity, etc.) of Li-enriched giants relative to the Li-normal giants. A discussion of the possible origins of Li-rich stars is provided in Section 5.5. Section 5.6 concludes the chapter with some ideas for further advancing understanding of Li-rich giants.

5.2 Data sample

For the current study, we start with the red giant sample of Deepak and Reddy (2019), which includes 51,982 low mass ($M \leq 2$ M$_\odot$) stars with reliable atmospheric parameters (i.e., `flag_cannon` = 0) from the GALAH DR2 survey (Buder *et al.* 2018). As discussed before, the GALAH DR2 provides quantitatively derived abundances of 23 elements, from Li to Eu, for these giants. Except for Li, O, Al and Fe, the abundances are based on the assumption of Local Thermodynamic Equilibrium (LTE). Non-LTE Li abundances are obtained from recipes provided by (Lind *et al.* 2009a). O abundances are estimated from the O triplet (O I 7772 Å, 7774 Å, and 7775 Å) using 1D non-LTE corrections based on the model atom and non-LTE radiative transfer code described in Amarsi *et al.* (2015, 2016), but using 1D MARCS model atmospheres. Al abundance are measured from the Al I

lines 6696.023, 6698.673, 7835.309 and 7836.134 Å using 1D non-LTE corrections by Nordlander and Lind (2017). The condition `flag_cannon` = 0 ensures that to a high probability that none of the considered giants is a binary star (Buder *et al.* 2018). In the HR diagram, the chosen stars occupy the space defined by 3800 K $\leq T_{\rm eff} \leq$ 5200 K and 0.3 $\leq \log(L/{\rm L}_{\odot}) \leq$ 3.2 dex. This space includes giants from the base of the red giant branch (RGB) through its tip to the red clump and the early asymptotic giant branch (AGB) phase. All of the selected giants are expected to have reliable atmospheric parameters (i.e., `flag_cannon` = 0) and uncertainties in Teff of only 100 K and of parallax ($\sigma_{\Pi}/\Pi \leq 0.15$). The typical error in absolute luminosity is about 0.05 dex (see Deepak and Reddy 2019, for more details). In this sample, there are 335 Li-rich RGB stars with Li abundance, A(Li) $\geq$ 1.80 $\pm$ 0.14 dex of which 20 are super Li-rich with A(Li) $\geq$ 3.20 dex. Specific gravity ($\log g$) for giants of RGB sample ranges from 0.45 to 4.10 dex, with the majority of the Li enriched giants falling in a narrow strip defined by *logg* from 2.0 to 2.9 dex. The typical error in the $\log g$ is about 0.19 dex, while the maximum error is about 0.22 dex. The samples of normal and Li-enriched giants span the same intervals in effective temperature.

It would be interesting to understand whether some of the lowest Li abundances are indeed measurements. Unfortunately, we do not have access to the actual stellar spectra to examine. Yet, we made an effort to estimate the fraction of giants for which abundances may be upper limits. For this, we estimated the detection limit for the Li line 6707.7Å using a relation δ(EW) = 1.6$\times(\omega\ \delta x)^{0.5}$/SNR (Cayrel 1988). By using the signal-to-noise ratio (SNR) of individual stars given in the GALAH catalogue, pixel size (δx) as 0.047Å, and FWHM (w) as 0.24Å for the spectral resolution, we obtain δ(EW) $\approx$ 2.5 mÅ. For this study, we adopt Li abundance as measurement if the Li line EW is more than or equal to three times that of δ(EW). By estimating EWs using the lowest Li abundances in the sample across the Teff range and comparing them with the adopted limit, we estimate that about 2% of stars might be upper limits or uncertain, and the rest are measurements.

Required atomic data for Li line for conversion from given abundance to EW is taken from Ghezzi *et al.* (2009). To predict the EW corresponding to the given lowest Li abundance across the sample temperature range, we used the radiative transfer code MOOG 2013 version (Sneden 1973) and LTE stellar atmospheric models from Castelli and Kurucz (2003) using atmospheric parameters given in the GALAH catalogue.

5.2.1 Samples by Luminosity

To a first approximation, cuts in the H-R diagram by luminosity and effective temperature sample stars over a range in mass and metallicity but at similar evolutionary stages. The H-R diagram in Figure 5.1 is broken into four regions. The two seemingly most relevant regions for investigations of Li-rich stars are outlined in the figure. The region bounded by $\log(L/L_{\odot})$ from 1.5 to 1.9 and $Teff_{GALAH}$ from 4650 K to 5200 K includes giants experiencing He-core burning. This region (here, the red clump or RC sample) contains the majority of the normal, Li-rich and super Li-rich giants. Below the RC strip in the figure are stars chosen as possible candidates belonging to the bump on the first ascent of the red giant branch (the LB sample). This is defined in the figure by the luminosity limits 1.3 and 1.5, and effective temperature limits 4500 K and 5000 K. Considering the range of mass and metallicity of the sample, a small overlap between RC and LB boxes can not be ruled out. However, the majority of the He-core burning giants are in the RC box. The two remaining selections in the H-R diagram are (i) stars more luminous than the RC and LB stars, that is, stars with luminosities between 1.9 and 3.0 (the maximum limit for the figure) (here, labelled as RC^{+} stars but the sample likely includes stars on the RGB up to its tip) and (ii) subgiant stars with luminosities between 0.3 and 1.3 (i.e., less luminous than the LB sample, here LB^{-} stars). Our selection from the GALAH survey provides the following numbers of giants across the four groups: 5951 (RC^{+}), 17909 (RC), 5518 (LB), and 17670

(LB^-) of which 31, 229, 23, and 27 are Li-rich, respectively. These numbers cover all metallicities.

5.3 Analysis

Our search for clues to the origins of Li-rich giants relies on the determination of differences in the abundance ratios [X/Fe] between Li-normal and Li-rich giants in the same evolutionary phase with the same average luminosity, effective temperature and metallicity [Fe/H]. Abundances may also depend on the micro turbulence. Within a given luminosity class, the distribution of the microturbulence velocities for the Li-rich, super Li-rich and normal giants are identical. The test is based on the assumption that any systematic error in abundance will be identical for Li-normal and Li-rich (including the super Li-rich) giants. We divide each of our four evolutionary phases RC^+, RC, LB and LB^- into the four metallicity ([Fe/H]) bins -0.5 to -0.3, -0.3 to -0.1, -0.1 to 0.1 and 0.1 to 0.3 dex centred at -0.4, -0.2, 0.0 and $+0.2$ dex, respectively. (Metal-poor ([Fe/H] < -0.5) giants are not considered because Li-rich giants at these metallicities are exceedingly rare (see Figure 2 of Deepak and Reddy 2019). Their rarity may be due simply to the small samples of metal-poor giants in the GALAH survey and a low occurrence rate for Li-rich giants, as reported for more metal-rich giants, or to the production of Li-rich giants decreasing with decreasing metallicity.) For each luminosity sample, relative abundances [X/Fe] at [Fe/H] = $+0.2$, 0.0, -0.2 and -0.4 are determined provided that a sufficient number of abundances are present in the GALAH database. It is important that Li-rich giants be compared with Li-normal giants of the same luminosity class because different ranges in effective temperature and surface gravity may be involved, for example, an inspection of

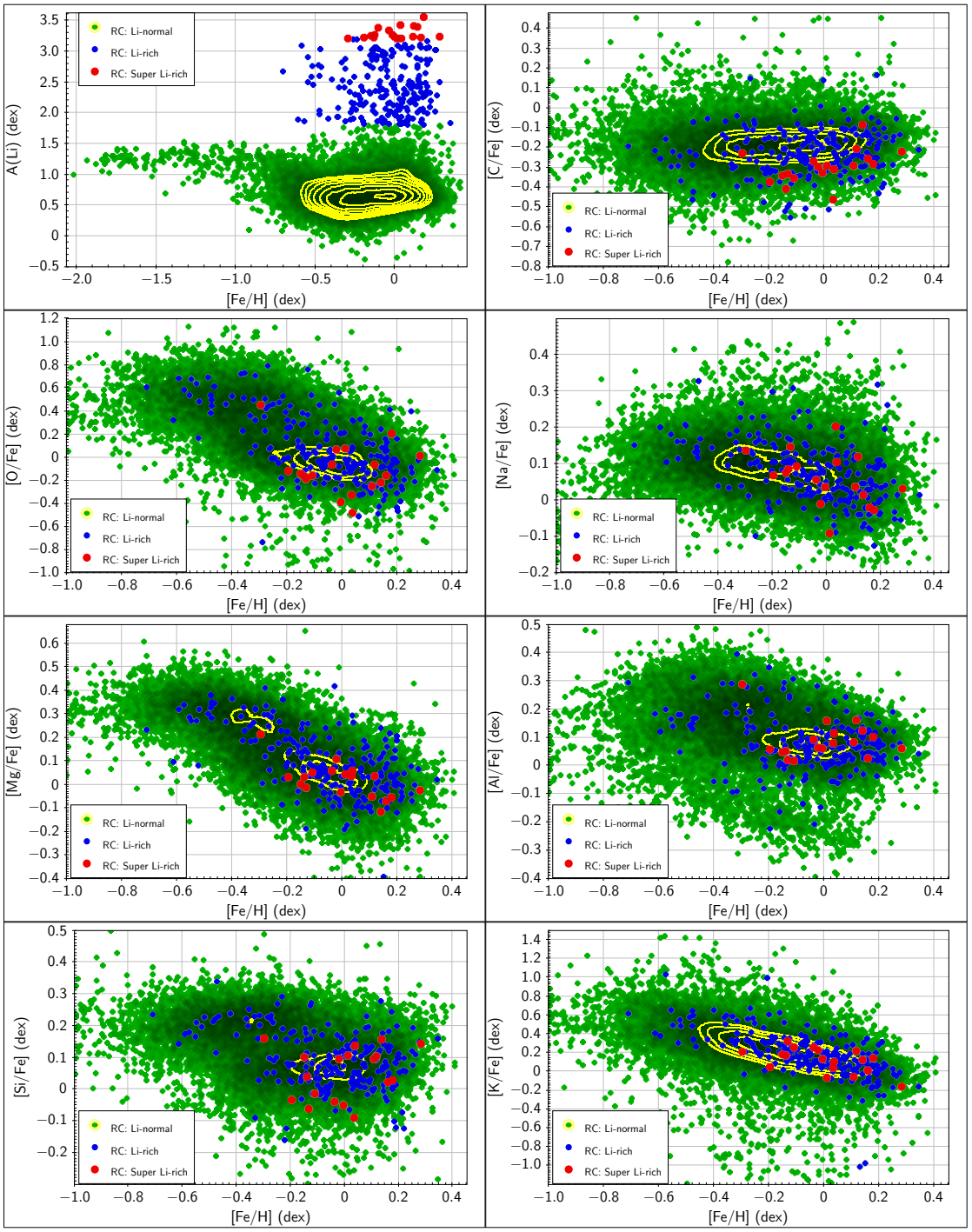


FIGURE 5.2: Distribution of elemental abundances of Li-normal, rich and super-rich giants of red-clump (RC) sample. The yellow contours in each panel represent the density of Li normal giants and are provided to ease the visualisation of the positions of the Li-rich and super Li-rich giants with respect to the Li normal giants.

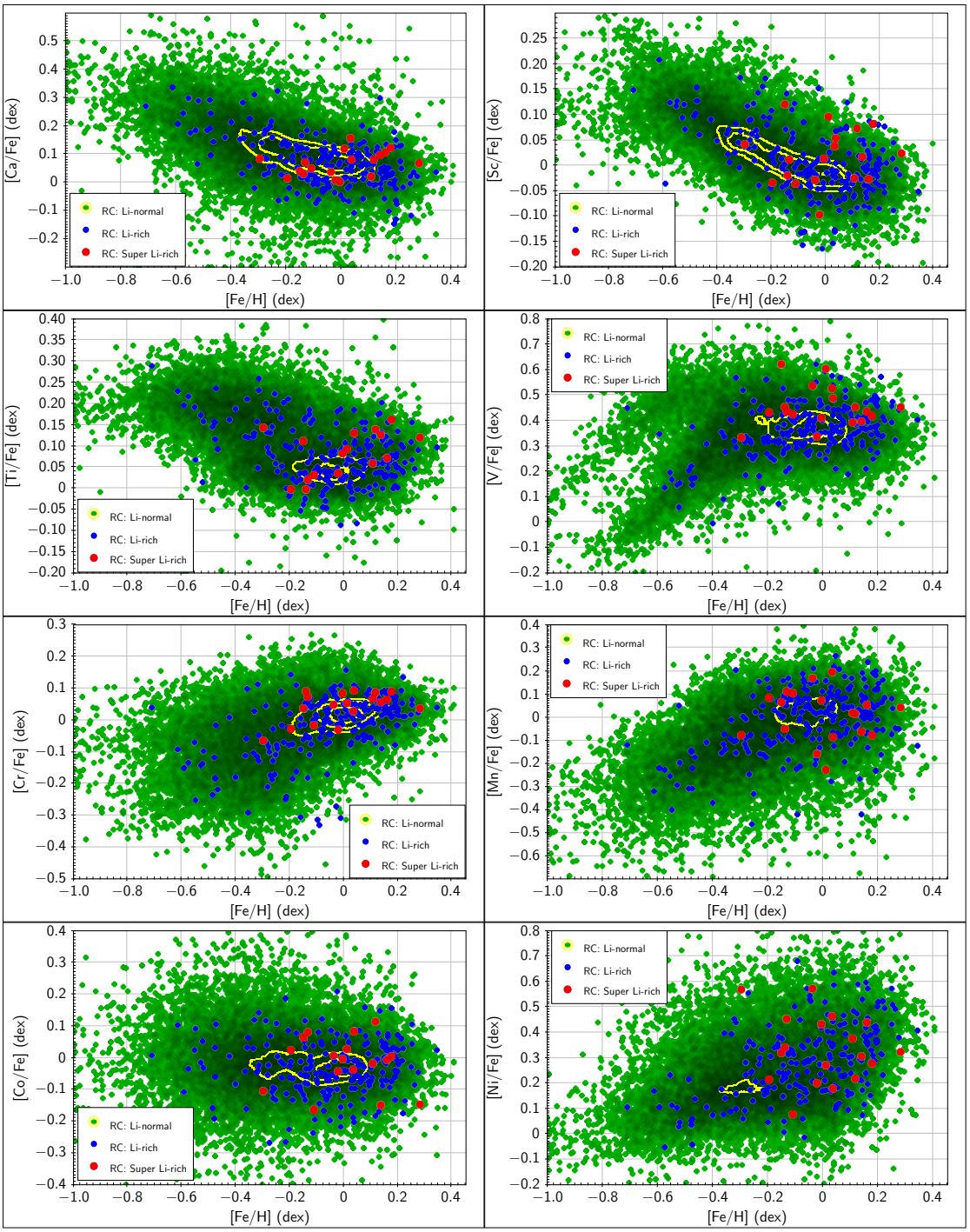


Figure 5.2 - *continued*

TABLE 5.1: Mean [Fe/H], A(Li) and [X/Fe] abundances with the standard error of the mean (SEM) for all the 21 elements given in the GALAH survey for Li-normal and Li-rich giants of each of the four luminosity samples. Results are tabulated for four [Fe/H] ranges. In the cases where the number of stars (data points) is less than five, we have provided the average of the abundance error given in the GALAH survey, and all such cases are marked with an asterisk (*).

	RGB,	RC^+ stars by [Fe/H] intervals				RC stars by [Fe/H] intervals			
	Li-	(-0.5, -0.3)	(-0.3, -0.1)	(-0.1, 0.1)	(0.1, 0.3)	(-0.5, -0.3)	(-0.3, -0.1)	(-0.1, 0.1)	(0.1, 0.3)
Stars	normal	1937	1415	538	25	3947	5147	4813	1800
	rich	7	13	5	1	18	58	84	59
[Fe/H]	normal	-0.402±0.001	-0.212±0.001	-0.031±0.002	0.133±0.007	-0.388±0.001	-0.200±0.001	-0.004±0.001	0.168±0.001
	rich	-0.441±0.019	-0.183±0.014	-0.049±0.015	0.137±0.054*	-0.392±0.015	-0.186±0.008	0.002±0.006	0.172±0.006
A(Li)	normal	0.116±0.010	0.203±0.012	0.288±0.020	0.557±0.116	0.632±0.003	0.650±0.003	0.714±0.003	0.723±0.005
	rich	2.550±0.175	2.236±0.090	2.278±0.169	1.893±0.117*	2.397±0.089	2.537±0.061	2.408±0.049	2.553±0.058
[C/Fe]	normal	-0.198±0.002	-0.186±0.002	-0.184±0.004	-0.124±0.037	-0.203±0.002	-0.197±0.001	-0.186±0.001	-0.167±0.002
	rich	-0.286±0.026	-0.265±0.021	-0.190±0.044	-0.183±0.019*	-0.240±0.031	-0.262±0.017	-0.221±0.012	-0.207±0.014
[O/Fe]	normal	0.367±0.008	0.164±0.009	0.021±0.012	-0.067±0.056	0.358±0.004	0.170±0.004	-0.007±0.003	-0.073±0.005
	rich	0.281±0.118	0.005±0.073	-0.385±0.165	-0.186±0.082*	0.463±0.046	0.115±0.038	-0.018±0.022	-0.103±0.025
[Na/Fe]	normal	0.108±0.002	0.094±0.003	0.088±0.005	0.138±0.026	0.113±0.001	0.095±0.001	0.071±0.001	0.052±0.002
	rich	0.171±0.041	0.123±0.027	0.191±0.041	0.258±0.039*	0.148±0.017	0.111±0.010	0.060±0.008	0.033±0.011
[Mg/Fe]	normal	0.190±0.004	0.065±0.004	-0.036±0.007	-0.034±0.037	0.244±0.002	0.139±0.002	0.036±0.002	-0.009±0.002
	rich	0.196±0.027	0.040±0.057	-0.167±0.063	-0.039±0.061*	0.287±0.014	0.135±0.015	0.037±0.012	0.021±0.013
[Al/Fe]	normal	0.228±0.003	0.163±0.003	0.105±0.004	0.031±0.021	0.161±0.002	0.124±0.002	0.077±0.001	0.074±0.002
	rich	0.277±0.053	0.159±0.025	0.055±0.032	0.081±0.034*	0.144±0.034	0.089±0.016	0.057±0.009	0.073±0.007
[Si/Fe]	normal	0.203±0.004	0.150±0.004	0.132±0.006	0.074±0.021	0.156±0.002	0.115±0.001	0.078±0.001	0.094±0.002
	rich	0.161±0.058	0.164±0.041	-0.014±0.031	0.099±0.055*	0.180±0.023	0.097±0.013	0.067±0.008	0.079±0.010

Table 5.1 - *continued*

	RGB,	RC^+ stars by [Fe/H] intervals				RC stars by [Fe/H] intervals			
	Li-	(-0.5, -0.3)	(-0.3, -0.1)	(-0.1, 0.1)	(0.1, 0.3)	(-0.5, -0.3)	(-0.3, -0.1)	(-0.1, 0.1)	(0.1, 0.3)
[K/Fe]	normal	0.099±0.006	0.030±0.007	-0.025±0.010	0.042±0.059	0.359±0.004	0.232±0.003	0.113±0.003	0.005±0.005
	rich	0.231±0.093	0.071±0.066	0.095±0.042	0.109±0.070*	0.466±0.032	0.277±0.025	0.140±0.016	-0.008±0.030
[Ca/Fe]	normal	0.136±0.002	0.089±0.002	0.054±0.004	0.045±0.024	0.159±0.002	0.103±0.001	0.064±0.001	0.045±0.002
	rich	0.166±0.024	0.114±0.022	0.080±0.013	0.058±0.042*	0.170±0.020	0.088±0.011	0.053±0.007	0.042±0.010
[Sc/Fe]	normal	0.121±0.002	0.072±0.002	0.013±0.003	-0.071±0.017	0.075±0.001	0.025±0.001	-0.014±0.001	-0.030±0.001
	rich	0.181±0.025	0.058±0.022	-0.028±0.015	-0.048±0.035*	0.076±0.011	0.032±0.008	-0.022±0.007	-0.008±0.006
[Ti/Fe]	normal	0.200±0.002	0.147±0.002	0.108±0.003	0.045±0.011	0.151±0.001	0.104±0.001	0.069±0.001	0.073±0.001
	rich	0.229±0.026	0.131±0.023	0.069±0.014	0.023±0.028*	0.147±0.015	0.079±0.009	0.053±0.006	0.076±0.006
[V/Fe]	normal	0.433±0.002	0.404±0.002	0.359±0.003	0.296±0.016	0.326±0.002	0.381±0.001	0.371±0.001	0.351±0.002
	rich	0.420±0.047	0.416±0.039	0.371±0.033	0.212±0.043*	0.284±0.032	0.349±0.013	0.393±0.010	0.392±0.009
[Cr/Fe]	normal	-0.047±0.002	-0.017±0.002	-0.001±0.003	0.004±0.016	-0.094±0.002	-0.047±0.001	0.008±0.001	0.024±0.001
	rich	-0.004±0.027	-0.034±0.015	0.036±0.021	-0.039±0.042*	-0.098±0.026	-0.046±0.013	-0.002±0.010	0.034±0.006
[Mn/Fe]	normal	-0.206±0.004	-0.143±0.005	-0.080±0.007	0.022±0.030	-0.136±0.002	-0.060±0.002	-0.009±0.002	-0.002±0.003
	rich	-0.213±0.062	-0.162±0.032	-0.016±0.061	-0.001±0.047*	-0.141±0.029	-0.025±0.017	0.018±0.014	0.018±0.015
[Co/Fe]	normal	0.074±0.002	0.042±0.003	0.010±0.003	-0.084±0.017	-0.013±0.002	-0.017±0.001	-0.026±0.001	-0.028±0.002
	rich	0.070±0.026	0.004±0.024	-0.053±0.014	-0.091±0.038*	-0.050±0.039	-0.054±0.015	-0.042±0.009	-0.017±0.010
[Ni/Fe]	normal	0.217±0.003	0.233±0.003	0.261±0.006	0.347±0.029	0.203±0.002	0.240±0.002	0.276±0.002	0.351±0.003
	rich	0.174±0.031	0.222±0.038	0.223±0.065	0.217±0.049*	0.170±0.034	0.259±0.016	0.305±0.015	0.364±0.016
[Cu/Fe]	normal	0.071±0.002	0.057±0.003	0.013±0.004	-0.046±0.023	-0.017±0.001	0.029±0.001	0.020±0.001	0.054±0.002
	rich	-0.034±0.020	0.048±0.034	-0.051±0.047	-0.216±0.045*	-0.048±0.020	-0.019±0.012	-0.028±0.009	0.023±0.011

Table 5.1 - *continued*

	RGB,	RC^+ stars by [Fe/H] intervals				RC stars by [Fe/H] intervals			
	Li-	(-0.5, -0.3)	(-0.3, -0.1)	(-0.1, 0.1)	(0.1, 0.3)	(-0.5, -0.3)	(-0.3, -0.1)	(-0.1, 0.1)	(0.1, 0.3)
[Zn/Fe]	normal	0.068±0.006	-0.035±0.007	-0.069±0.011	0.089±0.061	0.271±0.003	0.160±0.003	0.048±0.003	0.029±0.004
	rich	-0.041±0.138	0.012±0.100	-0.149±0.095	-0.023±0.058*	0.448±0.030	0.189±0.023	0.090±0.023	0.040±0.022
[Y/Fe]	normal	0.071±0.005	0.148±0.006	0.287±0.010	0.312±0.050	0.046±0.003	0.050±0.003	0.119±0.003	0.106±0.005
	rich	0.062±0.055	0.150±0.048	0.230±0.055	0.278±0.063*	0.069±0.033	0.108±0.023	0.100±0.022	0.077±0.024
[Ba/Fe]	normal	0.105±0.006	0.243±0.007	0.360±0.010	0.510±0.071	0.186±0.004	0.276±0.003	0.351±0.003	0.296±0.004
	rich	0.235±0.233	0.203±0.182	0.577±0.108	0.592±0.073*	0.246±0.223	0.394±0.230	0.390±0.189	0.308±0.018
[La/Fe]	normal	0.045±0.003	0.081±0.003	0.101±0.004	0.018±0.035	-0.054±0.002	-0.011±0.002	0.023±0.002	-0.019±0.002
	rich	0.163±0.046	0.064±0.025	0.064±0.040	0.020±0.038*	-0.058±0.031	0.007±0.015	-0.006±0.015	-0.020±0.011
[Eu/Fe]	normal	0.257±0.004	0.177±0.004	0.106±0.006	-0.039±0.044	0.173±0.002	0.103±0.002	0.036±0.002	-0.005±0.003
	rich	0.468±0.079	0.146±0.036	-0.032±0.044	0.053±0.043*	0.204±0.024	0.094±0.019	-0.021±0.015	0.009±0.018

	RGB,	LB stars by [Fe/H] intervals				LB^- stars by [Fe/H] intervals			
	Li-	(-0.5, -0.3)	(-0.3, -0.1)	(-0.1, 0.1)	(0.1, 0.3)	(-0.5, -0.3)	(-0.3, -0.1)	(-0.1, 0.1)	(0.1, 0.3)
Stars	normal	1229	1590	1592	481	2663	4498	5511	3298
	rich	0	5	5	7	0	1	5	12
[Fe/H]	normal	-0.388±0.002	-0.197±0.001	-0.008±0.001	0.176±0.002	-0.385±0.001	-0.192±0.001	-0.002±0.001	0.180±0.001
	rich	—	-0.192±0.026	0.029±0.019	0.212±0.024	—	-0.202±0.079*	-0.004±0.018	0.167±0.014
A(Li)	normal	0.617±0.006	0.651±0.005	0.671±0.005	0.676±0.010	0.979±0.005	1.000±0.004	1.015±0.003	1.010±0.004
	rich	—	2.390±0.182	2.392±0.203	2.408±0.148	—	1.916±0.132*	2.012±0.171	2.186±0.150
[C/Fe]	normal	-0.177±0.003	-0.184±0.003	-0.177±0.002	-0.162±0.005	-0.113±0.003	-0.147±0.002	-0.158±0.002	-0.156±0.002
	rich	—	-0.252±0.054	-0.197±0.021	-0.152±0.036	—	-0.200±0.027*	-0.160±0.048	-0.213±0.030

Table 5.1 - *continued*

	RGB,	LB stars by [Fe/H] intervals				LB$^-$ stars by [Fe/H] intervals			
	Li-	(-0.5, -0.3)	(-0.3, -0.1)	(-0.1, 0.1)	(0.1, 0.3)	(-0.5, -0.3)	(-0.3, -0.1)	(-0.1, 0.1)	(0.1, 0.3)
[O/Fe]	normal	0.377±0.007	0.188±0.007	0.020±0.006	-0.045±0.011	0.314±0.004	0.142±0.003	0.004±0.003	-0.065±0.004
	rich	—	0.306±0.111	-0.217±0.072	-0.261±0.095	—	0.248±0.114*	0.070±0.079	-0.109±0.036
[Na/Fe]	normal	0.108±0.002	0.067±0.002	0.036±0.002	0.029±0.004	0.089±0.001	0.042±0.001	0.003±0.001	0.019±0.001
	rich	—	0.141±0.038	0.026±0.017	-0.022±0.020	—	0.073±0.053*	0.028±0.022	0.021±0.038
[Mg/Fe]	normal	0.267±0.003	0.158±0.003	0.062±0.003	0.003±0.006	0.265±0.002	0.167±0.002	0.090±0.002	0.063±0.002
	rich	—	0.152±0.049	0.041±0.036	-0.012±0.031	—	0.355±0.084*	0.149±0.028	0.011±0.024
[Al/Fe]	normal	0.235±0.004	0.179±0.003	0.114±0.003	0.090±0.004	0.192±0.003	0.127±0.002	0.082±0.001	0.083±0.002
	rich	—	0.100±0.021	-0.003±0.032	0.013±0.026	—	0.083±0.047*	0.124±0.043	0.053±0.013
[Si/Fe]	normal	0.188±0.003	0.139±0.003	0.108±0.003	0.124±0.004	0.147±0.002	0.092±0.002	0.055±0.001	0.070±0.002
	rich	—	0.121±0.047	0.027±0.086	0.105±0.036	—	0.161±0.077*	0.073±0.017	0.020±0.019
[K/Fe]	normal	0.220±0.007	0.116±0.006	0.014±0.006	-0.020±0.012	0.243±0.004	0.131±0.003	0.005±0.003	-0.085±0.004
	rich	—	0.246±0.041	-0.006±0.022	-0.075±0.153	—	-0.256±0.108*	0.027±0.062	0.063±0.086
[Ca/Fe]	normal	0.181±0.003	0.117±0.002	0.070±0.002	0.032±0.005	0.180±0.002	0.109±0.002	0.055±0.001	0.038±0.002
	rich	—	0.154±0.019	0.066±0.027	0.002±0.030	—	0.244±0.059*	0.046±0.033	-0.019±0.026
[Sc/Fe]	normal	0.126±0.002	0.098±0.002	0.067±0.002	0.023±0.003	0.117±0.001	0.083±0.001	0.056±0.001	0.064±0.001
	rich	—	-0.001±0.016	-0.056±0.022	-0.047±0.033	—	0.116±0.050*	0.087±0.022	0.020±0.013
[Ti/Fe]	normal	0.197±0.002	0.148±0.002	0.118±0.002	0.103±0.003	0.182±0.002	0.128±0.001	0.092±0.001	0.090±0.001
	rich	—	0.082±0.055	0.037±0.034	0.075±0.037	—	0.164±0.039*	0.113±0.070	0.033±0.024
[V/Fe]	normal	0.482±0.003	0.469±0.002	0.438±0.002	0.384±0.004	0.443±0.002	0.455±0.002	0.450±0.001	0.439±0.002
	rich	—	0.331±0.041	0.382±0.037	0.402±0.019	—	0.515±0.063*	0.464±0.062	0.390±0.034

Table 5.1 - *continued*

	RGB,	LB stars by [Fe/H] intervals				LB$^-$ stars by [Fe/H] intervals			
	Li-	(-0.5, -0.3)	(-0.3, -0.1)	(-0.1, 0.1)	(0.1, 0.3)	(-0.5, -0.3)	(-0.3, -0.1)	(-0.1, 0.1)	(0.1, 0.3)
[Cr/Fe]	normal	-0.037±0.003	0.003±0.002	0.040±0.002	0.040±0.002	-0.020±0.002	0.008±0.001	0.039±0.001	0.059±0.001
	rich	—	-0.085±0.045	0.051±0.026	0.050±0.025	—	-0.082±0.063*	0.001±0.012	0.025±0.021
[Mn/Fe]	normal	-0.134±0.004	-0.087±0.004	-0.042±0.004	-0.016±0.008	-0.098±0.002	-0.039±0.002	-0.001±0.002	0.022±0.002
	rich	—	-0.001±0.043	0.130±0.057	-0.001±0.060	—	-0.254±0.066*	0.048±0.051	0.038±0.026
[Co/Fe]	normal	0.063±0.003	0.042±0.003	0.030±0.003	0.010±0.004	0.048±0.003	0.026±0.002	0.012±0.002	0.019±0.002
	rich	—	-0.078±0.032	-0.039±0.030	-0.010±0.025	—	0.125±0.054*	0.012±0.049	0.085±0.033
[Ni/Fe]	normal	0.219±0.003	0.236±0.003	0.272±0.003	0.345±0.006	0.191±0.002	0.212±0.002	0.230±0.002	0.272±0.002
	rich	—	0.167±0.029	0.372±0.017	0.359±0.069	—	0.112±0.066*	0.223±0.055	0.250±0.038
[Cu/Fe]	normal	0.081±0.003	0.110±0.002	0.099±0.003	0.115±0.004	0.056±0.002	0.089±0.001	0.091±0.001	0.128±0.002
	rich	—	0.005±0.029	-0.022±0.047	0.072±0.033	—	0.134±0.063*	0.051±0.028	0.064±0.025
[Zn/Fe]	normal	0.118±0.004	0.029±0.004	-0.035±0.005	-0.016±0.01	0.096±0.003	0.028±0.002	-0.035±0.002	-0.041±0.003
	rich	—	0.191±0.097	0.126±0.104	0.138±0.064	—	0.153±0.078*	0.165±0.067	0.012±0.044
[Y/Fe]	normal	0.017±0.006	0.032±0.005	0.108±0.006	0.126±0.011	0.005±0.004	0.030±0.003	0.074±0.003	0.055±0.004
	rich	—	0.121±0.066	0.271±0.090	0.139±0.103	—	-0.287±0.088*	-0.068±0.034	-0.002±0.068
[Ba/Fe]	normal	-0.030±0.006	0.066±0.006	0.147±0.005	0.164±0.010	-0.053±0.005	0.026±0.003	0.034±0.003	-0.040±0.003
	rich	—	0.323±0.232	0.377±0.108	0.298±0.113	—	-0.204±0.102*	0.057±0.160	0.139±0.054
[La/Fe]	normal	0.023±0.004	0.051±0.003	0.063±0.003	0.008±0.005	0.039±0.003	0.068±0.002	0.068±0.002	0.018±0.003
	rich	—	-0.118±0.097	0.030±0.045	-0.055±0.053	—	0.065±0.053*	0.104±0.045	0.014±0.031
[Eu/Fe]	normal	0.247±0.004	0.161±0.004	0.084±0.004	0.014±0.007	0.221±0.003	0.120±0.003	-0.003±0.003	-0.107±0.004
	rich	—	0.133±0.059	-0.008±0.047	0.040±0.059	—	0.248±0.058*	0.018±0.080	-0.139±0.080

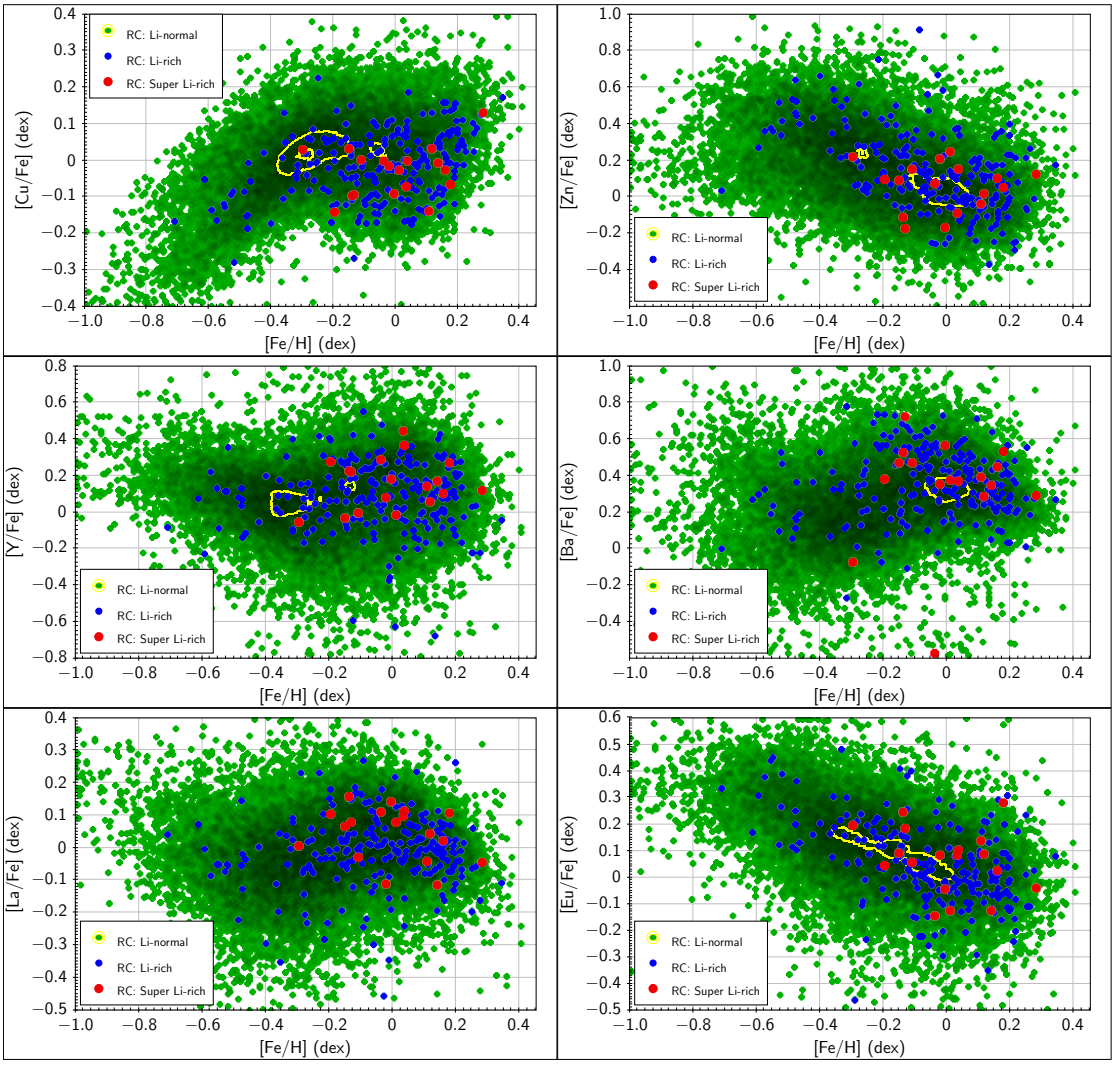


Figure 5.2 - *continued*

Figure 5.1 suggests that the RC$^+$ stars are systematically cooler and of lower surface gravity than the LB stars. Mean [X/Fe] along with standard error of the mean (SEM) corresponding to each of the 21 elements from C to Eu for both Li-normal and Li-rich populations in each of the luminosity samples are summarized in Table 5.1. For Li, we have provided the average value of A(Li) calculated after culling out giants ($\approx 2\%$) for which provided Li abundances are thought to be upper limits or uncertain, and for Fe, the actual mean value of [Fe/H] corresponding to each metallicity bin is given. (The mean values of [Fe/H] offer a check on the difference in the actual mean of two populations in a particular metallicity bin, which can be quite large if distribution along [Fe/H] is not symmetric or homogeneous).

Inspection of Table 5.1 shows that [X/Fe] from O to Eu are the same for Li-normal, Li-rich and super Li-rich giants within any luminosity class and [Fe/H] interval. The case of C is discussed separately in Section 5.4.4. To illustrate further the lack of dependence of [X/Fe] on the Li abundance, we show in Figures 5.2 the run of [X/Fe] with [Fe/H] for X = C to Eu for the giants of RC sample. These figures confirm, of course, the numerical results in Table 5.1. The similarity of [X/Fe] in a given luminosity class and [Fe/H] interval across the Li abundance range serves to challenge theories on how Li enrichment may occur. Two challenges will be mentioned here.

First, there is a possibility that Li-enrichment might be coupled with the *s*-process, as in the creation of a Li-enriched giant by mass-transfer from a *s*-process and Li-enriched AGB star but this idea is eliminated by the lack of differences in [Y/Fe], [Ba/Fe] and [La/Fe] between Li-normal and the Li-rich giants at a given [Fe/H] and for a given luminosity class. Second, the accretion of external material (e.g., planets or brown dwarves) may also result in a Li-enriched giant. Accretion may result in abundance changes for some elements in addition to Li enrichment. For example, the accretion of Earth-like planets may result in abundance enrichments dependent on the volatility of an element, i.e., on an element's condensation temperature. There is no hint of such a dependence in Table 5.1 and Figure 5.2. For example, in the RC luminosity range and the interval centred on [Fe/H] = 0.0, the difference between [X/Fe] for the Li-normal and Li-enriched giants in Table 5.1 is within limit +0.06 and −0.07 for O to Eu with no dependence on an element's condensation temperature. Perhaps, the primary lesson from Table 5.1 and Figure 5.2 is that one should look to the simplest theories for an explanation of Li-rich giants (Occam's razor!).

Quite independently of a search for clues to Li enrichment, Table 5.1 and Figure 5.2 are essential tools for mapping the chemical evolution of elements in the thin and thick disc. (Results for the halo are not plotted in this figure.) Figure 5.2

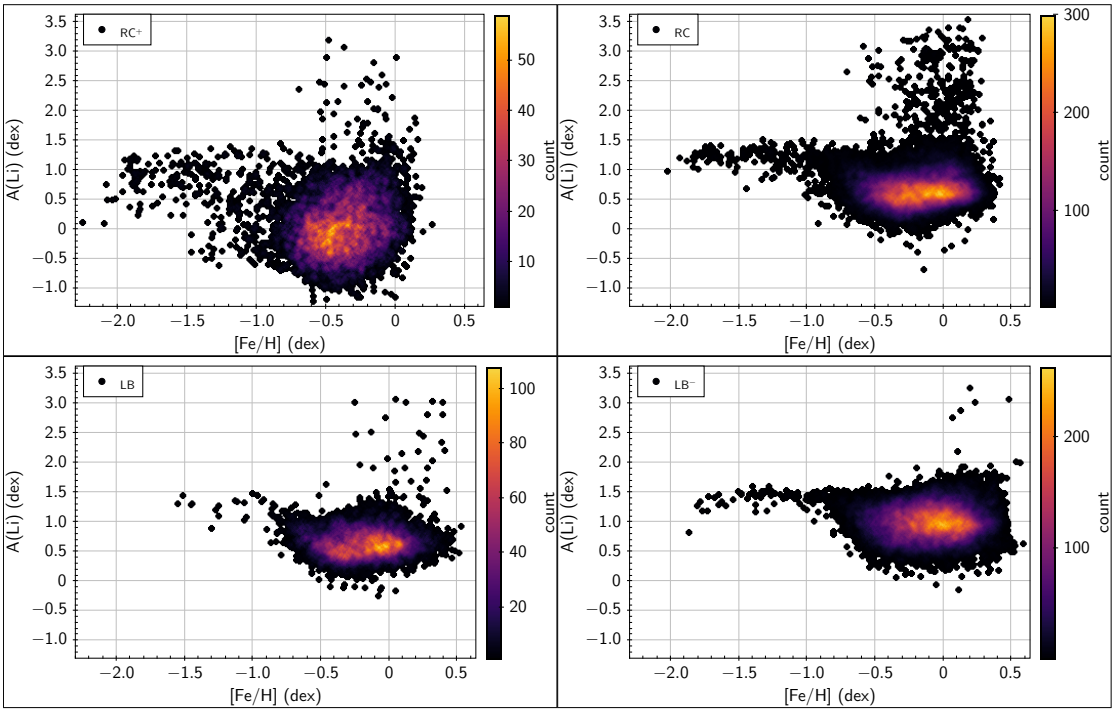


FIGURE 5.3: Lithium versus [Fe/H] for the GALAH sample across the four luminosity samples RC^+, RC, LB and LB^-.

generally appears consistent with the many surveys now in the literature (e.g., Reddy *et al.* 2003, 2006; Li *et al.* 2018a; Buder *et al.* 2019). With respect to the consensus from prior surveys, two kinds of anomalies are apparent in Figure 5.2. First, the run of [X/Fe] with [Fe/H] for elements shows unexpected structure. Second, the [X/Fe] – [Fe/H] distribution is offset clearly from previous results. Some elements combine aspects of (i) and (ii). In category (i), Al and V stand out in that there is a run of low [Al/Fe] and [V/Fe] below the main body of the results. In addition, but not apparent from Figure 5.2, many low values of [Ti/Fe] and [Ba/Fe] have been reported. In category (ii), the obvious cases are again V as well as Ni and Ba. These anomalies are discussed fully in the reference paper on the GALAH observations and their analysis (Buder *et al.* 2019). The anomalies of type (i) were excluded in calculating the entries in Table 5.1. Type (ii) offsets are assumed to be unaffected by the Li abundance for a given luminosity and metallicity interval. Ti, along with Si and Mg, is one of the most precisely measured elements in the GALAH survey, however, due to issues in the wavelength

solution of the red channel (covering 6478 – 6737 Å) and spikes in the infrared channel (covering 7585 – 7887 Å) of the HERMES spectrograph, several Mg, Si, and Ti abundances show values below [Mg/Fe], [Si/Fe] and [Ti/Fe] of −0.3, and as suggested by Buder *et al.* (2018), training set distances are the probable reason for these errors, and while working with data from the GALAH survey, one should avoid such affected abundances when possible. In our study, we have excluded all such stars while calculating the mean and standard error of the mean (SEM) for the distribution of Mg, Si, Ti and Ba, but have included these stars in evaluating statistics for other elements with good abundances.

5.4 Lithium and other stellar properties

5.4.1 Lithium and luminosity

Investigation of the Li abundances, including the distribution of the Li-rich giants with luminosity and metallicity relative to Li-normal giants, is possible with the GALAH sample because whatever selection effects may have entered into the selection of survey stars, the effects are unlikely to have biassed the selection of the Li-rich giants relative to normal giants. Distribution of the Li abundances with [Fe/H] for disc giants in the four luminosity samples RC^+, RC, LB and LB^- is shown in Figure 5.3. In each luminosity sample, the Li-rich and super Li-rich stars are found at [Fe/H] > -0.7 dex. In this [Fe/H] range, the occurrence and the frequency of occurrence of Li-rich (including super Li-rich) giants are highest for the RC sample and apparently increase with [Fe/H]: the frequency (in %) is 0.5, 1.1, 1.7 and 3.3 as [Fe/H] increases from the most metal-poor interval centred on −0.4, through [Fe/H] −0.2 and 0.0 to the most metal-rich box at [Fe/H] = +0.2. The total number of Li-rich giants in the RC sample with [Fe/H] from −0.5 to +0.3 dex is 219 out of a Li-normal population of 15707 for a [Fe/H]-independent

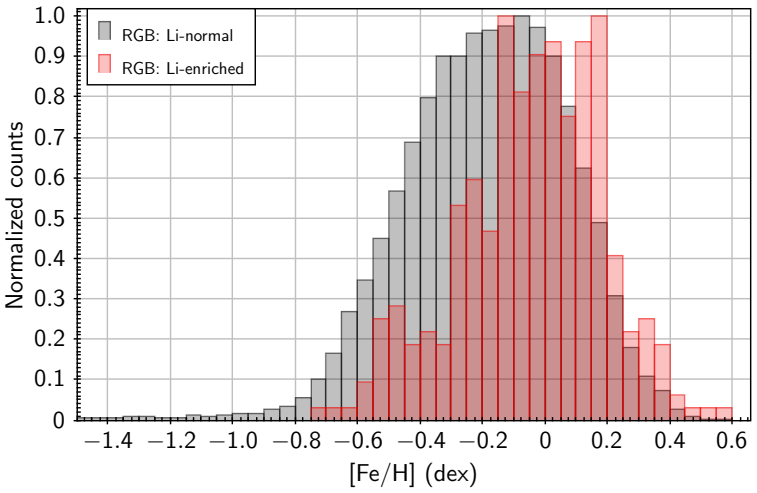


FIGURE 5.4: Normalized frequency distribution for Li-enriched and normal giants along [Fe/H]-axis.

frequency of 1.4%. In the most luminous sample RC^+, the frequency of occurrence is slightly less than 1% in each [Fe/H] bin: 26 Li-rich giants in a total sample of 3915 giants for a mean frequency of occurrence of 0.7%. The occurrence of Li-rich giants in the LB sample is of considerable interest because of suggestions that internal conditions responsible for the luminosity 'bump' may be ripe for Li production. The total number of Li-normal giants in the LB sample is 4892 with 17 Li-rich stars; the frequency of occurrence of Li-rich giants over the [Fe/H] range in Table 5.1 is 0.3%, a lower frequency than in the RC sample. Finally, the statistics for the subgiant or LB^- sample: 15971 stars and just 18 Li-rich stars for a frequency of occurrence of 0.1% over the [Fe/H] interval above -0.5. There is a clear indication from these frequencies that the phenomenon of Li-rich giants is primarily associated with He-core burning ('clump') giants, but as we discuss below, these statistics do not necessarily imply that Li production is associated with the He-core burning phase or with the He-core flash immediately preceding He-core burning in low mass giants.

As an alternative presentation of the [Fe/H]-dependence of the frequency of occurrence for Li-enriched giants, in Figure 5.4 we show the frequency distribution of Li-enriched and normal giants along [Fe/H]-axis. Seeing this plot, it is clear

that the density distribution for Li-rich giants is shifted by about 0.2 dex towards higher metallicity relative to the distribution for the Li-normal giants, i.e., the frequency of occurrence of Li-rich giants increases with increasing [Fe/H].

Our result that the frequency of occurrence of Li-rich giants increases with increasing [Fe/H] was anticipated by Casey *et al.* (2019) from the survey of the low-resolution LAMOST spectra, which garnered the staggering total of 2330 Li-rich giants defined as having a lithium abundance $A(\mathrm{Li}) \geq 1.5$, a limit lower than our limit by 0.3 dex. Their frequency of occurrence in the interval $[\mathrm{Fe/H}] = 0.0 \pm 0.1$ and overall luminosities was 0.6%. Our estimate for the same [Fe/H] interval and all luminosities is 0.8%, but for $A(\mathrm{Li}) \geq 1.8$ in fair agreement with Casey *et al.* (2019) despite our tighter definition of a Li-rich giant.

The observed frequency of occurrence of Li-rich giants and its change with metallicity are quantities which theories about the origins of Li-rich giants should replicate. A mechanism to produce Li is, of course, the crucial ingredient for any theory, but contributing factors include a star's initial (main sequence) Li abundance, Li depletion (rotational mixing?) on the main sequence and correct modelling of the first dredge-up. A close quantitative reproduction of the observed frequency of occurrence will be a stiff challenge.

5.4.2 Lithium and mass

There is interest in how the Li-rich giants are distributed in stellar mass. Stellar masses have been estimated, as in Deepak and Reddy (2019), using the formula $log(M/\mathrm{M}_{\odot}) = log(L/\mathrm{L}_{\odot}) + logg - log\mathrm{g}_{\odot} + 4 \times log(\mathrm{Teff}_{\odot}/\mathrm{Teff}_{\mathrm{GALAH}})$, where we used $\log \mathrm{g}_{\odot} = 4.44$ dex and $\mathrm{Teff}_{\odot} = 5772$ K for the solar values. Values of effective temperature, $\mathrm{Teff}_{\mathrm{GALAH}}$, and logarithmic surface gravity, $\log g$, are adopted from the GALAH catalog (Buder *et al.* 2018) and the values of luminosities are based

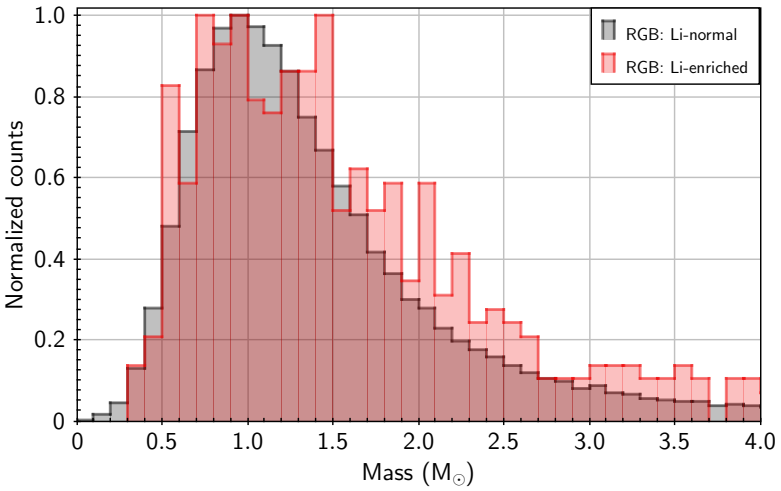


FIGURE 5.5: Normalized frequency distributions for Li-enriched and normal giants along mass-axis.

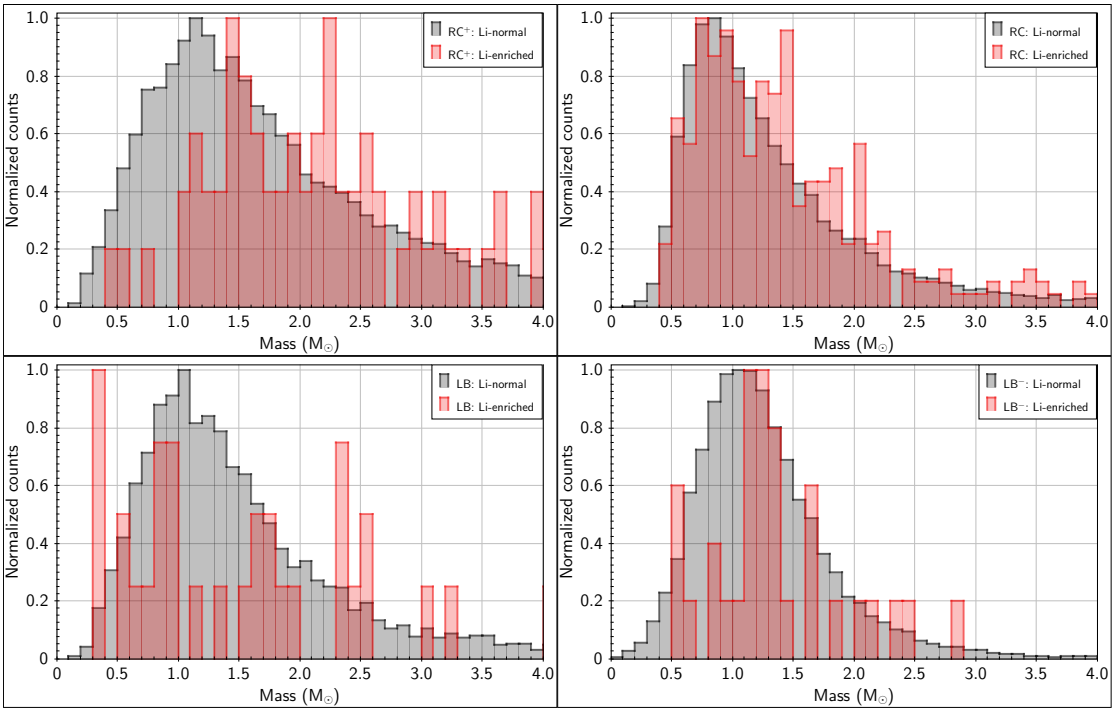


FIGURE 5.6: Normalized frequency distributions for Li-enriched and normal giants of RC$^+$, RC, LB and LB$^-$ samples along mass-axis.

on parallaxes and apparent magnitudes taken from the Gaia catalogue. We used bolometric correction based on $\mathrm{Teff_{GALAH}}$ and the relation given in Andrae *et al.* (2018). Values of luminosities given in the Gaia and those derived in this study using $\mathrm{Teff_{GALAH}}$ agree well with each other. The difference between the two values corresponds to a $\sigma \approx 0.02$ dex. Uncertainties in the derived luminosity values due to errors in parallax and $\mathrm{Teff_{GALAH}}$ are $\sigma_{L/L_\odot} \leq 0.05$ dex for most of the stars.

Masses of all the 64,493 giants of the GALAH survey populating the red giant region defined by $3800 \leq \mathrm{Teff_{GALAH}} \leq 5200$ K and $0.3 \leq \log(\mathrm{L/L_\odot}) \leq 3.2$ dex, and having reliable stellar parameters (`flag_cannon` = 0) along with small uncertainties in effective temperature ($\sigma_{\mathrm{Teff_{GALAH}}} \leq 100$ K) and parallax ($\sigma_\Pi/\Pi \leq 0.15$) are estimated. The typical error in the estimated masses is about 50%. Also, by comparison of the stars' positions with theoretical isochrones in the Luminosity–Effective temperature and Surface gravity–Effective temperature planes, we found that most of the giants in our sample are low mass giants (with $M \leq 2$ $\mathrm{M_\odot}$). In Figure 5.5, we show the normalized frequency distributions for masses of Li-rich and normal giants. Inspection of the figure suggests that the probability of becoming a Li-rich giant is essentially independent of a star's mass. Also, the probability of conversion to a Li-rich giant decreases sharply above about $3\mathrm{M_\odot}$ and vanishes above about $6\mathrm{M_\odot}$.

It is of interest to also know if the mass distribution of Li-rich and normal giants of $\mathrm{RC^+}$, RC, LB and $\mathrm{LB^-}$ samples show any difference when considered individually. In Figure 5.6, we have shown the normalized frequency distribution for masses of Li-rich and normal giants for all of the four groups. For all four groups, spreads in distribution for Li-rich and normal giants along the mass axis are similar. Also, based on the Kolmogorov-Smirnov test (K-S test), we found that the distribution for Li-rich and normal giants of $\mathrm{LB^-}$ and LB groups are statistically similar with a significance level of better than 5%. However, in the case of $\mathrm{RC^+}$ and RC samples, the K-S test failed to find similarity in the distributions of Li-rich and normal

giants with a significance level of 5% and further favours an alternative hypothesis that the cumulative distribution function (CDF) of Li normal giants is larger than the CDF of Li-rich giants.

Estimated masses from the above equation with their typical uncertainty are in some cases very low (< 0.6 M$_\odot$), which may appear to be unphysical in that the giant's age exceeds that of the *Galaxy*. Severe mass loss as a giant may reconcile low mass and age. The referee directed our attention to the giant star KIC 4937011 or W007017 in the open cluster NGC 6819. This giant is Li-rich with A(Li) = 2.3 (Anthony-Twarog *et al.* 2013) with a location in the H-R diagram below the red boundary of the cluster's red clump. Asteroseismology gives the star a mass $M = 0.71 \pm 0.08$ M$_\odot$ and shows that it has the structure of a RC star (Handberg *et al.* 2017). One may speculate that this star experienced a severe loss of mass at the He-core flash. Mass loss is *not* a common event in this cluster: Handberg *et al.* (2017) from *Kepler* asteroseismology show that the cluster's RGB and RC giants have very similar masses – $M = 1.61 \pm 0.02$ M$_\odot$ for RGB giants and $M = 1.64 \pm 0.02$ M$_\odot$ for the RC giants. Thus, KIC 4937011 is an exceptional Li-rich star. Does it have relatives among the GALAH survey's Li-rich giants?

5.4.3 Lithium and rotational velocity

It is of interest to know how the Li-enriched and normal giants are distributed in stellar rotational velocity as rotational velocities of stars have been linked to Li enhancement scenarios such as mergers (Siess and Livio 1999), tidal interactions between binary stars (Casey *et al.* 2019).

The GALAH survey provides the projected rotational velocity ($V_\mathrm{p} = V_\mathrm{rot} sini$, where "$i$" is the inclination angle). Derived values of V_p are based on spectral linewidths, which also consist of effects of macro- and micro-turbulence velocities,

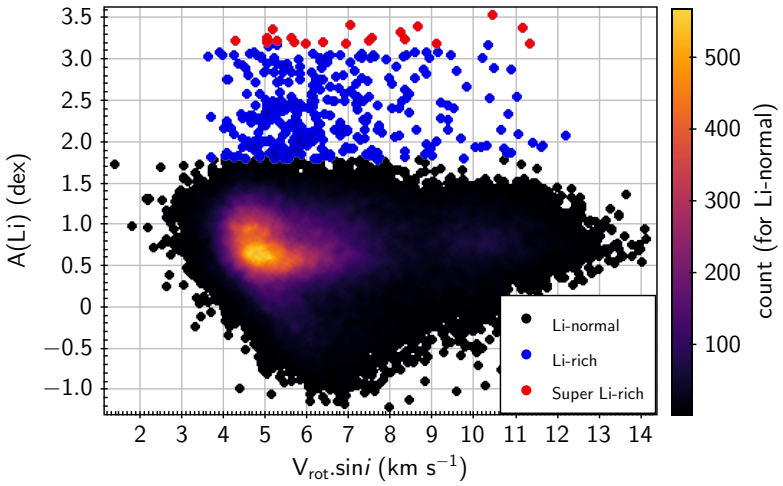


FIGURE 5.7: A(Li) versus the projected stellar rotational velocity ($V_{\rm rot}\sin i$) for our sample of giants from the GALAH survey. The projected rotational velocities are based on spectral line widths, which also consist of effects of macro- and micro-turbulence velocities; their combined effect on spectral width is not insignificant.

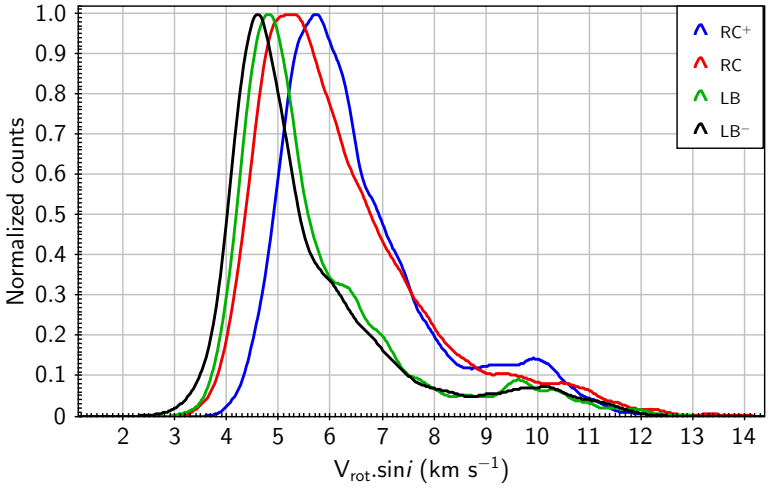


FIGURE 5.8: Normalized density distribution in projected stellar rotational velocity ($V_{\rm rot}\sin i$) for our sample of RC^{+}, RC, LB and LB^{-} normal giants.

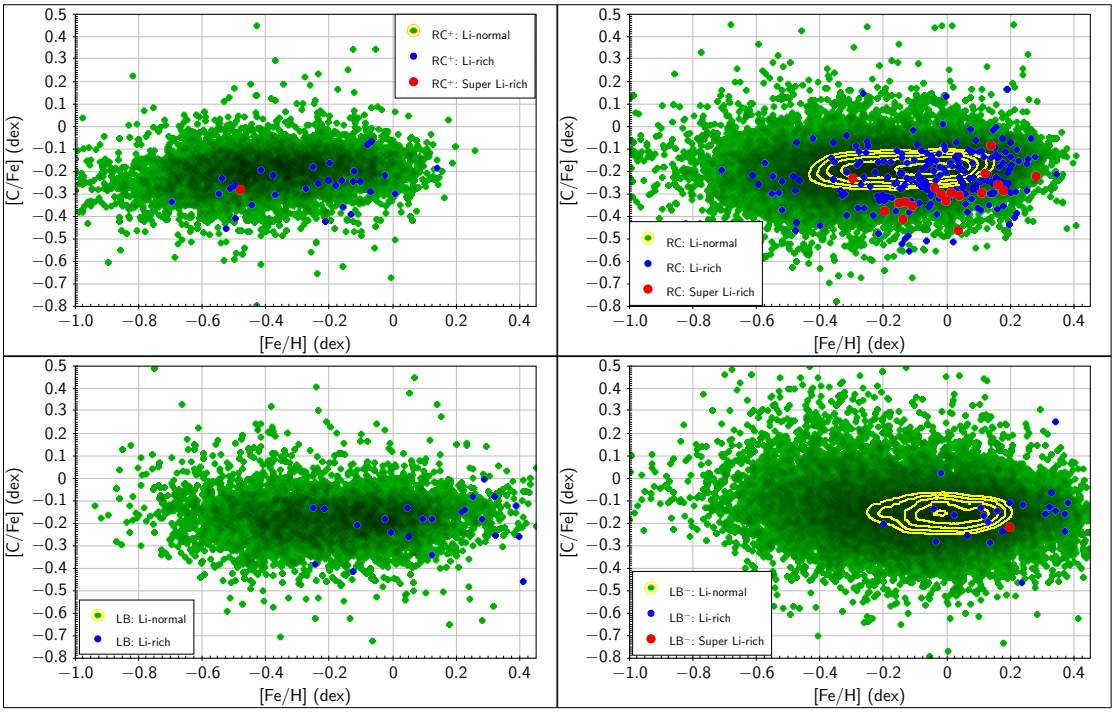


FIGURE 5.9: [C/Fe]] versus [Fe/H] for Li-normal, rich and super-rich giants of RC^+, RC, LB and LB^- samples.

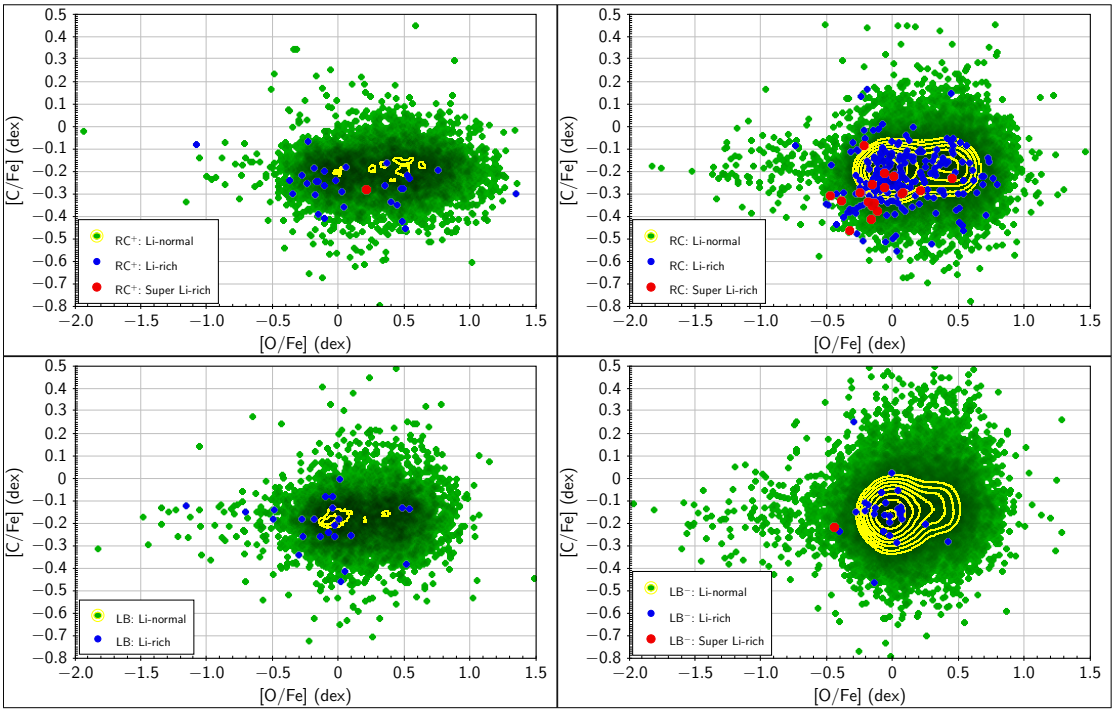


FIGURE 5.10: [C/Fe] versus [O/Fe] for Li-normal, rich and super-rich giants of RC^+, RC, LB and LB^- samples.

their combined effect on spectral width is not insignificant. With that caution, we plot the distribution of projected rotational velocity among red giants of normal and enhanced Li. The average value of $V_{\rm p}$ seems to increase as stars evolve along the RGB, as shown in Figure 5.8. Values for RC^{+} giants, most evolved among our giants, have an average 2 km s^{-1} higher values compared to the least evolved giants of LB^{-}. Given the moderate spectral resolution ($\lambda/\Delta\lambda = 28,000$ or 10 km s^{-1}) and the presence of atmospheric (microturbulence and macroturbulence) motions of several km s^{-1}, it is sufficient to note that no particular trend of $V_{\rm rot}$ of Li-rich giants compared to Li normal giants (see Figure 5.7) has been noticed. Although there is no discernible difference between the rotational velocity distributions for normal and Li-rich giants within a given luminosity sample, it is seen from Figure 5.1 that with but a single exception the super Li-rich stars belong to the RC sample.

5.4.4 Lithium and the Carbon Abundance

Comparison of elemental abundances C to Eu in Li-normal and Li-rich giants is a potentially powerful clue to the origins of the Li enrichment. In Figure 5.2, abundances for the RC sample are shown. The Li versus [Fe/H] distribution is shown in the top-left panel, with the density of points representing Li-normal giants shown by the yellow contours. For these density contours, suitable smoothing and scaling (linear or logarithmic) are used depending on the distribution in the individual plots. The purpose of using contours in Figure 5.2 is to identify the maximum density region for Li normal giants and to see if the occurrence of Li-rich and super Li-rich giants favour any particular [Fe/H] and [X/Fe] (and so the density value corresponding to each contour do not need to be specified). Li-rich and super Li-rich giants are denoted (here and in all panels) by blue and red-filled points, respectively. Other panels of this figure show [X/Fe] versus [Fe/H] where X runs successively from C to Eu. Abundance differences between the normal

and Li-rich giants will be seen as a displacement of the Li-rich (blue dots) and/or the super Li-rich (red dots) giants with respect to the normal giants (green dots and the yellow contours) with displacements in one or both of the axes [X/Fe] and [Fe/H]. In an earlier section, we commented on two applications of the [X/Fe] values to test ideas on forming Li-rich giants: a test involving abundances as a function of condensation temperature and another looking for correlation with *s*-process abundances. Here, we consider the carbon abundances.

Inspection of the panel showing [C/Fe] versus [Fe/H] (Figure 5.9) suggests that Li-rich giants and normal giants have the same [C/Fe] deficiency, a deficiency attributed to the first dredge-up. The super Li-rich giants, as noted earlier, have, however, a systematically lower [C/Fe] than the normal and the Li-rich giants by almost 0.2 dex and this difference in [C/Fe] may increase at lower [Fe/H]. Our sample of super Li-rich giants appears confined to the more metal-rich giants (i.e., the thin disc), say [Fe/H] ≥ -0.2 with a lone example at [Fe/H] $= -0.3$. In contrast, the Li-rich giants are spread roughly uniformly over the [Fe/H] range covered by the normal giants – see, Figure 5.9 which shows the [C/Fe] versus [Fe/H] plots for the RC^+, RC, LB and LB^- samples. Although the populations of giants in the luminosity samples RC^+, LB and LB^- are smaller than the well-populated RC sample, the RC^+ sample exhibits the same lower [C/Fe] values for Li-enhanced giants as the RC sample: each of the RC^+, LB and LB^- samples show no (or a very slight) difference in [C/Fe] between the normal Li and Li-rich stars. More obviously and as noted previously, there is an almost complete absence of super Li-rich giants in the RC^+, LB and LB^- samples: just one super Li-rich giant in the RC^+ and another in the LB sample and one cannot exclude the possibility that these are merely misclassifications which really belong to the RC sample.

The implication of the lower [C/Fe] for the super Li-rich giants may be that prior to or concurrently with becoming a Li-rich the giant experiences an episode of internal mixing and additional exposure to the CN-cycle following evolution through the

LB$^-$ and LB phases but prior to the RC phase. This episode of mixing brings additional CN-cycled and Li-enriched material to the surface to create the super Li-rich giant. The observation that the Li-rich and normal giants are similarly distributed in the [C/Fe] – [Fe/H] plane suggests the episode of Li production may be unrelated to the first dredge-up held responsible for the decrease in the C abundance. Destruction of C and its conversion to N by the CN cycle preserves the sum of the C and N abundances. The sum provides a valuable test of CN cycling, but unfortunately, the GALAH survey does not provide the N abundance. Note that the GALAH C abundance is derived from a C I line with a negligible isotopic wavelength shift and, hence, the C abundance is the sum of the ^{12}C and ^{13}C abundances. The ^{12}C/^{13}C ratio provides additional insight into CN cycling.

If the additional reduction of C in super Li-rich giants is a consequence of mixing in giants, there is a possibility that O might be reduced with a concomitant further increase in the N abundance and that Na might also be enhanced by a small amount. Nitrogen will be enhanced with the expectation that the sum of the C and N abundances will be conserved. Figure 5.2 for RC giants includes panels for [O/Fe] and [Na/Fe]. Inspection of the panels shows that [O/Fe] for the super Li-rich giants in the thin disc have the [O/Fe] of the normal giants. The same conclusion about [O/Fe] applies to the Li-rich giants in both the thin and thick discs. However, Figure 5.10 suggest a positive correlation between [C/Fe] and [O/Fe] among super Li-rich giants, i.e., super Li-rich giants with lower [C/Fe] also have lower [O/Fe]. In this figure, the stars with [O/Fe] < 0.2 dex are thin disc stars, while the stars with [O/Fe] > 0.2 dex are thick disc stars. Although the super Li-rich giants are chemically distinct from the normal giants, they are well distributed in the kinematical plane (Deepak and Reddy 2019). Similarly, the [Na/Fe] values of super Li-rich and Li-rich giants do not distinguish these giants from the large population of normal giants. These are not surprising results for O and Na because deep mixing is required to alter their surface abundances and, in addition, the deep mixing may destroy Li and result in a depleted, not enhanced,

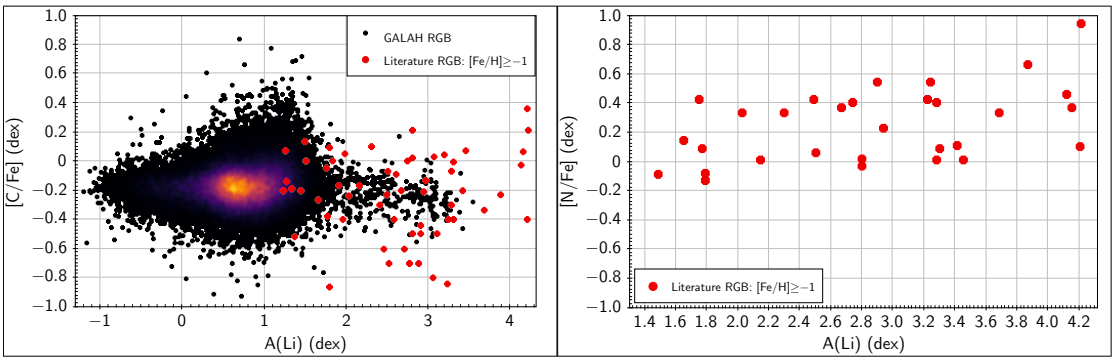


FIGURE 5.11: Abundances of C and N for known Li-enriched (including a few normal) giants in literature. For carbon, the RGB sample extracted from the GALAH survey is also plotted in the background.

surface Li abundance.

To set the picture expected of C and N abundances, we estimate the effect of conversion of C to N by the CN-cycle using the solar abundances for the initial composition of a [Fe/H] = 0 giant: $A(C)_{\odot} = 8.43 \pm 0.05$, $A(N)_{\odot} = 7.83 \pm 0.05$ and $A(O)_{\odot} = 8.69 \pm 0.05$ are solar C, N, and O abundances, respectively, taken from Asplund *et al.* (2009) which is the same reference as used Buder *et al.* (2018). Li-rich and normal giants show a C under abundance [C/Fe] $\simeq -0.2$, which, if the sum of the solar C and N abundances is conserved, translates to [N/Fe] $\simeq +0.4$. Similarly, the super Li-rich giants at [Fe/H] = 0 show [C/Fe] $\simeq -0.3$ and then [N/Fe] $\simeq +0.5$ is expected. Abundance uncertainties in the solar or reference abundances contribute about ± 0.05 to these estimates for the N abundance. These estimates assume that the C abundance includes both isotopes ^{12}C and ^{13}C. If the C abundance comes from CH lines and is thus primarily ^{12}C the predicted N abundance might be reduced by about 0.12 dex for $^{12}C/^{13}C \sim 3$. If the ON-cycle were to also be involved, the sum of the C, N and O abundances is conserved, but since the solar O abundance is greater than the solar C abundance and far greater than the solar N abundance, larger increases of [N/Fe] occur for even mild conversions of O to N.

Nitrogen as N I lines are not detectable in spectra of red giants but are readily sensed through lines of the CN radical via its red and violet systems. (The NH molecule is also detectable at 3360 Å and possibly too via the NH infrared vibration-rotation lines near 3 microns.) Carbon is also available through CH lines near 4300 Å. Combining CN and CH lines provides the N abundance but with the potential for an anti-correlation between the C and N abundances resulting from systematic errors in the C abundances from CH being transferred to the CN analysis. Also, there is the prospect of elemental abundances from a molecule differing systematically from abundances from atomic lines, especially from high-excitation lines such as the C I lines; the atomic and molecular lines are formed in different regions (deep versus shallow) of the stellar photosphere. In an attempt to explore the C-N connection for Li-enriched giants, we have considered two ways of determining the N abundance for Li-enriched giants, including some in the GALAH survey: (i) Li-rich giants have been analysed previously by many different investigators for C and O (and many other elements) using high-resolution optical spectra, and (ii) the low-resolution LAMOST survey of millions of giants covers the blue CH and CN bands and Xiang *et al.* (2019) have calibrated LAMOST abundances including C and N using abundances from high-resolution optical (GALAH) and infrared (APOGEE) surveys.

In seeking the N abundances of Li-rich giants, we searched the literature for analyses of high-resolution optical spectra and collected Li abundances along with abundances of other elements, as available, as well as stellar parameters. Data for about 400 giants were compiled. Results for giants which were not Li-rich were included as reported in the papers describing the analysis of Li-rich giants, but no special effort was made to include normal giants analyzed similarly by the authors reporting on the Li-rich giants. Selection of giants was restricted to members of the disc, i.e., [Fe/H] > -1.0, the same limit as applied to the selection of Li-rich giants from the GALAH survey. It is also important to note that many of the Li-enriched giants studied in the literature are not field stars and belong to globular

clusters. Depending on the metallicity, etc. of the clusters, the MS-turnoff and position of RGB tracks can vary widely along Teff and luminosity axis, which can further induce scatter in Li and CNO abundances. To avoid any contamination from such giants, we excluded stars with Teff > 5200 K and $logg > 4.1$ dex (which is the same limit as for our RGB sample from the GALAH survey). This limit also makes sure that we only have giants from the literature. This resulted in a sample of about 250 giants, some of which have been observed and analysed multiple times. It is also important to note that studies in the literature have used different atomic and molecular lines to estimate the C abundances. Some of these lines are highly divergent; for example, the most divergent C I line at 5380 Å yield more than an order of magnitude higher C abundance than that from the Swan system C_2 line (5135 Å) at 4700 K (Luck and Heiter 2007, and references therein). So in this study, to avoid any contamination, we have excluded the C abundances, which are estimated only from the C I line at 5380 Å.

Results from the literature are generally in good accord with those from the GALAH survey as in Figure 5.2. A partial presentation is provided in Figure 5.11 where [X/Fe] versus A(Li) is provided for X = C and N. Scatter in these plots must partially arise from combining results by different investigators. The few remarkable outliers may also arise from errors in analysis. Results in Figure 5.11 are generally consistent with ours. The novel contribution of Figure 5.11 is, of course, the panel providing the results for [N/Fe]. Our expectation is that [N/Fe] should be close to +0.4 if, as seen in Figure 5.11, [C/Fe] is about −0.2. In Figure 5.11, [N/Fe] is close to expectation but slightly greater than expected. Note, however, that a systematic overabundance of the C abundance necessarily results in an underabundance of the N abundance thanks to the use of the CH and CN molecules in the C and N abundance analysis. The $^{12}C/^{13}C$ ratios also taken from the literature are shown in Figure 5.12 as a function of A(Li). There is a large spread in the isotopic ratio at all Li abundances from normal to the super Li-rich giants.

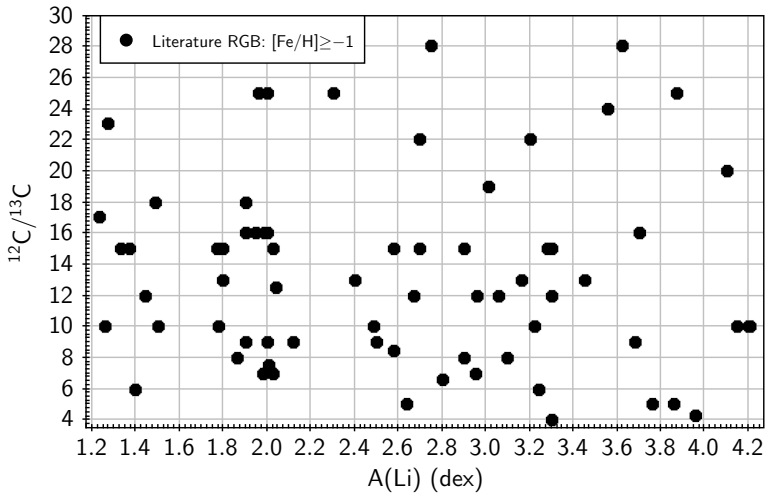


FIGURE 5.12: $^{12}C/^{13}C$ versus Li abundances for known Li-enriched (along with a few normal) giants in the literature.

The recent study by Xiang *et al.* (2019) of LAMOST spectra provides a catalogue of abundances of 16 elements (C, N, O, Na, Mg, Al, Si, Ca, Ti, Cr, Mn, Fe, Co, Ni, Cu, and Ba, of which N is of our main interest) of about 6 million stars from ~ 8 million low-resolution (R $\sim$ 1800) spectra from the LAMOST DR5. Abundances were extracted from the LAMOST spectra using training sets of high-resolution spectra provided by GALAH and APOGEE abundances. Nitrogen abundances for our giants in the GALAH survey are provided by the LAMOST-GALAH calibrated abundances. (There is very little overlap between the APOGEE sample, which is primarily from the northern hemisphere, and the GALAH sample, which primarily covers the southern hemisphere.) LAMOST N abundances are provided from the CH and CN bands in the blue. We cross-matched our red giant sample with the LAMOST catalogue based on a star's positional coordinates with a maximum error of one arc-sec in the star's position and found about 1800 common giants. We further restricted our sample to only those giants for which estimated N abundances are available (i.e., excluded the stars with a default value of -999, which was assigned when the code is enabled to estimate the abundance, see Xiang *et al.* (2019) for more details). This resulted in a sample of 1793 giants (here, the $\mathrm{RGB_{GL}}$ sample) of which 14 are Li-rich (with $A(\mathrm{Li}) \geq 1.8$ dex) and three (with $A(\mathrm{Li}) \geq 3.2$ dex) are super Li-rich (with $A(\mathrm{Li}) \geq 3.2$ dex).

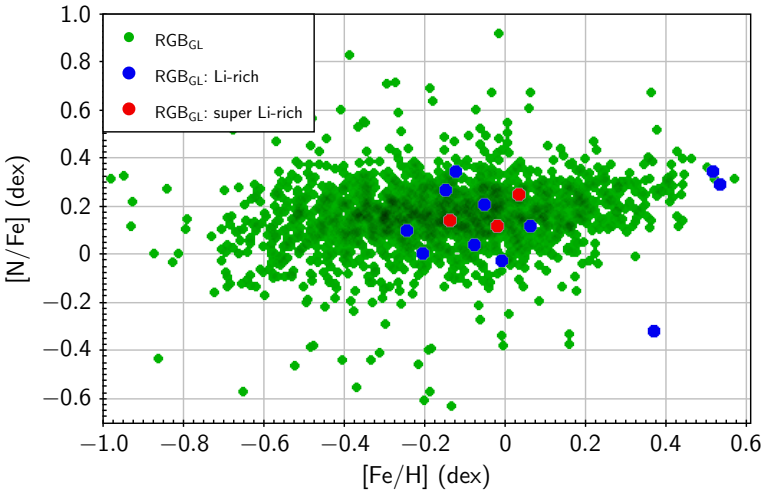


FIGURE 5.13: Distribution of [N/Fe] versus [Fe/H] for a sample of common giants among the GALAH and LAMOST surveys (sample RGB$_{GL}$).

In Figure 5.13, N abundances provided by Xiang *et al.* (2019) for giants common to the GALAH and LAMOST surveys are shown as a function of [Fe/H]. This figure in which giants are not separated into the luminosity classes LB$^-$ to RC$^+$ suggests that Li-rich and super Li-rich giants share the same N abundance with the normal giants. This result is somewhat surprising given that the super Li-rich giants appear to be more C-depleted than other giants. The mean N abundance is very similar to that provided by our search of the literature (Figure 5.11).

Given that the GALAH abundances are used as a training set for the low-resolution LAMOST survey, one expects the [X/Fe] versus [Fe/H] relations from GALAH to be a close match to the calibrated LAMOST abundances. (In a few cases, as noted in Section 5.3 the GALAH abundances appear to be subject to a systematic error.) In Figure 5.14, we compare [X/Fe] versus [Fe/H] for X = C, O and Na for common giants from the two surveys, again the giants are not broken into luminosity classes.

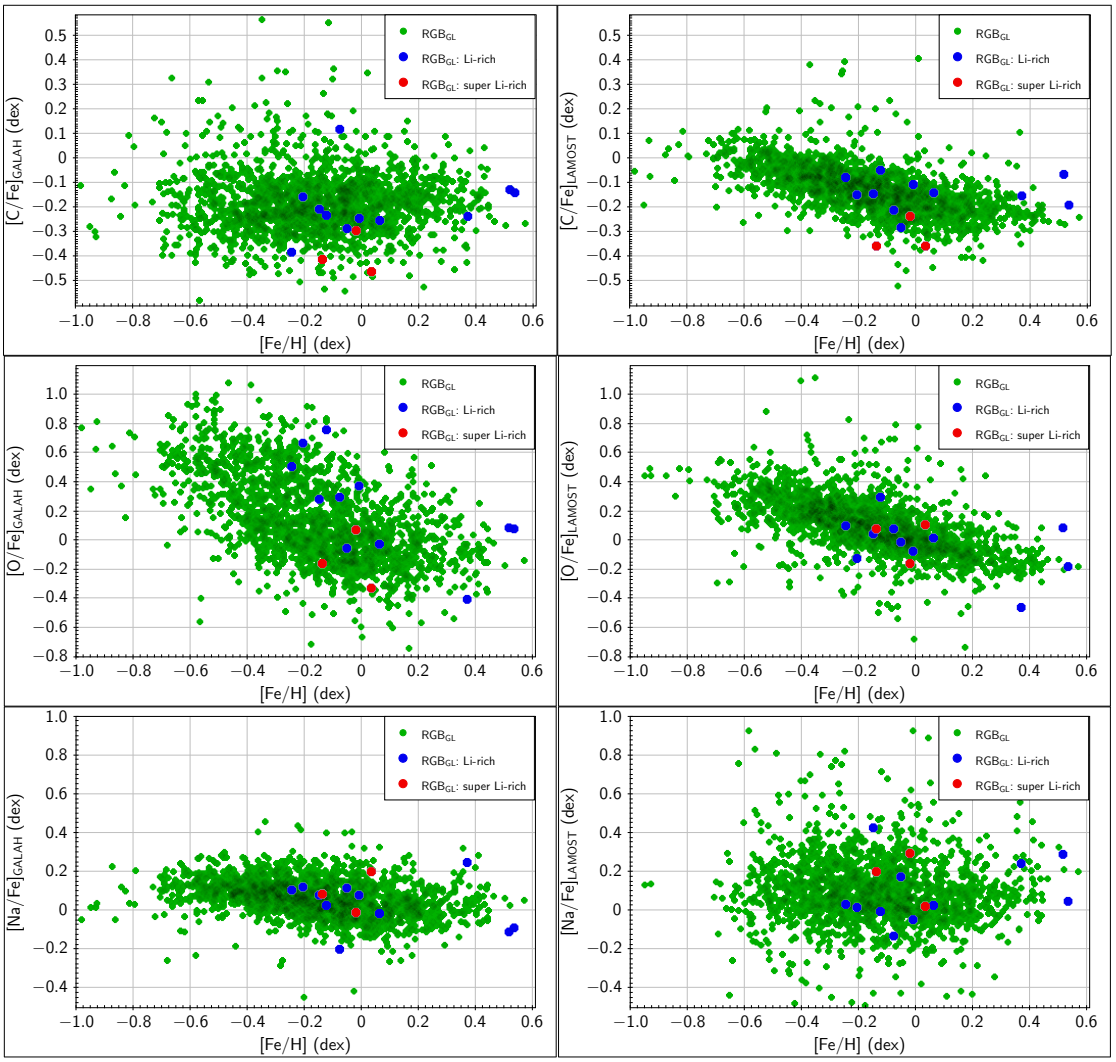


FIGURE 5.14: [C/Fe], [O/Fe], and [Na/Fe] versus [Fe/H] for common giants among GALAH and LAMOST. The left and right panels show the abundance from the GALAH and LAMOST surveys, respectively.

5.5 Creation of a Lithium enriched giant

For several decades, three potential reservoirs of Li that a normal giant may call upon to effect its conversion to a Li-rich giant, even a super Li-rich giant, have been proposed. A primary unresolved issue is how a reservoir may be tapped to convert a normal star to a Li-rich giant.

:– One reservoir is material orbiting a star – planets and substellar masses M $\leq$ 0.065M$_{\odot}$ – which a giant may engulf. (Brown dwarfs of mass greater than

0.065M$\odot$ destroy Li internally.) Since this material is expected to have retained its original Li (both ^{7}Li and ^{6}Li and also ^{9}Be), capture by the giant will raise the Li (and Be) abundance of the giant's atmosphere and convective envelope. The Li abundance of the Li-rich giant depends in part on the mass of circumstellar material and its Li abundance.

:– A second potential reservoir is the star's internal supply of ^{3}He which, under the right circumstances, may be converted to ^{7}Li by the reaction $^{3}\mathrm{He}(\alpha,\nu)^{7}\mathrm{Be}$ and subsequent electron-capture $^{7}\mathrm{Be}(\mathrm{e}^{-},\nu)^{7}\mathrm{Li}$. A key to the successful appearance of ^{7}Li at the giant's surface is that the ^{7}Be synthesis by α-captures must occur in a convective envelope which allows conversion of some ^{3}He to ^{7}Be but permits an adequate amount of ^{7}Be (and ^{7}Li) to be convected to lower temperatures and, thus, avoid near instantaneous destruction by α-captures. Of course, the convective envelope will return ^{7}Li to the deeper hotter layers and so expose it to destruction by α-captures as additional ^{3}He may be converted to ^{7}Be.

:- The third possible reservoir of Li is a companion and more massive star which evolves to become an AGB giant. Luminous AGB stars are predicted and known to have Li-enriched envelopes (Smith and Lambert 1989). The origin of the freshly synthesized Li is again the star's ^{3}He. Then, a measure of mass transfer from the luminous AGB star to its companion could result in a Li-rich giant (or main sequence) star. Since luminous AGB stars have experienced considerable enrichment with products of the *s*-process, the Li-rich giant would be expected to show marked *s*-process as well as Li-enrichment. None of the Li-rich giants in our GALAH survey is *s*-process enriched, and thus, we do not discuss this possible reservoir further. This binary scenario is the process by which classical Ba and CH giants are created.

5.5.1 Thoughts on the external reservoir

An extensive literature on theoretical and observational aspects of Li enrichment resulting from the accretion of circumstellar material now exists with its origin traceable to Alexander's (1967) suggestion that ingestion of a planet by a red giant would boost the star's Li abundance. Theoretical studies (e.g., Aguilera-Gómez *et al.* 2016a) have considered ingestion of brown dwarfs, Jupiter-like and Earth-like planets. Brown dwarfs with a mass M≤ 0.065M$_{\odot}$ are expected to preserve their Li and at least partially offset the reduction of the Li abundance arising from the first dredge-up. In some calculations, the brown dwarf is considered to be metal-rich relative to the companion star. In many calculations, Jovian planets are assumed to have the same composition as the initial main sequence star, i.e., the same mass fraction of Li. Calculations incorporating ingestion of terrestrial planets clearly adopt a composition different from that of the main sequence, including a composition representative of the present Earth; the Li abundance is raised on ingestion, but relative abundances of volatiles and non-volatiles may be altered. In each case, not only is the giant's surface Li abundance raised by ingestion, but the isotopic ratio ^{6}Li/^{7}Li is presumably raised close to its original value and the stellar Be abundance too is raised to partially correct for the dilution of Be by the first dredge-up.

For estimates of the Li abundance of red giants post-ingestion of circumstellar material, we turn to Aguilera-Gómez *et al.* (2016a) who examined accretion of brown dwarfs and planets Jupiter and Earth by low mass stars with [Fe/H] from 0 to -2.0. A maximum mass to accreted material and, hence, a maximum Li abundance for the post-accretion giant is set by their demonstration that brown dwarfs with masses greater than 15 Jovian masses (15M$_{J}$) are ingested but dissolve in the giant's radiative core below its convective envelope. In these calculations, a giant's main sequence progenitor is assumed to have not destroyed Li in its outer envelope. Li depletion in main sequence stars is a common phenomenon and, thus,

the calculations may overestimate the Li abundance following an accretion event. Destruction of accreted Li by the giant is included in the calculations. A $1.5M_{\odot}$ giant with [Fe/H] = 0 with an initial abundance A(Li) = 3.3, the meteoritic value, after ingestion of a $15M_{J}$ brown dwarf with an initial composition 2.5 times solar (including Li) has a predicted Li abundance A(Li) = 1.8. This Li abundance is reduced to A(Li) = 1.6 if the brown dwarf has a solar composition. The Li abundance is slightly higher for a $1M_{\odot}$ giant. These abundances are insensitive to the initial stellar abundance of Li but not to the assumed Li abundance of the brown dwarf. Of course, the giant's predicted post-accretion Li abundance is much lower after accreting a Jovian or an Earth-like planet. For a fixed initial Li abundance for the accreted material, the giant's final Li abundance is insensitive to its initial [Fe/H] and insensitive to the point on the giant branch at which ingestion begins. Indeed, the final Li abundance for $1M_{\odot}$ for a fixed initial Li abundance increases by about 0.4 dex as [Fe/H] drops from 0.0 to -2.0. Since the initial Li abundance decreases with decreasing [Fe/H] in the Galactic disc (Lambert and Reddy 2004), the predicted Li abundance of a giant is, in practice, sure to decrease with decreasing [Fe/H].

These calculations, as Aguilera-Gómez *et al.* (2016a) emphasize, cannot account for the most Li-enriched giants and, indeed, even our lower limit A(Li) = 1.8 for a Li-rich giant is at the limit of their calculations. Of course, the giant's final Li abundance may be additionally increased by the ingestion of more than a single brown dwarf, Jovian or terrestrial planet. For example, Melo et al.'s (2005) simpler recipe suggests that A(Li) = 2.5 is attainable with ingestion of 100 Jupiters. A couple of additional observations. First, giants with planets and including Li-rich planets with planets are known (Adamów *et al.* 2018) and the likelihood that some giants have experienced ingestion seems high and the question is how does one recognize such giants even if the Li abundance does not cross the threshold to be classified as Li-rich.

One test involves the Be abundance derived from the Be II 3131 Å resonance lines. Surface Be abundance of a giant is diluted by the first dredge-up and replenished by ingestion of circumstellar material. The point that Be has not increased above first dredge-up values in Li enriched stars has been made previously (Melo *et al.* 2005; Takeda and Tajitsu 2017). This is certainly a valid point against the external reservoir as a source of Li for Li-rich and especially for super Li-rich giants. But since Be abundance determinations are relatively rare, a giant which has ingested circumstellar material, including its own planets, may await discovery among nearby giants.

Ingestion of Earth-like planets will change the relative abundances of the elements. A recent interpretation of the composition differences between HD 240429 and HD 240430, solar-type stars forming a comoving pair, has proposed that HD 240430 has accreted 15 Earth masses of material with the composition of the Earth (Oh *et al.* 2018). This accretion results in HD 240430 (relative to HD 240429) having a higher abundance by about 0.2 dex of refractory elements with a condensation temperature above about 1200 K but a similar abundance of less volatile elements like C, N, O and Na. Adopting the bulk composition of the Earth from McDonough (2003), a good fit is obtained to the abundance differences between the two stars. Table 5.1 and Figure 5.2 show that abundance differences between normal and Li-enriched giants are small across elements with different condensation temperatures and absence of a correlation of abundance differences with condensation temperature provides an opportunity to set a limit on the accretion of Earth-like material by the Li enriched giants. A giant's convective envelope includes about 60% of the mass of the giant's mass (Aguilera-Gómez *et al.* 2016a). The addition of 10 Earth-like planets would increase the abundance of refectory elements by about 0.05 dex relative to less volatile elements such as O and Na. Abundance differences [X/Fe] in Table 1 are generally less than 0.05 dex. For example, abundance differences for the RC sample in the [Fe/H] interval +0.1 to +0.3 dex run from −0.03 to +0.04 dex excluding C. Thus, Li-enriched giants have ingested little

to no Earth-like planets.

5.5.2 Thoughts on the internal reservoir

Application of a giant's internal ^{3}He supply to the puzzle of Li-enriched stars demands a trigger for mixing between deep layers where conversion of ^{3}He to ^{7}Be occurs and the surface where an overabundance of ^{7}Li (and possibly ^{7}Be) occurs. As noted above, a novel result of this analysis is that many Li-enriched giants share the slight C deficiency of normal giants, which is the expected consequence of the first dredge-up. It is also the case that the ^{12}C/^{13}C ratio of Li-rich and super Li-rich giants span the range from 5 to 25 also exhibited by normal giants (Kumar *et al.* 2011; Adamów *et al.* 2018). This shared pattern of C elemental and isotopic abundances suggests that the ^{3}He-to-^{7}Li conversion may operate independently of the processes providing the internal composition changes to C, N and O, which are revealed as surface composition changes by the first dredge-up. This independence appears broken in the case of the super Li-rich giants where additional C deficiency was found but without a clear difference in the ^{12}C/^{13}C ratio (Figure 5.12).

All ^{7}Li produced from the internal reservoir comes from the decay of ^{7}Be with its 53-day half-life against electron capture. Takeda and Tajitsu (2017) noted that the isotopic wavelength shift for the Be II 3130-3131 Å resonance lines suffice in a high-resolution spectrum to put the ^{7}Be line to the red and clear of the stable ^{9}Be line. Their two comparisons of the spectrum of a Li-rich giant with the spectrum of a normal giant with nearly identical atmospheric parameters showed no evidence of a ^{7}Be contribution to the spectrum of the Li-rich giant but a marked but expected ^{9}Be deficiency in both stars. There may be a tantalizing hint of ^{7}Be in the spectrum of two super Li-rich giants whose spectra are shown by Melo et al. (2005, compare their Figures 3 and 4). Spectra of these giants around 3130

Å are rich in atomic and molecular (OH) lines, and a careful accounting of these blending lines is required before claiming detection of ^{7}Be or even ^{9}Be.

It would be of interest to calculate from a model of a giant the probability that an observable amount of ^{7}Be may be convected to the surface before it undergoes electron capture and conversion to ^{7}Li. In the convective envelope, Be is fully ionized, and thus the ^{7}Be's lifetime is greatly enhanced over its natural 53 days for the neutral atom. Transport over the stellar envelope, a distance of about 50 solar radii, in just 53 days requires a velocity of about 8 km s^{-1}, which would appear to be a stiff requirement, but the increase in the lifetime of the bare ^{7}Be nucleus may reduce the demanded convective velocity to a physically relevant value. A maximum ^{7}Be abundance equal to the maximum Li abundance of A(Li) = 4.5 observed in a Li-rich K giant after six half-lives at even the natural 53-day half-life provides a ^{7}Be abundance A(^{7}Be) = 1.6 at the stellar surface, an abundance slightly exceeding the initial (i.e., solar) of ^{9}Be. Thus, it may appear possible that super Li-rich giants may show detectable amounts of ^{7}Be, but this possibility demands that the giant be currently experiencing conversion of ^{3}He to ^{7}Be in its interior. On cessation of ^{7}Be production, ^{7}Be in the atmosphere decays with its 53-day half-life, a fleeting second with respect to the 100-200 million year life of the He-core burning clump giant. Acquisition of high-resolution spectra around 3130 Å of Li-enriched giants is of interest. Positive identification of ^{7}Be would be proof not only that the Li production originated with the ^{3}He internal reservoir but that ^{3}He conversion to ^{7}Be and ^{3}He is occurring presently in that giant. Ignition of ^{3}He as a source of ^{7}Li can not synthesise ^{9}Be, the sole stable isotope of Be.

Even with the attribution of Li production to the ^{3}He internal reservoir, there remains the challenge of identifying why only 1% of giants experience substantial Li enrichment at their surfaces. This challenge is sharpened if, as evidence is now trending, the key event in a Li-rich giant's life is its He-core flash at the tip of the red giant branch. Casey *et al.* (2019) argue that it is tidal spin-up by a stellar

companion that triggers the conversion of ^{3}He to ^{7}Li. A merit of this proposal is that it is open to a straightforward test: radial velocity observations should reveal the companion star.

5.6 Concluding remarks

In conclusion, the compositions of Li-rich and the super Li-rich giants across the elements considered by the GALAH survey are identical but for slightly lower [C/Fe] values in the super Li-rich giants. The distribution of the [C/Fe] values for the Li-rich giants resembles that for the normal giants. This analysis of GALAH abundances appears to be the first extensive differential survey to examine compositions of Li-rich and super Li-rich giants along with normal giants in the search for differences between the Li-enriched and normal giants. Although the literature on the compositions of Li-enriched giants is now quite extensive, few studies have tackled a fair sample of the Li-enriched giants and a comparable sample of normal giants in order to minimize systematic errors in the analyses. Among published studies, we note that by Takeda and Tajitsu (2017) whose sample contained 20 Li enriched giants including five super Li-rich and all but two giants with a Li abundance $A(\mathrm{Li}) \geq 2.0$. Takeda and Tajitsu (2017) obtained C, O. Na, S and Zn abundances by line selections and methods previously used for a large sample of normal giants. (These authors also derived Be abundances for five Li-enriched giants and estimated the ^{6}Li/^{7}Li ratio.) Elemental abundances for the Li-rich giants were not all exactly in line with those of normal giants. Of interest to understanding the origins of Li-rich giants, the [C/Fe] values of about half of the sample were much in excess of the values for normal giants of similar metallicity. About eight Li-rich giants had a positive [C/Fe] value at metallicities for which normal giants had a negative [C/Fe] value comparable to the GALAH values. (The C abundance was provided by the C I 5380 Å line.) This divergence in [C/Fe] values

with the GALAH values is not understood. In principle, Li-rich giants may be created through mass transfer from a Li-rich AGB star which could be C-rich but would also be expected to be *s*-process enriched. Our sample of Li-rich giants is not *s*-process enriched. The *Gaia-ESO* survey of Li-rich giants (Casey *et al.* 2016; Smiljanic *et al.* 2018) has provided information on the compositions of a few giants indicating essentially normal compositions relative to normal giants.

Our observation that the Li-rich giants and normal giants have the same compositions, including for species (e.g., C, N and O) whose surface abundances are affected by the first dredge-up suggests that the addition of Li to create a Li-rich giant occurs independently of the abundance changes wrought by CN-cycling in the deep interior. Although a few Li-rich giants may result from the accretion of external material, the majority of these giants have Li abundances indicating internal production of Li from ^{3}He conversion to ^{7}Be and the latter's decay to ^{7}Li (i.e., the Cameron-Fowler mechanism). Demonstration that the super Li-rich giants are more severely depleted in C than the normal Li-rich giants may indicate that their production of ^{7}Be was accompanied by additional CN-cycling.

We also found that the probability of becoming a Li-rich giant is independent of the star's mass, although the majority of the Li-rich giants are found to be low mass ($M \leq 2$ M$_{\odot}$). Both the Li-enriched and normal giants are also found to have similar projected rotational velocities, which suggests that Li-enrichment in giants is not linked to scenarios such as mergers, tidal interaction between binary stars, etc. The frequency of occurrence of Li-rich giants among normal giants is about 1 per cent and, as found by Casey *et al.* (2019), this frequency increases with increasing metallicity.

As shown in Figure 5.1, the great majority of Li-rich giants are He-core burning giants, but there are minorities with an apparent connection to the red giant

branch, possibly to the luminosity bump, and to the red giant branch at luminosities above the bump and to evolution along the early-AGB following He-core burning at the clump. All but one of the super Li-rich giants appears as a He-core burning or clump giant. (Low luminosity Li-rich stars in Figure 5.1 at effective temperatures of about 5200 K may be stars for which the first dredge-up is as yet incomplete.) Distribution of Li-rich giants in their version of Figure 5.1 led Casey *et al.* (2019) to conclude that production of a Li-rich giant does not occur exclusively at the luminosity bump or the tip of the red giant branch, but their Li abundance estimates are from the low resolution ($\sim$ 1800) LAMOST spectra. The stars become Li-rich either "at a random time on the giant branch or at the start of the helium-burning phase, and remain lithium-rich for about 2 x 10^6 yr". Between the tip of the red giant branch and the He-core burning phase is the He-core flash in low-mass giants. This core flash is, among some observers, a prime source of internal disturbance resulting in Li-enrichment at a giant's surface. Theoretical evidence in support of the suspicion is lacking, however. Casey *et al.* (2019) argue with theoretical backing that the conversion of ^{3}He to ^{7}Be with eventual decay to ^{7}Li is triggered by tidal interactions between the giant and a stellar companion. As Casey *et al.* (2019) note in a concluding paragraph, their proposal about tidal interactions is testable by a search for binary companions to Li-rich giants. It will be interesting to see if Li-rich giants do indeed have binary companions and if the nature of the binaries accounts for the distribution of Li abundances and, in particular, for the occurrence of super Li-rich giants with their additional depletion of carbon.

Chapter 6

Li abundances and asteroseismology of red giants: understanding the evolution of lithium in giants based on asteroseismic parameters*

6.1 Introduction

Thanks in part to the astrometric data provided by the *Gaia* satellite (Gaia Collaboration *et al.* 2016b, 2018b; Lindegren *et al.* 2018) and measured abundance (including Li) of a large sample of stars by the GALAH survey, now we know that most of the Li-rich giants (with $A(\mathrm{Li}) \geq 1.7$) are core He-burning (CHeB) giants, also known as the red clump (RC) giants (Chapter 4 or Deepak and Reddy 2019),

*This chapter is published in Deepak and Lambert (2021a)

and these giants are similar to Li-normal giants in all other aspects like chemical composition (except Li abundance), mass, metallicity and rotation (Chapter 5 or Deepak *et al.* 2020). Studies also suggest that the Li enrichment in giants is associated with the violent He-core flash at the tip of the RGB phase. A suspicion that the He-core flash in some low mass stars may result in Li enrichment from the conversion of internal ^{3}He to ^{7}Be and subsequent decay to ^{7}Li was aired by Brown *et al.* (1989a). This suspicion has now been supported by theoretical work (Schwab 2020) showing that an *ad hoc* prescription of internal chemical mixing may account for ^{7}Li enrichment from the He core flash and thus in the resultant RC giant. Schwab suggests that the introduced *ad hoc* mixing may result from internal gravity waves excited by turbulent convection arising from the He core flash.

Apart from Li enrichment in CHeB giants, some studies also suggest Li enrichment in giants with an inert He core at the luminosity bump (Martell *et al.* 2021). To find if Li enrichment is associated with the luminosity bump or not, it is crucial to first make a very accurate separation between CHeB giants and giants on the luminosity bump. In the $T_{\rm eff}$-luminosity plot (i.e., the HR diagram), the red clump and luminosity bump are located in very close proximity (Figure 4.1 and 5.1). Considering the large range in mass and metallicity of sample stars along with the associated errors in the estimated luminosity and $T_{\rm eff}$, we can not neglect the contamination among these two samples. Asteroseismic analysis of giants offers a solution to this issue. The CHeB giants and inter He-core giants can be accurately distinguished using asteroseismic analysis (Bedding *et al.* 2011; Mosser *et al.* 2011).

In this study, we combine data from the literature on asteroseismology with Li abundances for giants. Asteroseismology, as well recognized previously, allows one to distinguish core He-burning (here, CHeB) giants from those on the RGB, which are H-shell burning. The CHeB giants can further be separated into lower mass stars that experienced the He-core flash and higher mass stars, igniting and

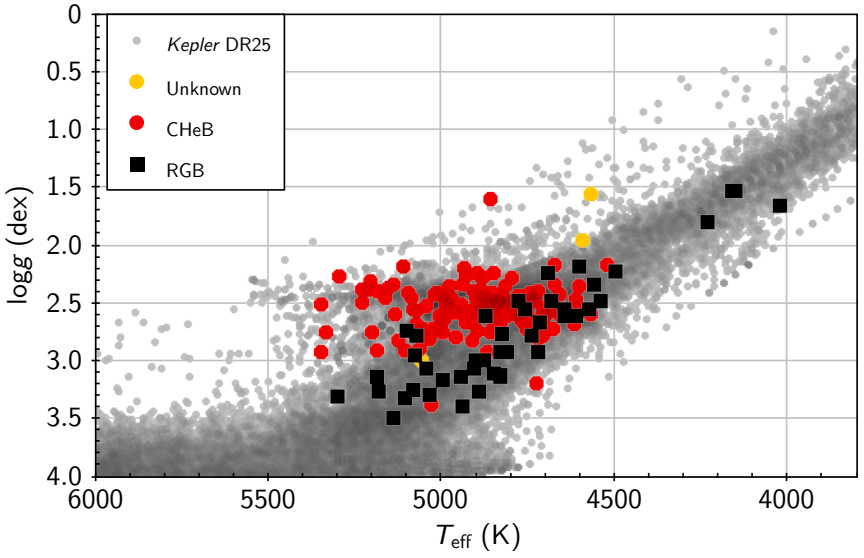


FIGURE 6.1: The spectroscopic HR diagram for giants in the KRBS sample along with *Kepler* DR25 stars in the background. Here, RGB are inert He core stars with H-shell burning, and CHeB are core He-burning giants, while 'Unknown' are the ones with unclassified evolutionary phases.

burning core He quiescently. A mass of $M \sim 2.2$ M$_\odot$ for solar metallicity stars separates low-mass CHeB giants experiencing a He-core flash from high-mass giants avoiding the flash. Theoretical modelling of RGB and CHeB giants shows that the measurable asteroseismic parameters may be used to distinguish these two classes of giants. Furthermore, the CHeB giants of all masses have similar interior structures and thus similar asteroseismic properties, but these properties vary according to mass. In this study, we explore the Li abundances among giants with asteroseismic data.

6.2 Data sample

Much of the asteroseismic data on red giants comes from observations conducted by the *CoRoT* (Auvergne *et al.* 2009) and *Kepler* satellites (Borucki *et al.* 2010). Bedding *et al.* (2011) provides a history of ground-based (and satellite) pursuit

of asteroseismic data. Photometry of giants provides a power spectrum exhibiting many frequencies which correspond to pure acoustic pressure (p modes) and gravity modes (g modes) as well as mixed modes (Beck *et al.* 2011). The mixed modes show a complicated spectrum; however, p- and g-modes are evenly spaced in frequency and period, respectively. The p modes are often characterized by the frequency of maximum oscillation power ($\nu_{\rm max}$) in μHz and large frequency spacing ($\Delta\nu$) in μHz. Unlike p modes, the g waves propagate through the core. They are characterized by the period spacing $\Delta\Pi_l$ defined as the difference between the periods of g modes of the same degree and consecutive radial orders. In this work, we use the asymptotic period spacing $\Delta\Pi_1$, which is the asymptotic g mode period spacing for $l = 1$ in sec.

In the ($\Delta\Pi_1$,$\Delta\nu$) plane, low mass CHeB and RGB stars with $M \leq 1.8$ M$_\odot$ are well separated (see below) such that the evolutionary phase of a star may be assigned (Bedding *et al.* 2011) and, thus, the variation of Li abundance with evolutionary phase may be explored. However, for stars with $M >$1.8 M$_\odot$, also known as secondary red clump giants (Bedding *et al.* 2011), there is a significant overlap between tracks for the CHeB and RGB phases which makes it challenging to assign an evolutionary phase based on the classical definition correctly, i.e., based on the distribution in the ($\Delta\Pi_1$,$\Delta\nu$) plane. Their evolutionary phase, however, can be assigned in a non-classical way as done by Kallinger *et al.* (2012) and the one by Elsworth *et al.* (2017).

We first searched the literature for giants with a known Li abundance in *Kepler*'s field of view. From Martell and Shetrone (2013); Anthony-Twarog *et al.* (2013); Silva Aguirre *et al.* (2014); Molenda-Żakowicz *et al.* (2014); Jofré *et al.* (2015); Takeda and Tajitsu (2017); Kumar *et al.* (2018); Singh *et al.* (2019b,a); Deliyannis *et al.* (2019) and Yan *et al.* (2021), we found a total of 574 giants with measured Li abundances in the *Kepler* field.

There are four open clusters (NGC 6791, NGC 6811, NGC 6819 and NGC 6866) in the *Kepler* field, while the lone open cluster NGC 6633 is in *CoRoT* field of view. NGC 6819 is the only well-studied with both Li and seismic data (Deliyannis *et al.* 2019). For the other three clusters in the *Kepler* field, Li abundances are available only for a few stars; for example, Molenda-Żakowicz *et al.* (2014) provides Li abundances of five G-type red clump stars of NGC 6811. These five giants and giants of NGC 6819 are now part of our sample. Li abundances for the giants of NGC 6866 and NGC 6791 are apparently unavailable.

Most of the studies in the literature provide the LTE Li abundance from the neutral Li resonance line at 6707 Å. Given the large range in Li abundance across the sample, the modest corrections for non-LTE effects for a typical giant seem unimportant. Abundance increases for the non-LTE effect for the 6707 Å Li line, as provided by Lind *et al.* (2009a) can range from close to zero for the hottest giants to about 0.4 dex for cool, metal-rich giants. For giants where the 6707 Å line is strong, the abundance analysis, including non-LTE corrections, is more reliably made using the excited Li lines at 6103 Å and 8126 Å.

Many of the observations in our initial list of giants are repeat observations. To eliminate repeat entries, we adopt the Li abundance (along with stellar parameters) from the spectroscopic study with the highest spectral resolution. For stars observed at comparable spectral resolutions in different studies, we adopt the entry with the highest signal-to-noise (SNR) ratio. If both spectral resolution and SNR are similar, then the entry from the latest study is considered. This resulted in a final sample of 514 unique giant stars in the *Kepler* field for which Li abundances are also available.

To get the asteroseismic data for these giants, we restrict our search to Bedding *et al.* (2011); Mosser *et al.* (2012); Stello *et al.* (2013); Mosser *et al.* (2014); Vrard *et al.* (2016); Elsworth *et al.* (2017); Hon *et al.* (2017); Yu *et al.* (2018) and Vrard

et al. (2018), along with the source papers of the giants from which Li abundances are taken. In these studies, we found a total of 612 asteroseismic data entries for our 514 unique stars. Data entries mainly include the evolutionary phase classifications along with some of the seismic parameters, like $\nu_{\rm max}$, $\Delta\nu$ and $\Delta\Pi_1$. For the majority of the entries, the evolutionary phase classification is given with $\nu_{\rm max}$ and $\Delta\nu$, while $\Delta\Pi_1$ is available for a small number of stars. We eliminate repeat entries by adopting data from the latest study. While selecting the data, preference is given to studies in which uncertainties in the seismic parameters are also provided. If $\Delta\Pi_1$ is missing from the selected study for a star, then we add its most recent measurement (if available) from other studies (and, of course, by giving preference to the study in which uncertainty in $\Delta\Pi_1$ is also provided). This resulted in a final sample of 187 unique stars (hereafter, the KRBS sample, where 'K' stands for the *Kepler* mission, and 'RBS' stands for our 'red-giant branch sample'). In the sample KRBS, both $\nu_{\rm max}$ and $\Delta\nu$ are available for 187 stars while $\Delta\Pi_1$ is available for only 64 stars.The KBRS consists of 44 RGBs, 140 core-He-burning (CHeB) and three giants with an unclassified evolutionary phases.[†] [‡]

The spectroscopic Hertzsprung-Russell diagram (sHRD) for the sample KRBS along with stars from 25^{th} Data Release of the *Kepler* stellar properties catalog (hereafter, *Kepler* DR25; Mathur *et al.* 2017), in the background are shown in Figure 6.1. For stars in the sample KRBS, we used effective surface temperature ($T_{\rm eff}$) from the *Kepler* DR25 while surface gravity ($\log g$) estimates are taken from the papers where Li abundances are taken.

[†]Spectroscopic and asteroseismic data for giants in our final sample is available at DOI: `https://doi.org/10.5281/zenodo.4519625`.

[‡]Comments from a post-publication email communication with Professor Benoît Mosser regarding giants with unclassified evolutionary phase in our list. 1) The oscillation spectrum of KIC 5112751 has a poor signal-to-noise ratio. 2) KIC 5024272 and KIC 5024750 have a status as evolved RGB or evolved AGB; a recent method is tried to disentangle the evolutionary stages of these stars (Mosser *et al.* 2019), but it fails here due to a too low SNR. 3) KIC 6221548 burns its core helium in the secondary clump, with a mass of about 2.3 $M_\odot$; its location in the Mass - A(Li) diagram seems consistent.

6.3 Results

6.3.1 Asteroseismic mass for sample stars

The mass of a RGB or a CHeB star with asteroseismic data may be determined using the following well-known scaling relations (see, e.g., Stello *et al.* 2009; Kallinger *et al.* 2010; Mosser *et al.* 2010).

$$\frac{M_{SR}}{M_{\odot}} = m \left(\frac{\nu_{\rm max}}{\nu_{\rm max,\odot}}\right)^{3} \left(\frac{\Delta\nu}{\Delta\nu_{\odot}}\right)^{-4} \left(\frac{T_{\rm eff}}{T_{\rm eff,\odot}}\right)^{3/2} \tag{6.1}$$

here, $T_{\rm eff,\odot}$ = 5777 K, $\Delta\nu_{\odot}$ = 135.1 ± 0.1 μHz and $\nu_{\rm max,\odot}$ = 3090 ± 30 μHz are reference solar values (Huber *et al.* 2011) while m is a scaling factor. The scaling relation is known to vary slightly for stars depending on their evolutionary phase. For example, Mosser *et al.* (2010) found that for giant stars, the value of m is 0.89 ± 0.07 for $\Delta\nu_{\odot}$ = 135.5 μHz, $\nu_{\rm max,\odot}$ = 3050 μHz, and $T_{\rm eff,\odot}$ = 5777 K. In the current study, we use the original scaling relation (i.e., with m = 1). For more recent updates, see Hekker (2020). We also estimated uncertainties in mass through error propagation. Mass is determined for all the 184 giants for which asteroseismic data is available; however, estimation of the corresponding uncertainty is not possible for seven giants due to the unavailability of uncertainties in seismic data. Mean uncertainty in estimated mass is 0.15 ± 0.11 $M_{\odot}$. For 181 of our sample stars, seismic mass estimates are also available from the original studies reporting the asteroseismic data. Our mass estimates from equation 6.1 are lower by only 0.002 ± 0.018 $M_{\odot}$ than estimates in these studies. This difference and the slight scatter in the mass differences are likely due to small systematic and random differences in the adopted effective temperatures and reference solar seismic parameters.

Instead of just relying on the above scaling relations, we also estimated seismic

masses for our sample stars using PARAM (da Silva *et al.* 2006; Miglio *et al.* 2013).[§] PARAM provides Bayesian estimation of stellar parameters (including mass) using PARSEC isochrones from Bressan *et al.* (2012). In the current study, we use PARAM in its asteroseismology mode with other conditions as default, except Bayesian priors, which are estimated for the age interval from 0.1 to 14 Gyr. For each star, the input parameters are $T_{\rm eff}$, [Fe/H], $\nu_{\rm max}$ and $\Delta\nu$ along with their uncertainties and a star's evolutionary phase classification. Hereafter, we refer to estimated masses from PARAM by $M_{\texttt{PARAM}}$. For seven of our sample stars for which uncertainties in $\nu_{\rm max}$ and $\Delta\nu$ are not available, we assumed uncertainties of 0.1 and 0.05 μHz, respectively. The distribution of masses for our sample stars estimated from scaling relation and from PARAM are shown in Figure 6.2. The scaling relation suggests the mass range of CHeB stars extends down to $M \simeq 0.5$ M$_\odot$, which seems implausible on account of very long main sequence lifetimes.

6.3.2 Li as a function of stellar mass

Variations of Li abundance with stellar mass are potentially valuable clues to the origins of Li enrichment in RGB and CHeB giants. A(Li) as a function of a star's mass as estimated from scaling relation (M_{SR}) and from PARAM ($M_{\texttt{PARAM}}$) is shown in Figure 6.2. Errors in the estimated masses are shown as black error bars. The majority of giants in our sample have A(Li) higher than 1.5. This is a selection bias. However, the lack of low-Li giants will not affect our analysis as we are more concerned about the presence of giants with Li higher than the expected value. According to standard models of stellar evolution, A(Li) in low-mass giants after they have undergone the first dredge-up is expected to be lower than $\sim$ 1.5 dex. Hence, all the giants with A(Li) higher than 1.5 can be safely assumed as Li-enriched, and their presence across the range of stellar parameters, like mass and asteroseismic parameters, is enough to draw conclusions about processes that may

[§]http://stev.oapd.inaf.it/cgi-bin/param_1.3

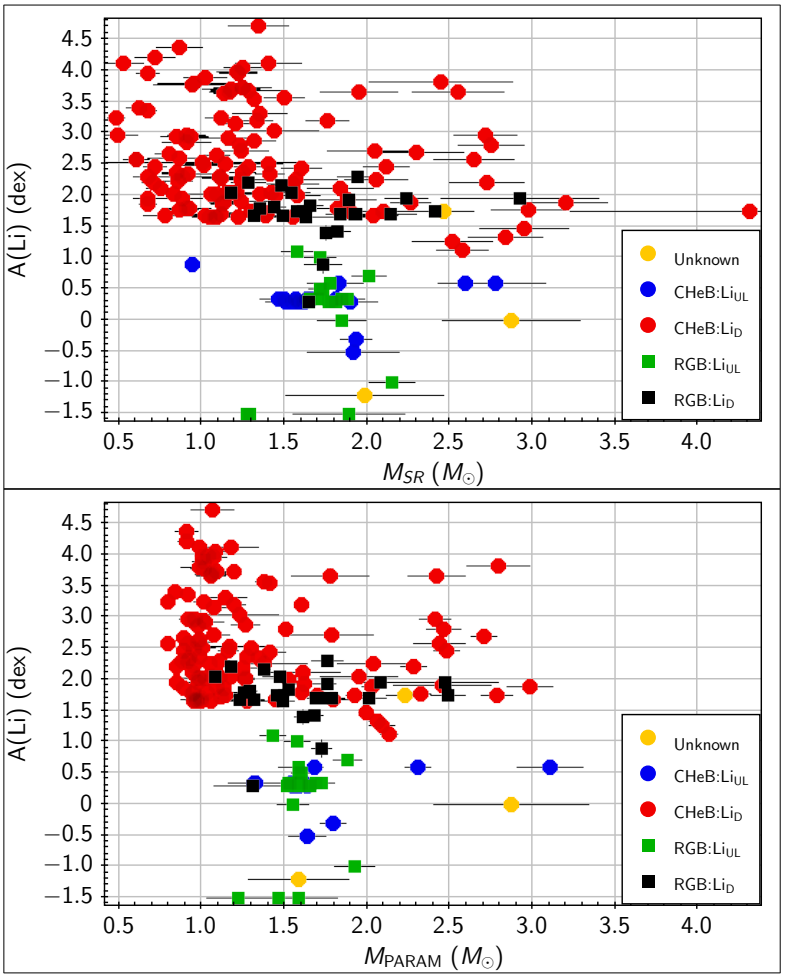


FIGURE 6.2: A(Li) as a function of stellar mass estimated from the scaling relation (top panel) and from `PARAM` (bottom panel). Errors in mass estimates are shown as black error bars. Filled red and blue circles are core He-burning giants with Li detections and upper limits, respectively. Filled black and green squares are RGB giants with H-shell burning with Li detections and upper limits, respectively.

be responsible for Li-enrichment in these giants. The necessity of having giants with a low A(Li) becomes absolute only if one wants to estimate the Li-rich giants' occurrence rate as a function of these stellar parameters, which is not a goal of this study. Hence, the lack of low A(Li) giants in our sample will not affect our conclusions.

Li in our sample of RGB giants has a maximum value of A(Li) at an average of $\simeq 2.3$ (black squares) in stars with masses from about 1-3 $M_\odot$. Other RGB giants

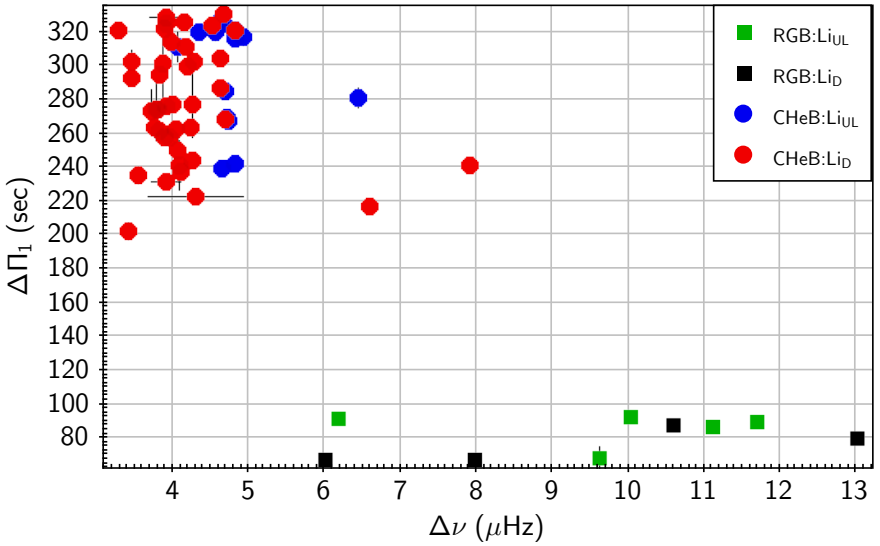


FIGURE 6.3: Distribution for our sample stars in the $\Delta\Pi_1 - \Delta\nu$ plane. Used labels are the same as in Figure 6.2.

(green squares) provide only an upper limit to A(Li) with A(Li) extending to -1.5 over apparently a narrow mass range centred on about 1.6-1.8 $M_\odot$, but this may be an illusion resulting from the small sample.

Mass estimates for the CHeB giants extend beyond the mass of 2.25 $M_\odot$, which is considered to be the maximum mass for a RGB star to experience the He-core flash, a leading suspect for Li-enrichment via conversion of ^{3}He (Iben 1967). The vast majority of the CHeB giants in our sample are Li-rich and even very Li-rich with $A(\mathrm{Li}) \geq 4$. Li-rich stars with $A(\mathrm{Li}) \geq 2$ are not restricted to giants expected to have suffered a He-core flash, i.e., $M \leq 2.25$ $M_\odot$. For a few CHeB giants, the Li 6707Å feature is undetectable, and an upper limit is set for the Li abundance (blue circles).

6.3.3 Predicted evolution in the $\Delta\Pi_1 - \Delta\nu$ plane

The $\Delta\Pi_1$ versus $\Delta\nu$ distribution for 64 sample stars is shown in Figure 6.3. These are the stars in our sample for which $\Delta\Pi_1$ is available. As expected, both RGB

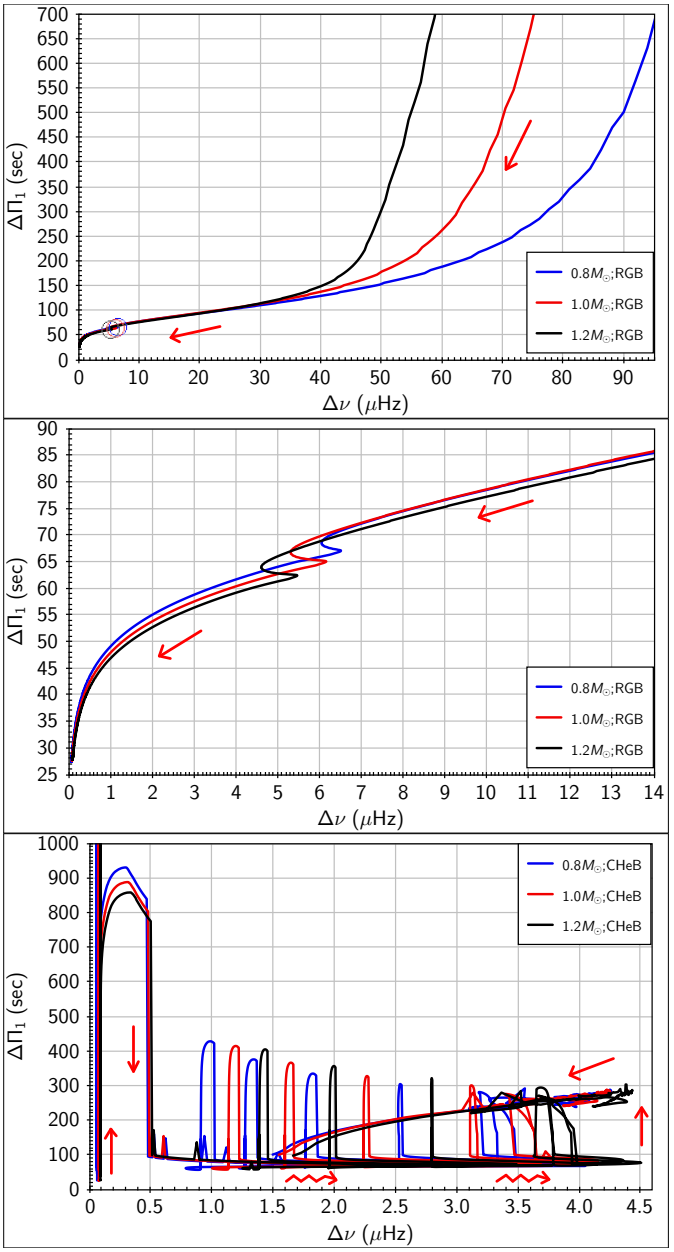


FIGURE 6.4: Evolutionary tracks for solar-metallicity model stars with masses 0.8 (blue line), 1.0 (red line) and 1.2 $M_\odot$ (black line) in $\Delta\Pi_1 - \Delta\nu$ plane. The RGB phase is shown in the top and middle panels, while the CHeB phase is shown in the bottom panel. Arrows indicate the global direction of the evolution of model stars. Open circles in the top panel indicate the position of the luminosity bump for each of the three masses. In the middle panel, the luminosity bump occurs at the obvious 'S-type' loop in the tracks. The initial He core flash at $\Delta\nu < 0.1$ μHz) is very strong. However, the actual peak value may be even higher and missed due to the finite step size. This and other early episodes of He core flash occur in a brief phase at a luminosity well above the RC.

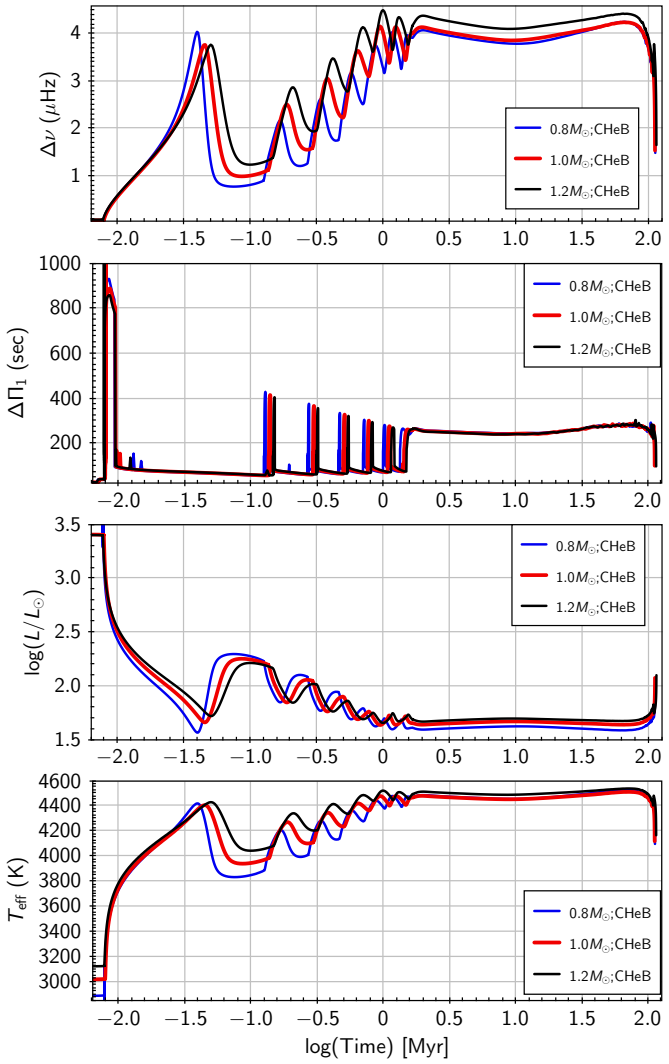


FIGURE 6.5: Variation of $\Delta\nu$, $\Delta\Pi_1$, luminosity and $T_{\rm eff}$ as a function of time (in millions of years) during the CHeB phase for solar-metallicity model stars of masses 0.8, 1.0 and 1.2 $M_\odot$. A base-10 log scale is used for the time axis to highlight the fact that giants in the CHeB phase spend almost their entire life in a relatively stable state except for the brief He-flashing region at the start.

(filled squares) and CHeB (filled circles) are well separated. Indeed, the differences between $\Delta\Pi_1$ and $\Delta\nu$ were the primary criteria for assigning the evolutionary phase.

Gross differences in the asteroseismic data between CHeB and RGB giants are the basis for assigning a giant to one of these evolutionary phases. Less striking changes of asteroseismic data are expected from the changing internal structure of

a giant, be it as the star evolves along the RGB or as the He-core of a CHeB star exhausts its He. Such changes may prove to be the basis for identifying the precise location of a RGB or a CHeB giant in its evolution. To quantify the evolution of giants in the $\Delta\Pi_1 - \Delta\nu$ plane, we make use of the *Modules for Experiments in Stellar Astrophysics* (`MESA`; Paxton *et al.* 2011, 2013, 2015, 2018).

We started with the `MESA` model constructed by Schwab (2020). We activated the output columns for asteroseismic parameters and also decreased the step interval to get fine details about the core He-flash phase. [¶] Then, we evolved models of solar-metallicity stars of masses 0.8, 1.0, and 1.2 $M_\odot$ until the centre mass fraction of ^{4}He drops below 10^{-6} to conclude the CHeB phase.

The evolutionary tracks for the red-giant phases – RGB and CHeB – of these stars are shown in Figure 6.4. Arrows indicate the global direction of the evolution of giants along the tracks. In the top panel, the RGB branch corresponds to the tracks with $\Delta\nu \lesssim 40$ μHz, which are nearly identical for $M \lesssim 1.8$ $M_\odot$ (Stello *et al.* 2013). For masses $M \geq 1.9$ $M_\odot$, evolutionary tracks (not shown in this panel) provide an increasing $\Delta\Pi_1$ at a given $\Delta\nu$ (Stello *et al.* 2013). Prior to entry to the RGB, the tracks in the top panel are separated by mass. Evolution up the RGB is shown in more detail in the middle panel where the $\Delta\nu$ range matches that shown in Figure 6.3. The location of the luminosity bump is indicated in the top panel and revealed in the middle panel by the 'S-type' loops at $\Delta\nu \simeq 6$ μHz. Locating the luminosity bump among giants in the asteroseismic sample is relevant to the exploration of Li among giants because Li production via thermohaline instabilities at the luminosity bump has been proposed (Charbonnel and Zahn 2007). The RGB and CHeB `MESA` tracks are shown for solar metallicity models but are insensitive to a factor of two changes in metallicity and unchanged when initial rotation $\Omega_{\rm ZAMS}/\Omega_{\rm crit}$ is changed between zero and 0.4.

[¶]The `MESA` model constructed by Schwab (2020) is available at DOI: `https://doi.org/10.5281/zenodo.3960434`

The CHeB phase begins in the bottom left of the lower panel, where the RGB track ends with readjustment to the He-core flash (Figure 6.4). Thanks to the small step size, we can also see the positions of subsequent mini He-flashes. These subsequent He-flashes are weaker compared to the initial strong He flash because re-ignition of He occurs but less violently (Mocák *et al.* 2010). For all three model stars of mass 0.8, 1.0 and 1.2 $M_{\odot}$, temporal evolution from start to end of the CHeB phase is illustrated by Figure 6.5. A base-10 log scale is used for the time axis considering the short duration of the He-flashing region compared to the total duration of the CHeB phase. The figure shows the variation of the star's asteroseismic parameters, luminosity and $T_{\rm eff}$. All three model stars undergo mini-He core flashes following the initial strong He-flash. Temporal evolution for all three masses is very similar in form. By far, most of the time in the core He-burning phase is spent on the path from about $(\Delta\nu, \Delta\Pi_1)$ = (4.5,300) to (1.5,100), as shown clearly in Figure 6.5.

The long-duration portions of the tracks for the three masses cover the majority of the observations for CHeB stars in Figure 6.3. The He core flashes last only for about 1 Myr, and hence, very few CHeB stars will be observed during this phase. For the major episode of CHeB, $\Delta\Pi_1$ ranges from about 150 to 320 sec. This is broadly consistent with observations in Figure 6.3. Indeed, just three CHeB giants with $\Delta\nu \simeq 7$ μHz are obvious outliers. This trio may be secondary RC giants (Bedding *et al.* 2011; Stello *et al.* 2013).

6.3.4 Li as a function of $\Delta\nu$ and $\Delta\Pi_1$ in giants

Our comparison of observed Li abundances for RGB and CHeB giants with their asteroseismic data is made in two steps. First we compare the Li abundances with the $\Delta\nu$ measurements (Figure 6.6) and then with the $\Delta\Pi_1$ data (Figure 6.7). This

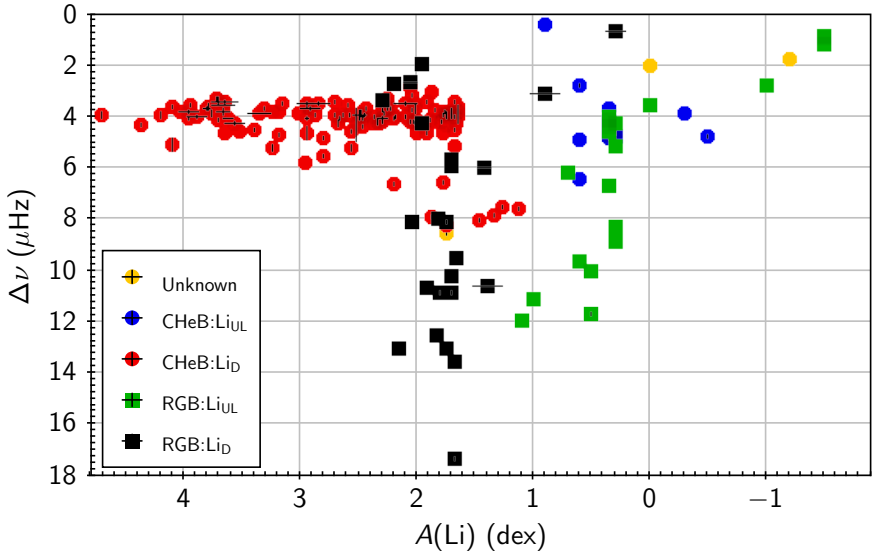


FIGURE 6.6: A(Li) as a function of $\Delta\nu$ for our sample stars. Used labels are the same as in Figure 6.2.

separation is made because not every giant in our sample has both $\Delta\Pi_1$ and $\Delta\nu$ available.

A(Li) as a function of $\Delta\nu$ for 187 giants is shown in Figure 6.6. The figure resembles the luminosity versus A(Li) plots with the RGB tip towards the top-right corner. As previously, RGB and CHeB giants are represented by filled squares and circles, respectively, as indicated by the key. For the RGB stars, the $\Delta\nu$ range about 0 to 18 μHz spans the range covered by Figure 6.4 with stars spanning the luminosity bump (LB) and a few stars nearing the RGB tip ($\Delta\nu \simeq 1\mu$Hz). Many of the RGB giants along almost the entire RGB have the $A(\mathrm{Li}) \simeq 1.5 - 2.0$, as expected for post-dredge-up giants. In this small sample, there is no indication that the LB denotes a change in A(Li) measurements except for a slight increase in the measured A(Li) for $\Delta\nu \leq 6\mu$Hz. RGB giants with A(Li) upper limits may have resulted from extraordinary Li destruction on the main sequence or in the transition to the RGB. Figure 6.6 shows that the upper limits for RGB giants trend to their lowest A(Li) as $\Delta\nu$ declines and, thus, as the giants approach the RGB tip and the limit $A(\mathrm{Li}) \sim -1.5$.

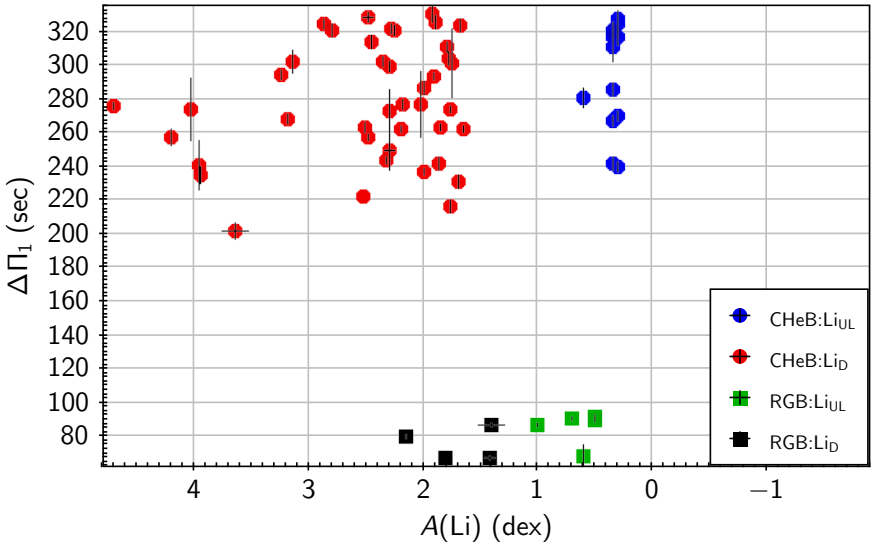


FIGURE 6.7: Li abundances in RGB and core-He-burning (CHeB) giants as a function of their gravity-mode period spacing ($\Delta\Pi_1$). Used labels are the same as in Figure 6.2.

Giants belonging to the CHeB phase, including secondary RC stars, are shown as filled circles in Figure 6.6 and are concentrated around 4 μHz. The few higher values of $\Delta\nu$ likely arise from secondary RC stars, all with detectable Li. Several stars with lower $\Delta\nu$ may be identified as more advanced in the CHeB. Almost every CHeB giant is Li-rich, i.e., has $A(\mathrm{Li}) \geq 1.5$, but a few stars with lower Li abundances, including a sample with A(Li) upper limits as low as -0.5.

Li abundances as a function of $\Delta\Pi_1$ for our sample stars are shown in Figure 6.7. The few RGB giants have $\Delta\Pi_1$ between about 60 and 90 sec about as expected from Figure 6.4. The CHeB giants span the range in $\Delta\Pi_1$ about as expected from Figure 6.4 except the absence of CHeB giants with very low $\Delta\nu$ and high $\Delta\Pi_1$. The dearth of CHeB giants with $\Delta\Pi_1 < 200$ in our observational sample is due to the very fast evolution of giants in this phase (Figure 6.5). In general, the figure is suggesting a decreasing trend in A(Li) with an increase in $\Delta\Pi_1$.

6.4 Discussion and Conclusions

In this study, we assemble data from the literature on asteroseismology and Li abundances for giants. Our final sample of 187 giants consists of 44 RGB, 140 CHeB and three giants with unclassified evolutionary phases.

First, to investigate the mass dependence of Li enrichment in giants, we estimated masses for our sample stars from asteroseismic scaling relations as well as from the `PARAM`, which provides isochrones-based Bayesian estimates using asteroseismic data. Estimated masses for the CHeB giants from asteroseismic scaling relation extend down to about 0.5 $M_{\odot}$, which is not the case for mass estimates from the `PARAM`. The presence of such low-mass giants in the CHeB phase seems implausible on account of very long main-sequence lifetimes compared to the Galaxy's age. However, it might be explained by a large mass loss in the giant phase or an issue with the asteroseismic scaling relations. Nevertheless, after comparison with isochrone-based mass estimates from the `PARAM`, our first impression is that there is an issue with mass estimates from scaling relation for giants in the CHeB phase. A more detailed study with a larger sample is needed to further resolve this issue.

The distribution of Li-rich giants as a function of mass is of particular interest. It can provide clues about processes leading to Li enrichment in giants. For example, if Li enrichment is associated with core He-flash only, then all the Li-rich giants are supposed to have masses lower than the maximum mass expected to have suffered a core He-flash, i.e. $M \leq 2.25$ $M_{\odot}$. However, in our sample, we have a significant number of Li-rich CHeB giants with masses higher than 2.25 $M_{\odot}$ (Figure 6.2). This suggests that whilst the core He-flash may be the dominant process leading to Li enrichment in low-mass giants, there is a secondary process leading to Li enrichment in the more massive stars.

To study the evolution of Li in giants, one of the primary tasks is to untangle giants

of different evolutionary phases (like RGB, CHeB, etc.). This can be done either based on the star's position in the HR diagram or using asteroseismology. In this study, our goal is to understand changes in asteroseismic parameters (especially $\Delta\Pi_1$ and $\Delta\nu$) of giants as they evolve. For this, we used the `MESA` models. Thanks to the consideration of very small step size, models reveal the very minute and vital information regarding the variation of seismic parameters during the red giant phase and suggest the presence of subsequent mini He-flashes along with the initial strong core He-flash (Figure 6.4). However, all of this activity occurs in a brief evolutionary phase before the giant assumes its steady state phase of core He-burning.

Based on observational data, we explored the variation of A(Li) as a function of seismic parameter $\Delta\nu$ and $\Delta\Pi_1$. From the distribution of A(Li) as a function of $\Delta\nu$, which is similar to the distribution of A(Li) as a function of luminosity, we found no indication of Li enrichment near the luminosity bump. Also, A(Li) trends to $\sim$ -1.5 dex as $\Delta\nu$ approaches zero, i.e. near the RGB tip.

Evolution of Li as a function of $\Delta\Pi_1$ is of particular interest. Data suggest a decreasing trend in A(Li) with an increase in asymptotic period spacing $\Delta\Pi_1$ for CHeB giants (Figure 6.7). In CHeB giants, the presence of higher A(Li) at lower $\Delta\Pi_1$ points towards Li enrichment at the early stage of the CHeB phase. Also, the dearth of CHeB giants with $\Delta\Pi_1 < 200$ can be explained by the fast evolution of giants in this phase (Figure 6.5). A more detailed study of stellar models will benefit understanding the evolution of Li near the RGB tip. One way to further this study is to get asymptotic period spacing $\Delta\Pi_1$, which is available for only 64 of the total 187 giants in our sample.

Many giants in the RGB and CHeB phases have now been probed for their asteroseismic data but lack spectroscopic measurements of Li and other elemental abundances. Expansion of our small samples of asteroseismic and Li data on RGB

and CHeB giants would be of great interest for several reasons. For example, CHeB giants and RGB giants at the luminosity bump partially overlap in the HR diagram, and spectroscopic separation is difficult, but asteroseismic data provides a certain identification of these two evolutionary phases. Expansion of our sample would finally answer the question about the extent of surface Li enrichment for giants evolving through the luminosity bump. In this regard, data from the ongoing Large Sky Area Multi-Object Fibre Spectroscopic Telescope (LAMOST)-*Kepler*/K2 survey will be beneficial. In a similar spirit, expansion of the CHeB sample should allow examination of the Li enrichment as a function of stellar mass and also of the age of a CHeB star. Much remains to be done by observers and theoreticians.

Data Availability

The data underlying this article are available at DOI: `https://doi.org/10.5281/zenodo.4519625`.

Chapter 7

Lithium in red giants: the roles of the He-core flash and the luminosity bump*

7.1 Introduction

Since the first discovery of a Li-rich giant by Wallerstein and Sneden (1982), the almost four-decade-old mystery behind the origin of Li-rich giants has now progressed to identifying the exact process of Li-enrichment in these giants. All the recent studies (Deepak and Reddy 2019; Deepak *et al.* 2020; Kumar *et al.* 2020; Martell *et al.* 2021) now confirms that almost all the Li-rich giants are He-core burning giant stars. Asteroseismic studies of relatively smaller samples further support this conclusion (Silva Aguirre *et al.* 2014; Singh *et al.* 2019a; Yan *et al.*

*This chapter is published in Deepak and Lambert (2021b)

2021; Deepak and Lambert 2021a; Singh *et al.* 2021). All the proposed explanations in all these studies involve internal production of Li through the well known Cameron-Fowler mechanism first recognised by Cameron and Fowler (1971).

Cameron and Fowler (1971) suggested this mechanism involving He-burning shell flashes to account for the rare carbon stars like WZ Cas (McKellar 1940) and WX Cyg (Sanford 1950) with very strong 6707 Å lines. In modern parlance, these carbon stars are examples of luminous AGB stars experiencing helium shell-burning episodes and the third dredge-up. Lithium, carbon and *s*-process enrichment are predicted by contemporary modelling and observed in luminous AGB giants (Smith and Lambert 1989). However, for K giants like HD 112127, which are not luminous AGB stars, two evolutionary phases have received the most attention with respect to Li enrichment: giants at the so-called luminosity bump (LB) on the RGB and more luminous low-mass giants at the RGB's tip, which experience a He-core flash before evolving to the red clump (horizontal branch) as a He-core burning giant.

Suspicions about the association of the He-core flash with Li synthesis were aired in the first survey for Li-rich giants by Brown *et al.* (1989a) and raised subsequently by others. For example, Deepak and Reddy (2019) found that most of the Li-rich giants in the GALAH DR2 survey belong to the red clump phase. These suspicions were wonderfully raised to a near-certainty by Kumar *et al.* (2020) whose analysis of Li abundances of giants in the GALAH DR2 survey led to the bold suggestion that *only* He-core burning giants were Li-rich and, thus, that Li synthesis occurs at or immediately following the He-core flash. They asserted that Li enrichment of He-core burning giants is 'ubiquitous' and confined to these giants; that is – all low-mass giants experiencing a He-core flash synthesize Li at a level from very mild to severe to contaminate the RC giant which follows the flash. Subsequent studies of asteroseismology of He-core burning giants with A(Li) determinations suggest that Li abundances following the He-core flash may decline with age (Deepak and

Lambert 2021a; Singh *et al.* 2021). The common assumption is that the Li results from the Cameron-Fowler mechanism. Kumar *et al.* (2020) did not detail the mechanism's application to the He-core flash. A recent theoretical exploration (Schwab 2020) is discussed below.

Adaptation of the ^{3}He reservoir to Li production has also been connected to RGB giants experiencing the LB. This 'bump' on the RGB occurs at the point when the H-burning shell moves outward across an H-discontinuity. The evolution of the star reverses course, and it moves slowly and slightly down the RGB before reversing again and continuing to evolve up the RGB. This manoeuvre introduces a clumping of stars on the RGB. At the time of this LB, operation of the Cameron-Fowler mechanism occurs through a thermohaline instability expected on theoretical grounds (Eggleton *et al.* 2008; Lagarde *et al.* 2011) and suggested as a possible way to account for Li enriched giants (e.g., Martell *et al.* 2021). But definitive observational identification of Li-enriched LB giants remains open.[†]

In this study, we concentrate on the exploitation of the recent GALAH survey of stellar abundances, with the focus here on the Li abundances of low-mass red giants. Our primary goal is to set Li production limits by the He-core flash as a function of stellar mass and initial metallicity. Our secondary goal is to search for Li enrichment by LB giants. Our observational inquiry based on the latest data release DR3 from the GALAH survey is supported by predictions of Li abundances from calculations performed using the Modules for Experiments in Stellar Astrophysics (`MESA`; Paxton *et al.* 2011, 2013, 2015, 2018, 2019) suite of computer programmes.

[†]Thermohaline instability at the LB has also been suggested as a way to change a giant's surface ^{12}C/^{13}C ratio.

7.2 Data sample

Recent observational advances in understanding Li-rich giants have largely come from combining spectroscopic abundance surveys with astrometric data from the *Gaia* satellite (Gaia Collaboration *et al.* 2016b). Li (and other) elemental abundances from the GALAH DR2 survey have been used by Deepak and Reddy (2019); Deepak *et al.* (2020); Kumar *et al.* (2020) with Martell *et al.* (2021) using the DR3 results. The LAMOST survey was considered by Deepak *et al.* (2020) for C, N and O (but not for Li) for stars in common with the GALAH DR2. LAMOST's Li abundances were explored by Singh *et al.* (2019a) for stars in the Kepler field of view and in detail by Yan *et al.* (2021).

Here, we consider the third data release (DR3) of the GALAH survey. Our analysis is devoted to low-mass giants with a metallicity [Fe/H] representative of the Galactic disc, say $-1 \lesssim$ [Fe/H] $\lesssim +0.5$. GALAH DR3 (and DR2) provides too few metal-poor halo giants to probe the matter of Li-richness among the halo population. As a secondary interest, we make a foray into possible abundance anomalies introduced into RC giants by the He-core flash, which converts a giant at the RGB tip to a He-core burning giant on the RC.

The Third Data Release of the Galactic Archaeology with the HERMES survey provides stellar parameters and elemental abundances derived from 678,423 spectra for 588,571 unique stars observed with the HERMES spectrograph at the Anglo-Australian Telescope between November 2013 and February 2019 (see Buder *et al.* 2021, for more detail on the data release). It is also accompanied by several value-added-catalogues (VAC) providing various other intrinsic, kinematic and dynamical properties of the observed stars (hereafter, GALAH+ DR3).[‡] `GALAH_DR3_main_allspec_v1.fits` is one of the two main catalogues of

[‡]The GALAH+ DR3 data is available at `https://cloud.datacentral.org.au/teamdata/GALAH/public/GALAH_DR3/`

GALAH+ DR3 and includes stellar parameters and overall abundances of about 30 chemical species derived for each of the observed spectra. This catalogue also includes abundances derived for each individual line for all the elements. We joined this catalogue with the VAC `GALAH_DR3_VAC_ages_v1.fits`, which provides other stellar parameters like age, mass, distances, luminosity, etc., estimated using Bayesian Stellar Parameter Estimation code (BSTEP, Sharma *et al.* 2018). The two catalogues are joined using the recommended method of using the internal ID for each GALAH observation provided in the `sobject_id` column. To eliminate multiple entries of a star in the catalogue and to select the entry with the highest signal-to-noise, we restrict our sample to stars with `flag_repeat` = 0. We further restrict our sample to stars with reliable stellar parameters (`flag_sp` = 0) and metallicity (`flag_fe_h` = 0), which lead to abandoning of stars with $T_{\rm eff} < 4100$ K. We also discarded all the stars with uncertainty in temperature ($\sigma_{T_{\rm eff}}$) and luminosity ($\sigma_{\log(L/{\rm L}_\odot)}$) of more than 200 K and 0.2, respectively. This resulted in a sample of about 425 thousand stars. Sample stars are shown in Figure 7.1 in the form of the HR diagram. Note that the sample is not mass limited, and the large scatter in the figure can be attributed in part to the presence of relatively massive stars (with masses 2−5 $M_\odot$) in the sample. For each sample star, uncertainties in luminosity and temperature are also shown in the background, however, due to crowding, they are visible only for the star on the boundaries. From this sample, we select giant stars with temperatures from 4100 to 5600 K and luminosity $\log(L/{\rm L}_\odot)$ from 0.3 to 3.4 dex. This selection of 159,841 stars is shown within the dotted green box in Figure 7.1 (hereafter, the RBS, which stands for the red-giant branch sample).

Except for Martell *et al.* (2021), previous discussions of Li abundances in giants based on the GALAH survey drew on the DR2 catalogue. Of interest to the present study is the fact that our sample of RBS giants from the DR3 catalogue is approximately doubled over our previous sample from DR2 (Deepak *et al.* 2020), abundance quality flagging is also improved, including the provision of upper limits

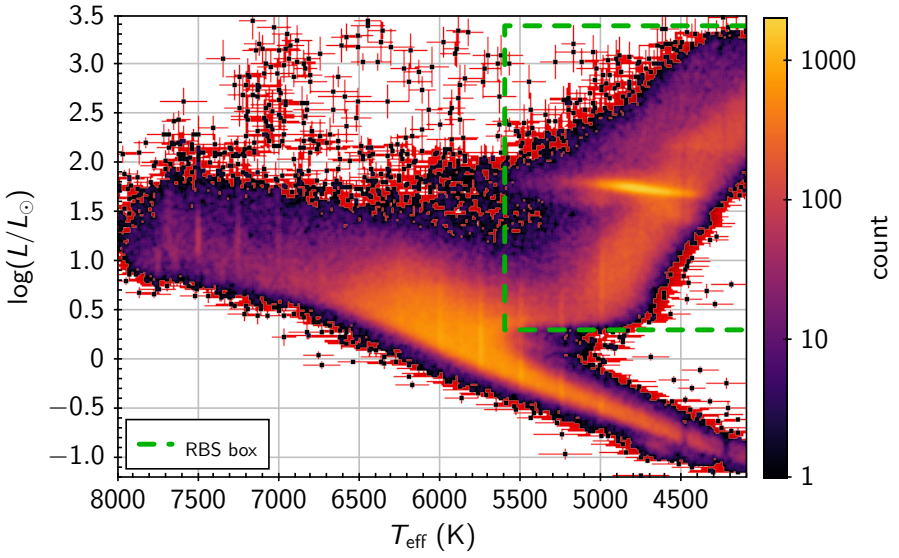


FIGURE 7.1: Sample stars in a HR diagram also showing the selection of red giants (the RBS) within the green box. For all the stars, uncertainty in luminosity and temperature are also plotted in the background as red error bars.

and abundances are now provided for 31 rather than 21 elements previously. In the case of the 335 Li-rich giants found by Deepak and Reddy (2019) in the DR2 catalogue, Li abundances of common stars in DR2 and DR3 show only a slight systematic change: the least Li-rich are slightly less Li-rich, and the super Li-rich giants are slightly more Li-rich. Our assessment is that the differences between the data releases have not affected principal conclusions about Li in giants in the RBS collection studied in previous works. The increase in the RBS sample offers the chance to search for new properties of Li-rich giants and to explore already covered properties in more detail.

7.2.1 Elemental abundances

The GALAH+ DR3 survey provides the elemental abundance ratio [X/Fe][§] for up to 30 chemical elements per star with X = Li, C, O, Na, Mg, Al, Si, K, Ca, Sc, Ti,

[§]For two elements, X and Y, with number densities N_X and N_Y, the elemental abundance ratio $[X/Y] \equiv \log(N_X/N_Y)_{\rm star} - \log(N_X/N_Y)_{\rm Sun}$.

V, Cr, Mn, Co, Ni, Cu, Zn, Rb, Sr, Y, Zr, Mo, Ru, Ba, La, Ce, Nd, Sm, and Eu. Abundances for most of the elements were considered in detail in Section 5.3 using the DR2 catalogue. The global analysis of [X/Fe] will not be reexamined here. Previously, the only detectable difference between [X/Fe] for Li-rich, Li super-rich and normal giants was that Li super-rich giants were slightly underabundant in [C/Fe] but see Martell *et al.* (2021).

For Li, the DR3 catalogue provides the non-LTE correction for the Li abundance provided by the 6707 Å resonance doublet (for more details, see Buder *et al.* 2021, and references therein). We convert the [Li/Fe] using the non-LTE Li and LTE Fe abundances into A(Li) using A(Li) = [Li/Fe] + [Fe/H] + $A(\mathrm{Li})_{\odot}$, where $A(\mathrm{Li})_{\odot}$ is the solar Li abundance for which we adopt $A(\mathrm{Li})_{\odot} = 1.05 \pm 0.10$ dex, which is the value used for the GALAH data (see Buder *et al.* 2021, for more details). The DR3 catalogue also provides uncertainties ($\sigma_{[\mathrm{X/Fe}]}$ available in corresponding `e_X_fe` column) and a quality flag (`flag_X_fe`) for each of abundance entry. `flag_X_fe` can have any value from 0, 1 and 32, where flag 0 means provided abundance is reliable, 1 means provided abundance is an upper limit, and 32 means no reliable measurement reported. In this study, we will use `flag_X_fe` = 0 for elements except for Li. In the case of Li, `flag_Li_fe` = 0 will be used to identify a Li-enriched star, while for the Li-normal stars, we will use all three flags to avoid discarding stars with a relatively lower Li-abundance from the sample. Throughout the chapter, we will specify if we are considering a sample of stars for which DR3 notes a detection of Li or considering the larger sample combining stars with a detection or an upper limit of the Li 6707 Å line.

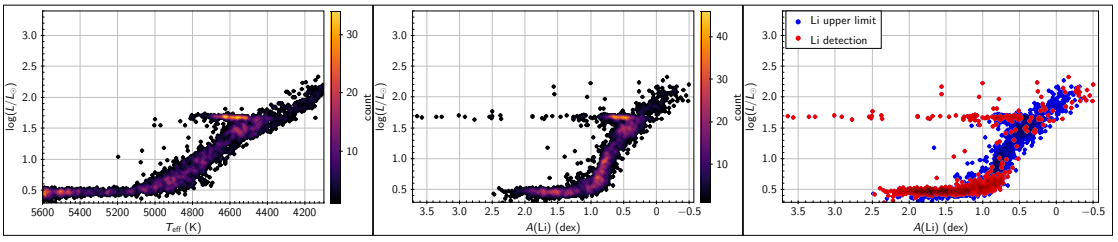


FIGURE 7.2: HR diagram and A(Li) as a function of luminosity for the RBS giants with masses $M/\mathrm{M}_{\odot} = 1.10 \pm 0.02$ and metallicity [Fe/H] $= 0.00 \pm 0.10$ dex. The left and middle panels show giants with both Li detections and upper limits with light yellow colour, indicating a higher density of stars. In the rightmost panel, giants with Li detections are shown in red, while giants with Li upper limits are in blue.

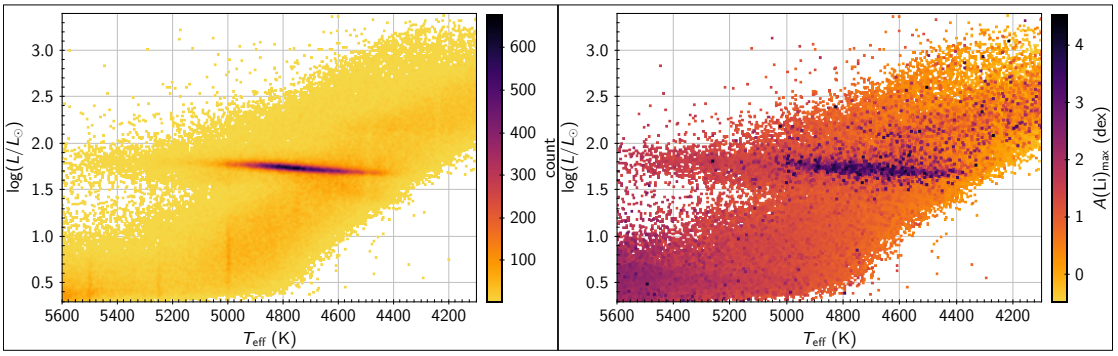


FIGURE 7.3: The HR diagram for the RBS giants. The colour in the left and right panels represents the linear density and maximum A(Li) abundances, respectively. Note that the density visualization scale in the left-side panel is linear, but in Figure 7.1 scale is logarithmic.

7.3 Lithium-rich giants: overview

Our principal endeavour is to use the GALAH DR3 RBS sample (Figure 7.1) to (i) explore closely the Li enrichment attributable to the He-core flash in low-mass red clump giants and (ii) probe more thoroughly than before the Li enrichment predicted from thermohaline mixing at the luminosity bump on the RGB. Li-enrichment by the He-core flash was empirically proven by Kumar *et al.* (2020) from analysis of the GALAH DR2 Li abundances for giants, but theoretical predictions of Li-enrichment are lacking apart from the recent exploration by Schwab

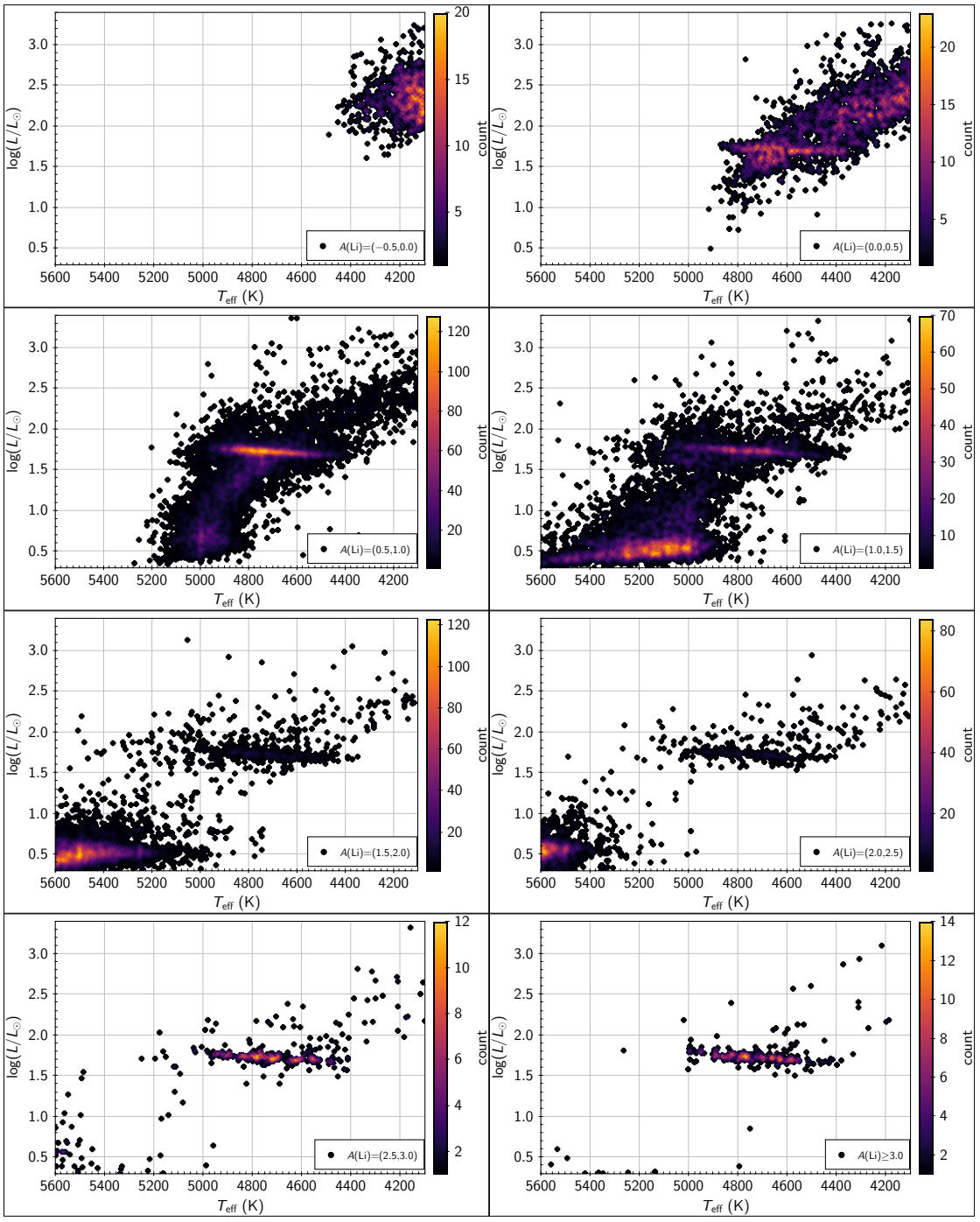


FIGURE 7.4: HR diagrams for the RBS giants for Li abundances in different abundance intervals. All giants shown here have a Li detection (i.e., flag_Li_fe=0).

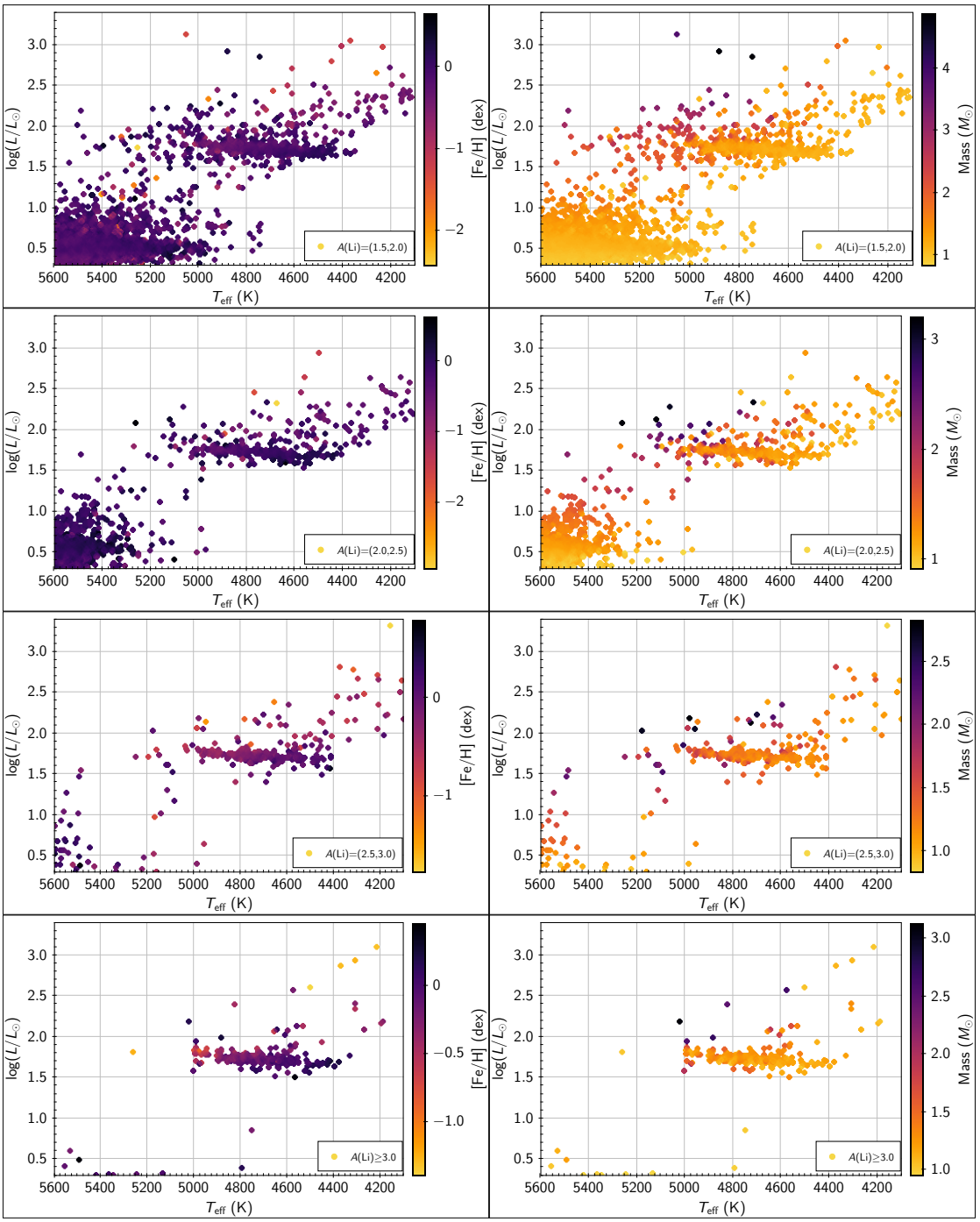


FIGURE 7.5: Li abundance maps along with metallicity and mass information in colour for the RBS giants in the HR diagram. All the giants shown here have Li detections (i.e., flag_Li_fe=0).

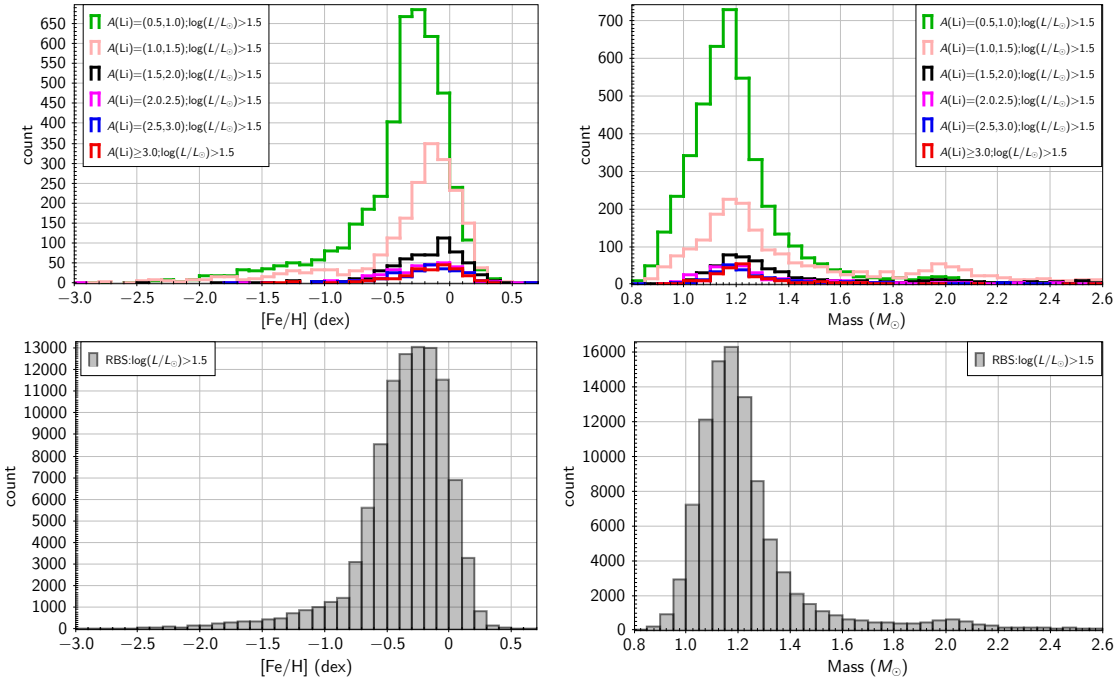


FIGURE 7.6: Top row: Metallicity and mass histograms for giants plotted in Figure 7.5. Histograms are shown for different Li abundance intervals, as shown in the keys in the two panels. Bottom row: Metallicity and mass histograms for entire RBS sample with $\log(L/\mathrm{L}_\odot) > 1.5$.

(2020). In contrast to this observational–theoretical imbalance regarding Li enrichment in red clump giants, theoretical modelling of Li-enrichment at the luminosity bump (Eggleton *et al.* 2008; Lagarde *et al.* 2011) may be more advanced than observational efforts.

To provide an intriguing glimpse into the relative roles of the two evolutionary phases of possible Li enrichment, Figure 7.2 shows in the left panel the HR diagram for the narrow range of masses $M = 1.10 \pm 0.02$ $\mathrm{M}_\odot$ and metallicities [Fe/H]$= 0.00 \pm 0.10$ shown below to be rich in Li enriched giants. The middle and rightmost panels show the relation between A(Li) and luminosity. The left and middle panels show giants with both Li detections and upper limits, while in the rightmost panel, giants with Li detections are shown in red, while giants with Li upper limits are in blue. The gross features of the three panels are readily recognizable. The HR diagram begins with subgiants at $\log(L/\mathrm{L}_\odot) \sim 0.5$ and leads into the RGB

with its tip at $\log(L/\mathrm{L}_\odot) \simeq 3.5$. There is a steady decrease of the Li abundance A(Li) up the RGB. The LB occurs on the RGB at a luminosity just below that of the RC. At the LB, there is a noticeable increase in the counts. Superimposed on the RGB in the HR diagram is the RC at $\log(L/\mathrm{L}_\odot) \simeq 1.7$, and this marks a large spread in lithium abundance up to $A(\mathrm{Li}) \sim 4$. Apart from a few outliers at luminosities above and below the RC's luminosity, this selection does not indicate Li enrichment associated with a density increase on the RGB arising from the LB. If this selection by mass and metallicity from the RBS is representative, the outstanding message is that Li enrichment among RC giants, as Kumar *et al.* (2020) noted, is a striking feature. But Figure 7.2 also suggests that a search for Li enrichment associated with the LB may require subtle procedures because at the mass and metallicity ranges explored in Figure 7.2 (and at neighbouring mass and metallicities) Li enrichment from the LB appears not to be a major process.

In our effort to advance the story of Li-enrichment in giants at the red clump post-He-core flash stage and in other giants at the luminosity bump on the RGB, we combine Li abundances from the GALAH DR3 survey with stellar evolution calculations for low mass stars from the `MESA` suite of computer programmes. Our focus on possibilities of Li-enrichment in RC and LB low mass Population I giants does not mean that Li enrichment cannot occur in giants other than at the RC or LB phases, as in mass transfer to a star from a Li-rich AGB companion (again, Li synthesis occurs via ^{3}He) or in Population II giants or by other mechanisms such as engulfment of planetary bodies (Alexander 1967).

7.3.1 He-core burning giants - the red clump

In Figure 7.1, the prominent feature superimposed on the red giant branch (RGB) at $\log(L/\mathrm{L}_\odot) \simeq 1.7$ is the red clump (RC) comprised of giants burning He in their core. As noted in the Introduction, Kumar *et al.* (2020)'s vital contribution

was to show that observations demand that all RC giants in the GALAH survey were enriched in Li to differing degrees relative to stars at the tip of the RGB, the immediate predecessors of RC giants, that is Li enrichment in RC giants is 'ubiquitous', i.e., even RC giants with the lowest Li abundance, $A(\mathrm{Li}) \simeq -0.5$, are Li enriched. Lithium production was attributed to the He-core flash occurring at the RGB tip as the star ignites its He core. Giants with masses less than about 2.25 $M_\odot$ at solar metallicity [Fe/H] = 0 experience a He-core flash at the tip of the RGB. The upper mass limit for a He-core flash decreases slightly for metal-poor stars (Karakas 2010). The existence of the flash has stimulated theoretical speculation on the possibility of internal mixing and associated nucleosynthesis including the production of Li from ^{3}He and enrichment of the surface of the RC giant with Li. Consideration of lithium abundances among RC stars is the principal concern of our study. (Extension of the RC to hotter temperatures, as in globular clusters, marks the horizontal branch (HB), but here we use RC to refer to the entire temperature range.)

Lithium abundances among the RC giants span several dex (Kumar *et al.* 2020). A simple map of Li abundance over the HR diagram is provided in Figure 7.3. The left-hand side panel shows the number density of giants across the RBS. The presence of the RC is obvious from about 4600 K to, perhaps, 5400 K, with a peak ratio of counts in the mid-RC strip to the counts on either side of about 7. The Li map in the right-hand side panel is colour-coded according to the Li abundance and makes clear that most Li-rich giants are on or maybe evolved from the RC.

More detailed maps of Li abundances are provided in the eight panels of Figure 7.4 showing HR diagrams for giants with $A(\mathrm{Li})$ abundances in the intervals -0.5-0.0, 0.0-0.5, 0.5-1.0, 1.0-1.5, 1.5-2.0, 2.0-2.5, 2.5-3.0 and > 3.0. The full RBS includes stars of mass from about 0.8 $M_\odot$ to 2.5 $M_\odot$. The low Li abundance panels in Figure 7.4 clearly show the results of the first dredge-up (FDU) affecting subgiants and early residents on the RGB, most notably in the $A(\mathrm{Li}) = 1.0$-1.5

and 1.5-2.0 panels at the luminosity $\log(L/\mathrm{L}_{\odot}) \sim 0.5$. The limit $A(\mathrm{Li}) \geq 1.5$ with representation across four panels corresponds approximately to the Li abundance expected following the first dredge-up, a value which has often been adopted in discussions of Li-rich giants as the lower boundary for a Li-rich giant. (Note that lithium post-FDU is further depleted in the lower mass giants – see below.) Li abundances in these four panels include giants in which clearly Li has been enriched. Inspection of each of these panels confirms that Li-enriched stars appear tightly confined to the RC and also to a few stars more luminous and generally cooler than the RC, i.e., to stars which may have exhausted He-burning in their core and evolved off the RC. For each of these four samples, there is a clear gap between the RC giants and the lower luminosity RGB giants, i.e., all giants which are Li-enriched are RC giants. There is potential confusion at luminosities above the RC between post-RC (early AGB) giants and RGB stars up to the tip of the RGB, at $\log(L/\mathrm{L}_{\odot}) \approx 3.4$. (There may also be a possibility of confusion provided by Li-rich giants at the luminosity bump on the RGB, an issue discussed in Section 7.5). In the panel covering the lowest Li abundances, $A(\mathrm{Li}) = -0.5$ to -0.0, no stars are seen on the RC, and the majority are likely RGB giants with a luminosity below that of the RGB tip. Since further evolution to the RGB tip may result in even lower Li abundances, RC giants emerging from the RGB tip without experiencing Li enrichment will have maximum Li abundances $A(\mathrm{Li}) \lesssim 0.0$. But there are very few RC giants with this low Li abundance and, therefore, Li synthesis at some level from the He-core flash may occur in all giants transitioning from the RGB to the RC, as suggested by Kumar *et al.* (2020).

Consideration of the panels in Figure 7.4 provides additional information. First, we explore the metallicity and mass dependence of Li-rich giants (see, for example, Deepak *et al.* 2020). The metallicities (colour-coded) show that Li-rich RC giants are predominantly of near-solar metallicities (Figure 7.5). This is not a new result; see, for example, Figures 3 and 4 from Deepak *et al.* (2020) and Figure 5 from Martell *et al.* (2021) but extends earlier results by showing that the metallicity

histograms are only weakly dependent on the Li abundance. Histograms of the metallicity for RC and (presumed) evolved RC stars in Figure 7.6 well illustrate that Li-rich giants are certainly representatives of the Galactic thin disc and its spread in metallicity.

Another family of histograms (Figure 7.6, top-right panel) is provided for the masses of the Li-rich RC giants. As Figure 7.6 shows, the Li-rich giants have a narrow distribution peaking at about 1.1 $M_{\odot}$. The histograms extend earlier results by showing that the mass distribution is independent of Li abundance. There is perhaps a slight increase in mass from the cool to the warm end of the RC. Distribution of Li abundances across the RBS by mass shows Li-rich RC giants from 0.8 $M_{\odot}$ to 2.3 $M_{\odot}$ with, of course, the most prominent sampling around 1.1 $M_{\odot}$ to 1.2 $M_{\odot}$.

The histograms in the bottom panels of Figure 7.6 refer to the full sample covered by the RBS at luminosities $\log(L/L_{\odot}) > 1.5$. Note the large increase in counts between this sample and the histograms compiled from selected Li abundance intervals in the upper part of the figure. More importantly, note the overall similarities in the two sets of histograms. To first order, this suggests that the frequency of Li-enriched RC giants is approximately independent of mass and metallicity. The two sets of histograms appear most similar for intermediate Li abundances inviting the idea that levels of Li enrichment may vary with mass and metallicity.

Close scrutiny of Figure 7.4 suggests several insights into Li production at the He-core flash. Most obviously, the RC's location in the HR diagram is independent of the Li abundance. For example, the mean luminosity of the RC's core at the mean effective temperature of 4775±100 K is $\log(L/L_{\odot}) = 1.73$ to within ±0.05 across the bottom four panels in Figure 7.4. The mild increase in luminosity with increasing effective temperature is independent of Li abundance. Similarly, the RC's width at a given effective temperature appears to be constant across these

panels with the exception of a mild increase at the lowest Li abundances, which may be related to the increase in the sample size at the lowest Li abundances. The range of effective temperatures spanned by the RC in the panels is independent of Li abundance above $A(\mathrm{Li}) \geq 1.5$. Also, the proportion of giants at luminosities above the RC is similar for the four panels. These characteristics about the RC and the Li abundance show that the gross properties of RC stars appear independent of the He-core flash's ability to synthesize Li.

However, stellar evolutionary calculations fail not only to account for Li enhancement in RC giants but also do not account for their considerable spread in effective temperature at approximately constant luminosity. Such calculations predict a 1 $\mathrm{M}_{\odot}$ of about solar metallicity to have approximately the observed luminosity at around 4500K. These are two failures of standard calculations, but one supposes that while their resolutions may be related, they cannot be tightly coupled because Li abundances are independent of a star's effective temperature.

It seems remarkable that the vast majority of Li-enriched giants have very similar characteristics, i.e., they are or were He-core burning giants of about 1 $\mathrm{M}_{\odot}$ and near-solar metallicity. Figure 7.5 shows that among apparent exceptions are subgiants ($\log(L/\mathrm{L}_{\odot}) \sim 0.7$ with $T_{\mathrm{eff}} \sim 5000 - 5600$ K) whose numbers decline with increasing $A(\mathrm{Li})$. These are, in all likelihood, normal stars of about 1 $\mathrm{M}_{\odot}$ and near-solar metallicity at different stages of an incomplete FDU. Figure 7.5 also shows a few higher mass stars with a luminosity spanning that of the RC. These too are stars observed before the completion of their FDU. Two Li enriched giants at ∼4800 K and at a luminosity well below that of the RC in $A(\mathrm{Li}) \geq 3.0$ panel in Figure 7.4 arouse our curiosity. Both of these giants are of solar mass. This pair "Gaia DR2 5507464674226166144" and "Gaia DR2 3340856632069339776" with $A(\mathrm{Li}) = 3.09 \pm 0.11$ and 3.51 ± 0.11, respectively, deserve detailed study.

In essence, setting aside a few stars, our selection of Li-enriched stars from the RBS is dominated by stars of about a solar mass and a solar metallicity.

7.4 MESA modelling for low-mass stars

To further our understanding of Li in giants, we use `MESA` models to predict the Li abundance from the main sequence along the RGB to the RC for stars in the mass and metallicity ranges covered by our RBS. Lithium dilution by the FDU and lithium evolution to the RGB's tip is modelled by `MESA`. The potential episode of Li enrichment of the atmosphere resulting from the He-core flash is not included. Also, AGB stars experiencing the third dredge-up and possible Li enrichment are neither included in the selection of giants from our RBS nor in our use of the `MESA` modules.

Our initial interest in the `MESA` predictions for Li abundances focussed on predicted Li abundances for red giants up to the RGB tip and their comparison with the observations over the mass and metallicity ranges adequately sampled by the RBS (Figure 7.7). Such a comparison is also a resource with which to search for non-standard episodes of Li enrichment (or destruction) such as may occur on the RGB or by engulfment of planetary material (Alexander 1967).

7.4.1 Predicted Li abundances to the RGB tip

In pursuit of the predicted Li abundances in giants, we began with the `MESA` model for a solar mass and solar metallicity model assembled by Schwab (2020).[¶] Based on our needs, we made some changes to Schwab's `inlist`. The prescription now

[¶]Schwab's `MESA` model is available at `https://doi.org/10.5281/zenodo.3960434`.

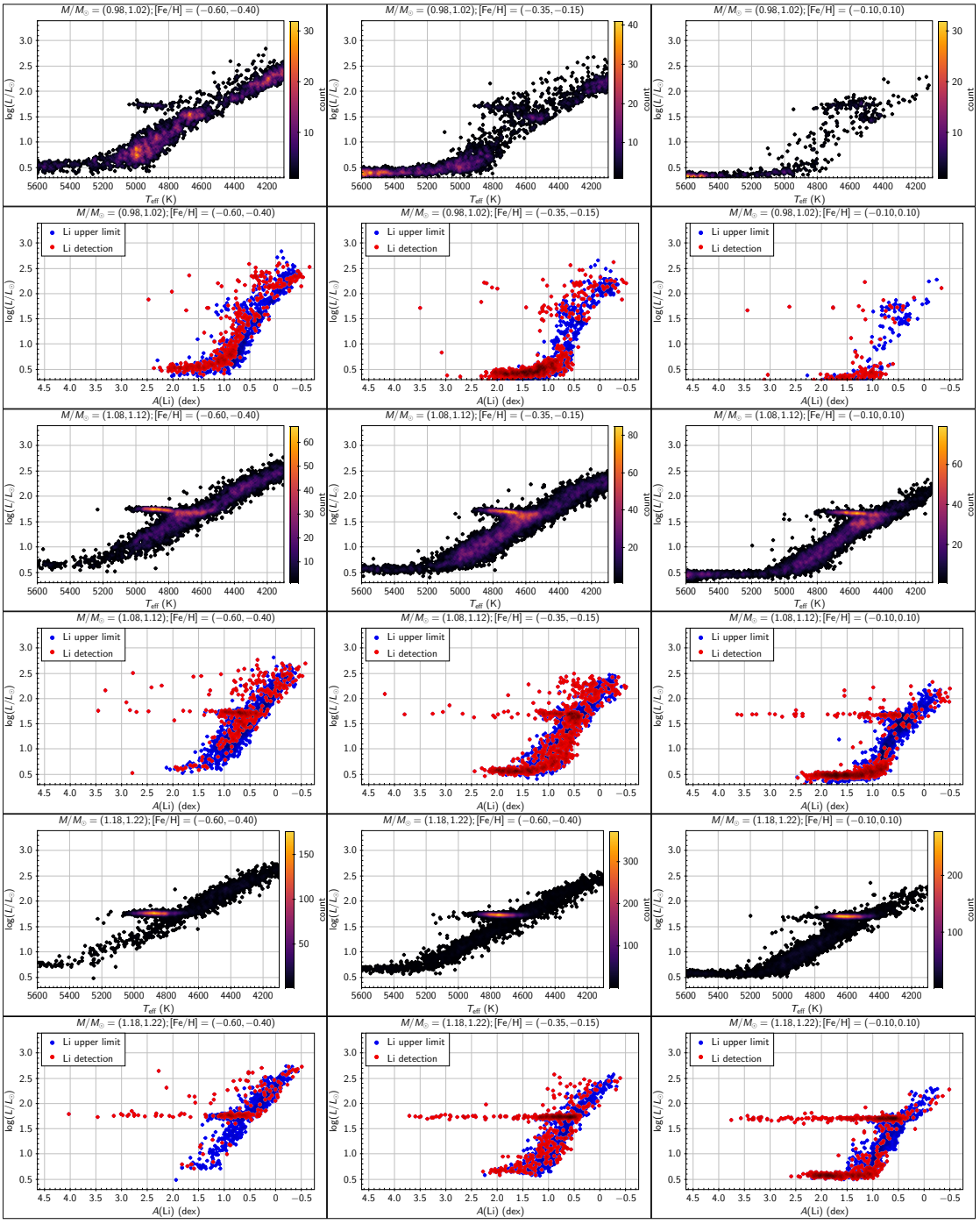


FIGURE 7.7: HR diagram (odd-numbered rows) and A(Li) as a function of luminosity (even-numbered rows) for the RBS stars selected with mass and metallicity range as mentioned in panels' titles. In luminosity-A(Li) panels, giants with Li detections are shown in red, while giants with Li upper limits are shown in blue.

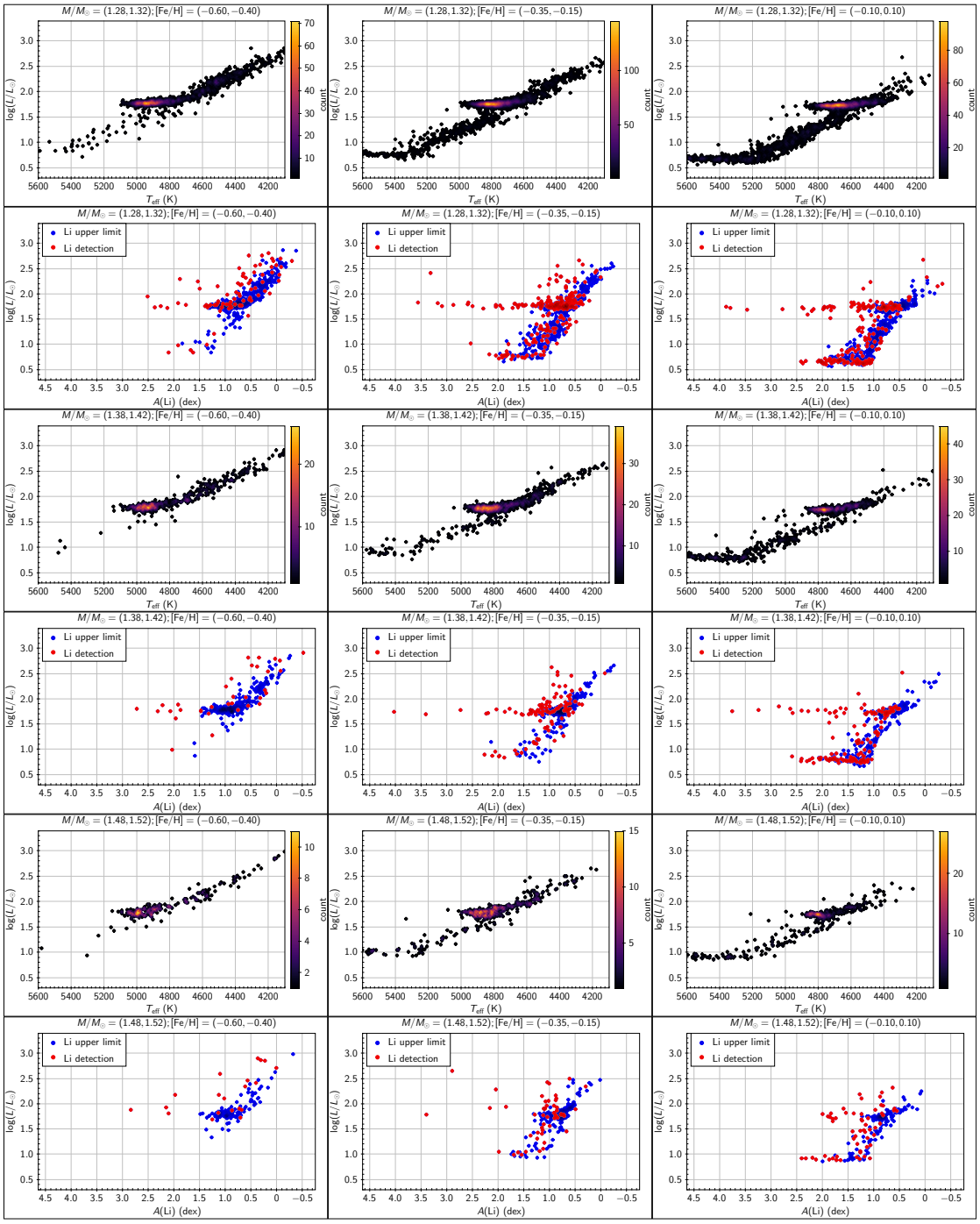


Figure 7.7 - *continued*

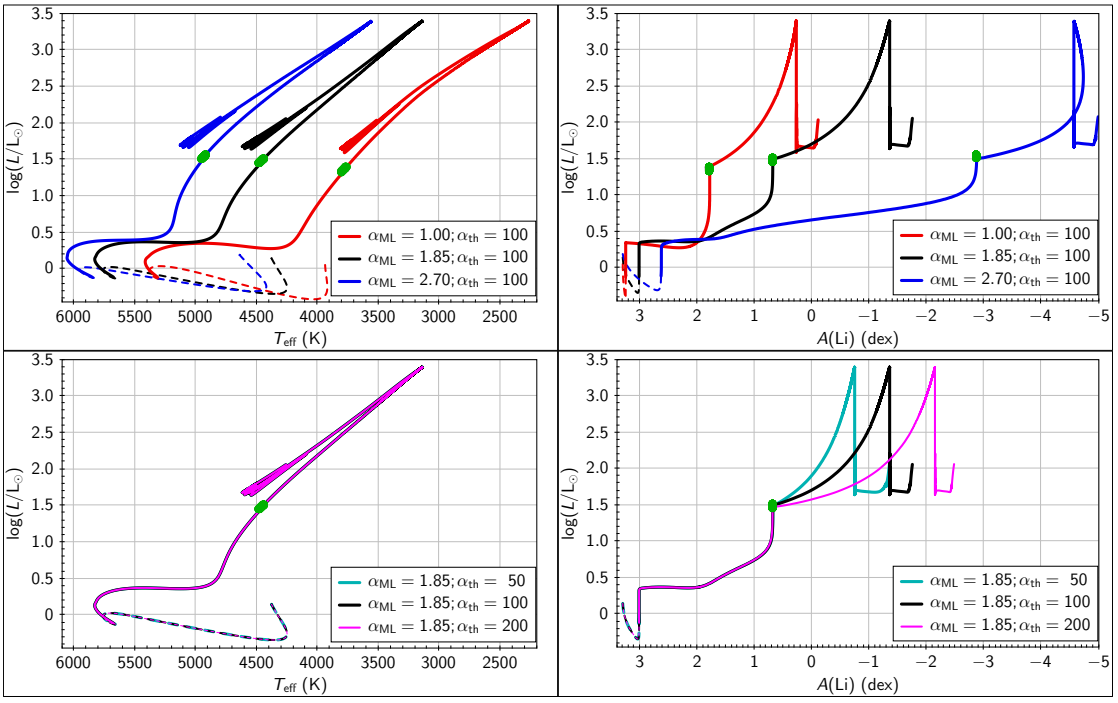


FIGURE 7.8: HR diagrams and A(Li) as a function of luminosity for solar mass and solar metallicity models with different $\alpha_{\rm ML}$ and $\alpha_{\rm th}$. The top and bottom panels show a model's sensitivity to $\alpha_{\rm ML}$ and $\alpha_{\rm th}$, respectively. Dashed lines show pre-main-sequence evolution, while solid lines show the evolution from the zero-age main sequence (ZAMS). On each track, the LB's position is marked by the green coloured blob.

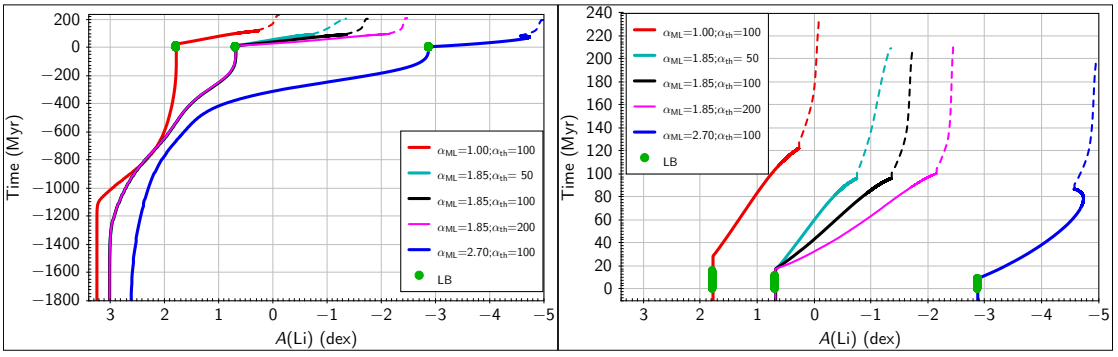


FIGURE 7.9: Temporal evolution of Li for solar mass and solar metallicity models with different $\alpha_{\rm ML}$ and $\alpha_{\rm th}$. Time is shown relative to the onset of LB. Model's sensitivity to both $\alpha_{\rm ML}$ and $\alpha_{\rm th}$ is shown. The left-hand side panel covers evolution from about the sub-giant phase to the CHeB phase, while the right-hand side panel covers evolution from near RGB on-wards. Evolution up to the RGB tip is shown as solid lines, while dashed lines show the evolution in the CHeB phase. On each track, the LB's position is marked by the green coloured blob. Timestep in each case varies from about 0.1 to 0.2 million years (Myr) during the LB, and further decreases as the star ascend the RGB.

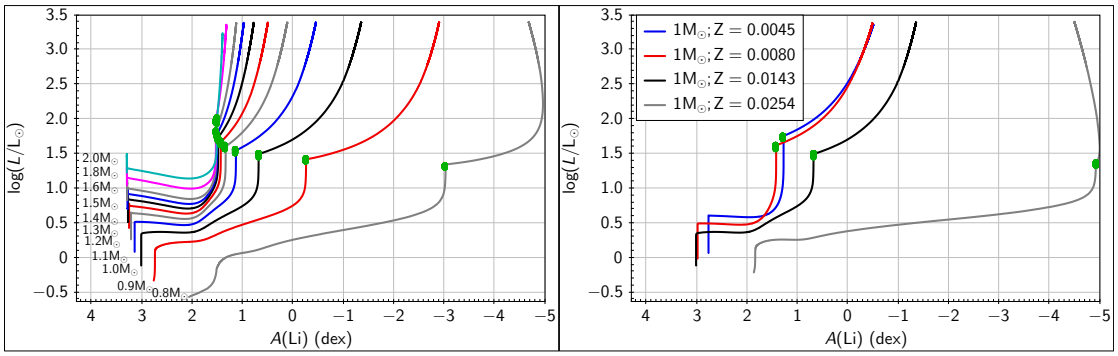


FIGURE 7.10: Left-hand side panel: Predicted evolution of A(Li) as a function of luminosity for solar metallicity (Z = 0.0143) giants. Masses of 0.8 $M_\odot$ to 2.0 $M_\odot$ are shown, as labelled. Right-hand side panel: Predicted evolution of A(Li) as a function of luminosity for 1$M_\odot$ mass models with metallicities Z = 0.0045, 0.0080, 0.0143, and 0.0254, which are equivalent to [Fe/H] = -0.50, -0.25, 0.00, and 0.25 dex, respectively. For all models, we use $\alpha_{\rm ML}$ = 1.85, $\alpha_{\rm th}$ = 100 and initial surface rotation $\Omega_{int}/\Omega_{crit}$ = 0. For each of the case, evolution is shown from the ZAMS to the RGB tip. For all the masses, LBs are marked by green coloured blobs. The abrupt change in A(Li) occurring at about $\log(L/L_\odot) \sim 1.5$ is attributable to the onset of thermohaline mixing at the LB.

includes phenomena like rotation, semi-convection, etc., along with additional resolution controls.[‖] For our calculations, we use `MESA` version 15140. Convection in `MESA` is treated using the mixing length theory (MLT) of convection, and for the current exploration, we use its default formalism from Cox and Giuli (1968). For our models, we use the `MESA`'s available recipe for thermohaline mixing adapted from Kippenhahn *et al.* (1980). We also use convective premixing (Paxton *et al.* 2019), which is specified by the condition `use_Ledoux_criterion = .true.` and `do_conv_premix = .true.` in the code. In `MESA` models, the strength of the thermohaline mixing is set by a dimensionless efficiency parameter $\alpha_{\rm th}$ (Paxton *et al.* 2013). Thermohaline mixing is initiated when the inversion of the mean molecular weight creates the LB and the region is formally stable against convection. Mixing in the interior at this time may result in Li synthesis. This fresh Li will appear at the giant's surface if the Li enters the deep convective envelope. For cases where there is no overlap between the region of Li synthesis and the convective envelope, the surface Li abundance will be unaltered at its post-FDU value. Subsequent

[‖]The source files for our solar mass and metallicity `MESA` models, along with the outputs for all the cases studied in this work, are available at `https://doi.org/10.5281/zenodo.5086893`.

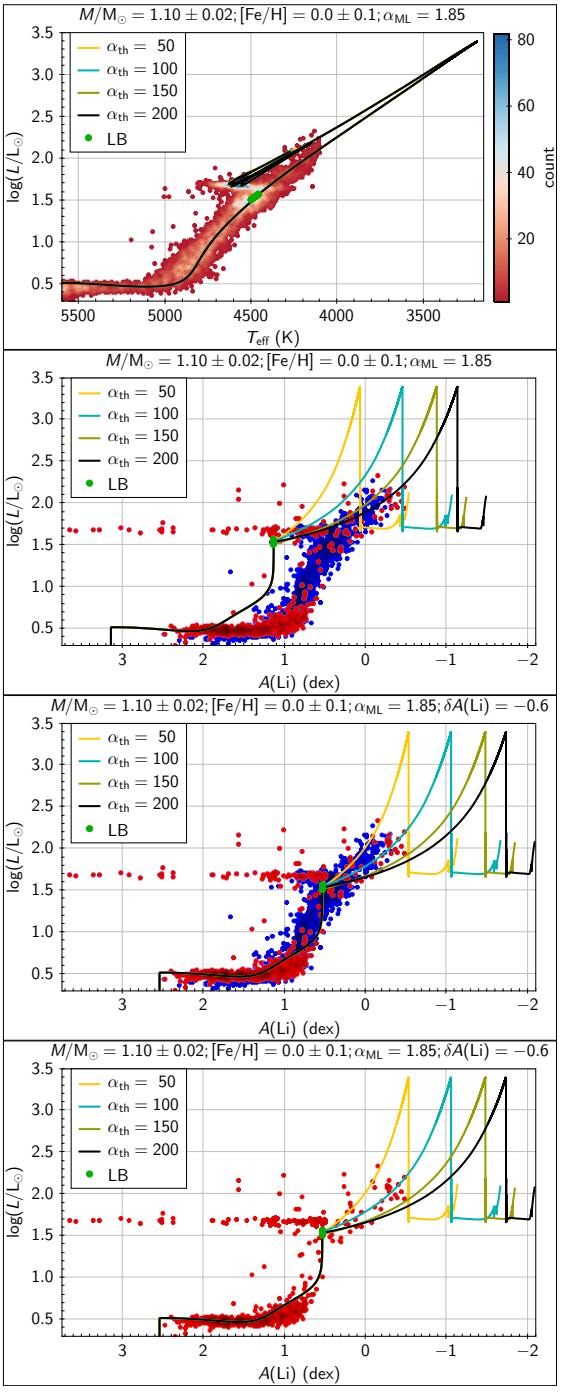


FIGURE 7.11: Observed and predicted HR diagram (top panel) and A(Li) as a function of luminosity (middle and bottom panels) for RBS giants of masses 1.10 ± 0.02 $M_\odot$ and metallicity 0.0 ± 0.1 dex. Predictions are shown for best fit model with $\alpha_{ML} = 1.85$ along with $\alpha_{th} = 50$, 100, 150 and 200. The bottom panel shows luminosity-A(Li) trends after adjustment to Li abundance level. In A(Li)-luminosity panels, giants with Li detections are shown in red, while giants with Li upper limits are shown in blue.

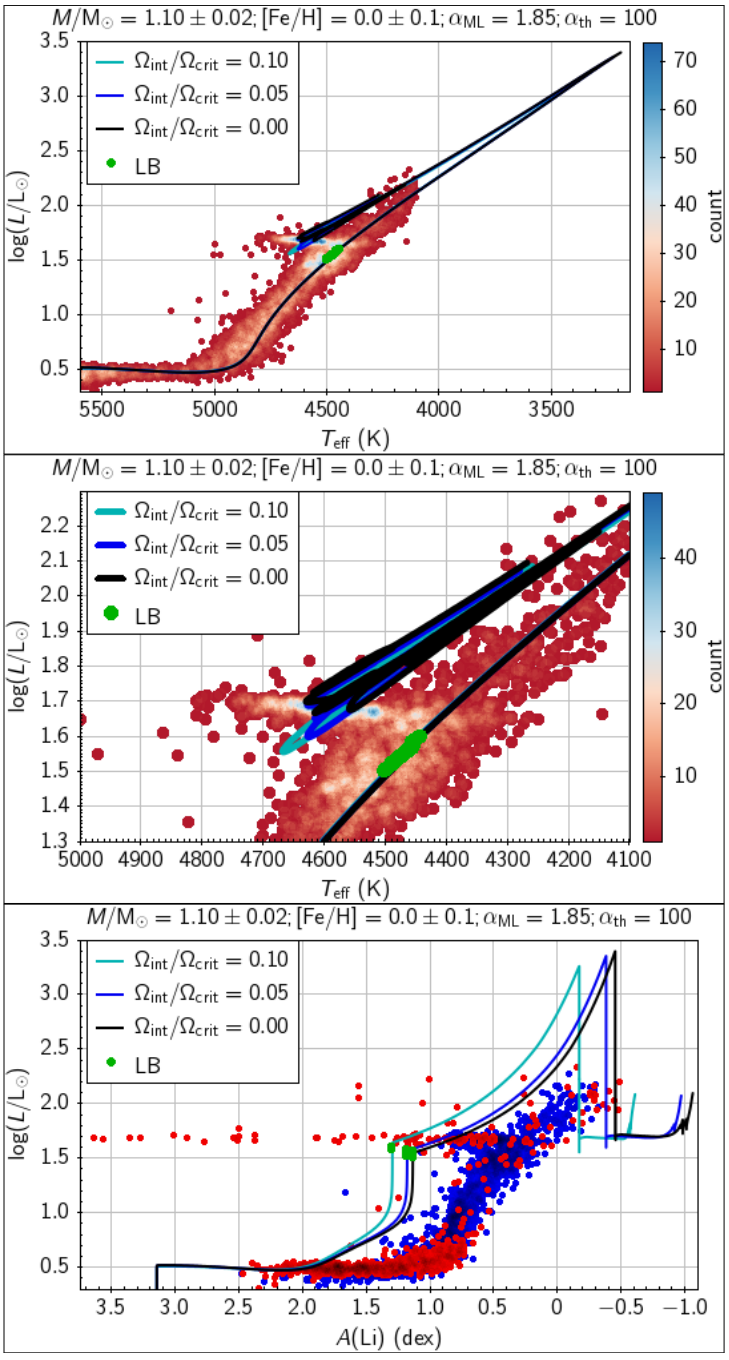


FIGURE 7.12: Observed and predicted HR diagram (top panel and middle panel) and A(Li) as a function of luminosity (bottom panel) for RBS giants of masses 1.10 ± 0.02 $M_\odot$ and metallicity 0.0 ± 0.1 dex. Predictions are shown for the best-fit model with $\alpha_{ML} = 1.85$ and $\alpha_{th} = 100$ along with initial surface rotation $\Omega_{int}/\Omega_{crit} = 0.00$, 0.05, and 0.10, which are equivalent to an initial surface rotation of about 0, 15, and 30 kms^{-1}, respectively. In A(Li)-luminosity panels, giants with Li detections are shown in red, while giants with Li upper limits are shown in blue.

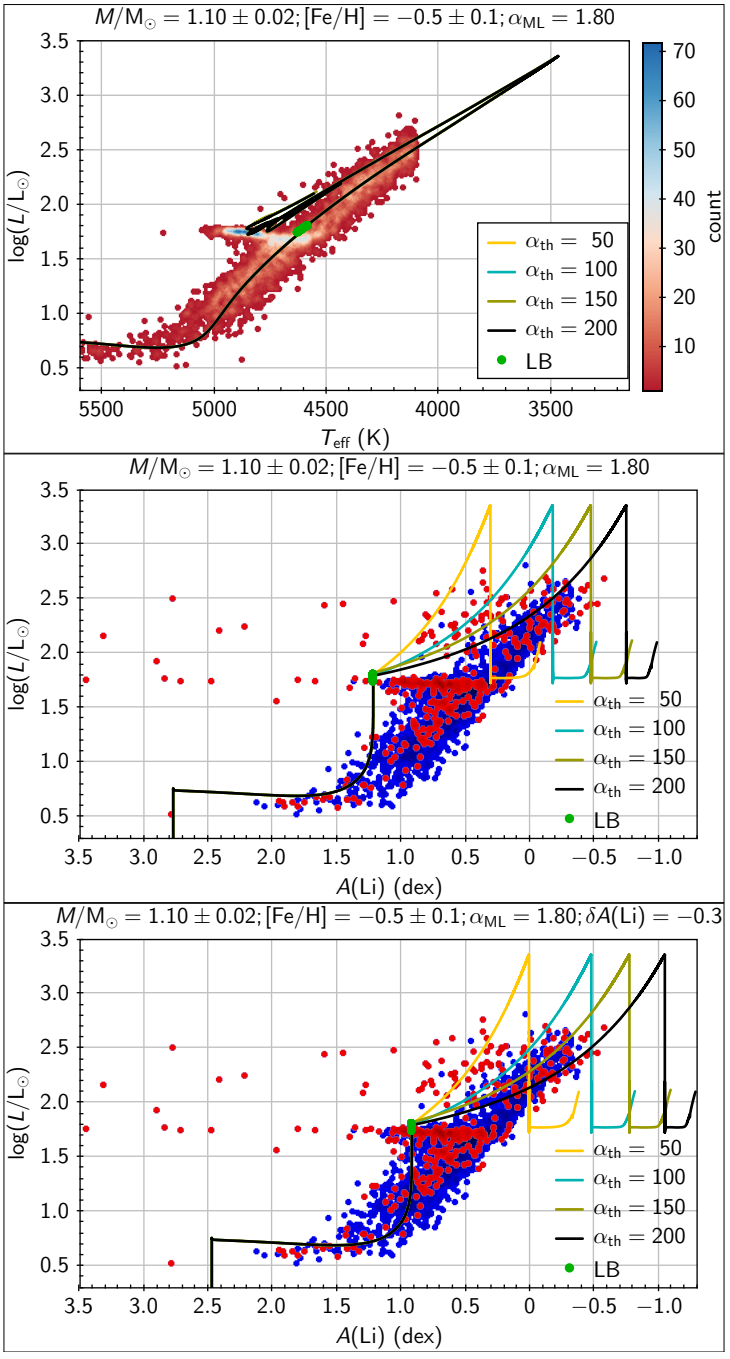


FIGURE 7.13: Observed and predicted HR diagram (top panel) and A(Li) as a function of luminosity (middle and bottom panel) for RBS giants of masses 1.10 ± 0.02 $M_\odot$ and metallicity -0.50 ± 0.10 dex. Prediction are shown for best fit models with α_{ML} = 1.80 along with α_{th} = 50, 100, 150 and 200. In A(Li)-luminosity panels, giants with Li detections are shown in red, while giants with Li upper limits are shown in blue.

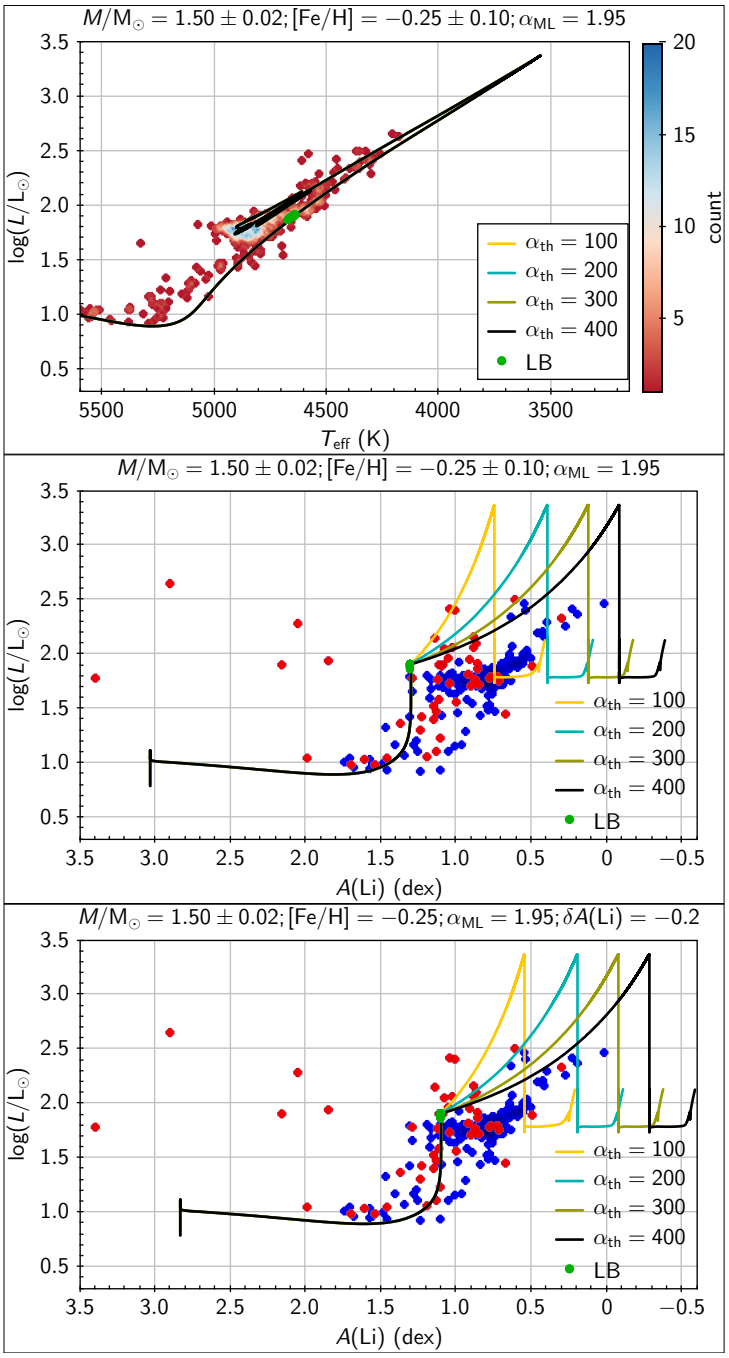


FIGURE 7.14: Observed and predicted HR diagram (top panel) and A(Li) as a function of luminosity (bottom panel) for RBS giants of masses 1.50 ± 0.02 $M_\odot$ and metallicity -0.25 ± 0.10 dex. Prediction are shown for best fit model with α_{ML} = 1.95 and α_{th} = 100, 200, 300 and 400. The bottom panel shows luminosity-A(Li) trends after adjustment to Li abundance level. In A(Li)-luminosity panels, giants with Li detections are shown in red, while giants with Li upper limits are shown in blue.

overlap with the convective envelope is predicted to generally reduce the surface Li abundance. Another parameter in `MESA` modelling is the mixing length ($\alpha_{\rm ML}$) for which we generally adopt a value of about 1.85 times the pressure scale height. Semi-convective mixing is also considered with efficiency $\alpha_{\rm sc} = 0.1$ (Paxton *et al.* 2013). Our models use the standard `MESA pp_and_cno_extras` nuclear network, which includes 25 species and the reactions covering the pp-chains and CNO-cycles. Our adopted `MESA` nuclear reaction rates are the same as used by Schwab (2020). GALAH's abundances are scaled to the solar composition from Asplund *et al.* (2009). We also use the same abundance mixture and related opacity tables (`a09`, `a09_co` and `lowT_fa05_a09p` with condition `use_Type2_opacities = .true.`) from `MESA`'s `kap` module. Mass loss is not considered. A recipe for rotation is included in our models. However, in general, most of our models are non-rotating, i.e., the initial surface rotation is set at $\Omega_{\rm int}/\Omega_{\rm crit} = 0.0$, and the detailed effect of rotation is discussed only for a few cases (see Section 7.4.1.1). Also, unlike Schwab (2020), our models do not include the *ad hoc* flash-induced diffusive mixing in the He core at the RGB tip. (However, if required, it can be easily turned on in our final prescription also.)

Selection of timestep is very crucial in the evolution of models as it helps to decide the next timestep and assist in the solution for the new structure and composition (see Paxton *et al.* 2011; Lattanzio *et al.* 2015, for more details). In `MESA`, it is primarily controlled using parameter `varcontrol_target`. In our initial test runs, we used the default minimum value of `varcontrol_target` $= 10^{-4}$ for the evolution of solar metallicity models of masses 0.8 to 2.2 $M_\odot$ in 0.1 $M_\odot$ intervals. Thermohaline mixing was present in all the models except for the 1.8 $M_\odot$ case. We also noticed that the adoption of a slightly higher value (about three times than the default value) of `varcontrol_target` resulted in no Li reduction (i.e., missing thermohaline mixing) in the post-LB phase for masses higher than about 1.2 $M_\odot$ until the model has already evolved near to the tip of RGB. As a fix to this issue, we forced smaller timesteps by adopting a lower value of the parameter

`time_delta_coeff` = 0.75 than its default value of unity. Adoption of this lower timestep resulted in no significant effect on the Li trends for the cases where Li reduction near the LB was possible with a larger timestep.

Models are begun in the pre-main sequence phase at the point where the core first becomes radiative. Approach to zero-age main sequence (ZAMS) is shown by dotted lines in Figures 7.8 and 7.10. Initial Li abundances dependent on metallicity are consistent with the Li abundances in local stars (Lambert and Reddy 2004; Deepak and Reddy 2020b; Randich *et al.* 2020): A(Li) = 3.57, 3.30, 3.04 and 2.78 for [Fe/H] = $+0.25, 0.00, -0.25$ and -0.50, respectively. Li depletion dependent on $\alpha_{\rm ML}$ occurs on the approach to the ZAMS: for the preferred value $\alpha_{\rm ML} \simeq 1.85$ (see below) depletion is ~ 0.3 and ~ 0.15 dex for solar metallicity stars of masses 1.0 and 1.1 $M_{\odot}$, respectively (Table 7.1). Evolution is followed along the RGB and through the He-core flash at the culmination of the RGB and to He-burning in the RC CHeB giant. We evolve all our models until the central mass fraction of ^{4}He drops below 10^{-6} to conclude the CHeB phase.

We first study the sensitivity of the model predictions to $\alpha_{\rm ML}$ and $\alpha_{\rm th}$. We evolved 1 $M_{\odot}$ and solar metallicity models with $\alpha_{\rm ML}$ = 1.00, 1.85, and 2.70, while keeping $\alpha_{\rm th}$ = 100. For $\alpha_{\rm th}$, we evolved 1 $M_{\odot}$ and solar metallicity models with $\alpha_{\rm th}$ = 50, 100, and 200, while keeping $\alpha_{\rm ML}$ fixed to 1.85. The HR diagram and A(Li) trends as a function of luminosity for all these cases are shown in Figure 7.8 from the ZAMS through the RGB tip to the end of core-He burning. The top panels show the effect of $\alpha_{\rm ML}$, and the bottom panels illustrate sensitivity to $\alpha_{\rm th}$. An increase in $\alpha_{\rm ML}$ leads to the expected evolutionary track shifts to higher temperatures. Higher $\alpha_{\rm ML}$ also leads to increased depletion of Li during the FDU. The temporal evolution of Li in our model stars is shown in Figure 7.9, which suggests that adoption of higher $\alpha_{\rm ML}$ leads to increased as well as prolonged depletion of Li as the star ascends the RGB. A closer look at Figure 7.8 and 7.9 also suggests that for a given set of input parameters, models with lower $\alpha_{\rm ML}$ experience slightly

delayed Li reduction at the LB in comparison to models with higher $\alpha_{\rm ML}$. Solar mass and metallicity models with $\alpha_{\rm ML}$ = 1.00, 1.85, and 2.70 starts experiencing post-LB Li reduction after about 29, 17, and 9 Myrs, respectively, from the onset of LB. However, for all three cases, the actual timestep during LB's evolution ranges from about 0.1 to 0.2 million years (Myr) and further decreases as the star evolves towards the tip of RGB. These timesteps are very small compared to the duration of LB and delays in Li reduction. The delay in the post-LB Li reduction is sensitive to the timestep and decreases with a decrease in the timestep. A test run with a smaller timestep by adopting `time_delta_coeff` = 0.50 and 0.25 (which resulted in a timestep of about 0.1 and 0.05 Myr, respectively) for a solar mass model with $\alpha_{\rm ML}$ = 1.00 resulted in delays of about 8 and 6 Myr, respectively, along with almost tripling the computation time. It may be of interest to note that the duration of the LB depends on the assumed value of $\alpha_{\rm ML}$ and is longer for smaller values of $\alpha_{\rm ML}$. Similar is the case for the overall age of the stars, i.e. stars with lower $\alpha_{\rm ML}$ evolve more slowly (Figure 7.9). The evolutionary tracks are insensitive to $\alpha_{\rm th}$, but Li depletion commencing at the LB is, as anticipated, dependent on $\alpha_{\rm th}$.

To obtain model predictions for various masses, we evolve solar metallicity models stars of masses 0.8 to 1.6 $M_\odot$ in steps of 0.1 $M_\odot$ and 1.6 to 2.0 in steps of 0.2 $M_\odot$ from the ZAMS to the RGB tip. The role of metallicity in the evolution of A(Li) during the RGB was explored by 1 $M_\odot$ models with metallicities Z = 0.0045, 0.0080, 0.0143, and 0.0254, which are equivalent to [Fe/H] = -0.50, -0.25, 0.00 and 0.25 dex, respectively. For all models, we used $\alpha_{\rm ML}$ = 1.85, $\alpha_{\rm th}$ = 100 and initial surface rotation $\Omega_{\rm int}/\Omega_{\rm crit}$ = 0. Changes in the Li abundance are shown in the left-hand side panel of Figure 7.10 for the series of solar metallicity models. Metallicity dependence of the Li abundance evolution is shown in the right-hand side panel of Figure 7.10 for 1 $M_\odot$ models. The initial temperature, luminosity and A(Li) along with their values at ZAMS, at the onset of LB and at RGB tip for models in Figure 7.10 are tabulated in Table 7.1.

TABLE 7.1: The initial temperature, luminosity and A(Li) along with their values at ZAMS, at the onset of LB and at the tip of the RGB for the models shown in Figure 7.10 and 7.15.

$M/\mathrm{M}_\odot$	Z	Temperature (K) at				log $(L/\mathrm{L}_\odot)$ at				A(Li) at			
		PMS	ZAMS	LB	RGB-tip	PMS	ZAMS	LB	RGB-tip	PMS	ZAMS	LB	RGB-tip
0.8	0.0143	4082	4894	4422	3028	-0.19	-0.56	1.32	3.40	3.30	2.07	-3.03	-4.67
0.9	0.0143	4243	5323	4430	3087	-0.01	-0.33	1.42	3.40	3.30	2.77	-0.26	-2.90
1.0	0.0045	4681	6165	4600	3454	0.36	0.07	1.76	3.36	2.78	2.77	1.28	-0.50
1.0	0.0080	4533	5936	4537	3307	0.26	-0.01	1.62	3.38	3.04	2.99	1.43	-0.49
1.0	0.0143	4380	5678	4438	3141	0.15	-0.11	1.51	3.40	3.30	3.02	0.68	-1.35
1.0	0.0254	4262	5403	4351	2940	0.06	-0.21	1.37	3.40	3.57	1.87	-4.92	-4.49
1.1	0.0143	4491	5966	4455	3189	0.29	0.09	1.57	3.40	3.30	3.15	1.13	-0.45
1.2	0.0143	4580	6231	4469	3230	0.41	0.27	1.62	3.39	3.30	3.22	1.34	0.12
1.3	0.0143	4651	6510	4474	3267	0.53	0.43	1.68	3.39	3.30	3.26	1.44	0.50
1.4	0.0143	4708	6863	4477	3300	0.63	0.58	1.73	3.39	3.30	3.28	1.49	0.78
1.5	0.0143	4754	7305	4486	3331	0.73	0.71	1.78	3.39	3.30	3.29	1.51	0.98
1.6	0.0143	4789	7768	4493	3361	0.82	0.83	1.82	3.39	3.30	3.29	1.53	1.13
1.8	0.0143	4838	8628	4462	3433	0.99	1.05	1.97	3.36	3.30	3.30	1.53	1.32
2.0	0.0143	4866	9388	4494	3570	1.14	1.23	2.01	3.24	3.30	3.30	1.51	1.40
2.2	0.0143	4878	10091	4373	3886	1.28	1.39	2.26	2.89	3.30	3.30	1.50	1.46

Conditions promoting thermohaline mixing begin at a luminosity around the LB. Surface Li abundance is affected by Li destruction and formation in the interior and by the connection between the interior and the outer convective envelope. Prescriptions for surface Li on the RGB predict, in general, an appreciable loss of Li beginning around the LB's luminosity, see examples in Figures 7.8 and 7.10. A decline of Li on the ascent of the RGB results when the convective envelope taps the region of Li synthesis. The predicted Li abundance is necessarily sensitive to the detailed modelling of thermohaline mixing, as well as stellar mass and composition. Lattanzio *et al.* (2015) discuss Li abundance predictions for a 1.25 $M_\odot$ solar metallicity model given by five different codes. Across these codes, the reduction of the Li abundance post-LB varies considerably for comparable mixing coefficients. An increase in A(Li) at luminosities just below the RGB tip is predicted under some conditions for some codes. (Late (small) increases in Li abundance are seen in Figure 7.8 for the 0.8 $M_\odot$ model with [Fe/H] = 0 and the 1.0 $M_\odot$ models with [Fe/H] = 0.) Such late small increases of Li will not be detectable in DR3 and similar surveys of K giants. In Figure 7.8, the evolution of A(Li) is continued beyond the He-core flash to the termination of He core burning. It is at the He-core flash followed by a slight Li decrease as a RC giant. (Li synthesis at the He-core flash is not included in our models.)

A goal of our study is to confront the `MESA` models with the HR diagrams and luminosity-A(Li) trends displayed in Figure 7.7 where in all panels, we distinguish between Li abundance measurements and upper limits. Within the constraints of `MESA` models, it is apparent that the value of $\alpha_{\rm ML}$ may be determined independently of $\alpha_{\rm th}$ from an observed HR diagram. Then, the determination of the best fit to the luminosity-A(Li) trend for a given mass-metallicity combination may proceed by adjustment of $\alpha_{\rm th}$. But, perhaps, the most striking observation is that the luminosity-A(Li) trend is very similar across all ($M_\odot$,[Fe/H]) pairings well sampled by the RBS, but the `MESA` predictions in Figure 7.8 and 7.10 show a diverse set of luminosity-A(Li) trends. Ahead of detailed comparisons, it is apparent that

the fits of MESA Li predictions to observations in Figure 7.7 will range in quality. Notably lacking among the observed trends in Figure 7.7 are examples matching predictions where the Li abundance is effectively constant over the RGB from completion of the FDU through the LB's luminosity to the RGB's tip.**

Investigation of mixing on the RGB is well worthy of study because observations of Li on the RGB end at a luminosity of $\log(L/\mathrm{L}_\odot) \sim 2.2$ well short of the RGB tip at $\log(L/\mathrm{L}_\odot) \sim 3.4$. Thus, inference of the Li abundance at the RGB's tip involves a substantial extrapolation from the known Li abundances. It is the Li abundance at the tip which sets the low bound to the Li abundance among RC clump giants, i.e., the RC giants which did not experience Li addition as a result of the He-core flash.

7.4.1.1 Constraining thermohaline mixing from Li predictions for red giants

To investigate thermohaline mixing in red giants from the MESA models, we start with the sample of giants with mass $M/\mathrm{M}_\odot = 1.10 \pm 0.02$ and $[\mathrm{Fe/H}] = 0.00 \pm 0.10$. As discussed above, the evolutionary track is sensitive to α_{ML} and insensitive to α_{th}. A model with $\alpha_{\mathrm{ML}} = 1.85 \pm 0.05$ provides a good match to the observations (Figure 7.11). Li abundances for $\alpha_{\mathrm{th}} = 50, 100, 150$ and 200 were predicted. Predictions and observations are compared in the bottom panels of Figure 7.11.

Predicted A(Li) throughout the observed luminosity range is higher than the observed value. This offset, apparently independent of luminosity, may be negated by subtracting 0.6 dex from observed Li abundances, as achieved in the bottom panel of Figure 7.11 showing a fair fit between predicted and observed Li abundances. The short segment of the RGB above the LB with observed Li abundances (after

**The mass and metallicity trends shown in Figure 7.10 are qualitatively similar to those provided by Charbonnel and Lagarde (2010) from the STAREVOL-GENEVA Code.

application of the offset) is fitted with $\alpha_{\rm th} \sim 100 \pm 50$. When predictions of Li abundances are extrapolated to the RGB's tip, a Li abundance $A(\mathrm{Li}) \simeq -1.0 \pm 0.3$ is obtained. Setting aside the question of the -0.6 offset in Li abundance, the final match of prediction to observation might seem acceptable. Two points deserve attention. First, the decline of observed Li abundances on the RGB does not clearly show the abrupt change predicted to occur at the LB's luminosity. However, as starkly shown by the bottom panel in the figure, the RGB at luminosities below the LB is poorly represented by giants with Li detections and, thus, the true slope may be ill-determined.

Origins of the above Li abundance offset may be imagined. (Also, the presence of Li upper limits among similar giants with Li abundances shows processes actively depleting Li are common among these stars, as giants or in earlier evolutionary phases.) Li in a main-sequence star survives in a very thin skin at the surface. Should depletion occur via the skin's base (prior to the FDU), the Li abundance post-FDU will be reduced from its predicted value. Unless the Li-containing skin is convective, the depletion of Li will not be seen in the main sequence star yet revealed in the post-FDU giant. Similarly, mass loss from the surface of the main-sequence star may not affect its Li surface abundance but will be revealed by the FDU. There are examples of main-sequence stars with reduced Li abundances. The Sun is a notable example with an abundance of about 2.3 dex less than its initial abundance. Surely, the most extraordinary examples belong to the so-called Li-dip discovered by Boesgaard and Tripicco (1986) in the Hyades at a mass of $M \sim 1.4\mathrm{M}_{\odot}$. This dip shifts to lower masses with decreasing metallicity (Balachandran 1990). Chen *et al.* (2001) map this decline: at [Fe/H] = 0.0 and -0.50, the mass corresponding to the dip is $M \simeq 1.40$ $\mathrm{M}_{\odot}$ and 1.26 $\mathrm{M}_{\odot}$, respectively, suggesting that the Li-dip is not the primary origin for the Li offset required in Figure 7.11. Severe, even moderate, reductions of Li abundance in main sequence stars result in non-detection of Li in giants such that reductions cannot be quantified. It is curious that when well-populated with Li abundance measurements, the A(Li) -

luminosity relations for the RGB in Figure 7.7 have a smooth outer boundary suggesting uniform initial Li abundances and effectively identical treatment of Li from the main sequence to the post-FDU giant. The other boundary defined by Li abundance limits from non-detection of the Li I 6707 Å line may be ragged and arises from stars which experienced Li loss prior to the RGB.[††]

To understand the effect of rotation, we evolved a 1.1 $M_\odot$ solar metallicity model with initial surface rotation $\Omega_{\rm int}/\Omega_{\rm crit} = 0.00$, 0.05, and 0.10 which are equivalent to an initial surface rotation of about 0, 15, and 30 $\rm kms^{-1}$, respectively. A comparison of predictions with the observational data is shown in Figure 7.12. Predicted HRDs for both rotating and non-rotating models are similar except for slight disagreements at the RC and the RGB's tip. (HRDs of the rotating and non-rotating models also disagree at the main sequence, but not shown here.) Rotating models show slightly lower luminosity and slightly higher temperatures for the RC star compared to non-rotating models. This behaviour of rotating models at the RC is in contrast to observations and suggests that giants post-He-Core-flash have small or no rotation. The RGB's tip for rotating models lies at a slightly lower luminosity compared to non-rotating models (see the bottom panel of Figure 7.12). The figure suggests that rotating models experience smaller Li depletion during the FDU compared to non-rotating models. However, `MESA`'s implementation of rotation-induced mixing is but one realization of this complex physical process - see Charbonnel and Lagarde (2010) for an alternative prescription and different Li depletions.

Other samples in Figure 7.7 from the RBS were studied to compare predicted with observed HR diagrams and the luminosity-A(Li) trends. Predictions comparable to observations can be produced with small acceptable changes to $\alpha_{\rm ML}$ and $\alpha_{\rm th}$. As a test of a fit to a metal-poor selection, we consider the sample for (M,[Fe/H])

[††]It may be worth remarking that Li, with its survival limited to a main-sequence star's outer skin, differs greatly in its response to the FDU from the C, N and O elemental and isotopic abundances traditionally identified as measures of the FDU.

= $(1.10 \pm 0.02 M_{\odot}, -0.50 \pm 0.10)$ - see Figure 7.13. The HR diagram is well fit with a slightly lower $\alpha_{\rm ML} = 1.80 \pm 0.05$. For this sample, the predicted luminosity of the LB falls slightly above the predicted/observed luminosity of the RC. The LB is not obvious from the observed HR diagram because it is merged with the RC. The middle panel of Figure 7.13 shows a mildly satisfactory match between observed and predicted A(Li)-luminosity trends. An additional offset of about -0.3 to the predicted A(Li) is required to get a better fit. The predicted Li-luminosity trend with a sharp break in slope at the LB's luminosity seems a poor match to the observed trend, as set by giants with Li abundance detections. In contrast to Figure 7.11, Li detections span the RGB from its base to the limiting luminosity. The short segment of the RGB above the LB with observed Li abundances (after application of the offset) is fitted with a slightly higher $\alpha_{th} \sim 150 \pm 50$. Extrapolation of predicted Li trends to the RGB tip gives a Li abundance A(Li) $\simeq$ -0.8 $\pm$ 0.3 at the RGB tip.

As a representative sample of higher mass giants, we consider the (M,[Fe/H]) = $(1.50 \pm 0.02 M_{\odot}, -0.25 \pm 0.10)$ selection - see Figure 7.14. The rather sparse HRD is again well fit with $\alpha_{\rm ML} = 1.95 \pm 0.05$. The LB is not prominent in the observed HR diagram. The predicted luminosity of the LB falls slightly above the predicted/observed luminosity of the RC. Due to the small sample size, especially very few giants with a Li detection, the observed A(Li) trend is not very well defined by giants more luminous than the LB. An offset of -0.2 to the Li abundance level is required to match the luminosity-(Li) trend for giants less luminous than the RC. The predicted trend of Li abundance with luminosity again changes the slope at the LB's luminosity and may not match the smoother observed trend. The segment of giants more luminous than the RC suggests $\alpha_{\rm th} \simeq 300 \pm 100$, a value almost three times higher than required for 1.1 $M_{\odot}$ stars. Extrapolation of predicted Li trends to the RGB's tip gives a Li abundance $A(\mathrm{Li}) \simeq -0.1 \pm 0.3$.

TABLE 7.2: Input parameters for the best-fit models along with lithium abundances at the start of the different evolutionary phases for the three (M, [Fe/H]) cases studied in details in Section 7.4.1.1.

Mass	[Fe/H]	Model parameters			δA(Li)	A(Li) after correction for δA(Li) at			
($M_\odot$)	(dex)	Z	α_{ML}	α_{th}	(dex)	PMS	ZAMS	LB	RGB-tip
1.1	-0.50	0.0045	1.80 ± 0.05	150 ± 50	-0.3	2.48	2.48	0.92	-0.77 ± 0.3
1.1	0.00	0.0143	1.85 ± 0.05	100 ± 50	-0.6	2.70	2.55	0.53	-1.05 ± 0.3
1.5	-0.25	0.0080	1.95 ± 0.05	300 ± 100	-0.2	2.84	2.83	1.10	-0.08 ± 0.3

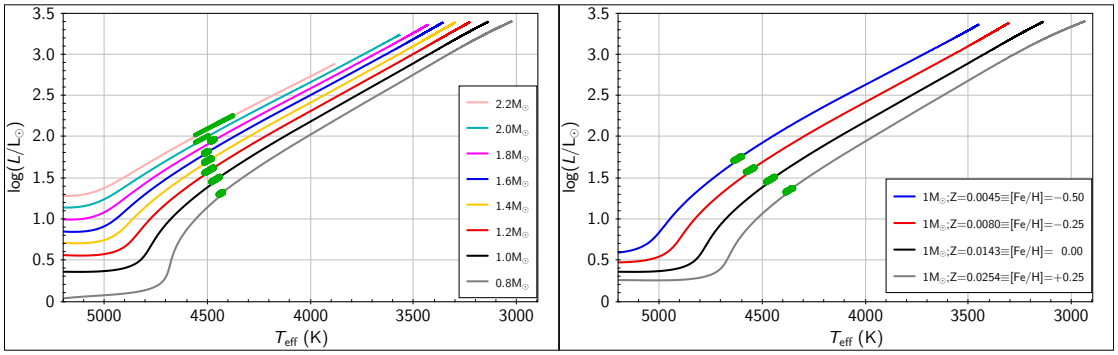


FIGURE 7.15: Left panel: HR diagram showing tracks for RGB phase for solar metallicity (Z = 0.0143) models of masses from 0.8 to 2.2 in steps of 0.2 $M_\odot$. Right panel: RGB tracks for solar mass models of metallicity Z = 0.0045, 0.0080, 0.0143, and 0.0254, which is equivalent to [Fe/H] = -0.50, -0.25, 0.00 and 0.25, respectively. Shown tracks are for models with α_{ML} = 1.85 and α_{th} = 100. The luminous end for each of the tracks marks the position of the RGB tip. Also, in each case, the green blob marks the position of LB.

Final results from detailed modelling for the above three (M, [Fe/H]) cases are summarized in Table 7.2.

7.4.2 MESA predictions for the red clump

Our MESA models include the He-core flash but not the possibility of accompanying Li synthesis. In low-mass stars, there is not a single flash, but a series of He-core flashes of declining severity as He-core burning is established (Thomas 1967; Despain 1981; Bildsten *et al.* 2012; Deepak and Lambert 2021a) and the

star's luminosity drops from its value at the RGB tip to the value of the RC.[‡‡] This decline occurs so quickly that very few stars are expected to be observed in this approach to the RC. During the RC phase, the luminosity and effective temperature are little changed for about 100 Myr for a giant of about 1 $M_\odot$. As He-core burning transitions to He-shell burning with continuing H-shell burning, luminosity increases and effective temperature decreases in the transitions from the RC to the AGB. RC evolution according to `MESA` models for 0.8, 1.0 and 1.2 $M_\odot$ stars of solar metallicity is shown in Figure 7.16. Initial lithium abundances for these RC models are assumed to be the low values achieved at the tip of the RGB. A small additional decrease in Li abundance is predicted on the RC and in the initial ascent of the AGB (Figure 7.9 and 7.16). An increase of the Li abundance resulting from the third dredge-up is not expected until the AGB model reaches a luminosity exceeding that of the RGB tip and an effective temperature of 3000 K or cooler.

Notably, observations and `MESA` predictions disagree sharply in two regards. First, the luminosity and effective temperature of the post-He-core flash RC models are in good agreement with observations for the coolest examples in Figure 7.5 but cannot account for the RC's extension to higher temperatures (Figure 7.3 and 7.4) at nearly a constant luminosity and nearly the same mass. For example, the 1 $M_\odot$ model in Figure 7.16 at 10 Myr has the luminosity $\log(L/L_\odot) = 1.70$ and $T_{\rm eff} = 4518$ K which compares favourably with the values for the coolest RC stars in Figure 7.5. Second, these standard `MESA` models necessarily have the very low A(Li) of their RGB progenitors and cannot account for the highly variable Li enrichment of all - 'ubiquitous' enrichment (Kumar *et al.* 2020) – RC stars across their temperature range. One may speculate that these two disagreements between observations and models may have a single explanation or at least related explanations.

[‡‡]Iben (2012b) provides a detailed discussion of a solar metallicity 1 $M_\odot$ model through its He-core flashes to the third dredge-up on the AGB.

Lithium synthesis at the He core flash was recently investigated by Schwab (2020) using a 1 $M_\odot$ solar metallicity `MESA` model. He demonstrated that the high Li abundance in RC stars may be explained by an event that occurs at the time of the first and strongest He-core flash. Three versions of Li synthesis and mixing events shown in Schwab's Figure 4 give final Li abundances from about 3.7 to 1.0. The mixing introduced by Schwab is diffusive and defined by a mixing coefficient. Another parameter is the duration of the mixing event. Li may also be destroyed in a subsequent weaker He-core flash. Schwab remarks that excitation of internal gravity waves by turbulent convection during the core flash may provide the basis for the mixing, which he describes by an *ad hoc* mixing coefficient. These exploratory calculations do suggest that the He-core flash and attendant Li synthesis may account for varying degrees of Li enrichment seen in RC giants (Figure 7.4).

7.5 Lithium enrichment at the luminosity bump?

Lithium synthesis at the He-core flash results in an abundance increase between a star at the RGB tip and the RC. In a parallel endeavour, one may search for Li abundance increases in stars at or just following the LB. Theory and observation, as discussed above, anticipate that Li abundance changes resulting from the LB are expected to be revealed subsequently as the star ascends the RGB. In general, the Li abundance post-LB is predicted to be unchanged or to decline steadily up the RGB. Nonetheless, the history of Li among giants suggests that one may usefully see if exceptional Li-rich giants are to be found at about the luminosity of the LB. `MESA` predictions for the LB's location in the HR diagram are shown in Figure 7.15 for solar composition models with $\alpha_{\rm ML} = 1.8$. This figure shows that the LB's luminosity increases with stellar mass and crosses the RC's luminosity at $M \simeq 1.6 M_\odot$. The LB occurs at somewhat higher luminosities and higher

temperatures for metal-poor stars (Figure 7.15). The similarity in the luminosity of RC and LB for low-mass giants potentially complicates the identity of Li-enriched stars in a luminosity-A(Li) diagram.

Attribution of Li enrichment directly to the LB seems possible for those (mass, metallicity) pairings providing a LB luminosity operationally distinguishable by more than 0.2 dex from the RC's luminosity. At [Fe/H] = 0, this condition corresponds to $M \leq 1.2\mathrm{M}_{\odot}$ for a LB luminosity less than that of the RC or $M \leq 1.0\mathrm{M}_{\odot}$ for a LB luminosity greater than that of the RC. At [Fe/H] = -0.25, these limits are reduced by about $0.2\mathrm{M}_{\odot}$. Figure 7.7 shows that only the search among the samples with a luminosity less than that of the RC is practical for the DR3 survey; far too few giants with $M \geq 1.6\mathrm{M}_{\odot}$ are included in DR3.

One suitable sample is shown in Figure 7.2. The distinct locations of the RC and LB are well shown. Surely, the outstanding feature in the luminosity- A(Li) diagram is the wide range of Li abundances at the RC's luminosity. At the LB's luminosity, there are no giants with an obvious Li enrichment; most of the Li abundances are upper limits. Several panels in Figure 7.7 confirm this result for other (mass, metallicity) combinations.

Figure 7.7 shows that for all (mass, metallicity) combinations, the Li abundance post-LB declines at a similar rate as the giant evolves beyond the LB. If significant Li enrichment were to occur at the LB, it may vary even between stars with identical properties, as it does among RC giants. Then, the width of the A(Li) – $\log(L/\mathrm{L}_{\odot})$ trend on the RGB above the LB would be increased relative to the width below the LB. In principle, this test of Li enrichment at the LB seems applicable to all (mass, metallicity) combinations provided that the RGB is well populated. Unfortunately, the presence of many upper limits to the Li abundances impairs the test. In addition, at luminosities above the RC and LB, Li-enriched RGB stars are difficult to isolate from evolved Li-enriched RC giants.

Our conclusion that Li-rich giants do not occur on the RGB **at** the LB differs from remarks made by Martell *et al.* (2021) from their analysis of Li-rich giants in the GALAH DR3 survey. They conclude that lithium enrichment is not limited to RC giants but is also present among an appreciable number of RGB giants: "red clump stars are 2.5 times as likely to be lithium-rich as red giant branch stars." This disagreement with our analysis may arise from Martell *et al.*'s use of Kiel diagrams ($T_{\rm eff}, \log g$) where giants are assigned to either the RGB or the RC using the Bayesian probability estimates provided in column `is_redclump_bstep`. Giants with `is_redclump_bstep` ≥ 0.5 and *WISE* W_2 absolute magnitude in the range $|W_2 + 1.63| \leq 0.80$ are classified as RC giants, while giants with `is_redclump_bstep` < 0.5 or absolute magnitude outside the range $|W_2 + 1.63| \leq 0.80$ are classified as RGB giants. This results in a classification of all the luminous giants with $W_2 <$ -2.43 or $log(L/{\rm L}_\odot) \gtrapprox 2.1$ as RGB giants, which in actuality are expected to be a mixture of RGB, early CHeB, and post-RC giants. The use of Bayesian estimates, which vary with luminosity, effective temperature and metallicity, appears to have introduced some intermixing of the RGB and RC populations. We prefer to assign evolutionary phases using a giant's location in the HR diagram ($\log(L/{\rm L}_\odot), T_{\rm eff}$) with respect to the appropriate evolutionary track. As noted above, there are regions in the HR diagram where ambiguities may arise depending on the accuracy of the parameters used to place a giant on the HR diagram, for example, at the confluence of the RC and the RGB.

In summary, Li enrichment *at* the LB is not detected in the giants well represented by DR3. An upper limit to the Li abundance increase of about 0.3 dex is suggested by visual inspection of Figure 7.7. This may provide a novel challenge to the theoretical modelling of thermohaline mixing at the LB.

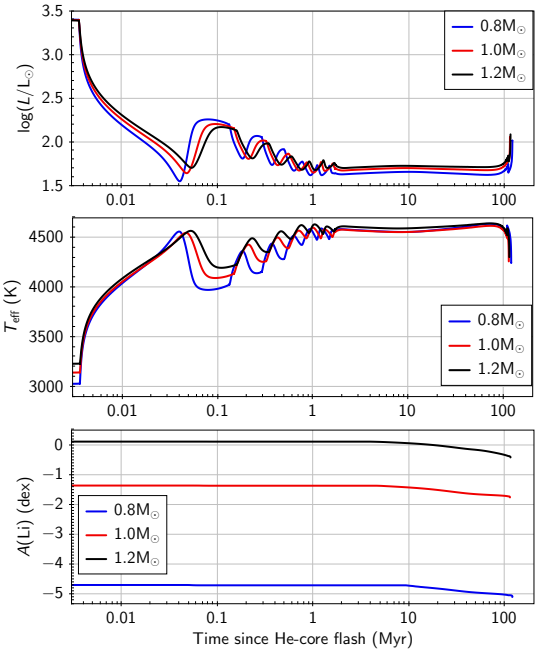


FIGURE 7.16: Variation of luminosity, T_{eff} and A(Li) as a function of time (in million years) during the CHeB phase for solar-metallicity model stars of masses 0.8, 1.0 and 1.2 $M_{\odot}$ with $\alpha_{ML} = 1.85$ and $\alpha_{th} = 100$. For the time axis, a base-10 log scale is used to highlight the fact that CHeB giants spend almost their entire life in a relatively stable state except for the brief He-flashing region, which lasts for about 1-2 Myr from the He-core flash. In the CHeB phase, giants also experience additional Li depletion. This Li depletion starts at approximately about 5 Myr after the He-core flash for a solar mass and solar metallicity star.

7.6 Compositions of red clump giants

The chemical composition of Li-enriched giants has been studied by Deepak *et al.* (2020), which is covered in Chapter 5, to a great extent based on the GALAH DR2 and then by Martell *et al.* (2021) based on data from the GALAH DR3. The conclusion is clear: compositions of Li-rich giants are not distinguishable from other giants. Here, attention is returned specifically to the RC giants. All of these stars have been affected by the He-core flash, which led to alterations of the Li abundance by an amount varying from small to substantial. In the examination of the [X/Fe] versus [Fe/H] plots, the emphasis here is on elements affected by He-burning and *s*-processing. The earlier conclusion about compositions of Li enriched and normal giants is confirmed.

Unfortunately, elements provided by the GALAH survey are not well suited to probing surface contamination by products of He burning mixed to the surface during the short-lived episode of He-core flashes or the longer period of He-core burning. Just 229 giants in the RC luminosity strip (with $\log(L/\mathrm{L}_{\odot})$ of 1.6-1.9) have a determined C abundance. Nitrogen, which might be affected via associated H-burning CN-cycling, is not provided in the GALAH survey. Oxygen, which is well represented in this survey, shows the [O/Fe] versus [Fe/H] relation expected for thin-disc giants with no alterations dependent on Li abundance. This suggests that, although internal He-burning may have altered surface Li abundances, oxygen which is possibly a direct product of He-burning has not been altered.

Coupling of *s*-processing with He-burning is a theoretical possibility. GALAH provides 11 elements from Rb to Sm as at least partial monitors of an *s*-process and Eu as a measure of the *r*-process. For four elements - Rb, Sr, Mo and Ru - abundances are sparsely reported. Among the RC giants, there is no evidence that the abundances of these 11 elements differ according to their Li abundances or differ at all from the [X/Fe] versus [Fe/H] trends expected for the thin disc.

In brief, elements examined across the RBS sample of RC giants show no abundance anomalies except for Li, but this conclusion can not yet be extended to principal products of He-burning (C and N and their isotopes) for lack of observations.

The [X/Fe] versus [Fe/H] for X = Sr, Mo and Ru show an odd bifurcation. A majority of the measurements provide [X/Fe] $\simeq 0$, as found for other *s*-process dominated elements, but a minority of giants suggest a second trend of increasing [X/Fe] with decreasing [Fe/H] attaining [X/Fe] $\sim +1$ at [Fe/H] ~ -0.4. Is this exceptional behaviour a reflection of systematic errors, perhaps linked to the misidentification of lines?

7.7 Concluding remarks

Since their discovery in 1982 by Wallerstein and Sneden, Li-rich giants have occasioned considerable attention by both observers and theoreticians searching for the evolutionary phases at which a stellar atmosphere's Li abundance may be increased by up to several dex. For red giants considered as single stars, the search for internal lithium production has been directed at two evolutionary phases in low mass giants (say, $M \lesssim 2\mathrm{M}_{\odot}$): the luminosity bump on the RGB and the He-core flash. It is now clear that an overwhelming majority of lithium-rich red giants are He-core burning giants, members of the so-called red clump, featuring lithium synthesized by the Cameron-Fowler mechanism during (presumably) the He-core flashes occurring in the RC star's predecessor at the RGB's tip. Detectable Li synthesis is not detectable at the luminosity bump. The preeminence of the idea that the majority of lithium-rich giants are He-core burners ends a long debate about the relative roles of the red clump and the luminosity bump. (The role of binary stars in creating Li-rich giants has been examined. Casey *et al.* (2019) proposed that Li was synthesized in a RGB giant when Li synthesis was triggered by perturbations arising from a companion star. The observation that the binary frequency for Li-rich giants resembles that for Li normal giants Jorissen *et al.* (2020) is a challenge to the universal viability of this binary hypothesis.)

The conclusion about the dominance of the He-core flash in creating Li-rich giants was strengthened by Kumar et al.'s (2020) use of the GALAH DR2 survey. Kumar *et al.* noted that the population of the Li-rich population was at the luminosity of the red clump with Li abundances A(Li) spanning from about -0.5 to $+3.7$. Red clump residents have evolved from the RGB and most likely from a star at the RGB's luminosity tip. Thus, the lithium abundance at the RGB's tip provides the baseline for a clump giant. Kumar *et al.* inferred by extrapolation of the GALAH abundances for the RGB that the abundance at the tip was $A(\mathrm{Li}) \sim -0.9$. Thus, this baseline and the Li abundance range -0.5 to $+3.7$ for RC giants led Kumar

et al. to a conclusion that all RC residents were enriched in lithium: across the range of Li abundances, the enrichment is slight to dramatic. Kumar *et al.* referred to lithium enrichment as 'ubiquitous' among red clump giants. Our probing of red clump giants in the GALAH DR3 endorses Kumar *et al.*'s conclusions about the ubiquity of lithium enrichment among RC giants.

`MESA` models do not fully account for the run of Li abundance along the RGB. Across the sample examined here, the maximum predicted Li abundances of RGB giants are about 0.2 - 0.6 dex greater than observed, which suggests a loss of Li within the main sequence star prior to the RGB. Loss of Li is also suggested by the absence of detectable Li in many RGB giants. All mass-metallicity samples of RGB giants exhibit a smooth decrease of Li abundance with increasing luminosity, but the `MESA` predictions provide for a steeper decline of Li abundance at luminosities above that of the LB. A possible resolution of this discrepancy is to invoke missing 'physics' in the models, such as rotation-induced mixing.

Our analysis shows that the lithium-enriched population peaks at a mass $M \simeq 1.1$ $M_\odot$ and metallicity [Fe/H] $\simeq -0.2$. These values reflect the mass and metallicity distributions of the GALAH population as a whole. The lithium richest and lithium poorest stars in a mass-metallicity combination may appear at the same effective temperature and at the same luminosity. The ubiquity of Li enrichment among RC giants demands redefinition and restatement of the frequency of Li-rich giants among a population, previously stated to be at the few per cent level. If ubiquity is the correct description for RC giants, all such giants with mass $M \simeq$ 1.1 $M_\odot$ and metallicity [Fe/H] $\simeq -0.2$ have experienced the addition of fresh Li to their atmosphere. Future investigations exploring red giants beyond the masses and metallicities well covered by the RBS are awaited with interest.

MESA models fail to account for observations of RC giants. (Li synthesis was not included in our models.) There is an observed spread in effective temperature

(and Li abundance) for giants of a given mass and metallicity. But models predict He-core burning to occur at essentially a single effective temperature before the star evolves to the AGB phase at lower temperatures and higher luminosity. This observed spread in effective temperature and an uncorrelated spread in Li abundance suggests that the sequence of He-core flashes initiating the RC phase at the RGB's tip may result in internal adjustments not considered by `MESA` (and similar models). The primary search for the origin of the effective temperature spread among red clump giants must be led by theoreticians. This issue, however, may be explored by examining compositions of red clump giants across their full spread in effective temperature. No abundance anomalies are shown by the GALAH compositions, but key nuclides are very incompletely reported (as C) or not reported at all (as N).

The luminosity bump has been offered as an opportunity to enhance the surface lithium abundance. Guided by the `MESA` predictions on the bump's location, we searched for a direct association with Li-enriched giants. Across the mass and metallicity combinations providing HRDs with well-populated RGBs, we found no evidence for the presence of Li-enriched giants at the LB: an upper limit of 0.3 dex to the increase in Li abundance is set. This provides an interesting limit with which to test calculations of lithium synthesis occurring at the luminosity bump. Such synthesis does directly affect the Li abundance development on the RGB above the LB, where without obvious exception, the Li abundances are less than at pre-LB RGB values.

The saga of the origins of lithium enrichment in low-mass red giants has now transitioned to the challenge of providing a clear picture of Li synthesis at the He-core flashes in luminous RGB giants. Clarification of the identification of Li-enriched giants is a notable achievement, but questions concerning the quantitative accounting for giants' lithium abundances remain, most especially difficult questions about the He-core flashes and their effect on the structure of red clump giants

which may in many cases depart markedly from the clump giants described by standard evolution calculations. Although direct observations of Li abundance at the LB have not been found, observations of Li and light nuclides (C, N and O) affected by thermohaline and other forms of mixing along the full RGB deserve pursuit before the understanding of RGB giants may be deemed complete. Undoubtedly, as the history of lithium in observational astronomy reminds us, other puzzles about the lithium abundance among giants as single and binary stars will occur unexpectedly.

Data Availability

The source files for our solar mass and metallicity `MESA` models, along with the outputs for all the cases studied in this work, are available at `https://doi.org/10.5281/zenodo.5086893`.

Chapter 8

Contribution of low-mass stars towards the Galactic Li evolution*

8.1 Introduction

As discussed in Chapter 3, Li has significantly increased in the Galactic disc compared to the amount of Li found in the old, metal-poor halo stars, as well as the theoretically predicted value from the standard BBN models. Various sources, like galactic cosmic ray spallation, nova explosions, AGB stars, nucleosynthesis in evolved low-mass stars, etc., are known to produce Li and believed to contribute towards the Galactic Li evolution Romano *et al.* (2001). Of these sources, the low-mass stars, which are also the most common stars in the Galaxy (Salpeter 1955), are believed to be one of the significant contributors of Li in the Galaxy (Romano *et al.* 2001).

*Part of this chapter is published in Deepak and Reddy (2020a,b).

This chapter provides an overview of Li's evolution in low-mass stars and their contribution towards the Galactic Li evolution. For this study, we make use of the stellar sample from Deepak and Reddy (2018) and Deepak and Lambert (2021b), described in Section 3.2 of Chapter 4 and Section 7.2 of 7, respectively. We also make use of a sample of giants with measured Li abundance and asteroseismic parameters from Deepak and Lambert (2021a).

8.2 Evolution of Li in low-mass giant stars: an overview

Li's presence in low-mass red giants has occasioned considerable interest across the evolutionary phases from subgiant, the red giant branch, the red clump He-core burning giant to the asymptotic giant branch and then to the post-asymptotic giant branch followed by ejection of the envelope with the stellar residual present as a white dwarf. Lithium present at low abundance in a giant's main sequence progenitor is depleted in the giant because the deep convective envelope drastically dilutes the Li abundance. This major episode of dilution occurs as the giant evolves to the base of the first red giant branch (RGB). This stage is known as the first dredge-up (FDU). Continuing depletion of Li occurs in the lowest mass RGB giants beyond the completion of the FDU. Given that the effect of the FDU in low-mass giants is to lower the envelope's Li abundance by approximately a factor of about 100, a red giant post-FDU of about solar metallicity is expected to have a Li abundance of A(Li) $\sim$ 1.5. A Li abundance of about this value represents the anticipated *upper* limit for a giant's Li abundance because Li may have experienced depletion, dilution or diffusion in a main sequence star's outer envelope well prior to the FDU and the giant's convective envelope may post-FDU destroy additional Li. Thus, a Li-rich giant has been widely known as one with an abundance A(Li)$\geq$ 1.5. Since the first discovery of a Li-rich giant by Wallerstein

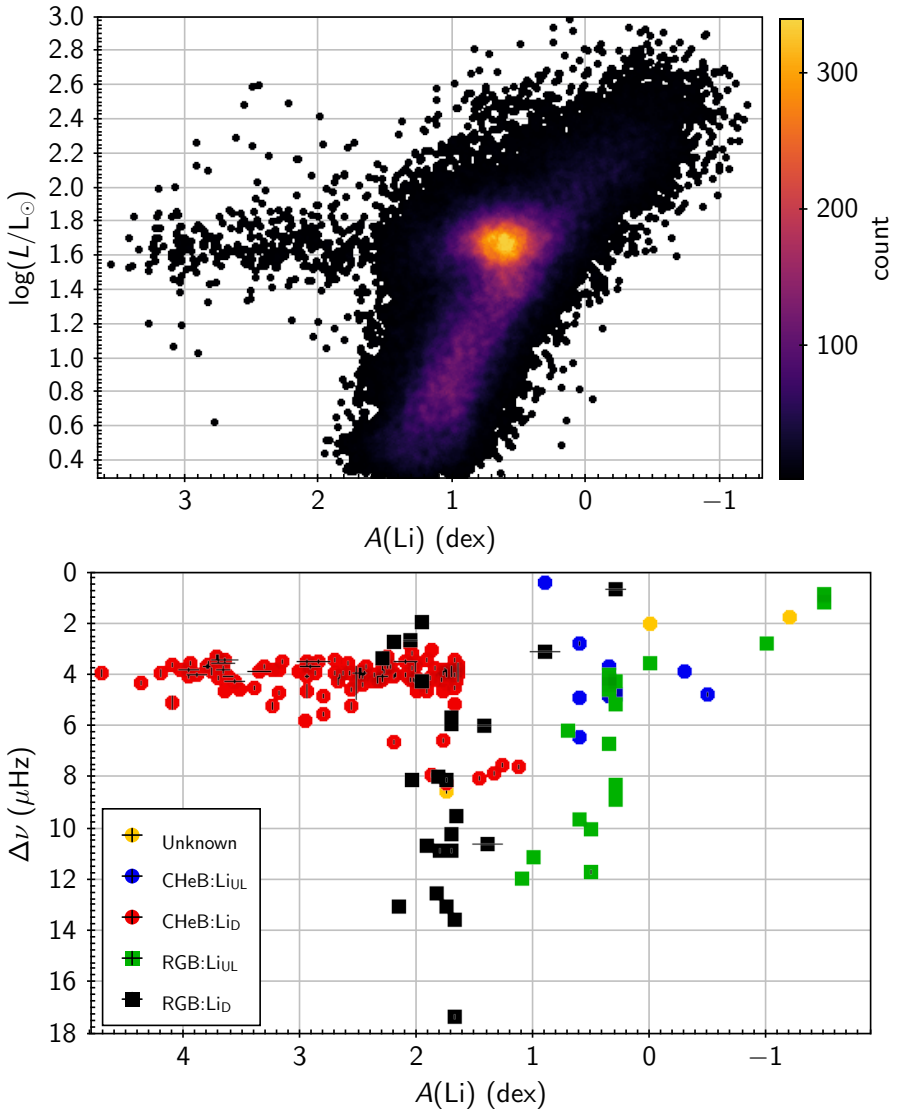


FIGURE 8.1: Top panel: Li as a function of luminosity for the sample of low-mass giants from Deepak and Reddy (2019). Bottom panel: Li as a function of large frequency spacing $\Delta\nu$ for the sample of giants from Deepak and Lambert (2021a). In the bottom panel, errors in Li abundance and $\Delta\nu$ are shown using black-colored error bars corresponding to each of the stars. Also, Filled red and blue circles are core He-burning giants with Li detections and upper limits, respectively. Filled black and green squares are RGB giants with H-shell burning with Li detections and upper limits, respectively.

and Sneden (1982), thousands of Li-rich giants have been discovered in recent years based on the data from the large spectroscopic surveys such as the *Gaia*-ESO, GALAH and LAMOST surveys (Casey *et al.* 2016; Deepak and Reddy 2019; Gao *et al.* 2019; Deepak and Lambert 2021b; Martell *et al.* 2021; Yan *et al.* 2021). Li-rich giants are rare, representing a per cent or so of K giants in the Galactic disc (Deepak and Reddy 2019). Now we know that all of the Li-rich giants are core He-burning red giants and are indistinguishable (except Li abundance) from the Li normal giants of similar evolutionary phases (see Chapter 4 to 7).

Evolution of Li as a function of luminosity during RGB phase for the sample of giants from Deepak and Reddy (2019), selected from the GALAH DR2 survey, is shown in the top panel of Figure 8.1. Similar distributions, along with HRDs, for mass and metallicity-restricted samples are shown in Figure 7.7 of Chapter 7. The bottom panel of Figure 8.1 shows the evolution of Li as a function of large frequency spacing $\Delta\nu$ for a sample of giants with measured Li and asteroseismic analysis (based on the sample from Deepak and Lambert 2021a). In all these figures, a star moves from the bottom left corner to the top right corner as it evolves in the RGB phase. During this time, the star's Li gets depleted due to enhanced mixing and approaches a value as low as -1 dex in giants near the tip of RGB. However, all the red clump stars have much higher Li abundance than this lower limit and Li abundances of their predecessor on the RGB, suggesting Li enrichment in all these low-mass stars.

8.2.1 Li production in low-mass giants

The discovery of a high amount of Li in HD 112127 and others led to speculations about Li production in these red giants. Almost all proposed explanations involve Li production tied to a giant's interior layer of ^{3}He. This He isotope at low abundance is present in a star from its birth, with additional amounts produced

in low mass stars by initial steps of the *pp*-chain in main sequence H-burning. Li production from ^{3}He is straightforward for a nuclear astrophysicist: the reaction $^3\mathrm{He}(\alpha,\gamma)^7\mathrm{Be}$ is followed by electron capture $^7\mathrm{Be}(\mathrm{e}^-,\nu_e)^7\mathrm{Li}$. For the stellar astrophysicist, this link requires coupling the hot reaction site where ^{7}Li is created but also destroyed by protons to the cool stellar atmosphere where the Li may survive and is observed. This necessary coupling acknowledges too that the intermediary ^{7}Be has a half-life of just 53 days. The giant's stellar convective envelope is required to bring the fresh (^{7}Be and) ^{7}Li to the atmosphere with, of course, the convection also returning ^{7}Li to the interior for destruction and replenishment. This coupling of nuclear and stellar astrophysics first recognized by Cameron (1955) is now widely known as the Cameron-Fowler mechanism. Cameron and Fowler (1971) suggested this mechanism involving He-burning shell flashes to account for the rare carbon stars like WZ Cas (McKellar 1940) and WX Cyg (Sanford 1950) with very strong 6707 Å lines. In modern parlance, these carbon stars are examples of luminous AGB stars experiencing helium shell-burning episodes and the third dredge-up. Lithium, carbon and *s*-process enrichment are predicted by contemporary modelling and observed in luminous AGB giants (Smith and Lambert 1989). In the case of K giants like HD 112127, which are not luminous AGB stars, the suspicions about the association of the He-core flash with Li synthesis were aired in the first survey for Li-rich giants by Brown *et al.* (1989a) and raised subsequently by others. We now know that Li enrichment in these giants happens during the first strong core He-flash (Deepak and Lambert 2021a,b; Singh *et al.* 2021).

8.2.2 Contribution of low-mass giants towards the Galactic Li-enrichment

We now know that all the low-mass stars experience Li-enrichment via internal production during the He-core flash phase resulting in Li-enriched red-clump stars. One of the ways Li from these Li-enriched RC stars can end up in the ISM is

through mass loss during fluctuations when the star is in the Asymptotic Giant Branch (AGB) phase. However, due to continued mixing during the RC phase, the enriched Li survives only for about 2 Myr compared to the total time of about 100 Myr a Sun-like low-mass star spend in the RC phase. Because of this, these low-mass stars can not contribute from this enriched Li towards the Galactic Li enrichment during the post-RC phase, as this enriched Li would have been destroyed much before stars reached that stage of evolution. However, some of the studies, for example, Tomasko (1970); Cole and Deupree (1981) and references therein, suggest mass loss during the core He-flash. With this mass loss during the core He-flash, the freshly created Li in the giants can be thrown out into the ISM and thus contribute to the Galactic Li enrichment.

8.3 Summary and future plan

Based on spectroscopic data from the GALAH survey along with the astrometric data from the *Gaia* survey, we have performed a detailed study of the evolution of Li in low-mass stars. We also used the MESA models to understand the evolution of these stars and Li among them. These studies led to the discovery of the internal production of Li in low-mass giants through the Cameron-Fowler mechanism during the He-core flashing phase, which is known to be very violent. During the violent He-core flashes, especially the first strongest He-core flash, stars are known to shed some of the material from their outer envelope to the ISM. Through this mechanism, stars having Li-enriched atmospheres can significantly contribute to Galactic Li enrichment. Further studies are required for a more detailed understanding of the mass loss experienced by giants during the core He-flashing phase across mass and metallicity range and then quantify the amount of Li contribution from these stars towards the Galactic Li enrichment.

Chapter 9

Study of stellar substructures in the Galactic halo based on the data from the LAMOST and *Gaia* surveys

9.1 Introduction

The Galactic halo's stars are relics from the earlier times of the Galaxy and are believed to hold information about the events (like dwarf galaxy mergers) from that time. Hard to measure accurate astrometric parameters and chemical abundances are key to uncovering the origin of these stars and the formation and evolution histories of the Galaxy. There were only a few accurate distance measurements until the advent of the Hipparchus space mission in the 1990s, which provided astrometry for a couple of hundred thousand stars in the solar neighbourhood with unprecedented accuracy. Measured distances with derived stellar kinematic motion

(U, V, W) coupled with high-resolution spectroscopic surveys of controlled samples within the solar neighbourhood revealed the existence of distinct structures (like the thin and the thick disc) within the Galaxy (e.g., Edvardsson *et al.* 1993; Reddy *et al.* 2003, 2006). Studies identified many a smaller clustering or overdensity of stars as streams both in the halo and in the disc. However, their origins are not well understood owing to the limited sample. Studies also suggested that the halo contains stars of different populations that have different chemical and kinematic properties (Nissen and Schuster 1997, 2010; Stephens and Boesgaard 2002; Jonsell *et al.* 2005; Ishigaki *et al.* 2010). Launch of the *Gaia* satellite and its data release brought the issue of the origin of Galactic sub-structures into sharp focus. Thanks to the Gaia space mission and its unprecedented accurate astrometry for a much larger sample of stars than the earlier Hipparchus mission, many of the structures in the Galaxy are now well-defined. However, we have yet to understand the precise origin of each of these substructures and how they are related to each other within the Galaxy.

Several other studies, for example Fulbright (2000); Stephens and Boesgaard (2002); Gratton *et al.* (2003); Carollo *et al.* (2007); Nissen and Schuster (2010, 2011); Schuster *et al.* (2012); Haywood *et al.* (2018); Hayes *et al.* (2018); Helmi *et al.* (2018); Brook *et al.* (2020) and references therein, have reported the presence of two different halo populations in the solar neighbourhood. The presence of spatial and kinematical substructures in the Galactic halo are some of the key pieces of evidence for the working of cosmological ΛCDM model (for example, see recent reviews Helmi 2008; Klement 2010)

The Gaia collaboration, based on the second data release from the Gaia satellite, has shown two well-separated main sequences in the colour-magnitude diagram (CMD) for the Galactic halo (Gaia Collaboration *et al.* 2018a). Similarly, based on CMD, ages and metallicity distribution, recent studies (see Haywood *et al.* 2018; Gallart *et al.* 2019) have also found the bi-modal population in the Galactic halo.

The recent study Gallart *et al.* (2019) has shown that these two halo populations are of approximately the same age with significantly different average metallicities. Based on a comparison with results from galactic simulation, the study attributes the in-situ origin for the red sequence, and the metal-poor blue sequence to the external origin of the accretion of dwarf galaxies.

Accurate kinematics and atmospheric composition of a large sample of stars are critical to piecing together the puzzle. While kinematics provide present morphology, elemental abundances offer insights into the origins of stars as different elements formed in different environments in different epochs. The ratio $[\alpha/\mathrm{Fe}]^*$, average abundance of α-process elements (mainly Mg, Si, Ca and Ti) can be used as a temporal probe to study the formation history of the Galaxy because the α elements are understood to have been produced mainly during type II supernovae (SNe) which explode on a short time scale ($\sim 10^7$ years), whereas elements like iron (Fe), nickel (Ni) are produced in type Ia SNe which happen on a much longer timescale ($\sim 10^9$ years). Stephens and Boesgaard (2002) have shown that $[\alpha/\mathrm{Fe}]$ is anti-correlated with the apogalactic orbital distance. The outer halo (i.e., the accreted component) has a comparatively lower $[\alpha/\mathrm{Fe}]$, but with a large scatter, than the inner halo (i.e., the dissipative component) (Jonsell *et al.* 2005). Based on the maximum vertical distance from the galactic plane (Zmax), Ishigaki *et al.* (2010) divided the sample (with metallicity -2 < [Fe/H] < -1) into two groups with |Zmax| > 5 kpc and |Zmax| < 5 kpc, and found that [Mg/Fe] for the latter group (with |Zmax| < 5 kpc) tend to be about 0.1 dex higher compared to the first. The low-α halo stars are thought to have accreted from dwarf galaxies. On the other hand, various studies based on numerical simulations and observations have suggested that the high-α stars may have formed “in situ" in the Galactic bulge or disc, and then “heated" to halo kinematics during the merger of satellite galaxies (Zolotov *et al.* 2009, 2010; Purcell *et al.* 2010; Di Matteo *et al.* 2011; Qu *et al.* 2011). Many recent studies, like Myeong *et al.* (2019); Koppelman *et al.*

*For two elements, X and Y, the elemental abundance ratio $[X/Y] \equiv \log(N_X/N_Y)_{\mathrm{star}} - \log(N_X/N_Y)_{\mathrm{Sun}}$, where N_X and N_Y are number densities of element X and Y, respectively.

(2019); Belokurov *et al.* (2020); Feuillet *et al.* (2020); Horta *et al.* (2021); Limberg *et al.* (2021), have provided evidence for the presence of accreted substructures in the halo.

To further understand the formation and evolution histories of the Galactic halo, one needs to study chemical and kinematical properties along with the ages of a large number of halo stars. For this purpose, we use astrometric data from the *Gaia* survey along with spectroscopic data from the LAMOST survey. The stellar sample is discussed in Section 9.2. Section 9.3 provide a brief overview of the halo. The selection of various substructures in the halo is discussed in Section 9.4. A comparison of CMDs of these substructures is provided in Section 9.6. In Section 9.7, we discuss various properties (like metallicity, age and orbital parameters) of these substructures. In Section 9.8, we discuss the possible origin of these substructures and also provide some ideas for further advancing our understanding of the formation and evolution history of the Galactic halo and the Galaxy itself.

9.2 Data sample

Our aim for this study is to have a large data sample with good astrometry and photometry (including extinction data) along with good spectroscopic parameters so that halo substructures covering a wide range of kinematics can be identified and then their various kinematic and chemical properties along with their distributions in the colour-magnitude diagram can be studied. We started with *Gaia* survey second data release (hereafter *Gaia* DR2), which is the largest astrometric catalogue available to date. It provides a five-parameter astrometric solution (i.e., stars' position coordinates, proper motions and parallaxes) and photometric data in the *Gaia* G, BP, and RP-band magnitudes covering wavelength bands of [330-1050], [330-680], and [630-1050] nm, respectively, for about 1.7 billion stars (Jordi

et al. 2010a; Gaia Collaboration *et al.* 2018b). However, the *Gaia* DR2 survey provides extinction data only for a small fraction of stars. The lack of extinction correction to the magnitude and colour of sample stars may lead to a large scatter in the CMD considering halo stars cover a large distance and can also be found at lower galactic latitudes where extinction is expected to be very high due to the presence of dust and gas. To mitigate this problem, we combined the *Gaia* DR2 catalogue with the catalogue of *V*-band extinctions provided by Queiroz *et al.* (2020) from the Bayesian isochrone-fitting code `StarHorse` for the LAMOST DR5 survey.[†] `StarHorse` is a `Python` tool that uses Bayesian analysis of spectroscopic, photometric, and astrometric data to infer distances, extinction, ages, and masses of field stars. Source matching between the two catalogues is done using the *Gaia* DR2 source identifier provided in the catalogue from `StarHorse`. We then added the spectroscopic data from the LAMOST DR5 survey provided by Xiang *et al.* (2019).[‡] For this, we first restricted the selection of unique stars with the highest SNR by using `UQFLAG == 1` and then cross-match the two catalogues based on sky coordinates with a maximum separation of 5 arcsec. This results in a sample of about five million unique stars with the highest SNR from the LAMOST DR5. About 99 and 95 per cent of stars in the final cross-match are within 1.0 and 0.5 arcsec. We further restrict the data to good quality spectroscopic measurements with `QFLAG_CHI2 == good`, `TEFF_FLAG == 1`, `LOGG_FLAG == 1` and `FEH_FLAG == 1`. The sample is also restricted to stars with standard error in *V*-band extinction $\sigma_{A_{\rm V}} \leq 0.2$.

For good quality astrometric data from the *Gaia* survey, we restricted the sample to stars with parallax error (σ_{Π}) of less than 20%. To retain stars with good quality proper motions along RA and DEC (i.e., $\rm PM_{RA}$ and $\rm PM_{DEC}$), we restricted the sample to stars with $\sigma_{\rm PM} \leq 0.2$ mas yr^{-1} or 20 per cent. Data is also filtered to remove stars with bad astrometric parameters by restricting sample to stars

[†]`StarHorse` output catalogue for LAMOST DR5 survey is available at the Leibniz Institute for Astrophysics (AIP) web-page `https://data.aip.de/aqueiroz2020`

[‡]The LAMOST DR5 catalogue is available at `http://dr5.lamost.org/doc/vac`.

which qualify the following criteria (Gaia Collaboration *et al.* 2018a; Lindegren *et al.* 2018):

$$\texttt{astrometric_chi2_al}/(\texttt{astrometric_n_good_obs_al} - 5) < 1.44 \times max(1, exp(-0.4 \times (\texttt{phot_g_mean_mag} - 19.5))) \quad (9.1)$$

where, `astrometric_chi2_al`, `astrometric_n_good_obs_al` and `phot_g_mean_mag` are astrometric goodness-of-fit (χ^2) value in the along-scan (AL) direction, number of good AL observations and apparent G-band mean magnitude, respectively. Finally, we have a sample of about 3.27 million stars with good-quality astrometric and spectroscopic data along with good-quality extinction measurements. From this large sample, we selected a sample of halo stars with transverse velocity (V_T) $\geq$ 200 km s^{-1}.[§] This resulted in a sample of 59 909 stars (henceforth, we call it the 'halo' sample).

We estimated the orbital properties (like, $R_{\rm peri}$, $R_{\rm apo}$, eccentricity, $|Z_{\rm max}|$, angular momentum components, total orbital energy E, etc.) of all the sample stars using the `Python` package `galpy` (Bovy 2015; Mackereth and Bovy 2018). Orbits are integrated in `McMillan17` potential (McMillan 2017) for 10 Gyr at 1 Myr intervals using astrometric parameters from *Gaia* and RVs from the LAMOST DR5 survey (for more details, see section 2.2.3).

We also estimated the ages and masses of our sample stars using *qoyllur-quipu* code (`q`^{2}; Ramírez *et al.* 2014), as described in Section 2.2.4. For these calculations, we used astrometric data from the *Gaia* DR2 survey, while the spectroscopic parameters (like stellar parameters, metallicity, [α/Fe], etc.) from the LAMOST DR5 survey. Our age and mass estimates are more reliable for main sequence (MS) and MS turn-off stars due to comparatively well-spaced isochrones in the main-sequence (MS) and MS turn-off (MST) phases. Hence, discussion on age

[§]$V_T = (4.74/\Pi) \times (\mu_\alpha^2 + \mu_\beta^2)^{1/2}$, where Π is parallax in milli-arc-second, and μ_α and μ_β are the proper motions in milli-arc-second per year in the right ascension and declination, respectively.

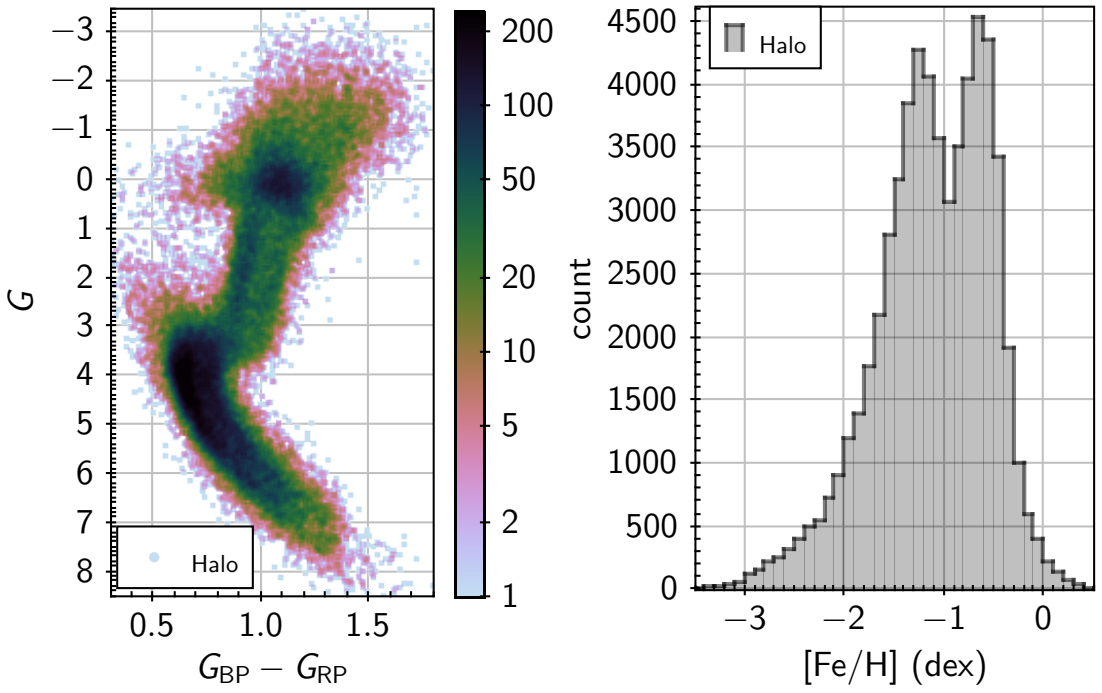


FIGURE 9.1: Color-magnitude diagram and metallicity function for the selected sample of halo stars. A bi-modal distribution is clearly visible in both CMD and metallicity function.

and mass is restricted to the MS and MST stars selected with *Gaia*'s absolute G-band magnitude higher than three. To further remove stars with dubious ages, we restrict our discussion to stars with standard error in age, $\sigma_{\rm Age} \leq 2$ Gyr. Standard error in the estimated masses ($\sigma_{\rm Mass}$) for about 82 and 99 per cent of our sample stars is less than 0.05 and 0.1 $M_\odot$, respectively.

9.3 The Galactic halo: An overview

The kinematically selected halo sample is shown in CMD in the left panel of Figure 9.1. The G, $G_{\rm BP}$ and $G_{\rm RP}$ are *Gaia*'s absolute G, BP and RP band magnitude,

and are estimated using

$$\begin{aligned} G &= \texttt{phot_g_mean_mag} + 5 + 5 \times log(\Pi/1000) - A_G \\ G_{\rm BP} &= \texttt{phot_bp_mean_mag} + 5 + 5 \times log(\Pi/1000) - A_{G_{\rm BP}} \\ G_{\rm RP} &= \texttt{phot_rp_mean_mag} + 5 + 5 \times log(\Pi/1000) - A_{G_{\rm RP}} \end{aligned} \tag{9.2}$$

where, `phot_g_mean_mag`, `phot_bp_mean_mag` and `phot_rp_mean_mag` are *Gaia*'s apparent G, BP and RP band magnitudes. Π is Gaia's parallax in milliarcseconds. and A_G, $A_{G_{\rm BP}}$ and $A_{G_{\rm RP}}$ are *Gaia*'s G, BP and RP band extinctions derived from the V-band extinctions (A_V) provided by Queiroz *et al.* (2020). For conversion of A_V to *Gaia*'s extinctions, we used the recipe introduced in Danielski *et al.* (2018) and implemented by Gaia Collaboration *et al.* (2018a).

The CMD for the halo sample, shown in the left panel of Figure 9.1, clearly suggests a bi-model population in both main-sequence (MS) and red-giants branch (RGB). Of the two populations, the one on the right-hand side (i.e., with a higher colour index) is known as the 'red' sequence, while the other on the left-hand side (with a lower colour index) is known as the 'blue' sequence. The origin of these two colour sequences has been associated with a major merging event – when the Gaia-Enceladus or Gaia Sausage (GE/S) galaxy merged with the progenitor of the Milky Way – which occurred earlier during the formation of the Galaxy. The blue sequence halo population is understood to be the remnant of the Gaia-Enceladus galaxy. On the other hand, the red sequence halo population is believed to consist of Milky Way's in situ halo and disc's old stars, which are believed to have gained more energetic orbits during the merging event (see Gallart *et al.* 2019, and references therein). As shown in the right-hand panel of Figure 9.1, the bi-model metallicity distribution is the main reason for the bi-model distribution in the CMD. These two sequences are also known to have significant metallicity overlap (Gallart *et al.* 2019). This metallicity overlap and possible errors in the colour index because of hard-to-accurately measure extinctions make it very difficult to

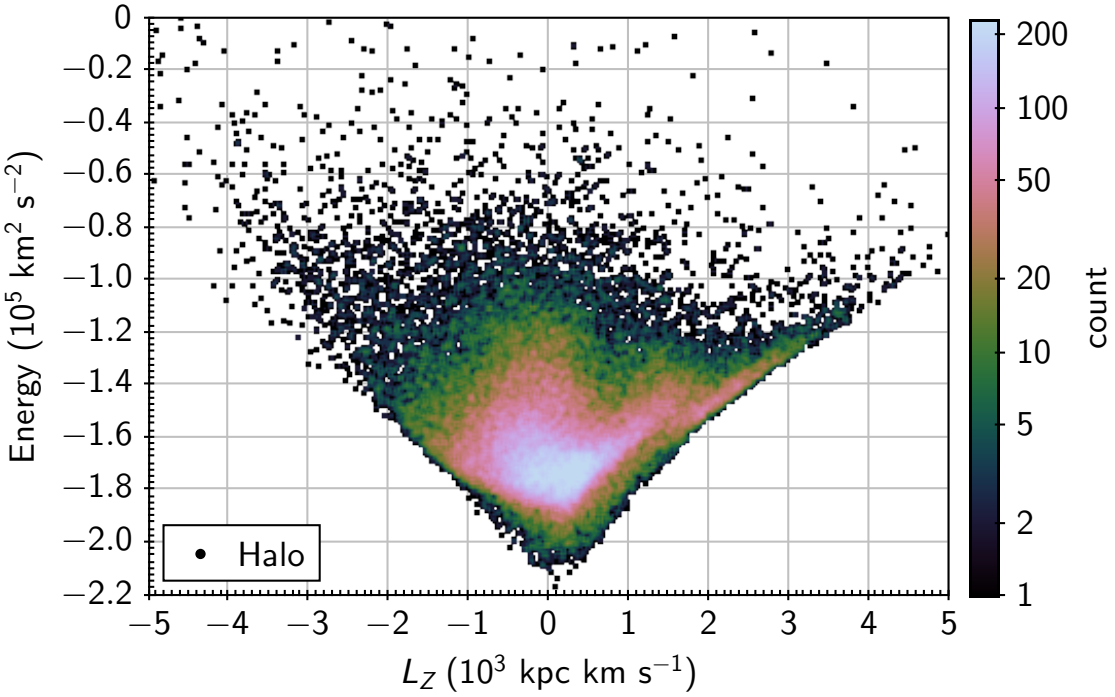


FIGURE 9.2: Energy-L_Z distribution for the kinetically selected halo stars.

accurately separate these two major sequences based on the distribution in the CMD. This also renders the detection of other relatively fainter substructures in the halo. Hence, as discussed in the next section, we separate various substructures in the halo based on stars' kinematic properties.

9.4 Stellar Substructures in the Galactic halo

Figure 9.2 shows the distribution of orbital energy (E) as a function of angular momentum along the Z axis (L_Z) for our kinematically selected sample of halo stars. A brief comparison with previous studies like Horta *et al.* (2021) and references therein suggest the presence of various stellar groups like Gaia-Enceladus/Sausage (GE/S), Thamnos, Sequoia, Halmi stream (H99), etc., along with disc stars with large tangential velocities. Below we describe the identification of these substructures in the halo based on kinematic properties. Unlike Horta *et al.* (2021), we

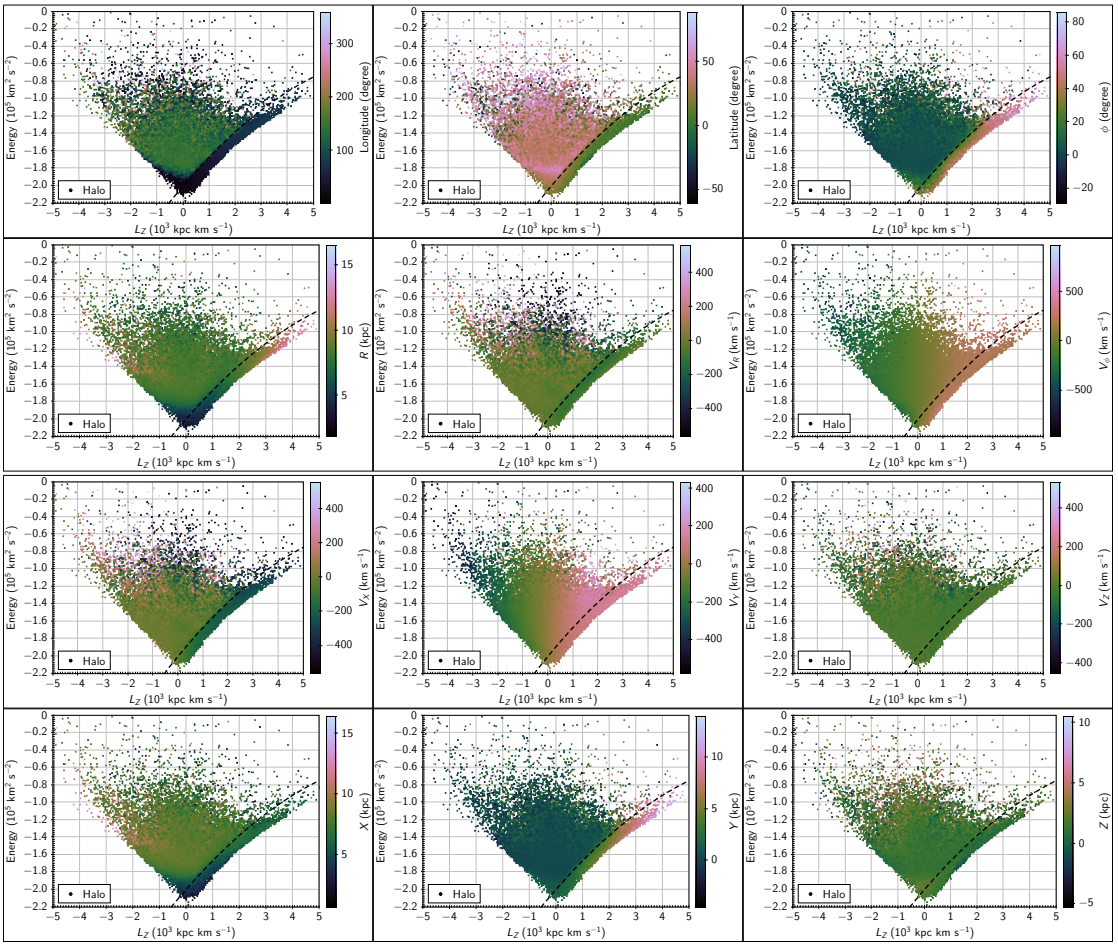


FIGURE 9.3: Kinetically selected sample of halo stars in E-L_Z plane. Stars' sky coordinates, radial distance from the Galactic center R, radial velocity V_R, ϕ, and circular velocity V_ϕ are shown in color in the top two panels. Stars' position coordinates (X, Y, Z) and space velocities (V_X, V_Y, V_Z) are shown in color in the bottom two panels. The dotted black line represents the quadratic equation $E = -2 \times 10^5 + 35 \times L_Z - 0.002 \times L_Z^2$ and separates the probable disc stars with large tangential velocity (i.e., stars with $E < -2 \times 10^5 + 35 \times L_Z - 0.002 \times L_Z^2$) from more certain halo stars (with $E > -2 \times 10^5 + 35 \times L_Z - 0.002 \times L_Z^2$).

prefer not to make any initial major selection based on the chemical composition of stars considering LAMOST's low spectral resolution and also to avoid any possible bias in chemical compositions of substructures due to such selection.

9.4.1 Hot disc sample: Stars with the Galactic disc-like properties but hotter kinematics in our halo sample

We start with separating the possible Galactic disc stars with high tangential velocities, which appear to be buried inside our kinematically selected sample of halo stars. Figure 9.3, shows the kinetically selected sample of halo stars in E-L_Z plane with stars' sky coordinates, radial distance from the Galactic centre R, radial velocity V_R, ϕ, and circular velocity V_ϕ in colour in the top two panels while stars' position coordinates (X, Y, Z) and space velocities (V_X, V_Y, V_Z) in colour in the bottom two panels. Across the range of positive L_Z, stars in the lowest energy bands are spatially as well as kinematically different from the rest of the stars in the halo sample. Spatially, these stars are at lower galactic latitude (with $|b| \lesssim 30^\circ$ and peak distribution at $|b| \approx 13^\circ$) and also lower galactic longitude ($l \approx 55 \pm 35^\circ$). Kinematically, as apparent from the ϕ, V_ϕ, R and V_R distributions, these stars also have relatively large circular and radial velocities. The same is apparent from the distribution of X, Y, Z and V_X, V_Y, V_Z (Figure 9.3). The dotted black line across the panels in Figure 9.3 separates these stars from the remaining halo stars. The dotted black line represents the quadratic equation $E = -2 \times 10^5 + 35 \times L_Z - 0.002 \times L_Z^2$. We classify stars with $E < -2 \times 10^5 + 35 \times L_Z - 0.002 \times L_Z^2$ as disc stars with large tangential velocity. These criteria resulted in a sample of 4810 stars having disc-like spatial distribution but relatively hotter kinematic (henceforth, we refer to this as the hot-disc sample or, in short, the HD sample).

9.4.2 Splash

As can be seen in Figure 9.2, another major pro-grade substructure is present adjacent to the HD. This substructure is linked to the 'Splash' population identified by Belokurov *et al.* (2020). The selection of the Splash population is shown in

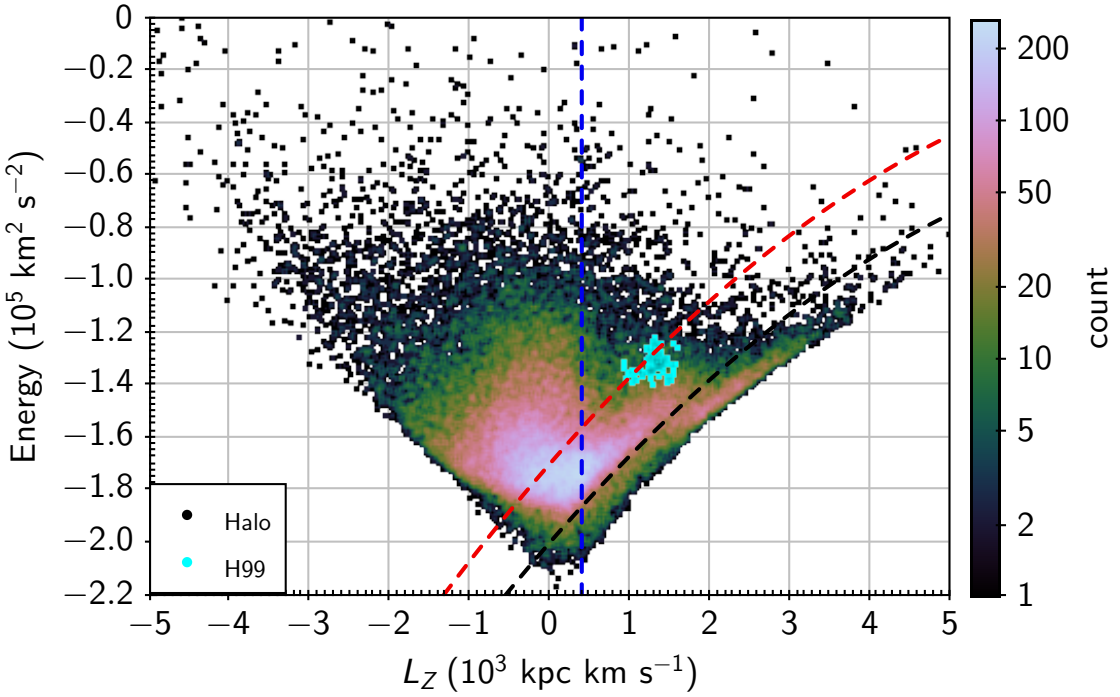


FIGURE 9.4: Kinetically selected sample of halo stars in E-L_Z plane. The dotted black and red lines represent the quadratic equation $E = -2\times10^5 + 35\times L_Z - 0.002\times L_Z^2$ and $(E = -1.7\times10^5 + 35\times L_Z - 0.002\times L_Z^2)$, respectively, and encloses the stars belong to the Splash. Selection of Splash's stars is further restricted to $L_Z > 0.4\times10^3$ kpc km s^{-1} to avoid contamination from retro-grade populations. Members of the Helmi stream (H99) are shown in cyan color.

Figure 9.4. The stars between dotted black line ($E > -2\times10^5 + 35\times L_Z - 0.002\times L_Z^2$) and red line ($E < -1.7\times10^5 + 35\times L_Z - 0.002\times L_Z^2$) are potential members of the Splash. However, for $L_Z < 0.4\times10^3$ kpc km s^{-1}, a significant overlap between Splash's stars and stars belonging to other retro-grade substructures. To avoid contamination from the retrograde stars, we restrict our selection to stars with $L_Z > 0.4\times10^3$ kpc km s^{-1}. This resulted in a sample of 11577 stars.

9.4.3 Helmi stream

The Helmi stream (Helmi *et al.* 1999) is another pro-grade substructure hidden well inside the halo stars. It is one of the first dynamical groups discovered using the astrometric data from the *Hipparcos* mission. For the selection of Helmi stream's

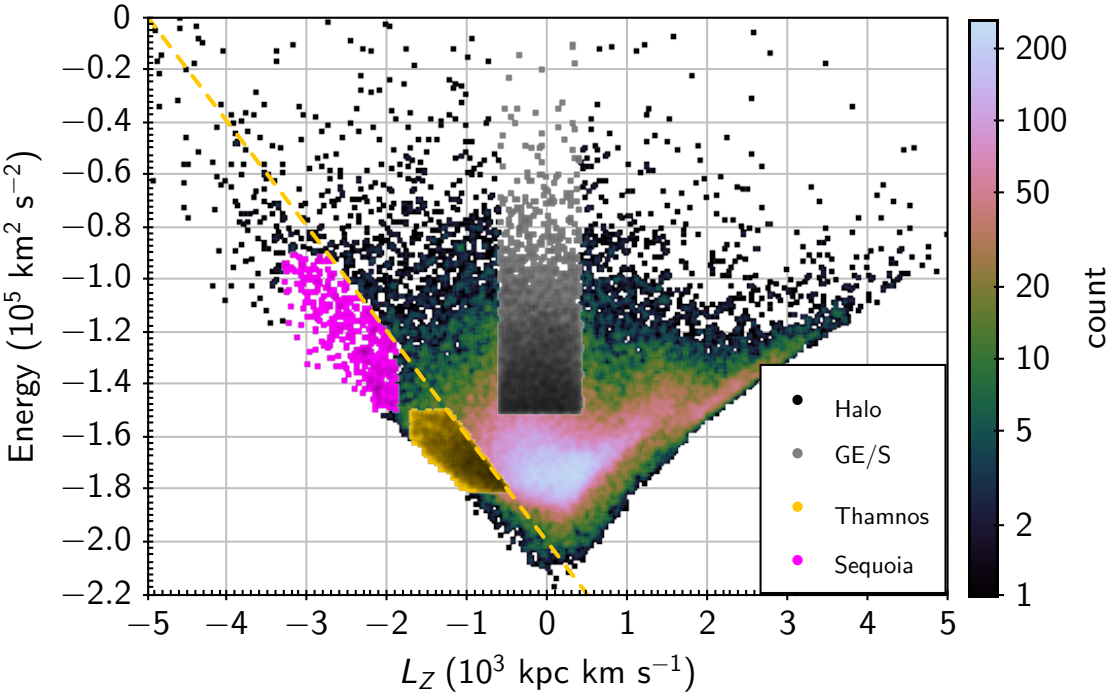


FIGURE 9.5: Selection of Gaia-Enceladus/Sausage, Thamnos and sequoia. The whole sample of kinematically selected halo stars is shown in the background. GE/S stars are selected with $E \gtrsim -1.5 \times 10^5$ km s^{-2} and -600 $\leq L_Z \leq$ 400 kpc km s^{-1}. The dotted yellow line represents the quadratic equation $E < -2\times10^5 - 40\times L_Z$. Stars below the dotted yellow line and with $-1.8\times10^5 < E < -1.5\times10^5$ km^2 s^{-2} and $-1700 < L_Z < -500$ kpc km s^{-1} are classified as Thamnos stars, while Sequoia's selection is restricted to stars with $-1.5\times10^5 < E < -0.9\times10^5$ km^2 s^{-2} and $-3300 < L_Z < -1900$ kpc km s^{-1}.

stars, we use a 5D kinematic criteria based on inference from previous studies like Helmi *et al.* (1999); Limberg *et al.* (2021). Selection is restricted to stars with 90< V_Y < 190 km s^{-1}, -140000 < E < -120000 km^2 s^{-2}, 900 < L_Z < 1600 kpc km s^{-1} and 0 < J_R < 500 kpc km s^{-1}. This resulted in a sample of 93 stars (hereafter, H99 sample). The location of H99's stars in the E-L_Z plane is shown in Figure 9.4.

9.4.4 Gaia-Enceladus/Sausage

Gaia-Enceladus/Sausage is a major accreted component of the halo (Myeong *et al.* 2019) and readily visible in the E-L_Z plane at about zero angular momentum. At lower energies ($\lesssim -1.6 \times 10^5$ km s^{-2}), it overlaps with Splash. However, for $E \gtrsim -1.5 \times 10^5$ km s^{-2}, GE/S and Splash stars are well separated. Also, at negative L_Z, it further merges with other retro-grade components (like Thamnos and Sequoia). As shown in Figure 9.5, we restrict our GE/S sample selection to $E \gtrsim -1.5 \times 10^5$ km s^{-2} and -600 $\leq L_Z \leq$ 400 kpc km s^{-1}. This resulted in a sample of 6263 stars.

9.4.5 Thamnos and Sequoia

Thamnos and Sequoia are two major highly retrograde components of the Galactic halo (Koppelman *et al.* 2019; Myeong *et al.* 2019; Limberg *et al.* 2021). Based on inference from the previous studies, we restrict search for Thamnos and Sequoia's to stars $E < -2 \times 10^5 - 40 \times L_Z$. Further, Thamnos is restricted to stars with $-1.8 \times 10^5 < E < -1.5 \times 10^5$ km^2 s^{-2} and $-1700 < L_Z < -500$ kpc km s^{-1}, while Sequoia is restricted to stars with $-1.5 \times 10^5 < E < -0.9 \times 10^5$ km^2 s^{-2} and $-3300 < L_Z < -1900$ kpc km s^{-1}. This resulted in 3006 Thamnos and 306 Sequoia member stars. Selection is shown in Figure 9.5.

9.5 Low- and high-α disc stars in the HD sample

[α/Fe] versus [Fe/H] distribution for the HD sample is shown in the top-left panel of Figure 9.6. This distribution is similar to the well-known thick disc population's distribution. To further understand the HD's properties, we divide the sample into

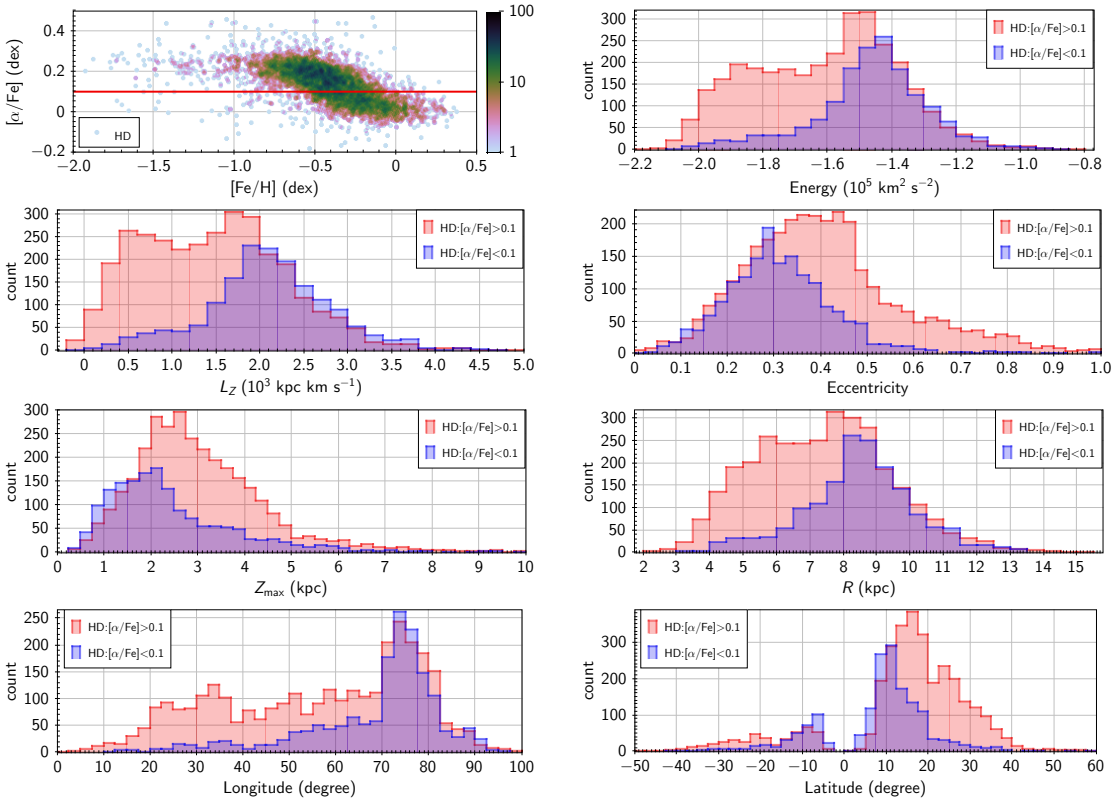


FIGURE 9.6: $[\alpha/\mathrm{Fe}]$ versus [Fe/H] distribution for the hot-disc (HD) sample is shown in the top-left panel while the remaining panels show histograms for various spatial and kinematic properties of the HD's high- and low-α stars. Selection of the HD's high- and low-α samples is shown in the top-left panel, where the red horizontal line (with $[\alpha/\mathrm{Fe}] = 0.1$ dex) separates the high-α stars (with $[\alpha/\mathrm{Fe}] > 0.1$) from the low-$\alpha$ stars having $[\alpha/\mathrm{Fe}] < 0.1$.

low- and high-α stars about $[\alpha/\mathrm{Fe}] = 0.1$ dex. There are 3167 stars with $[\alpha/\mathrm{Fe}] > 0.1$ and 1643 stars with $[\alpha/\mathrm{Fe}] < 0.1$ (hereafter, we refer to these as high- and low-α HD samples, respectively).

Spatial and kinematic properties of high- and low-α HD samples are shown across the panels in Figure 9.6. The low-α HD stars have higher energy E and angular momentum L_Z than the high-α HD stars, which also span comparatively larger ranges in both E and L_Z. The low-α HD stars have comparatively more circular orbits (with peak eccentricity, $e \approx 0.3$) than the high-α HD stars for which peak e is ~ 0.4. Spatially, low-α HD stars are in the inner region of the Galactic plane (with peak $|b| \sim 10°$) compared to high-α HD stars (with peak $|b| \sim 10°$ 18°).

Most of the low-α HD stars are at lower $|Z|_{\rm max}$ (with a mean $|Z|_{\rm max}$ of about 1.8 kpc) compared to the high-α HD stars, which have a mean $|Z|_{\rm max}$ of about 2.4 kpc. However, in the Galactic plane, most of the low-α HD stars are away from the Galactic centre and are located at $l \sim 75°$. On the other hand, the high-α HD stars are almost uniformly distributed from $l \sim 20$ to 85°, except for a slightly higher accumulation at $l \sim 75°$. The mean radial distance of low-α HD stars from the GC is about 8.5 kpc which is the same as the solar distance. On the other hand, the high-α stars have a mean radial distance of about seven kpc from the GC and span a large radial distance range. In the direction away from the GC, the star count for both low- and high-α samples is similar, but in contrast, towards the GC, the number of high-α is large by many folds. Samples distribution in $|Z|_{\rm max}$ and radial distance R suggest that our sample of low-α stars is more localized in the solar neighbourhood compared to the high-α sample.

9.6 Comparison of CMDs of the halo's components and importance of kinematic segregation of these components

Colour-magnitude diagrams (CMDs) for the kinematically selected substructures in the halo are shown in Figure 9.7. All the substructures, except for the HD (and its low- and high-α components), have well-populated MS and RGB. The HD is dominated mainly by giant stars only. The CMD for the entire halo sample is shown in the top-left panel of the figure. The figure clearly suggests the presence of two colour sequences in both MS and RGB. As discussed previously in Section 9.3, these two colour sequences correspond to the halo's two major components, the Splash and GE/S. The difference in the metallicities of these two components is the primary reason for the presence of these two colour sequences. And as

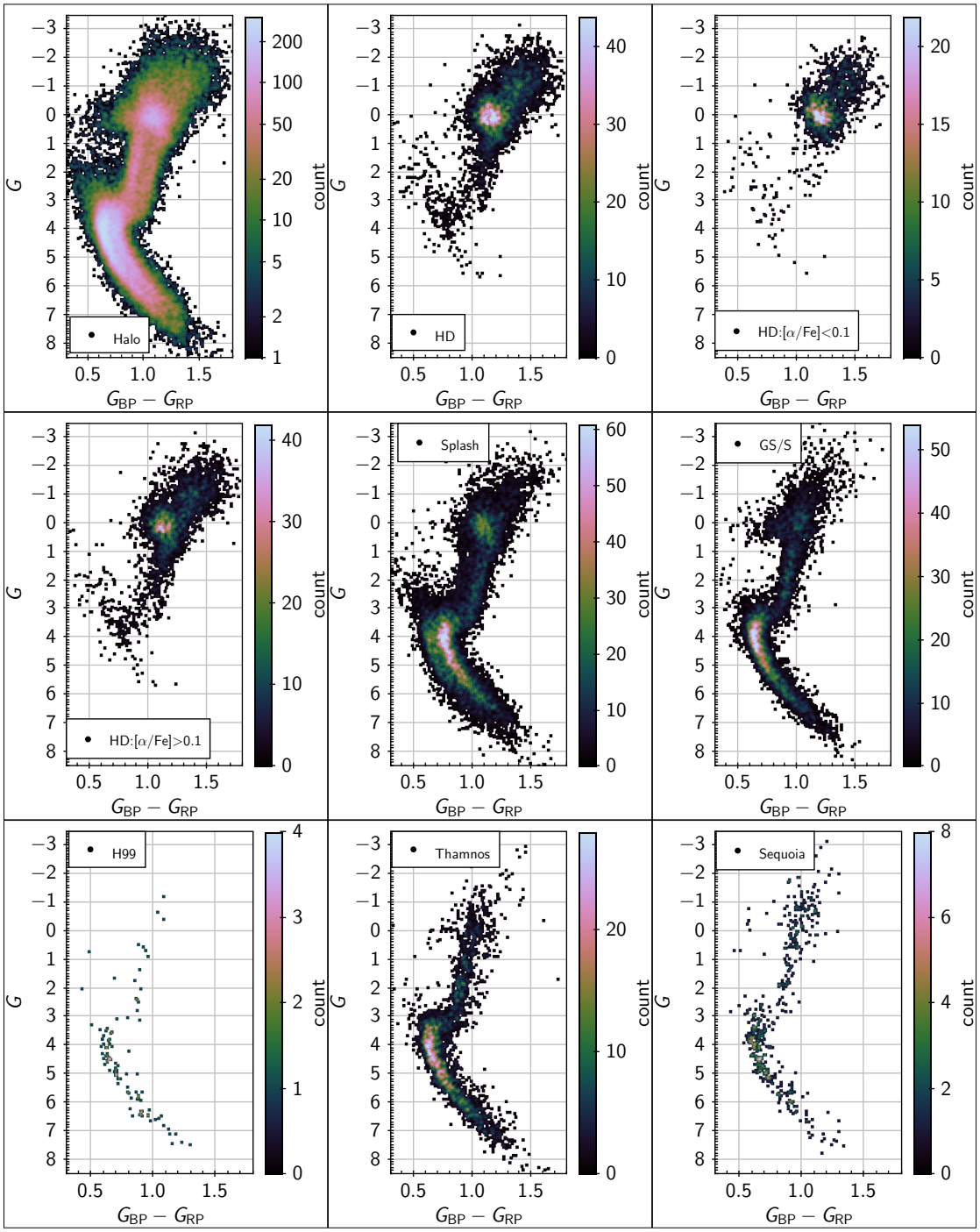


FIGURE 9.7: Color-magnitude diagram for the halo sample along with all the identified components/substructures of the halo.

mentioned before, clean segregation of these two sequences purely based on the distribution in the CMD is difficult due to possible errors in the estimated colours and overlap in CMDs due to overlapping metallicities. The overlap in CMDs of the two major components of halo, Splash and GE/S, is clearly evident from corresponding panels in Figure 9.7, which are based on kinematically selected samples of these two components. Apart from the difficulty in clean segregation of these two major components, the figure also suggests that it would have been impossible to identify other small substructures purely based on the distribution in the CMD, as all these small substructures would have ended up as contaminates among the samples of the two major components, the Splash and the GE/S.

9.7 Metallicity, age, and kinematic properties of the halo's components

Of our kinematically selected six halo substructures, HD and Splash, along with the Helmi stream (H99), are pro-grade, i.e. rotating in the same direction as the Galactic disc about the Galactic centre. On the other hand, Thamnos and Sequoia are highly retro-grade substructures. The GE/S consists of both pro-grade and retro-grade stars; however, it is also slightly retrograde on average. To find clues about the origins of these substructures, we study the distributions of their metallicity, age and kinematic parameters. The metallicity and age histograms for all the identified substructures in the Galactic halo are shown in left- and right-hand panels Figure 9.8, respectively. Similarly, the left- and right-hand panels of Figure 9.9 show the eccentricity and $|Z|_{\rm max}$ histograms, respectively, for all the identified substructures in the halo. Statics from these distributions are summarised in Table 9.1, where the best possible measures for the central and peak values are given in bold. Results from these distributions are discussed in the following sections.

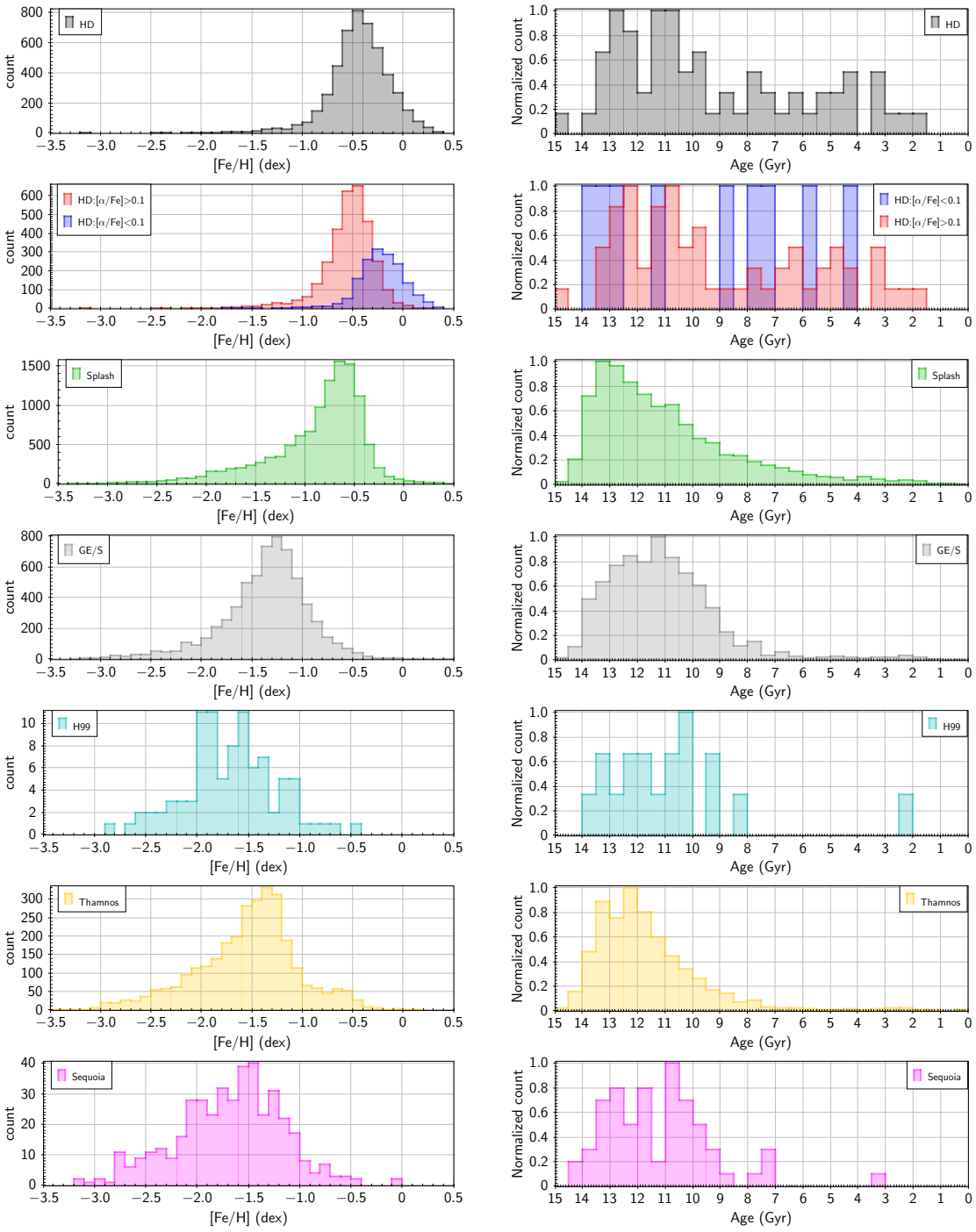


FIGURE 9.8: Metallicity and age histograms for all the substructures in the Galactic halo. Histograms for the low- and high-α populations in the HD samples are also shown.

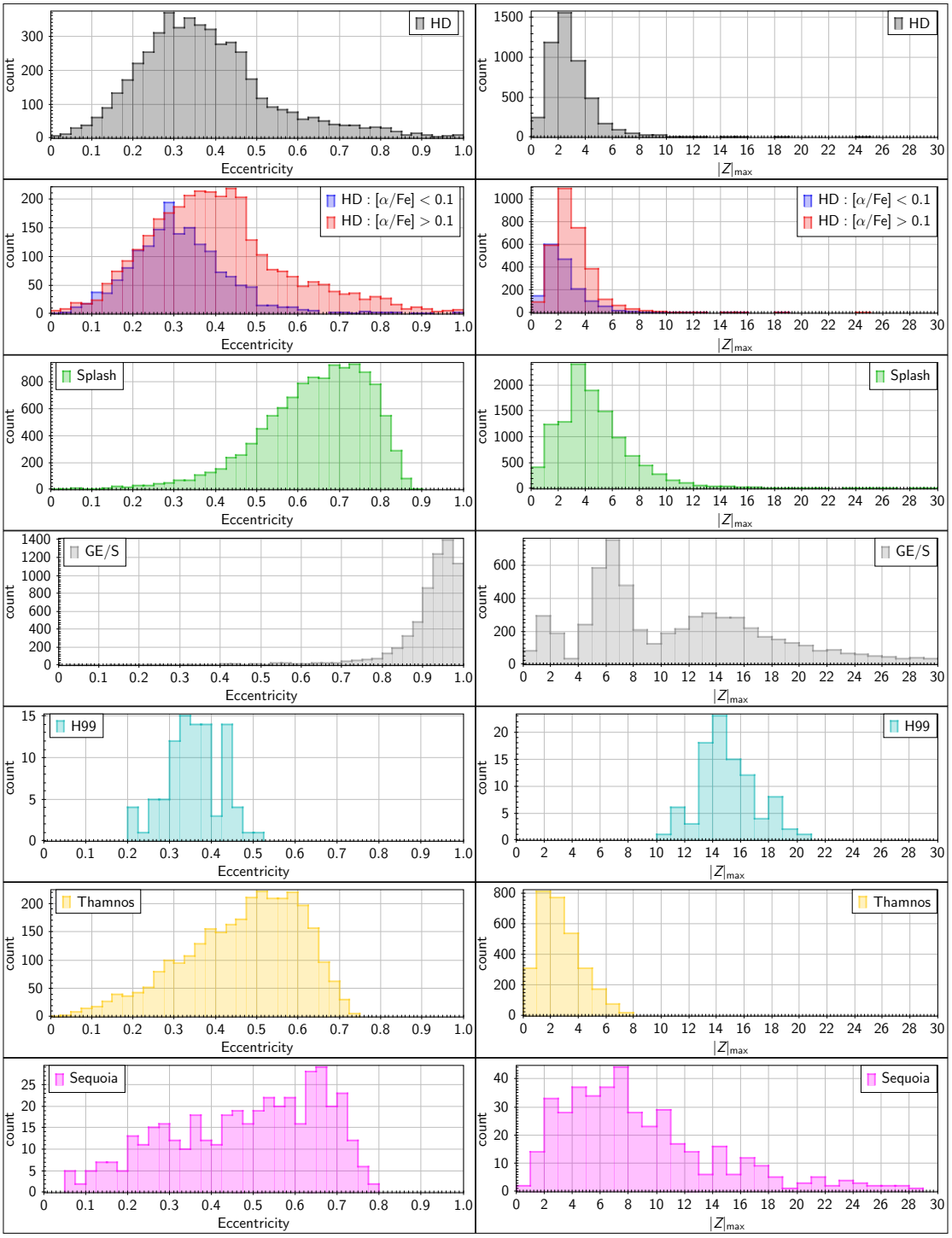


FIGURE 9.9: Histograms of the orbital eccentricity and maximum vertical distance from the Galactic plane ($|Z|_{\max}$) for all the substructures in the Galactic halo. Histograms for the low- and high-α populations in the HD samples are also shown.

TABLE 9.1: Mean, SD, median, median absolute deviation (MAD), mode and skew values for metallicity, age, eccentricity and $|Z|_{\max}$ distributions for selected samples of halo's substructures. The data entries in bold are the best possible measures for the central/ peak values for each sample are given in bold.

Substructure	[Fe/H]					Age				
	Count	Mean ± SD (dex)	Median ± MAD (dex)	Mode (dex)	Skew	Count	Mean ± SD (Gyr)	Median ± MAD (Gyr)	Mode (Gyr)	Skew
HD	4810	**-0.43 ± 0.30**	-0.42 ± 0.17	-0.40	**-1.10**	69	9.27 ± 3.39	10.25 ± 2.32	**12.21**	**-0.60**
HD: low-α	1643	**-0.22 ± 0.24**	-0.21 ± 0.14	-0.19	-1.18	9	9.36 ± 3.26	8.70 ± 3.05	7.38	-0.12
HD: high-α	3167	**-0.55 ± 0.27**	-0.51 ± 0.13	-0.43	-1.84	60	9.08 ± 3.40	10.25 ± 2.31	**12.59**	**-0.52**
Splash	11577	-0.89 ± 0.50	**-0.75 ± 0.24**	-0.47	**-1.31**	2573	10.99 ± 2.57	11.67 ± 1.42	**13.03**	**-1.33**
GE/S	6263	-1.37 ± 0.45	**-1.31 ± 0.23**	-1.19	-0.77	1464	11.06 ± 2.10	**11.26 ± 1.20**	**11.66**	-1.63
Thamnos	3006	-1.54 ± 0.51	-1.48 ± 0.27	**-1.36**	-0.41	765	11.60 ± 2.02	12.03 ± 1.01	**12.89**	**-2.05**
Sequoia	421	-1.68 ± 0.53	-1.64 ± 0.34	**-1.56**	-0.27	66	11.19 ± 1.94	11.52 ± 1.30	**12.18**	**-1.20**
H99	93	**-1.68 ± 0.45**	**-1.68 ± 0.29**	**-1.68**	**0.08**	18	10.75 ± 2.54	**11.14 ± 1.26**	11.92	-2.07
	Eccentricity					$\|Z\|_{max}$				
	Count	Mean ± SD	Median ± MAD	Mode	Skew	Count	Mean ± SD (kpc)	Median ± MAD (kpc)	Mode (kpc)	Skew
HD	4810	0.37 ± 0.16	**0.35 ± 0.09**	0.31	**0.87**	4810	2.90 ± 1.65	**2.58 ± 0.84**	1.94	**2.54**
HD: low-α	1643	0.32 ± 0.12	**0.30 ± 0.07**	0.26	**0.96**	1643	2.50 ± 1.62	2.10 ± 0.76	**1.30**	**2.70**
HD: high-α	3167	0.40 ± 0.17	**0.39 ± 0.10**	0.37	**0.68**	3167	3.11 ± 1.63	2.82 ± 0.81	**2.24**	**2.65**
Splash	11577	0.64 ± 0.13	**0.66 ± 0.09**	**0.70**	**-0.91**	11577	4.73 ± 2.82	4.22 ± 1.47	**3.20**	**1.83**
GE/S	6263	0.91 ± 0.11	**0.94 ± 0.03**	**1.00**	**-3.51**	6263	**14.15 ± 20.69**	10.79 ± 4.92	4.07	**16.42**
Thamnos	3006	0.47 ± 0.14	**0.49 ± 0.10**	0.53	**-0.57**	3006	2.73 ± 1.49	2.53 ± 1.00	**2.13**	**0.73**
Sequoia	421	0.48 ± 0.18	**0.51 ± 0.14**	0.57	**-0.42**	421	8.93 ± 5.78	7.43 ± 3.18	**4.43**	**1.29**
H99	93	**0.36 ± 0.06**	**0.36 ± 0.04**	**0.36**	**-0.19**	93	15.06 ± 2.01	**14.80 ± 1.18**	14.28	0.37

9.7.1 HD population

As shown in the top-left panel of Figure 9.8, the majority of stars in the HD population have metallicity [Fe/H] from about -1.5 to 0.4 dex with a mean [Fe/H] of -0.43 dex and a standard deviation (SD) of 0.30 dex. The distribution is not symmetric and has a small negative skew of -1.10. Metallicity functions for the HD's low- and high-α populations are also shown. The mean [Fe/H] for HD's low-α population is -0.22 with a SD of 0.24, while the mean [Fe/H] for the high-α population is -0.55 with a SD of 0.27. This difference in mean metallicity among these two populations of HD is primarily due to how these two populations are segregated based on [α/Fe] abundance (see the top-left panel of Figure 9.6).

The HD population consist of stars with a wide range in age, with ages ranging from about 2 to 14 Gyr (see the top-right panel of Figure 9.8). The distribution slightly peaks at 12.21 Gyr and is highly skewed towards the younger age (Table 9.1). The age distributions for the low- and high-α populations are similar to the HD population, and the difference, if any, can be attributed to the small sample size.

Kinematically, the majority of the HD's stars follow a slightly elliptical orbit. The sample has a median eccentricity of 0.35 with a median absolute deviation (MAD) of 0.09 (Table 9.1). However, some of the HD's stars have highly elliptical orbits with eccentricity ranging from about 0.5 to 1.0. Because of this, the distribution is skewed towards the higher eccentricity (Figure 9.9). As shown in Figure 9.10, these high eccentricity stars are slightly metal-poor. The figure also suggests a slightly decreasing trend in eccentricity with an increase in metallicity for HD's stars. As shown in Figure 9.9, the HD's low-α stars have more circular orbits with a median eccentricity of 0.30 (and MAD of 0.07) compared to the high-α population for which median eccentricity is 0.39 with MAD of 0.10. The distribution of $|Z|_{\rm max}$ for the HD population is also asymmetric and has a positive skew of 2.54. Most

of the HD's stars are within $|Z|_{\rm max} < 6$ kpc. The sample has a median $|Z|_{\rm max}$ of 2.58 kpc with a MAD of 0.84 kpc. The $|Z|_{\rm max}$ distribution for the low- and high-α populations is also highly skewed with skewness of 2.70 and 2.65, respectively. The $|Z|_{\rm max}$ distribution for the low- and high-α populations peaks at about 1.30 and 2.24, respectively (Table 9.1), suggesting the low-α population is more restricted to the Galactic disc than the HD's high-α population.

9.7.2 Splash

Splash is one of the major pro-grade components of the halo. It is also the most metal-rich after the HD population. Its metallicity distribution is highly asymmetric and skewed towards the metal-poor end with a skewness of -1.31 (Figure 9.8 and Table 9.1). The sample has a median metallicity of -0.75 dex with a MAD of 0.24 dex. Similar to the metallicity, Splash's age distribution is also very asymmetric and skewed towards the younger age, with a skewness of -1.33. The age distribution peaks at 13.03 Gyr and is highly skewed towards the younger age, with about 50 per cent of the stars born in about the first 2 Gyr (i.e., from about 14 to 12 Gyr ago) while the majority of the stars from the remaining 50 per cent are born from about 12 to 5 Gyr ago (Figure 9.8 and Table 9.1).

Kinematically, the majority of Splash's stars have highly elliptical orbits. The median orbital eccentricity for the sample is 0.66, with a MAD of 0.09. However, the sample's eccentricity distribution is highly skewed towards the lower eccentricity with a skewness of -0.91 (Figure 9.9 and Table 9.1). Due to this, a more accurate measure of the sample's eccentricity is its mode which is 0.70. As shown in Figure 9.10, the distribution of eccentricity as a function of [Fe/H] for the Splash is distinct from other populations. The Splash's stars have a maximum eccentricity of about 0.85, and this maximum eccentricity is independent of the stars' metallicity. Additionally, the total spread in eccentricity increases with an increase in

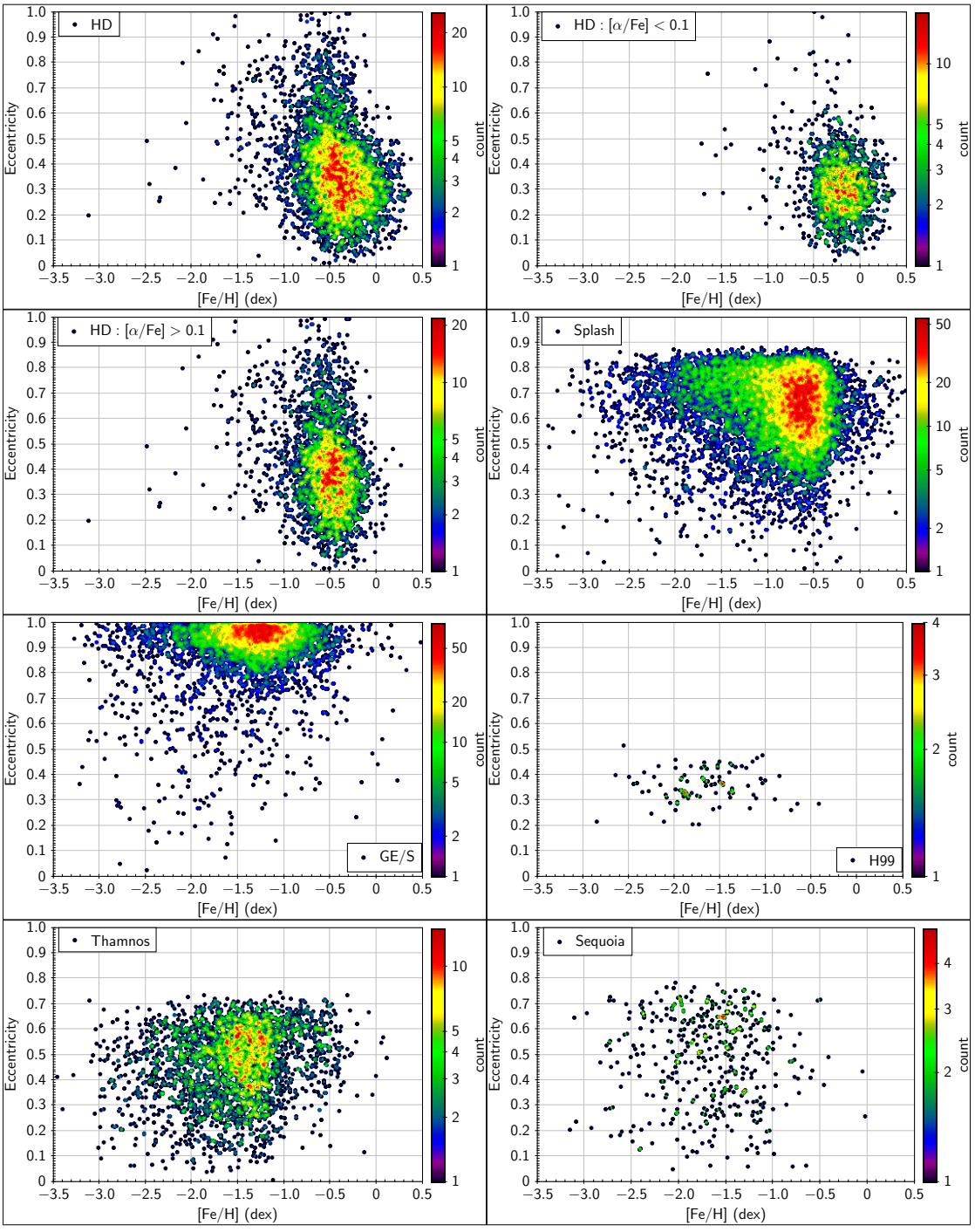


FIGURE 9.10: Orbital eccentricity as a function of metallicity for all the substructures in the Galactic halo. Distributions for the low- and high-α populations in the HD samples are also shown.

metallicity. Due to highly eccentric orbits, Splash's stars also reach comparatively larger distances from the Galactic plane. The $|Z|_{\rm max}$ distribution for the Splash peaks at 3.20. However, due to a highly skewed distribution towards the higher $|Z|_{\rm max}$, about 16, 50, and 84 per cent of Splash's stars have $|Z|_{\rm max}$ lower than 2.2, 4.2, and 7.0, respectively.

9.7.3 Gaia-Enceladus/Sausage (GE/S)

The metallicity distribution function for the GE/S is relatively symmetric and has a median [Fe/H] of -1.31 with a MAD of 0.23 dex (Figure 9.8 and Table 9.1). The age function for the GE/S sample is also approximately symmetric and has a median age of 11.26 Gyr with a MAD of 1.20 Gyr. Also, about 94 per cent of GE/S stars are older than 8 Gyr, suggesting star formation in GE/S ceased sometime before 8 Gyr ago.

Kinematically, the GE/S stars are on nearly parabolic orbits, with the sample having a peak and median orbital eccentricity of one and 0.94 $\pm$ 0.03, respectively (Table 9.1). Distribution is skewed towards the lower eccentricity with a skewness of -3.51. Because of nearly parabolic orbits, the GE/S stars span a wide range in $|Z|_{\rm max}$ ranging from about zero to 30 kpc, and has mean $|Z|_{\rm max}$ of 14.15 kpc with a very large SD of 20.69 kpc. Also, interestingly, the sample suggests three peaks in $|Z|_{\rm max}$ distribution for the GE/S sample (Figure 9.9). These three peaks have peak $|Z|_{\rm max}$ values of about 1.5, 6.5 and 14 kpc. More interestingly, the widths of these peaks also appear to increase with an increase in their peak $|Z|_{\rm max}$. Further studies are required to find if these three peaks are due to the presence of some real kinematic substructures in the GE/S sample.

9.7.4 Thamnos and Sequoia

The Thamnos and Sequoia are the two most metal-poor and highly retro-grade sub-structures in our selected sample of halo stars. Both of these stellar populations span a similar range in metallicity but peak at slightly different metallicities (Figure 9.8). The metallicity distribution for the Thamnos and Sequoia peaks at -1.36 and -1.56 dex, respectively (Table 9.1). Both of these populations also span approximately similar ranges in age; however, their distributions peak at slightly different ages. For Thamnos, the age distribution peaks at 12.89 Gyr, while for Sequoia, it peaks at 12.18 Gyr. Similar to the GE/S, most of the stars in these two populations are older than about 8 Gyr. The presence of a few young stars in the samples can be attributed to either possible contamination in the sample or an error in the age estimation.

Kinematically, stars of both Thamnos and Sequoia have near-circular to highly elliptical orbits. The median eccentricity for the Thamnos and Sequoia are 0.49 $\pm$ 0.10 and 0.51 $\pm$ 0.14, respectively. Eccentricity distributions for both populations are skewed towards the lower eccentricity (Figure 9.9). As shown in the bottom panels of Figure 9.10, even with relatively smaller sample sizes, both Thamnos and Sequoia have the largest scatter in eccentricity versus [Fe/H] plane. Also, for both populations, there is no apparent correlation between stars' orbital eccentricity and metallicity. The two populations have considerable difference in $|Z|_{\rm max}$ distribution (Figure 9.5). The Sequoia stars span a larger range in $|Z|_{\rm max}$ with a peak $|Z|_{\rm max}$ of 4.43 kpc compared to the Thamnos, which has a peak $|Z|_{\rm max}$ of 2.13 kpc. Also, all the Thamnos stars have $|Z|_{\rm max} < 8$ kpc, while only about 50 per cent of the Sequoia's stars have $|Z|_{\rm max} < 8$ kpc.

9.7.5 Helmi stream (H99)

As shown in Figure 9.8, the metallicity of H99 stars ranges from about -2.9 to -0.6 dex. The mean [Fe/H] for the H99 sample is -1.68, with an SD of 0.45 dex. Our metallicity estimate is higher than mean [Fe/H] $= -2.3 \pm 0.5$, recently reported by Limberg *et al.* (2021). One of the main reasons for this disagreement appears to be the relatively small sample in Limberg *et al.* (2021), which has a total of 18 stars compared to our sample of 93 stars. Most of the H99's stars are older than 8 Gyr. The median age of the H99 sample is 11.14 Gyr with a MAD of 1.26 Gyr. Kinematically, the H99 stars have slightly elliptical orbits with a mean orbital eccentricity of about 0.36 ± 0.06, which is in agreement with the mean eccentricity of 0.40 ± 0.08 from Limberg *et al.* (2021). The median $|Z|_{\rm max}$ for the sample is 14.80 kpc with a MAD of 1.18 kpc.

9.8 Discussion and concluding remarks

Stars' kinematics, age and metallicities, when combined, provide a powerful tool to understand the formation and evolution of a galaxy. In this study, we use these three properties to find clues about the formation and evolution of the outermost component of the Milky Way (MW). We used data from the LAMOST survey, which is one of the largest ground-based spectroscopic surveys. More importantly, besides the large sample size, it provides good coverage of metal-poor stars with metallicities up to about -3.5 dex. As the focus of this work is to study the Galactic halo, which consists of relatively metal-poor stars, the LAMOST survey provides an excellent opportunity to study the Galactic halo. From the LAMOST DR5 catalogue (Xiang *et al.* 2019), we kinematically selected a sample of halo stars. Further, based on the distribution in the orbital energy versus momentum plane, we selected samples of substructures in this sample.

The CMD for the selected sample of halo stars, as shown in Figure 9.1, readily suggest the presence of two colour sequences in the MS as well as the RGB. As discussed in Section 9.3, the difference in the metallicities of the halo's two major components (the GE/S and the Splash, also known as the blue and red sequence, respectively) is the reason behind this bi-model CMD for halo. Previous studies like Gallart *et al.* (2019) segregated these two colour sequences based on the distribution in the CMD. However, as shown in Figure 9.7 and discussed in Section 9.6, there is a significant overlap between CMDs of the GE/S and Splash. The CMDs for the other small substructures also overlap with the CMDs for these two major substructures of the halo. These overlaps among the CMDs and possible errors in the colour estimates make it difficult to accurately segregate the halo's substructures purely based on the distribution in the CMD and highlight the importance of the kinematic segregation of these substructures.

Out of our kinematically selected substructures in the galactic halo, the Splash is the largest one, followed by the GE/S. The Splash and GE/S have median metallicities of -0.75 ± 0.24 and -1.31 ± 0.23, respectively, and are primarily responsible for the appearance of two colour sequences in the halo's CMD. The HD population is the most metal-rich with a mean metallicity of -0.43 ± 0.30 and consists of both young and old stars. Most of the HD's stars are on disc stars' like orbits with median orbital eccentricity of 0.35 ± 0.09 and $|Z|_{\rm max} \lesssim 5$ kpc (Figure 9.9 and Table 9.1).

All the selected halo sub-structures, except the HD population, are relatively old, with some of their member stars as old as the Universe itself (i.e. about 14 Gyr old). The Splash has a peak age of 13.03 Gyr and is about 1.5 Gyr older than the GE/S, whose peak and median ages are 11.66 and 11.26 ± 1.20 Gyr, respectively. Also, most Splash and GE/S stars are older than about 8 Gyr. These age estimates are in agreement with many previous studies like (Schuster *et al.* 2012; Hawkins *et al.* 2014; Ge *et al.* 2016); however, they are in contrast to a recent study by

Gallart *et al.* (2019) which suggests that both GE/S and Splash (i.e., blue and red colour sequence, respectively) have the same peak age of 13.4 Gyr. For the Splash, our age estimate is in agreement with Gallart *et al.* (2019)'s age estimate. However, for the GE/S, our age estimate is about 2 Gyr lower than the age estimate provided by Gallart *et al.* (2019). The disagreement between our age estimates (which are in agreement with many previous studies) and Gallart *et al.* (2019) appears to be related to the segregation of these two halo's populations in Gallart *et al.* (2019). As discussed above and in Section 9.6, the Galactic halo is home to many substructures, of which the Splash and GE/S are the two major ones. The selection of Splash and GE/S samples purely based on the distribution in the CMD is expected to result in large contamination due to overlap in metallicity and the presence of other small substructures in the halo. Our selection of halo's sub-structures is based on stars' kinematics and is independent of their metallicity and distribution in the CMD.

The difference in the peak ages of Splash and GE/S can be explained based on the environment in which these two halo populations may have formed. The parabolic orbits (with peak orbital eccentricity of about unity) and large $|Z|_{\rm max}$ of GE/S stars hint toward their accreted origin. The GE/S is believed to be a remnant of accreted dwarf galaxy Gaia-Enceladus/Sausage, while the Splash is believed to consist of in situ formed stars in the Milky Way (Helmi *et al.* 2018; Gallart *et al.* 2019; Koppelman *et al.* 2019). Based on simulations, studies also suggest an initial mass ratio of about 4:1 between progenitors of the Milky Way and the GE/S. The higher mass galaxies are understood to form stars at a more accelerated pace compared to the low-mass Galaxies (e.g., Kauffmann *et al.* 2003; Juneau *et al.* 2005; Guglielmo *et al.* 2015). Chemically, a higher mass galaxy is also understood to evolve faster compared to a low-mass galaxy (Erb *et al.* 2006). Splash's higher metallicity but lower peak age compared to the GE/S population support the idea that the GE/S originated from a less massive progenitor compared to the progenitor of the Milky Way. A sudden drop in age distribution at about

8 Gyr for the GE/S (Figure 9.8) suggest that the star formation in the GE/S progenitor ceased sometime more than 8 Gyr ago. This may be either due to GE/S progenitor running out of gas to form more new stars or its gas getting stripped off due to interaction with the Milky Way. The age distribution of the Splash population is a lot different than the GE/S. Since its peak age at about 13 Gyr ago, there has been a continuous exponential decay in star count (Figure 9.8), which can result from Milky Way's gas settling in the disc and need not be directly related to the GE/S merger with the Milky Way. Also, about 10 per cent of the Splash's stars are younger than 8 Gyr. Gallart *et al.* (2019)'s sample also confirms the presence of young stars in halo's components (see the left-hand panel of Figure 2 of Gallart *et al.* 2019). The existence of these young stars in the Splash can be explained by the dynamical migration of stars from the Galactic disc and bulge to higher energy orbitals.

The age distribution of the HD sample roughly matches the GE/S's age distribution. Although not very clear due to the small sample size of the HD population, a sudden drop in the HD's age distribution can be seen at about 9 Gyr, which roughly coincide with the sudden drop in the age distribution for the GE/S population. This similarity in the age distribution (especially the drop in count around 8 Gyr) along with the disc-like spatial and kinematic features of the HD sample but with relatively energetic orbits than the disc stars suggests that the encounter between the GE/S and the Milky Way may have helped these stars gain higher energy orbits.

Thamnos and Sequoia are the two most metal-poor substructures among our selected substructures in the halo and have peak metallicities of -1.36 and -1.56, respectively. The Thamnos and Sequoia are believed to be remnants of two small dwarf galaxies which merged with the progenitor of the Milky Way (Koppelman *et al.* 2019; Myeong *et al.* 2019; Limberg *et al.* 2021). These two populations are also highly retrograde with mean rotational velocities with respect to the LSR

of about 360 and 530 km s^{-1}, respectively. Both of these populations have stars with circular to highly elliptical orbits with median eccentricities of 0.49 ± 0.10 and 0.51 ± 0.14, respectively. Their age distributions are similar to the GE/S's age distribution, with very few or no stars younger than 8 Gyr. The higher peak metallicity and older age of the Thamnos compared to the Sequoia is possible if the progenitor of the Thamnos was slightly more massive than the progenitor of the Sequoia, resulting in faster star formation and chemical evolution in the Thamnoscompared to the Sequoia.

In conclusion, the lower metallicity and lower peak star formation age of halo's three accreted components (the GE/S, Thamnos and Sequoia) compared to the pro-grade, in situ components like Splash and HD, favours the ΛCMD model of galaxy formation in which smaller dwarf galaxies merge with the large complex galaxies like the Milky Way.

To get a more accurate picture of the formation history of the Galactic halo and the Galaxy, further studies of the chemical compositions of these substructures are needed. However, the LMAOST's low resolution is not adequate to resolve the differences in the compositions of these substructures. As discussed in the next chapter, we employ data from the GALAH survey for this purpose.

Chapter 10

Chemodynamic studies of the Galactic disc and halo

10.1 Introduction

In the last chapter, we used the data from the LMAOST survey in combination with the astrometric information of stars from the *Gaia* survey to identify various substructures in the Galactic halo. This large sample of halo stars from the combination of the LAMOST and *Gaia* survey helped to identify multiple substructures in the halo and also provided opportunities to look into the orbital properties of stars in these substructures along with the metallicity and age functions. However, due to very low spectral resolution ($\sim$ 1800), the LAMOST data is not adequate to resolve the difference in the chemical properties of these substructures. For example, the difference in the mean [α/Fe] of the known low- and high-α population of the Galactic halo is about 0.1 dex (Nissen and Schuster 2010), which

will be difficult to resolve with the abundances from the LAMOST survey. Hence to chemically understand the various substructures in the halo, in this study, we make use of the data from the GALAH survey, which has a spectral resolution of $\sim$ 28000. We also compare the properties of the halo's substructures with the samples of the thin and thick discs.

10.2 Data Sample

For this study, we start with the third data release of the GALAH survey (GALAH DR3 Buder *et al.* 2021). As described previously in Chapter 7 (see Section 7.2), the GALAH DR3 survey consist of 588,571 unique stars derived from 678,423 spectra observed with the HERMES spectrograph at the Anglo-Australian Telescope with a spectral resolution of $\sim$ 28000. The third data release is also accompanied by several value data catalogues (VAC) providing other intrinsic, kinematic and dynamical properties of the observed stars and is collectively known as the GALAH+ DR3 survey.* `GALAH_DR3_main_allspec_v1.fits` is one of the two main catalogues of GALAH+ DR3 and includes stellar parameters and overall abundances of about 30 chemical species derived for each of the observed spectra. This catalogue also includes abundances derived for each individual line for all the elements. We joined this catalogue with the VAC `GALAH_DR3_VAC_ages_v1.fits`, which provides other stellar parameters like age, mass, distances, luminosity, etc., estimated using Bayesian Stellar Parameter Estimation code (BSTEP, Sharma *et al.* 2018). The two catalogues are joined using the recommended method of using the unique internal ID for each GALAH observation provided in the `sobject_id` column. For each of the star's entries in the GALAH DR3 catalogue, we also added all the available astrometric and photometric information from the second data release of

*The GALAH+ DR3 data is available at `https://cloud.datacentral.org.au/teamdata/GALAH/public/GALAH_DR3/`

the *Gaia* survey (Gaia Collaboration *et al.* 2018b). For this, we used the common Gaia DR2 source id provided in the GALAH DR3 catalogue.

The GALAH DR3 has a data entry for each of the 678,423 observed spectra but only 588,571 unique stars leading to multiple entries for some of the stars in the catalogue. To eliminate multiple entries of a star in the catalogue and to select the entry with the highest signal-to-noise, we restrict our sample to stars with `flag_repeat` = 0. We further restrict our sample to stars with reliable stellar parameters (`flag_sp` = 0) and metallicity (`flag_fe_h` = 0), which lead to abandoning of stars with $T_{\rm eff} < 4100$ K. As described previously in chapter 7 (see section 7.2.1), the GALAH DR3 provides a quality flag (`flag_X_fe`) for each of abundance [X/Fe] entry (where X = Li, C, O, Na, Mg, Al, Si, K, Ca, Sc, Ti, V, Cr, Mn, Co, Ni, Cu, Zn, Rb, Sr, Y, Zr, Mo, Ru, Ba, La, Ce, Nd, Sm, and Eu). `flag_X_fe` can have any value from 0, 1 and 32, where flag 0 means provided abundance is reliable, 1 means provided abundance is an upper limit, and 32 means no reliable measurement reported. In this study, we use only the reliable abundances, i.e. the abundances with `flag_X_fe` = 0 (for more details, see section 7.2.1 of chapter 7). However, considering relatively weak absorption lines for some of the chemical elements (like Li, C, Rb, Sr, Mo, and Ru), their corresponding abundance quality flags are expected to be nonzero. Hence, the selection of a global sample with a zero abundance flag for each of the elements together will lead to the discarding of a large fraction of stars. To avoid this, we consider the abundance flag individually when talking about that particular element. Also, similar to the sample of halo stars from the LAMOST survey in Chapter 7, we excluded all the stars with possibly bad astrometric data in the *Gaia* DR2 using equation 9.1. We further restrict the sample to stars with a parallax error (σ_{Π}) less than 20%. This resulted in a final sample of 418,225 unique stars with good stellar and astrometric data.

The Toomre diagram for this stellar sample from the GALAH survey is shown

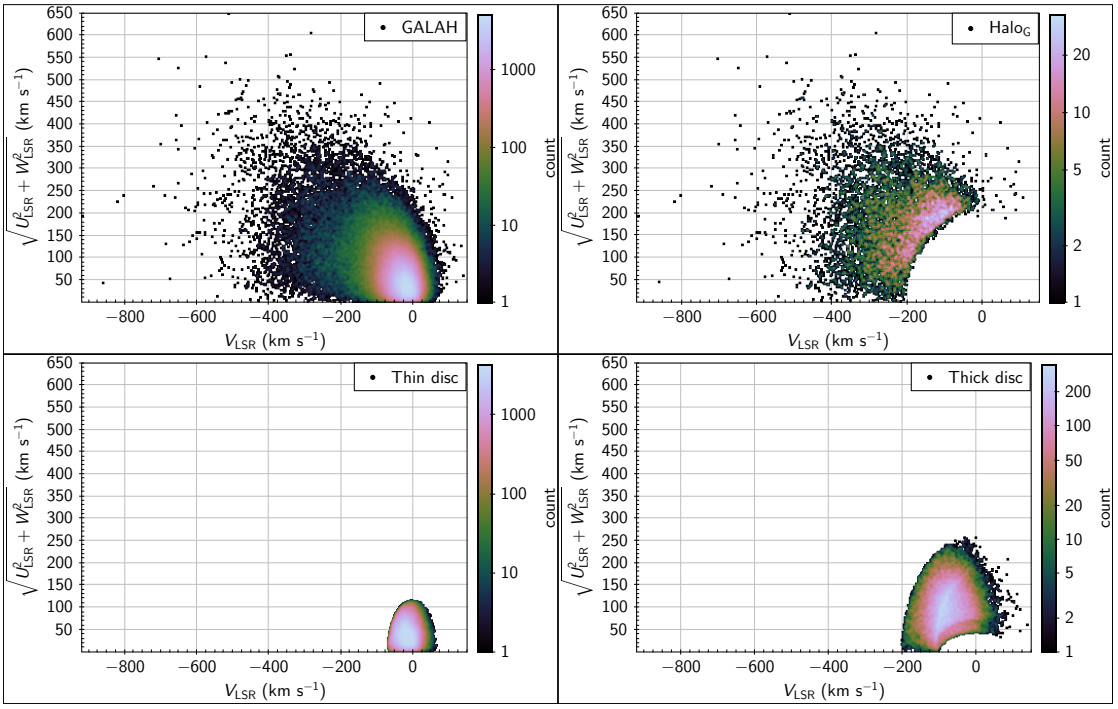


FIGURE 10.1: Top-left panel: The distribution of the GALAH DR3 stars in the form of the Toomre Diagram. Top-right panel: The Toomre diagram for the selected sample of halo stars from the GALAH survey (Halo$_G$). The selected samples of thin and thick disc stars from the GALAH survey are shown in the bottom left and right panels, respectively.

in the top-left panel of Figure 10.1. For each of the stars, the Galactic space velocities (U, V, W) are estimated as described in Section 2.2.1. For this, we used the stars' proper motions and parallax along with corresponding uncertainties from the *Gaia* DR2 survey and line of radial velocity (RV) from the GALAH DR3 survey. These space velocities are further corrected for solar motion using Sun's motion with respect to the LSR from Dehnen and Binney (1998). Also, similar to the sample of stars from the LAMOST survey in the last chapter, we estimated the orbital properties (like $R_{\rm peri}$, $R_{\rm apo}$, eccentricity, $|Z_{\rm max}|$, angular momentum components, total orbital energy E, etc.) of all the sample stars using the `Python` package `galpy` (Bovy 2015; Mackereth and Bovy 2018). Orbits are integrated in `McMillan17` potential (McMillan 2017) for 10 Gyr at 1 Myr intervals using astrometric parameters from *Gaia* and RVs from the GALAH DR3 survey (for more details, see section 2.2.3).

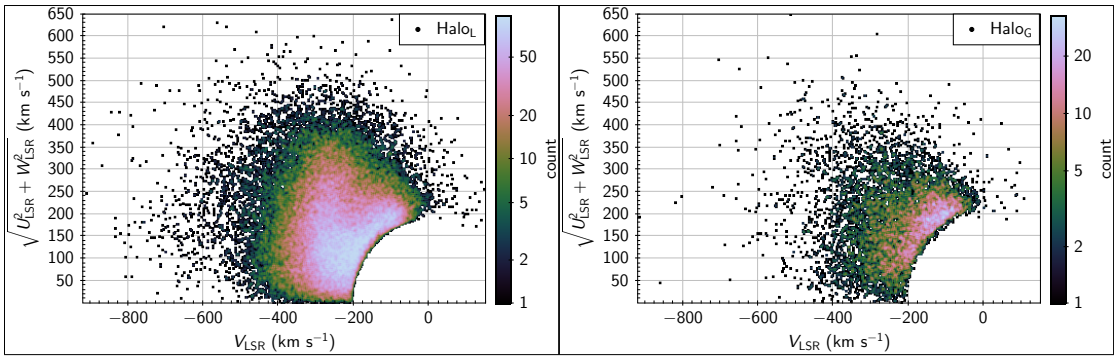


FIGURE 10.2: The left and right-hand panels show the Toomre diagram for the samples of halo stars from the LAMOST survey (Halo$_L$) and the GALAH survey (Halo$_G$). The sample Halo$_G$ from the GALAH survey is about eight times smaller than the sample Halo$_L$ from the LAMOST survey. The number of retrograde stars (i.e. the stars with V_{LSR} < -200 km s^{-1}) in the Halo$_G$ sample is also relatively less than the Halo$_L$ sample.

10.2.1 Stellar sample of the Galactic halo and its substructures

Similar to the selection of halo stars from the LAMOST survey in the previous chapter, we select the sample of halo stars from the GALAH survey with a transverse velocity (V$_T$) $\geq$ 200 km s^{-1}.[†] This resulted in a sample of 8091 halo stars (henceforth, we call it the 'halo' or 'halo$_G$'sample, where 'G' in the subscript indicates that this sample is from the GALAH survey). The distribution of this sample in the form of the Toomre diagram is shown in the top-right corner of Figure 10.1 and in the right-hand panel of Figure 10.2. The halo sample from the GALAH survey is about eight times smaller than the sample of 59 909 halo stars from the LAMOST survey (henceforth, we call it the 'halo$_L$' sample, where 'L' in the subscript indicates that the sample is from the LAMOST survey). A comparison of the Toomre diagram for the halo stars sample from the LAMOST and GALAH survey (i.e. sample halo$_L$ and halo$_G$) is shown in Figure 10.2. Other than the difference in the size of these two samples, the halo$_G$ sample lacks retrograde stars (with $V_{LSR} < -200$ km s^{-1}) and is dominated primarily by prograde

[†]V$_T$ = (4.74/Π) $\times$ (μ_α^2+μ_β^2)$^{1/2}$, where Π is parallax in milli-arc-second, and μ_α and μ_β are the proper motions in milli-arc-second per year in the right ascension and declination, respectively.

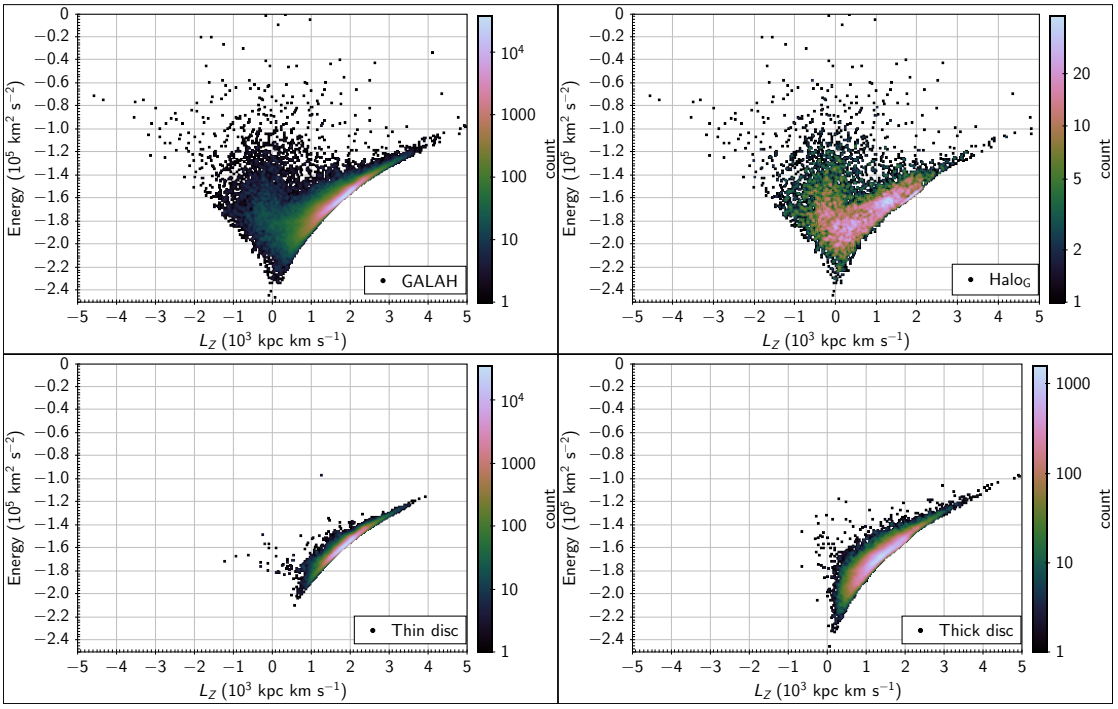


FIGURE 10.3: Top-left panel: The distribution of the GALAH DR3 stars in Energy-L_Z plane. Top-right panel: Energy-L_Z distribution for the kinetically selected sample of halo stars. Energy-L_Z distribution for the kinetically selected samples of thin and thick disc stars are shown in the bottom left and right panels, respectively.

stars. In contrast, the halo$_L$ sample has good prograde and retrograde star coverage. Considering the relatively large number of retrograde stars in the halo stars sample halo$_L$ from the LAMOST survey, which are believed to be the remnant of the accreted dwarf galaxies, we will also make use of the halo$_L$ sample for the comparison of some of the global properties like stellar age and orbital parameters. (For more details about the halo$_L$ sample, see Section 9.2 for Chapter 9.)

The distribution of the GALAH sample and halo stars sample halo$_G$ in orbital energy versus orbital angular momentum L_Z are shown in the top-left and top-right panels of Figure 10.3, respectively. A comparison between the distribution of halo stars samples from the LAMOST and GALAH survey (i.e. sample halo$_L$ and halo$_G$) is shown in Figure 10.4. Unlike the halo stars sample from the LAMOST survey, the GALAH's halo sample has relatively fewer stars with $L_Z \lessapprox 0$. The lack of these stars (known as retrograde stars due to their motion opposite to

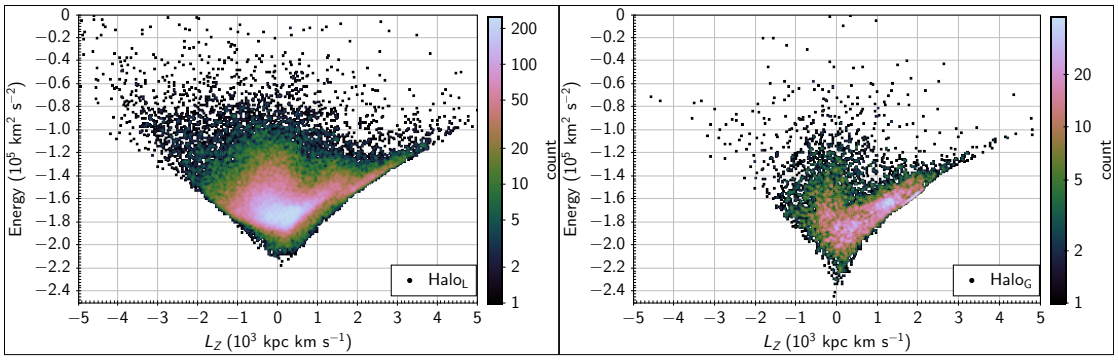


FIGURE 10.4: The left and right-hand panels show the distribution in Energy-L_Z plane for the samples of halo stars from the LAMOST survey (Halo$_L$) and the GALAH survey (Halo$_G$). Compared to the Halo$_L$ sample, the Halo$_G$ has relatively fewer stars with retrograde orbits (i.e. stars with $L_Z < 0$).

the direction of the Galactic disc rotation) in these stars is primarily due to the magnitude limit in the GALAH survey, which targets relatively much brighter stars compared to the fainter limit of the LAMOST survey. Similar to the selection of stars belonging to different sub-structure of the halo in the previous chapter, based on the stars' distribution in the energy-L_Z plane and using other orbital properties, we select samples of stars from halo$_G$ belonging to different halo sub-structures (see Section 9.4 of Chapter 9 for more details). This resulted in samples of 2905 stars having disc-like spatial distribution but hotter kinematic distribution (hereafter, we refer to this sample as the hot-disc sample or, in short, the HD sample), 1373 stars belonging to the Splash, 591 stars Gaia-Enceladus/Sausage, 201 belonging to the Thamnos, and just 21 belong to the Sequoia.

10.2.2 Selection of the thin and thick disc stars

To better understand the origin and evolution of the Galactic halo and various components, it is important to compare their properties with the corresponding properties of thin and thick discs, which are believed to have in situ origins. We select thin and thick disc samples from the GALAH based on stars' kinematic membership probabilities to be in the thin and thick disc. These membership

probabilities are calculated as discussed in section 2.2.2. Stars with a minimum probability of 80% to be in the Galactic thin disc are defined as thin-disc stars. Similarly, stars with a minimum probability of 80% to be in the Galactic thick disc are defined as thick-disc stars. This resulted in a sample of 269 055 thin disc stars and 50 355 thick disc stars (hereafter, we refer to these samples as the 'thin disc' and 'thick disc' samples, respectively). The Toomre diagram for the thin and thick disc stars is shown in the bottom two panels of Figure 10.1 while distribution in the energy versus L_Z plane is shown in the bottom two panels of Figure 10.7.

10.3 Metallicity for the thin-disc, thick-disc and halo sub-structures

Metallicity functions for the thin and thick discs are shown in the top-left and top-right panels of Figure 10.5. The two stellar disc populations significantly overlap in metallicity but peak at different metallicities. Metallicity function for the thin disc peaks at [Fe/H] = -0.05, and more than 96 per cent of the thin disc stars have metallicity in a span of one dex centred at this peak [Fe/H]. In the case of the thick disc, [Fe/H] distribution peaks at -0.45 dex and about 92 per cent of the thick disc stars fall within a span of one dex centred at this peak metallicity. Both of the populations have approximately uni-modal Gaussian metallicity distributions. Single peak Gaussian distribution fits for the thin and thick discs are shown in the red dotted line. For the thin disc, the fitted Gaussian has a mean [Fe/H] of about -0.111 with a standard deviation (SD) of 0.248 dex. The thick population is slightly metal-poor with a mean [Fe/H] of about -0.396 with an SD of about 0.294 dex. Normalized metallicity distribution for the sample of Galactic halo stars from the GALAH survey (i.e., sample halo_G) as well as the LAMOST survey (i.e. sample halo_L) is shown in the bottom left corner. The halo_L readily suggests a bi-model metallicity population in the Galactic halo. However, such bi-model

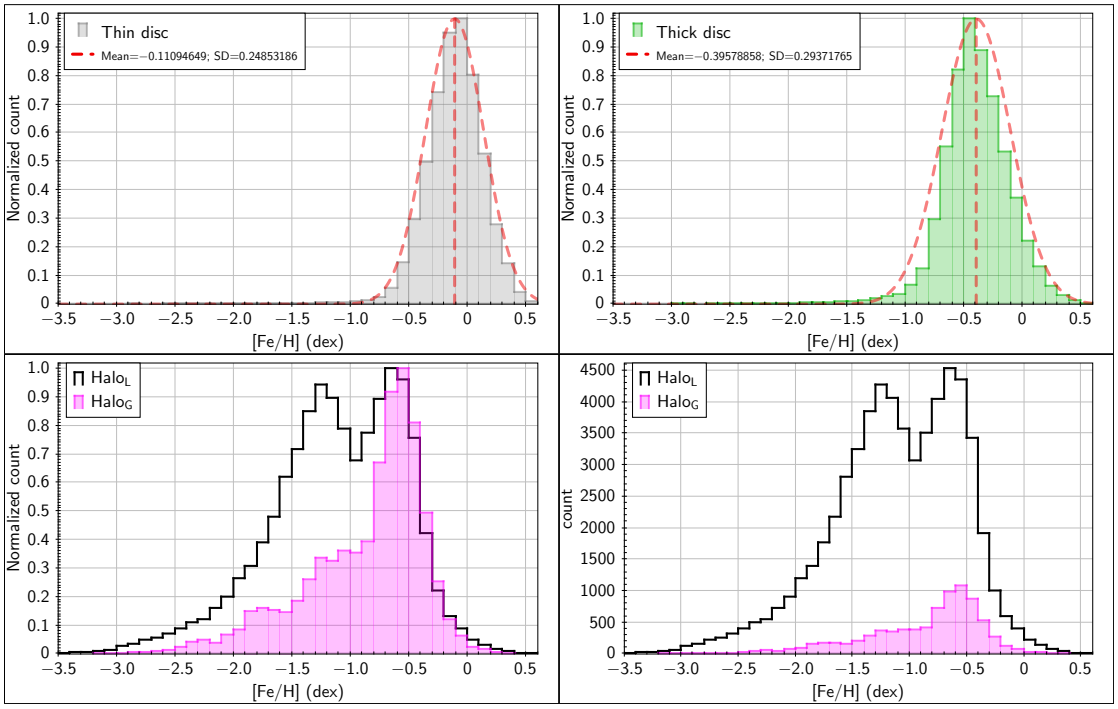


FIGURE 10.5: Top-left and top-right hand panels show the normalized metallicity functions for the selected samples of the thin and thick disc stars, respectively. A single peak Gaussian fit to the metallicity distribution is also shown as the red dotted line for both thin and thick samples. The thin disc sample has a mean [Fe/H] of about -0.111 with a standard deviation (SD) of about 0.248. The thick disc sample has a slightly lower mean [Fe/H] of -0.396 with a SD of 0.294. The normalized metallicity function for the selected samples of halo stars from the LAMOST survey (Halo$_L$) and GALAH survey (Halo$_G$) is shown in the bottom-left panel. Metallicity functions with actual star count in the metallicity bins are shown in the bottom-right panel.

metallicity distribution is not apparent from the Halo$_G$ sample. This is due to the lack of metal-poor stars in the GALAH survey, which primarily covers the Galactic disc stars. Metal-rich stars dominate the halo$_G$ sample. The bottom-left panel of Figure 10.5 shows a comparison of the actual number of halo stars as a function of [Fe/H] in both the halo$_G$ and halo$_L$ sample. As mentioned previously, the halo$_G$ sample is about eight times smaller than sample halo$_L$.

To check for the effects of smaller sample size and lack of metal-poor stars in sample halo$_G$ compared to halo$_L$, in Figure 10.6, we have shown the comparison of the metallicity distributions for all the sub-samples from sample halo$_G$ and

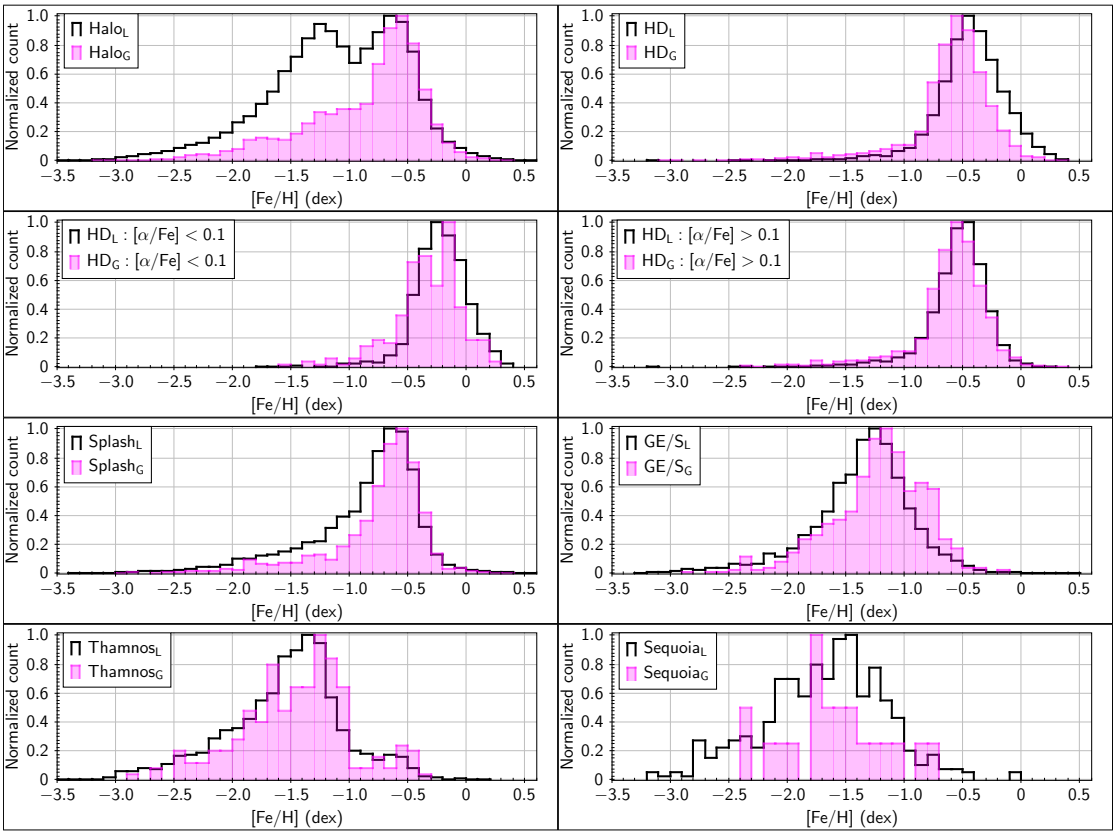


FIGURE 10.6: Metallicity functions for the samples of halo's sub-structures selected from the GALAH and LAMOST survey (shown in magenta and black, respectively). The letters 'L' and 'G' in the sample's subscripts indicate their parent survey name.

halo$_L$. Across the panels in the figure, the metallicity functions for the LAMOST's samples are well defined, considering a sufficiently good number of stars. On the other hand, in the case of samples from the GALAH survey, the distributions are not so well defined due to the very small sample sizes. However, the distribution for samples from both surveys looks approximately similar and also spans similar ranges in [Fe/H]. Hence, even with comparatively fewer stars and a lack of metal-poor stars, the selected samples of halo's substructures are good representative samples and can be further employed to understand the chemical natures of these substructures.

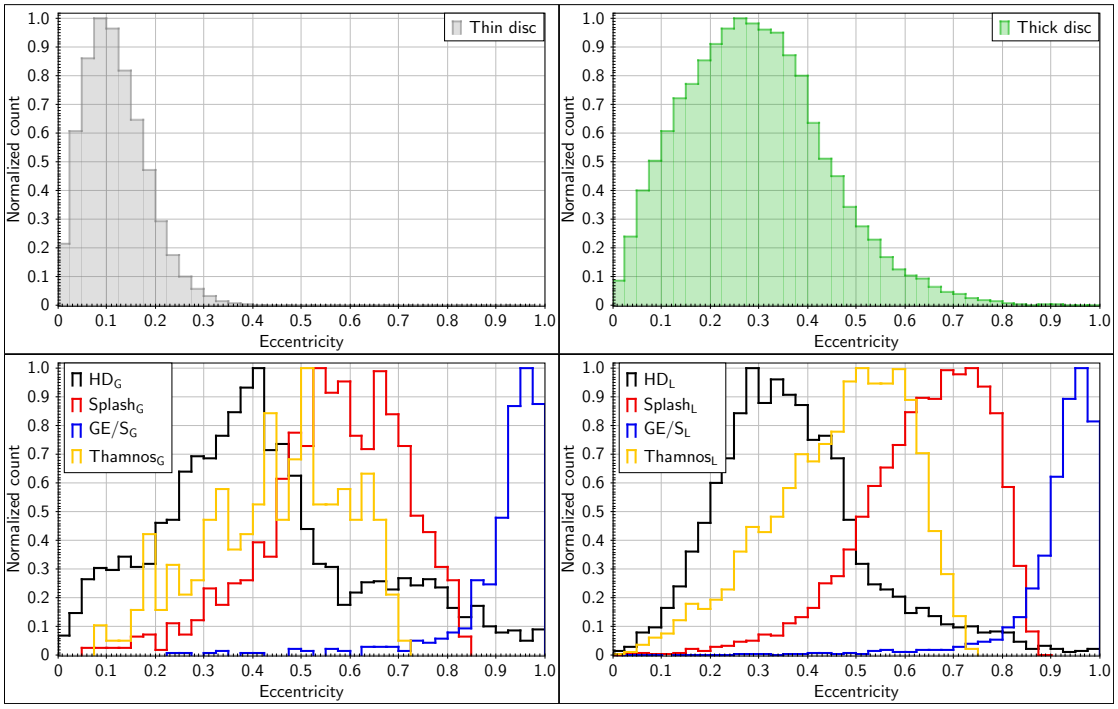


FIGURE 10.7: Orbital eccentricity functions for the thin and thick disc are shown in the top-left and top-right hand panels, respectively. The eccentricity function for the samples of halo's substructures selected from the GALAH and LAMOST surveys is shown in the bottom-left and bottom-right panels, respectively. The letters 'G' and 'L' in the subscript of the samples' names shown in the legends indicate the sample's parent survey.

10.4 Eccentricity functions for the thin disc, thick disc and halo sub-structures

Orbital eccentricity distribution for the sample of the thin and thick disc stars is shown in the top-left and top-right panels of Figure 10.7. The distribution shows that most thin disc stars have approximately circular orbits. Eccentricity distribution for the thin disc stars peaks at about 0.1, with about 42, 71, 88, 96, and 98 per cent of the stars having eccentricity less than about 0.10, 0.15, 0.20, 0.25 and 0.30, respectively. On the other hand, the thick disc stars have slightly more elliptical orbits than the thin disc stars. Their distribution peaks at an eccentricity of about 0.27, with 54, 67, 78, 86, and 91 per cent of the stars having eccentricity less than 0.30, 0.35, 0.40, 0.45, and 0.50, respectively.

Eccentricity distribution for the HD, Splash, Gaia-Enceladus/Sausage, and Thamnos samples selected from the GALAH and LAMOST samples are shown in the bottom-left and bottom-right hand panels, respectively, of Figure 10.7. Due to the relatively small sample size, the histograms for the halo stars samples selected from the GALAH survey are highly distorted. However, considering the distributions' span and apparent peaks, these histograms are roughly in agreement with the histogram for samples from the LAMOST survey, which is about eight times larger in size. The eccentricity distribution for the HD sample is similar to the thick disc sample. For both the thick disc sample and HD_L (i.e., HD sample from the LAMOST survey), the eccentricity distribution peaks at about 0.3, suggesting that both have similar orbitals. Among the four sub-samples of halo stars shown in the figure, GE/S has the highest eccentricity of near unity, so GE/S's stars follow near parabolic orbits. The Splash and Thamnos are also highly elliptical, with peak eccentricity of about 0.70 and 0.55, respectively.

10.5 Stellar ages of the thin disc, thick disc and halo's sub-structures

Stellar ages are estimated using *qoyllur-quipu* code ($\texttt{q}^2$; Ramírez *et al.* 2014), as described in Section 2.2.4. For these calculations, we used stars' distance from the *Gaia* DR2 survey and spectroscopic parameters (like stellar parameters, metallicity, [α/Fe], etc.) from the GALAH DR3 survey. The estimated ages are more reliable for main sequence (MS) and MS turn-off stars due to comparatively well-resolved isochrones during these phases. Hence, for discussion on age, we restrict our samples to stars with *Gaia*'s absolute *G*-band magnitude higher than three. Stars' absolute *G*-band magnitudes are estimated based on *Gaia*'s apparent *G*-band magnitude (provided in column `phot_g_mean_mag`) and parallax using the relation 9.2. These magnitudes are also corrected for extinction. For this *G*-band

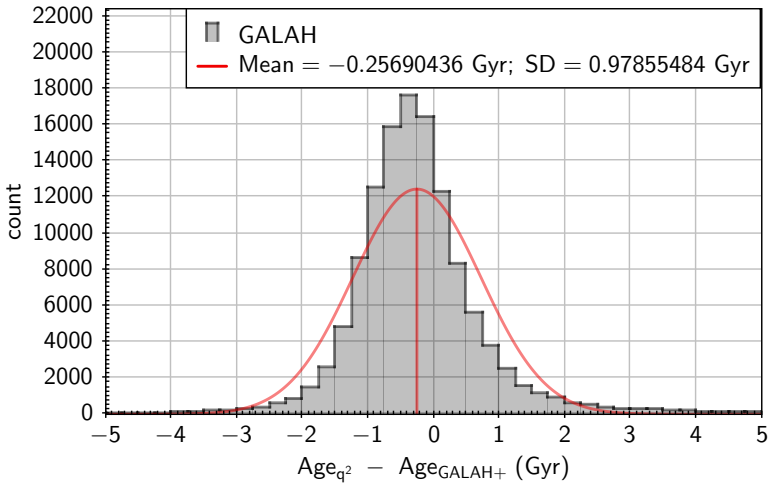


FIGURE 10.8: Comparison of stellar ages determined in this study using $\mathfrak{q}^2$ and ages provided along with the third data release of the GALAH survey. A single peak Gaussian fit, with mean ≈ -0.2569 Gyr and SD ≈ 0.9786 Gyr is also shown in red.

extinction (A_G) is calculated based on the V-band extinction from the GALAH DR3 catalogue using the recipe introduced in Danielski *et al.* (2018) and implemented by Gaia Collaboration *et al.* (2018a). To further remove stars with dubious ages, we restricted our samples to stars with standard error in age ($\sigma_{\rm Age}$) less than 2 Gyr.

The third data release of the GALAH survey also includes stellar ages estimated using Bayesian Stellar Parameter Estimation code (BSTEP, Sharma *et al.* 2018). Similar to our age estimates, the GALAH's age estimates also suffer from accuracy issues for giants. However, as shown in Figure 10.8, for MS and MS turn-off stars (selected with *Gaia*'s absolute G-band magnitude higher than three), these two age estimates are in good agreement. The mean difference in these two age estimates is about 0.26 Gyr with a standard deviation of about 0.98 Gyr.

Age distribution for the Galactic thin and thick disc is shown in the top-left and top-right panel of Figure 10.9. As can be readily seen from the figure, the thin disc is comparatively very young, with the distribution function peaking at about 5 Gyr. About 60 per cent of the thin-disc stars have ages between 3 to 7 Gyr,

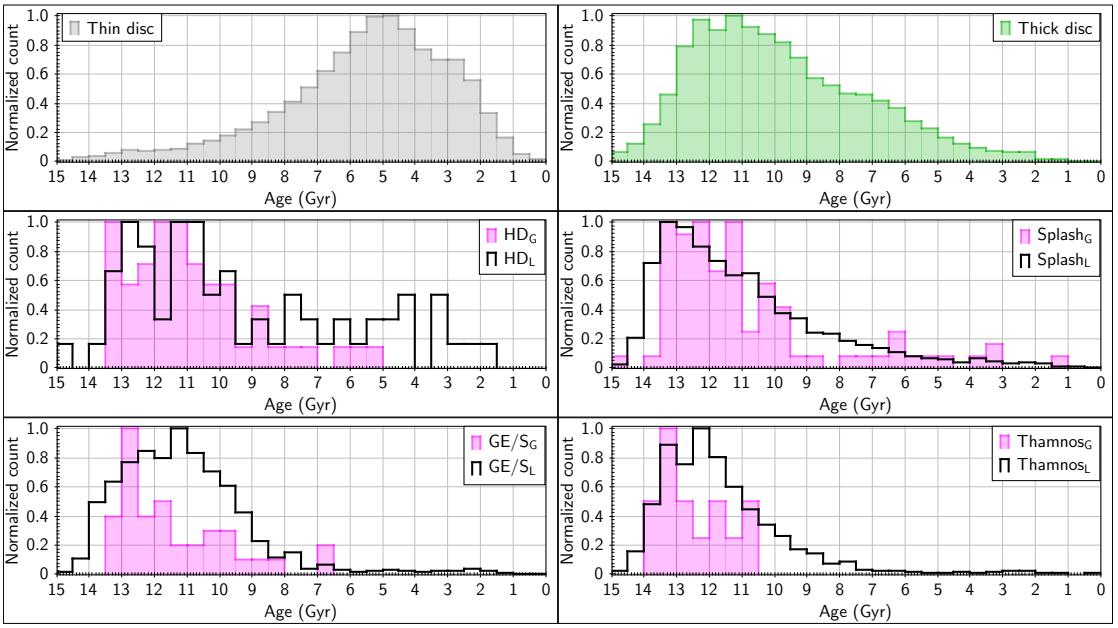


FIGURE 10.9: Age functions for the thin disc (top-left panel) and the thick disc (top-right panel). The bottom two rows show the age function for four major substructures in the selected samples of halo stars from the GALAH and LAMOST surveys shown in the filled magenta histogram and black histograms, respectively. The letter 'G' and 'L' in the subscript of the sample's name stands for GALAH and LAMOST survey and indicates the parent survey from which samples are withdrawn.

while 80 per cent of thin-disc stars have ages between 2 to 8 Gyr. A few of the thin disc stars are as old as the Universe itself (i.e. about 14 Gyr old), suggesting the star formation in the Galactic disc started at the earliest stage of the Galaxy formation (i.e. about 14). The age distribution for the thin disc is also not symmetric about the peak value. As we move towards the higher age end from the peak value, the distribution resembles an exponentially decreasing function. However, on the younger age side, the distribution is approximately linear. This suggests that the star formation in the thin disc has been going on from the time Galaxy was formed about 14 Gyr ago. During the initial years, the rate of star formation was very low, but it exponentially increased until peak star formation about 5 Gyr ago. However, since the last five Gyr, after reaching the peak of star formation, the rate of newly formed stars appears to be decreasing almost linearly with time. One of the possible reasons for the drop in star formation rate is a relative drop in the availability of the raw material (i.e. dust and gas) and other

favourable conditions required to form new stars. However, it is to be noted that the age for some of the thin disc stars is even less than a Gyr, suggesting star formation in the thin disc is still going on.

The thick disc population, as shown in the top-right panel of Figure 10.9, has a peak age of about 11.50 Gyr. About 57 per cent of the thick-disc stars have ages between 9.50 to 13.50 Gyr, while about 71 per cent of the thick-disc stars has ages between 8.50 to 14.50 Gyr. Also, about 94 per cent of the thick-disc stars are older than the thin disc's peak age of 5 Gyr. Similar to the thin disc, the age distribution of the thick disc is also not symmetric about the peak of the distribution at 11.50 Gyr. However, in contrast to the thin disc, the distribution for the thick disc falls very rapidly as we move towards the higher age from the peak but falls very slowly with an elongated tale for the younger stars. This suggests that the star formation in the thick disc started early on with the formation of the Galaxy. Also, in the starting, the star formation increased very rapidly with time and peaked at about 11.50 Gyr ago. However, since then, the star formations in the thick disc is decreasing slowly but continuously.

The age distribution function for the Galactic halo's population HD, Splash, GE/S and Thamnos are shown in the bottom two rows of Figure 10.9. Distributions are shown for samples selected from the GALAH survey (in magenta) as well as from the LAMOST survey (in black). The histograms for the samples selected from the GALAH data are not well-defined due to the relatively small sample size; however, these histograms roughly agree well with the histograms for the corresponding sample from the LAMOST data. All four halo populations are relatively old. The presence of a slowly decreasing tale of young stars in HD and Splash samples and total span in age similar to the thick disc suggest that these two halo populations have experienced star formation histories similar to the thick disc. However, HD and Splash appear to have run out of raw material to continue this accelerated formation of new stars and hence attained peak star formation earlier than the

thick disc. The age distribution for the GE/S and Thamnos suggests that these two populations also experienced peak star formation around the same time when the star formation peaked in the thick disc. However, unlike the thick disc, the star formation in the GE/S and Thamnos ceased very rapidly. This is evident from the fact that more than 90 per cent of stars in GE/S and Thamnos are older than 9 Gyr, while only about 66 per cent of the thick disc are older than 9 Gyr.

10.6 Chemical compositions of the thin disc, thick disc, and components of the Galactic halo: Abundances of the α-process elements

To further find clues about the origin and differences in the evolution of the Galactic disc's and halo's components, we search for the differences in their abundance ratios [X/Fe]. In this work, we restrict our analysis to α-process element O, Mg, Si, Ca and Ti, and lithium (discussed later in Section 10.7). A run for [X/Fe] as a function of [Fe/H] for all the five α-process elements (with X = O, Mg, Si, Ca, and Ti) for the selected samples of the thin disc, thick disc and five major components of the Galactic halo is shown in Figure 10.10. (For simplicity, hereafter, we refer to the abundance ratio [X/Fe] for all the five α-process elements as [α/Fe].) Selection for each chemical species is made separately, and only the stars with the most reliable abundance measurements are considered. For example, in a plot for abundance ratio [X/Y], only the stars with abundance flag `flag_X_fe` = 0 and `flag_Y_fe` = 0 are plotted. Also, for ease in identifying the regions where most of the stars are located, we have shown the number density distributions with a 'rainbow' colour scheme in which red represents the highest number density while dark violet (or black) represents the lowest number density. The number density distribution is shown for all components except for the Thamnos and Sequoia due

to their relatively smaller samples. The figure readily suggests that for a given kinematic group (i.e., thin disc, thick disc or any of the halo's components), all the α-process elements follow a similar abundance trend due to shared production sites. (Small differences, if any exist, are primarily due to non-uniform samples across the five α-elements.) On the other hand, the variation in abundance trend for a particular chemical element among different Galaxy components indicates different chemical history (see Figure 10.10).

The thin disc stars have the highest value of abundance ratio [α/Fe] for all five α-elements in the metal-poor region and follow a decreasing trend in [α/Fe] with an increase in [Fe/H]. The metal-poor thin disc stars also have the largest scatter in [α/Fe]. At solar metallicity (i.e., [Fe/H] = 0), the mean abundance of α-elements in the thin disc is approximately the same as in the Sun, i.e. [α/Fe] $\approx$ 0. The thick disc, on the other hand, has a very distinct [α/Fe] distribution compared to the thin disc. The metal-poor thick disc stars (with [Fe/H] $\lessapprox$ -0.5) have a mean [α/Fe] of about 0.3 dex. However, the scatter in [α/Fe] distribution for the metal-poor thick disc stars also increases with an increase in [Fe/H]. For example, the total scatter in [Mg/Fe] for the thick disc stars at [Fe/H] of -2.0 and -0.5 is about 0.5 and 1.2, respectively. In the metal-rich region (with [Fe/H] > -0.5), the thick disc follows a decreasing trend in [α/Fe] abundances with an increase in [Fe/H], and also has approximately constant scatter in [α/Fe]. At solar metallicity, the mean [α/Fe] for the thick disc is slightly higher than the thin disc. For example, at [Fe/H] =0, the mean [Mg/Fe] for the thin disc is about 0.1 dex, which is about 0.1 dex higher than the mean [Mg/Fe] of the thin disc.

As can be seen from Figure 10.10, the [α/Fe] abundance of the HD and Splash are similar to the thick disc. However, unlike the thick disc, both HD and Splash lack metal-rich stars with lower [α/Fe] abundance. A comparison of [Mg/Fe] in the HD, Splash and the thick disc is provided in the top-left panel of Figure 10.11. At [Fe/H] = -0.5, both HD and Splash have a mean [Mg/Fe] of about 0.3 dex, which is

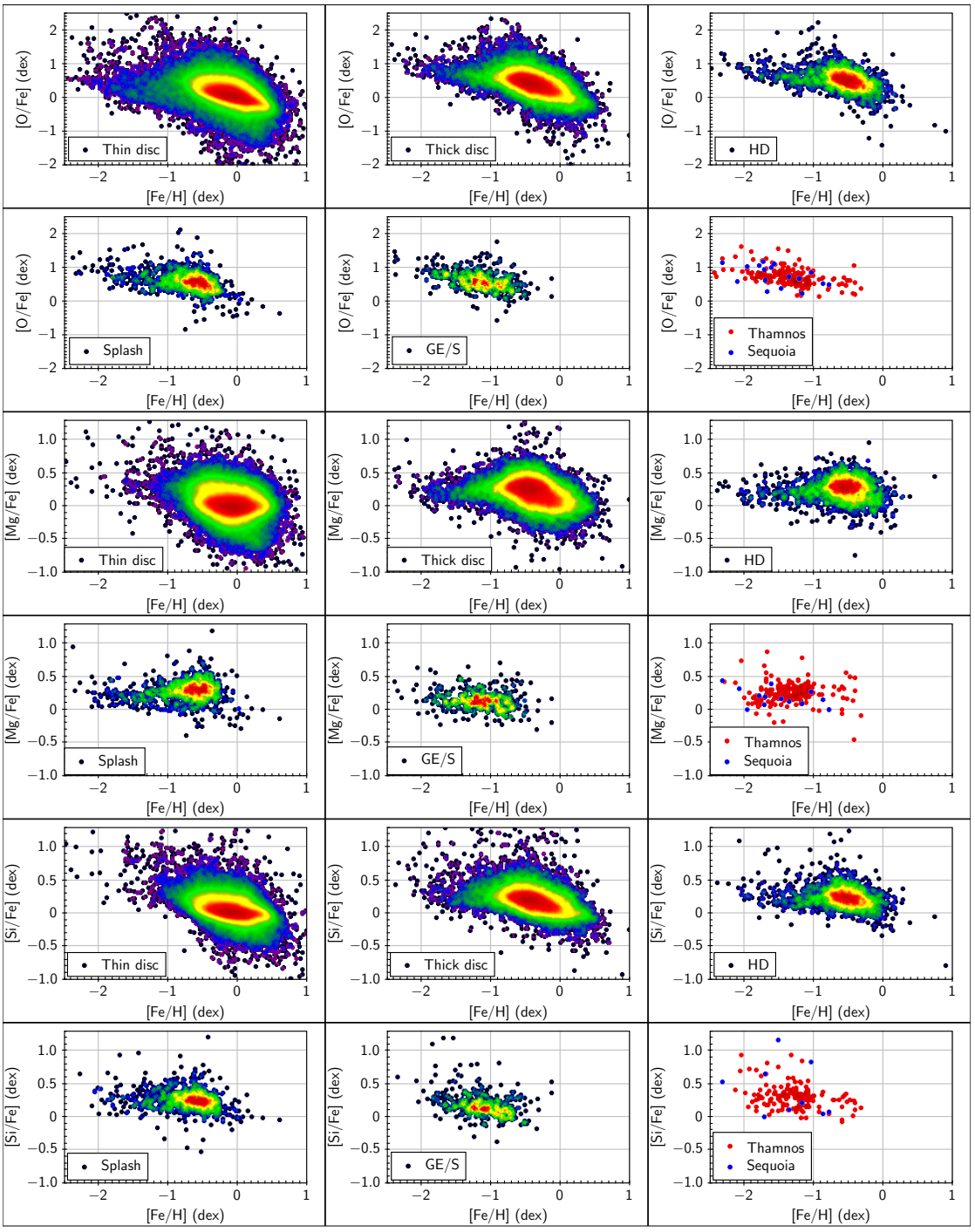


FIGURE 10.10: Abundance ratio [X/Fe] as a function of [Fe/H] for α-process elements O, Mg, Si, Ca and Ti provided in the GALAH DR3 survey for selected samples of the thin and thick disc along with five major substructures in the halo. All the stars shown here have measured abundances in the GALAH DR3 survey and are selected using `flag_X_fe` = 0. For example, a plot for abundance ratio [X/Y] includes only the stars with abundance flag `flag_X_fe` = 0 and `flag_Y_fe` = 0. Except in the case of the Thamnos and Sequoia, plots show density distribution with 'rainbow' as the adopted colour scheme in which red represents the highest density while dark violet (or black) represents the lowest density.

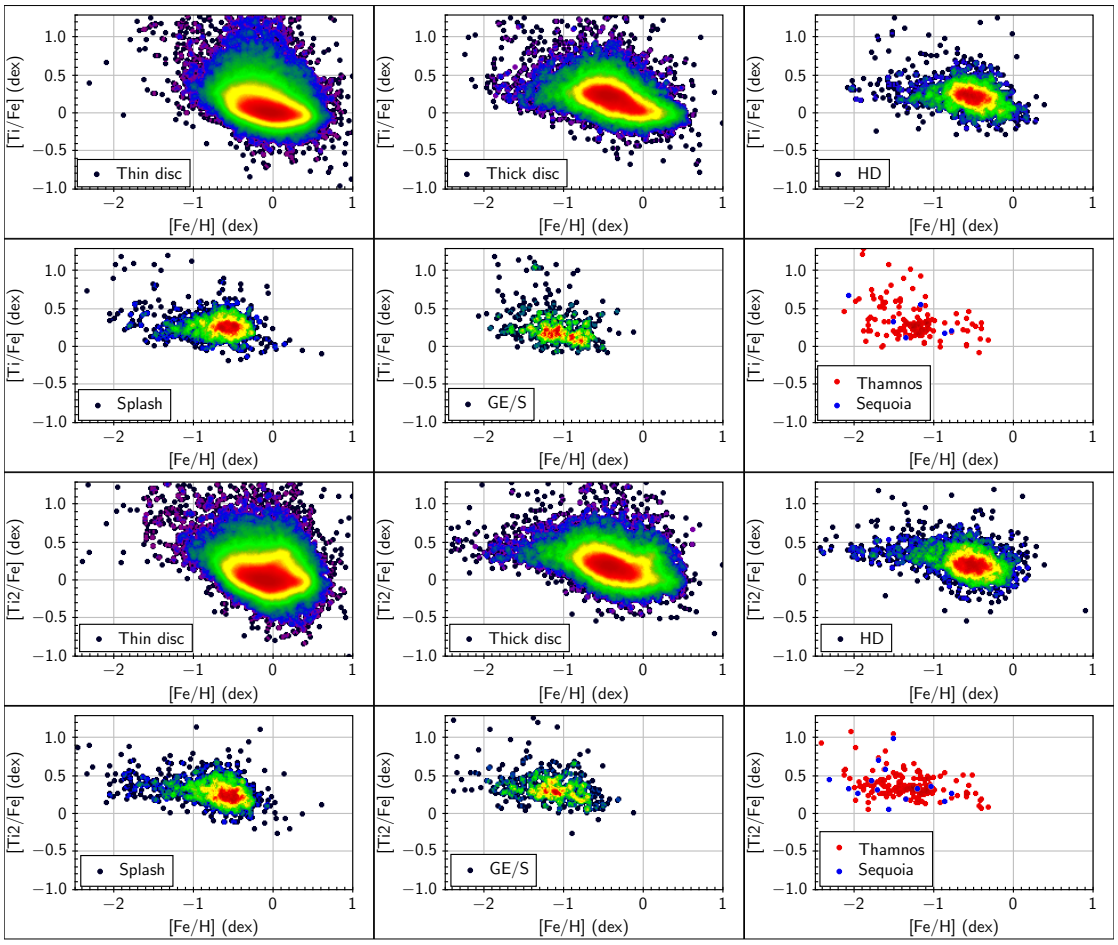


Figure 10.10 - *continued*

the same as the mean [Mg/Fe] for the thick disc at this sub-solar metallicity. The α-abundances of the Thamnos are also similar to the HD and Splash. It also lacks metal-rich stars with lower [α/Fe]. A comparison of [Mg/Fe] in the Thamnos, HD and Splash is shown in the bottom-left panel of Figure 10.11. The Thamnos has a mean [Mg/Fe] of about 0.25 dex at its peak [Fe/H] of -1.36 (Table 9.1).

The GE/S, along with the Sequoia, have distinct distribution of [α/Fe] abundances compared to the other selected components of the Galactic disc and halo (Figure 10.10). Unlike the thick disc, HD, Splash and Thamnos, the GE/S and Sequoia follow a decreasing trend in [α/Fe] abundance in the metal-poor region also. Comparisons of [Mg/Fe] abundances of GE/S and Sequoia with halo's prograde components (HD and Splash) and the thick disc are shown in the right-hand

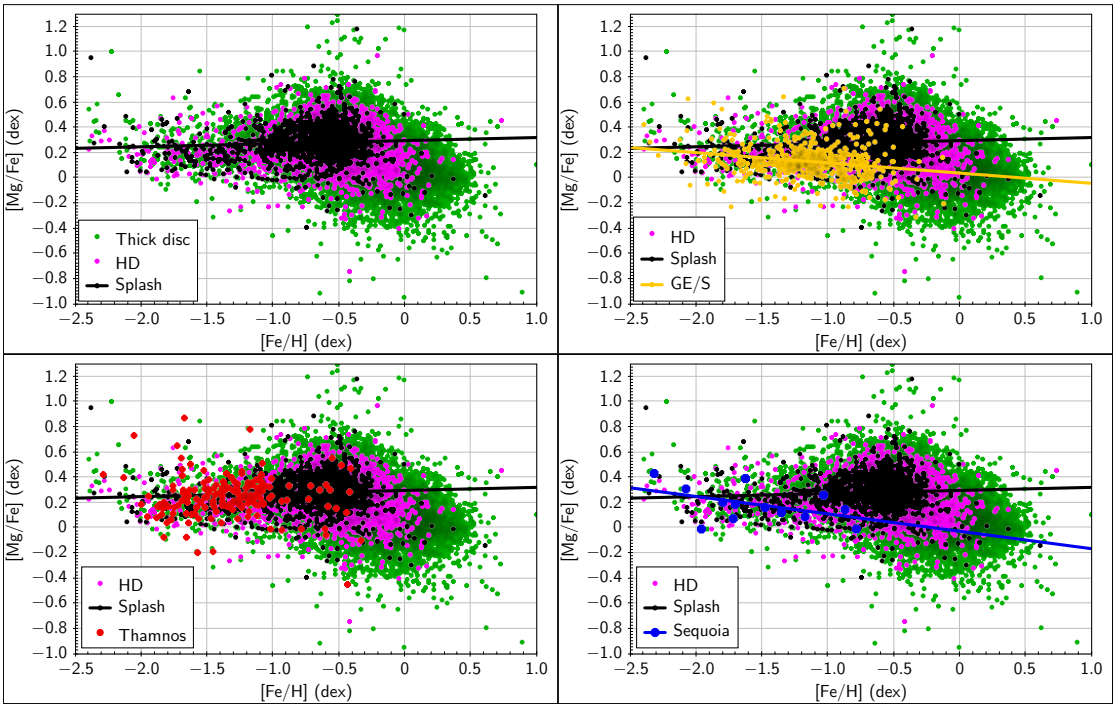


FIGURE 10.11: Abundance ratio [Mg/Fe] as a function of [Fe/H] for selected samples of the thick disc and five major substructures in the halo. All the stars shown here have measured Mg and Fe abundances in the GALAH DR3 survey and are selected using `flag_mg_fe` = 0 and `flag_fe_h` = 0. The linear fits to the Splash, GE/S and Sequoia are shown as the black, yellow and blue lines, respectively.

panels of Figure 10.11. The figure clearly suggests that at lower metallicity, both GE/S and Sequoia have the same mean [Mg/Fe] as in HD, Splash and thick disc. At [Fe/H] of about -2.0, both GE/S and Sequoia have a mean [Mg/Fe] of about 0.2 dex, which is the same as the mean [Mg/Fe] in the HD, Splash and thick disc at this metallicity. However, at [Fe/H] of -1.0, the mean [Mg/Fe] in the GE/S and Sequoia is about 0.1 dex, which is about 0.15 dex lower than the mean [Mg/Fe] of about 0.25 dex in the HD, Splash and thick disc.

10.6.1 Insights into the formation of different Galactic components based on [α/Fe] trends

The amount of α-process elements relative to iron in the thin disc, which is also the youngest among the Galactic disc and halo components, follows a decreasing trend with an increase in iron. As discussed previously in Section 1.5, the exploding high-mass stars as Type II supernovae (SNII) are primary contributors of the α-process elements. On the other hand, the exploding low-mass stars as Type Ia supernovae (SNIa) contribute most of the iron peak elements. Hence, the decreasing trend in [α/Fe] as a function of an increase in [Fe/H] suggests an increase in the rate of SNIa compared to SNII in the Galactic thin disc. The initial higher [α/Fe] in metal-poor thin-disc stars is understood to be due to a higher rate of SNII earlier times in the inner region of the Galaxy (e.g. Edvardsson *et al.* 1993; Reddy *et al.* 2003, and references therein), which resulted in enrichment of ISM with α-elements before the star formation in the thin disc peaked about 5 Gyr ago (Figure 10.9). The presence of a large scatter in [α/Fe] abundance for the metal-poor thin-disc stars suggested a poorly mixed gas at the time of formation of these metal-poor stars. Some of these stars, however, may be younger and have originated from the Galactic bulge, which is known to have stars with a wide range in metallicity and α abundances. Further studies of other chemical species covering light elements and neutron-capture elements are needed to find the contribution of poorly mixed gas and the Galactic bulge towards the large scatter in [α/Fe] abundances in metal-poor thin-disc stars.

Unlike the thin disc, the thick disc has a more complex distribution of [α/Fe] abundances (Figure 10.10). In the [Fe/H] range from about -2.5 to -0.5 dex, the maximum [Mg/Fe] at a given [Fe/H] increases with an increase in [Fe/H], suggesting dominating contribution of α-process elements from the SNII. Also, in this metallicity range, the total spread in [Mg/Fe] at a given [Fe/H] is also increasing with an increase in [Fe/H], suggesting the α-elements contribution from

SNII was not uniform throughout the Galaxy, and the gas was poorly mixed during the formation of the thick disc. For [Fe/H] > -0.5 dex, the decreasing trend in [Mg/Fe] with respect to an increase in [Fe/H] gives rise to the well-known knee-like distribution for the thick disk and suggests dominating contribution of iron from SNIa at the later stage of thick disk formation. These trends are in agreement with previous studies, for example, Edvardsson *et al.* (1993); Reddy *et al.* (2006). The thin disk is understood to have formed during the merger of a gas-rich system with the progenitor of the Milky Way about 10 Gyr ago (e.g., see Haywood *et al.* 2018; Hayes *et al.* 2018; Helmi *et al.* 2018; Gallart *et al.* 2019; Koppelman *et al.* 2019; Belokurov *et al.* 2020, and references therein). The retrograde component HD and Splash, having [α/Fe] abundances similar to the thick disc (except lack of α-poor stars), are also believed to have originated during this or a same or a similar merging event (Belokurov *et al.* 2020). The GE/S is the largest accreted component in the Galactic halos and is known to be the remnant of the last merger in the Milky Way's history and has a progenitor mass of about one-fourth of the mass of Milky Way's progenitor. As shown in Figure 10.11, the decreasing [Mg/Fe] as a function of [Fe/H] for the GE/S suggest that it GE/S has undergone a distinct chemical evolution than the Milky Way's thick disk and other *in situ* components like the HD and Splash. The [α/Fe] abundance distribution for the Sequoia is similar to the GE/S, suggesting the progenitors of both has undergone similar chemical histories. On the other hand, [α/Fe] abundance trends of the Thamnos (which is also believed to be a remnant of a dwarfs galaxy) are similar to the Milky Way's *situ* components like HD and Splash, and suggest that not all the dwarf galaxies which merged with the Milky Way's progenitors had similar chemical evolution. To understand their chemical evolution in more detail, we need to further study the full spectrum of chemical elements provided in the GALAH survey to cover different nucleosynthetic processes.

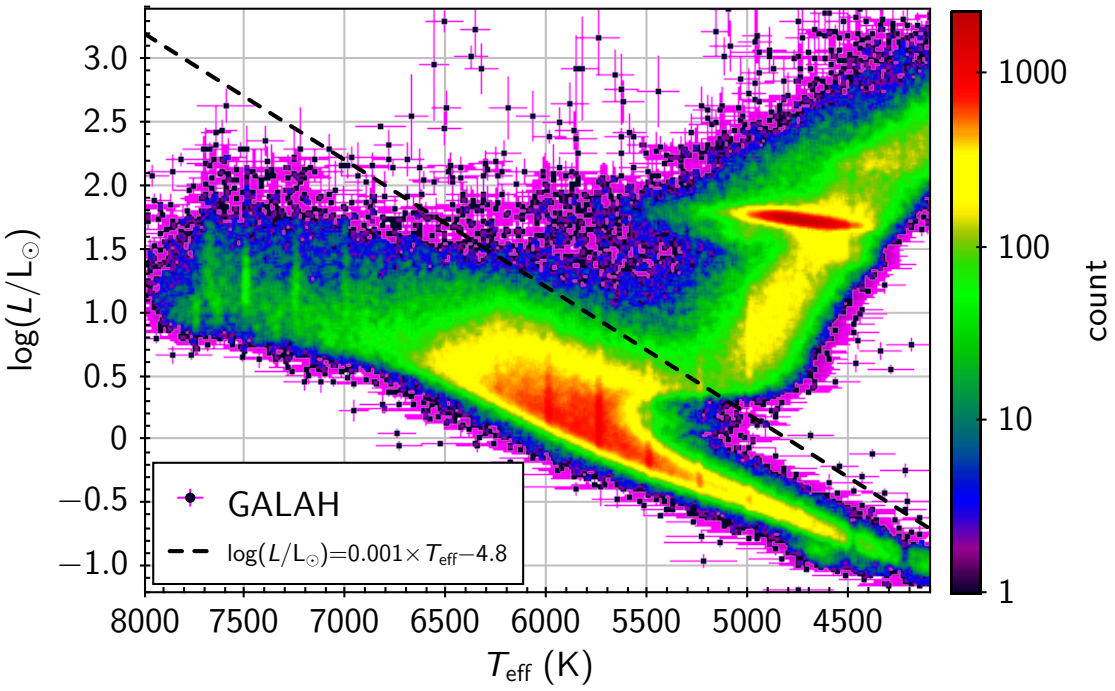


FIGURE 10.12: The HR diagram for the selected sample of stars from the GALAH DR3 survey. Uncertainty in luminosity and temperature are plotted in the background as magenta error bars for all the stars. The dotted-black line $\log(L/L_\odot) = 0.001 \times T_{\rm eff} - 4.8$ marks the approximate separation between dwarfs (below the line) from giants (above the line). These dwarfs are further used to understand the distribution of Li in the Galactic disc and the various substructures in the Galactic halo.

10.7 Lithium abundance across the components of the Galactic halo and disc

As discussed previously in Chapter 3, Li is another interesting element to look into the evolution of different components of the Galaxy. One of the burning questions about the evolution of Li is if it is constant across the components of the Galactic halo and how it is evolving in these components compared to the components of the Galactic disc. In Chapter 3, we studied Li's Galactic evolution based on its distribution in the Toomre diagram and also its variation as a function of metallicity. However, this study uses more well-defined samples of the disc and halo components based on stars' kinematics. For this study, we restrict

our selection to dwarf stars as Li in the atmosphere of these stars is known to represent the original Li of the natal gas cloud from which these stars are formed. Selection of the dwarf stars is shown in Figure 10.12, where the entire GALAH sample is plotted in luminosity-$T_{\rm eff}$ plane and stars below the dotted-black line $\log(L/\mathrm{L}_{\odot}) = 0.001 \times T_{\rm eff} - 4.8$ are selected as the dwarf. The same criteria are applied for selecting sub-samples of dwarfs from our selected samples of the thin disc, thick disc, and halo components.

The distribution of Li as a function of metallicity for the Galactic disc and halo's components is shown in Figure 10.13. Except in the case of the Thamons and Sequoia, plots show density distribution with a 'rainbow' colour scheme in which red represents the highest number density while dark violet (or black) represents the lowest number density. Thamnos and Sequoia's stars are shown as filled red circles and blue squares in the bottom-right panel, respectively. Also, for each of the stars, the error in Li abundance A(Li) and metallicity [Fe/H] are shown in the background as cyan-coloured error bars. Below we discuss some of the results from these plots.

10.7.1 Li in the Galactic thin and thick disc

The distribution of Li as a function of [Fe/H] for the thin and thick disc dwarfs is shown in the top-left and top-right panels of Figure 10.13. On a visual inspection of the two panels, the spread appears slightly larger for the thin disc sample compared to the thick disc sample due to the large difference in sample size (the sample of thin disc dwarfs with measured Li abundances is about 26 times larger than the thick disc sample). However, both thin and thick disc samples have approximately similar spread in Li abundances. The spread is dependent on metallicity and increases with an increase in metallicity with a maximum in super-solar metallicities. Also, as can be seen from the figure, the number of stars at super-solar metallicity

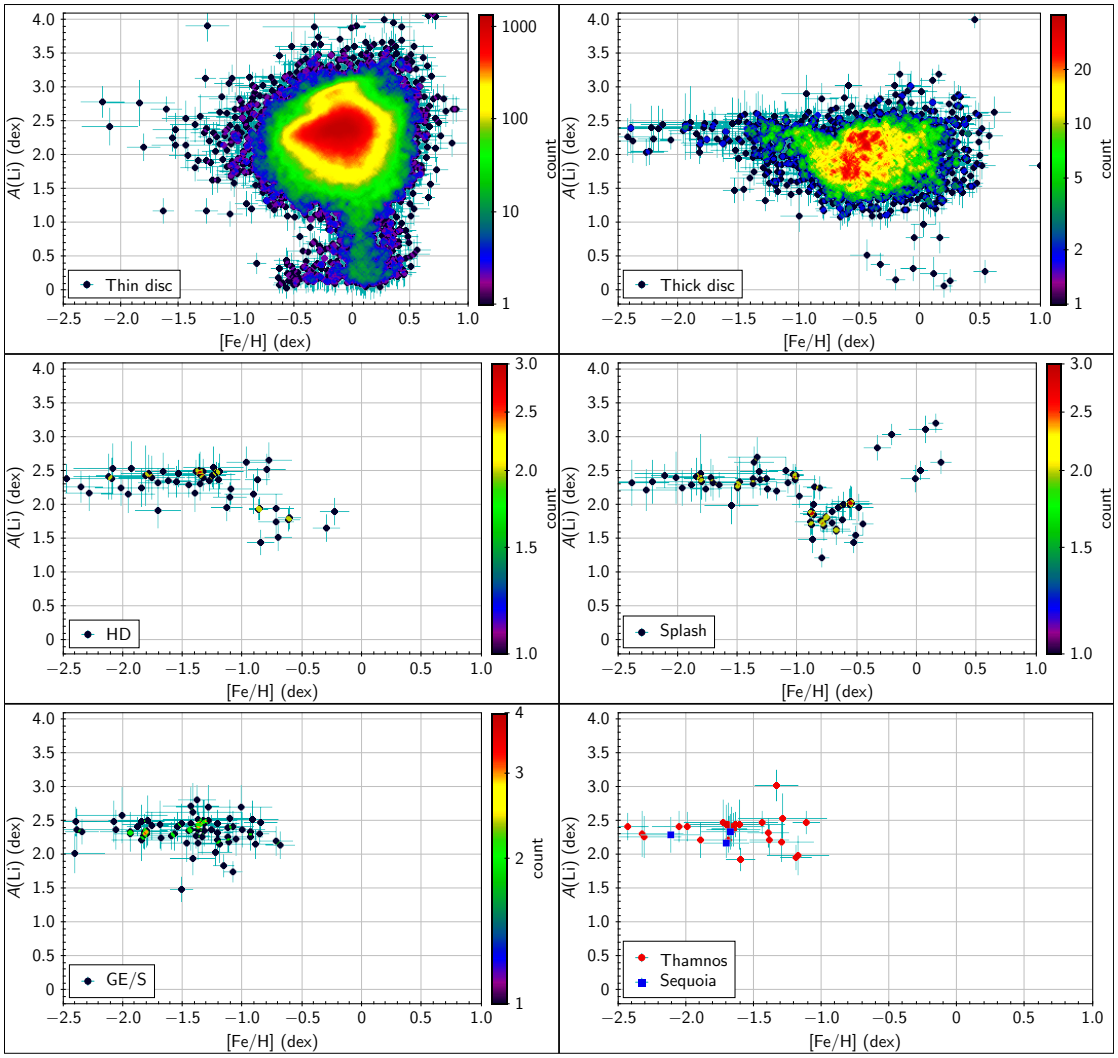


FIGURE 10.13: Distribution of lithium abundance A(Li) as a function of metallicity for dwarfs of the thin and thick disc are shown in the top-left and top-right panels, respectively. The bottom two rows show the distribution of Li abundance as a function of metallicity for substructures in the Galactic halo. For each of the stars, the error in Li abundance A(Li) and metallicity [Fe/H] are also shown in the background using cyan-coloured error bars. Except in the case of the Thamnos and Sequoia, plots show density distribution with a 'rainbow' colour scheme in which red represents the highest density while dark violet (or black) represents the lowest density. Thamnos and Sequoia's stars are shown in the bottom-right panel as filled red circles and blue squares, respectively. All the shown stars have measured Li abundance in the GALAH DR3 survey.

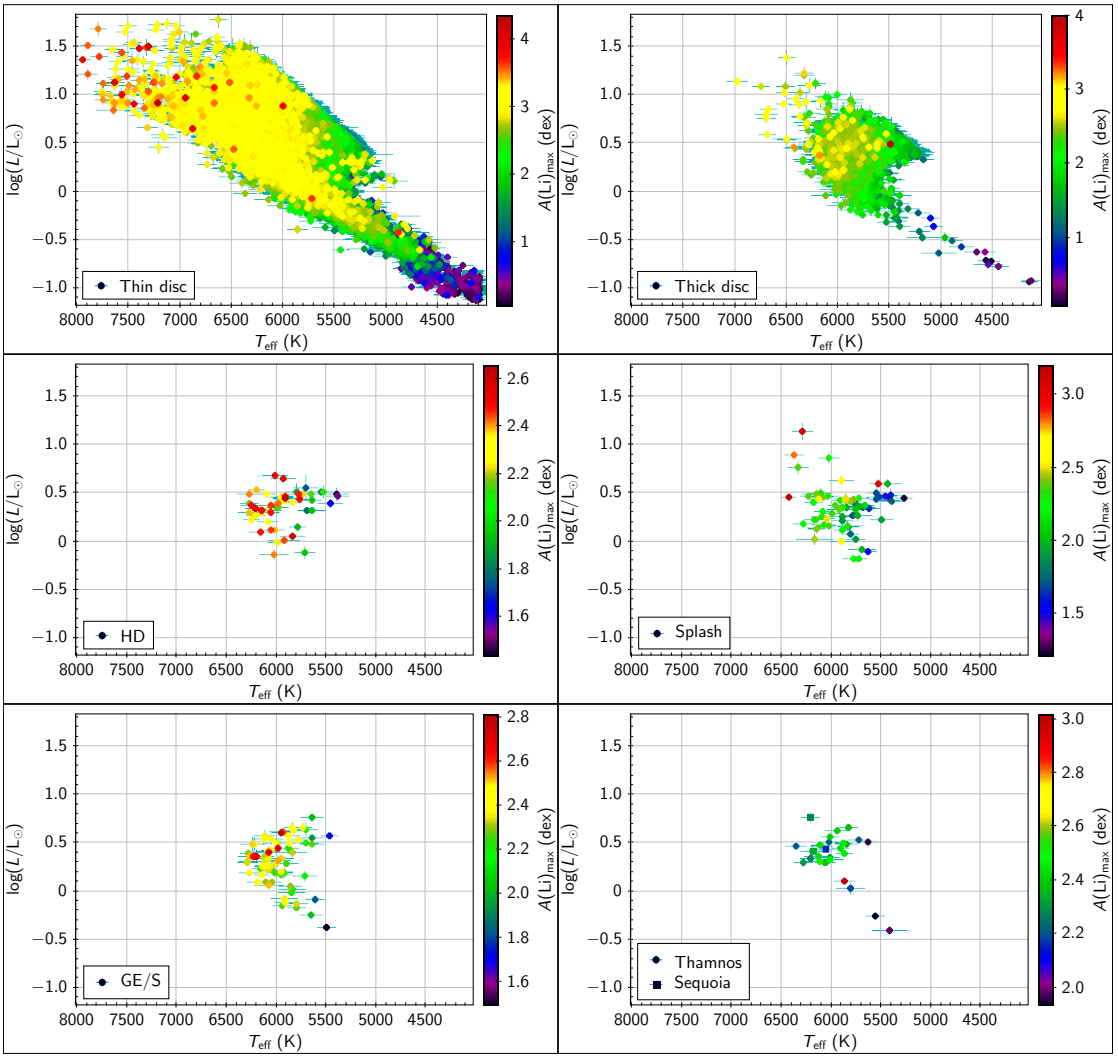


FIGURE 10.14: Top-left and top-right panels show the distribution of the thin and thick disc dwarfs in luminosity versus temperature plane. The bottom two rows show the distribution of the halo's substructures in the luminosity versus temperature plane. In each case, maximum Li abundance at a pixel is encoded in the data point's colour using a 'rainbow' colour scheme. The amount of Li corresponding to each colour is provided in the colour bar. For each star, errors in the luminosity and temperature are also shown in the background using cyan-coloured error bars. All the shown stars have measured Li abundance in the GALAH DR3 survey.

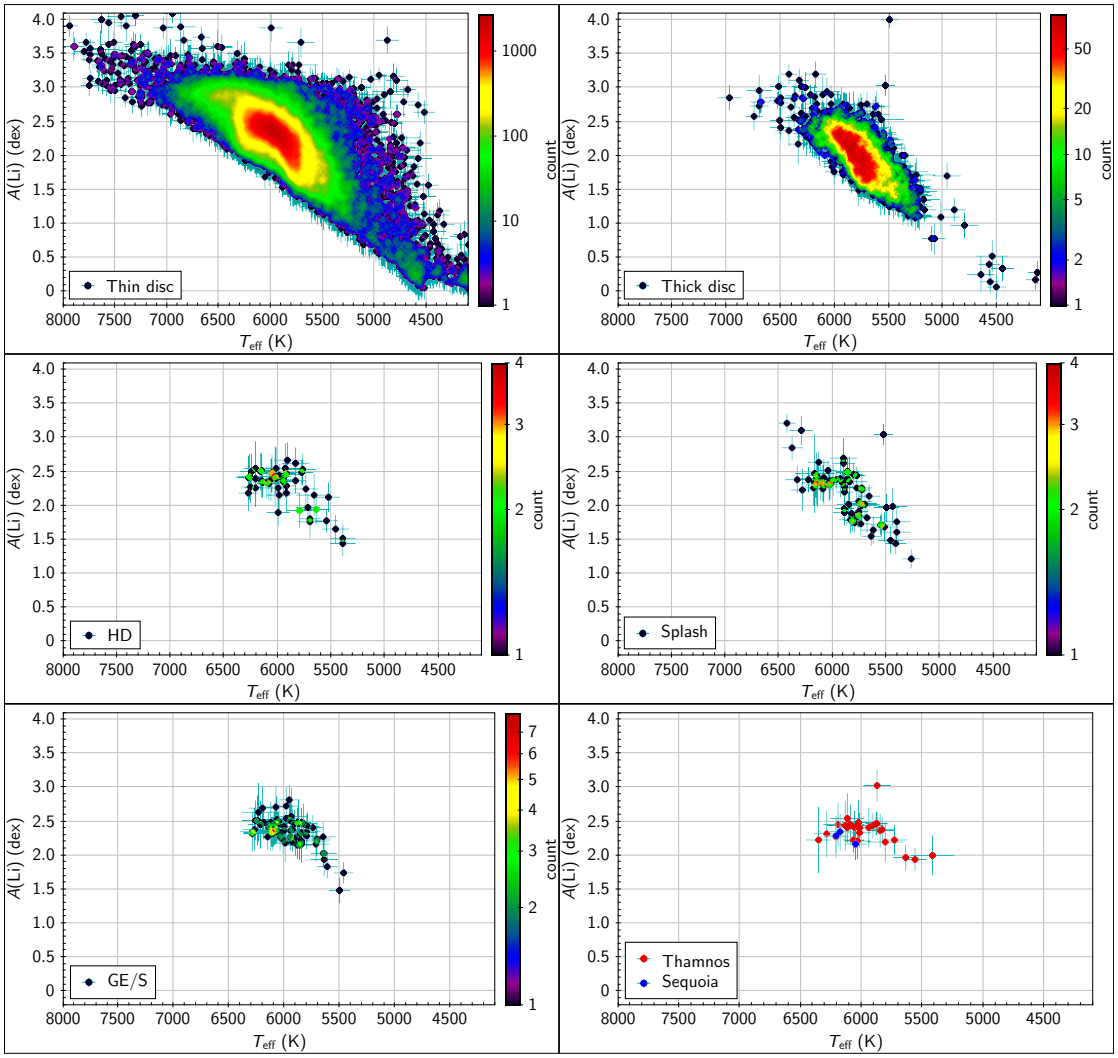


FIGURE 10.15: The top-left and top-right panels show the distribution of Li abundance as a function of surface brightness temperature for dwarfs of the thin and thick disc, respectively. The bottom two rows show distributions for dwarfs in the Galactic halo's substructures. For each star, errors in the A(Li) and temperature are also shown in the background using cyan-coloured error bars. Except in the case of the Thamnos and Sequoia, plots show density distribution with a 'rainbow' colour scheme in which red represents the highest density while dark violet (or black) represents the lowest density. The Thamnos and Sequoia's stars are shown in the bottom-right panel as filled red circles and blue squares, respectively. All the shown stars have measured Li abundance in the GALAH DR3 survey.

is lower than the solar and sub-solar metallicities, suggesting this spread in Li abundance is not due to sampling bias. The majority of thin disc stars in the sub-solar metallicity region with [Fe/H] from -0.5 to 0.5 have A(Li) of about 1.8 to 2.8 dex with a mean value of about 2.3 dex. On the other hand, the majority of the thick stars have [Fe/H] of about -1.0 to 0.0 dex with A(Li) ranging from 1.5 to 2.0 dex and mean A(Li) of about 2.0, which is lower than the mean A(Li) for the thin disc.

One of the distribution features in these plots is the extended tail consisting of stars with low Li abundance in the sub-solar metallicity region. To find the reason behind the relatively lower Li in these stars, as shown in Figure 10.14, we plotted the samples in the form of the HRD with the colour of data point representing the maximum Li abundance. The 'rainbow' colour scheme is used in which red represents the highest Li abundance while dark violet (or black) represents the lowest Li abundance. As expected, the figure suggests a positive correlation between stars' Li abundance and surface brightness temperature. All the cool dwarfs have very low Li abundance. To more clearly see the relation between Li abundance and temperature, in Figure 10.15, we have shown the distribution of Li as a function of surface brightness temperature for dwarfs of the thin and thick disc. Similar to Figure 10.12, this figure also suggests that all the low Li stars are cool dwarfs and measured Li abundance in these stars decreases with further decrease in temperature. Low Li in these cool dwarf stars is believed to be due to pre-main-sequence depletion (e.g., Xiong and Deng 2009, and references therein).

Another surprising result from the panels for the thin and thick disc in Figure 10.13 to 10.15 is the presence of dwarfs with A(Li) $\gtrapprox$ 3.2 dex. Of the total 87747 and 3282 dwarfs stars with measured Li abundance in the thin and thick disc samples, 176 and 2 dwarfs, respectively, have A(Li) higher than 3.2 dex. The majority of these dwarfs with unexpectedly higher Li are hot dwarfs with $T_{\rm eff} >$ 6500 K; however, a few of these are also cool G and K type dwarfs with $T_{\rm eff} < 6000$

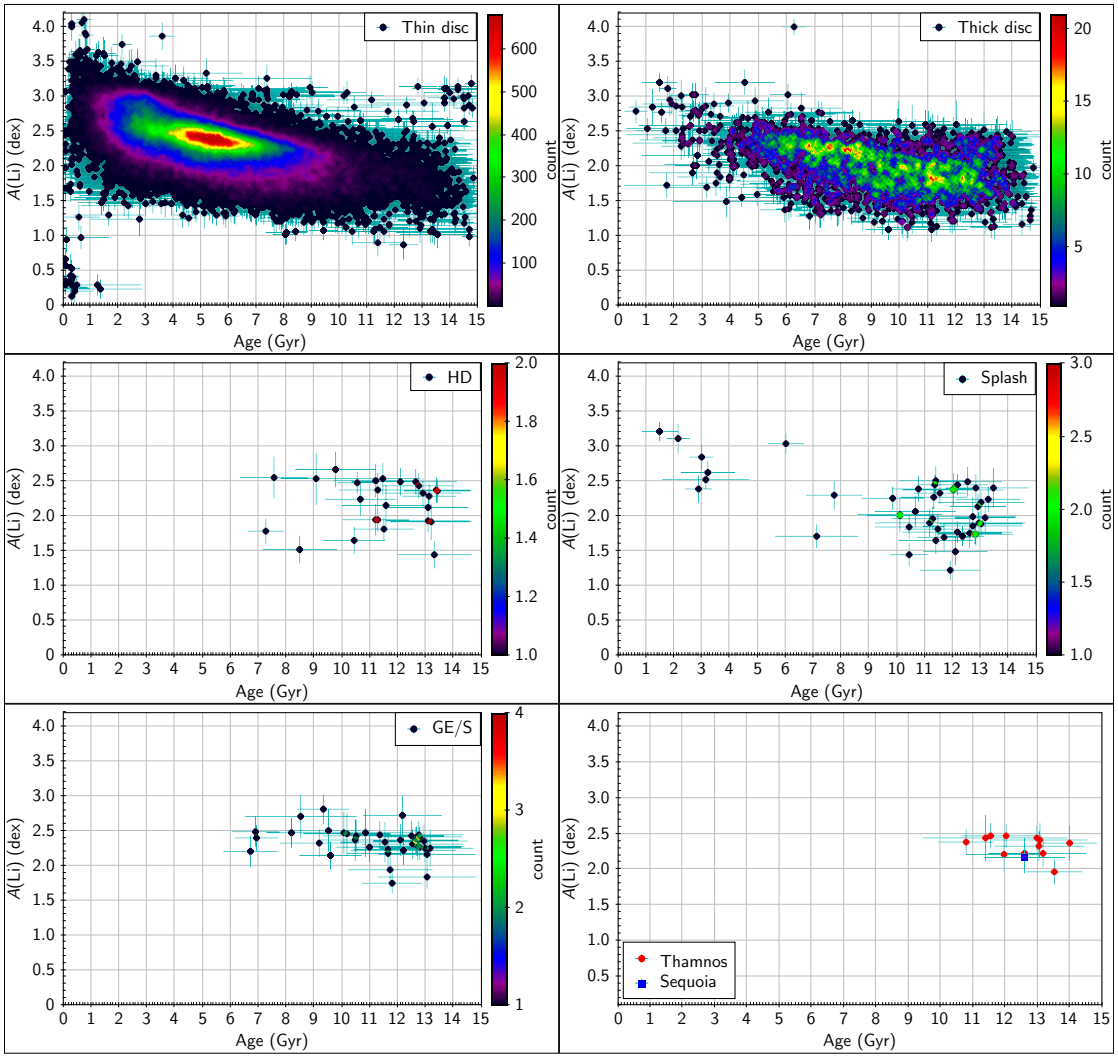


FIGURE 10.16: The top-left and top-right panels show lithium abundance A(Li) as a function of stellar age for dwarfs of the Galactic thin and thick disc, respectively. The bottom two rows show lithium abundance A(Li) as a function of stellar age for dwarfs in the Galactic halo's substructures. For each star, the error in the A(Li) and ages are also shown in the background using cyan-coloured error bars. Except in the case of the Thamnos and Sequoia, plots show density distribution with a 'rainbow' colour scheme in which red represents the highest density while dark violet (or black) represents the lowest density. The Thamnos and Sequoia's stars are shown in the bottom-right panel as filled red circles and blue squares, respectively. All the stars shown here have measured Li abundance in the GALAH DR3 survey. Also, only the dwarfs with reliable age estimates are plotted here (see Section 10.5 for more details).

K. As there is no known mechanism for Li production among such dwarf stars and so the amount of Li in their atmosphere should not be more than the Li content in the natal gas cloud from which these stars are formed, i.e. ISM, which is about 3.2 dex. Hence, the presence of higher Li in these dwarfs needs further investigation. To find clues behind the higher Li in these dwarfs, as shown in Figure 10.16, we plotted Li abundance as a function of stars' age. A(Li)-age distributions for the thin and thick disc dwarfs are shown in the top-left and top-right panels. Both figures suggest an increasing trend in Li abundance with a decrease in the star's age, i.e. young stars have higher Li compared to older stars. The large spread in the Li abundance among stars of similar age is due to the dependence of the Li depletion rate on stars' mass and metallicity. The thin disc's stars with high Li abundance are relatively very young compared to the mean age of the thin disc. Some of these stars are even less than a Gyr old, suggesting that either the current amount of Li in the ISM is much higher than 3.2 dex or the gas clouds from which these stars are born were locally enriched in Li by astrophysical events like exploding stars. Similar to the thin disc, the lone thick disc star with unexpectedly high A(Li) of about 4.0 dex is also very young compared to the mean age of the thick disc. Further investigations, like studying the distribution of these dwarfs in the Galaxy and identifying their natal gas cloud and other sibling stars born from that gas cloud, are needed to uncover the mystery behind high Li in these stars.

In the metal-poor region with [Fe/H] $<$ -1.5, the thick disc stars have a nearly constant maximum A(Li) of about 2.4 dex. This constant plateau of maximum A(Li) with respect to the metallicity is in agreement with the well-known spite plateau. As we move to the higher metallicity, the plateau of maximum Li rises slowly but gradually with respeIn contrast to the thick disc, Li in metal-rich thin disc stars increases more rapidly, suggesting more active production of Li in the thin disc. Also, interestingly, Li in metal-poor thin disc stars is much higher (about two to three times) than the expected plateau at about 2.4 dex. These metal-poor thin disc stars with high Li are about 4 to 6 Gyr old, i.e., are nearly the same age

as the thin disc. The very low metallicity content, along with age and kinematics similar to the thin disc stars, suggest that these stars might have originated from the Galactic bulge. Further detailed chemical analysis is needed to understand the origin of these metal-poor thin disc stars and their high Li abundance.

10.7.2 Li across the components of the Galactic halo

The distribution of Li as a function of [Fe/H] for the halo's five major components (HD, Splash, GE/S, Thamnos and Sequoia) are shown in the bottom two rows of Figure 10.13. Li abundance in the metal-poor stars (with [Fe/H] $<$ -1.5) of all the halo's components, along with the thick disc, strictly agrees with the well-known Spite plateau. The accreted origins of the GE/S, Thamnos and Sequoia, along with the agreement between Li in their metal-poor stars with the Spite plateau, confirm the universality of the observed Spite plateau and suggest that the different star formation environments in the progenitors of these components left no imprints on Li abundances of member stars. These results are in agreement with (Molaro *et al.* 2020; Simpson *et al.* 2021), who studied the Li abundance of the GE/S stars compared to the Milky Way's metal-poor stars. Unlike metal-poor stars, Li in some of the stars with [Fe/H] $>$ -1.5 is higher than the Spite plateau. As can be seen in Figure 10.16, these stars with higher Li are relatively younger than the majority of other stars in their corresponding samples, suggesting these stars were possibly formed from slightly Li enriched ISM like in the case of the Milky Way's thin disc stars. For stars with [Fe/H] $>$ -1.0 dex, a sudden drop in A(Li) can be seen in the HD and Splash, which can not be confirmed for the GE/S, Thamnos and Sequoia due to a lack of metal-rich stars in the selected samples (Figure 10.13). To find the origin of lower Li in these metal-rich stars, we have shown HRDs in Figure 10.12 with Li abundance in colour. The figure suggests that these metal-rich stars with lower Li are either somewhat cooler dwarfs or post-MS stars, which have already started experiencing Li depletion due to first-dredge-up (FDU).

10.8 Summary

In this work, we primarily studied the abundances of the α-process elements and lithium in kinematically selected components of the Galactic disc and halo based on data collected from the GALAH DR3. Considering the majority of stars in the GALAH belong to the Galactic disc, a comparison is made between the kinematic coverage of the sample of halo stars selected from the GALAH with the larger sample from the LAMOST survey (see Section 10.2). We then studied the metallicity, eccentricity and age function for the Galactic thin and thick disk along with the prorate and retrograde components of the halo. Results from relatively smaller samples of halo stars from the GALAH survey are in good agreement with the results based on the larger samples from the LAMOST survey (for more details, see Section 10.3, 10.4 and 10.5). We also compared our age estimates with the age estimates provided in the GALAH survey, and both are found to be in good agreement (see Section 10.5). In Section 10.6, we studied the distribution of α-process elements across the selected samples of the thin disc and thick disc along with the prograde and retrograde components of the Galactic halo. Based on the abundance trends of the α-process, a brief discussion on the formation histories of these Galactic components is provided in Section 10.6.1. Finally, in Section 10.7, we studied the evolution of lithium in the Galactic thin disc and thick disc along with kinetically selected components of the halo.

Chapter 11

Conclusions, key results and future plan

In this chapter, we provide conclusions by highlighting the novel results obtained in the thesis and future plans.

11.1 Thesis conclusions and key results

This thesis is devoted to the chemo-dynamic studies of our home galaxy, the Milky Way, to understand its formation and evolution histories. The study primarily addressed three major questions in the field of the formation and evolution histories of the Galaxy: 1) The evolution of Li in the Galaxy, 2) The evolution of Li in low-mass stars and their contribution towards the Galactic Li evolution, and 3) Formation and evolution of the Galactic halo and disc's components. A summary of works carried out and key results obtained is provided below.

1. **Evolution of Lithium in the Galaxy:**

   To understand the evolution of Li in the Galaxy, we used spectroscopic data from the second data release of the GALAH survey in combination with the stars' astrometric and photometric information from the *Gaia* survey. In agreement with previous studies, Li is found to have significantly increased in the Galaxy compared to the primordial value based on observations of old, metal-poor halo stars as well as the theoretical prediction from the standard BBN models using baryonic density measured from space missions such as the Wilkinson Microwave Anisotropy Probe (WMAP). The metal-poor dwarfs with [Fe/H] $<$ -0.8 dex confirms the existence of the well-known spite plateau at A(Li) $\sim$ 2.3 dex. The absence of any correlation between maximum Li in these metal-poor stars and their galactic space velocity's rotational component indicates that the Li in these metal-poor stars is primordial. It is, however, not clear if the current amount of Li in these metal-poor stars is the same as the initial Li produced during the BBN or has almost constantly depleted across the metallicity range through astration by spallation processes (Mathews *et al.* 1990).

   In the sub-solar metallicity range with [Fe/H] from -0.8 to 0.0 dex, Li has increased significantly from the initial value of about 2.3 to the present value of about 3.3 dex. Li in super-solar metallicity dwarfs is found to be decreasing with an increase in metallicity. This decrease in Li is thought to be related to the dynamic history of the Galaxy, for example, the possible radial migration of stars from the inner regions of the Galaxy (Guiglion *et al.* 2019). However, we found no significant difference in the kinematic properties of super-solar metallicity dwarfs compared to dwarfs with solar metallicity. More recent studies, like Randich *et al.* (2020); Charbonnel *et al.* (2021), contradict the previous findings of decreasing Li in super-solar metallicity dwarfs and found that the observed decreasing trend is due to bias in sample selection.

   In conclusion, Li has significantly increased in the Galactic disc. However, the source of such a large-scale Li production is still not clear. (For more

details, see Chapter 3, and Deepak and Reddy 2020a,b).

2. **Evolution of Li in stars and its role in the Galactic Li evolution:**

   The search for an explanation for the large-scale Li enrichment in the Galaxy led us to understand the evolution of Li in low-mass stars. Low-mass stars (with mass < 2 $M_{\odot}$) are most common in the Galaxy and consist of about 80 per cent of the Galactic stellar mass (Salpeter 1955). In general, stars are known to be sinks for Li as Li burns at relatively low temperatures of about 2.5×10^6 K, and is sensitive to enhanced mixing during the first dredge-up (FDU), which leads to rapid dilution of Li in stars' outer envelopes as they evolve from the main sequence. Because of this, a red giant post-FDU of about solar metallicity is expected to have a Li abundance of $A(\mathrm{Li}) \sim 1.5$. However, since the first discovery by Wallerstein and Sneden (1982), about a per cent of giant stars are known to have unexpectedly higher Li. All such giants with $A(\mathrm{Li})$ higher than ~ 1.5 are known as Li-rich giant stars. The source of higher Li in this small group of giant stars was not clear until the publications of our results from a series of studies from 2019 onwards. Before this, a number of theories, like giants getting Li enriched through planets engulfment, were proposed to explain the higher amount of Li in these giant stars.

   To understand the evolution of Li in low-mass stars and uncover the almost four-decade-old puzzle about the origin of Li-rich giant stars, we performed a number of studies using spectroscopic data from the GALAH survey in combination with astrometric and photometric data from the *Gaia* survey. In our first study from this series (Deepak and Reddy 2019), covered in Chapter 4, we discovered 335 new Li-rich giants stars (with $A(\mathrm{Li}) \geq 1.8$ dex) of which 20 are super Li-rich with $A(\mathrm{Li}) \geq 3.2$ dex. This discovery of 335 new Li-rich giant stars helped to double the number of known Li-rich giant stars at that time. We also found that most of these Li-rich giant stars populate

the red clump region, which, when combined with stellar evolutionary timescales on RGB, indicates that the Li enhancement origin may lie at RGB tip during He-flash rather than by external source of merging of sub-stellar objects or during luminosity bump evolution. Further, to see if these Li-rich stars belong to any particular kinematic group in the Galaxy, we looked into their kinematic distribution. We found that they are found throughout the Galaxy, although they are relatively more prevalent among giants of the thin disc compared to the thick disc and halo. (For more details, see Chapter 4 and Deepak and Reddy 2019.)

In the follow-up study (Deepak *et al.* 2020), covered in Chapter 5, we search for clues about the origin of Li-rich and super Li-rich giants by studying their chemical compositions and physical properties relative to Li-normal giants of similar temperature and luminosity ranges. For this, abundances of 21 chemical species, from C to Eu, are adopted from the GALAH DR2 survey. We found that Li-rich and super Li-rich giants are chemically similar to Li-normal giants. We also found that the probability of becoming a Li-rich giant is approximately independent of a star's mass, although the majority of the Li-rich giants are found to be low mass ($M \leq 2$ M$_{\odot}$). The frequency of occurrence of Li-enriched giants among normal giants is about one per cent and slightly dependent on metallicity ([Fe/H]). Li-enriched and normal giants are found to have a similar projected rotational velocity, suggesting that Li-enrichment in giants is not linked to scenarios such as mergers and tidal interaction between binary stars. (For more details, see Chapter 5 and Deepak *et al.* 2020.)

To further confirm the connection between the He-core flash and Li-enrichment in the low-mass stars, we studied the correlation between giants' Li abundance and asteroseismic parameters based on asteroseismic data collected from the literature for giants with known Li abundances. Whilst most of the Li-rich giants in the sample have masses less than 1.5 $M_{\odot}$, they are also present up to and beyond the maximum mass expected to have suffered a

core He-flash, i.e. $M \leq 2.25\ M_{\odot}$: this suggests contributions from other processes towards Li enrichment. To understand the evolution of giants in the $\Delta\Pi_1 - \Delta\nu$ plane, we use the `MESA` models, which show the presence of mini He-flashes following the initial strong core He-flash. From the distribution of A(Li) as a function of $\Delta\nu$, which is similar to the distribution of A(Li) as a function of luminosity, we find no indication of Li enrichment near the luminosity bump. Also, A(Li) trends to $\sim$ -1.5 dex near the RGB tip. The data for the CHeB giants also suggest a decrease in A(Li) with an increase in the gravity mode period spacing $\Delta\Pi_1$, which is known to increase with time at the start of the CHeB phase suggesting the enriched Li in He-core burning giants decreases as stars evolve. (For more details, see Chapter 6 and Deepak and Lambert 2021a.)

Finally, in our most recent study Deepak and Lambert (2021b), covered in Chapter 7, we used the data from the third data release of the GALAH survey to understand the roles of the He-core flash and the luminosity bump. The rare examples of Li-enriched stars with abundances A(Li) $\geq$ 1.5 are confirmed to be He-core burning stars belonging to or evolved from the red clump with similar masses and metallicity: $M \simeq 1.1 \pm 0.2 M_{\odot}$ and [Fe/H] $\simeq -0.3 \pm 0.3$. Li enrichment over the Li abundance present in a star's predecessor at the tip of the red giant branch likely occurs in all these red clump stars. Examination of the elemental abundances (C to Eu) in the GALAH catalogue shows no anomalous abundances in red clump giants and, in particular, no dependence on the Li abundance, which ranges over at least five dex. Lithium synthesis is attributed to the He-core flash occurring in stars at the tip of the red giant branch. Models from the `MESA` match the observed evolution of these stars along the red giant branch and to the red clump but only at the low effective temperature end of the observed spread of red clump giants. The run of Li abundance on the red giant branch is fairly well reproduced by `MESA` models. A speculation is presented that the series of He-core flashes not only leads to ^{7}Li synthesis from a star's

internal reservoir of ^{3}He but also may lead to internal restructuring leading to the observed effective temperature spread of red clump stars at about a constant luminosity. Giants exhibiting marked Li enrichments are not found at other evolutionary phases and, in particular, not directly associated with the luminosity bump on the red giant branch for which the Li abundance increase does not exceed 0.3 dex. (For more details, see Chapter 7 and Deepak and Lambert 2021b.)

In conclusion, our studies on the evolution of Li in low-mass stars suggest that all the low-mass stars experience Li depletion as they evolve from the main sequence to the RGB. This depletion of Li continues as the star evolves on the RGB. Because of this, giants are left with a very low amount of Li as they reach near the RGB tip. However, soon after, during the He-core flashing phase, all the low-mass stars are found to experience a varying amount of Li enrichment, which ranges over at least five dexes. We found that this sudden Li enrichment is associated with the first strongest He-core flash. Stars are also known to experience mass loss during the He-core flash. Hence, we speculate that some of the enriched Li may be thrown out into the interstellar medium (ISM) during the He flashing phase and contribute to the Galactic Li enrichment. Further studies are required to precisely understand and quantify the amount of mass loss across the stellar mass and metallicity range. Studies are also needed to quantify the amount of Li added to the ISM during such mass-loss events.

3. **Formation and evolution of the Galactic halo and disc**

The Galactic halo, the outermost stellar component of the Galaxy, is believed to be home to the remnant of many dwarfs galaxies after they merged with the progenitor of the Milky Way. Understanding the halo's formation and evolution histories hold the key to understanding the formation and evolution of the Galaxy. To understand the formation and evolution of the halo, we used spectroscopic data from the fifth data release of the

LAMOST survey (Xiang *et al.* 2019) in combination with the astrometric and photometric data from the *Gaia* survey. The colour-magnitude diagram (CMD) for the kinematically selected sample of halo stars follows a bi-model colour sequence on the main sequence as well as on the RGB. The sample also has a bi-model metallicity distribution, which is understood to be the main reason for the two colour sequences and corresponds to the two largest stellar groups in the halo, namely the Gaia-Enceladus/Sausage (GE/S; with lower metallicity) and the Splash (with higher metallicity). However, precise segregation of these two sequences is not possible purely based on the distribution in the CMD due to significant overlap in the CMD due to metallicity overlap and possible errors with the colour estimates. These two populations, however, are well separated in the orbital energy versus angular momentum (L_Z) plane. Hence, we select samples of these two and other prominent stellar substructures in the halo sample based on the distribution in the orbital energy versus the angular momentum (L_Z) plane. From the halo, we selected samples of six substructures, of which three (the HD, Splash and Helmi stream H99) are prograde, while the other three (the Gaia-Enceladus/Sausage (GE/S), Thamnos and Sequoia) are retrograde. Chemically, the HD population is the most metal-rich with a mean metallicity of -0.43 ± 0.30, while the Thamnos and Sequoia are most metal-poor with peak metallicities of -1.36 and -1.56, respectively. The Splash and GE/S have median metallicities of -0.75 ± 0.24 and -1.31 ± 0.23, respectively (Figure 9.8 and Table 9.1). All of these substructures are relatively old, with some of their member stars as old as the Universe itself. In contrast to a recent study by Gallart *et al.* (2019), we found that the Splash (also known as the red sequence and inner halo) is about 1.5 Gyr older than the GE/S population (also known as the blue sequence and outer halo). These results, however, are in agreement with most of the other previous studies, for example, Schuster *et al.* (2012); Hawkins *et al.* (2014); Ge *et al.* (2016). The primary reason for the disagreement between the difference in the ages

of the Splash and GE/S from our age estimates and Gallart *et al.* (2019) appears to be related to a possible issue with segregation of these two halo's populations based on the distribution in the CMD in Gallart *et al.* (2019). Additionally, the younger age and lower metallicity of the GE/S compared to the Splash agrees with the understanding that the GE/S is a remnant of dwarf galaxy Gaia-Enceladus/Sausage, which merged with the progenitor of the Milky Way and has a mass of about one-fourth of the mass of the Milky Way' progenitor. The sudden drop in age distribution for the GE/S population about 8 Gyr ago (Figure 9.8) indicate that the star formation in the GE/S progenitor ceased sometime more than 8 Gyr ago either due to the GE/S progenitor running out of gas to form more new stars or its gas getting stripped off due to interaction with the Milky Way. On the other hand, since the peak age at about 13 Gyr ago, the almost exponential decay in star formation in the Splash may be due to Milky Way's gas settling in the disc and need not be directly related to the GE/S merger with the Milky Way. Additionally, the similarity between the age distribution of the HD and the GE/S populations along with HD's disc-like properties, except the hotter kinematics, suggest that the merger encounter between the progenitors of the GE/S and the Milky Way may be responsible for the HD stars' hotter kinematics. In conclusion, the lower metallicity and lower peak star formation age of halo's three accreted components (the GE/S, Thamnos and Sequoia) compared to the prograde, in situ components like the Splash and HD, favour the ΛCMD model of galaxy formation in which smaller dwarf galaxies merge with relatively large galaxies leading to the formation of complex galaxies like Milky Way. (For more details, see Chapter 9.)

To get a more accurate picture of the formation and evolution histories of the Galactic halo and the Galaxy, we further studied the chemical composition of these components in Chapter 10. Our analysis is restricted to the α-process elements (O, Mg, Si, Ca and Ti) and lithium. The [α/Fe] abundance trends in the HD, Splash and Thamnos are found to be similar to the metal-poor

stars of the Galactic thick disk. On the other hand, the GE/S and Sequoia have experienced similar evolution of α-process elements. The maximum Li in metal-poor dwarf stars of both accreted (e.g., the GE/S, Thamnos and Sequoia) and in situ components (e.g., the thick disc, HD and Splash) is found to be in agreement with the well know Spite Plateau. We also discovered unexpectedly higher Li (even higher than the currently accepted A(Li) of about 3.2 dex in ISM) in the thin and thick disc dwarfs. Further studies are needed to understand the source of this higher Li in these dwarfs. (For more details, see Chapter 10.)

11.2 Future plan

To get a more clear picture of the formation and evolution of the Galactic halo and the Galaxy, we plan to study the full spectrum of chemical species provided by the GALAH survey. We also plan to study the distribution of these chemical species as functions of stars' spatial and orbital parameters, which is expected to provide more details about how these chemical elements evolved across different regions of the Galaxy. For this purpose, we also plan to include the spectroscopic data from the Sloan Digital Sky Survey (SDSS)/Apache Point Observatory Galactic Evolution Experiment (APOGEE) survey.

Additionally, the upcoming third data release (DR3) from the *Gaia* survey is expected to increase the sample stars with measured radial velocities by many-fold. The *Gaia*'s DR3 is also expected to have spectroscopically measured abundances of about a dozen chemical species for millions of stars, hence providing a golden opportunity to study kinematics and chemical compositions of many more dynamical groups in the Milky Way, which is expected to further assist our understanding

of the formation and evolution histories of the Milky Way in more detail. Additionally, more data releases from the ongoing ground-based spectroscopic surveys (like the GALAH, APOGEE, LAMOST and Gaia-ESO survey) are expected to supplement the *Gaia*'s data with more high quality and resolution stellar spectra and derived abundances of more chemical species. We plan to use these upcoming data sets to further understand the formation and evolution of the Milky Way.

Also, to understand the contribution of low-mass stars toward the Galactic Li enrichment, we plan to study the mass loss scenarios during the He-core flash.

Bibliography

1997, *The HIPPARCOS and TYCHO catalogues. Astrometric and photometric star catalogues derived from the ESA HIPPARCOS Space Astrometry Mission*, ESA Special Publication, 1200, ESA Publications Division, Noordwijk, Netherlands. [ADS]

Adamów, M., Niedzielski, A., Kowalik, K., Villaver, E., Wolszczan, A., Maciejewski, G. and Gromadzki, M., 2018, "Tracking Advanced Planetary Systems (TAPAS) with HARPS-N. VI. HD 238914 and TYC 3318-01333-1: two more Li-rich giants with planets", *Astron. Astrophys.*, **613**, A47. [DOI], [ADS], [arXiv:1801.04379 [astro-ph.SR]]

Aguilera-Gómez, Claudia, Chanamé, Julio, Pinsonneault, Marc H. and Carlberg, Joleen K., 2016a, "On Lithium-rich Red Giants. I. Engulfment of Substellar Companions", *Astrophys. J.*, **829**(2), 127. [DOI], [ADS], [arXiv:1605.05332 [astro-ph.SR]]

Aguilera-Gómez, Claudia, Chanamé, Julio, Pinsonneault, Marc H. and Carlberg, Joleen K., 2016b, "On Lithium-rich Red Giants: Engulfment on the Giant Branch of Trumpler 20", *Astrophys. J. Lett.*, **833**(2), L24. [DOI], [ADS], [arXiv:1609.07492 [astro-ph.SR]]

Alexander, J. B., 1967, "A possible source of lithium in the atmospheres of some red giants", *The Observatory*, **87**, 238–240. [ADS]

Amarsi, A. M., Asplund, M., Collet, R. and Leenaarts, J., 2015, "The Galactic chemical evolution of oxygen inferred from 3D non-LTE spectral-line-formation calculations.", *Mon. Not. Roy. Astron. Soc.*, **454**, L11–L15. [DOI], [ADS], [arXiv:1508.04857 [astro-ph.SR]]

Amarsi, A. M., Asplund, M., Collet, R. and Leenaarts, J., 2016, "Non-LTE oxygen line formation in 3D hydrodynamic model stellar atmospheres", *Mon. Not. Roy. Astron. Soc.*, **455**(4), 3735–3751. [DOI], [ADS], [arXiv:1511.01155 [astro-ph.SR]]

Anders, F., Chiappini, C., Minchev, I., Miglio, A., Montalbán, J., Mosser, B., Rodrigues, T. S., Santiago, B. X., Baudin, F., Beers, T. C., da Costa, L. N., García, R. A., García-Hernández, D. A., Holtzman, J., Maia, M. A. G., Majewski, S., Mathur, S., Noels-Grotsch, A., Pan, K., Schneider, D. P., Schultheis, M., Steinmetz, M., Valentini, M. and Zamora, O., 2017, "Red giants observed by CoRoT and APOGEE: The evolution of the Milky Way's radial metallicity gradient", *Astron. Astrophys.*, **600**, A70. [DOI], [ADS], [arXiv:1608.04951 [astro-ph.GA]]

Andrae, René, Fouesneau, Morgan, Creevey, Orlagh, Ordenovic, Christophe, Mary, Nicolas, Burlacu, Alexandru, Chaoul, Laurence, Jean-Antoine-Piccolo, Anne, Kordopatis, Georges, Korn, Andreas, Lebreton, Yveline, Panem, Chantal, Pichon, Bernard, Thévenin, Frédéric, Walmsley, Gavin and Bailer-Jones, Coryn A. L., 2018, "Gaia Data Release 2. First stellar parameters from Apsis", *Astron. Astrophys.*, **616**, A8. [DOI], [ADS], [arXiv:1804.09374 [astro-ph.SR]]

Anthony-Twarog, Barbara J., Deliyannis, Constantine P., Rich, Evan and Twarog, Bruce A., 2013, "A Lithium-rich Red Giant Below the Clump in the Kepler Cluster, NGC 6819", *Astrophys. J. Lett.*, **767**(1), L19. [DOI], [ADS], [arXiv:1303.2984 [astro-ph.SR]]

Arnett, David, 1996, *Supernovae and Nucleosynthesis: An Investigation of the History of Matter from the Big Bang to the Present*, Princeton University Press, Princeton. [ADS]

Arnett, W. David, 1969, "A Possible Model of Supernovae: Detonation of ^{12}C", *Astrophys. Space Sci.*, **5**(2), 180–212. [DOI], [ADS]

Arnett, W. David, 1971, "An Analytic Approach to the Evolution of Degenerate Carbon Cores of Stars", *Astrophys. J.*, **169**, 113. [DOI], [ADS]

Arnould, M. and Norgaard, H., 1975, "The Explosive Thermonuclear Formation of 7Li and 11B", *Astron. Astrophys.*, **42**, 55. [ADS]

Asplund, Martin, Lambert, David L., Nissen, Poul Erik, Primas, Francesca and Smith, Verne V., 2006, "Lithium Isotopic Abundances in Metal-poor Halo Stars", *Astrophys. J.*, **644**(1), 229–259. [DOI], [ADS], [arXiv:astro-ph/0510636 [astro-ph]]

Asplund, Martin, Grevesse, Nicolas, Sauval, A. Jacques and Scott, Pat, 2009, "The Chemical Composition of the Sun", *Ann. Rev. Astron. Astrophys.*, **47**(1), 481–522. [DOI], [ADS], [arXiv:0909.0948 [astro-ph.SR]]

Audouze, Jean and Truran, James W., 1973, "A Possible Explanation for the Origin of Lithium, Beryllium, and Boron", *Astrophys. J.*, **182**, 839–846. [DOI], [ADS]

Auvergne, M., Bodin, P., Boisnard, L., Buey, J. T., Chaintreuil, S., Epstein, G., Jouret, M., Lam-Trong, T., Levacher, P., Magnan, A., Perez, R., Plasson, P., Plesseria, J., Peter, G., Steller, M., Tiphène, D., Baglin, A., Agogué, P., Appourchaux, T., Barbet, D., Beaufort, T., Bellenger, R., Berlin, R., Bernardi, P., Blouin, D., Boumier, P., Bonneau, F., Briet, R., Butler, B., Cautain, R., Chiavassa, F., Costes, V., Cuvilho, J., Cunha-Parro, V., de Oliveira Fialho, F., Decaudin, M., Defise, J. M., Djalal, S., Docclo, A., Drummond, R., Dupuis, O., Exil, G., Fauré, C., Gaboriaud, A., Gamet, P., Gavalda, P., Grolleau, E., Gueguen, L., Guivarc'h, V., Guterman, P., Hasiba, J., Huntzinger, G., Hustaix, H., Imbert, C., Jeanville, G., Johlander, B., Jorda, L., Journoud, P., Karioty, F., Kerjean, L., Lafond, L., Lapeyrere, V., Landiech, P., Larqué, T., Laudet, P., Le Merrer, J., Leporati, L., Leruyet, B., Levieuge, B., Llebaria, A., Martin, L., Mazy, E., Mesnager, J. M., Michel, J. P., Moalic, J. P., Monjoin, W.,

Naudet, D., Neukirchner, S., Nguyen-Kim, K., Ollivier, M., Orcesi, J. L., Ottacher, H., Oulali, A., Parisot, J., Perruchot, S., Piacentino, A., Pinheiro da Silva, L., Platzer, J., Pontet, B., Pradines, A., Quentin, C., Rohbeck, U., Rolland, G., Rollenhagen, F., Romagnan, R., Russ, N., Samadi, R., Schmidt, R., Schwartz, N., Sebbag, I., Smit, H., Sunter, W., Tello, M., Toulouse, P., Ulmer, B., Vandermarcq, O., Vergnault, E., Wallner, R., Waultier, G. and Zanatta, P., 2009, "The CoRoT satellite in flight: description and performance", *Astron. Astrophys.*, **506**(1), 411–424. [DOI], [ADS], [arXiv:0901.2206 [astro-ph.SR]]

Bañados, Eduardo, Venemans, Bram P., Mazzucchelli, Chiara, Farina, Emanuele P., Walter, Fabian, Wang, Feige, Decarli, Roberto, Stern, Daniel, Fan, Xiaohui, Davies, Frederick B., Hennawi, Joseph F., Simcoe, Robert A., Turner, Monica L., Rix, Hans-Walter, Yang, Jinyi, Kelson, Daniel D., Rudie, Gwen C. and Winters, Jan Martin, 2018, "An 800-million-solar-mass black hole in a significantly neutral Universe at a redshift of 7.5", *Nature*, **553**(7689), 473–476. [DOI], [ADS], [arXiv:1712.01860 [astro-ph.GA]]

Balachandran, Suchitra, 1990, "Lithium Depletion and Rotation in Main-Sequence Stars", *Astrophys. J.*, **354**, 310. [DOI], [ADS]

Beck, P. G., Bedding, T. R., Mosser, B., Stello, D., Garcia, R. A., Kallinger, T., Hekker, S., Elsworth, Y., Frandsen, S., Carrier, F., De Ridder, J., Aerts, C., White, T. R., Huber, D., Dupret, M. A., Montalbán, J., Miglio, A., Noels, A., Chaplin, W. J., Kjeldsen, H., Christensen-Dalsgaard, J., Gilliland, R. L., Brown, T. M., Kawaler, S. D., Mathur, S. and Jenkins, J. M., 2011, "Kepler Detected Gravity-Mode Period Spacings in a Red Giant Star", *Science*, **332**(6026), 205. [DOI], [ADS]

Bedding, Timothy R., Mosser, Benoit, Huber, Daniel, Montalbán, Josefina, Beck, Paul, Christensen-Dalsgaard, Jørgen, Elsworth, Yvonne P., García, Rafael A., Miglio, Andrea, Stello, Dennis, White, Timothy R., De Ridder, Joris, Hekker, Saskia, Aerts, Conny, Barban, Caroline, Belkacem, Kevin, Broomhall, Anne-Marie, Brown, Timothy M., Buzasi, Derek L., Carrier, Fabien, Chaplin,

William J., di Mauro, Maria Pia, Dupret, Marc-Antoine, Frandsen, Søren, Gilliland, Ronald L., Goupil, Marie-Jo, Jenkins, Jon M., Kallinger, Thomas, Kawaler, Steven, Kjeldsen, Hans, Mathur, Savita, Noels, Arlette, Silva Aguirre, Victor and Ventura, Paolo, 2011, "Gravity modes as a way to distinguish between hydrogen- and helium-burning red giant stars", *Nature*, **471**(7340), 608–611. [DOI], [ADS], [arXiv:1103.5805 [astro-ph.SR]]

Beers, Timothy C., Drilling, John S., Rossi, Silvia, Chiba, Masashi, Rhee, Jaehyon, Führmeister, Birgit, Norris, John E. and von Hippel, Ted, 2002, "Metal Abundances and Kinematics of Bright Metal-poor Giants Selected from the LSE Survey: Implications for the Metal-weak Thick Disk", *Astron. J.*, **124**(2), 931–948. [DOI], [ADS], [arXiv:astro-ph/0204339 [astro-ph]]

Belladitta, S., Moretti, A., Caccianiga, A., Spingola, C., Severgnini, P., Della Ceca, R., Ghisellini, G., Dallacasa, D., Sbarrato, T., Cicone, C., Cassarà, L. P. and Pedani, M., 2020, "The first blazar observed at z $>$ 6", *Astron. Astrophys.*, **635**, L7. [DOI], [ADS], [arXiv:2002.05178 [astro-ph.CO]]

Belokurov, Vasily, Sanders, Jason L., Fattahi, Azadeh, Smith, Martin C., Deason, Alis J., Evans, N. Wyn and Grand, Robert J. J., 2020, "The biggest splash", *Mon. Not. Roy. Astron. Soc.*, **494**(3), 3880–3898. [DOI], [ADS], [arXiv:1909.04679 [astro-ph.GA]]

Bensby, T., Feltzing, S. and Lundström, I., 2003, "Elemental abundance trends in the Galactic thin and thick disks as traced by nearby F and G dwarf stars", *Astron. Astrophys.*, **410**, 527–551. [DOI], [ADS]

Bensby, T., Feltzing, S., Lundström, I. and Ilyin, I., 2005, "α-, r-, and s-process element trends in the Galactic thin and thick disks", *Astron. Astrophys.*, **433**(1), 185–203. [DOI], [ADS], [arXiv:astro-ph/0412132 [astro-ph]]

Bensby, T., Alves-Brito, A., Oey, M. S., Yong, D. and Meléndez, J., 2011, "A First Constraint on the Thick Disk Scale Length: Differential Radial Abundances in

K Giants at Galactocentric Radii 4, 8, and 12 kpc", *Astrophys. J. Lett.*, **735**(2), L46. [DOI], [ADS], [arXiv:1106.1914 [astro-ph.GA]]

Bensby, T., Feltzing, S. and Oey, M. S., 2014, "Exploring the Milky Way stellar disk. A detailed elemental abundance study of 714 F and G dwarf stars in the solar neighbourhood", *Astron. Astrophys.*, **562**, A71. [DOI], [ADS], [arXiv:1309.2631 [astro-ph.GA]]

Bildsten, Lars, Brown, Edward F., Matzner, Christopher D. and Ushomirsky, Greg, 1997, "Lithium Depletion in Fully Convective Pre-Main-Sequence Stars", *Astrophys. J.*, **482**(1), 442–447. [DOI], [ADS], [arXiv:astro-ph/9612155 [astro-ph]]

Bildsten, Lars, Paxton, Bill, Moore, Kevin and Macias, Phillip J., 2012, "Acoustic Signatures of the Helium Core Flash", *Astrophys. J. Lett.*, **744**(1), L6. [DOI], [ADS], [arXiv:1111.6867 [astro-ph.SR]]

Bland-Hawthorn, J., Sharma, S. and Freeman, K., 2014, "GALAH survey: chemically tagging the thick disk", in *EAS Publications Series*, EAS Publications Series, 67-68, pp. 219–226, Cambridge University Press, The Edinburgh Building, Cambridge CB2 8RU, UK. [DOI], [ADS], [arXiv:1504.01765 [astro-ph.GA]]

Blumenthal, G. R., Faber, S. M., Primack, J. R. and Rees, M. J., 1984, "Formation of galaxies and large-scale structure with cold dark matter.", *Nature*, **311**, 517–525. [DOI], [ADS]

Boesgaard, A. M. and Steigman, G., 1985, "Big Bang nucleosynthesis: theories and observations.", *Ann. Rev. Astron. Astrophys.*, **23**, 319–378. [DOI], [ADS]

Boesgaard, A. M. and Tripicco, M. J., 1986, "Lithium in the Hyades Cluster", *Astrophys. J. Lett.*, **302**, L49. [DOI], [ADS]

Böhm-Vitense, Erika, 1992, *Introduction to Stellar Astrophysics*, Cambridge University Press, Cambridge, UK. [ADS]

Bonifacio, P. and Molaro, P., 1997, "The primordial lithium abundance", *Mon. Not. Roy. Astron. Soc.*, **285**(4), 847–861. [DOI], [ADS], [arXiv:astro-ph/9611043 [astro-ph]]

Bonsack, Walter K., 1959, "The Abundance of Lithium and Convective Mixing in Stars of Type.", *Astrophys. J.*, **130**, 843. [DOI], [ADS]

Bonsack, Walter K. and Greenstein, Jesse L., 1960, "The Abundance of Lithium in T Tauri Stars and Related Objects.", *Astrophys. J.*, **131**, 83. [DOI], [ADS]

Borucki, William J., Koch, David, Basri, Gibor, Batalha, Natalie, Brown, Timothy, Caldwell, Douglas, Caldwell, John, Christensen-Dalsgaard, Jørgen, Cochran, William D., DeVore, Edna, Dunham, Edward W., Dupree, Andrea K., Gautier, Thomas N., Geary, John C., Gilliland, Ronald, Gould, Alan, Howell, Steve B., Jenkins, Jon M., Kondo, Yoji, Latham, David W., Marcy, Geoffrey W., Meibom, Søren, Kjeldsen, Hans, Lissauer, Jack J., Monet, David G., Morrison, David, Sasselov, Dimitar, Tarter, Jill, Boss, Alan, Brownlee, Don, Owen, Toby, Buzasi, Derek, Charbonneau, David, Doyle, Laurance, Fortney, Jonathan, Ford, Eric B., Holman, Matthew J., Seager, Sara, Steffen, Jason H., Welsh, William F., Rowe, Jason, Anderson, Howard, Buchhave, Lars, Ciardi, David, Walkowicz, Lucianne, Sherry, William, Horch, Elliott, Isaacson, Howard, Everett, Mark E., Fischer, Debra, Torres, Guillermo, Johnson, John Asher, Endl, Michael, MacQueen, Phillip, Bryson, Stephen T., Dotson, Jessie, Haas, Michael, Kolodziejczak, Jeffrey, Van Cleve, Jeffrey, Chandrasekaran, Hema, Twicken, Joseph D., Quintana, Elisa V., Clarke, Bruce D., Allen, Christopher, Li, Jie, Wu, Haley, Tenenbaum, Peter, Verner, Ekaterina, Bruhweiler, Frederick, Barnes, Jason and Prsa, Andrej, 2010, "Kepler Planet-Detection Mission: Introduction and First Results", *Science*, **327**(5968), 977. [DOI], [ADS]

Bovy, Jo, 2015, "galpy: A python Library for Galactic Dynamics", *Astrophys. J. Suppl.*, **216**(2), 29. [DOI], [ADS], [arXiv:1412.3451 [astro-ph.GA]]

Bovy, Jo, Rix, Hans-Walter, Liu, Chao, Hogg, David W., Beers, Timothy C. and Lee, Young Sun, 2012, "The Spatial Structure of Mono-abundance Subpopulations of the Milky Way Disk", *Astrophys. J.*, **753**(2), 148. [DOI], [ADS], [arXiv:1111.1724 [astro-ph.GA]]

Bressan, Alessandro, Marigo, Paola, Girardi, Léo., Salasnich, Bernardo, Dal Cero, Claudia, Rubele, Stefano and Nanni, Ambra, 2012, "PARSEC: stellar tracks and isochrones with the PAdova and TRieste Stellar Evolution Code", *Mon. Not. Roy. Astron. Soc.*, **427**(1), 127–145. [DOI], [ADS], [arXiv:1208.4498 [astro-ph.SR]]

Brook, Chris B., Kawata, Daisuke, Gibson, Brad K., Gallart, Carme and Vicente, Andrés, 2020, "Explaining the chemical trajectories of accreted and in-situ halo stars of the Milky Way", *Mon. Not. Roy. Astron. Soc.*, **495**(3), 2645–2651. [DOI], [ADS], [arXiv:2001.02187 [astro-ph.GA]]

Brown, Jeffery A., Sneden, Christopher, Lambert, David L. and Dutchover, Edward Jr., 1989a, "A Search for Lithium-rich Giant Stars", *Astrophys. J. Suppl.*, **71**, 293. [DOI], [ADS]

Brown, Jeffery A., Sneden, Christopher, Lambert, David L. and Dutchover, Edward, Jr., 1989b, "A Search for Lithium-rich Giant Stars", *Astrophys. J. Suppl.*, **71**, 293. [DOI], [ADS]

Buder, S., Lind, K., Ness, M. K., Asplund, M., Duong, L., Lin, J., Kos, J., Casagrande, L., Casey, A. R., Bland-Hawthorn, J., de Silva, G. M., D'Orazi, V., Freeman, K. C., Martell, S. L., Schlesinger, K. J., Sharma, S., Simpson, J. D., Zucker, D. B., Zwitter, T., Čotar, K., Dotter, A., Hayden, M. R., Hyde, E. A., Kafle, P. R., Lewis, G. F., Nataf, D. M., Nordlander, T., Reid, W., Rix, H. W., Skúladóttir, Á., Stello, D., Ting, Y. S., Traven, G., Wyse, R. F. G. and Galah Collaboration, 2019, "The GALAH survey: An abundance, age, and kinematic inventory of the solar neighbourhood made with TGAS", *Astron. Astrophys.*, **624**, A19. [DOI], [ADS], [arXiv:1804.05869 [astro-ph.SR]]

Buder, Sven, Asplund, Martin, Duong, Ly, Kos, Janez, Lind, Karin, Ness, Melissa K., Sharma, Sanjib, Bland-Hawthorn, Joss, Casey, Andrew R., de Silva, Gayandhi M., D'Orazi, Valentina, Freeman, Ken C., Lewis, Geraint F., Lin, Jane, Martell, Sarah L., Schlesinger, Katharine J., Simpson, Jeffrey D., Zucker, Daniel B., Zwitter, Tomaž, Amarsi, Anish M., Anguiano, Borja, Carollo, Daniela, Casagrande, Luca, Čotar, Klemen, Cottrell, Peter L., da Costa, Gary, Gao, Xudong D., Hayden, Michael R., Horner, Jonathan, Ireland, Michael J., Kafle, Prajwal R., Munari, Ulisse, Nataf, David M., Nordlander, Thomas, Stello, Dennis, Ting, Yuan-Sen, Traven, Gregor, Watson, Fred, Wittenmyer, Robert A., Wyse, Rosemary F. G., Yong, David, Zinn, Joel C., Žerjal, Maruša and Galah Collaboration, 2018, "The GALAH Survey: second data release", *Mon. Not. Roy. Astron. Soc.*, **478**(4), 4513–4552. [DOI], [ADS], [arXiv:1804.06041 [astro-ph.SR]]

Buder, Sven, Sharma, Sanjib, Kos, Janez, Amarsi, Anish M., Nordlander, Thomas, Lind, Karin, Martell, Sarah L., Asplund, Martin, Bland-Hawthorn, Joss, Casey, Andrew R., de Silva, Gayandhi M., D'Orazi, Valentina, Freeman, Ken C., Hayden, Michael R., Lewis, Geraint F., Lin, Jane, Schlesinger, Katharine J., Simpson, Jeffrey D., Stello, Dennis, Zucker, Daniel B., Zwitter, Tomaž, Beeson, Kevin L., Buck, Tobias, Casagrande, Luca, Clark, Jake T., Čotar, Klemen, da Costa, Gary S., de Grijs, Richard, Feuillet, Diane, Horner, Jonathan, Kafle, Prajwal R., Khanna, Shourya, Kobayashi, Chiaki, Liu, Fan, Montet, Benjamin T., Nandakumar, Govind, Nataf, David M., Ness, Melissa K., Spina, Lorenzo, Tepper-García, Thor, Ting, Yuan-Sen, Traven, Gregor, Vogrinčič, Rok, Wittenmyer, Robert A., Wyse, Rosemary F. G., Žerjal, Maruša and GALAH Collaboration, 2021, "The GALAH+ survey: Third data release", *Mon. Not. Roy. Astron. Soc.*, **506**(1), 150–201. [DOI], [ADS], [arXiv:2011.02505 [astro-ph.GA]]

Cameron, A. G. W., 1955, "Origin of Anomalous Abundances of the Elements in Giant Stars.", *Astrophys. J.*, **121**, 144. [DOI], [ADS]

Cameron, A. G. W. and Fowler, W. A., 1971, "Lithium and the s-PROCESS in Red-Giant Stars", *Astrophys. J.*, **164**, 111. [DOI], [ADS]

Carlberg, Joleen K., Cunha, Katia and Smith, Verne V., 2016, "Lithium Inventory of 2 M $_{\odot}$ Red Clump Stars in Open Clusters: A Test of the Helium Flash Mechanism", *Astrophys. J.*, **827**(2), 129. [DOI], [ADS], [arXiv:1608.01678 [astro-ph.SR]]

Carollo, Daniela, Beers, Timothy C., Lee, Young Sun, Chiba, Masashi, Norris, John E., Wilhelm, Ronald, Sivarani, Thirupathi, Marsteller, Brian, Munn, Jeffrey A., Bailer-Jones, Coryn A. L., Fiorentin, Paola Re and York, Donald G., 2007, "Two stellar components in the halo of the Milky Way", *Nature*, **450**(7172), 1020–1025. [DOI], [ADS], [arXiv:0706.3005 [astro-ph]]

Casagrande, L., Schönrich, R., Asplund, M., Cassisi, S., Ramírez, I., Meléndez, J., Bensby, T. and Feltzing, S., 2011, "New constraints on the chemical evolution of the solar neighbourhood and Galactic disc(s). Improved astrophysical parameters for the Geneva-Copenhagen Survey", *Astron. Astrophys.*, **530**, A138. [DOI], [ADS], [arXiv:1103.4651 [astro-ph.GA]]

Casey, A. R., Ruchti, G., Masseron, T., Randich, S., Gilmore, G., Lind, K., Kennedy, G. M., Koposov, S. E., Hourihane, A., Franciosini, E., Lewis, J. R., Magrini, L., Morbidelli, L., Sacco, G. G., Worley, C. C., Feltzing, S., Jeffries, R. D., Vallenari, A., Bensby, T., Bragaglia, A., Flaccomio, E., Francois, P., Korn, A. J., Lanzafame, A., Pancino, E., Recio-Blanco, A., Smiljanic, R., Carraro, G., Costado, M. T., Damiani, F., Donati, P., Frasca, A., Jofré, P., Lardo, C., de Laverny, P., Monaco, L., Prisinzano, L., Sbordone, L., Sousa, S. G., Tautvaišienė, G., Zaggia, S., Zwitter, T., Delgado Mena, E., Chorniy, Y., Martell, S. L., Silva Aguirre, V., Miglio, A., Chiappini, C., Montalban, J., Morel, T. and Valentini, M., 2016, "The Gaia-ESO Survey: revisiting the Li-rich giant problem", *Mon. Not. Roy. Astron. Soc.*, **461**(3), 3336–3352. [DOI], [ADS], [arXiv:1603.03038 [astro-ph.SR]]

Casey, Andrew R., Ho, Anna Y. Q., Ness, Melissa, Hogg, David W., Rix, Hans-Walter, Angelou, George C., Hekker, Saskia, Tout, Christopher A., Lattanzio, John C., Karakas, Amanda I., Woods, Tyrone E., Price-Whelan, Adrian M. and Schlaufman, Kevin C., 2019, "Tidal Interactions between Binary Stars Can Drive Lithium Production in Low-mass Red Giants", *Astrophys. J.*, **880**(2), 125. [DOI], [ADS], [arXiv:1902.04102 [astro-ph.SR]]

Cassisi, Santi, Salaris, Maurizio and Pietrinferni, Adriano, 2016, "The red giant branch phase transition: Implications for the RGB luminosity function bump and detections of Li-rich red clump stars", *Astron. Astrophys.*, **585**, A124. [DOI], [ADS], [arXiv:1510.07870 [astro-ph.SR]]

Castelli, F. and Kurucz, R. L., 2003, "New Grids of ATLAS9 Model Atmospheres", in *Modelling of Stellar Atmospheres*, (Eds.) Piskunov, N., Weiss, W. W., Gray, D. F., IAU Symposium, 210, p. A20, Astronomical Society of the Pacific, California, USA. [ADS], [arXiv:astro-ph/0405087 [astro-ph]]

Casuso, E. and Beckman, J. E., 2004, "The K-dwarf problem and the time-dependence of gaseous accretion to the Galactic disc", *Astron. Astrophys.*, **419**, 181–190. [DOI], [ADS]

Cayrel, R., 1988, "Data Analysis", in *The Impact of Very High S/N Spectroscopy on Stellar Physics*, (Eds.) Cayrel de Strobel, G., Spite, Monique, IAU Symposium, 132, p. 345, Kluwer Academic Publishers, Dordrecht, Netherlands. [ADS]

Chandrasekhar, S., 1931, "The highly collapsed configurations of a stellar mass", *Mon. Not. Roy. Astron. Soc.*, **91**, 456–466. [DOI], [ADS]

Chandrasekhar, S., 1935, "The highly collapsed configurations of a stellar mass (Second paper)", *Mon. Not. Roy. Astron. Soc.*, **95**, 207–225. [DOI], [ADS]

Chandrasekhar, S., 1984, "On Stars, Their Evolution and Their Stability", *Science*, **226**(4674), 497–505. [DOI], [ADS]

Charbonnel, C. and Balachandran, S. C., 2000, "The Nature of the lithium rich giants. Mixing episodes on the RGB and early-AGB", *Astron. Astrophys.*, **359**, 563–572. [ADS], [arXiv:astro-ph/0005280 [astro-ph]]

Charbonnel, C. and Lagarde, N., 2010, "Thermohaline instability and rotation-induced mixing. I. Low- and intermediate-mass solar metallicity stars up to the end of the AGB", *Astron. Astrophys.*, **522**, A10. [DOI], [ADS], [arXiv:1006.5359 [astro-ph.SR]]

Charbonnel, C. and Zahn, J. P., 2007, "Thermohaline mixing: a physical mechanism governing the photospheric composition of low-mass giants", *Astron. Astrophys.*, **467**(1), L15–L18. [DOI], [ADS], [arXiv:astro-ph/0703302 [astro-ph]]

Charbonnel, C., Borisov, S., de Laverny, P. and Prantzos, N., 2021, "The behaviour of lithium at high metallicity in the Milky Way. Selection effects in the samples and the possible role of atomic diffusion", *Astron. Astrophys.*, **649**, L10. [DOI], [ADS], [arXiv:2104.14311 [astro-ph.GA]]

Chen, Y. Q., Nissen, P. E., Benoni, T. and Zhao, G., 2001, "Lithium abundances for 185 main-sequence stars: Galactic evolution and stellar depletion of lithium", *Astron. Astrophys.*, **371**, 943–951. [DOI], [ADS], [arXiv:astro-ph/0104053 [astro-ph]]

Chiba, Masashi and Beers, Timothy C., 2000, "Kinematics of Metal-poor Stars in the Galaxy. III. Formation of the Stellar Halo and Thick Disk as Revealed from a Large Sample of Nonkinematically Selected Stars", *Astron. J.*, **119**(6), 2843–2865. [DOI], [ADS], [arXiv:astro-ph/0003087 [astro-ph]]

Christensen-Dalsgaard, Jørgen, 2015, "On the red-giant luminosity bump", *Mon. Not. Roy. Astron. Soc.*, **453**(1), 666–670. [DOI], [ADS], [arXiv:1507.05531 [astro-ph.SR]]

Coc, Alain, Goriely, Stéphane, Xu, Yi, Saimpert, Matthias and Vangioni, Elisabeth, 2012, "Standard Big Bang Nucleosynthesis up to CNO with an Improved Extended Nuclear Network", *Astrophys. J.*, **744**(2), 158. [DOI], [ADS], [arXiv:1107.1117 [astro-ph.CO]]

Coc, Alain, Uzan, Jean-Philippe and Vangioni, Elisabeth, 2014, "Standard big bang nucleosynthesis and primordial CNO abundances after Planck", *J. Cosmol. Astropart. Phys.*, **2014**(10), 050. [DOI], [ADS], [arXiv:1403.6694 [astro-ph.CO]]

Cole, P. W. and Deupree, R. G., 1981, "The violent phase of the core helium flash.", *Astrophys. J.*, **247**, 607–613. [DOI], [ADS]

Couch, R. G. and Arnett, W. D., 1975, "Carbon ignition and burning in degenerate stellar cores.", *Astrophys. J.*, **196**, 791–803. [DOI], [ADS]

Cox, J. P. and Giuli, R. T., 1968, *Principles of stellar structure*, Gordon & Breach, New York. [ADS]

Cropper, M., Katz, D., Sartoretti, P., Prusti, T., de Bruijne, J. H. J., Chassat, F., Charvet, P., Boyadjian, J., Perryman, M., Sarri, G., Gare, P., Erdmann, M., Munari, U., Zwitter, T., Wilkinson, M., Arenou, F., Vallenari, A., Gómez, A., Panuzzo, P., Seabroke, G., Allende Prieto, C., Benson, K., Marchal, O., Huckle, H., Smith, M., Dolding, C., Janßen, K., Viala, Y., Blomme, R., Baker, S., Boudreault, S., Crifo, F., Soubiran, C., Frémat, Y., Jasniewicz, G., Guerrier, A., Guy, L. P., Turon, C., Jean-Antoine-Piccolo, A., Thévenin, F., David, M., Gosset, E. and Damerdji, Y., 2018, "Gaia Data Release 2. Gaia Radial Velocity Spectrometer", *Astron. Astrophys.*, **616**, A5. [DOI], [ADS], [arXiv:1804.09369 [astro-ph.IM]]

Cunha, Katia and Smith, Verne V., 2006, "Chemical Evolution of the Galactic Bulge as Derived from High-Resolution Infrared Spectroscopy of K and M Red Giants", *Astrophys. J.*, **651**(1), 491–501. [DOI], [ADS], [arXiv:astro-ph/0607393 [astro-ph]]

Cyburt, Richard H., Fields, Brian D. and Olive, Keith A., 2008, "An update on the big bang nucleosynthesis prediction for ^{7}Li: the problem worsens", *J. Cosmol. Astropart. Phys.*, **2008**(11), 012. [DOI], [ADS], [arXiv:0808.2818 [astro-ph]]

da Silva, L., Girardi, L., Pasquini, L., Setiawan, J., von der Lühe, O., de Medeiros, J. R., Hatzes, A., Döllinger, M. P. and Weiss, A., 2006, "Basic physical parameters of a selected sample of evolved stars", *Astron. Astrophys.*, **458**(2), 609–623. [DOI], [ADS], [arXiv:astro-ph/0608160 [astro-ph]]

Danielski, C., Babusiaux, C., Ruiz-Dern, L., Sartoretti, P. and Arenou, F., 2018, "The empirical Gaia G-band extinction coefficient", *Astron. Astrophys.*, **614**, A19. [DOI], [ADS], [arXiv:1802.01670 [astro-ph.SR]]

D'Antona, F. and Montalbán, J., 2003, "Efficiency of convection and Pre-Main Sequence lithium depletion", *Astron. Astrophys.*, **412**, 213–218. [DOI], [ADS], [arXiv:astro-ph/0309348 [astro-ph]]

Deepak and Lambert, David L., 2021a, "Lithium abundances and asteroseismology of red giants: understanding the evolution of lithium in giants based on asteroseismic parameters", *Mon. Not. Roy. Astron. Soc.*, **505**(1), 642–648. [DOI], [ADS], [arXiv:2104.11741 [astro-ph.SR]]

Deepak and Lambert, David L., 2021b, "Lithium in red giants: the roles of the He-core flash and the luminosity bump", *Mon. Not. Roy. Astron. Soc.*, **507**(1), 205–224. [DOI], [ADS], [arXiv:2107.04624 [astro-ph.SR]]

Deepak and Reddy, Bacham E., 2018, "Radial Velocity Comparison of Gaia DR2 and RAVE DR5 Survey: A Systematic Offset in Radial Velocities among a Group of Highly Accurate Radial Velocity Stars", *Astron. J.*, **156**(4), 170. [DOI], [ADS], [arXiv:1807.11716 [astro-ph.SR]]

Deepak and Reddy, Bacham E., 2019, "Study of Lithium-rich giants with the GALAH spectroscopic survey", *Mon. Not. Roy. Astron. Soc.*, **484**(2), 2000–2008. [DOI], [ADS], [arXiv:1901.03832 [astro-ph.SR]]

Deepak and Reddy, Bacham E., 2020a, "Lithium enrichment in the Galaxy: A study using the GALAH and Gaia surveys", in *Galactic Dynamics in the Era of Large Surveys*, (Eds.) Valluri, Monica, Sellwood, J. A., IAU Symposium, 353, pp. 16–18, Cambridge University Press, The Edinburgh Building, Cambridge CB2 8RU, UK. [DOI], [ADS]

Deepak and Reddy, Bacham Eswar, 2020b, "Lithium in the Galaxy: current status and contribution from the low-mass giants?", *Mem. Societa Astronomica Italiana*, **91**, 134–137. [ADS]

Deepak, Lambert, David L. and Reddy, Bacham E., 2020, "Abundance analyses of Li-enriched and normal giants in the GALAH survey", *Mon. Not. Roy. Astron. Soc.*, **494**(1), 1348–1365. [DOI], [ADS], [arXiv:2003.05381 [astro-ph.SR]]

Dehnen, Walter and Binney, James J., 1998, "Local stellar kinematics from HIPPARCOS data", *Mon. Not. Roy. Astron. Soc.*, **298**(2), 387–394. [DOI], [ADS], [arXiv:astro-ph/9710077 [astro-ph]]

Deliyannis, Constantine P., Anthony-Twarog, Barbara J., Lee-Brown, Donald B. and Twarog, Bruce A., 2019, "Li Evolution and the Open Cluster NGC 6819: A Correlation between Li Depletion and Spindown in Dwarfs More Massive Than the F-Dwarf Li-Dip", *Astron. J.*, **158**(4), 163. [DOI], [ADS], [arXiv:1909.04523 [astro-ph.SR]]

Deliyannis, Constantine Plato, 1990, *Primordial Lithium, Stellar Evolution, and Cosmology: Lithium in Halo Stars from Standard, Diffusive, and Rotational Stellar Evolution and Implications for Cosmology*, Ph.D. thesis, Yale University., New Haven, CT. [ADS]

Denissenkov, P. A., 2012, "A New Twist in the Evolution of Low-mass Stars", *Astrophys. J. Lett.*, **753**, L3. [DOI], [ADS], [arXiv:1203.1948 [astro-ph.SR]]

Denissenkov, P. A. and Merryfield, W. J., 2011, "Thermohaline Mixing: Does it Really Govern the Atmospheric Chemical Composition of Low-mass Red Giants?", *Astrophys. J. Lett.*, **727**, L8. [DOI], [ADS], [arXiv:1011.2191 [astro-ph.SR]]

Despain, K. H., 1981, "Low-mass evolution - Zero-age main sequence to asymptotic giant branch", *Astrophys. J.*, **251**, 639–653. [DOI], [ADS]

Di Matteo, P., Lehnert, M. D., Qu, Y. and van Driel, W., 2011, "The formation of a thick disk through the heating of a thin disk: Agreement with orbital eccentricities of stars in the solar neighborhood", *Astron. Astrophys.*, **525**, L3. [DOI], [ADS], [arXiv:1011.3825 [astro-ph.CO]]

Dominguez, Inma, Chieffi, Alessandro, Limongi, Marco and Straniero, Oscar, 1999, "Intermediate-Mass Stars: Updated Models", *Astrophys. J.*, **524**(1), 226–241. [DOI], [ADS], [arXiv:astro-ph/9906030 [astro-ph]]

Douchin, F. and Haensel, P., 2001, "A unified equation of state of dense matter and neutron star structure", *Astron. Astrophys.*, **380**, 151–167. [DOI], [ADS], [arXiv:astro-ph/0111092 [astro-ph]]

Dumont, T., Palacios, A., Charbonnel, C., Richard, O., Amard, L., Augustson, K. and Mathis, S., 2021, "Lithium depletion and angular momentum transport in solar-type stars", *Astron. Astrophys.*, **646**, A48. [DOI], [ADS], [arXiv:2012.03647 [astro-ph.SR]]

Edvardsson, B., Andersen, J., Gustafsson, B., Lambert, D. L., Nissen, P. E. and Tomkin, J., 1993, "The chemical evolution of the galactic disk. I. Analysis and results.", *Astron. Astrophys.*, **500**, 391–442. [ADS]

Eggen, O. J., Lynden-Bell, D. and Sandage, A. R., 1962, "Evidence from the motions of old stars that the Galaxy collapsed.", *Astrophys. J.*, **136**, 748. [DOI], [ADS]

Eggleton, Peter P., 1971, "The evolution of low mass stars", *Mon. Not. Roy. Astron. Soc.*, **151**, 351. [DOI], [ADS]

Eggleton, Peter P., Dearborn, David S. P. and Lattanzio, John C., 2008, "Compulsory Deep Mixing of ^{3}He and CNO Isotopes in the Envelopes of Low-Mass Red Giants", *Astrophys. J.*, **677**(1), 581–592. [DOI], [ADS], [arXiv:0706.2710 [astro-ph]]

Elsworth, Yvonne, Hekker, Saskia, Basu, Sarbani and Davies, Guy R., 2017, "A new method for the asteroseismic determination of the evolutionary state of red-giant stars", *Mon. Not. Roy. Astron. Soc.*, **466**(3), 3344–3352. [DOI], [ADS], [arXiv:1612.04751 [astro-ph.SR]]

Erb, Dawn K., Shapley, Alice E., Pettini, Max, Steidel, Charles C., Reddy, Naveen A. and Adelberger, Kurt L., 2006, "The Mass-Metallicity Relation at z>~2", *Astrophys. J.*, **644**(2), 813–828. [DOI], [ADS], [arXiv:astro-ph/0602473 [astro-ph]]

Evans, D. W., Riello, M., De Angeli, F., Carrasco, J. M., Montegriffo, P., Fabricius, C., Jordi, C., Palaversa, L., Diener, C., Busso, G., Cacciari, C., van Leeuwen, F., Burgess, P. W., Davidson, M., Harrison, D. L., Hodgkin, S. T., Pancino, E., Richards, P. J., Altavilla, G., Balaguer-Núñez, L., Barstow, M. A., Bellazzini, M., Brown, A. G. A., Castellani, M., Cocozza, G., De Luise, F., Delgado, A., Ducourant, C., Galleti, S., Gilmore, G., Giuffrida, G., Holl, B., Kewley, A., Koposov, S. E., Marinoni, S., Marrese, P. M., Osborne, P. J., Piersimoni, A., Portell, J., Pulone, L., Ragaini, S., Sanna, N., Terrett, D., Walton, N. A., Wevers, T. and Wyrzykowski, Ł., 2018, "Gaia Data Release 2. Photometric content and validation", *Astron. Astrophys.*, **616**, A4. [DOI], [ADS], [arXiv:1804.09368 [astro-ph.IM]]

Feng, Yu, Di-Matteo, Tiziana, Croft, Rupert A., Bird, Simeon, Battaglia, Nicholas and Wilkins, Stephen, 2016, "The BlueTides simulation: first galaxies and reionization", *Mon. Not. Roy. Astron. Soc.*, **455**(3), 2778–2791. [DOI], [ADS], [arXiv:1504.06619 [astro-ph.CO]]

Feuillet, Diane K., Feltzing, Sofia, Sahlholdt, Christian L. and Casagrande, Luca, 2020, "The SkyMapper-Gaia RVS view of the Gaia-Enceladus-Sausage - an investigation of the metallicity and mass of the Milky Way's last major merger", *Mon. Not. Roy. Astron. Soc.*, **497**(1), 109–124. [DOI], [ADS], [arXiv:2003.11039 [astro-ph.GA]]

Fields, Brian D., 2011, "The Primordial Lithium Problem", *Annual Review of Nuclear and Particle Science*, **61**(1), 47–68. [DOI], [ADS], [arXiv:1203.3551 [astro-ph.CO]]

Francis, Charles and Anderson, Erik, 2009, "Calculation of the local standard of rest from 20 574 local stars in the New Hipparcos Reduction with known radial velocities", *New Astronomy*, **14**(7), 615–629. [DOI], [ADS], [arXiv:0812.4032 [astro-ph]]

Freeman, Ken and Bland-Hawthorn, Joss, 2002, "The New Galaxy: Signatures of Its Formation", *Ann. Rev. Astron. Astrophys.*, **40**, 487–537. [DOI], [ADS], [arXiv:astro-ph/0208106 [astro-ph]]

Fryer, Chris L., 1999, "Mass Limits For Black Hole Formation", *Astrophys. J.*, **522**(1), 413–418. [DOI], [ADS], [arXiv:astro-ph/9902315 [astro-ph]]

Fulbright, Jon P., 2000, "Abundances and Kinematics of Field Halo and Disk Stars. I. Observational Data and Abundance Analysis", *Astron. J.*, **120**(4), 1841–1852. [DOI], [ADS], [arXiv:astro-ph/0006260 [astro-ph]]

Fulbright, Jon. P., McWilliam, Andrew and Rich, R. Michael, 2007, "Abundances of Baade's Window Giants from Keck HIRES Spectra. II. The Alpha and Light Odd Elements", *Astrophys. J.*, **661**(2), 1152–1179. [DOI], [ADS], [arXiv:astro-ph/0609087 [astro-ph]]

Fusi-Pecci, F. and Renzini, A., 1976, "On total mass loss in stars with M $\lneqq$ 8 M sun.", *Astron. Astrophys.*, **46**, 447–454. [ADS]

Gaia Collaboration, Prusti, T., de Bruijne, J. H. J., Brown, A. G. A., Vallenari, A., Babusiaux, C., Bailer-Jones, C. A. L., Bastian, U., Biermann, M., Evans, D. W., Eyer, L., Jansen, F., Jordi, C., Klioner, S. A., Lammers, U., Lindegren, L., Luri, X., Mignard, F., Milligan, D. J., Panem, C., Poinsignon, V., Pourbaix, D., Randich, S., Sarri, G., Sartoretti, P., Siddiqui, H. I., Soubiran, C., Valette, V., van Leeuwen, F., Walton, N. A., Aerts, C., Arenou, F., Cropper,

M., Drimmel, R., Høg, E., Katz, D., Lattanzi, M. G., O'Mullane, W., Grebel, E. K., Holland, A. D., Huc, C., Passot, X., Bramante, L., Cacciari, C., Castañeda, J., Chaoul, L., Cheek, N., De Angeli, F., Fabricius, C., Guerra, R., Hernández, J., Jean-Antoine-Piccolo, A., Masana, E., Messineo, R., Mowlavi, N., Nienartowicz, K., Ordóñez-Blanco, D., Panuzzo, P., Portell, J., Richards, P. J., Riello, M., Seabroke, G. M., Tanga, P., Thévenin, F., Torra, J., Els, S. G., Gracia-Abril, G., Comoretto, G., Garcia-Reinaldos, M., Lock, T., Mercier, E., Altmann, M., Andrae, R., Astraatmadja, T. L., Bellas-Velidis, I., Benson, K., Berthier, J., Blomme, R., Busso, G., Carry, B., Cellino, A., Clementini, G., Cowell, S., Creevey, O., Cuypers, J., Davidson, M., De Ridder, J., de Torres, A., Delchambre, L., Dell'Oro, A., Ducourant, C., Frémat, Y., García-Torres, M., Gosset, E., Halbwachs, J. L., Hambly, N. C., Harrison, D. L., Hauser, M., Hestroffer, D., Hodgkin, S. T., Huckle, H. E., Hutton, A., Jasniewicz, G., Jordan, S., Kontizas, M., Korn, A. J., Lanzafame, A. C., Manteiga, M., Moitinho, A., Muinonen, K., Osinde, J., Pancino, E., Pauwels, T., Petit, J. M., Recio-Blanco, A., Robin, A. C., Sarro, L. M., Siopis, C., Smith, M., Smith, K. W., Sozzetti, A., Thuillot, W., van Reeven, W., Viala, Y., Abbas, U., Abreu Aramburu, A., Accart, S., Aguado, J. J., Allan, P. M., Allasia, W., Altavilla, G., Álvarez, M. A., Alves, J., Anderson, R. I., Andrei, A. H., Anglada Varela, E., Antiche, E., Antoja, T., Antón, S., Arcay, B., Atzei, A., Ayache, L., Bach, N., Baker, S. G., Balaguer-Núñez, L., Barache, C., Barata, C., Barbier, A., Barblan, F., Baroni, M., Barrado y Navascués, D., Barros, M., Barstow, M. A., Becciani, U., Bellazzini, M., Bellei, G., Bello García, A., Belokurov, V., Bendjoya, P., Berihuete, A., Bianchi, L., Bienaymé, O., Billebaud, F., Blagorodnova, N., Blanco-Cuaresma, S., Boch, T., Bombrun, A., Borrachero, R., Bouquillon, S., Bourda, G., Bouy, H., Bragaglia, A., Breddels, M. A., Brouillet, N., Brüsemeister, T., Bucciarelli, B., Budnik, F., Burgess, P., Burgon, R., Burlacu, A., Busonero, D., Buzzi, R., Caffau, E., Cambras, J., Campbell, H., Cancelliere, R., Cantat-Gaudin, T., Carlucci, T., Carrasco, J. M., Castellani, M., Charlot, P., Charnas, J., Charvet, P., Chassat, F., Chiavassa, A., Clotet, M., Cocozza,

G., Collins, R. S., Collins, P., Costigan, G., Crifo, F., Cross, N. J. G., Crosta, M., Crowley, C., Dafonte, C., Damerdji, Y., Dapergolas, A., David, P., David, M., De Cat, P., de Felice, F., de Laverny, P., De Luise, F., De March, R., de Martino, D., de Souza, R., Debosscher, J., del Pozo, E., Delbo, M., Delgado, A., Delgado, H. E., di Marco, F., Di Matteo, P., Diakite, S., Distefano, E., Dolding, C., Dos Anjos, S., Drazinos, P., Durán, J., Dzigan, Y., Ecale, E., Edvardsson, B., Enke, H., Erdmann, M., Escolar, D., Espina, M., Evans, N. W., Eynard Bontemps, G., Fabre, C., Fabrizio, M., Faigler, S., Falcão, A. J., Farràs Casas, M., Faye, F., Federici, L., Fedorets, G., Fernández-Hernández, J., Fernique, P., Fienga, A., Figueras, F., Filippi, F., Findeisen, K., Fonti, A., Fouesneau, M., Fraile, E., Fraser, M., Fuchs, J., Furnell, R., Gai, M., Galleti, S., Galluccio, L., Garabato, D., García-Sedano, F., Garé, P., Garofalo, A., Garralda, N., Gavras, P., Gerssen, J., Geyer, R., Gilmore, G., Girona, S., Giuffrida, G., Gomes, M., González-Marcos, A., González-Núñez, J., González-Vidal, J. J., Granvik, M., Guerrier, A., Guillout, P., Guiraud, J., Gúrpide, A., Gutiérrez-Sánchez, R., Guy, L. P., Haigron, R., Hatzidimitriou, D., Haywood, M., Heiter, U., Helmi, A., Hobbs, D., Hofmann, W., Holl, B., Holland, G., Hunt, J. A. S., Hypki, A., Icardi, V., Irwin, M., Jevardat de Fombelle, G., Jofré, P., Jonker, P. G., Jorissen, A., Julbe, F., Karampelas, A., Kochoska, A., Kohley, R., Kolenberg, K., Kontizas, E., Koposov, S. E., Kordopatis, G., Koubsky, P., Kowalczyk, A., Krone-Martins, A., Kudryashova, M., Kull, I., Bachchan, R. K., Lacoste-Seris, F., Lanza, A. F., Lavigne, J. B., Le Poncin-Lafitte, C., Lebreton, Y., Lebzelter, T., Leccia, S., Leclerc, N., Lecoeur-Taibi, I., Lemaitre, V., Lenhardt, H., Leroux, F., Liao, S., Licata, E., Lindstrøm, H. E. P., Lister, T. A., Livanou, E., Lobel, A., Löffler, W., López, M., Lopez-Lozano, A., Lorenz, D., Loureiro, T., MacDonald, I., Magalhães Fernandes, T., Managau, S., Mann, R. G., Mantelet, G., Marchal, O., Marchant, J. M., Marconi, M., Marie, J., Marinoni, S., Marrese, P. M., Marschalkó, G., Marshall, D. J., Martín-Fleitas, J. M., Martino, M., Mary, N., Matijevič, G., Mazeh, T., McMillan, P. J., Messina, S., Mestre, A., Michalik, D., Millar, N. R., Miranda, B. M. H., Molina, D., Molinaro, R.,

Molinaro, M., Molnár, L., Moniez, M., Montegriffo, P., Monteiro, D., Mor, R., Mora, A., Morbidelli, R., Morel, T., Morgenthaler, S., Morley, T., Morris, D., Mulone, A. F., Muraveva, T., Musella, I., Narbonne, J., Nelemans, G., Nicastro, L., Noval, L., Ordénovic, C., Ordieres-Meré, J., Osborne, P., Pagani, C., Pagano, I., Pailler, F., Palacin, H., Palaversa, L., Parsons, P., Paulsen, T., Pecoraro, M., Pedrosa, R., Pentikäinen, H., Pereira, J., Pichon, B., Piersimoni, A. M., Pineau, F. X., Plachy, E., Plum, G., Poujoulet, E., Prša, A., Pulone, L., Ragaini, S., Rago, S., Rambaux, N., Ramos-Lerate, M., Ranalli, P., Rauw, G., Read, A., Regibo, S., Renk, F., Reylé, C., Ribeiro, R. A., Rimoldini, L., Ripepi, V., Riva, A., Rixon, G., Roelens, M., Romero-Gómez, M., Rowell, N., Royer, F., Rudolph, A., Ruiz-Dern, L., Sadowski, G., Sagristà Sellés, T., Sahlmann, J., Salgado, J., Salguero, E., Sarasso, M., Savietto, H., Schnorhk, A., Schultheis, M., Sciacca, E., Segol, M., Segovia, J. C., Segransan, D., Serpell, E., Shih, I. C., Smareglia, R., Smart, R. L., Smith, C., Solano, E., Solitro, F., Sordo, R., Soria Nieto, S., Souchay, J., Spagna, A., Spoto, F., Stampa, U., Steele, I. A., Steidelmüller, H., Stephenson, C. A., Stoev, H., Suess, F. F., Süveges, M., Surdej, J., Szabados, L., Szegedi-Elek, E., Tapiador, D., Taris, F., Tauran, G., Taylor, M. B., Teixeira, R., Terrett, D., Tingley, B., Trager, S. C., Turon, C., Ulla, A., Utrilla, E., Valentini, G., van Elteren, A., Van Hemelryck, E., van Leeuwen, M., Varadi, M., Vecchiato, A., Veljanoski, J., Via, T., Vicente, D., Vogt, S., Voss, H., Votruba, V., Voutsinas, S., Walmsley, G., Weiler, M., Weingrill, K., Werner, D., Wevers, T., Whitehead, G., Wyrzykowski, Ł., Yoldas, A., Žerjal, M., Zucker, S., Zurbach, C., Zwitter, T., Alecu, A., Allen, M., Allende Prieto, C., Amorim, A., Anglada-Escudé, G., Arsenijevic, V., Azaz, S., Balm, P., Beck, M., Bernstein, H. H., Bigot, L., Bijaoui, A., Blasco, C., Bonfigli, M., Bono, G., Boudreault, S., Bressan, A., Brown, S., Brunet, P. M., Bunclark, P., Buonanno, R., Butkevich, A. G., Carret, C., Carrion, C., Chemin, L., Chéreau, F., Corcione, L., Darmigny, E., de Boer, K. S., de Teodoro, P., de Zeeuw, P. T., Delle Luche, C., Domingues, C. D., Dubath, P., Fodor, F., Frézouls, B., Fries, A., Fustes, D., Fyfe, D., Gallardo, E., Gallegos, J., Gardiol, D., Gebran, M., Gomboc, A.,

Gómez, A., Grux, E., Gueguen, A., Heyrovsky, A., Hoar, J., Iannicola, G., Isasi Parache, Y., Janotto, A. M., Joliet, E., Jonckheere, A., Keil, R., Kim, D. W., Klagyivik, P., Klar, J., Knude, J., Kochukhov, O., Kolka, I., Kos, J., Kutka, A., Lainey, V., LeBouquin, D., Liu, C., Loreggia, D., Makarov, V. V., Marseille, M. G., Martayan, C., Martinez-Rubi, O., Massart, B., Meynadier, F., Mignot, S., Munari, U., Nguyen, A. T., Nordlander, T., Ocvirk, P., O'Flaherty, K. S., Olias Sanz, A., Ortiz, P., Osorio, J., Oszkiewicz, D., Ouzounis, A., Palmer, M., Park, P., Pasquato, E., Peltzer, C., Peralta, J., Péturaud, F., Pieniluoma, T., Pigozzi, E., Poels, J., Prat, G., Prod'homme, T., Raison, F., Rebordao, J. M., Risquez, D., Rocca-Volmerange, B., Rosen, S., Ruiz-Fuertes, M. I., Russo, F., Sembay, S., Serraller Vizcaino, I., Short, A., Siebert, A., Silva, H., Sinachopoulos, D., Slezak, E., Soffel, M., Sosnowska, D., Straižys, V., ter Linden, M., Terrell, D., Theil, S., Tiede, C., Troisi, L., Tsalmantza, P., Tur, D., Vaccari, M., Vachier, F., Valles, P., Van Hamme, W., Veltz, L., Virtanen, J., Wallut, J. M., Wichmann, R., Wilkinson, M. I., Ziaeepour, H. and Zschocke, S., 2016a, "The Gaia mission", *Astron. Astrophys.*, **595**, A1. [DOI], [ADS], [arXiv:1609.04153 [astro-ph.IM]]

Gaia Collaboration, Prusti, T., de Bruijne, J. H. J., Brown, A. G. A., Vallenari, A., Babusiaux, C., Bailer-Jones, C. A. L., Bastian, U., Biermann, M., Evans, D. W., Eyer, L., Jansen, F., Jordi, C., Klioner, S. A., Lammers, U., Lindegren, L., Luri, X., Mignard, F., Milligan, D. J., Panem, C., Poinsignon, V., Pourbaix, D., Randich, S., Sarri, G., Sartoretti, P., Siddiqui, H. I., Soubiran, C., Valette, V., van Leeuwen, F., Walton, N. A., Aerts, C., Arenou, F., Cropper, M., Drimmel, R., Høg, E., Katz, D., Lattanzi, M. G., O'Mullane, W., Grebel, E. K., Holland, A. D., Huc, C., Passot, X., Bramante, L., Cacciari, C., Castañeda, J., Chaoul, L., Cheek, N., De Angeli, F., Fabricius, C., Guerra, R., Hernández, J., Jean-Antoine-Piccolo, A., Masana, E., Messineo, R., Mowlavi, N., Nienartowicz, K., Ordóñez-Blanco, D., Panuzzo, P., Portell, J., Richards, P. J., Riello, M., Seabroke, G. M., Tanga, P., Thévenin, F., Torra, J., Els, S. G., Gracia-Abril, G., Comoretto, G., Garcia-Reinaldos, M., Lock, T., Mercier, E.,

Altmann, M., Andrae, R., Astraatmadja, T. L., Bellas-Velidis, I., Benson, K., Berthier, J., Blomme, R., Busso, G., Carry, B., Cellino, A., Clementini, G., Cowell, S., Creevey, O., Cuypers, J., Davidson, M., De Ridder, J., de Torres, A., Delchambre, L., Dell'Oro, A., Ducourant, C., Frémat, Y., García-Torres, M., Gosset, E., Halbwachs, J. L., Hambly, N. C., Harrison, D. L., Hauser, M., Hestroffer, D., Hodgkin, S. T., Huckle, H. E., Hutton, A., Jasniewicz, G., Jordan, S., Kontizas, M., Korn, A. J., Lanzafame, A. C., Manteiga, M., Moitinho, A., Muinonen, K., Osinde, J., Pancino, E., Pauwels, T., Petit, J. M., Recio-Blanco, A., Robin, A. C., Sarro, L. M., Siopis, C., Smith, M., Smith, K. W., Sozzetti, A., Thuillot, W., van Reeven, W., Viala, Y., Abbas, U., Abreu Aramburu, A., Accart, S., Aguado, J. J., Allan, P. M., Allasia, W., Altavilla, G., Álvarez, M. A., Alves, J., Anderson, R. I., Andrei, A. H., Anglada Varela, E., Antiche, E., Antoja, T., Antón, S., Arcay, B., Atzei, A., Ayache, L., Bach, N., Baker, S. G., Balaguer-Núñez, L., Barache, C., Barata, C., Barbier, A., Barblan, F., Baroni, M., Barrado y Navascués, D., Barros, M., Barstow, M. A., Becciani, U., Bellazzini, M., Bellei, G., Bello García, A., Belokurov, V., Bendjoya, P., Berihuete, A., Bianchi, L., Bienaymé, O., Billebaud, F., Blagorodnova, N., Blanco-Cuaresma, S., Boch, T., Bombrun, A., Borrachero, R., Bouquillon, S., Bourda, G., Bouy, H., Bragaglia, A., Breddels, M. A., Brouillet, N., Brüsemeister, T., Bucciarelli, B., Budnik, F., Burgess, P., Burgon, R., Burlacu, A., Busonero, D., Buzzi, R., Caffau, E., Cambras, J., Campbell, H., Cancelliere, R., Cantat-Gaudin, T., Carlucci, T., Carrasco, J. M., Castellani, M., Charlot, P., Charnas, J., Charvet, P., Chassat, F., Chiavassa, A., Clotet, M., Cocozza, G., Collins, R. S., Collins, P., Costigan, G., Crifo, F., Cross, N. J. G., Crosta, M., Crowley, C., Dafonte, C., Damerdji, Y., Dapergolas, A., David, P., David, M., De Cat, P., de Felice, F., de Laverny, P., De Luise, F., De March, R., de Martino, D., de Souza, R., Debosscher, J., del Pozo, E., Delbo, M., Delgado, A., Delgado, H. E., di Marco, F., Di Matteo, P., Diakite, S., Distefano, E., Dolding, C., Dos Anjos, S., Drazinos, P., Durán, J., Dzigan, Y., Ecale, E., Edvardsson, B., Enke, H., Erdmann, M., Escolar, D., Espina, M., Evans, N. W., Eynard

Bontemps, G., Fabre, C., Fabrizio, M., Faigler, S., Falcão, A. J., Farràs Casas, M., Faye, F., Federici, L., Fedorets, G., Fernández-Hernández, J., Fernique, P., Fienga, A., Figueras, F., Filippi, F., Findeisen, K., Fonti, A., Fouesneau, M., Fraile, E., Fraser, M., Fuchs, J., Furnell, R., Gai, M., Galleti, S., Galluccio, L., Garabato, D., García-Sedano, F., Garé, P., Garofalo, A., Garralda, N., Gavras, P., Gerssen, J., Geyer, R., Gilmore, G., Girona, S., Giuffrida, G., Gomes, M., González-Marcos, A., González-Núñez, J., González-Vidal, J. J., Granvik, M., Guerrier, A., Guillout, P., Guiraud, J., Gúrpide, A., Gutiérrez-Sánchez, R., Guy, L. P., Haigron, R., Hatzidimitriou, D., Haywood, M., Heiter, U., Helmi, A., Hobbs, D., Hofmann, W., Holl, B., Holland, G., Hunt, J. A. S., Hypki, A., Icardi, V., Irwin, M., Jevardat de Fombelle, G., Jofré, P., Jonker, P. G., Jorissen, A., Julbe, F., Karampelas, A., Kochoska, A., Kohley, R., Kolenberg, K., Kontizas, E., Koposov, S. E., Kordopatis, G., Koubsky, P., Kowalczyk, A., Krone-Martins, A., Kudryashova, M., Kull, I., Bachchan, R. K., Lacoste-Seris, F., Lanza, A. F., Lavigne, J. B., Le Poncin-Lafitte, C., Lebreton, Y., Lebzelter, T., Leccia, S., Leclerc, N., Lecoeur-Taibi, I., Lemaitre, V., Lenhardt, H., Leroux, F., Liao, S., Licata, E., Lindstrøm, H. E. P., Lister, T. A., Livanou, E., Lobel, A., Löffler, W., López, M., Lopez-Lozano, A., Lorenz, D., Loureiro, T., MacDonald, I., Magalhães Fernandes, T., Managau, S., Mann, R. G., Mantelet, G., Marchal, O., Marchant, J. M., Marconi, M., Marie, J., Marinoni, S., Marrese, P. M., Marschalkó, G., Marshall, D. J., Martín-Fleitas, J. M., Martino, M., Mary, N., Matijevič, G., Mazeh, T., McMillan, P. J., Messina, S., Mestre, A., Michalik, D., Millar, N. R., Miranda, B. M. H., Molina, D., Molinaro, R., Molinaro, M., Molnár, L., Moniez, M., Montegriffo, P., Monteiro, D., Mor, R., Mora, A., Morbidelli, R., Morel, T., Morgenthaler, S., Morley, T., Morris, D., Mulone, A. F., Muraveva, T., Musella, I., Narbonne, J., Nelemans, G., Nicastro, L., Noval, L., Ordénovic, C., Ordieres-Meré, J., Osborne, P., Pagani, C., Pagano, I., Pailler, F., Palacin, H., Palaversa, L., Parsons, P., Paulsen, T., Pecoraro, M., Pedrosa, R., Pentikäinen, H., Pereira, J., Pichon, B., Piersimoni, A. M., Pineau, F. X., Plachy, E., Plum, G., Poujoulet, E., Prša, A., Pulone, L.,

Ragaini, S., Rago, S., Rambaux, N., Ramos-Lerate, M., Ranalli, P., Rauw, G., Read, A., Regibo, S., Renk, F., Reylé, C., Ribeiro, R. A., Rimoldini, L., Ripepi, V., Riva, A., Rixon, G., Roelens, M., Romero-Gómez, M., Rowell, N., Royer, F., Rudolph, A., Ruiz-Dern, L., Sadowski, G., Sagristà Sellés, T., Sahlmann, J., Salgado, J., Salguero, E., Sarasso, M., Savietto, H., Schnorhk, A., Schultheis, M., Sciacca, E., Segol, M., Segovia, J. C., Segransan, D., Serpell, E., Shih, I. C., Smareglia, R., Smart, R. L., Smith, C., Solano, E., Solitro, F., Sordo, R., Soria Nieto, S., Souchay, J., Spagna, A., Spoto, F., Stampa, U., Steele, I. A., Steidelmüller, H., Stephenson, C. A., Stoev, H., Suess, F. F., Süveges, M., Surdej, J., Szabados, L., Szegedi-Elek, E., Tapiador, D., Taris, F., Tauran, G., Taylor, M. B., Teixeira, R., Terrett, D., Tingley, B., Trager, S. C., Turon, C., Ulla, A., Utrilla, E., Valentini, G., van Elteren, A., Van Hemelryck, E., van Leeuwen, M., Varadi, M., Vecchiato, A., Veljanoski, J., Via, T., Vicente, D., Vogt, S., Voss, H., Votruba, V., Voutsinas, S., Walmsley, G., Weiler, M., Weingrill, K., Werner, D., Wevers, T., Whitehead, G., Wyrzykowski, Ł., Yoldas, A., Žerjal, M., Zucker, S., Zurbach, C., Zwitter, T., Alecu, A., Allen, M., Allende Prieto, C., Amorim, A., Anglada-Escudé, G., Arsenijevic, V., Azaz, S., Balm, P., Beck, M., Bernstein, H. H., Bigot, L., Bijaoui, A., Blasco, C., Bonfigli, M., Bono, G., Boudreault, S., Bressan, A., Brown, S., Brunet, P. M., Bunclark, P., Buonanno, R., Butkevich, A. G., Carret, C., Carrion, C., Chemin, L., Chéreau, F., Corcione, L., Darmigny, E., de Boer, K. S., de Teodoro, P., de Zeeuw, P. T., Delle Luche, C., Domingues, C. D., Dubath, P., Fodor, F., Frézouls, B., Fries, A., Fustes, D., Fyfe, D., Gallardo, E., Gallegos, J., Gardiol, D., Gebran, M., Gomboc, A., Gómez, A., Grux, E., Gueguen, A., Heyrovsky, A., Hoar, J., Iannicola, G., Isasi Parache, Y., Janotto, A. M., Joliet, E., Jonckheere, A., Keil, R., Kim, D. W., Klagyivik, P., Klar, J., Knude, J., Kochukhov, O., Kolka, I., Kos, J., Kutka, A., Lainey, V., LeBouquin, D., Liu, C., Loreggia, D., Makarov, V. V., Marseille, M. G., Martayan, C., Martinez-Rubi, O., Massart, B., Meynadier, F., Mignot, S., Munari, U., Nguyen, A. T., Nordlander, T., Ocvirk, P., O'Flaherty, K. S., Olias Sanz, A., Ortiz, P., Osorio, J., Oszkiewicz, D., Ouzounis, A., Palmer, M.,

Park, P., Pasquato, E., Peltzer, C., Peralta, J., Péturaud, F., Pieniluoma, T., Pigozzi, E., Poels, J., Prat, G., Prod'homme, T., Raison, F., Rebordao, J. M., Risquez, D., Rocca-Volmerange, B., Rosen, S., Ruiz-Fuertes, M. I., Russo, F., Sembay, S., Serraller Vizcaino, I., Short, A., Siebert, A., Silva, H., Sinachopoulos, D., Slezak, E., Soffel, M., Sosnowska, D., Straižys, V., ter Linden, M., Terrell, D., Theil, S., Tiede, C., Troisi, L., Tsalmantza, P., Tur, D., Vaccari, M., Vachier, F., Valles, P., Van Hamme, W., Veltz, L., Virtanen, J., Wallut, J. M., Wichmann, R., Wilkinson, M. I., Ziaeepour, H. and Zschocke, S., 2016b, "The Gaia mission", *Astron. Astrophys.*, **595**, A1. [DOI], [ADS], [arXiv:1609.04153 [astro-ph.IM]]

Gaia Collaboration, Babusiaux, C., van Leeuwen, F., Barstow, M. A., Jordi, C., Vallenari, A., Bossini, D., Bressan, A., Cantat-Gaudin, T., van Leeuwen, M., Brown, A. G. A., Prusti, T., de Bruijne, J. H. J., Bailer-Jones, C. A. L., Biermann, M., Evans, D. W., Eyer, L., Jansen, F., Klioner, S. A., Lammers, U., Lindegren, L., Luri, X., Mignard, F., Panem, C., Pourbaix, D., Randich, S., Sartoretti, P., Siddiqui, H. I., Soubiran, C., Walton, N. A., Arenou, F., Bastian, U., Cropper, M., Drimmel, R., Katz, D., Lattanzi, M. G., Bakker, J., Cacciari, C., Castañeda, J., Chaoul, L., Cheek, N., De Angeli, F., Fabricius, C., Guerra, R., Holl, B., Masana, E., Messineo, R., Mowlavi, N., Nienartowicz, K., Panuzzo, P., Portell, J., Riello, M., Seabroke, G. M., Tanga, P., Thévenin, F., Gracia-Abril, G., Comoretto, G., Garcia-Reinaldos, M., Teyssier, D., Altmann, M., Andrae, R., Audard, M., Bellas-Velidis, I., Benson, K., Berthier, J., Blomme, R., Burgess, P., Busso, G., Carry, B., Cellino, A., Clementini, G., Clotet, M., Creevey, O., Davidson, M., De Ridder, J., Delchambre, L., Dell'Oro, A., Ducourant, C., Fernández-Hernández, J., Fouesneau, M., Frémat, Y., Galluccio, L., García-Torres, M., González-Núñez, J., González-Vidal, J. J., Gosset, E., Guy, L. P., Halbwachs, J. L., Hambly, N. C., Harrison, D. L., Hernández, J., Hestroffer, D., Hodgkin, S. T., Hutton, A., Jasniewicz, G., Jean-Antoine-Piccolo, A., Jordan, S., Korn, A. J., Krone-Martins, A., Lanzafame, A. C., Lebzelter, T., Löffler, W., Manteiga, M., Marrese, P. M., Martín-Fleitas, J. M.,

Moitinho, A., Mora, A., Muinonen, K., Osinde, J., Pancino, E., Pauwels, T., Petit, J. M., Recio-Blanco, A., Richards, P. J., Rimoldini, L., Robin, A. C., Sarro, L. M., Siopis, C., Smith, M., Sozzetti, A., Süveges, M., Torra, J., van Reeven, W., Abbas, U., Abreu Aramburu, A., Accart, S., Aerts, C., Altavilla, G., Álvarez, M. A., Alvarez, R., Alves, J., Anderson, R. I., Andrei, A. H., Anglada Varela, E., Antiche, E., Antoja, T., Arcay, B., Astraatmadja, T. L., Bach, N., Baker, S. G., Balaguer-Núñez, L., Balm, P., Barache, C., Barata, C., Barbato, D., Barblan, F., Barklem, P. S., Barrado, D., Barros, M., Bartholomé Muñoz, L., Bassilana, J. L., Becciani, U., Bellazzini, M., Berihuete, A., Bertone, S., Bianchi, L., Bienaymé, O., Blanco-Cuaresma, S., Boch, T., Boeche, C., Bombrun, A., Borrachero, R., Bouquillon, S., Bourda, G., Bragaglia, A., Bramante, L., Breddels, M. A., Brouillet, N., Brüsemeister, T., Brugaletta, E., Bucciarelli, B., Burlacu, A., Busonero, D., Butkevich, A. G., Buzzi, R., Caffau, E., Cancelliere, R., Cannizzaro, G., Carballo, R., Carlucci, T., Carrasco, J. M., Casamiquela, L., Castellani, M., Castro-Ginard, A., Charlot, P., Chemin, L., Chiavassa, A., Cocozza, G., Costigan, G., Cowell, S., Crifo, F., Crosta, M., Crowley, C., Cuypers, J., Dafonte, C., Damerdji, Y., Dapergolas, A., David, P., David, M., de Laverny, P., De Luise, F., De March, R., de Martino, D., de Souza, R., de Torres, A., Debosscher, J., del Pozo, E., Delbo, M., Delgado, A., Delgado, H. E., Diakite, S., Diener, C., Distefano, E., Dolding, C., Drazinos, P., Durán, J., Edvardsson, B., Enke, H., Eriksson, K., Esquej, P., Eynard Bontemps, G., Fabre, C., Fabrizio, M., Faigler, S., Falcão, A. J., Farràs Casas, M., Federici, L., Fedorets, G., Fernique, P., Figueras, F., Filippi, F., Findeisen, K., Fonti, A., Fraile, E., Fraser, M., Frézouls, B., Gai, M., Galleti, S., Garabato, D., García-Sedano, F., Garofalo, A., Garralda, N., Gavel, A., Gavras, P., Gerssen, J., Geyer, R., Giacobbe, P., Gilmore, G., Girona, S., Giuffrida, G., Glass, F., Gomes, M., Granvik, M., Gueguen, A., Guerrier, A., Guiraud, J., Gutié, R., Haigron, R., Hatzidimitriou, D., Hauser, M., Haywood, M., Heiter, U., Helmi, A., Heu, J., Hilger, T., Hobbs, D., Hofmann, W., Holland, G., Huckle, H. E., Hypki, A., Icardi, V., Janßen, K., Jevardat de Fombelle, G., Jonker, P. G., Juhász, Á. L., Julbe, F., Karampelas,

A., Kewley, A., Klar, J., Kochoska, A., Kohley, R., Kolenberg, K., Kontizas, M., Kontizas, E., Koposov, S. E., Kordopatis, G., Kostrzewa-Rutkowska, Z., Koubsky, P., Lambert, S., Lanza, A. F., Lasne, Y., Lavigne, J. B., Le Fustec, Y., Le Poncin-Lafitte, C., Lebreton, Y., Leccia, S., Leclerc, N., Lecoeur-Taibi, I., Lenhardt, H., Leroux, F., Liao, S., Licata, E., Lindstrøm, H. E. P., Lister, T. A., Livanou, E., Lobel, A., López, M., Managau, S., Mann, R. G., Mantelet, G., Marchal, O., Marchant, J. M., Marconi, M., Marinoni, S., Marschalkó, G., Marshall, D. J., Martino, M., Marton, G., Mary, N., Massari, D., Matijevič, G., Mazeh, T., McMillan, P. J., Messina, S., Michalik, D., Millar, N. R., Molina, D., Molinaro, R., Molnár, L., Montegriffo, P., Mor, R., Morbidelli, R., Morel, T., Morris, D., Mulone, A. F., Muraveva, T., Musella, I., Nelemans, G., Nicastro, L., Noval, L., O'Mullane, W., Ordénovic, C., Ordóñez-Blanco, D., Osborne, P., Pagani, C., Pagano, I., Pailler, F., Palacin, H., Palaversa, L., Panahi, A., Pawlak, M., Piersimoni, A. M., Pineau, F. X., Plachy, E., Plum, G., Poggio, E., Poujoulet, E., Prša, A., Pulone, L., Racero, E., Ragaini, S., Rambaux, N., Ramos-Lerate, M., Regibo, S., Reylé, C., Riclet, F., Ripepi, V., Riva, A., Rivard, A., Rixon, G., Roegiers, T., Roelens, M., Romero-Gómez, M., Rowell, N., Royer, F., Ruiz-Dern, L., Sadowski, G., Sagristà Sellés, T., Sahlmann, J., Salgado, J., Salguero, E., Sanna, N., Santana-Ros, T., Sarasso, M., Savietto, H., Schultheis, M., Sciacca, E., Segol, M., Segovia, J. C., Ségransan, D., Shih, I. C., Siltala, L., Silva, A. F., Smart, R. L., Smith, K. W., Solano, E., Solitro, F., Sordo, R., Soria Nieto, S., Souchay, J., Spagna, A., Spoto, F., Stampa, U., Steele, I. A., Steidelmüller, H., Stephenson, C. A., Stoev, H., Suess, F. F., Surdej, J., Szabados, L., Szegedi-Elek, E., Tapiador, D., Taris, F., Tauran, G., Taylor, M. B., Teixeira, R., Terrett, D., Teyssand ier, P., Thuillot, W., Titarenko, A., Torra Clotet, F., Turon, C., Ulla, A., Utrilla, E., Uzzi, S., Vaillant, M., Valentini, G., Valette, V., van Elteren, A., Van Hemelryck, E., Vaschetto, M., Vecchiato, A., Veljanoski, J., Viala, Y., Vicente, D., Vogt, S., von Essen, C., Voss, H., Votruba, V., Voutsinas, S., Walmsley, G., Weiler, M., Wertz, O., Wevers, T., Wyrzykowski, Ł., Yoldas, A., Žerjal, M., Ziaeepour, H., Zorec, J., Zschocke, S.,

Zucker, S., Zurbach, C. and Zwitter, T., 2018a, "Gaia Data Release 2. Observational Hertzsprung-Russell diagrams", *Astron. Astrophys.*, **616**, A10. [DOI], [ADS], [arXiv:1804.09378 [astro-ph.SR]]

Gaia Collaboration, Brown, A. G. A., Vallenari, A., Prusti, T., de Bruijne, J. H. J., Babusiaux, C., Bailer-Jones, C. A. L., Biermann, M., Evans, D. W., Eyer, L., Jansen, F., Jordi, C., Klioner, S. A., Lammers, U., Lindegren, L., Luri, X., Mignard, F., Panem, C., Pourbaix, D., Randich, S., Sartoretti, P., Siddiqui, H. I., Soubiran, C., van Leeuwen, F., Walton, N. A., Arenou, F., Bastian, U., Cropper, M., Drimmel, R., Katz, D., Lattanzi, M. G., Bakker, J., Cacciari, C., Castañeda, J., Chaoul, L., Cheek, N., De Angeli, F., Fabricius, C., Guerra, R., Holl, B., Masana, E., Messineo, R., Mowlavi, N., Nienartowicz, K., Panuzzo, P., Portell, J., Riello, M., Seabroke, G. M., Tanga, P., Thévenin, F., Gracia-Abril, G., Comoretto, G., Garcia-Reinaldos, M., Teyssier, D., Altmann, M., Andrae, R., Audard, M., Bellas-Velidis, I., Benson, K., Berthier, J., Blomme, R., Burgess, P., Busso, G., Carry, B., Cellino, A., Clementini, G., Clotet, M., Creevey, O., Davidson, M., De Ridder, J., Delchambre, L., Dell'Oro, A., Ducourant, C., Fernández-Hernández, J., Fouesneau, M., Frémat, Y., Galluccio, L., García-Torres, M., González-Núñez, J., González-Vidal, J. J., Gosset, E., Guy, L. P., Halbwachs, J. L., Hambly, N. C., Harrison, D. L., Hernández, J., Hestroffer, D., Hodgkin, S. T., Hutton, A., Jasniewicz, G., Jean-Antoine-Piccolo, A., Jordan, S., Korn, A. J., Krone-Martins, A., Lanzafame, A. C., Lebzelter, T., Löffler, W., Manteiga, M., Marrese, P. M., Martín-Fleitas, J. M., Moitinho, A., Mora, A., Muinonen, K., Osinde, J., Pancino, E., Pauwels, T., Petit, J. M., Recio-Blanco, A., Richards, P. J., Rimoldini, L., Robin, A. C., Sarro, L. M., Siopis, C., Smith, M., Sozzetti, A., Süveges, M., Torra, J., van Reeven, W., Abbas, U., Abreu Aramburu, A., Accart, S., Aerts, C., Altavilla, G., Álvarez, M. A., Alvarez, R., Alves, J., Anderson, R. I., Andrei, A. H., Anglada Varela, E., Antiche, E., Antoja, T., Arcay, B., Astraatmadja, T. L., Bach, N., Baker, S. G., Balaguer-Núñez, L., Balm, P., Barache, C., Barata, C., Barbato, D., Barblan, F., Barklem, P. S., Barrado, D., Barros, M., Barstow,

M. A., Bartholomé Muñoz, S., Bassilana, J. L., Becciani, U., Bellazzini, M., Berihuete, A., Bertone, S., Bianchi, L., Bienaymé, O., Blanco-Cuaresma, S., Boch, T., Boeche, C., Bombrun, A., Borrachero, R., Bossini, D., Bouquillon, S., Bourda, G., Bragaglia, A., Bramante, L., Breddels, M. A., Bressan, A., Brouillet, N., Brüsemeister, T., Brugaletta, E., Bucciarelli, B., Burlacu, A., Busonero, D., Butkevich, A. G., Buzzi, R., Caffau, E., Cancelliere, R., Cannizzaro, G., Cantat-Gaudin, T., Carballo, R., Carlucci, T., Carrasco, J. M., Casamiquela, L., Castellani, M., Castro-Ginard, A., Charlot, P., Chemin, L., Chiavassa, A., Cocozza, G., Costigan, G., Cowell, S., Crifo, F., Crosta, M., Crowley, C., Cuypers, J., Dafonte, C., Damerdji, Y., Dapergolas, A., David, P., David, M., de Laverny, P., De Luise, F., De March, R., de Martino, D., de Souza, R., de Torres, A., Debosscher, J., del Pozo, E., Delbo, M., Delgado, A., Delgado, H. E., Di Matteo, P., Diakite, S., Diener, C., Distefano, E., Dolding, C., Drazinos, P., Durán, J., Edvardsson, B., Enke, H., Eriksson, K., Esquej, P., Eynard Bontemps, G., Fabre, C., Fabrizio, M., Faigler, S., Falcão, A. J., Farràs Casas, M., Federici, L., Fedorets, G., Fernique, P., Figueras, F., Filippi, F., Findeisen, K., Fonti, A., Fraile, E., Fraser, M., Frézouls, B., Gai, M., Galleti, S., Garabato, D., García-Sedano, F., Garofalo, A., Garralda, N., Gavel, A., Gavras, P., Gerssen, J., Geyer, R., Giacobbe, P., Gilmore, G., Girona, S., Giuffrida, G., Glass, F., Gomes, M., Granvik, M., Gueguen, A., Guerrier, A., Guiraud, J., Gutiérrez-Sánchez, R., Haigron, R., Hatzidimitriou, D., Hauser, M., Haywood, M., Heiter, U., Helmi, A., Heu, J., Hilger, T., Hobbs, D., Hofmann, W., Holland, G., Huckle, H. E., Hypki, A., Icardi, V., Janßen, K., Jevardat de Fombelle, G., Jonker, P. G., Juhász, Á. L., Julbe, F., Karampelas, A., Kewley, A., Klar, J., Kochoska, A., Kohley, R., Kolenberg, K., Kontizas, M., Kontizas, E., Koposov, S. E., Kordopatis, G., Kostrzewa-Rutkowska, Z., Koubsky, P., Lambert, S., Lanza, A. F., Lasne, Y., Lavigne, J. B., Le Fustec, Y., Le Poncin-Lafitte, C., Lebreton, Y., Leccia, S., Leclerc, N., Lecoeur-Taibi, I., Lenhardt, H., Leroux, F., Liao, S., Licata, E., Lindstrøm, H. E. P., Lister, T. A., Livanou, E., Lobel, A., López, M., Managau, S., Mann, R. G., Mantelet, G., Marchal, O.,

Marchant, J. M., Marconi, M., Marinoni, S., Marschalkó, G., Marshall, D. J., Martino, M., Marton, G., Mary, N., Massari, D., Matijevič, G., Mazeh, T., McMillan, P. J., Messina, S., Michalik, D., Millar, N. R., Molina, D., Molinaro, R., Molnár, L., Montegriffo, P., Mor, R., Morbidelli, R., Morel, T., Morris, D., Mulone, A. F., Muraveva, T., Musella, I., Nelemans, G., Nicastro, L., Noval, L., O'Mullane, W., Ordénovic, C., Ordóñez-Blanco, D., Osborne, P., Pagani, C., Pagano, I., Pailler, F., Palacin, H., Palaversa, L., Panahi, A., Pawlak, M., Piersimoni, A. M., Pineau, F. X., Plachy, E., Plum, G., Poggio, E., Poujoulet, E., Prša, A., Pulone, L., Racero, E., Ragaini, S., Rambaux, N., Ramos-Lerate, M., Regibo, S., Reylé, C., Riclet, F., Ripepi, V., Riva, A., Rivard, A., Rixon, G., Roegiers, T., Roelens, M., Romero-Gómez, M., Rowell, N., Royer, F., Ruiz-Dern, L., Sadowski, G., Sagristà Sellés, T., Sahlmann, J., Salgado, J., Salguero, E., Sanna, N., Santana-Ros, T., Sarasso, M., Savietto, H., Schultheis, M., Sciacca, E., Segol, M., Segovia, J. C., Ségransan, D., Shih, I. C., Siltala, L., Silva, A. F., Smart, R. L., Smith, K. W., Solano, E., Solitro, F., Sordo, R., Soria Nieto, S., Souchay, J., Spagna, A., Spoto, F., Stampa, U., Steele, I. A., Steidelmüller, H., Stephenson, C. A., Stoev, H., Suess, F. F., Surdej, J., Szabados, L., Szegedi-Elek, E., Tapiador, D., Taris, F., Tauran, G., Taylor, M. B., Teixeira, R., Terrett, D., Teyssandier, P., Thuillot, W., Titarenko, A., Torra Clotet, F., Turon, C., Ulla, A., Utrilla, E., Uzzi, S., Vaillant, M., Valentini, G., Valette, V., van Elteren, A., Van Hemelryck, E., van Leeuwen, M., Vaschetto, M., Vecchiato, A., Veljanoski, J., Viala, Y., Vicente, D., Vogt, S., von Essen, C., Voss, H., Votruba, V., Voutsinas, S., Walmsley, G., Weiler, M., Wertz, O., Wevers, T., Wyrzykowski, Ł., Yoldas, A., Žerjal, M., Ziaeepour, H., Zorec, J., Zschocke, S., Zucker, S., Zurbach, C. and Zwitter, T., 2018b, "Gaia Data Release 2. Summary of the contents and survey properties", *Astron. Astrophys.*, **616**, A1. [DOI], [ADS], [arXiv:1804.09365 [astro-ph.GA]]

Gallart, Carme, Bernard, Edouard J., Brook, Chris B., Ruiz-Lara, Tomás, Cassisi, Santi, Hill, Vanessa and Monelli, Matteo, 2019, "Uncovering the birth of the

Milky Way through accurate stellar ages with Gaia", *Nature Astronomy*, **3**, 932–939. [DOI], [ADS], [arXiv:1901.02900 [astro-ph.GA]]

Gao, Qi, Shi, Jian-Rong, Yan, Hong-Liang, Yan, Tai-Sheng, Xiang, Mao-Sheng, Zhou, Yu-Tao, Li, Chun-Qian and Zhao, Gang, 2019, "Lithium-rich Giants in LAMOST Survey. I. The Catalog", *Astrophys. J. Suppl.*, **245**(2), 33. [DOI], [ADS], [arXiv:1912.08431 [astro-ph.SR]]

Garcia-Berro, Enrique and Iben, I., 1994, "On the Formation and Evolution of Super–Asymptotic Giant Branch Stars with Cores Processed by Carbon Burning. I. SPICA to Antares", *Astrophys. J.*, **434**, 306. [DOI], [ADS]

Ge, Z. S., Bi, S. L., Chen, Y. Q., Li, T. D., Zhao, J. K., Liu, K., Ferguson, J. W. and Wu, Y. Q., 2016, "Ages of 70 Dwarfs of Three Populations in the Solar Neighborhood: Considering O and C Abundances in Stellar Models", *Astrophys. J.*, **833**(2), 161. [DOI], [ADS], [arXiv:1612.01622 [astro-ph.SR]]

Genova, F., Egret, D., Bienaymé, O., Bonnarel, F., Dubois, P., Fernique, P., Jasniewicz, G., Lesteven, S., Monier, R., Ochsenbein, F. and Wenger, M., 2000, "The CDS information hub. On-line services and links at the Centre de Données astronomiques de Strasbourg", *Astron. Astrophys. Suppl.*, **143**, 1–7. [DOI], [ADS]

Ghezzi, L., Cunha, K., Smith, V. V., Margheim, S., Schuler, S., de Araújo, F. X. and de la Reza, R., 2009, "Measurements of the Isotopic Ratio ^{6}Li/^{7}Li in Stars with Planets", *Astrophys. J.*, **698**(1), 451–460. [DOI], [ADS], [arXiv:0903.4873 [astro-ph.SR]]

Gilmore, G. and Reid, N., 1983, "New light on faint stars - III. Galactic structure towards the South Pole and the Galactic thick disc.", *Mon. Not. Roy. Astron. Soc.*, **202**, 1025–1047. [DOI], [ADS]

Gilmore, G. and Wyse, R. F. G., 1985, "The abundance distribution in the inner spheroid.", *Astron. J.*, **90**, 2015–2026. [DOI], [ADS]

Gilmore, Gerard, Wyse, Rosemary F. G. and Kuijken, Konrad, 1989, "Kinematics, chemistry, and structure of the Galaxy.", *Ann. Rev. Astron. Astrophys.*, **27**, 555–627. [DOI], [ADS]

Gilroy, Kalpana Krishnaswamy, 1989, "Carbon Isotope Ratios and Lithium Abundances in Open Cluster Giants", *Astrophys. J.*, **347**, 835. [DOI], [ADS]

Gonzalez, Oscar A. and Gadotti, Dimitri, 2016, "The Milky Way Bulge: Observed Properties and a Comparison to External Galaxies", in *Galactic Bulges*, (Eds.) Laurikainen, Eija, Peletier, Reynier, Gadotti, Dimitri, Astrophysics and Space Science Library, 418, p. 199, Springer International Publishing, Cham. [DOI], [ADS], [arXiv:1503.07252 [astro-ph.GA]]

Gratton, R. G., Carretta, E., Desidera, S., Lucatello, S., Mazzei, P. and Barbieri, M., 2003, "Abundances for metal-poor stars with accurate parallaxes. II. alpha -elements in the halo", *Astron. Astrophys.*, **406**, 131–140. [DOI], [ADS], [arXiv:astro-ph/0305358 [astro-ph]]

Greenstein, Jesse L. and Richardson, Robert S., 1951, "Lithium and the Internal Circulation of the Sun.", *Astrophys. J.*, **113**, 536. [DOI], [ADS]

Guglielmo, Valentina, Poggianti, Bianca M., Moretti, Alessia, Fritz, Jacopo, Calvi, Rosa, Vulcani, Benedetta, Fasano, Giovanni and Paccagnella, Angela, 2015, "The star formation history of galaxies: the role of galaxy mass, morphology and environment", *Mon. Not. Roy. Astron. Soc.*, **450**(3), 2749–2763. [DOI], [ADS], [arXiv:1504.01594 [astro-ph.GA]]

Guiglion, G., de Laverny, P., Recio-Blanco, A., Worley, C. C., De Pascale, M., Masseron, T., Prantzos, N. and Mikolaitis, Š., 2016, "The AMBRE project: Constraining the lithium evolution in the Milky Way", *Astron. Astrophys.*, **595**, A18. [DOI], [ADS], [arXiv:1608.03411 [astro-ph.GA]]

Guiglion, G., Chiappini, C., Romano, D., Matteucci, F., Anders, F., Steinmetz, M., Minchev, I., de Laverny, P. and Recio-Blanco, A., 2019, "Explaining the

decrease in ISM lithium at super-solar metallicities in the solar vicinity", *Astron. Astrophys.*, **623**, A99. [DOI], [ADS], [arXiv:1902.01660 [astro-ph.GA]]

Handberg, R., Brogaard, K., Miglio, A., Bossini, D., Elsworth, Y., Slumstrup, D., Davies, G. R. and Chaplin, W. J., 2017, "NGC 6819: testing the asteroseismic mass scale, mass loss and evidence for products of non-standard evolution", *Mon. Not. Roy. Astron. Soc.*, **472**(1), 979–997. [DOI], [ADS], [arXiv:1707.08223 [astro-ph.SR]]

Hasselquist, Sten, Zasowski, Gail, Feuillet, Diane K., Schultheis, Mathias, Nataf, David M., Anguiano, Borja, Beaton, Rachael L., Beers, Timothy C., Cohen, Roger E., Cunha, Katia, Fernández-Trincado, José G., García-Hernández, D. A., Geisler, Doug, Holtzman, Jon A., Johnson, Jennifer, Lane, Richard R., Majewski, Steven R., Moni Bidin, Christian, Nitschelm, Christian, Roman-Lopes, Alexandre, Schiavon, Ricardo, Smith, Verne V. and Sobeck, Jennifer, 2020, "Exploring the Stellar Age Distribution of the Milky Way Bulge Using APOGEE", *Astrophys. J.*, **901**(2), 109. [DOI], [ADS], [arXiv:2008.03603 [astro-ph.GA]]

Hawkins, K., Jofré, P., Gilmore, G. and Masseron, T., 2014, "On the relative ages of the α-rich and α-poor stellar populations in the Galactic halo", *Mon. Not. Roy. Astron. Soc.*, **445**(3), 2575–2588. [DOI], [ADS], [arXiv:1409.3431 [astro-ph.GA]]

Hayes, Christian R., Majewski, Steven R., Shetrone, Matthew, Fernández-Alvar, Emma, Allende Prieto, Carlos, Schuster, William J., Carigi, Leticia, Cunha, Katia, Smith, Verne V., Sobeck, Jennifer, Almeida, Andres, Beers, Timothy C., Carrera, Ricardo, Fernández-Trincado, J. G., García-Hernández, D. A., Geisler, Doug, Lane, Richard R., Lucatello, Sara, Matthews, Allison M., Minniti, Dante, Nitschelm, Christian, Tang, Baitian, Tissera, Patricia B. and Zamora, Olga, 2018, "Disentangling the Galactic Halo with APOGEE. I. Chemical and Kinematical Investigation of Distinct Metal-poor Populations", *Astrophys. J.*, **852**(1), 49. [DOI], [ADS], [arXiv:1711.05781 [astro-ph.GA]]

Haywood, M., Di Matteo, P., Lehnert, M. D., Snaith, O., Khoperskov, S. and Gómez, A., 2018, "In Disguise or Out of Reach: First Clues about In Situ and Accreted Stars in the Stellar Halo of the Milky Way from Gaia DR2", *Astrophys. J.*, **863**(2), 113. [DOI], [ADS], [arXiv:1805.02617 [astro-ph.GA]]

Haywood, Misha, Di Matteo, Paola, Lehnert, Matthew D., Katz, David and Gómez, Ana, 2013, "The age structure of stellar populations in the solar vicinity. Clues of a two-phase formation history of the Milky Way disk", *Astron. Astrophys.*, **560**, A109. [DOI], [ADS], [arXiv:1305.4663 [astro-ph.GA]]

Heger, A., Fryer, C. L., Woosley, S. E., Langer, N. and Hartmann, D. H., 2003, "How Massive Single Stars End Their Life", *Astrophys. J.*, **591**(1), 288–300. [DOI], [ADS], [arXiv:astro-ph/0212469 [astro-ph]]

Hekker, Saskia, 2020, "Scaling relations for solar-like oscillations: a review", *Frontiers in Astronomy and Space Sciences*, **7**, 3. [DOI], [ADS], [arXiv:1907.10457 [astro-ph.SR]]

Helmi, Amina, 2008, "The stellar halo of the Galaxy", *Astron. Astrophys. Rev.*, **15**(3), 145–188. [DOI], [ADS], [arXiv:0804.0019 [astro-ph]]

Helmi, Amina, White, Simon D. M., de Zeeuw, P. Tim and Zhao, Hongsheng, 1999, "Debris streams in the solar neighbourhood as relicts from the formation of the Milky Way", *Nature*, **402**(6757), 53–55. [DOI], [ADS], [arXiv:astro-ph/9911041 [astro-ph]]

Helmi, Amina, Babusiaux, Carine, Koppelman, Helmer H., Massari, Davide, Veljanoski, Jovan and Brown, Anthony G. A., 2018, "The merger that led to the formation of the Milky Way's inner stellar halo and thick disk", *Nature*, **563**(7729), 85–88. [DOI], [ADS], [arXiv:1806.06038 [astro-ph.GA]]

Henden, Arne A., Levine, Stephen, Terrell, Dirk and Welch, Douglas L., 2015, "APASS - The Latest Data Release", in *American Astronomical Society Meeting Abstracts #225*, American Astronomical Society Meeting Abstracts, 225, 336.16, American Astronomical Society, ˙[ADS]

Herschel, William, 1785, "On the Construction of the Heavens.", *Philosophical Transactions of the Royal Society of London Series I*, **75**, 213–266. [ADS]

Hill, V., Lecureur, A., Gómez, A., Zoccali, M., Schultheis, M., Babusiaux, C., Royer, F., Barbuy, B., Arenou, F., Minniti, D. and Ortolani, S., 2011, "The metallicity distribution of bulge clump giants in Baade's window", *Astron. Astrophys.*, **534**, A80. [DOI], [ADS], [arXiv:1107.5199 [astro-ph.GA]]

Hon, Marc, Stello, Dennis and Yu, Jie, 2017, "Deep learning classification in asteroseismology", *Mon. Not. Roy. Astron. Soc.*, **469**(4), 4578–4583. [DOI], [ADS], [arXiv:1705.06405 [astro-ph.SR]]

Horta, Danny, Schiavon, Ricardo P., Mackereth, J. Ted, Pfeffer, Joel, Mason, Andrew C., Kisku, Shobhit, Fragkoudi, Francesca, Allende Prieto, Carlos, Cunha, Katia, Hasselquist, Sten, Holtzman, Jon, Majewski, Steven R., Nataf, David, O'Connell, Robert W., Schultheis, Mathias and Smith, Verne V., 2021, "Evidence from APOGEE for the presence of a major building block of the halo buried in the inner Galaxy", *Mon. Not. Roy. Astron. Soc.*, **500**(1), 1385–1403. [DOI], [ADS], [arXiv:2007.10374 [astro-ph.GA]]

Huber, D., Bedding, T. R., Stello, D., Hekker, S., Mathur, S., Mosser, B., Verner, G. A., Bonanno, A., Buzasi, D. L., Campante, T. L., Elsworth, Y. P., Hale, S. J., Kallinger, T., Silva Aguirre, V., Chaplin, W. J., De Ridder, J., García, R. A., Appourchaux, T., Frandsen, S., Houdek, G., Molenda-Żakowicz, J., Monteiro, M. J. P. F. G., Christensen-Dalsgaard, J., Gilliland, R. L., Kawaler, S. D., Kjeldsen, H., Broomhall, A. M., Corsaro, E., Salabert, D., Sanderfer, D. T., Seader, S. E. and Smith, J. C., 2011, "Testing Scaling Relations for Solar-like Oscillations from the Main Sequence to Red Giants Using Kepler Data", *Astrophys. J.*, **743**(2), 143. [DOI], [ADS], [arXiv:1109.3460 [astro-ph.SR]]

Iben, Icko and Renzini, Alvio, 1984, "Single star evolution I. Massive stars and early evolution of low and intermediate mass stars", *Phys. Rep*, **105**(6), 329–406. [DOI], [ADS]

Iben, Icko Jr., 1967, "Stellar Evolution.VI. Evolution from the Main Sequence to the Red-Giant Branch for Stars of Mass 1 M_{sun}, 1.25 M_{sun}, and 1.5 M_{sun}", *Astrophys. J.*, **147**, 624. [DOI], [ADS]

Iben, I., Jr., 1974, "Post main sequence evolution of single stars.", *Ann. Rev. Astron. Astrophys.*, **12**, 215–256. [DOI], [ADS]

Iben, Icko, Jr., 2012a, *Stellar Evolution Physics, Volume 1: Physical Processes in Stellar Interiors*, Cambridge University Press, Cambridge, UK. [ADS]

Iben, Icko, Jr., 2012b, *Stellar Evolution Physics, Volume 2: Advanced Evolution of Single Stars*, Cambridge University Press, Cambridge, UK. [ADS]

Ishigaki, Miho, Chiba, Masashi and Aoki, Wako, 2010, "Chemical Abundances of Outer Halo Stars in the Milky Way", *Pub. Astron. Soc. Japan*, **62**, 143. [DOI], [ADS], [arXiv:0912.0329 [astro-ph.GA]]

Ishigaki, Miho N., Chiba, Masashi and Aoki, Wako, 2012, "Chemical Abundances of the Milky Way Thick Disk and Stellar Halo. I. Implications of [α/Fe] for Star Formation Histories in Their Progenitors", *Astrophys. J.*, **753**(1), 64. [DOI], [ADS], [arXiv:1205.2406 [astro-ph.GA]]

Ivezić, Željko, Beers, Timothy C. and Jurić, Mario, 2012, "Galactic Stellar Populations in the Era of the Sloan Digital Sky Survey and Other Large Surveys", *Ann. Rev. Astron. Astrophys.*, **50**, 251–304. [DOI], [ADS], [arXiv:1308.6386 [astro-ph.GA]]

Izzo, Luca, Della Valle, Massimo, Mason, Elena, Matteucci, Francesca, Romano, Donatella, Pasquini, Luca, Vanzi, Leonardo, Jordan, Andres, Fernandez, José Miguel, Bluhm, Paz, Brahm, Rafael, Espinoza, Nestor and Williams, Robert, 2015, "Early Optical Spectra of Nova V1369 Cen Show the Presence of Lithium", *Astrophys. J. Lett.*, **808**(1), L14. [DOI], [ADS], [arXiv:1506.08048 [astro-ph.SR]]

Jeffries, R. D., Jackson, R. J., James, David J. and Cargile, P. A., 2009, "Low-mass members of the young cluster IC 4665 and pre-main-sequence lithium depletion", *Mon. Not. Roy. Astron. Soc.*, **400**(1), 317–329. [DOI], [ADS], [arXiv:0908.1317 [astro-ph.SR]]

Jofré, E., Petrucci, R., García, L. and Gómez, M., 2015, "KIC 9821622: An interesting lithium-rich giant in the Kepler field", *Astron. Astrophys.*, **584**, L3. [DOI], [ADS], [arXiv:1510.07192 [astro-ph.SR]]

Johnson, Dean R. H. and Soderblom, David R., 1987, "Calculating Galactic Space Velocities and Their Uncertainties, with an Application to the Ursa Major Group", *Astron. J.*, **93**, 864. [DOI], [ADS]

Jonsell, K., Edvardsson, B., Gustafsson, B., Magain, P., Nissen, P. E. and Asplund, M., 2005, "Chemical abundances in 43 metal-poor stars", *Astron. Astrophys.*, **440**(1), 321–343. [DOI], [ADS], [arXiv:astro-ph/0505118 [astro-ph]]

Jordi, C., Gebran, M., Carrasco, J. M., de Bruijne, J., Voss, H., Fabricius, C., Knude, J., Vallenari, A., Kohley, R. and Mora, A., 2010a, "Gaia broad band photometry", *Astron. Astrophys.*, **523**, A48. [DOI], [ADS], [arXiv:1008.0815 [astro-ph.IM]]

Jordi, C., Gebran, M., Carrasco, J. M., de Bruijne, J., Voss, H., Fabricius, C., Knude, J., Vallenari, A., Kohley, R. and Mora, A., 2010b, "Gaia broad band photometry", *Astron. Astrophys.*, **523**, A48. [DOI], [ADS], [arXiv:1008.0815 [astro-ph.IM]]

Jorissen, A., Van Winckel, H., Siess, L., Escorza, A., Pourbaix, D. and Van Eck, S., 2020, "Li-rich K giants, dust excess, and binarity", *Astron. Astrophys.*, **639**, A7. [DOI], [ADS], [arXiv:2007.05442 [astro-ph.SR]]

Juneau, Stéphanie, Glazebrook, Karl, Crampton, David, McCarthy, Patrick J., Savaglio, Sandra, Abraham, Roberto, Carlberg, Raymond G., Chen, Hsiao-Wen, Le Borgne, Damien, Marzke, Ronald O., Roth, Kathy, Jørgensen, Inger, Hook,

Isobel and Murowinski, Richard, 2005, "Cosmic Star Formation History and Its Dependence on Galaxy Stellar Mass", *Astrophys. J. Lett.*, **619**(2), L135–L138. [DOI], [ADS], [arXiv:astro-ph/0411775 [astro-ph]]

Jungman, Gerard, Kamionkowski, Marc, Kosowsky, Arthur and Spergel, David N., 1996, "Cosmological-parameter determination with microwave background maps", *Physical Review D*, **54**(2), 1332–1344. [DOI], [ADS], [arXiv:astro-ph/9512139 [astro-ph]]

Kallinger, T., Weiss, W. W., Barban, C., Baudin, F., Cameron, C., Carrier, F., De Ridder, J., Goupil, M. J., Gruberbauer, M., Hatzes, A., Hekker, S., Samadi, R. and Deleuil, M., 2010, "Oscillating red giants in the CoRoT exofield: asteroseismic mass and radius determination", *Astron. Astrophys.*, **509**, A77. [DOI], [ADS]

Kallinger, T., Hekker, S., Mosser, B., De Ridder, J., Bedding, T. R., Elsworth, Y. P., Gruberbauer, M., Guenther, D. B., Stello, D., Basu, S., García, R. A., Chaplin, W. J., Mullally, F., Still, M. and Thompson, S. E., 2012, "Evolutionary influences on the structure of red-giant acoustic oscillation spectra from 600d of Kepler observations", *Astron. Astrophys.*, **541**, A51. [DOI], [ADS], [arXiv:1203.3134 [astro-ph.SR]]

Kapteyn, J. C., 1922, "First Attempt at a Theory of the Arrangement and Motion of the Sidereal System", *Astrophys. J.*, **55**, 302. [DOI], [ADS]

Karakas, A. I., 2010, "Updated stellar yields from asymptotic giant branch models", *Mon. Not. Roy. Astron. Soc.*, **403**(3), 1413–1425. [DOI], [ADS], [arXiv:0912.2142 [astro-ph.SR]]

Katz, D., Sartoretti, P., Cropper, M., Panuzzo, P., Seabroke, G. M., Viala, Y., Benson, K., Blomme, R., Jasniewicz, G., Jean-Antoine, A., Huckle, H., Smith, M., Baker, S., Crifo, F., Damerdji, Y., David, M., Dolding, C., Frémat, Y., Gosset, E., Guerrier, A., Guy, L. P., Haigron, R., Janßen, K., Marchal, O., Plum, G., Soubiran, C., Thévenin, F., Ajaj, M., Allende Prieto, C., Babusiaux, C.,

Boudreault, S., Chemin, L., Delle Luche, C., Fabre, C., Gueguen, A., Hambly, N. C., Lasne, Y., Meynadier, F., Pailler, F., Panem, C., Royer, F., Tauran, G., Zurbach, C., Zwitter, T., Arenou, F., Bossini, D., Gerssen, J., Gómez, A., Lemaitre, V., Leclerc, N., Morel, T., Munari, U., Turon, C., Vallenari, A. and Žerjal, M., 2019, "Gaia Data Release 2. Properties and validation of the radial velocities", *Astron. Astrophys.*, **622**, A205. [DOI], [ADS], [arXiv:1804.09372 [astro-ph.IM]]

Kauffmann, Guinevere, Heckman, Timothy M., White, Simon D. M., Charlot, Stéphane, Tremonti, Christy, Peng, Eric W., Seibert, Mark, Brinkmann, Jon, Nichol, Robert C., SubbaRao, Mark and York, Don, 2003, "The dependence of star formation history and internal structure on stellar mass for 10^5 low-redshift galaxies", *Mon. Not. Roy. Astron. Soc.*, **341**(1), 54–69. [DOI], [ADS], [arXiv:astro-ph/0205070 [astro-ph]]

Kim, Yong-Cheol, Demarque, Pierre, Yi, Sukyoung K. and Alexand er, David R., 2002, "The Y^2 Isochrones for α-Element Enhanced Mixtures", *Astrophys. J. Suppl.*, **143**(2), 499–511. [DOI], [ADS], [arXiv:astro-ph/0208175 [astro-ph]]

Kippenhahn, R., Ruschenplatt, G. and Thomas, H. C., 1980, "The time scale of thermohaline mixing in stars", *Astron. Astrophys.*, **91**(1-2), 175–180. [ADS]

Kippenhahn, Rudolf, Weigert, Alfred and Weiss, Achim, 2012, *Stellar Structure and Evolution*, Springer, Berlin, Heidelberg. [DOI], [ADS]

Kirby, Evan N., Fu, Xiaoting, Guhathakurta, Puragra and Deng, Licai, 2012, "Discovery of Super-Li-rich Red Giants in Dwarf Spheroidal Galaxies", *Astrophys. J. Lett.*, **752**(1), L16. [DOI], [ADS], [arXiv:1205.1057 [astro-ph.SR]]

Kirby, Evan N., Guhathakurta, Puragra, Zhang, Andrew J., Hong, Jerry, Guo, Michelle, Guo, Rachel, Cohen, Judith G. and Cunha, Katia, 2016, "Lithium-rich Giants in Globular Clusters", *Astrophys. J.*, **819**(2), 135. [DOI], [ADS], [arXiv:1601.01315 [astro-ph.SR]]

Klement, Rainer J., 2010, "Halo streams in the solar neighborhood", *Astron. Astrophys. Rev.*, **18**(4), 567–594. [DOI], [ADS], [arXiv:1007.3257 [astro-ph.GA]]

Knapp, G. R., 1986, "Mass Loss from Evolved Stars. VI. Mass-Loss Mechanisms and Luminosity Evolution", *Astrophys. J.*, **311**, 731. [DOI], [ADS]

Knapp, G. R. and Morris, M., 1985, "Mass Loss from Evolved Stars. III. Mass Loss Rates for 50 Stars from CO J = 1–0 Observations", *Astrophys. J.*, **292**, 640. [DOI], [ADS]

Komatsu, E., Smith, K. M., Dunkley, J., Bennett, C. L., Gold, B., Hinshaw, G., Jarosik, N., Larson, D., Nolta, M. R., Page, L., Spergel, D. N., Halpern, M., Hill, R. S., Kogut, A., Limon, M., Meyer, S. S., Odegard, N., Tucker, G. S., Weiland, J. L., Wollack, E. and Wright, E. L., 2011, "Seven-year Wilkinson Microwave Anisotropy Probe (WMAP) Observations: Cosmological Interpretation", *Astrophys. J. Suppl.*, **192**(2), 18. [DOI], [ADS], [arXiv:1001.4538 [astro-ph.CO]]

Koppelman, Helmer H., Helmi, Amina, Massari, Davide, Price-Whelan, Adrian M. and Starkenburg, Tjitske K., 2019, "Multiple retrograde substructures in the Galactic halo: A shattered view of Galactic history", *Astron. Astrophys.*, **631**, L9. [DOI], [ADS], [arXiv:1909.08924 [astro-ph.GA]]

Kumar, Yerra Bharat, Reddy, Bacham E. and Lambert, David L., 2011, "Origin of Lithium Enrichment in K Giants", *Astrophys. J. Lett.*, **730**(1), L12. [DOI], [ADS], [arXiv:1102.2299 [astro-ph.SR]]

Kumar, Yerra Bharat, Reddy, B. E., Muthumariappan, C. and Zhao, G., 2015, "Far-infrared study of K giants in the solar neighborhood: Connection between Li enrichment and mass-loss", *Astron. Astrophys.*, **577**, A10. [DOI], [ADS], [arXiv:1503.01548 [astro-ph.SR]]

Kumar, Yerra Bharat, Singh, Raghubar, Reddy, Bacham E. and Zhao, Gang, 2018, "Two New Super Li-rich Core He-burning Giants: A New Twist to the Long Tale of Li Enhancement in K Giants", *Astrophys. J. Lett.*, **858**(2), L22. [DOI], [ADS], [arXiv:1804.10955 [astro-ph.SR]]

Kumar, Yerra Bharat, Reddy, Bacham E., Campbell, Simon W., Maben, Sunayana, Zhao, Gang and Ting, Yuan-Sen, 2020, "Discovery of ubiquitous lithium production in low-mass stars", *Nature Astronomy*, **4**, 1059–1063. [DOI], [ADS], [arXiv:2007.07045 [astro-ph.SR]]

Kunder, Andrea, Kordopatis, Georges, Steinmetz, Matthias, Zwitter, Tomaž, McMillan, Paul J., Casagrande, Luca, Enke, Harry, Wojno, Jennifer, Valentini, Marica, Chiappini, Cristina, Matijevič, Gal, Siviero, Alessandro, de Laverny, Patrick, Recio-Blanco, Alejandra, Bijaoui, Albert, Wyse, Rosemary F. G., Binney, James, Grebel, E. K., Helmi, Amina, Jofre, Paula, Antoja, Teresa, Gilmore, Gerard, Siebert, Arnaud, Famaey, Benoit, Bienaymé, Olivier, Gibson, Brad K., Freeman, Kenneth C., Navarro, Julio F., Munari, Ulisse, Seabroke, George, Anguiano, Borja, Žerjal, Maruša, Minchev, Ivan, Reid, Warren, Bland-Hawthorn, Joss, Kos, Janez, Sharma, Sanjib, Watson, Fred, Parker, Quentin A., Scholz, Ralf-Dieter, Burton, Donna, Cass, Paul, Hartley, Malcolm, Fiegert, Kristin, Stupar, Milorad, Ritter, Andreas, Hawkins, Keith, Gerhard, Ortwin, Chaplin, W. J., Davies, G. R., Elsworth, Y. P., Lund, M. N., Miglio, A. and Mosser, B., 2017, "The Radial Velocity Experiment (RAVE): Fifth Data Release", *Astron. J.*, **153**(2), 75. [DOI], [ADS], [arXiv:1609.03210 [astro-ph.SR]]

Kwok, S., 1982, "From red giants to planetary nebulae.", *Astrophys. J.*, **258**, 280–288. [DOI], [ADS]

Kwok, S., Purton, C. R. and Fitzgerald, P. M., 1978, "On the origin of planetary nebulae.", *Astrophys. J. Lett.*, **219**, L125–L127. [DOI], [ADS]

Lagarde, N., Charbonnel, C., Decressin, T. and Hagelberg, J., 2011, "Thermohaline instability and rotation-induced mixing. II. Yields of ^{3}He for low- and intermediate-mass stars", *Astron. Astrophys.*, **536**, A28. [DOI], [ADS], [arXiv:1109.5704 [astro-ph.SR]]

Lambert, David L. and Reddy, Bacham E., 2004, "Lithium abundances of the local thin disc stars", *Mon. Not. Roy. Astron. Soc.*, **349**(2), 757–767. [DOI], [ADS], [arXiv:astro-ph/0401259 [astro-ph]]

Lattanzio, J., Frost, C., Cannon, R. and Wood, P. R., 1996, "Hot bottom burning in intermediate mass stars", *Mem. Societa Astronomica Italiana*, **67**, 729. [ADS]

Lattanzio, J. C., Siess, L., Church, R. P., Angelou, G., Stancliffe, R. J., Doherty, C. L., Stephen, T. and Campbell, S. W., 2015, "On the numerical treatment and dependence of thermohaline mixing in red giants", *Mon. Not. Roy. Astron. Soc.*, **446**(3), 2673–2688. [DOI], [ADS], [arXiv:1410.6517 [astro-ph.SR]]

Lecureur, A., Hill, V., Zoccali, M., Barbuy, B., Gómez, A., Minniti, D., Ortolani, S. and Renzini, A., 2007, "Oxygen, sodium, magnesium, and aluminium as tracers of the galactic bulge formation", *Astron. Astrophys.*, **465**(3), 799–814. [DOI], [ADS], [arXiv:astro-ph/0610346 [astro-ph]]

Lemaître, G., 1927, "Un Univers homogène de masse constante et de rayon croissant rendant compte de la vitesse radiale des nébuleuses extra-galactiques", *Annales de la Société Scientifique de Bruxelles*, **47**, 49–59. [ADS]

Li, C., Zhao, G., Zhai, M. and Jia, Y., 2018a, "The Formation and Evolution of Galactic Disks with APOGEE and the Gaia Survey", *Astrophys. J.*, **860**, 53. [DOI], [ADS]

Li, Haining, Aoki, Wako, Matsuno, Tadafumi, Bharat Kumar, Yerra, Shi, Jianrong, Suda, Takuma and Zhao, Gang, 2018b, "Enormous Li Enhancement Preceding Red Giant Phases in Low-mass Stars in the Milky Way Halo", *Astrophys. J. Lett.*, **852**(2), L31. [DOI], [ADS], [arXiv:1801.00090 [astro-ph.SR]]

Limberg, Guilherme, Rossi, Silvia, Beers, Timothy C., Perottoni, Hélio D., Pérez-Villegas, Angeles, Santucci, Rafael M., Abuchaim, Yuri, Placco, Vinicius M., Lee, Young Sun, Christlieb, Norbert, Norris, John E., Bessell, Michael S., Ryan,

Sean G., Wilhelm, Ronald, Rhee, Jaehyon and Frebel, Anna, 2021, "Dynamically Tagged Groups of Very Metal-poor Halo Stars from the HK and Hamburg/ESO Surveys", *Astrophys. J.*, **907**(1), 10. [DOI], [ADS], [arXiv:2011.08305 [astro-ph.GA]]

Lind, K., Asplund, M. and Barklem, P. S., 2009a, "Departures from LTE for neutral Li in late-type stars", *Astron. Astrophys.*, **503**, 541–544. [DOI], [ADS], [arXiv:0906.0899 [astro-ph.SR]]

Lind, K., Primas, F., Charbonnel, C., Grundahl, F. and Asplund, M., 2009b, "Signatures of intrinsic Li depletion and Li-Na anti-correlation in the metal-poor globular cluster NGC 6397", *Astron. Astrophys.*, **503**(2), 545–557. [DOI], [ADS], [arXiv:0906.2876 [astro-ph.SR]]

Lindegren, L., Hernández, J., Bombrun, A., Klioner, S., Bastian, U., Ramos-Lerate, M., de Torres, A., Steidelmüller, H., Stephenson, C., Hobbs, D., Lammers, U., Biermann, M., Geyer, R., Hilger, T., Michalik, D., Stampa, U., McMillan, P. J., Castañeda, J., Clotet, M., Comoretto, G., Davidson, M., Fabricius, C., Gracia, G., Hambly, N. C., Hutton, A., Mora, A., Portell, J., van Leeuwen, F., Abbas, U., Abreu, A., Altmann, M., Andrei, A., Anglada, E., Balaguer-Núñez, L., Barache, C., Becciani, U., Bertone, S., Bianchi, L., Bouquillon, S., Bourda, G., Brüsemeister, T., Bucciarelli, B., Busonero, D., Buzzi, R., Cancelliere, R., Carlucci, T., Charlot, P., Cheek, N., Crosta, M., Crowley, C., de Bruijne, J., de Felice, F., Drimmel, R., Esquej, P., Fienga, A., Fraile, E., Gai, M., Garralda, N., González-Vidal, J. J., Guerra, R., Hauser, M., Hofmann, W., Holl, B., Jordan, S., Lattanzi, M. G., Lenhardt, H., Liao, S., Licata, E., Lister, T., Löffler, W., Marchant, J., Martin-Fleitas, J. M., Messineo, R., Mignard, F., Morbidelli, R., Poggio, E., Riva, A., Rowell, N., Salguero, E., Sarasso, M., Sciacca, E., Siddiqui, H., Smart, R. L., Spagna, A., Steele, I., Taris, F., Torra, J., van Elteren, A., van Reeven, W. and Vecchiato, A., 2018, "Gaia Data Release 2. The astrometric solution", *Astron. Astrophys.*, **616**, A2. [DOI], [ADS], [arXiv:1804.09366 [astro-ph.IM]]

Lindegren, Lennart and Dravins, Dainis, 2003, "The fundamental definition of "radial velocity"", *Astron. Astrophys.*, **401**, 1185–1201. [DOI], [ADS], [arXiv:astro-ph/0302522 [astro-ph]]

Longland, R., Lorén-Aguilar, P., José, J., García-Berro, E. and Althaus, L. G., 2012, "Lithium production in the merging of white dwarf stars", *Astron. Astrophys.*, **542**, A117. [DOI], [ADS], [arXiv:1205.2538 [astro-ph.SR]]

Luck, R. Earle and Heiter, Ulrike, 2007, "Giants in the Local Region", *Astron. J.*, **133**(6), 2464–2486. [DOI], [ADS]

Mackereth, J. Ted and Bovy, Jo, 2018, "Fast Estimation of Orbital Parameters in Milky Way-like Potentials", *Pub. Astron. Soc. Pac.*, **130**(993), 114 501. [DOI], [ADS], [arXiv:1802.02592 [astro-ph.GA]]

Martell, S. L. and Shetrone, M. D., 2013, "Lithium-rich field giants in the Sloan Digital Sky Survey", *Mon. Not. Roy. Astron. Soc.*, **430**(1), 611–620. [DOI], [ADS], [arXiv:1301.0163 [astro-ph.SR]]

Martell, Sarah L., Simpson, Jeffrey D., Balasubramaniam, Adithya G., Buder, Sven, Sharma, Sanjib, Hon, Marc, Stello, Dennis, Ting, Yuan-Sen, Asplund, Martin, Bland-Hawthorn, Joss, De Silva, Gayandhi M., Freeman, Ken C., Hayden, Michael, Kos, Janez, Lewis, Geraint F., Lind, Karin, Zucker, Daniel B., Zwitter, Tomaž, Campbell, Simon W., Čotar, Klemen, Horner, Jonathan, Montet, Benjamin and Wittenmyer, Rob, 2021, "The GALAH survey: a census of lithium-rich giant stars", *Mon. Not. Roy. Astron. Soc.*, **505**(4), 5340–5355. [DOI], [ADS], [arXiv:2006.02106 [astro-ph.SR]]

Mathews, G. J., Alcock, C. R. and Fuller, G. M., 1990, "Galactic Chemical Evolution with Low and High Primordial Lithium", *Astrophys. J.*, **349**, 449. [DOI], [ADS]

Mathur, Savita, Huber, Daniel, Batalha, Natalie M., Ciardi, David R., Bastien, Fabienne A., Bieryla, Allyson, Buchhave, Lars A., Cochran, William D., Endl,

Michael, Esquerdo, Gilbert A., Furlan, Elise, Howard, Andrew, Howell, Steve B., Isaacson, Howard, Latham, David W., MacQueen, Phillip J. and Silva, David R., 2017, "Revised Stellar Properties of Kepler Targets for the Q1-17 (DR25) Transit Detection Run", *Astrophys. J. Suppl.*, **229**(2), 30. [DOI], [ADS], [arXiv:1609.04128 [astro-ph.SR]]

Matteucci, Francesca, 2012, *Chemical Evolution of Galaxies*, Springer, Berlin, Heidelberg. [DOI], [ADS]

Matteucci, Francesca, Molero, Marta, Aguado, David S. and Romano, Donatella, 2021, "The evolution of Lithium: implications of a universal Spite plateau", *Mon. Not. Roy. Astron. Soc.*, **505**(1), 200–206. [DOI], [ADS], [arXiv:2104.11504 [astro-ph.GA]]

McDonough, W. F., 2003, "Compositional Model for the Earth's Core", *Treatise on Geochemistry*, **2**, 568. [DOI], [ADS]

McKellar, A., 1940, "Intense λ 6708 Resonance Doublet of Li I in the Spectrum of WZ Cassiopeiae", *Pub. Astron. Soc. Pac.*, **52**(310), 407. [DOI], [ADS]

McMillan, Paul J., 2017, "The mass distribution and gravitational potential of the Milky Way", *Mon. Not. Roy. Astron. Soc.*, **465**(1), 76–94. [DOI], [ADS], [arXiv:1608.00971 [astro-ph.GA]]

McWilliam, Andrew and Rich, R. Michael, 1994, "The First Detailed Abundance Analysis of Galactic Bulge K Giants in Baade's Window", *Astrophys. J. Suppl.*, **91**, 749. [DOI], [ADS]

Meléndez, Jorge and Ramírez, Iván, 2004, "Reappraising the Spite Lithium Plateau: Extremely Thin and Marginally Consistent with WMAP Data", *Astrophys. J. Lett.*, **615**(1), L33–L36. [DOI], [ADS], [arXiv:astro-ph/0409383 [astro-ph]]

Melo, C. H. F., de Laverny, P., Santos, N. C., Israelian, G., Randich, S., Do Nascimento, J. D., Jr. and de Medeiros, J. R., 2005, "On the nature of lithium-rich giant stars. Constraints from beryllium abundances", *Astron. Astrophys.*, **439**(1), 227–235. [DOI], [ADS], [arXiv:astro-ph/0504133 [astro-ph]]

Meneguzzi, M., Audouze, J. and Reeves, H., 1971, "The production of the elements Li, Be, B by galactic cosmic rays in space and its relation with stellar observations.", *Astron. Astrophys.*, **15**, 337. [ADS]

Miglio, A., Chiappini, C., Morel, T., Barbieri, M., Chaplin, W. J., Girardi, L., Montalbán, J., Valentini, M., Mosser, B., Baudin, F., Casagrande, L., Fossati, L., Silva Aguirre, V. and Baglin, A., 2013, "Galactic archaeology: mapping and dating stellar populations with asteroseismology of red-giant stars", *Mon. Not. Roy. Astron. Soc.*, **429**(1), 423–428. [DOI], [ADS], [arXiv:1211.0146 [astro-ph.GA]]

Minchev, I., Chiappini, C. and Martig, M., 2013, "Chemodynamical evolution of the Milky Way disk. I. The solar vicinity", *Astron. Astrophys.*, **558**, A9. [DOI], [ADS], [arXiv:1208.1506 [astro-ph.GA]]

Minchev, I., Chiappini, C. and Martig, M., 2014a, "Chemodynamical evolution of the Milky Way disk. II. Variations with Galactic radius and height above the disk plane", *Astron. Astrophys.*, **572**, A92. [DOI], [ADS], [arXiv:1401.5796 [astro-ph.GA]]

Minchev, I., Chiappini, C., Martig, M., Steinmetz, M., de Jong, R. S., Boeche, C., Scannapieco, C., Zwitter, T., Wyse, R. F. G., Binney, J. J., Bland-Hawthorn, J., Bienaymé, O., Famaey, B., Freeman, K. C., Gibson, B. K., Grebel, E. K., Gilmore, G., Helmi, A., Kordopatis, G., Lee, Y. S., Munari, U., Navarro, J. F., Parker, Q. A., Quillen, A. C., Reid, W. A., Siebert, A., Siviero, A., Seabroke, G., Watson, F. and Williams, M., 2014b, "A New Stellar Chemo-Kinematic Relation Reveals the Merger History of the Milky Way Disk", *Astrophys. J. Lett.*, **781**(1), L20. [DOI], [ADS], [arXiv:1310.5145 [astro-ph.GA]]

Mitler, Henri E., 1972, "Cosmic-ray production of deuterium, He^3, lithium, beryllium, and boron in the Galaxy", *Astrophys. Space Sci.*, **17**(1), 186–218. [DOI], [ADS]

Miyaji, S., Nomoto, K., Yokoi, K. and Sugimoto, D., 1980, "Supernova triggered by electron captures.", *Pub. Astron. Soc. Japan*, **32**, 303–329. [ADS]

Miyaji, Shigeki and Nomoto, Ken'ichi, 1987, "On the Collapse of 8–10 M_{sun} Stars Due to Electron Capture", *Astrophys. J.*, **318**, 307. [DOI], [ADS]

Mocák, M., Campbell, S. W., Müller, E. and Kifonidis, K., 2010, "The core helium flash revisited. III. From Population I to Population III stars", *Astron. Astrophys.*, **520**, A114. [DOI], [ADS], [arXiv:1003.3646 [astro-ph.SR]]

Mocák, M., Meakin, Casey A., Müller, E. and Siess, L., 2011, "A New Stellar Mixing Process Operating below Shell Convection Zones Following Off-center Ignition", *Astrophys. J.*, **743**(1), 55. [DOI], [ADS], [arXiv:1108.4433 [astro-ph.SR]]

Molaro, P., Cescutti, G. and Fu, X., 2020, "Lithium and beryllium in the Gaia-Enceladus galaxy", *Mon. Not. Roy. Astron. Soc.*, **496**(3), 2902–2909. [DOI], [ADS], [arXiv:2006.00787 [astro-ph.GA]]

Molenda-Żakowicz, J., Brogaard, K., Niemczura, E., Bergemann, M., Frasca, A., Arentoft, T. and Grundahl, F., 2014, "Spectroscopic study of the open cluster NGC 6811", *Mon. Not. Roy. Astron. Soc.*, **445**(3), 2446–2461. [DOI], [ADS], [arXiv:1409.5132 [astro-ph.SR]]

Monaco, L., Bonifacio, P., Sbordone, L., Villanova, S. and Pancino, E., 2010, "The lithium content of ω Centauri. New clues to the cosmological Li problem from old stars in external galaxies", *Astron. Astrophys.*, **519**, L3. [DOI], [ADS], [arXiv:1008.1817 [astro-ph.GA]]

Mortlock, Daniel J., Warren, Stephen J., Venemans, Bram P., Patel, Mitesh, Hewett, Paul C., McMahon, Richard G., Simpson, Chris, Theuns, Tom, Gonzáles-Solares, Eduardo A., Adamson, Andy, Dye, Simon, Hambly, Nigel C.,

Hirst, Paul, Irwin, Mike J., Kuiper, Ernst, Lawrence, Andy and Röttgering, Huub J. A., 2011, "A luminous quasar at a redshift of z = 7.085", *Nature*, **474**(7353), 616–619. [DOI], [ADS], [arXiv:1106.6088 [astro-ph.CO]]

Mosser, B., Belkacem, K., Goupil, M. J., Miglio, A., Morel, T., Barban, C., Baudin, F., Hekker, S., Samadi, R., De Ridder, J., Weiss, W., Auvergne, M. and Baglin, A., 2010, "Red-giant seismic properties analyzed with CoRoT", *Astron. Astrophys.*, **517**, A22. [DOI], [ADS], [arXiv:1004.0449 [astro-ph.SR]]

Mosser, B., Barban, C., Montalbán, J., Beck, P. G., Miglio, A., Belkacem, K., Goupil, M. J., Hekker, S., De Ridder, J., Dupret, M. A., Elsworth, Y., Noels, A., Baudin, F., Michel, E., Samadi, R., Auvergne, M., Baglin, A. and Catala, C., 2011, "Mixed modes in red-giant stars observed with CoRoT", *Astron. Astrophys.*, **532**, A86. [DOI], [ADS], [arXiv:1105.6113 [astro-ph.SR]]

Mosser, B., Goupil, M. J., Belkacem, K., Michel, E., Stello, D., Marques, J. P., Elsworth, Y., Barban, C., Beck, P. G., Bedding, T. R., De Ridder, J., García, R. A., Hekker, S., Kallinger, T., Samadi, R., Stumpe, M. C., Barclay, T. and Burke, C. J., 2012, "Probing the core structure and evolution of red giants using gravity-dominated mixed modes observed with Kepler", *Astron. Astrophys.*, **540**, A143. [DOI], [ADS], [arXiv:1203.0689 [astro-ph.SR]]

Mosser, B., Benomar, O., Belkacem, K., Goupil, M. J., Lagarde, N., Michel, E., Lebreton, Y., Stello, D., Vrard, M., Barban, C., Bedding, T. R., Deheuvels, S., Chaplin, W. J., De Ridder, J., Elsworth, Y., Montalban, J., Noels, A., Ouazzani, R. M., Samadi, R., White, T. R. and Kjeldsen, H., 2014, "Mixed modes in red giants: a window on stellar evolution", *Astron. Astrophys.*, **572**, L5. [DOI], [ADS], [arXiv:1411.1082 [astro-ph.SR]]

Mosser, B., Michel, E., Samadi, R., Miglio, A., Davies, G. R., Girardi, L. and Goupil, M. J., 2019, "Seismic performance", *Astron. Astrophys.*, **622**, A76. [DOI], [ADS], [arXiv:1812.11906 [astro-ph.SR]]

Mould, J. R., 1978, "Infrared spectroscopy of M dwarfs.", *Astrophys. J.*, **226**, 923–930. [DOI], [ADS]

Mowlavi, N., 1995, "Lithium Production and Hot Bottom Burning in AGB Stars", in *The Light Element Abundances*, (Ed.) Crane, Philippe, p. 297, Springer-Verlag, Berlin Heidelberg New York. [ADS]

Munari, U., Henden, A., Frigo, A., Zwitter, T., Bienaymé, O., Bland-Hawthorn, J., Boeche, C., Freeman, K. C., Gibson, B. K., Gilmore, G., Grebel, E. K., Helmi, A., Kordopatis, G., Levine, S. E., Navarro, J. F., Parker, Q. A., Reid, W., Seabroke, G. M., Siebert, A., Siviero, A., Smith, T. C., Steinmetz, M., Templeton, M., Terrell, D., Welch, D. L., Williams, M. and Wyse, R. F. G., 2014, "APASS Landolt-Sloan BVgri Photometry of RAVE Stars. I. Data, Effective Temperatures, and Reddenings", *Astron. J.*, **148**(5), 81. [DOI], [ADS], [arXiv:1408.5476 [astro-ph.SR]]

Myeong, G. C., Vasiliev, E., Iorio, G., Evans, N. W. and Belokurov, V., 2019, "Evidence for two early accretion events that built the Milky Way stellar halo", *Mon. Not. Roy. Astron. Soc.*, **488**(1), 1235–1247. [DOI], [ADS], [arXiv:1904.03185 [astro-ph.GA]]

Nissen, P. E. and Schuster, W. J., 1997, "Chemical composition of halo and disk stars with overlapping metallicities.", *Astron. Astrophys.*, **326**, 751–762. [ADS]

Nissen, P. E. and Schuster, W. J., 2010, "Two distinct halo populations in the solar neighborhood. Evidence from stellar abundance ratios and kinematics", *Astron. Astrophys.*, **511**, L10. [DOI], [ADS], [arXiv:1002.4514 [astro-ph.GA]]

Nissen, P. E. and Schuster, W. J., 2011, "Two distinct halo populations in the solar neighborhood. II. Evidence from stellar abundances of Mn, Cu, Zn, Y, and Ba", *Astron. Astrophys.*, **530**, A15. [DOI], [ADS], [arXiv:1103.4755 [astro-ph.GA]]

Nomoto, K., 1984, "Evolution of 8-10 solar mass stars toward electron capture supernovae. I - Formation of electron-degenerate O + NE + MG cores.", *Astrophys. J.*, **277**, 791–805. [DOI], [ADS]

Nomoto, K. and Hashimoto, M., 1988, "Presupernova evolution of massive stars.", *Phys. Rep*, **163**(1), 13–36. [DOI], [ADS]

Nomoto, Ken'ichi, 1987, "Evolution of 8–10 M_{sun} Stars toward Electron Capture Supernovae. II. Collapse of an O + NE + MG Core", *Astrophys. J.*, **322**, 206. [DOI], [ADS]

Nordlander, T. and Lind, K., 2017, "Non-LTE aluminium abundances in late-type stars", *Astron. Astrophys.*, **607**, A75. [DOI], [ADS], [arXiv:1708.01949 [astro-ph.SR]]

Oh, Semyeong, Price-Whelan, Adrian M., Brewer, John M., Hogg, David W., Spergel, David N. and Myles, Justin, 2018, "Kronos and Krios: Evidence for Accretion of a Massive, Rocky Planetary System in a Comoving Pair of Solar-type Stars", *Astrophys. J.*, **854**(2), 138. [DOI], [ADS], [arXiv:1709.05344 [astro-ph.SR]]

Oppenheimer, J. R. and Volkoff, G. M., 1939, "On Massive Neutron Cores", *Physical Review*, **55**(4), 374–381. [DOI], [ADS]

Osterbrock, Donald E., 1964, "Planetary Nebulae", *Ann. Rev. Astron. Astrophys.*, **2**, 95. [DOI], [ADS]

Paczyński, B., 1970, "Evolution of Single Stars. I. Stellar Evolution from Main Sequence to White Dwarf or Carbon Ignition", *Acta Astronomica*, **20**, 47. [ADS]

Paczyński, B., 1971, "Evolution of Single Stars. V. Carbon Ignition in Population I Stars", *Acta Astronomica*, **21**, 271. [ADS]

Palacios, A., Charbonnel, C. and Forestini, M., 2001, "The Lithium Flash. Thermal instabilities generated by lithium burning in RGB stars", *Astron. Astrophys.*, **375**, L9–L13. [DOI], [ADS], [arXiv:astro-ph/0106441 [astro-ph]]

Paxton, Bill, Bildsten, Lars, Dotter, Aaron, Herwig, Falk, Lesaffre, Pierre and Timmes, Frank, 2011, "Modules for Experiments in Stellar Astrophysics

(MESA)", *Astrophys. J. Suppl.*, **192**(1), 3. [DOI], [ADS], [arXiv:1009.1622 [astro-ph.SR]]

Paxton, Bill, Cantiello, Matteo, Arras, Phil, Bildsten, Lars, Brown, Edward F., Dotter, Aaron, Mankovich, Christopher, Montgomery, M. H., Stello, Dennis, Timmes, F. X. and Townsend, Richard, 2013, "Modules for Experiments in Stellar Astrophysics (MESA): Planets, Oscillations, Rotation, and Massive Stars", *Astrophys. J. Suppl.*, **208**(1), 4. [DOI], [ADS], [arXiv:1301.0319 [astro-ph.SR]]

Paxton, Bill, Marchant, Pablo, Schwab, Josiah, Bauer, Evan B., Bildsten, Lars, Cantiello, Matteo, Dessart, Luc, Farmer, R., Hu, H., Langer, N., Townsend, R. H. D., Townsley, Dean M. and Timmes, F. X., 2015, "Modules for Experiments in Stellar Astrophysics (MESA): Binaries, Pulsations, and Explosions", *Astrophys. J. Suppl.*, **220**(1), 15. [DOI], [ADS], [arXiv:1506.03146 [astro-ph.SR]]

Paxton, Bill, Schwab, Josiah, Bauer, Evan B., Bildsten, Lars, Blinnikov, Sergei, Duffell, Paul, Farmer, R., Goldberg, Jared A., Marchant, Pablo, Sorokina, Elena, Thoul, Anne, Townsend, Richard H. D. and Timmes, F. X., 2018, "Modules for Experiments in Stellar Astrophysics (MESA): Convective Boundaries, Element Diffusion, and Massive Star Explosions", *Astrophys. J. Suppl.*, **234**(2), 34. [DOI], [ADS], [arXiv:1710.08424 [astro-ph.SR]]

Paxton, Bill, Smolec, R., Schwab, Josiah, Gautschy, A., Bildsten, Lars, Cantiello, Matteo, Dotter, Aaron, Farmer, R., Goldberg, Jared A., Jermyn, Adam S., Kanbur, S. M., Marchant, Pablo, Thoul, Anne, Townsend, Richard H. D., Wolf, William M., Zhang, Michael and Timmes, F. X., 2019, "Modules for Experiments in Stellar Astrophysics (MESA): Pulsating Variable Stars, Rotation, Convective Boundaries, and Energy Conservation", *Astrophys. J. Suppl.*, **243**(1), 10. [DOI], [ADS], [arXiv:1903.01426 [astro-ph.SR]]

Peebles, P. J., 1966a, "Primeval Helium Abundance and the Primeval Fireball", *Physical Review L*, **16**(10), 410–413. [DOI], [ADS]

Peebles, P. J. E., 1965, "The Black-Body Radiation Content of the Universe and the Formation of Galaxies.", *Astrophys. J.*, **142**, 1317. [DOI], [ADS]

Peebles, P. J. E., 1966b, "Primordial Helium Abundance and the Primordial Fireball. II", *Astrophys. J.*, **146**, 542. [DOI], [ADS]

Perryman, M. A. C., Lindegren, L., Kovalevsky, J., Hoeg, E., Bastian, U., Bernacca, P. L., Crézé, M., Donati, F., Grenon, M., Grewing, M., van Leeuwen, F., van der Marel, H., Mignard, F., Murray, C. A., Le Poole, R. S., Schrijver, H., Turon, C., Arenou, F., Froeschlé, M. and Petersen, C. S., 1997, "The HIPPARCOS Catalogue", *Astron. Astrophys.*, **323**, L49–L52. [ADS]

Pinsonneault, M., 1997, "Mixing in Stars", *Ann. Rev. Astron. Astrophys.*, **35**, 557–605. [DOI], [ADS]

Pinsonneault, M. H., Deliyannis, Constantine P. and Demarque, P., 1992, "Evolutionary Models of Halo Stars with Rotation. II. Effects of Metallicity on Lithium Depletion, and Possible Implications for the Primordial Lithium Abundance", *Astrophys. J. Suppl.*, **78**, 179. [DOI], [ADS]

Pinsonneault, M. H., Walker, T. P., Steigman, G. and Narayanan, Vijay K., 1999, "Halo Star Lithium Depletion", *Astrophys. J.*, **527**(1), 180–198. [DOI], [ADS], [arXiv:astro-ph/9803073 [astro-ph]]

Planck, Max, 1910, "Zur Theorie der Wärmestrahlung", *Annalen der Physik*, **336**(4), 758–768. [DOI], [ADS]

Planck, Max, 1912, "Über die Begründung des Gesetzes der schwarzen Strahlung", *Annalen der Physik*, **342**(4), 642–656. [DOI], [ADS]

Planck Collaboration, Ade, P. A. R., Aghanim, N., Armitage-Caplan, C., Arnaud, M., Ashdown, M., Atrio-Barandela, F., Aumont, J., Baccigalupi, C., Banday, A. J., Barreiro, R. B., Bartlett, J. G., Battaner, E., Benabed, K., Benoît, A., Benoit-Lévy, A., Bernard, J. P., Bersanelli, M., Bielewicz, P., Bobin, J., Bock, J. J., Bonaldi, A., Bond, J. R., Borrill, J., Bouchet, F. R., Bridges, M., Bucher,

M., Burigana, C., Butler, R. C., Calabrese, E., Cappellini, B., Cardoso, J. F., Catalano, A., Challinor, A., Chamballu, A., Chary, R. R., Chen, X., Chiang, H. C., Chiang, L. Y., Christensen, P. R., Church, S., Clements, D. L., Colombi, S., Colombo, L. P. L., Couchot, F., Coulais, A., Crill, B. P., Curto, A., Cuttaia, F., Danese, L., Davies, R. D., Davis, R. J., de Bernardis, P., de Rosa, A., de Zotti, G., Delabrouille, J., Delouis, J. M., Désert, F. X., Dickinson, C., Diego, J. M., Dolag, K., Dole, H., Donzelli, S., Doré, O., Douspis, M., Dunkley, J., Dupac, X., Efstathiou, G., Elsner, F., Enßlin, T. A., Eriksen, H. K., Finelli, F., Forni, O., Frailis, M., Fraisse, A. A., Franceschi, E., Gaier, T. C., Galeotta, S., Galli, S., Ganga, K., Giard, M., Giardino, G., Giraud-Héraud, Y., Gjerløw, E., González-Nuevo, J., Górski, K. M., Gratton, S., Gregorio, A., Gruppuso, A., Gudmundsson, J. E., Haissinski, J., Hamann, J., Hansen, F. K., Hanson, D., Harrison, D., Henrot-Versillé, S., Hernández-Monteagudo, C., Herranz, D., Hildebrandt, S. R., Hivon, E., Hobson, M., Holmes, W. A., Hornstrup, A., Hou, Z., Hovest, W., Huffenberger, K. M., Jaffe, A. H., Jaffe, T. R., Jewell, J., Jones, W. C., Juvela, M., Keihänen, E., Keskitalo, R., Kisner, T. S., Kneissl, R., Knoche, J., Knox, L., Kunz, M., Kurki-Suonio, H., Lagache, G., Lähteenmäki, A., Lamarre, J. M., Lasenby, A., Lattanzi, M., Laureijs, R. J., Lawrence, C. R., Leach, S., Leahy, J. P., Leonardi, R., León-Tavares, J., Lesgourgues, J., Lewis, A., Liguori, M., Lilje, P. B., Linden-Vørnle, M., López-Caniego, M., Lubin, P. M., Macías-Pérez, J. F., Maffei, B., Maino, D., Mandolesi, N., Maris, M., Marshall, D. J., Martin, P. G., Martínez-González, E., Masi, S., Massardi, M., Matarrese, S., Matthai, F., Mazzotta, P., Meinhold, P. R., Melchiorri, A., Melin, J. B., Mendes, L., Menegoni, E., Mennella, A., Migliaccio, M., Millea, M., Mitra, S., Miville-Deschênes, M. A., Moneti, A., Montier, L., Morgante, G., Mortlock, D., Moss, A., Munshi, D., Murphy, J. A., Naselsky, P., Nati, F., Natoli, P., Netterfield, C. B., Nørgaard-Nielsen, H. U., Noviello, F., Novikov, D., Novikov, I., O'Dwyer, I. J., Osborne, S., Oxborrow, C. A., Paci, F., Pagano, L., Pajot, F., Paladini, R., Paoletti, D., Partridge, B., Pasian, F., Patanchon, G., Pearson, D., Pearson, T. J., Peiris, H. V., Perdereau, O., Perotto, L., Perrotta, F., Pettorino,

V., Piacentini, F., Piat, M., Pierpaoli, E., Pietrobon, D., Plaszczynski, S., Platania, P., Pointecouteau, E., Polenta, G., Ponthieu, N., Popa, L., Poutanen, T., Pratt, G. W., Prézeau, G., Prunet, S., Puget, J. L., Rachen, J. P., Reach, W. T., Rebolo, R., Reinecke, M., Remazeilles, M., Renault, C., Ricciardi, S., Riller, T., Ristorcelli, I., Rocha, G., Rosset, C., Roudier, G., Rowan-Robinson, M., Rubiño-Martín, J. A., Rusholme, B., Sandri, M., Santos, D., Savelainen, M., Savini, G., Scott, D., Seiffert, M. D., Shellard, E. P. S., Spencer, L. D., Starck, J. L., Stolyarov, V., Stompor, R., Sudiwala, R., Sunyaev, R., Sureau, F., Sutton, D., Suur-Uski, A. S., Sygnet, J. F., Tauber, J. A., Tavagnacco, D., Terenzi, L., Toffolatti, L., Tomasi, M., Tristram, M., Tucci, M., Tuovinen, J., Türler, M., Umana, G., Valenziano, L., Valiviita, J., Van Tent, B., Vielva, P., Villa, F., Vittorio, N., Wade, L. A., Wandelt, B. D., Wehus, I. K., White, M., White, S. D. M., Wilkinson, A., Yvon, D., Zacchei, A. and Zonca, A., 2014, "Planck 2013 results. XVI. Cosmological parameters", *Astron. Astrophys.*, **571**, A16. [DOI], [ADS], [arXiv:1303.5076 [astro-ph.CO]]

Purcell, Chris W., Bullock, James S. and Kazantzidis, Stelios, 2010, "Heated disc stars in the stellar halo", *Mon. Not. Roy. Astron. Soc.*, **404**(4), 1711–1718. [DOI], [ADS], [arXiv:0910.5481 [astro-ph.GA]]

Qu, Y., Di Matteo, P., Lehnert, M. D. and van Driel, W., 2011, "Characteristics of thick disks formed through minor mergers: stellar excesses and scale lengths", *Astron. Astrophys.*, **530**, A10. [DOI], [ADS], [arXiv:1102.1879 [astro-ph.GA]]

Queiroz, A. B. A., Anders, F., Chiappini, C., Khalatyan, A., Santiago, B. X., Steinmetz, M., Valentini, M., Miglio, A., Bossini, D., Barbuy, B., Minchev, I., Minniti, D., García Hernández, D. A., Schultheis, M., Beaton, R. L., Beers, T. C., Bizyaev, D., Brownstein, J. R., Cunha, K., Fernández-Trincado, J. G., Frinchaboy, P. M., Lane, R. R., Majewski, S. R., Nataf, D., Nitschelm, C., Pan, K., Roman-Lopes, A., Sobeck, J. S., Stringfellow, G. and Zamora, O., 2020, "From the bulge to the outer disc: StarHorse stellar parameters, distances,

and extinctions for stars in APOGEE DR16 and other spectroscopic surveys", *Astron. Astrophys.*, **638**, A76. [DOI], [ADS], [arXiv:1912.09778 [astro-ph.GA]]

Ramírez, I., Meléndez, J., Bean, J., Asplund, M., Bedell, M., Monroe, T., Casagrande, L., Schirbel, L., Dreizler, S., Teske, J., Tucci Maia, M., Alves-Brito, A. and Baumann, P., 2014, "The Solar Twin Planet Search. I. Fundamental parameters of the stellar sample", *Astron. Astrophys.*, **572**, A48. [DOI], [ADS], [arXiv:1408.4130 [astro-ph.SR]]

Ramírez, Solange V., Stephens, Andrew W., Frogel, Jay A. and DePoy, D. L., 2000, "Metallicity of Red Giants in the Galactic Bulge from Near-Infrared Spectroscopy", *Astron. J.*, **120**(2), 833–844. [DOI], [ADS], [arXiv:astro-ph/0003116 [astro-ph]]

Ramstedt, S., Schöier, F. L., Olofsson, H. and Lundgren, A. A., 2008, "On the reliability of mass-loss-rate estimates for AGB stars", *Astron. Astrophys.*, **487**(2), 645–657. [DOI], [ADS], [arXiv:0806.0517 [astro-ph]]

Rana, Narayan C., 1991, "Chemical evolution of the Galaxy.", *Ann. Rev. Astron. Astrophys.*, **29**, 129–162. [DOI], [ADS]

Randich, S., Pasquini, L., Franciosini, E., Magrini, L., Jackson, R. J., Jeffries, R. D., d'Orazi, V., Romano, D., Sanna, N., Tautvaišienė, G., Tsantaki, M., Wright, N. J., Gilmore, G., Bensby, T., Bragaglia, A., Pancino, E., Smiljanic, R., Bayo, A., Carraro, G., Gonneau, A., Hourihane, A., Morbidelli, L. and Worley, C. C., 2020, "The Gaia-ESO Survey: Galactic evolution of lithium at high metallicity", *Astron. Astrophys.*, **640**, L1. [DOI], [ADS], [arXiv:2007.02888 [astro-ph.SR]]

Rauch, Michael, Haehnelt, Martin, Bunker, Andrew, Becker, George, Marleau, Francine, Graham, James, Cristiani, Stefano, Jarvis, Matt, Lacey, Cedric, Morris, Simon, Peroux, Celine, Röttgering, Huub and Theuns, Tom, 2008, "A Population of Faint Extended Line Emitters and the Host Galaxies of Optically

Thick QSO Absorption Systems", *Astrophys. J.*, **681**(2), 856–880. [DOI], [ADS], [arXiv:0711.1354 [astro-ph]]

Reddy, Bacham E., Tomkin, Jocelyn, Lambert, David L. and Allende Prieto, Carlos, 2003, "The chemical compositions of Galactic disc F and G dwarfs", *Mon. Not. Roy. Astron. Soc.*, **340**(1), 304–340. [DOI], [ADS], [arXiv:astro-ph/0211551 [astro-ph]]

Reddy, Bacham E., Lambert, David L. and Allende Prieto, Carlos, 2006, "Elemental abundance survey of the Galactic thick disc", *Mon. Not. Roy. Astron. Soc.*, **367**(4), 1329–1366. [DOI], [ADS], [arXiv:astro-ph/0512505 [astro-ph]]

Reeves, Hubert, Audouze, Jean, Fowler, William A. and Schramm, David N., 1973, "On the Origin of Light Elements", *Astrophys. J.*, **179**, 909–930. [DOI], [ADS]

Rich, R. Michael and Origlia, Livia, 2005, "The First Detailed Abundances for M Giants in Baade's Window from Infrared Spectroscopy", *Astrophys. J.*, **634**(2), 1293–1299. [DOI], [ADS], [arXiv:astro-ph/0506051 [astro-ph]]

Rich, R. Michael, Origlia, Livia and Valenti, Elena, 2007, "The First Detailed Abundances for M Giants in the Inner Bulge from Infrared Spectroscopy", *Astrophys. J. Lett.*, **665**(2), L119–L122. [DOI], [ADS], [arXiv:0707.1855 [astro-ph]]

Ritossa, Claudio, Garcia-Berro, Enrique and Iben, Icko, Jr., 1996, "On the Evolution of Stars That Form Electron-degenerate Cores Processed by Carbon Burning. II. Isotope Abundances and Thermal Pulses in a 10 M_{sun} Model with an ONe Core and Applications to Long-Period Variables, Classical Novae, and Accretion-induced Collapse", *Astrophys. J.*, **460**, 489. [DOI], [ADS]

Rix, Hans-Walter and Bovy, Jo, 2013, "The Milky Way's stellar disk. Mapping and modeling the Galactic disk", *Astron. Astrophys. Rev.*, **21**, 61. [DOI], [ADS], [arXiv:1301.3168 [astro-ph.GA]]

Rojas-Arriagada, A., Recio-Blanco, A., Hill, V., de Laverny, P., Schultheis, M., Babusiaux, C., Zoccali, M., Minniti, D., Gonzalez, O. A., Feltzing, S., Gilmore,

G., Randich, S., Vallenari, A., Alfaro, E. J., Bensby, T., Bragaglia, A., Flaccomio, E., Lanzafame, A. C., Pancino, E., Smiljanic, R., Bergemann, M., Costado, M. T., Damiani, F., Hourihane, A., Jofré, P., Lardo, C., Magrini, L., Maiorca, E., Morbidelli, L., Sbordone, L., Worley, C. C., Zaggia, S. and Wyse, R., 2014, "The Gaia-ESO Survey: metallicity and kinematic trends in the Milky Way bulge", *Astron. Astrophys.*, **569**, A103. [DOI], [ADS], [arXiv:1408.4558 [astro-ph.GA]]

Roman, N. G., 1954, "A group of high velocity F-type stars.", *Astron. J.*, **59**, 307–312. [DOI], [ADS]

Romano, D., Matteucci, F., Ventura, P. and D'Antona, F., 2001, "The stellar origin of ^{7}Li. Do AGB stars contribute a substantial fraction of the local Galactic lithium abundance?", *Astron. Astrophys.*, **374**, 646–655. [DOI], [ADS], [arXiv:astro-ph/0105483 [astro-ph]]

Rukeya, Rejiefu, Lü, Guoliang, Wang, Zhaojun and Zhu, Chunhua, 2017, "Novae Contribution to the Galactic Lithium Enhancement", *Pub. Astron. Soc. Pac.*, **129**(977), 074 201. [DOI], [ADS]

Ryan, Sean G., Norris, John E. and Beers, Timothy C., 1999, "The Spite Lithium Plateau: Ultrathin but Postprimordial", *Astrophys. J.*, **523**(2), 654–677. [DOI], [ADS], [arXiv:astro-ph/9903059 [astro-ph]]

Ryan, Sean G., Beers, Timothy C., Olive, Keith A., Fields, Brian D. and Norris, John E., 2000, "Primordial Lithium and Big Bang Nucleosynthesis", *Astrophys. J. Lett.*, **530**(2), L57–L60. [DOI], [ADS], [arXiv:astro-ph/9905211 [astro-ph]]

Sadler, Elaine M., Rich, R. Michael and Terndrup, D. M., 1996, "K Giants in Baade's Window. II. The Abundance Distribution", *Astron. J.*, **112**, 171. [DOI], [ADS], [arXiv:astro-ph/9604045 [astro-ph]]

Salaris, M., Cassisi, S. and Weiss, A., 2002, "Red Giant Branch Stars: The Theoretical Framework", *Pub. Astron. Soc. Pac.*, **114**, 375–402. [DOI], [ADS], [astro-ph/0201387]

Salaris, Maurizio, Chieffi, Alessandro and Straniero, Oscar, 1993, "The alpha - enhanced Isochrones and Their Impact on the FITS to the Galactic Globular Cluster System", *Astrophys. J.*, **414**, 580. [DOI], [ADS]

Salpeter, Edwin E., 1955, "The Luminosity Function and Stellar Evolution.", *Astrophys. J.*, **121**, 161. [DOI], [ADS]

Sandage, Allan and Fouts, Gary, 1987, "New Subdwarfs. VI. Kinematics of 1125 High-Proper-Motion Stars and the Collapse of the Galaxy", *Astron. J.*, **93**, 74. [DOI], [ADS]

Sanford, Roscoe F., 1950, "An Atlas of Spectra of Six Stars of Classes R and N.", *Astrophys. J.*, **111**, 262. [DOI], [ADS]

Scalo, J. M., 1976, "Production of galactic ^{7}Li by slow mass loss.", *Astrophys. J.*, **206**, 795–799. [DOI], [ADS]

Schramm, D. N. and Wagoner, R. V., 1977, "Element production in the early universe.", *Annual Review of Nuclear and Particle Science*, **27**, 37–74. [DOI], [ADS]

Schuster, W. J., Moreno, E., Nissen, P. E. and Pichardo, B., 2012, "Two distinct halo populations in the solar neighborhood. III. Evidence from stellar ages and orbital parameters", *Astron. Astrophys.*, **538**, A21. [DOI], [ADS], [arXiv:1111.4026 [astro-ph.GA]]

Schwab, Josiah, 2020, "A Helium-flash-induced Mixing Event Can Explain the Lithium Abundances of Red Clump Stars", *Astrophys. J. Lett.*, **901**(1), L18. [DOI], [ADS], [arXiv:2009.01248 [astro-ph.SR]]

Searle, L. and Zinn, R., 1978, "Composition of halo clusters and the formation of the galactic halo.", *Astrophys. J.*, **225**, 357–379. [DOI], [ADS]

Shapiro, Stuart L. and Teukolsky, Saul A., 1983, *Black holes, white dwarfs, and neutron stars : the physics of compact objects*, WILEY-VCH Verlag GmbH & Co. KGaA, Weinheim. [DOI], [ADS]

Shapley, Harlow, 1930, *Star Clusters*, 2, McGraw-Hill, New York. [ADS]

Sharma, Sanjib, Stello, Dennis, Buder, Sven, Kos, Janez, Bland-Hawthorn, Joss, Asplund, Martin, Duong, Ly, Lin, Jane, Lind, Karin, Ness, Melissa, Huber, Daniel, Zwitter, Tomaz, Traven, Gregor, Hon, Marc, Kafle, Prajwal R., Khanna, Shourya, Saddon, Hafiz, Anguiano, Borja, Casey, Andrew R., Freeman, Ken, Martell, Sarah, De Silva, Gayandhi M., Simpson, Jeffrey D., Wittenmyer, Rob A. and Zucker, Daniel B., 2018, "The TESS-HERMES survey data release 1: high-resolution spectroscopy of the TESS southern continuous viewing zone", *Mon. Not. Roy. Astron. Soc.*, **473**(2), 2004–2019. [DOI], [ADS], [arXiv:1707.05753 [astro-ph.SR]]

Siess, Lionel and Livio, Mario, 1999, "The accretion of brown dwarfs and planets by giant stars - II. Solar-mass stars on the red giant branch", *Mon. Not. Roy. Astron. Soc.*, **308**(4), 1133–1149. [DOI], [ADS], [arXiv:astro-ph/9905235 [astro-ph]]

Silva Aguirre, V., Ruchti, G. R., Hekker, S., Cassisi, S., Christensen-Dalsgaard, J., Datta, A., Jendreieck, A., Jessen-Hansen, J., Mazumdar, A., Mosser, B., Stello, D., Beck, P. G. and de Ridder, J., 2014, "Old Puzzle, New Insights: A Lithium-rich Giant Quietly Burning Helium in Its Core", *Astrophys. J. Lett.*, **784**(1), L16. [DOI], [ADS], [arXiv:1402.6339 [astro-ph.SR]]

Simpson, Jeffrey D., Martell, Sarah L., Buder, Sven, Bland-Hawthorn, Joss, Casey, Andrew R., de Silva, Gayandhi M., D'Orazi, Valentina, Freeman, Ken C., Hayden, Michael, Kos, Janez, Lewis, Geraint F., Lind, Karin, Schlesinger, Katharine J., Sharma, Sanjib, Stello, Dennis, Zucker, Daniel B., Zwitter, Tomaž, Asplund, Martin, da Costa, Gary, Čotar, Klemen, Tepper-García, Thor, Horner, Jonathan, Nordlander, Thomas, Ting, Yuan-Sen, Wyse, Rosemary F. G. and GALAH Collaboration, 2021, "The GALAH survey: accreted stars also inhabit the Spite plateau", *Mon. Not. Roy. Astron. Soc.*, **507**(1), 43–54. [DOI], [ADS], [arXiv:2011.02659 [astro-ph.GA]]

Singh, Raghubar, Reddy, Bacham E., Bharat Kumar, Yerra and Antia, H. M., 2019a, "Survey of Li-rich Giants among Kepler and LAMOST Fields: Determination of Li-rich Giants' Evolutionary Phase", *Astrophys. J. Lett.*, **878**(1), L21. [DOI], [ADS], [arXiv:1906.03198 [astro-ph.SR]]

Singh, Raghubar, Reddy, Bacham E. and Kumar, Yerra Bharat, 2019b, "Spectroscopic study of two new super Li-rich red clump K giants", *Mon. Not. Roy. Astron. Soc.*, **482**(3), 3822–3830. [DOI], [ADS], [arXiv:1810.12509 [astro-ph.SR]]

Singh, Raghubar, Reddy, Bacham E., Campbell, Simon W., Kumar, Yerra Bharat and Vrard, Mathieu, 2021, "Tracking the Evolution of Lithium in Giants Using Asteroseismology: Super-Li-rich Stars Are Almost Exclusively Young Red-clump Stars", *Astrophys. J. Lett.*, **913**(1), L4. [DOI], [ADS], [arXiv:2104.12070 [astro-ph.SR]]

Smiljanic, R., Gauderon, R., North, P., Barbuy, B., Charbonnel, C. and Mowlavi, N., 2009, "CNONa and $^{12}C/^{13}C$ in giant stars of 10 open clusters", *Astron. Astrophys.*, **502**(1), 267–282. [DOI], [ADS], [arXiv:0810.1701 [astro-ph]]

Smiljanic, R., Franciosini, E., Randich, S., Magrini, L., Bragaglia, A., Pasquini, L., Vallenari, A., Tautvaišienė, G., Biazzo, K., Frasca, A., Donati, P., Delgado Mena, E., Casey, A. R., Geisler, D., Villanova, S., Tang, B., Sousa, S. G., Gilmore, G., Bensby, T., François, P., Koposov, S. E., Lanzafame, A. C., Pancino, E., Recio-Blanco, A., Costado, M. T., Hourihane, A., Lardo, C., de Laverny, P., Lewis, J., Monaco, L., Morbidelli, L., Sacco, G. G., Worley, C. C., Zaggia, S. and Martell, S., 2016, "The Gaia-ESO Survey: Inhibited extra mixing in two giants of the open cluster Trumpler 20?", *Astron. Astrophys.*, **591**, A62. [DOI], [ADS], [arXiv:1605.01945 [astro-ph.SR]]

Smiljanic, R., Franciosini, E., Bragaglia, A., Tautvaišienė, G., Fu, X., Pancino, E., Adibekyan, V., Sousa, S. G., Randich, S., Montalbán, J., Pasquini, L., Magrini, L., Drazdauskas, A., García, R. A., Mathur, S., Mosser, B., Régulo, C., de Assis Peralta, R., Hekker, S., Feuillet, D., Valentini, M., Morel, T.,

Martell, S., Gilmore, G., Feltzing, S., Vallenari, A., Bensby, T., Korn, A. J., Lanzafame, A. C., Recio-Blanco, A., Bayo, A., Carraro, G., Costado, M. T., Frasca, A., Jofré, P., Lardo, C., de Laverny, P., Lind, K., Masseron, T., Monaco, L., Morbidelli, L., Prisinzano, L., Sbordone, L. and Zaggia, S., 2018, "The Gaia-ESO Survey: properties of newly discovered Li-rich giants", *Astron. Astrophys.*, **617**, A4. [DOI], [ADS], [arXiv:1805.07077 [astro-ph.SR]]

Smith, Verne V. and Lambert, David L., 1989, "Synthesis of Lithium and s-Process Elements in Small Magellanic Cloud Asymptotic Giant Branch Stars", *Astrophys. J. Lett.*, **345**, L75. [DOI], [ADS]

Sneden, Christopher Alan, 1973, *Carbon and Nitrogen Abundances in Metal-Poor Stars.*, Ph.D. thesis, THE UNIVERSITY OF TEXAS AT AUSTIN. [ADS]

Solà, Joan and Gómez-Valent, Adrià, 2015, "The $\bar{\Lambda}$CDM cosmology: From inflation to dark energy through running Λ", *International Journal of Modern Physics D*, **24**(4), 1541003. [DOI], [ADS], [arXiv:1501.03832 [gr-qc]]

Spite, F. and Spite, M., 1982, "Abundance of lithium in unevolved stars and old disk stars : Interpretation and consequences.", *Astron. Astrophys.*, **115**, 357–366. [ADS]

Starrfield, S., Truran, J. W., Sparks, W. M. and Arnould, M., 1978, "On ^{7}Li production in nova explosions.", *Astrophys. J.*, **222**, 600–603. [DOI], [ADS]

Steinmetz, M., Zwitter, T., Siebert, A., Watson, F. G., Freeman, K. C., Munari, U., Campbell, R., Williams, M., Seabroke, G. M., Wyse, R. F. G., Parker, Q. A., Bienaymé, O., Roeser, S., Gibson, B. K., Gilmore, G., Grebel, E. K., Helmi, A., Navarro, J. F., Burton, D., Cass, C. J. P., Dawe, J. A., Fiegert, K., Hartley, M., Russell, K. S., Saunders, W., Enke, H., Bailin, J., Binney, J., Bland-Hawthorn, J., Boeche, C., Dehnen, W., Eisenstein, D. J., Evans, N. W., Fiorucci, M., Fulbright, J. P., Gerhard, O., Jauregi, U., Kelz, A., Mijović, L., Minchev, I., Parmentier, G., Peñarrubia, J., Quillen, A. C., Read, M. A., Ruchti, G., Scholz, R. D., Siviero, A., Smith, M. C., Sordo, R., Veltz, L., Vidrih, S.,

von Berlepsch, R., Boyle, B. J. and Schilbach, E., 2006, "The Radial Velocity Experiment (RAVE): First Data Release", *Astron. J.*, **132**(4), 1645–1668. [DOI], [ADS], [arXiv:astro-ph/0606211 [astro-ph]]

Stello, D., Chaplin, W. J., Basu, S., Elsworth, Y. and Bedding, T. R., 2009, "The relation between $\Delta\nu$ and ν_{max} for solar-like oscillations", *Mon. Not. Roy. Astron. Soc.*, **400**(1), L80–L84. [DOI], [ADS], [arXiv:0909.5193 [astro-ph.SR]]

Stello, Dennis, Huber, Daniel, Bedding, Timothy R., Benomar, Othman, Bildsten, Lars, Elsworth, Yvonne P., Gilliland, Ronald L., Mosser, Benoît, Paxton, Bill and White, Timothy R., 2013, "Asteroseismic Classification of Stellar Populations among 13,000 Red Giants Observed by Kepler", *Astrophys. J. Lett.*, **765**(2), L41. [DOI], [ADS], [arXiv:1302.0858 [astro-ph.SR]]

Stephens, Alex and Boesgaard, Ann Merchant, 2002, "Abundances from High-Resolution Spectra of Kinematically Interesting Halo Stars", *Astron. J.*, **123**(3), 1647–1700. [DOI], [ADS]

Tajitsu, Akito, Sadakane, Kozo, Naito, Hiroyuki, Arai, Akira and Aoki, Wako, 2015, "Explosive lithium production in the classical nova V339 Del (Nova Delphini 2013)", *Nature*, **518**(7539), 381–384. [DOI], [ADS], [arXiv:1502.05598 [astro-ph.SR]]

Takeda, Yoichi and Tajitsu, Akito, 2017, "On the observational characteristics of lithium-enhanced giant stars in comparison with normal red giants", *Pub. Astron. Soc. Japan*, **69**(4), 74. [DOI], [ADS], [arXiv:1706.02273 [astro-ph.SR]]

Thomas, David, Schramm, David N., Olive, Keith A. and Fields, Brian D., 1993, "Primordial Nucleosynthesis and the Abundances of Beryllium and Boron", *Astrophys. J.*, **406**, 569. [DOI], [ADS], [arXiv:astro-ph/9206002 [astro-ph]]

Thomas, H. C., 1967, "Sternentwicklung VIII. Der Helium-Flash bei einem Stern von 1. 3 Sonnenmassen", *Z. Astrophys.*, **67**, 420. [ADS]

Thorburn, J. A., 1994, "The Primordial Lithium Abundance from Extreme Subdwarfs: New Observations", *Astrophys. J.*, **421**, 318. [DOI], [ADS]

Ting, Yuan-Sen, Hawkins, Keith and Rix, Hans-Walter, 2018, "A Large and Pristine Sample of Standard Candles across the Milky Way: ∼100,000 Red Clump Stars with 3% Contamination", *Astrophys. J. Lett.*, **858**(1), L7. [DOI], [ADS], [arXiv:1803.06650 [astro-ph.SR]]

Tomasko, Martin G., 1970, "Hydrodynamics of the Helium Core Flash", *Astrophys. J.*, **162**, 125. [DOI], [ADS]

Trevisan, M., Barbuy, B., Eriksson, K., Gustafsson, B., Grenon, M. and Pompéia, L., 2011, "Analysis of old very metal rich stars in the solar neighbourhood", *Astron. Astrophys.*, **535**, A42. [DOI], [ADS], [arXiv:1109.6304 [astro-ph.SR]]

Trumpler, Robert Julius, 1930, "Preliminary results on the distances, dimensions and space distribution of open star clusters", *Lick Observatory Bulletin*, **420**, 154–188. [DOI], [ADS]

van den Bergh, S., 1962, "The frequency of stars with different metal abundances.", *Astron. J.*, **67**, 486–490. [DOI], [ADS]

Vangioni-Flam, Elisabeth, Cassé, Michel, Cayrel, Roger, Audouze, Jean, Spite, Monique and Spite, François, 1999, "Lithium-6: evolution from Big Bang to present", *New Astronomy*, **4**(4), 245–254. [DOI], [ADS], [arXiv:astro-ph/9811327 [astro-ph]]

Ventura, P., Di Criscienzo, M., Carini, R. and D'Antona, F., 2013, "Yields of AGB and SAGB models with chemistry of low- and high-metallicity globular clusters", *Mon. Not. Roy. Astron. Soc.*, **431**(4), 3642–3653. [DOI], [ADS], [arXiv:1303.3912 [astro-ph.SR]]

Vogelsberger, Mark, Genel, Shy, Springel, Volker, Torrey, Paul, Sijacki, Debora, Xu, Dandan, Snyder, Greg, Nelson, Dylan and Hernquist, Lars, 2014, "Introducing the Illustris Project: simulating the coevolution of dark and visible matter

in the Universe", *Mon. Not. Roy. Astron. Soc.*, **444**(2), 1518–1547. [DOI], [ADS], [arXiv:1405.2921 [astro-ph.CO]]

Vrard, M., Mosser, B. and Samadi, R., 2016, "Period spacings in red giants. II. Automated measurement", *Astron. Astrophys.*, **588**, A87. [DOI], [ADS], [arXiv:1602.04940 [astro-ph.SR]]

Vrard, M., Kallinger, T., Mosser, B., Barban, C., Baudin, F., Belkacem, K. and Cunha, M. S., 2018, "Amplitude and lifetime of radial modes in red giant star spectra observed by Kepler", *Astron. Astrophys.*, **616**, A94. [DOI], [ADS], [arXiv:1805.03690 [astro-ph.SR]]

Wagoner, Robert V., 1973, "Big-Bang Nucleosynthesis Revisited", *Astrophys. J.*, **179**, 343–360. [DOI], [ADS]

Wagoner, Robert V., Fowler, William A. and Hoyle, F., 1967, "On the Synthesis of Elements at Very High Temperatures", *Astrophys. J.*, **148**, 3. [DOI], [ADS]

Wallerstein, G. and Sneden, C., 1982, "A K giant with an unusually high abundance of lithium : HD 112127.", *Astrophys. J.*, **255**, 577–584. [DOI], [ADS]

Wang, Feige, Yang, Jinyi, Fan, Xiaohui, Yue, Minghao, Wu, Xue-Bing, Schindler, Jan-Torge, Bian, Fuyan, Li, Jiang-Tao, Farina, Emanuele P., Bañados, Eduardo, Davies, Frederick B., Decarli, Roberto, Green, Richard, Jiang, Linhua, Hennawi, Joseph F., Huang, Yun-Hsin, Mazzucchelli, Chiara, McGreer, Ian D., Venemans, Bram, Walter, Fabian and Beletsky, Yuri, 2018, "The Discovery of a Luminous Broad Absorption Line Quasar at a Redshift of 7.02", *Astrophys. J. Lett.*, **869**(1), L9. [DOI], [ADS], [arXiv:1810.11925 [astro-ph.GA]]

Wang, Feige, Yang, Jinyi, Fan, Xiaohui, Hennawi, Joseph F., Barth, Aaron J., Banados, Eduardo, Bian, Fuyan, Boutsia, Konstantina, Connor, Thomas, Davies, Frederick B., Decarli, Roberto, Eilers, Anna-Christina, Farina, Emanuele Paolo, Green, Richard, Jiang, Linhua, Li, Jiang-Tao, Mazzucchelli, Chiara, Nanni, Riccardo, Schindler, Jan-Torge, Venemans, Bram, Walter, Fabian, Wu, Xue-Bing

and Yue, Minghao, 2021, "A Luminous Quasar at Redshift 7.642", *Astrophys. J. Lett.*, **907**(1), L1. [DOI], [ADS], [arXiv:2101.03179 [astro-ph.GA]]

Weidemann, V., 1977, "Mass loss towards the white dwarf stage.", *Astron. Astrophys.*, **59**(3), 411–418. [ADS]

Wenger, M., Ochsenbein, F., Egret, D., Dubois, P., Bonnarel, F., Borde, S., Genova, F., Jasniewicz, G., Laloë, S., Lesteven, S. and Monier, R., 2000, "The SIMBAD astronomical database. The CDS reference database for astronomical objects", *Astron. Astrophys. Suppl.*, **143**, 9–22. [DOI], [ADS], [arXiv:astro-ph/0002110 [astro-ph]]

Wielen, Roland, 1988, "Dissolution of Star Clusters in Galaxies", in *The Harlow-Shapley Symposium on Globular Cluster Systems in Galaxies*, (Eds.) Grindlay, Jonathan E., Philip, A. G. Davis, IAU Symposium, 126, pp. 393–406, Kluwer Academic Publishers, Dordrecht, Netherlands. [ADS]

Woolf, Vincent M. and West, Andrew A., 2012, "The M dwarf problem in the Galaxy", *Mon. Not. Roy. Astron. Soc.*, **422**(2), 1489–1494. [DOI], [ADS], [arXiv:1202.3078 [astro-ph.SR]]

Worthey, Guy, Dorman, Ben and Jones, Lewis A., 1996, "The G Dwarf Problem Exists in Other Galaxies", *Astron. J.*, **112**, 948. [DOI], [ADS], [arXiv:astro-ph/9606017 [astro-ph]]

Xiang, Maosheng, Ting, Yuan-Sen, Rix, Hans-Walter, Sandford, Nathan, Buder, Sven, Lind, Karin, Liu, Xiao-Wei, Shi, Jian-Rong and Zhang, Hua-Wei, 2019, "Abundance Estimates for 16 Elements in 6 Million Stars from LAMOST DR5 Low-Resolution Spectra", *Astrophys. J. Suppl.*, **245**(2), 34. [DOI], [ADS], [arXiv:1908.09727 [astro-ph.SR]]

Xiong, D. R. and Deng, L., 2009, "Lithium depletion in late-type dwarfs", *Mon. Not. Roy. Astron. Soc.*, **395**(4), 2013–2028. [DOI], [ADS]

Yan, Hong-Liang, Shi, Jian-Rong, Zhou, Yu-Tao, Chen, Yong-Shou, Li, Er-Tao, Zhang, Suyalatu, Bi, Shao-Lan, Wu, Ya-Qian, Li, Zhi-Hong, Guo, Bing, Liu, Wei-Ping, Gao, Qi, Zhang, Jun-Bo, Zhou, Ze-Ming, Li, Hai-Ning and Zhao, Gang, 2018, "The nature of the lithium enrichment in the most Li-rich giant star", *Nature Astronomy*, **2**, 790–795. [DOI], [ADS], [arXiv:1809.00187 [astro-ph.SR]]

Yan, Hong-Liang, Zhou, Yu-Tao, Zhang, Xianfei, Li, Yaguang, Gao, Qi, Shi, Jian-Rong, Zhao, Gang, Aoki, Wako, Matsuno, Tadafumi, Li, Yan, Xu, Xiao-Dong, Li, Haining, Wu, Ya-Qian, Jin, Meng-Qi, Mosser, Benoit, Bi, Shao-Lan, Fu, Jian-Ning, Pan, Kaike, Suda, Takuma, Liu, Yu-Juan, Zhao, Jing-Kun and Liang, Xi-Long, 2021, "Most lithium-rich low-mass evolved stars revealed as red clump stars by asteroseismology and spectroscopy", *Nature Astronomy*, **5**, 86–93. [DOI], [ADS], [arXiv:2010.02106 [astro-ph.SR]]

Yang, Jinyi, Wang, Feige, Fan, Xiaohui, Barth, Aaron J., Hennawi, Joseph F., Nanni, Riccardo, Bian, Fuyan, Davies, Frederick B., Farina, Emanuele P., Schindler, Jan-Torge, Banados, Eduardo, Decarli, Roberto, Eilers, Anna-Christina, Green, Richard, Guo, Hengxiao, Jiang, Linhua, Li, Jiang-Tao, Venemans, Bram, Walter, Fabian, Wu, Xue-Bing and Yue, Minghao, 2021, "Probing Early Super-massive Black Hole Growth and Quasar Evolution with Near-infrared Spectroscopy of 37 Reionization-era Quasars at $6.3 < z <= 7.64$", *arXiv e-prints*, arXiv:2109.13942. [ADS], [arXiv:2109.13942 [astro-ph.GA]]

Yi, Sukyoung, Demarque, Pierre, Kim, Yong-Cheol, Lee, Young-Wook, Ree, Chang H., Lejeune, Thibault and Barnes, Sydney, 2001, "Toward Better Age Estimates for Stellar Populations: The Y^2 Isochrones for Solar Mixture", *Astrophys. J. Suppl.*, **136**(2), 417–437. [DOI], [ADS], [arXiv:astro-ph/0104292 [astro-ph]]

Yoshii, Y., 1982, "Density distribution of faint stars in the direction of the north galactic pole.", *Pub. Astron. Soc. Japan*, **34**, 365–379. [ADS]

Yu, Jie, Huber, Daniel, Bedding, Timothy R., Stello, Dennis, Hon, Marc, Murphy, Simon J. and Khanna, Shourya, 2018, "Asteroseismology of 16,000 Kepler Red Giants: Global Oscillation Parameters, Masses, and Radii", *Astrophys. J. Suppl.*, **236**(2), 42. [DOI], [ADS], [arXiv:1802.04455 [astro-ph.SR]]

Zappala, R. R., 1972, "Lithium Abundances of Stars in Open Clusters.", *Astrophys. J.*, **172**, 57. [DOI], [ADS]

Zhang, Xianfei and Jeffery, C. Simon, 2013, "White dwarf-red giant mergers, early-type R stars, J stars and lithium", *Mon. Not. Roy. Astron. Soc.*, **430**(3), 2113–2120. [DOI], [ADS], [arXiv:1301.0766 [astro-ph.SR]]

Zhao, Gang, Zhao, Yong-Heng, Chu, Yao-Quan, Jing, Yi-Peng and Deng, Li-Cai, 2012, "LAMOST spectral survey — An overview", *Research in Astronomy and Astrophysics*, **12**(7), 723–734. [DOI], [ADS]

Zoccali, M., Renzini, A., Ortolani, S., Greggio, L., Saviane, I., Cassisi, S., Rejkuba, M., Barbuy, B., Rich, R. M. and Bica, E., 2003, "Age and metallicity distribution of the Galactic bulge from extensive optical and near-IR stellar photometry", *Astron. Astrophys.*, **399**, 931–956. [DOI], [ADS], [arXiv:astro-ph/0210660 [astro-ph]]

Zolotov, Adi, Willman, Beth, Brooks, Alyson M., Governato, Fabio, Brook, Chris B., Hogg, David W., Quinn, Tom and Stinson, Greg, 2009, "The Dual Origin of Stellar Halos", *Astrophys. J.*, **702**(2), 1058–1067. [DOI], [ADS], [arXiv:0904.3333 [astro-ph.GA]]

Zolotov, Adi, Willman, Beth, Brooks, Alyson M., Governato, Fabio, Hogg, David W., Shen, Sijing and Wadsley, James, 2010, "The Dual Origin of Stellar Halos. II. Chemical Abundances as Tracers of Formation History", *Astrophys. J.*, **721**(1), 738–743. [DOI], [ADS], [arXiv:1004.3789 [astro-ph.GA]]